PhD

3rd CYCLE

FCUP
UA
UM
2024

MagMed - Novel Magnetic Nanostructures as Multimodal Nanocarriers for Cancer Therapies

Ricardo José Pires Magalhães

FC

U.PORTO
FACULDADE DE CIÊNCIAS
UNIVERSIDADE DO PORTO

universidade de aveiro

Universidade do Minho

MagMed - Novel Magnetic Nanostructures as Multimodal Nanocarriers for Cancer Therapies

Ricardo José Pires Magalhães
Doctoral Program in Physics
Faculty of Sciences of the University of Porto, University of Aveiro and University of Minho
2024

MagMed - Novel Magnetic Nanostructures as Multimodal Nanocarriers for Cancer Therapies

Ricardo José Pires Magalhães
Doutoramento em Física
Departamento de Física e Astronomia
2024

Orientador
Doutora Célia Tavares de Sousa, Investigador Auxiliar, Faculdade de Ciências da Universidade do Porto

Coorientador
Doutora Cláudia Daniela Oliveira de Lacerda Nunes Pinho, Investigador externo, Faculdade de Farmácia da Universidade do Porto

Coorientador
Doutor André Miguel Trindade Pereira, Professor Auxiliar, Faculdade de Ciências da Universidade do Porto

Universidade do Minho

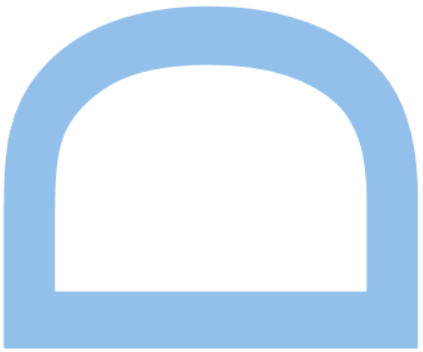

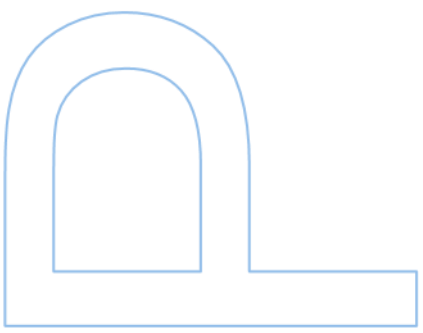

À minha família e amigos

Agradecimentos

O trabalho apresentado nesta tese seria impossível de realizar sem o contributo de várias pessoas pertencentes a diferentes instituições. Assim sendo, e na impossibilidade de agradecer a cada uma individualmente, deixo aqui o meu agradecimento a todos os que contribuíram para a realização deste longo percurso.

Em primeiro lugar agradeço à Doutora Célia Tavares de Sousa, não só pelo papel fundamental de orientador, mas também por toda a disponibilidade, ajuda, apoio, motivação e simpatia que me permitiram aprofundar o meu conhecimento na área científica e adquirir competências importantes para o futuro. Agradeço também toda a confiança depositada em mim para a realização deste trabalho, a qual me fez crescer dentro e fora do laboratório.

Agradeço também à Doutora Cláudia Pinho, por toda a ajuda, simpatia, disponibilidade para me receber no MB^2, tendo tido um papel crucial para o sucesso do trabalho apresentado nesta dissertação. Também quero agradecer por todas as dúvidas esclarecidas sobre temas com os quais não estava inicialmente tão familiarizado, o que me permitiu obter novos conhecimentos valiosos.

Quero agradecer ao Doutor André Miguel Trindade Pereira por me ter introduzido a este mundo tão interessante da nanotecnologia e motivado a prosseguir o meu trabalho nesta área. Quero igualmente agradecer toda a simpatia e motivação que foram fundamentais para este percurso.

À Doutora Mariana Proença um especial obrigado por toda a ajuda, disponibilidade e trabalho realizado na Universidade Politécnica de Madrid, sem os quais esta dissertação não teria sido possível.

À Doutora Sofia Costa Lima quero agradecer por me ter introduzido ao mundo da cultura celular e toda a simpatia para me ajudar nessa área que foi relativamente nova para mim.

À Doutora Carolina Redondo agradeço a hospitalidade e disponibilidade para me receber na Universidade do País Basco e integrar no seu grupo de investigação.

À Doutora Ana Espinosa um obrigado pela dispensa do seu tempo para me ajudar com a realização do meu trabalho experimental na Universidade Autónoma de Madrid.

Quero também agradecer a todas as pessoas dos diferentes grupos de investigação com quem me cruzei ao longo deste percurso, sem as quais não teria sido possível

chegar aqui. Em especial agradeço à Suellen, Sofia, Arlete, João Horta, Sara, Andreia Marinho, Andreia Granja, Ana e Xuan.

A todos os meus amigos e família, que também desempenharam um papel fundamental para a realização deste trabalho.

Finalmente, quero dar o meu maior agradecimento à melhor e mais especial pessoa que tenho a sorte de ter na minha vida, Rae. Esta tese existe só existe graças teu apoio constante, tanto nos bons como nos maus momentos.

Funding

This work was supported by the Portuguese Fundação para a Ciência e Tecnologia (FCT) and Programa Operacional Regional Norte (Fundo Social Europeu) under the projects SFRH/BD/148563/2019 and IF/01159/2015. This work was also financially supported by the FCT and Programa Operacional Competitividade e Internacionalização 2020 (Fundo Europeu de Desenvolvimento Regional) under the projects POCI-01-0141-FEDER-032527, PTDC/FIS-MAC/31302/2017, PTDC/CTM-CTM/28676/2017, PTDC/FIS-OTI/32257/2017, and Strategic Funding contract UIDB/04968/2020, from the Spanish Ministerio de Ciencia e Innovación under the project PID2020-117024GB-C42, and from European Union's Horizon 2020 research and innovation programme under the Marie Sklodowska-Curie Grant Agreement No. 734801. This work has also made use of the Spanish ICTS Network MICRONANOFABS.

Resumo

O cancro é notoriamente difícil de tratar, sendo que as terapias oncológicas atuais são frequentemente associadas a efeitos secundários indesejáveis, devido à sua citotoxicidade e mau direcionamento para o tumor. Consequentemente, várias estratégias promissoras têm sido propostas recentemente para reduzir esses efeitos adversos. Uma abordagem interessante envolve a entrega direcionada de fármacos anticancerígenas usando nanotransportadores biocompatíveis. Tendo em conta este propósito, vários sistemas coloidais para a entrega de drogas têm sido extensivamente investigados. No entanto, seria possível realizar um grande avanço neste tipo de terapia se os transportadores de drogas tivessem um duplo acionamento eficiente, nomeadamente tratamento e transporte/libertação do fármaco no local do tumor alvo. Uma outra estratégia terapêutica promissora é baseada na indução da morte de células cancerígenas através de atuação magneto-mecânica, usando nanomateriais magnéticos adequados.

O trabalho desenvolvido nesta tese está inserido neste contexto. Em particular, é introduzida uma abordagem inovadora através do desenvolvimento de uma nova geração de nanotransportadores multimodais direcionados. Envolvendo transportadores lipídicos nanoestruturados carregados com um fármaco anticancerígeno (doxorrubicina) e um núcleo magnético (nanopartículas superparamagnéticas de óxido de ferro), estes nanotransportadores possuem propriedades físico-químicas adequadas para aplicações biomédicas foram desenvolvidos. Adicionalmente, conseguimos funcionalizar a sua superfície de modo a aumentar o seu tempo de circulação sanguínea e promover uma entrega seletiva da droga às células cancerígenas. Estes sistemas também demonstraram sensibilidade ao pH e à temperatura, o que se traduziu num aumento da libertação do fármaco anticancerígeno com o aumento da temperatura e diminuição do pH. Consequentemente, permitiram um controlo sobre a libertação do fármaco anticancerígeno quando expostos a um estímulo consistindo num campo magnético alternado, devido à capacidade das nanopartículas superparamagnéticas de óxido de ferro de gerar calor.

A adequação destas nanoplataformas para induzir a morte de células cancerígenas *in vitro* através de uma ação combinada, envolvendo hipertermia magnética e libertação da droga promovida pelo aumento da temperatura, também foi avaliada. Como resultado, foram obtidos indícios de uma dupla ação bem-sucedida em células de cancro

de mama, a qual envolveu hipertermia magnética juntamente com libertação de doxorrubicina promovida pelo aumento de temperatura.

Por outro lado, novas nanoestruturas magnéticas com configurações de *spin* únicas foram otimizadas e o seu potencial para a indução magneto-mecânica da morte de células cancerígenas foi avaliado. Particularmente, nanofios de FePt forma produzidos por dois métodos diferentes, envolvendo eletrodeposição em moldes nanoporosos de óxido de alumínio anódico. Neste contexto, verificou-se que a abordagem usando eletrodeposição DC foi a mais adequada para a sua síntese, uma vez que originou nanoestructuras com um comprimento mais uniforme com um controlo sobre a sua composição. Por outro lado, através do processo de evaporação térmica em moldes de litografia de interferência, nanodiscos de Au/Fe/Au foram produzidos, exibindo um estado fundamental de vórtice de spins. Uma caracterização compreensiva destas nanoestruturas e dos nanotransportadores previamente mencionados, confirmou a sua adequabilidade para aplicações biomédicas.

O potencial destas nanoestruturas para induzir a morte de células cancerígenas através de atuação magneto-mecânica também foi avaliado. Ensaios de biocompatibilidade e internalização *in vitro*, realizados na ausência de um campo magnético externo, demonstraram que os nanofios e nanodiscos são/eram inócuos para células de cancro da mama, tendo sido, no entanto, eficientemente internalizados por essas entidades biológicas. De seguida, ensaios *in vitro* de morte celular induzida magneto-mecanicamente, usando ambos os tipos de nanoestruturas, indicaram uma redução da viabilidade celular dependente da concentração, onde a morte celular aumentou com o aumento da concentração das nanoestruturas.

A superfície dos nanodiscos foi funcionalizada com êxito para reduzir a sua internalização pelos macrófagos, levando a um prolongamento do seu tempo de circulação sanguínea e, simultaneamente, direcionamento para as células cancerígenas. Como resultado, verificou-se que a funcionalização não afetou a biocompatibilidade dessas nanoestruturas, enquanto a sua internalização pelos macrófagos foi significativamente reduzida. Além disso, os ensaios *in vitro* de morte celular magneto-mecanicamente induzida, usando nanoestruturas funcionalizadas, revelaram uma maior redução da viabilidade das células cancerígenas em comparação com as não funcionalizadas, quando considerando condições idênticas.

Palavras-chave: cancro, nanomedicina, nanomagnetismo, nanotransportadores, nanopartículas lipídicas, nanopartículas magnéticas, nanoestruturas magnéticas,

nanofabricação assistida por moldes, simulações micromagnéticas, aplicações biomédicas.

Abstract

Cancer is notoriously difficult to treat, and the current oncologic therapies are commonly associated with undesirable side effects, due to their cytotoxicity and poor tumour targeting. Consequently, various promising treatment strategies have been recently proposed to reduce those adverse effects. One interesting approach involves the targeted delivery of anticancer drugs using biocompatible nanocarriers. For this purpose, various colloidal drug delivery systems have been extensively investigated. Nevertheless, a major advance in this type of therapy could be achieved if drug carriers presented an efficient dual triggering, namely treatment and transport/release of the drug at the target tumour site. Another promising therapeutic strategy is based on the induction of the death of cancer cells through magneto-mechanical actuation, using suitable magnetic nanomaterials that can be also used as an imaging tool for a theragnostic approach.

The work developed in this thesis is inserted in a such context. Particularly, it introduces an innovative approach by developing a novel generation of multimodal targeted nanocarriers. Featuring nanostructured lipid carriers that encapsulate the chemotherapeutic agent doxorubicin and are embedded with a magnetic core of superparamagnetic iron oxide nanoparticles, these nanocarriers are designed with physicochemical properties that meet the exacting standards necessary for biomedical applications. Additionally, we were able to functionalize their surface to increase their blood circulation time and promote a selective drug delivery to the cancer cells. These systems also demonstrated pH and thermal sensitivity, which translated into an increased release of the anticancer drug under greater temperatures and lower pH conditions. Consequently, they allowed a control over the anticancer drug release when exposed to an alternating magnetic field stimulus, due to the superparamagnetic iron oxide nanoparticles heat-generating capacity.

The suitability of these nanoplatforms for inducing the death of cancer cells *in vitro* through a combined action, involving magnetic hyperthermia and drug release promoted by the temperature increase, was evaluated as well. As a result, it was obtained evidence of a successful dual action on breast cancer cells, involving magnetic hyperthermia together with doxorubicin release promoted by the temperature increase.

Also, novel magnetic nanostructures with unique spin configurations were optimized and their potential for magneto-mechanical induction of cancer cells death was assessed.

Particularly, FePt nanowires were produced through two different methods, involving electrodeposition into nanoporous anodic aluminium oxide templates. In this context, it was verified that a pulsed DC electrodeposition approach was the most suitable for their synthesis, as it resulted in nanostructures presenting a more uniform length with a controlled composition. On the other hand, through the process of thermal evaporation into interference lithography templates, Au/Fe/Au nanodiscs were engineered, exhibiting a spin-vortex ground state. Comprehensive characterization of these nanostructures, alongside the nanocarriers mentioned earlier, confirmed their suitability for biomedical applications.

The potential of these nanoarchitectures for inducing the death of cancer cells through magneto-mechanical actuation was also evaluated. *In vitro* biocompatibility and uptake assays, conducted without an external magnetic field, demonstrated that the nanowires and nanodiscs were innocuous to breast cancer cells, yet were efficiently internalized by those biological entities. Then, *in vitro* magneto-mechanically induced cell death assays, using both types of nanoarchitectures, indicated a concentration-dependent decrease of cell viability, where cell death increased with increasing concentration of nanostructures.

The surface of the nanodiscs was successfully functionalized to reduce their uptake by macrophages, leading to an increase of their blood circulation time, and, simultaneously, targeting of cancer cells. As a result, it was verified that the functionalization did not impact the biocompatibility of those nanostructures, while their uptake by macrophages was significantly reduced. Moreover, the *in vitro* magneto-mechanically induced cell death assays, using the functionalized nanoarchitectures, revealed a greater reduction of the viability of cancer cells in comparison to the non-functionalized ones, under identical conditions.

Keywords: cancer, nanomedicine, nanomagnetism, nanocarriers, lipid nanoparticles, magnetic nanoparticles, magnetic nanostructures, template-assisted nanofabrication, micromagnetic simulations, biomedical applications.

Table of Contents

List of Figures

List of Abbreviations and Symbols

2D	Two dimensional
3D	Three dimensional
ºC	Degree Celsius
$<H_A>$	Mean anisotropy field
A	Ampere
AAO	Anodic aluminium oxide
AC	Alternating current
AFD	Anisotropy field distribution
AMF	Alternating magnetic field
AMR	Anisotropic magnetoresistance
ANOVA	One-way analysis of variance
APTES	(3-aminopropyl) triethoxysilane
ARC	Anti-reflective coating
at.%	Atomic percentage
BBB	Blood–brain barrier
bcc	Body-centred cubic
BSA	Bovine serum albumen
B_0	External magnetic field
CARS	Coherent anti-Stokes Raman scattering
CEMUP	Centro de Microscopia Eletrónica da Universidade do Porto
CD44	Cluster of differentiation 44
cm	Centimetre
cm^2	Square centimetres
CPU	Central processing unit

d	Diameter
Da	Dalton
DC	Direct current
DDPH	2,2-Diphenyl-1-picrylhydrazyl
DLS	Dynamic light scattering
DMEM	Dulbecco's Modified Eagle's Medium
Dop-PEG	Dopamide-Polyethylene glycol
DOX	Doxorubicin
DTPA	Pentetic acid
EDL	Electric double layer
EDS	Energy-dispersive X-ray spectroscopy
EE	Encapsulation efficiency
EGF	Epidermal growth factor
ELS	Electrophoretic light scattering
emu	Electromagnetic unit
EPR	Enhanced permeability and retention
eV	Electronvolt
EXAFS	Extended X-ray absorption fine structure
FA	Folic acid
FACS	Fluorescence-activated cell sorting
FBS	Fetal Bovine Serum
FC	Field cooled
FCUP	Faculty of Sciences of the University of Porto
FDA	Food and drug administration
FFUP	Faculty of Pharmacy of the University of Porto
FSC	Forward scattered light

GEL	Gelucire 43/01
GPU	Graphics processing unit
GRAS	Generally recognized as safe
H	Magnetic field strength
h	Hours
H_a	Annihilation field
H_c	Coercivity
HCL	Hydrochloric acid
hcp	Hexagonal close-packed
HCT 116	Colon carcinoma epithelial cells
HeLa	Human cell line derived from cervical cancer cells
HL60	Leukemic cells
H_n	Nucleation field
H_r	Remanent magnetization
H_s	Switching field
HSAB	Hard-soft acid-base
$H^{\perp}_{Sat}$	Perpendicular saturation field
Hz	Hertz
ICPOES	Inductively coupled plasma-optical emission spectroscopy
IC_{50}	Half maximal inhibitory concentration
IFIMUP	Institute of Physics for Advanced Materials, Nanotechnology and Photonics
IgG	Immunoglobulin G
ILP	Intrinsic loss power
ISOM	Institute for Optoelectronic Systems and Microtechnology
J	Joule

j(t)	Current density curve
keV	Kiloelectronvolt
kOe	Kilooersted
kV	Kilovolt
L	Litre
LAQV	Associated Laboratory for Green Chemistry
LC	Loading Capacity
LDNLC	Nanostructured lipid carrier loaded with β-lapachone and doxorubicin
LLG	Landau-Lifshitz-Gilbert
m	Metre
mA	Milliamperes
MACS	Magnetic-activated cell sorting
mbar	Millibar
MBE	Molecular beam epitaxy
MFM	Magnetic force microscopy
mg	Milligram
MHT	Magnetic hyperthermia
MHz	Megahertz
min	Minute
mL	Millilitre
mM	Millimolar
mm	Millimetre
mmol	Millimole
MOKE	Magneto-optical Kerr effect
MPS	Mononuclear phagocyte system
MR	Magnetic resonance

MRI	Magnetic resonance imaging
ms	Milliseconds
M_{Sat}	Saturation magnetization
mTorr	Millitorr
mV	Millivolts
MW	Molecular weight
M_{xy}	Transverse magnetization
M_z	Longitudinal magnetization
NDs	Nanodiscs
NIR	Near-infrared
NIST	National Institute of Standards and Technology
NLCs	Nanostructured lipid carriers
NMR	Nuclear magnetic resonance
NTA	Nanoparticle tracking analysis
M_0	Net magnetization vector
nm	Nanometres
NMR	Nuclear magnetic resonance
NPs	Nanoparticles
NRs	Nanorods
NTs	Nanotubes
NWs	Nanowires
Oe	Oersted
OOMMF	Object oriented micro-magnetic framework
Pa	Pascal
PAA	Poly(acrylic acid)
PAL	Cetyl palmitate

PBS	Phosphate buffered saline
PDI	Polydispersity index
PED	Pulsed electrodeposition
PEG	Polyethylene glycol
pg	Picogram
pH	Potential of hydrogen
pN	Piconewton
psi	Pounds per square inch
Py	Permalloy
R	Radius
r	Aspect ratio
REQUIMTE	Network of Chemistry and Technology
RF	Radiofrequency
rpm	Rotations per minute
RPMI	Roswell Park Memorial Institute
RSM	Response surface methodology
R^2	Coefficient of determination
r_1	Longitudinal relaxivity
r_2	Transverse relaxivity
s	Seconds
SAF	Synthetic antiferromagnetic
SAF-PL-NPs	Phospholipid-coated synthetic antiferromagnetic nanoparticles
SAR	Specific heat absorption rate
SEM	Scanning electron microcopy
SH-PEG--COOH	Thiol-polyethylene glycol-carboxyl

SLNs	Solid lipid nanoparticles
SLP	Specific loss power
SPIONs	Superparamagnetic iron oxide nanoparticles
SQUID	Superconducting quantum interference device
SRS	Stimulated Raman scattering
SSC	Side scattered light
SSC-H	Height of the side scattered light
STEM	Scanning transmission electron microscopy
T	Tesla
t	Thickness
T_B	Blocking temperature
TEM	Transmission electron microscopy
THCP	Tetrakis(hydroxymethyl)phosphonium
THP-1	Human monocytic cell line
t_{off}	Rest pulse
t_{on}	Deposition pulse
UAM	Autonomous University of Madrid
UPM	Technical University of Madrid
UPV	University of the Basque Country
UV-Vis	Ultraviolet-visible
V	Volt
V_{dep}	Electrodeposition potential
VSM	Vibrating-sample magnetometer
W	Watt
Wb	Weber
XPS	X-ray photoelectron spectroscopy

XRD	X-ray diffraction
ZFC	Zero-field cooled
λ	Wavelength
µg	Microgram
µL	Microlitre
µm	Micrometre
τ	Néel relaxation time
τ_m	Measurement time
υ_a	Anti-symmetric stretches
υ_s	Symmetric stretches
Ω	Ohm

Thesis Outline

This thesis unfolds over nine meticulously structured chapters, delineating a comprehensive journey from theoretical foundations to groundbreaking applications in the field of magnetic nanomaterials for cancer treatment. It meticulously charts the path from initial concepts to the development and characterization of innovative nanomaterials, culminating in their potential biomedical applications, with chapter 1 covering the theoretical background; chapter 2 comprising the goals of this work; chapter 3 detailing the experimental techniques; chapters 4, 5, 6, and 7 providing the obtained results and their discussion; and chapter 8 presenting the conclusions together with the future perspectives..

Chapter 1 – Introduction: In this chapter, it is provided a theoretical background regarding magnetic nanomaterials, encompassing their fabrication processes and various biomedical applications. A particular focus is given to the specific types of nanomaterials used throughout this work, including superparamagnetic iron oxide nanoparticles, nanostructured lipid carriers, nanowires, and nanodiscs with a spin-vortex ground state.

Chapter 2 – Goal: The major goal of the work carried out is presented in this chapter, which is centred around the development of innovative approaches for cancer treatment based on functionalized magnetic-lipid nanoparticles and high aspect-ratio magnetic nanostructures, with unique spin configurations, that can act as versatile nanocarriers for triggering the death of cancer cells and, simultaneously, deliver multiple drug agents to the target site, thereby enhancing the treatment efficiency

Chapter 3 – Experimental Techniques: This chapter addresses the nanofabrication and characterization methods used in this thesis. Additionally, the methodologies used for performing micromagnetic simulations and in vitro cellular studies are presented.

Chapter 4 – Nanostructured Lipid Carriers: In this chapter, it is presented the complete characterization of the fabricated superparamagnetic iron oxide nanoparticles and various nanostructured lipid carriers formulations. Moreover, the thermal stability and pH-sensitivity of the produced formulations are also addressed as well as their response to external stimuli..

Chapter 5 – FePt Nanowires: A detailed characterization of the nanowires composed of FePt, obtained though electrodeposition into nanoporous anodic aluminium oxide, is presented in this chapter. The influence of different parameters associated with the

nanofabrication process is analysed in depth, so as to optimize their synthesis conditions. Moreover, micromagnetic simulations of these nanoarchitectures are presented, to gain a better understanding of the magnetization behaviour in those nanoarchitectures.

Chapter 6 – Au/Fe/Au Nanodiscs: This chapter addresses the characterization of Au/Fe/Au nanodiscs with a spin-vortex ground state, produced via thermal evaporation into interference lithography templates. Micromagnetic simulations of these nanostructures are also included, so as to get a better comprehension of the magnetization behaviour and support the experimental results.

Chapter 7 – Biomedical Applications: In this chapter, the suitability of the fabricated nanomaterials for different biomedical applications is assessed. Particularly, it is analysed the potential of the produced formulations of nanostructured lipid carriers loaded with superparamagnetic iron oxide nanoparticles for a dual cancer treatment approach, based on delivering anticancer drugs in combination with magnetic hyperthermia. Conversely, the suitability of the synthesized nanowires and nanodiscs for another oncological therapeutic strategy, namely magneto-mechanical induction of cancer cell death, is evaluated, considering both functionalized and non-functionalized nanostructures.

Chapter 8 – Final Remarks and Future Work: The conclusions of the work presented throughout this thesis are covered in this final chapter, together with the future perspectives

Through this structured exposition, the thesis here presented represents another step towards bridging the gap between nanomaterials' science and therapeutic innovation, offering novel strategies for cancer treatment.

1. Introduction

This first chapter addresses the physical properties and fabrication techniques of superparamagnetic and high aspect-ratio magnetic nanomaterials. Following this foundational overview, will go into the evaluation of the suitability of these nanomaterials for a variety of biomedical applications. This segment meticulously integrates the current state of art, providing a detailed account that highlights the significance and future prospects of these nanomaterials in the biomedical field.

1.1. Magnetic Nanomaterials

Nanotechnology is considered one of the most important emerging fields of science in the 21st century, being defined as the comprehension and control of matter at the nanoscale, typically in the range between ~ 1 and 100 nm. However, the precise boundaries of the nanoscale remain a topic of debate, with some definitions extending it to materials ranging from 1 up to 1000 nm in size.[1,2] Nevertheless, at such scale, unique phenomena that are not observed in a materials' bulk form, such as quantum confinement and high surface area effects, occur, which enable the development of new applications.[1–3] Among the various materials studied in this field, those with ferromagnetic properties, known as magnetic nanomaterials, have been gaining considerable attention for applications where remote control and manipulation through the application of external magnetic fields are essential, such as biomedical devices and high-density magnetic data storage, as they can be remotely controlled by external magnetic fields.[4–6] An aspect that characterizes this type of nanomaterials is that they have strong and permanent magnetic moments that tend to align themselves in the same direction, even in the absence of an external magnetic field.[7] In this context, nanomagnetism appears, which is the field that explores the magnetic properties of these nanomaterials.[8]

1.1.1. Nanomagnetism

When a material's dimensions are reduced down to the nanoscale, they become comparable to the critical length scales of physical phenomena, i.e. specific size ranges below which the physical properties of the material are modified.[9,10] In nanomagnetism, there are two main critical length scales, namely the exchange length and the domain wall width, due to their key roles in controlling the magnetic behaviour of magnetic nanomaterials.[11–13] The exchange length is described as the length below which atomic exchange interactions dominate over the magnetostatic fields and, consequently, the

formation of multiple magnetic domains becomes energetically unfavourable, since the alignment of magnetic moments is preferred.[13–15] This length scale is defined as:

$$L_{ex} = \sqrt{\frac{2A}{\mu_0 M_{Sat}^2}} \quad (1.1)$$

where A is an exchange stiffness constant, which provides a measure of the exchange interaction between neighboring spins, μ_0 is the vacuum magnetic permeability ($4\pi * 10^{-7}$ H/m), and M_{Sat}^2 is the saturation magnetization of the material.[13,16,17] For most ferromagnetic materials, such length ranges between 2 and 5 nm.[18]

On the other hand, the domain wall width represents the distance over which the magnetic polarization changes from one magnetic domain to the adjacent one, i.e. the transition region.[19] Consequently, when a ferromagnetic nanomaterial is smaller than the domain wall width, it tends to behave as a single magnetic domain.[20]

Consequently, when the dimensions of a magnetic body are reduced to match or fall below the critical length scales, only single-domain magnets can be obtained. This suggests that the size and shape of the magnetic element or particle can be used to tune their magnetic properties and behaviour.[13,21] In the following sections the most relevant magnetic nanomaterials for the development of this work will be addressed.

1.1.1.1. Magnetic Anisotropy

Magnetic anisotropy can be described as the directional dependence of a material's magnetic properties, as opposed to magnetic isotropy.[22] Particularly, in the absence of an external magnetic field, the magnetic moment of a magnetically isotropic material is not aligned along a preferential direction, whilst the magnetic moment of a magnetically anisotropic material is preferably oriented along an easy magnetization axis. This axis is an energetically favourable direction of spontaneous magnetization, being determined by various aspects, namely grain shape, crystal structure, and stress.[23,24] Furthermore, when the magnetization of a magnetically anisotropic material is aligned along its easy axis, it can point towards either of two opposite directions, since they typically are energetically equivalent.[24]

Alternatively, this axis can be considered as the crystallographic direction along which the lowest applied magnetic field is enough to achieve the saturation magnetization. On the other hand, the crystallographic direction along which the applied magnetic field required to reach the saturation magnetization is the largest is known as the hard magnetization axis (figure 1.1).[25,26]

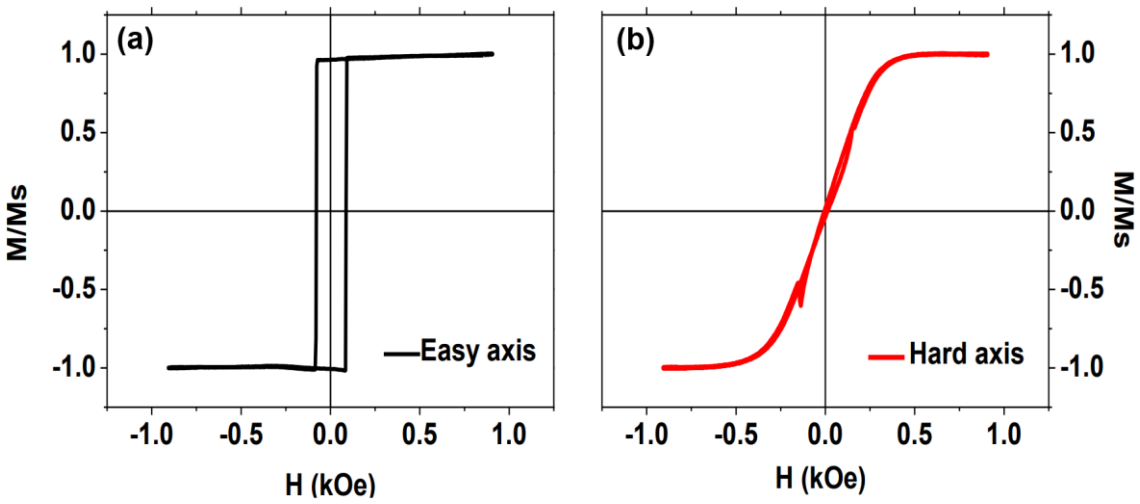

Figure 1.1 - Schematic hysteresis loops representing the application of an external magnetic field along the (a) easy and (b) hard magnetization axes. Adapted from [27]. Copyright 2019 Author licensed under a Creative Commons Attribution (CC BY-NC-ND 4.0 DEED) license.

The two major sources of magnetic anisotropy in a material are the magnetic dipole-dipole interaction and the spin–orbit coupling, which are associated with shape and magnetocrystalline anisotropy.[28,29] Regarding the magnetic dipole-dipole interactions, they result from the mutual attraction or repulsion between magnetic moments. These interactions have a long-range character, and they lead to the formation of a demagnetizing (or stray) field within the specimen, which is induced by the spatial arrangement of the magnetic moments inside it. Therefore, the shape of the material plays a key role in how these interactions manifest, leading to a contribution to the anisotropy that depends on the specimen's shape, known as shape anisotropy.[29–31]

On the other hand, the spin-orbit coupling results from the interaction between the spin angular momentum of an elementary particle (such as an electron) and its orbital angular momentum as it moves through an electromagnetic field, typically generated by an atomic nucleus.[32,33] This orbital angular momentum is influenced by the crystal field of the lattice, leading to a transfer of the lattice anisotropy to the elementary particle's spin. This phenomenon, known as magnetocrystalline anisotropy, plays a crucial role in determining the preferred orientation of magnetic moments within a crystalline material.[28,34] Dipole-dipole interactions also contribute to this type of anisotropy, although at a lower degree.[29,35] Furthermore, when a material experiences stress, the spin-orbit coupling is altered by the strain, leading to an effect known as magnetoelastic anisotropy.[29]

1.1.1.1.1. Superparamagnetic Nanoparticles

Superparamagnetism is a type of magnetism observed in small ferromagnetic or ferrimagnetic nanoparticles (NPs).[36] This form of magnetism is characterized by three features, namely absence of hysteresis, meaning that remanence and coercivity are zero, a high magnetic moment that follows the Langevin curve, and an overlapping of the magnetization curves measured under different temperatures, when magnetization is plotted as a function of the magnetic field strength (H) and temperature.[37]

A particularly interesting type of NPs where this magnetic behaviour is observed are superparamagnetic iron oxide NPs (SPIONs), due to their excellent superparamagnetic properties, controllable size, high surface area-to-volume ratio, as well as biocompatibility, typically presenting a diameter up to 30 nm.[38,39] These NPs are single domain nanostructures where the thermal energy overcomes the anisotropy energy barrier.[40,41] This happens when the sample volume is reduced below a critical value, or superparamagnetic limit, in which more energy is required to create a domain wall than to support the external magnetostatic energy of the single domain state (figure 1.2).[42,43]

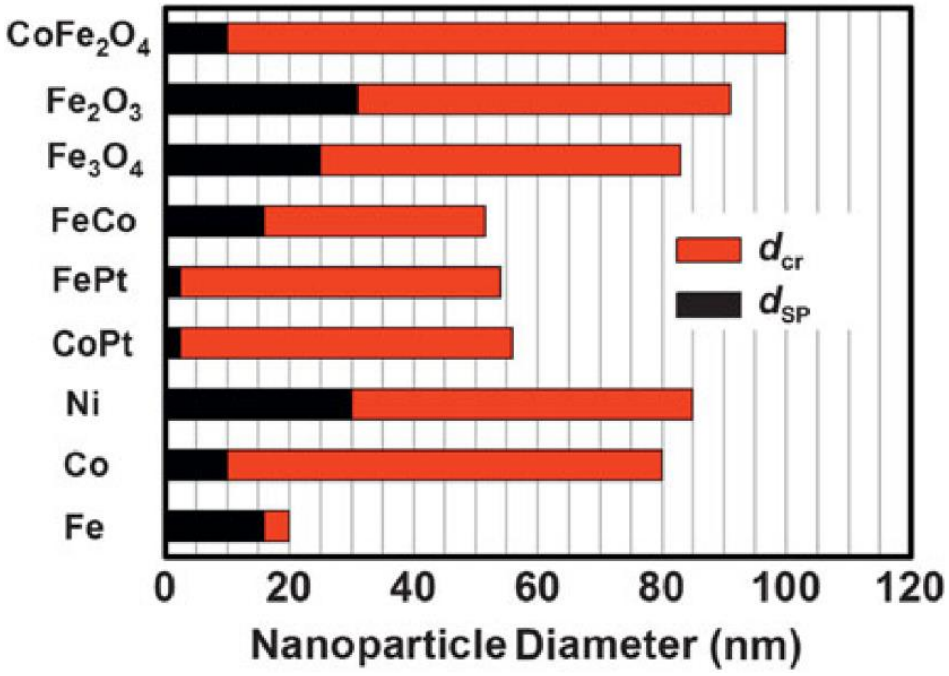

Figure 1.2 – Superparamagnetic limit (d_{SP}) and maximum monodomain size (d_{cr}) for spherical NPs with different compositions. From [44]. Reproduced with permission from Springer Nature.

Particularly, the magnetic anisotropy energy in a single-domain magnetic NP (E), i.e. the energy required to change the magnetization direction from a low energy direction, or easy magnetization axis, to a high energy direction, or hard magnetization axis, is defined as:

$$E(\theta) = K_{eff} V \sin(\theta)^2 \quad (1.2)$$

where K_{eff} is the anisotropy constant, V corresponds to the volume of the NP, and θ is the angle between the easy axis and the magnetization direction.[45,46] From this equation, it is possible to verify that $K_{eff}V$ represents the energy barrier between the two opposing directions along the easy magnetization axis, which are energetically equivalent (figure 1.3). Furthermore, with decreasing NP size such energy barrier decreases and, for a sufficiently small V, it may become so small that thermal excitations, even at room temperature, are sufficient to overcome it. As a result, fluctuations of the overall magnetic moment can occur within the particle, even when no external magnetic field is applied. Hence, the NP presents a behaviour that resembles a single paramagnetic spin, albeit with a magnetic moment that not only is several orders of magnitude larger, but also can thermally fluctuate over time.[47–50]

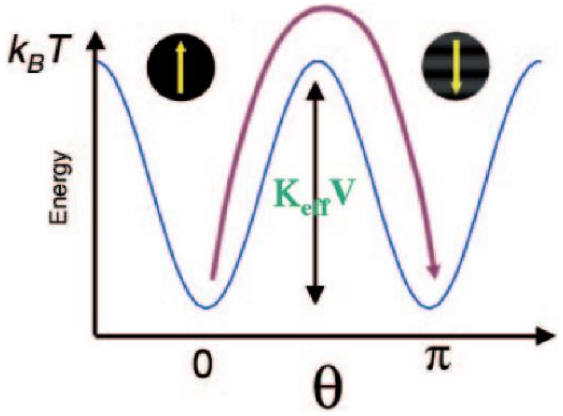

Figure 1.3 - Dependence of the anisotropy energy profile on the angle between the easy axis and the magnetization direction, considering a single domain NP with a purely uniaxial symmetry. Adapted from [51]. Reproduced with permission from Springer Nature.

In this situation, the magnetization of a NP fluctuates between its two equilibrium positions, i.e. the two orientations along the easy magnetization axis, and the average time it takes for the net magnetic moment to switch its orientation, due to thermal excitations, is known as the Néel relaxation time (τ_N), which is given by:[52–54]

$$\tau_N = \tau_0 \exp\left(\frac{K_{eff}V}{k_B T}\right) \quad (1.3)$$

where τ_0 is the attempt time or attempt period, which is a characteristic length of time of the material (for magnetite/maghemite it is in the order of 10^{-10} s), k_B is the Boltzmann constant, and T is the absolute temperature.[55]

Consequently, in the absence of an external magnetic field and if the duration over which the magnetic properties of the material are observed, or measured, i.e. the measurement

time (τ_m), is much longer than the Néel relaxation time (τ), then the resulting net magnetic moment is zero, due to the random fluctuations in the magnetization, and the system is said to be in a superparamagnetic state [figure 1.4(b)]. On the other hand, if the measurement time is much shorter than the Néel relaxation time, the system is said to be in a blocked state where net magnetic moment does not change throughout the measurement, since its direction does not flip [figure 1.4(a)]. In this case, the nanomaterial exhibits a typical paramagnet behaviour, albeit with a significantly larger magnetic susceptibility.[52,56]

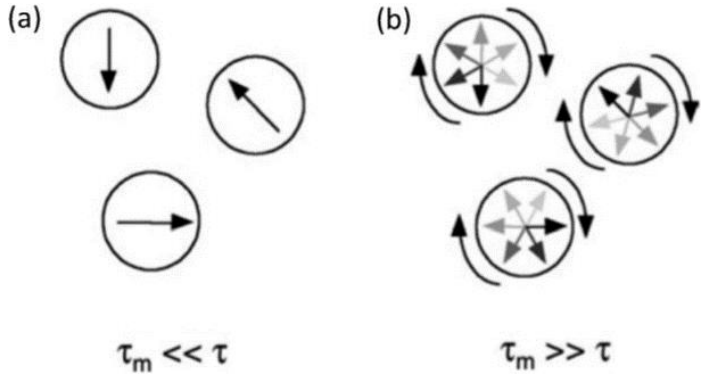

Figure 1.4 - Superparamagnetic NPs in a (a) quasi-stable blocked state and (b) freely rotating. Used with permission of IOP Publishing, Ltd, from [57]; permission conveyed through Copyright Clearance Center, Inc.

1.1.1.1.2. Nanodiscs with a Spin-Vortex Ground State

Magnetic nanostructures or nanoarchitectures, namely magnetic nanomaterials with a non-spherical shape, such as nanowires (NWs), nanorods (NRs), nanotubes (NTs), and nanodiscs (NDs), often appear as alternatives to magnetic NPs, as their geometry translates into intrinsic anisotropy properties that cause them to behave differently, depending on the direction of the applied magnetic field. Moreover, they have an increased surface area-to-volume ratio and higher magnetic moments, resulting from a prevalent shape anisotropy.[58,59]

In this context, due to the interplay between various energy terms, such as the dipolar, the exchange, and the anisotropy energy contributions, new exotic magnetic configurations have been observed. One example is the magnetic spin-vortex configuration, which appears as the ground state in ferromagnetic dots possessing various geometries (circular, elliptical, or triangular). In micro/nanodiscs, energy minimization leads the spins to form a curling state, where their orientation turns gradually. At the disc's edge, these spins are parallel to its surface, cancelling the total dipole energy while minimizing the loss of exchange energy. However, as they become closer to the centre of the disc, the angles among neighbouring spins increase until they

reach a point where confinement within the plane becomes untenable, leading to the formation of a vortex core where the magnetization is oriented perpendicular to the nanostructure's plane (figure 1.5).[60] Spin-vortices can be described by two parameters, namely the chirality, which describes the direction of rotation of the in-plane rotating magnetization (counterclockwise or clockwise), and the direction of the spin-vortex core's magnetization, also known as polarity (up or down).[61]

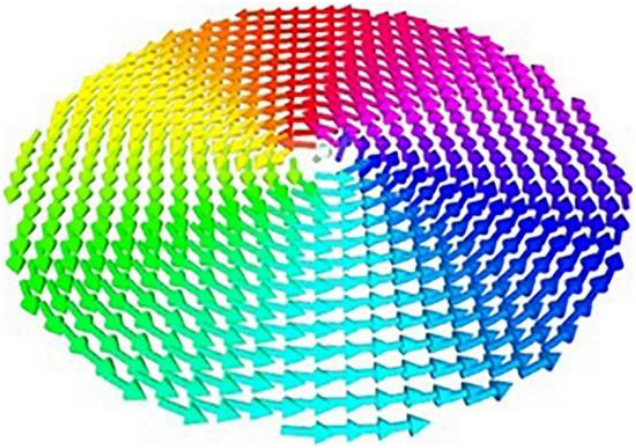

Figure 1.5 - Scheme of a spin-vortex ground state in a micro/nanodisc. Reprinted from [62], with the permission of AIP Publishing.

Such remanent magnetization distribution is energetically favourable for discs with low magnetocrystalline anisotropy and it can be deduced from the hysteresis loop's shape, or by direct observation through magnetic imaging techniques, such as magnetic force microscopy (MFM).[63–65] However, when conducting MFM experiments on soft magnetic materials, the results must be cautiously interpreted, since there are unavoidable tip-induced perturbations, which have to be considered.[66]

The magnetization in a disc with a spin-vortex ground state as a function of the applied magnetic field is represented in figure 1.6. Such hysteresis loop was measured for a permalloy (Py - $Fe_{80}Ni_{20}$) microdiscs array, which possessed a thickness of 60 nm and diameter of 0.2 μm.[63] As can be observed, when the disc is in a state of magnetic saturation and then the applied magnetic field is reduced (in module), there is the nucleation of the spin-vortex, which is accompanied by a sudden magnetization reduction. The magnetic field at which this phenomenon occurs is referred to as the nucleation field, H_n. Subsequently, there is a region where magnetization exhibits a linear response to the applied magnetic field, which is associated with the reversible motion of the spin-vortex core and encompasses the remanent state of the disc, characterized by virtually no magnetization [figure 1.6(a)]. Subsequentially, with increasing reverse-applied magnetic field, the individual magnetic moments increasingly tilt towards the field

direction, which causes the spin-vortex core to move perpendicularly to the direction of the applied magnetic field [figure 1.6(b, c)]. A further increase of such field leads to the expulsion of the spin-vortex from the disc. The magnetic field at which this phenomenon occurs is known as the vortex annihilation field, H_a, which is followed by the stabilization of the disc in a single-domain state.[63,67–69]

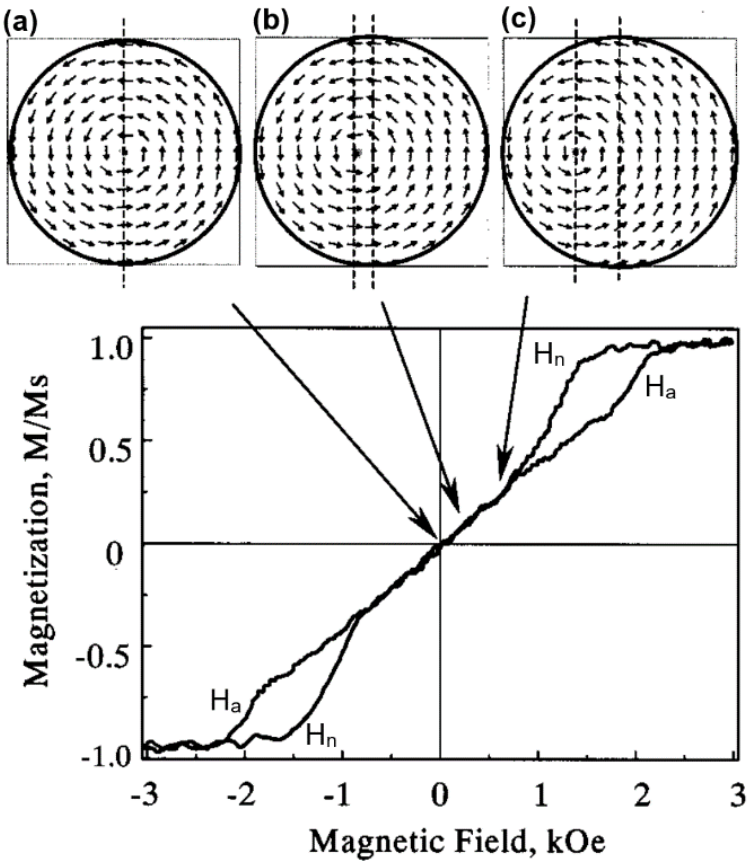

Figure 1.6 - Hysteresis loop of a Py microdiscs array illustrating a spin-vortex ground state: (a) remanent state; (b, c) movement of the vortex core with increasing magnetic field. Reprinted from [63], with the permission of AIP Publishing.

To better understand the magnetic behaviour of this type of nanostructures, it is crucial to analyse the parameters that influence the formation of a spin vortex ground state. Through theoretical and experimental studies, it has been demonstrated that such magnetization distribution depends on the material, geometry, but mainly on the nanostructure's aspect ratio, which can be considered as:[70,71]

$$\text{Aspect ratio} = \frac{\text{Long axis}}{\text{Short axis}} \tag{1.4}$$

In figure 1.7, an universal magnetic phase diagram, as a function of the thickness (t) and radius (R) of circular Py dots and in the absence of an external magnetic field, is represented, which was obtained from calculations of energies associated with the

single-domain and spin-vortex state.[72–75] As can be observed, the aspect ratio of the nanostructures plays a key role in the determination of their remanent spin configuration.[73]

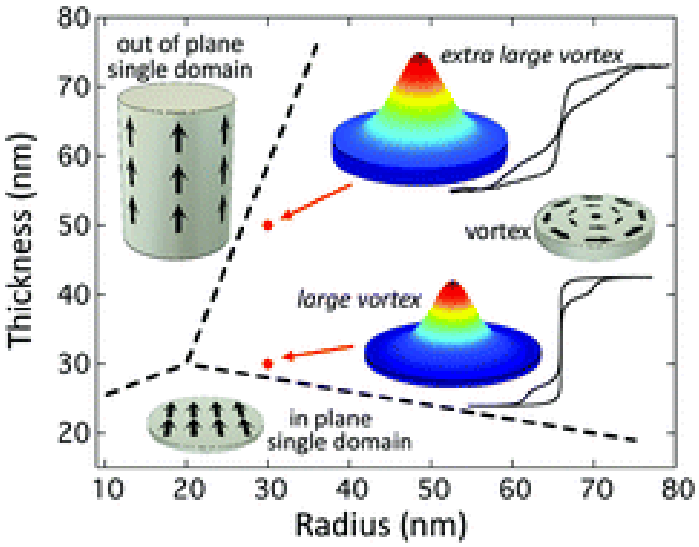

Figure 1.7 - Magnetic ground state phase diagram for Py dots, plotted as a function of their t and r. The dashed lines delineate the boundaries between areas characterized by distinct magnetic configurations, which are indicated by arrows within the cylinders. Used with permission of Royal Society of Chemistry, from [73]; permission conveyed through Copyright Clearance Center, Inc.

Consequently, to better understand the range of dimensions that lead to formation of a spin-vortex ground state, the magnetic behaviour of arrays of discs possessing various diameters (d's) and thicknesses (t's) has been extensively investigated by several authors. For example, Cowburn et al.[64] produced several arrays of supermalloy ($Ni_{75}Fe_{20}Mo_5$) NDs, possessing d's between 55 and 500 nm as well as t's ranging from 6 up to 15 nm, through the combination of electron beam lithography with electron beam evaporation. The obtained results are represented in figure 1.8(a), where it is possible to observe that the hysteresis loops vary with the nanostructures' dimensions. Additionally, some loops do not demonstrate the existence of a spin-vortex behaviour, having allowed the authors to empirically establish a phase diagram for the transition from vortex to single-domain behaviour [figure 1.8(b)].

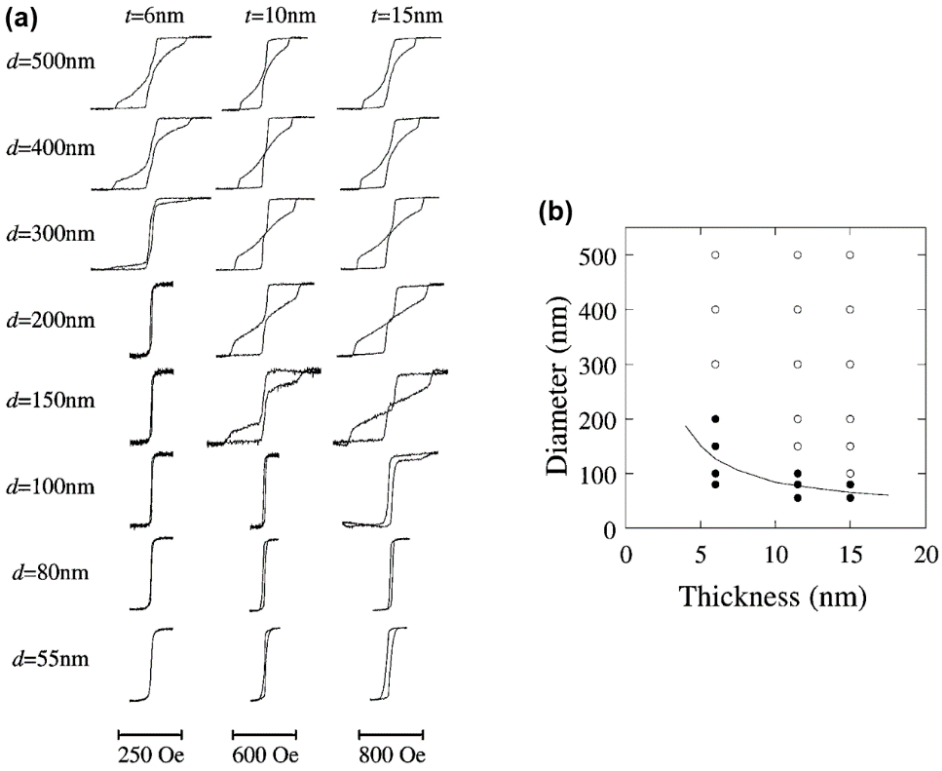

Figure 1.8 - (a) Hysteresis loops measured for discs with different d's and t's; (b) experimentally obtained phase diagram. •: spin-vortex state, ◦: single-domain state. The black line represents the lowest limit of the theoretical phase transition between the vortex state (above the line) and the single-domain state (below the line). Adapted from [64]. http://dx.doi.org/10.1103/PhysRevLett.83.1042. Copyright 1999 by the American Physical Society.

Later, Schneider et al.[69] performed an investigation into the magnetic properties of Py discs. These circular nanostructures presented a d varying between 180 and 950 nm, as well as a uniform t of 15 nm. This study revealed a significant dependence of H_a on the disc diameter, which was attributed to the growing influence of the magnetostatic self-energy as the nanostructure's d decreased. In contrast, H_n remained nearly constant, as depicted in figure 1.9.

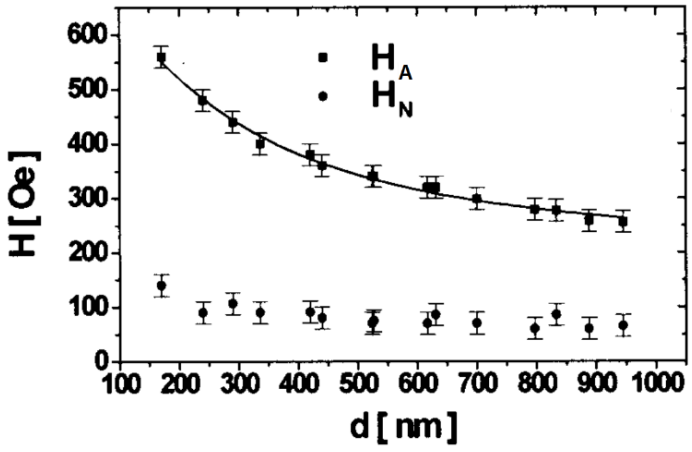

Figure 1.9 - Annihilation (H_A) and nucleation (H_N) fields as a function of Py discs' d. Reprinted from [69], with the permission of AIP Publishing.

In a subsequent work, Schneider et al.[65] carried out a similar analysis, but considering Py cylinders with varying t's (3, 5.5, 8.3, 15, as well as 20 nm) and d's ranging from 150 to 1000 nm. The primary focus of this study was to investigate the relationship between the characteristic vortex fields and the aspect ratio (represented as r = d/t) of these cylinders. As a result, the authors discovered that both H_a and H_n decreased r increased. Such behaviour indicated that single-domain and intermediary magnetic states, which precede the formation of a vortex configuration, became more stable at higher r. Furthermore, it was verified that, in the thinnest discs (t = 5.5 nm), the core of the vortex was not perfectly centred, resulting in a nonzero remanent magnetization. The authors proposed that such behaviour could be attributed to the possibility that the vortex can become pinned at positions where there is a local energy minimum, due to surface roughness effects.

Another study, by Fernandez et al.[76], addressed the magnetization reversal process in Co elliptical dots with t's ranging from 18 to 30 nm, through the use of MFM. Here, the authors emphasized the importance of the shape anisotropy term in determining the domain configuration in the dots, when they do not have a circular shape. Specifically, when the dots were saturated along their long axis, a uniformly magnetized state was observed at remanence. However, when they were saturated along their short axis, it was verified that they relax into a single-vortex state. The researchers suggested that this behaviour might be attributed to the array's microstructure, which led to the dominance of shape anisotropy over the magnetocrystalline anisotropy contribution.

In summary, experimental findings have confirmed that the values of the spin-vortex characteristic fields, i.e. H_a and H_n, and the slope of the linear section of the hysteresis loop exhibit significant dependencies on both the material properties and the nanostructures' size.[63,67,68]

Regarding the spin-vortex core, the magnetization direction at the disc's centre can randomly point up or down. This occurs because the up- and down-magnetizations are energetically equivalent when no external field is applied and, also, they are independent of the sense of the in-plane flux closure (clockwise or counterclockwise).[60,77] Nevertheless, Waeyenberge et al.[77] demonstrated that it was possible to switch the out-of-plane core polarization by applying brief pulses of a sinusoidal excitation field.

For the same reason, the sense of the in-plane flux closure is also random, in the absence of an external magnetic field.[78] However, some authors have demonstrated that it could be switched by applying a current pulse with appropriate amplitude, polarity, and

duration, or through the application of magnetic field pulses, with a controlled amplitude and duration.[79,80]

Up until this point, the magnetic behaviour of isolated dots with a spin-vortex ground state has been addressed. However, when arrays of nanoelements are considered, such as NDs fabricated through a template-assisted method, different behaviours have been observed, owing to the magnetostatic interactions between the nanostructures. As such, given the likely need for multiple identical nanostructures in an ordered arrangement in various applications, it becomes crucial to investigate the impact of the interdot distance. Therefore, a concise overview of some of the most noteworthy examples illustrating these effects is provided next.

In this context, Novosad et al.[67] presented experimental data and calculations that demonstrated a significant influence of interdot spacing on the vortex characteristic fields. This relationship is visually represented in figure 1.10, where two hysteresis loops corresponding to arrays of discs with varying interdot distances are depicted. As can be observed, although these loops maintain the expected spin-vortex-like shape, they exhibit distinct H_n and H_a values. Notably, these values, as well as the slope of the linear portion of the hysteresis loop, appear to be contingent not only on the dot's d and t but also on the interdot distance. Additionally, it is worth highlighting that H_n and H_a exhibit a decreasing trend as the interdot distance decreases. Conversely, there's an observable increase in the initial susceptibility of the vortex as such distance diminishes. This larger initial susceptibility implies that dot arrays characterized by robust interdot magnetostatic coupling (i.e. interdot distance < d/2) display greater mobility of the vortex core compared to an isolated dot of the same dimensions. Moreover, the decrease in characteristic field values can be attributed to the higher effective field experienced by each individual disc, resulting from the contributions from neighbouring discs combined with the applied external magnetic field.

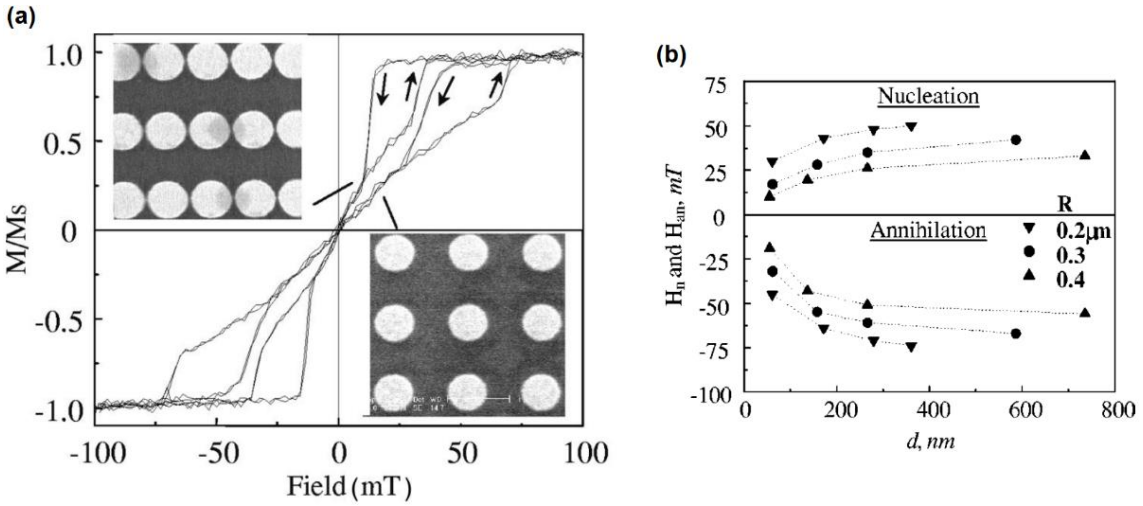

Figure 1.10 - (a) Hysteresis loops of two Py discs arrays (d = 0.8 μm, t = 80 nm) with interdot distances of 30 and 800 nm; (b) experimental H_n and H_a (represented as H_{an}) values in rectangular arrays of Py dots as a function of the dot diameter and interdot distance (represented as d). Adapted from [67]. https://doi.org/10.1103/PhysRevB.65.060402. Copyright 2002 by the American Physical Society.

Another study, by Mejía-López et al.[81], analysed the magnetic interactions among Fe NDs (d = 65 nm; t = 20 nm), as a function of the centre-to-centre dot distance through micromagnetic simulations, as well as experimentally. Considering the normalized distance as centre-to-centre dot distance/d, figure 1.11 illustrates how the characteristic vortex fields vary according to that parameter. As can be observed, these authors verified that as the dots become close to each other the absolute value of the vortex nucleation field increases. This behaviour was attributed to the magnetostatic interactions, which tend to favour a configuration where the dots are primarily magnetized along one direction. Consequently, an additional energy barrier for the transition from a single domain to the spin-vortex state is introduced, resulting in an increase in the H_n values. The H_a is also influenced by interdot interactions, albeit to a lesser extent, since the dipolar interactions between dots in the vortex state are weaker. Based on these results, the authors postulated that when the centre-to-centre dot distance exceeds approximately 3 times the dot's d (centre-to-centre dot distance ≥ 3d), both a dots array and an individual dot exhibit identical hysteresis loops. Additionally, for 2d ≤ centre-to-centre dot distance < 3d, it was verified that the hysteresis loop shape closely resembles that of non-interacting dots. Consequently, it was concluded that the magnetic properties of two interacting dots can be effectively described by the behaviour of non-interacting dots, when the centre-to-centre dot distance is greater or equal to 2d. Conversely, when the centre-to-centre dot distance is smaller than 2d, the interaction between two magnetic dots assumes a pronounced role and can considerably modify the magnetization reversal process.

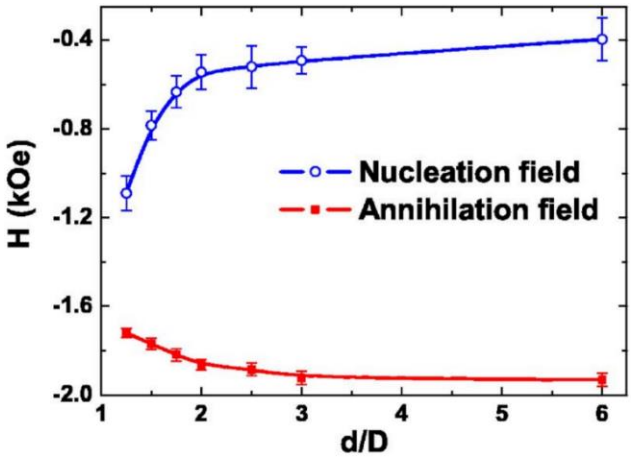

Figure 1.11 - H_n and H_a computed as a function of the normalized distance [centre-to-centre dot distance (represented as d)/diameter (represented as D)]. Reprinted from [81], with the permission of AIP Publishing.

Furthermore, as represented in figure 1.12, the authors observed deviations between simulated and experimental data, which was ascribed to two main factors: the variation in dot sizes and the imperfections in dot shape within the experimental setup. Additionally, the neglected interdot interactions, when the centre-to-centre dot distance is greater or equal to 2d, while not altering the fundamental shape of the hysteresis loop, might introduce minor quantitative adjustments.[81]

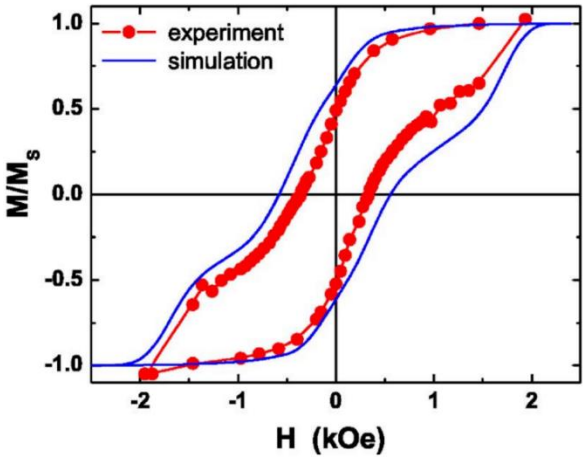

Figure 1.12 - Experimental and simulated hysteresis loops for a dots array possessing a centre-to-centre dot distance = 20 nm, t = 65 nm, and d = 110 nm. Reprinted from [81], with the permission of AIP Publishing.

From these two studies, there are two apparently contradictory results regarding the variation of H_n with the interdot distance, i.e. Novosad et al.[67] indicated that it decreases as the dots become closer while Mejía-López et al.[81] concluded that H_n increased for lower interdot distances. However, these are ”two sides of the same coin”, since the hysteresis loop in figure 1.12 is significantly wider than the one represented in figure 1.10(a). Therefore, the variation of H_n as a function of the interdot distance can be

interpreted in regard to the reverse-applied field, meaning that as the dots become closer, the reverse-applied field must be higher for the transition from a single domain to the spin-vortex state to occur, i.e. H_n increases with the decrease of the interdot distance, due to higher magnetostatic interactions.[67,81]

Guslienko et al.[82] also highlighted the significance of magnetostatic interactions in the magnetization reversal process of disc arrays, for interdot distances smaller than the radius of the discs. These authors developed an analytical model to describe the magnetization reversal process of a chain of interacting circular dots (interdot distance equal to 0.1 - 0.6 μm; t = 10 - 60 nm), as depicted in figure 1.13. Particularly, when the applied magnetic field was reduced, it was observed the initiation of the vortex nucleation in the two dots located at the ends of the chain, since they do not have neighbouring dots on one side and, therefore, experience a smaller effective magnetic field when compared to the dots located more centrally in the chain. Then, once a spin-vortex state is nucleated in those discs, the neighbouring discs are subsequently exposed to a reduced effective magnetic field and, consequently, a spin-vortex is more easily nucleated in those dots.

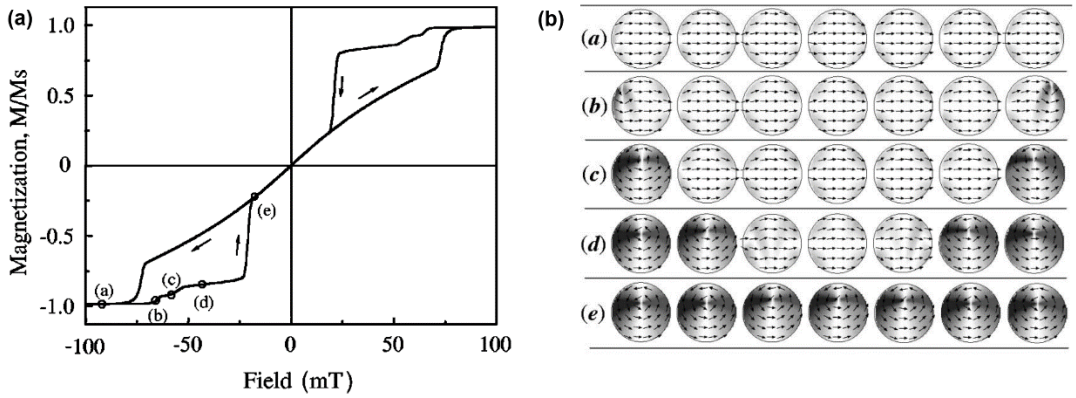

Figure 1.13 - (a) Simulated hysteresis loop for a chain of seven dots presenting an interdot distance equal to 0.4 μm, t = 60 nm, and d = 50 nm; (b) evolution of the spin structure in the simulated dots chain at various magnetic field, indicated by the open circles in figure (a). Adapted from [82]. http://dx.doi.org/10.1103/PhysRevB.65.024414. Copyright 2001 by the American Physical Society.

A similar observation was made by Zhu et al.[68], through the use of MFM. These authors found that the spin-vortex nucleation starts at the chain's edge, where the dots have less neighbouring dots, while the spin-vortex annihilation process is initiated at the centre of the chain, since these central discs experience the largest effective magnetic field, resulting from the contributions by their neighbours.

In the existing literature, more intricate phenomena have been documented. For example, Heyderman et al.[83]. verified that the distance between individual dots within an

array and their specific arrangement can result in the collective rotation of the magnetic spins (figure 1.14). In this work, the authors proposed that instead of a spin-vortex forming in each individual dot, a flux closure could occur through a series of dots, so as to minimize the magnetostatic energy.

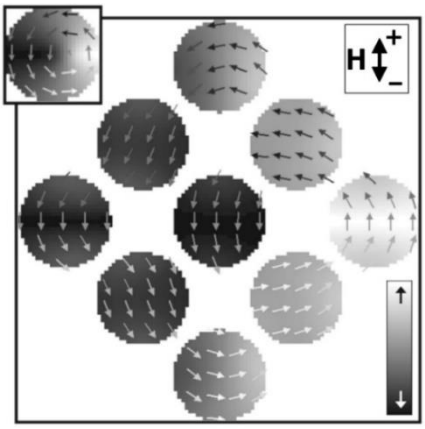

Figure 1.14 - Visual representation of a micromagnetic simulation demonstrating a flux closure through a Ni dot array, where the interdot distance is equal to 50 nm, t = 16 nm, and d = 20 nm. The inset represents the vortex state formed in an isolated dot. Reprinted from [83], with the permission of AIP Publishing.

Furthermore, Neal et al.[84] addressed the magnetization reversal of epitaxial Fe (1 0 0) discs with d = 2 μm, utilizing scanning Hall probe microscopy and supporting their findings through micromagnetic simulations. As a result, the simulations predicted the occurrence of a double vortex magnetization reversal process. Moreover, by comparing magnetic images with local induction loops at strategically chosen points on the disc, it was observed an agreement with this double vortex magnetization reversal mechanism.

1.1.1.1.3. One-Dimensional Nanostructures

Magnetic nanostructures with higher aspect ratios known as one-dimensional nanostructures, e.g. NWs, NTs, and NRs, are often considered as alternatives to the typical spherical magnetic NPs, because their elongated geometry results in intrinsic anisotropic properties that lead to distinct magnetic interactions.[58] These structures possess a larger surface area-to-volume ratio and exhibit higher magnetic moments, resulting from a prevalent shape anisotropy. Magnetic NWs, in particular, have been a subject of extensive research.[85–87] Segmented NWs have also gained significant attention due to their promising properties and potential applications.[88–91] In this context, numerous researchers have explored the interactions between different layers within the same NW.[92–94]

Regarding the magnetic properties of individual NWs, it has been theorized that for infinitely long cylinders, magnetization reversal primarily occurs in three distinct ways:

coherent rotation, magnetization curling, or magnetization buckling. In this context, it was discovered that the critical size required for a single-domain behaviour, i.e. the maximum size at which magnetization reversal occurs through coherent rotation, is practically independent of both magnetocrystalline anisotropy, as well as length. Instead, it depends solely on the exchange constant and the saturation magnetization and, as a result, is proportional to the characteristic length of the material. Consequently, the specific reversal mechanism adopted by the NW depends on the ratio between its R and the characteristic length of the material (figure 1.15).[86]

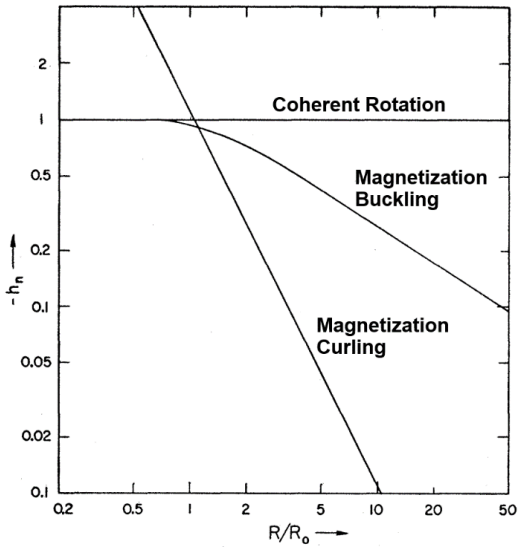

Figure 1.15 - Theoretical plot representing the nucleation field (h_n) of an infinite cylinder as a function of its R. $R_0 = A^{1/2}/I_s$ is the characteristic length of the material (A is the exchange constant and I_s is the saturation magnetization). Adapted from [86]. http://dx.doi.org/10.1103/PhysRev.106.446. Copyright 1957 by the American Physical Society.

Experimentally, Wernsdorfer et al.[95] demonstrated that in Ni NWs, with d's ranging from 40 to 100 nm, the magnetization reversal process is driven by the nucleation and propagation of a single magnetic domain along the nanostructure. Building upon this insight, Ferre et al.[96] proposed that in real systems, even when assuming a weak crystal anisotropy, the reversal behaviour should be described in terms of nucleation-propagation mechanisms. In this study, the authors analysed magnetic properties of electrodeposited Ni and Co NWs with d's ranging from 35 to 500 nm. Consequently, it was found that the intrinsic differences among the magnetization reversal mechanisms result from the interplay between magnetocrystalline and shape anisotropies. Specifically, it was observed that the Ni NWs' weak crystal anisotropy is overshadowed by their shape anisotropy, resulting in an easy magnetization axis aligned along the wire's longitudinal axis. In contrast, the Co NWs exhibit a more complex behaviour due to the significant crystal anisotropy originating from the hexagonal close-packed (hcp) growth of Co, having been verified that the easy magnetization axis of such nanostructures

strongly depends on the orientation of the hcp c-axis. Particularly, in the case of small-diameter Co NWs (d < 50 nm), the hcp c-axis is parallel to their longitudinal axis and, consequently, their behaviour closely resembles that of a single magnetic domain with an easy axis aligned along such direction. On the other hand, for NWs with larger d's, the authors concluded that the c-axis of the hcp structure tends to grow perpendicular to the nanostructure's longitudinal axis, due to the competition between the shape and crystal anisotropies. This leads to the formation of a multidomain magnetization configuration, where each individual magnetic domain is partially oriented along the direction normal to the wire's axis, which explains the decrease in coercivity observed in their measurements. Furthermore, such conclusion is in agreement with the findings reported by Proença et al.[97]

Furthermore, Ferre et al.[96] also demonstrated, using micromagnetic simulations, that the magnetization reversal process in small-diameter Ni wires (d < 50 nm) starts with the nucleation of a reversed magnetic domain at one end of the nanostructure. Moreover, it was verified that this reversed domain has a size smaller than three times the exchange length of Ni. When considering greater d's, the authors described a different mechanism, involving the existence of two critical fields, namely the nucleation field (H_n), which represents the point at which the magnetization of the system deviates from saturation and the magnetic domains start to reorient, as well as the switching field (H_s), which is the threshold at which an irreversible magnetization jump occurs, signifying a full reversal of the magnetic state. Particularly, it was concluded that the deviation from saturation occurs at both ends of the NW, leading to the formation of one magnetization vortex at each extremity, which then propagates along the nanostructure's longitudinal axis. The results of these simulations align with the work conducted by Hertel[98], who also conducted micromagnetic simulations of arrays of closely-packed Ni NWs (d = 40 nm, t = 1 μm, and period = 100 nm). Subsequently, Hertel and Kirschner[99] conducted additional research on the magnetization reversal dynamics of Ni NWs, through the use of micromagnetic simulations. In this study, the authors addressed the basic reversal modes, namely transverse wall and vortex wall, having verified that the first occurred for smaller d's (40 nm), while the latter took place when larger d's (60 nm) were considered. Additionally, simulations involving a cone-shaped Ni NW were performed so as to observe the transition between these two reversal modes and, consequently, analyse the diameter-dependent transition among them.

In another work, Strijkers et al.[100] investigated the magnetization behaviour in Co NWs with two different d's, i.e. 20 nm and 100 nm, through the use of nuclear magnetic

resonance (NMR). As a result, it was verified that when the nanostructure's length was reduced from 40 μm to 0.5 μm, its easy magnetization axis direction changed. Particularly, the longer NWs exhibited an easy axis perpendicular to the nanostructure's longitudinal axis, while for the shorter NWs the direction of such magnetization axis shifted, being parallel to their longitudinal axis. Additionally, the researchers observed that for Co NWs with d = 100 nm, the easy magnetization axis was perpendicular to the nanoarchitecture's longitudinal axis, in contrast to the behaviour of the NWs with d = 20 nm, which displayed a more isotropic behaviour, albeit with a slight tendency for the magnetization to align parallel to the NWs longitudinal axis. Similar results were obtained by Metzger et al.[101]

Regarding Co NWs as well, Pal et al.[102] conducted an analysis on the evolution of the easy axis orientation in those nanostructures as a function of their aspect ratio, i.e. length/d. This study involved both experimental data and micromagnetic simulations, having been verified that for larger aspect ratios (> 10), shape anisotropy represented the main contribution to the magnetic anisotropy, resulting in an easy magnetization axis aligned along the NW's longitudinal axis. Conversely, for aspect ratios below 3, they reported that magnetocrystalline anisotropy dominates, causing the easy magnetization axis to be oriented in a direction perpendicular to the NW's longitudinal axis. In the cases where the NW's aspect ratio fell in between these two values, the contributions from two anisotropies were found to be comparable, leading to subtle distinctions between the hysteresis loops along the long and short axes of the NW that are difficult to discern. Moreover, numerous researchers have explored various methods to influence the direction of the easy magnetization axis, not solely by altering the NW's dimensions but also by modifying its composition and investigating how it is influenced by the magnetoelastic anisotropy.[103–105]

A different study, conducted by Pignard et al.[106], analysed the magnetization reversal in Ni NWs with a 22 μm in length and d's of either 35 nm or 75 nm, through anisotropic magnetoresistance (AMR) measurements. This phenomenon leads to changes in the electrical resistivity of the NW as the angle between the directions of the electric current and magnetization is altered and, therefore, can be used as a probe of the orientation of the magnetization relative to the current.

In another work, Nielsch et al.[107] analysed the magnetic properties of periodic arrays of Ni NWs with d's of 30, 40, and 55 nm and a length equal to 1 μm, presenting a constant period of 100 nm. These authors suggested that the magnetic anisotropy of these arrays is a result of the interplay of various effective magnetic fields. Specifically, in cases where

the Ni NWs are compatible with a single domain structure, which is expected for d's lower than 55 nm, three contributions have to be taken into account, namely the macroscopic demagnetization field, which results from the average magnetic charges of the NWs in the array at its surface, the form effect of the individual NW, if magnetized along the pore axis, and the magnetocrystalline anisotropy energy. For such nanostructures, the authors observed an easy magnetization axis aligned with the NW's longitudinal axis. Additionally, it was verified that reducing the NWs' d from 55 to 30 nm resulted in improved hardness and higher coercivity, which was attributed to the reduction of macroscopic interactions between the NWs. Moreover, the domain structure, as represented in figure 1.16, was explained as resulting from an antiferromagnetic alignment. In this alignment, when considering only the nearest neighbour interaction, two out of the six nearest neighbouring NWs exhibit a parallel magnetization, while the remaining four display an antiparallel magnetization.

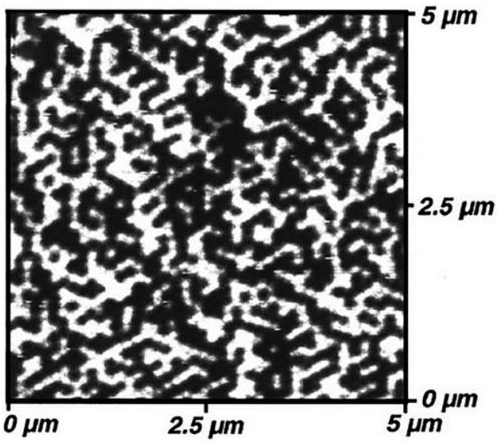

Figure 1.16 - MFM image of a periodic array of Ni NWs, with d = 40 nm, in the demagnetized state. Light regions: magnetization pointing upward; dark region: magnetization pointing downward. Reprinted from [107], with the permission of AIP Publishing.

Carignan et al.[103] also investigated the magnetic properties of Ni NWs arrays, composed of nanostructures with d's of 20, 40, and 170 nm. The hysteresis loops of these three types of arrays revealed an easy magnetization axis parallel to the NW longitudinal axis, along with a decreasing coercivity and remanence as d increased. This finding aligned with the observations made by Nielsch et al.[107]. Moreover, the authors observed differences in the hysteresis loops of the various arrays, which were attributed to the occurrence of different the magnetization reversal processes (figure 1.17). Particularly, for the NWs with a d of 20 nm, it was stated that magnetization reversal proceeds by coherent rotation, whereas in the d = 170 nm NWs such process occurs through a curling mode. The d = 40 nm NWs, on the other hand, have a magnetization reversal process that is at the transition between these two modes.

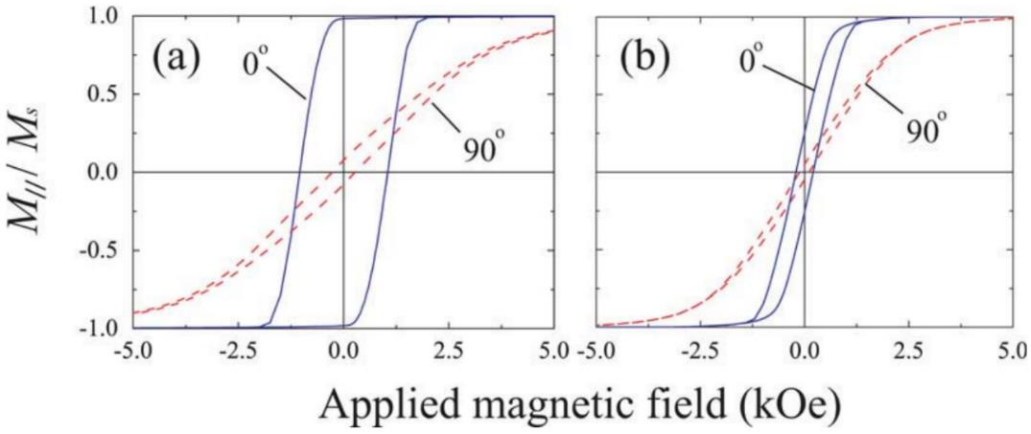

Figure 1.17 - Measured hysteresis loops of Ni NWs arrays involving nanostructures with a d of (a) 20 nm and (b) 170 nm, considering the external magnetic field parallel (0º) and perpendicular (90º) to the NWs' longitudinal axis. From [103]. © 2009 IEEE.

Regarding Fe NWs, Xiang et al.[108] investigated their magnetization reversal mechanisms, through micromagnetic simulations of individual Fe NWs presenting various lengths (20 - 1000 nm) and d's (6 - 50 nm). As can be observed in figure 1.18, different reversal mechanisms can occur depending on the nanostructure's diameter. Specifically, for the two lowest d's [figure 1.18(a) and figure 1.18(b)], the authors identified coherent rotation as the mechanism of magnetization reversal. For the NW with a d of 20 nm [figure 1.18(c)], it was verified that the reversal is associated with a vortex-like nucleation, which initiates at the two extremities of the NW. Regarding the nanostructure with the largest diameter [figure 1.18(d)], its magnetization reversal mechanism was found to be controlled by the buckling-like motion of larger vortices, not only occurring at the ends of the NW but also initiating in its middle sections.

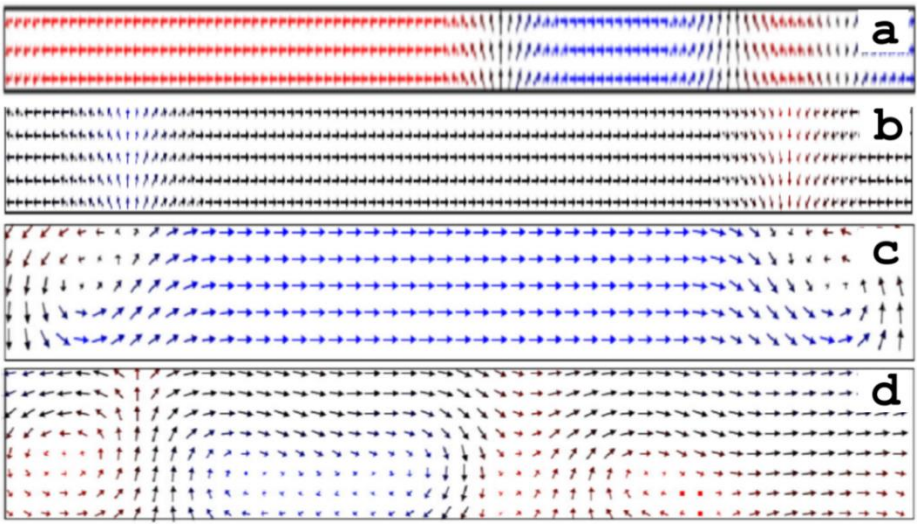

Figure 1.18 - Vector map of the spins' configuration at the moment the reversal is triggered in Fe NWs possessing a length of 200 nm and a d of (a) 6 nm; (b) 10 nm; (c) 20 nm; and (d) 30 nm. From [108]. Copyright 2011 IOP Publishing Limited (IOP) under the terms of the Creative Commons Attribution (CC BY) license.

Experimentally, Qin et al.[109] studied the magnetization reversal in arrays of Fe NWs presenting d's of 30, 50, as well as 70 nm, and with a period of 100 nm, having obtained results that align with the findings reported by Xiang et al.[108] These authors also addressed the influence of the magnetic interactions in a periodic array. As a result, it was verified that these interactions led to a reduction of the shape anisotropy effect, as they contributed to the development of an easy magnetization axis perpendicular to the nanostructure's longitudinal axis, while the NW's shape anisotropy contributed to an easy axis parallel to the nanoarchitecture's long axis (figure 1.19).

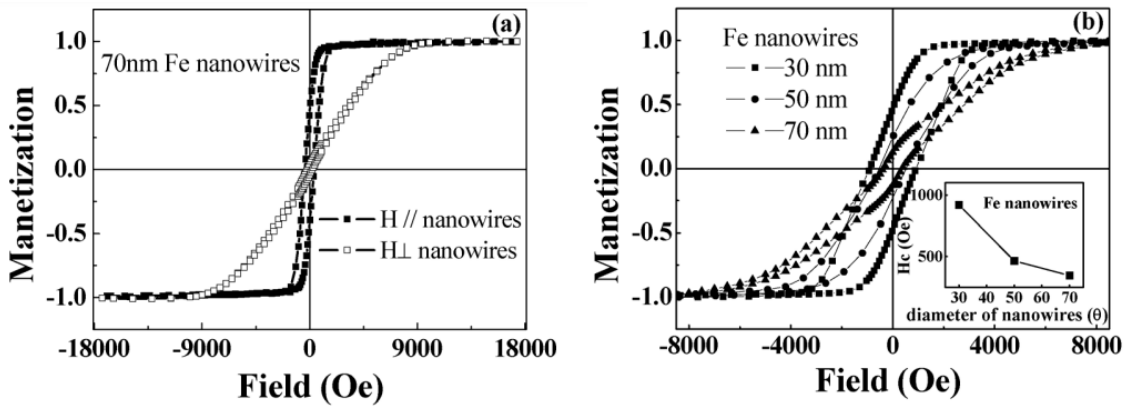

Figure 1.19 - (a) Hysteresis loop of a Fe NWs array, with d = 70 nm, considering the applied external magnetic field parallel (H//) or perpendicular (H⊥) to their longitudinal axis; (b) hysteresis loops for different Fe NWs arrays, possessing various diameters, obtained by applying the applied external magnetic field parallel to their longitudinal axis. Inset: coercivity (Hc) as a function of the NWs' diameter. From [109]. © 2012 IEEE

In another work, Ivanov et al.[110] conducted an extensive series of micromagnetic simulations of both isolated and arrays of NWs based on Py, Ni, Fe, and Co. These authors varied the d of the NWs within the range of 20 to 100 nm, while keeping a fixed length of 20 μm. Here, three main magnetization reversal modes were identified, namely coherent rotation, which involves a uniform rotation of the magnetization along the NW, transverse domain wall, which involves the nucleation and propagation of a domain wall oriented perpendicularly to the NW's longitudinal axis, and vortex domain wall, where a vortex-like domain wall is formed and propagates along the NW length. Furthermore, it was verified that, as the NW's d increases, the transition between the transverse and vortex domain wall modes depends solely on the material that composes the nanostructure, mainly its exchange length. On the other hand, the simulated hysteresis loops for individual NWs and arrays of 7 coexisting NWs revealed that, except for Co, the orientation of the nanostructure's easy magnetization axis did not significantly depend on its d, remaining parallel to the long axis of the NW. Moreover, it was observed that for all the considered NWs, the coercivity decreased as their d increased, which can be attributed to the scaling of shape anisotropy with the aspect ratio, i.e. length/d.

Regarding Co NWs, the orientation of the magnetocrystalline anisotropy with respect to the NW's longitudinal axis was found to impact their effective anisotropy. This led the authors to suggest that the magnetic properties of these nanostructures can be adjusted by controlling the crystal growth direction, or their composition (for NWs composed of Co-based alloys).

1.2. Fabrication of Nanomaterials

As technology and science develop, humanity not only has been improving their life quality, but has also been gaining a better understanding of the universe.[111,112] This evolutive process has led to a growing interest on the ability to fabricate, manipulate, and study structures at the nanoscale, since it is at that level many unique effects appear and most biological processes occur.[113–116] Such interest on the nm range, has led to the development of multiple techniques and equipment capable of improving our ability to comprehend, as well as employ, the distinct phenomena arising at this scale.[117]

The capacity to synthesize nanomaterials with an uniform and controlled shape and size, has led to their application in various fields.[118] Currently, there are multiple nanofabrication processes, which can be divided into two main categories: bottom-up and top-down (figure 1.20).[119] In the top-down approaches, the starting point is a bulk material, whose size is then reduced down to the nanoscale, examples include nanolithography and laser ablation.[120-122] These techniques offer various advantages, such as the fact that they can be used with a wide range of materials and also allow the control of the building units, which permits the creation of complex shapes.[123,124] Nonetheless, this type of methodologies come with a significant drawback: they have substantial costs, being required state-of-the-art nanofabrication facilities as well as time-intensive procedures to produce nanostructures on a large scale.[125,126]

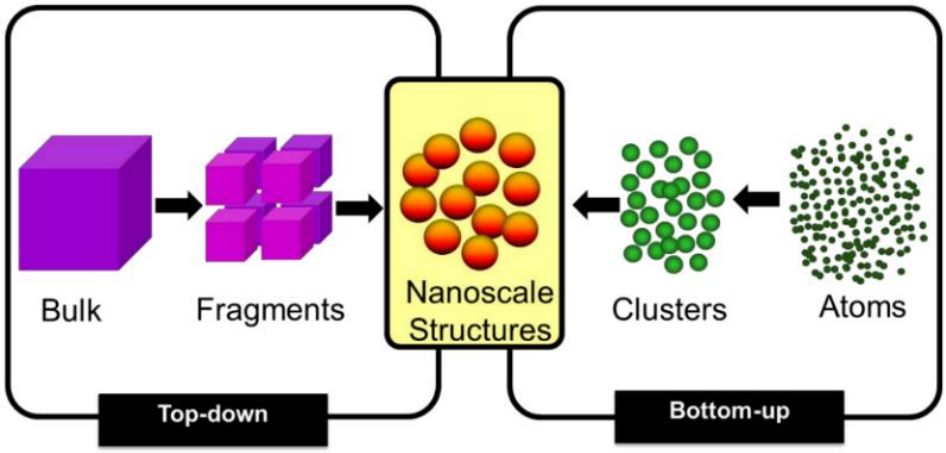

Figure 1.20 - Top-down versus bottom-up nanofabrication approaches. From [127]. Copyright 2015 Authors licensed under a Creative Commons Attribution (CC BY 3.0) license.

On the other hand, the bottom-up approaches utilize individual atoms or molecules as the foundational building blocks, resulting in a more precise and efficient synthetization process, while allowing a reduction of the production costs.[128–130] However, the range of materials that can be used in these methodologies is more limited, when compared to top-down strategies, and it is more difficult to control the assembly process through these techniques.[123,131] Nowadays, there are various fabrication strategies classified as bottom-up, such as co-precipitation in solution or electrochemical deposition.[132,133]

In this thesis, all the nanofabrication processes used are classified as bottom-up and, in the following sections, they will be described in detail.

1.2.1. Microwave-Assisted Co-Precipitation

Microwave-assisted co-precipitation is a versatile, non-expensive, simple, and quick nanofabrication technique employed multiple fields, which allows the synthetization of nanomaterials with easy control over their size, morphology, and composition.[134] In the particular case of SPIONs fabrication, iron oxides are synthesized by the co-precipitation of Fe^{2+} and Fe^{3+} aqueous salt solutions through the addition of a base, followed by controlled microwave heating, where microwave irradiation is used to heat a reaction mixture containing the iron oxides.[135,136]

Similarly to all forms of electromagnetic radiation, microwave radiation can be separated into both an electric field component and a magnetic field component.[137] When a given sample is exposed to such radiation, its electric component leads to an accelerated heating of the material due to a phenomenon known as dielectric heating, which involves two main heating mechanisms, namely dipolar polarization and ionic conduction.[138,139] Regarding dipolar polarization, the dipoles present in the sample attempt to align themselves along the direction of the electric field component associated with the microwave radiation. However, since that electric field is continuously oscillating, those molecular dipoles are always realigning themselves, following those oscillations. As a result, this leads to energy loss through molecular friction and rotation, as well as by dielectric loss, originating a heating of the sample.[140,141] Naturally, this heating effect is negligible if the involved dipoles align too fast with the electric field, which happens when the electromagnetic radiation has a low frequency, or if they are not capable of realigning themselves, which is the case when the electric field frequency is too high.[141] On the other hand, the ionic conduction heating mechanism involves the oscillation of ions in a solution, due to the presence of an alternating electric field associated with the microwave radiation, causing the ions to collide with their surrounding molecules or atoms. This causes a temperature increase in the sample, due to the loss of energy as

a result of the collisions and frictions.[140,142] Between these two mechanisms, the latter leads to a stronger heating effect in comparison to dipolar polarization.[141]

Compared to other fabrication methods of SPIONs, this strategy has some advantages, since the microwave energy is only transferred directly to the reaction components susceptible to microwave polarization. This leads to an enhanced energy efficiency, because only the reaction mixture is heated, eliminating the necessity to heat any reaction vessels, as opposed to other traditional heating methods. Therefore, due to this directed heating, the process of heating the reagents occurs significantly more rapidly compared to conventional methods. Consequently, the time required for the reaction to reach its activation energy is minimized, considerably shortening the overall reaction time. Additionally, this approach offers the advantages of diminishing undesired side reactions and by-products, as well as producing an internal homogeneous heating that promotes the nucleation throughout the entire sample at the same time, which diminishes the growth possibilities of the generated nuclei, resulting in the production of uniform particles possessing lower dimensions.[138,143,144]

1.2.2. Template-Assisted Methods

The fabrication of ordered arrays of one-dimensional nanostructures, e.g. NWs and NTs, has been drawing notable attention, due to the fact that they can be used for relevant applications, including catalysis, sensors, electronic devices, as well as energy harvesting and storage.[145,146] One of the simplest, and therefore most attractive approaches for the production of these arrays are template-assisted methods, where a material with cylindrical nanopores is used as a mask, or template, and then the desired material is grown inside those nanoholes through techniques such as, sol–gel, electrodeposition, or chemical vapor deposition.[146–148] With this bottom-up approach it becomes possible to precisely and easily control the size, as well as the shape, of the obtained nanostructures without costly equipment or time consuming processes.[146,149]

1.2.2.1. Nanoporous Anodic Aluminum Oxide (AAO) Templates

When Al is exposed to air, it is quickly coated by a passivating oxide layer with 2-3 nm in thickness, which prevents further surface oxidation. Based on this process, Buff showed, by 1857, that the electrochemical oxidation of aluminium in an aqueous solution, i.e. anodizing electrolyte, produced an oxide layer thicker than the natural one.[150–152] This process is based on maintaining a delicate equilibrium between two opposing electrochemical reactions driven by an electrical field: oxide formation at the metal/oxide (~60 %) and at the oxide/electrolyte interfaces, and oxide dissolution at the

oxide/electrolyte interface. These electrochemical processes can be summarily described as follows:[153–157]

- Oxide formation: $2Al(s) + 3H_2O(l) \rightarrow Al_2O_3(s) + 6H^+(aq) + 6e^-$ (1.5)
- Oxide dissolution: $Al_2O_3(s) + 6H^+(aq) \rightarrow 3Al_3\,(oxide) + 3H_2O(l)$ (1.6)

Such process became generally known as anodization, since the Al to be oxidized composes the anode within the electrolytic cell.[152] Over time, such technique has been widely employed in industrial scale applications, including, for example, Al cookware, vehicles, and electronic devices.[88,152]

This anodization process can produce two types of anodic aluminium oxide (AAO), also known as anodic alumina, films on the material surface, principally depending on the anodizing conditions, namely nonporous barrier-type oxide film and porous-type oxide film.[158,159]

This last type of oxide film (figure 1.21) has been attracting significant attention in the context of nanotechnology, because it constitutes an economic approach that facilitates the self-organized production of nanostructures, without requiring expensive lithographical tools, like, for example, e-beam lithography.[160]

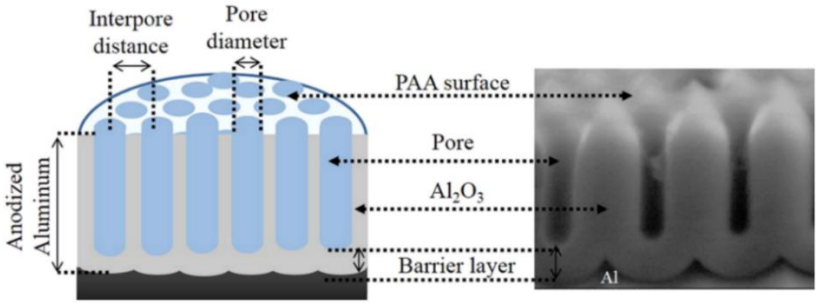

Figure 1.21 - Schematic illustration of a hexagonally packed nanopores array, in an AAO membrane, correlated to its cross-sectional view obtained by scanning electron microscopy (SEM). Reprinted from [88], with the permission of AIP Publishing.

As shown in figure 1.21, the hexagonally packed, similarly sized, and high aspect ratio nanopores, serve as a three-dimensional mask, which can be combined with various deposition procedures, namely electrodeposition, in order to fabricate ordered arrays of NWs or NTs.[146,161] Additionally, the d and length of the produced nanoarchitectures, as well as the distance between two neighbouring structures, can be controlled by modifying the template dimensions, which is achieved through changes in the anodization regime.[152,162]

Such aspects, have made nanoporous AAO templates a common choice for the fabrication of one-dimensional nanostructures.[162]

1.2.2.1.1. Two-Step Anodization Process

Al anodization can be performed by either applying a constant current or a fixed potential across the electrolytic cell, corresponding to galvanostatic or potentiostatic anodization modes, respectively.[163] Regarding the first, its main advantage is that the electric field does not change throughout the reaction, which results in a constant and controlled effective reaction rate, leading to a more controllable process that provides more reproducible templates.[164–166] On the other hand, under the same anodization conditions, potentiostatic anodization leads to the formation of AAO templates with a higher nanopore density and, furthermore, it allows an improved control over the uniformity and aspect ratio of the nanopores, since there is a linear relation among the applied voltage and the resulting AAO structural parameters, such as pore diameter, interpore distance, and the barrier layer thickness.[166,167] Consequently, this approach was the one selected for the experiments performed in this work.

During potentiostatic anodization of a given Al substrate, the process can be precisely controlled in real-time by monitoring the current density curve, j(t), throughout its duration.[168] An example of a typical j(t) curve representing a successful potentiostatic anodization of an Al substrate is represented in figure 1.22.

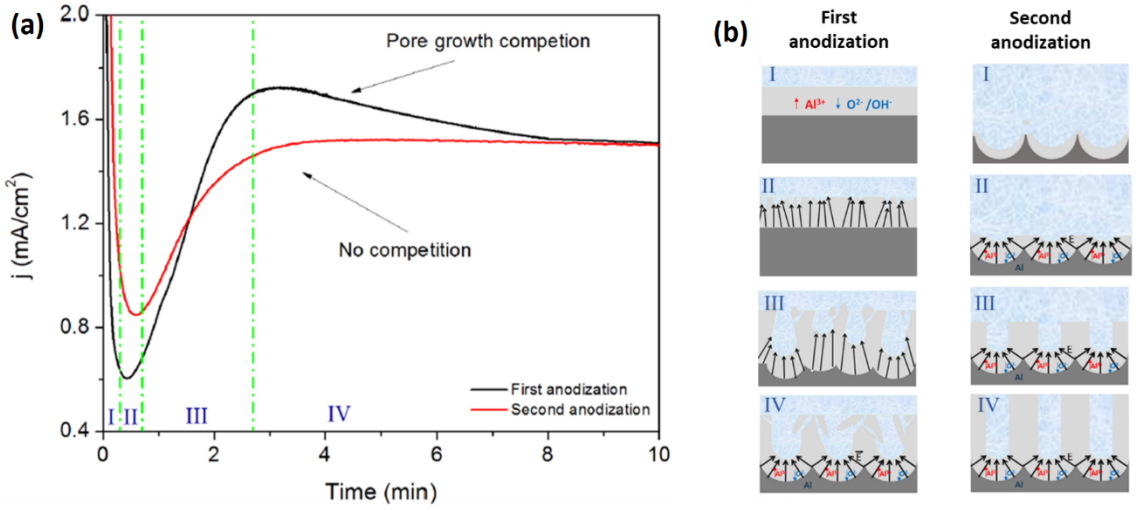

Figure 1.22 - (a) Current density, j, as a function of time for the first and second anodizations; (b) schematic representation of the AAO structure during the first and second anodizations. The roman numerals indicate the different phases of the anodization process identified through the current density curves. Adapted from [93]. Copyright 2018 Authors licensed under a Creative Commons Attribution (CC BY 4.0) license.

As can be observed, the j(t) curve has a characteristic shape, which can be divided into four stages, each representing a different phase of the Al anodization process.[169] In the

first stage, it is possible to verify a steep decrease of the current density, which corresponds to the formation of a high resistivity (> 10^9 Ω·cm) continuous AAO layer over the entire Al substrate's area.[88] This occurs because, in this phase, the oxide formation if faster than its dissolution, which can be attributed to the fact that metal surface is unstable and the electrolyte is in direct contact with it, as a result, oxygen ions can readily diffuse to the metal's surface to participate in the oxidation reaction.[166]

By maintaining a constant potential, the AAO thickness continues to increase and, consequently, the resistance gets higher, causing a reduction of the current density over time.[170,171] This leads to a lower the oxide formation rate as the time needed for the reactant species to diffuse throughout the entire barrier length is significantly longer.[172] Then, the decreasing trend in the current density stops and a minimum value is observed, which corresponds to the second stage.[173] During this phase, the electric field becomes more concentrated on imperfections that exist in the spontaneously formed barrier oxide layer. These imperfections consist of defects, impurities, or indentations that lead to an oxide layer with a non-uniform thickness. They can result from irregularities on the surface of the Al substrate and/or, for electrolytes with a pH lower than 5, from the considerable flow of Al^{3+} ions into the electrolytic bath that leads to areas where the formation of new oxide at the oxide/electrolyte interface is unstable, originating a thinner oxide layer in random spots.[157,173] As a result, the electric field lines converge at these regions where the oxide layer is thinner, which causes a localized heating due to electrical power dissipation resulting from the current increase.[88] Consequently, the oxide dissolution rate in those regions is increased, leading to the formation of numerous hemispherical depressions that correspond to the pore nucleation sites.[157] Therefore, the minimum observed during the second stage in the current density curve represents that an equilibrium between the oxide formation and its dissolution was achieved.[173]

Then, the current density increases towards a local maximum, corresponding to the initial stage of pore-nucleation and growth (third phase).[174] During this stage, the small concavities formed in the previous phase continue to grow deeper, since the electric field inside those formations is much larger than in the flat regions, leading to the development of multiple pore channels, which represent ionic conduction paths. Consequently, the system's resistance decreases and, therefore, there is an increase of the current density.[175] As the anodization time further increases, some pores will be deeper than others and, as a result, will grow faster than the more shallow ones. Moreover, there is a competition between pores for the volume available for oxidation, particularly, when shorter pores are encircled by deeper ones, the oxide layer becomes too thick for the

short pore to continue growing [figure 1.23(a)].[176] Simultaneously, the deeper pores will expand horizontally, leading to the formation of water-drop-shaped pore channels, which are characterized by small pore mouths and large pore bottoms [figure 1.23(b)]. Geometrically, the contact area between the barrier layer and the Al substrate achieves its maximum when the pore bottom has this water-drop-shape. Therefore, the ion current, which traverses the barrier layer, reaches a maximum value.[168,175,176]

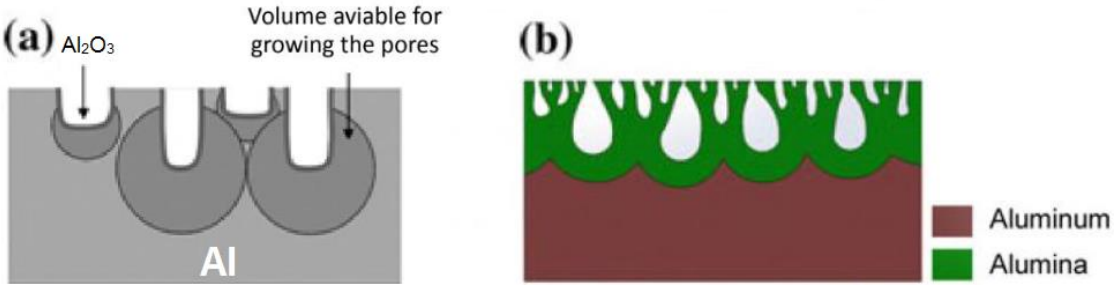

Figure 1.23 - (a) Natural selection mechanism, based on the available volume for growth, of the deeper pores at the expense of the shallower ones. Used with permission of IOP Publishing, Ltd, from [176]; permission conveyed through Copyright Clearance Center, Inc; (b) schematic representation of the water drop-shaped-pores. Used with permission of Springer Nature BV, from [175]; permission conveyed through Copyright Clearance Center, Inc.

Subsequently, the current density decreases, reaching a lower steady value, which corresponds to the fourth stage (figure 1.22). During this phase, the electric field lines become more concentrated at the bottom of the water-drop-shaped pores, as the length of their walls across the pore growth direction become greater. Consequently, the growth process mainly occurs at the pore bottom towards Al substrate, which leads to the development of U-shaped pores from the initial waterdrop-shaped ones. These newly formed pores provide lower contact area between the barrier layer and the Al substrate and, as a result, the current density is slightly reduced. Then, the structure of the pore bottom stabilizes and, consequently, the current density reaches a constant value.[175,177,178] This constant current density represents the existence of an equilibrium between the oxide dissolution and its formation and, therefore, indicates that the nanopores are growing at a constant rate.[88]

Nonetheless, this doesn't necessarily imply that the arrangement at the base of the pore remains constant during this phase, as self-origination of pores is continuously occurring via pore merging, division, and termination.[177] Consequently, throughout this stage an initially disorganized porous structure gradually transforms into a more organized arrangement by a self-ordering process that can extend over hours or even days of anodization.[178] Therefore, the self-ordering process occurs during the growth of the pores, once they have already been initiated.[175]

Then, after a certain period, the current density starts to decrease, which can be attributed to a diffusion limited mechanism.[179] Particularly, the anodization current is primarily associated with the migration of ionic species (such as O^{2-}, OH^{-}, or Al^{3+}) through the oxide layer at the base of the pores. This means that the flow of oxygen-containing anionic species from the electrolyte to the oxide growth interfaces dictates the anodization current.[180] Consequently, as the oxide layer grows, the nanopores get lengthier and, as a result, the diffusion path of those reactant species becomes increasingly longer, which limits their diffusion to the pores' bottom. This leads to a gradual modification of the electrolyte composition in that region as the reactant ions are not replenished at a sufficiently fast pace, which originates a corresponding decrease of the current density.[181–183]

Furthermore, it is important to note that, throughout this process, a continuous barrier layer always exists at the base of each pore. The thickness of this layer is primarily determined by the applied voltage, with minor variations observed based on the specific electrolyte and temperature conditions.[88]

In 1998, Masuda et al.[184] introduced an anodization technique capable of creating a self-assembled, well-organized hexagonal AAO structure. This approach is based on performing an initial anodization for a long time (≥ 16 h) in order to obtain a highly ordered nanopore array at the metal/oxide interface.[88] Then, the resulting oxide layer is removed by wet chemical etching, which originates an Al substrate with periodic concave patterns on its surface.[185] Subsequently, a second anodization is performed under identical conditions and, during this process, the nanoindentations present on the metal surface act as preferential pore nucleation sites.[186] As represented by the red line in figure 1.22 and in contrast to the first anodization, there is no damping in the current density curve when the second anodization is performed. This indicates the absence of competition among the nanopores as they grow, since a self-organized growth regime has already been established.[187,188] As a result, a highly organized nanopores array, possessing a closely packed hexagonal configuration of straight and parallel nanopore channels, is obtained (figure 1.24).[157]

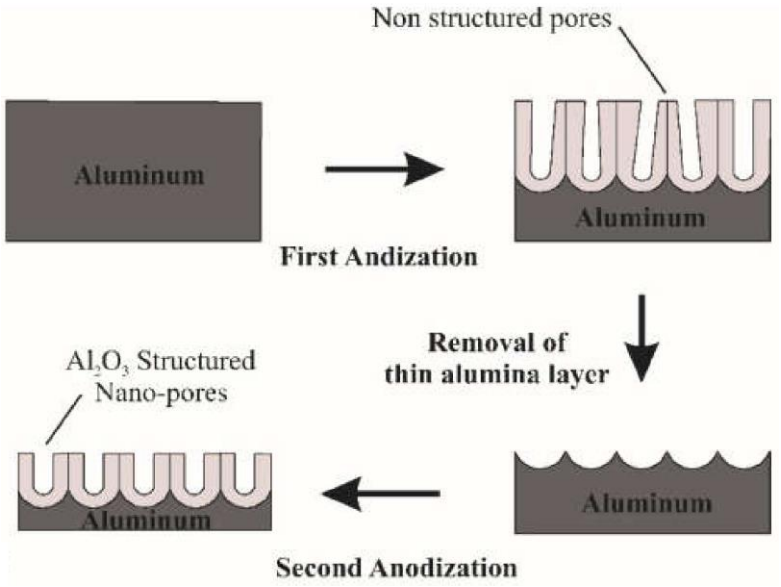

Figure 1.24 - Schematic representation of the two-step anodization process of Al. Adapted from [189]. Copyright 2020 Authors licensed under a Creative Commons Attribution (CC BY 4.0) license.

1.2.2.1.1.1. Non-Steady-State Anodization

The nanoporous templates resulting from the two-step anodization process represent a relatively simple, easy, and affordable way of fabricating one-dimensional nanostructures via electrodeposition. However, since AAO is electrically insulating, the barrier layer at the bottom of the nanopores has to be removed or thinned to a point where the electrons can tunnel through it in order to have a current flow between two current electrodes.[190] Regarding the latter approach, by applying an exponentially decreasing potential, after the second anodization, it is possible to reduce the thickness of such dielectric layer, a method known as non-steady-state anodization.[191] Such process is based on the following linear relation between the AAO barrier layer thickness (δ_b) and the anodization potential (V_{ap}):[192]

$$\delta_b = kV_{ap} \tag{1.7}$$

where k (~ 1.3 nm/V) represents a phenomenological constant.

Specifically, this approach exploits the dependence of the pore diameter on the anodization voltage, i.e. the pore's diameter decreases as the anodization voltage gets lower.[193] Particularly, when the anodization voltage is reduced, the oxide formation rate decreases, since the electric field for driving ions across the barrier layer becomes weaker. On the other hand, the field-assisted oxide dissolution becomes the dominating process, because the local chemical microenvironments at the bottom of the nanopores are not altered. As a result, the barrier layer thickness is reduced and, consequently, the

ionic current starts to increase, which leads to a higher oxide formation rate. Therefore, an equilibrium between oxide formation and dissolution will tend to build up again. In this context, if such balance is achieved before reducing the anodization potential one more time, then the process is called steady-state anodization. On the other hand, if the applied potential is lowered prior to the establishment of that equilibrium, the strategy is defined as non-steady-state anodization. This latter approach is characterized by a current density curve that decreases in a toothed shape as the potential is reduced, as represented in figure 1.25.[193–196]

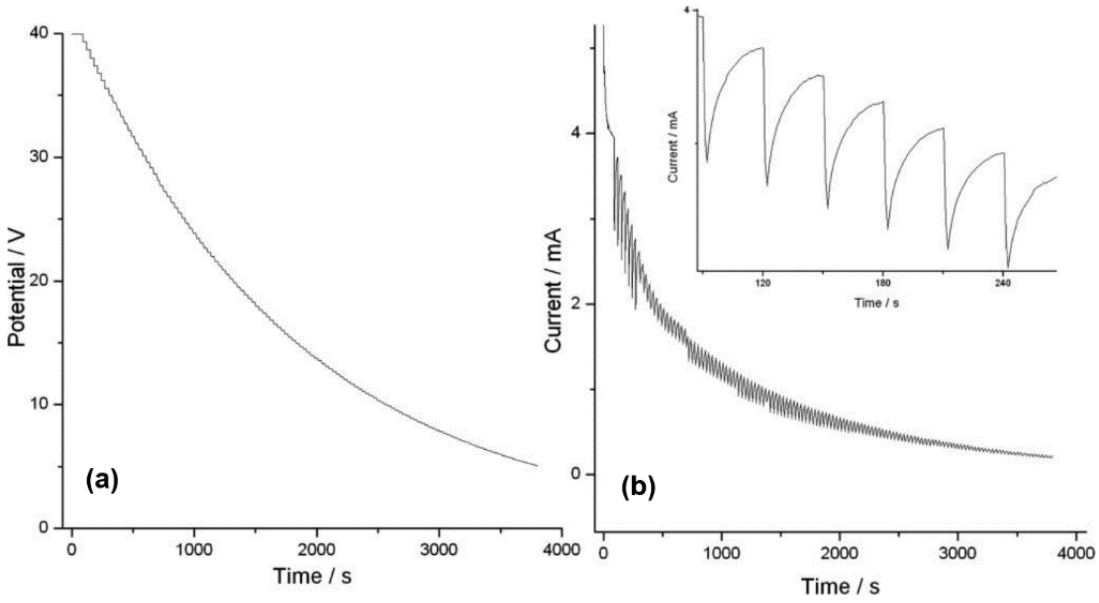

Figure 1.25 - (a) Time-dependent potential and (b) time-dependent current curves obtained during a non-steady-state anodization of AAO. The inset in (b) provides a magnified perspective of a section of the current curve. Used with permission of Royal Society of Chemistry, from [196]; permission conveyed through Copyright Clearance Center, Inc.

Due to the disparity between the formation and dissolution rates of the oxide, an excess of negative charges originating from oxygen-containing species, such as OH^- and $O2^{2-}$, will accumulate within the oxide layer. This buildup of negative charges occurs continually in the context of non-steady-state anodization. Then, when these negative charges reach a certain critical point, partial discharges may occur, giving rise to irregular, branched current pathways within the oxide layer.[196,197] As a result, a reproducible tree-like branched structure (also known as dendritic structure) is formed at the bottom of each nanopore (figure 1.26).[198]

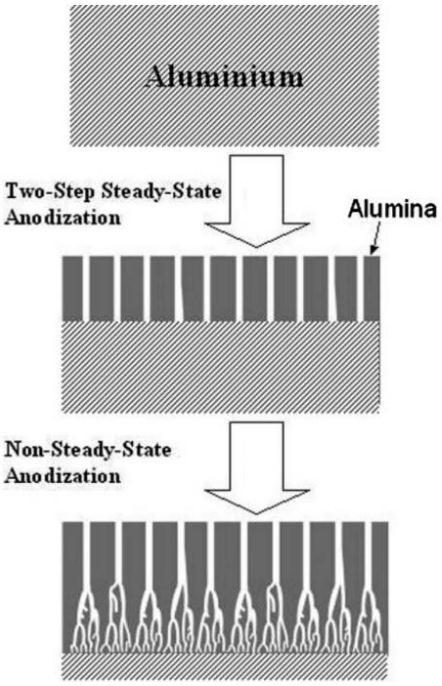

Figure 1.26 - Illustrative diagram depicting the manufacturing procedure of AAO templates with nanopores possessing a dendritic structure at their bottom. Used with permission of Royal Society of Chemistry, from [196]; permission conveyed through Copyright Clearance Center, Inc.

The porosity of the resulting template (P) can be calculated through the following equation:[198]

$$\mathrm{P} = \frac{2\pi}{\sqrt{3}}\left(\frac{\frac{\mathrm{D_p}}{2}}{\mathrm{D_{int}}}\right)^2 \tag{1.8}$$

where $\mathrm{D_p}$ is the pore diameter and $\mathrm{D_{int}}$ represents the interpore distance.

1.2.2.1.2. Hard Anodization

The main disadvantage of producing AAO templates through the previously described anodization regime, also known as mild anodization, is the long processing times, being required several days for fabricating that type of templates due to the low anodization rates (2 - 2.5 μm/h) at the applied potentials.[199] In order to overcome this limitation, a synthesis process known as hard anodization was introduced by Lee et al.[183] as a way to obtain thick nanoporous AAO films with a shorter processing time. This process involves the application of a significantly larger anodization voltage, which leads to considerably higher anodization rates (50 - 100 μ/h), as can be observed in figure 1.27.[183,200,201]

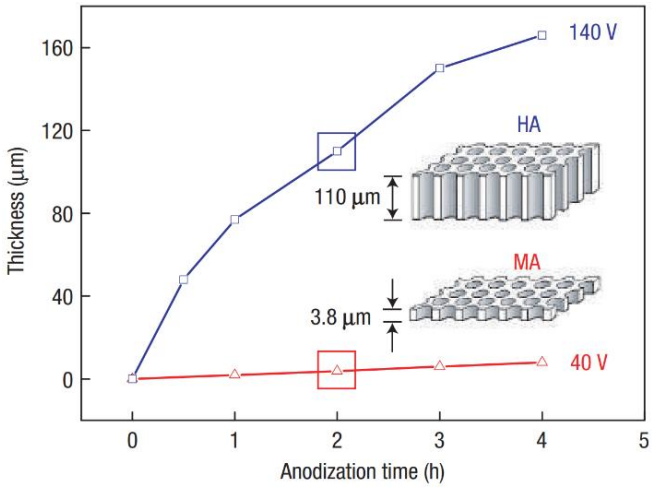

Figure 1.27 - AAO template thickness as a function of the anodization time for a hard anodization (HA) at 140 V (blue line) and a mild anodization (MA) at 40 V, considering oxalic acid as the electrolyte. Adapted from [183]. Reproduced with permission from Springer Nature

The resulting templates exhibit larger pore diameters and interpore distances than the ones produced using mild anodization, when maintaining the remaining anodization parameters unchanged, as those aspects, as well as the barrier layer thickness, have a positive correlation with the applied voltage, whose covariance varies with the considered pH, temperature, and electrolyte (figure 1.28).[202]

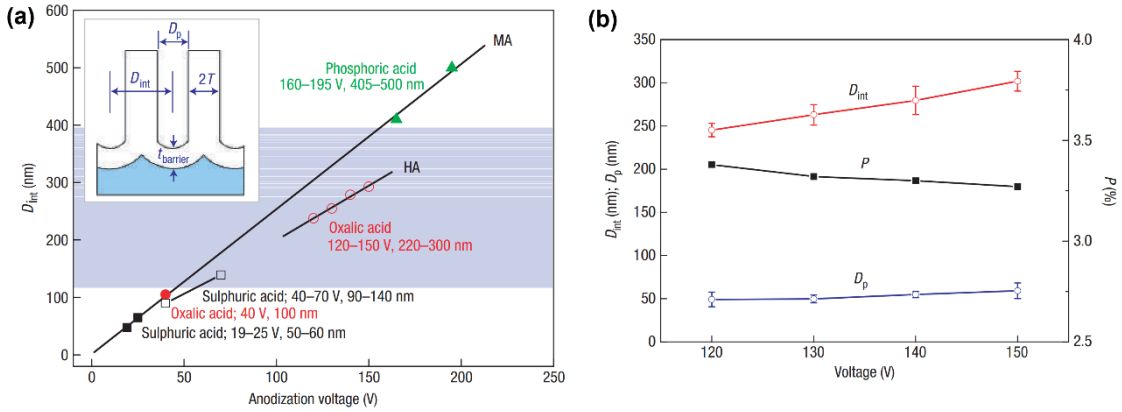

Figure 1.28 - (a) Variation of the interpore distance (D_{int}) with the anodization voltage in a mild anodization (MA) regime (sulfuric, oxalic, and phosphoric acid electrolytes) and in a hard anodization (HA) regime (sulfuric and oxalic); (b) Dependence of D_{int}, pore diameter (D_p), and template's porosity (P) on the hard anodization voltage, considering a 0.3 M oxalic acid electrolyte at 1 ºC. Adapted from [183]. Reproduced with permission from Springer Nature

However, if a high potential is directly applied to the Al substrate, the resulting AAO films are typically cracked due to the high current densities and possess numerous undesirable structural defects.[200] Consequently, in order to enhance the mechanical stability, as well as the structural integrity of the AAO templates produced by hard anodization, a pre-anodization under a mild regime is typically performed first so as to create an oxide layer (t > 400 nm). This initial oxide layer on the surface of the Al

substrate is thought to establish uniform pore nucleation sites during the first phases of high-voltage anodization, thereby preventing localized catastrophic events such as the localized flow of high electrical current.[200,203] Subsequently, the anodization voltage is gradually increased, at a constant rate (0.5 and 0.9 V/s), until a an adequate voltage (60-150 V) for hard anodization is reached, so as to prevent burning the sample.[203,204] After attaining the desired potential, the anodization voltage is kept constant during the time required for obtaining the template with the desired characteristics.[205] Finally, the anodization potential can be reduced to the one used in the pre-anodization step, so as to stabilize the barrier layer at the bottom of the nanopores.[93]

1.2.2.1.3. Electrodeposition into AAO Templates

A particularly interesting and useful approach for the fabrication of nanomaterials is a process known as electrodeposition, or electroplating, where an electric current is used to reduce dissolved cations of a given metal from a solution (electrolyte), in order to form a thin coating on a conductive object.[206,207]

Besides nanotechnology, this technique is also used in more contexts, such as decoration, protection against corrosion, and electroforming, since it presents several advantages when compared to other methods, including, for example, high purity and deposition rate, industrial applicability, as well as low costs.[208,209] Consequently, several authors have been studying the electrodeposition of different materials on multiple substrates, having shown that it is possible to obtain different coatings, with distinct characteristics, by varying the electrodeposited material as well as the electroplating conditions and substrate.[210,211]

Nevertheless, in the nanotechnology context, multiple researchers have been studying the electrodeposition of diverse nanostructures, not only for optimizing the electroplating conditions, but also to gain a better understanding about their growth mechanism, allowing the nanoarchitectures improvement as well as the fabrication processes amelioration.[208,212–216] In this context, the electrodeposition of one-dimensional nanostructures into AAO templates has been gaining a significant attention.[62]

A schematic diagram of a general electrodeposition setup for the synthetization of nanomaterials inside AAO membranes is represented in figure 1.29.

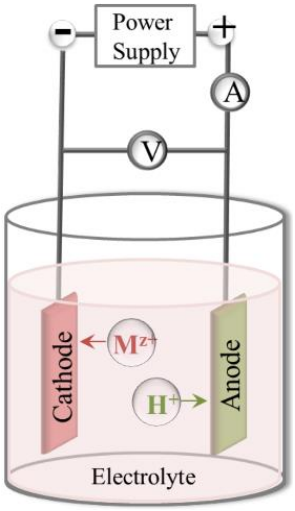

Figure 1.29 - Schematic representation of an electrolytic cell for the electrodeposition of a metal M from an aqueous solution (electrolyte). From [217]. Reproduced with permission from the author.

As can be observed, this process involves two electrodes, namely a cathode (or working electrode) and an anode (or counter electrode).[218] Consequently, during this process, two different electron transfer reactions take place at each electrode-electrolyte interface.[219] Particularly, at the cathode the overall reaction is:[220]

$$M^{z+}_{solution} + ze^- \rightarrow M_{lattice} \quad (1.9)$$

where M^{z+} are the metal ions in the electrolyte and z represents the number of electrons provided by an external power supply. However, electrolytes with complexed ions are frequently preferred for electrodeposition procedures, as they lead to finer-grained deposits and have excellent throwing power, i.e. allow a uniform deposition over a substrate, even when it is has an irregular shape. Additionally, complexed ion electrolytes are particularly useful for the co-deposition of alloys, as the deposition potential of each metal can be brought closer together when they are in a complexed state.[221–223] When performing electrodeposition from complexed ions, a chemical reaction occurs before the electrochemical one, according to:[224]

$$[ML_x]^{z+} \rightleftharpoons M^{z+} + xL \quad (1.10)$$

$$M^{z+} + ze^- \rightleftharpoons M \quad (1.11)$$

where L is a neutral ligand and x represents the number of ligands bound to the metal cation. From these two equations, it is possible to conclude that the complexed ions, i.e. $[ML_x]^{z+}$, are not directly reduced by the applied potential. Instead, they undergo a preceding chemical reaction, as described in the second equation, which transforms them into an electroactive state, M^{z+}. The rate constants associated with this chemical

reaction, which govern the formation and dissociation of the complex, are independent of the electrode potential, being solely determined by the nature of the complex itself. Subsequently, the electrochemically active species, M^{z+}, is reduced by electron transfer.[217,224]

From the equations above, it is possible to conclude that the electrodeposition of a single metal atom requires the transfer of z electrons, which is equivalent to a charge of ze. Therefore, for the deposition of one mole of the metal a total of $N_A ze = zF$ coulombs are required (N_A represents the Avogadro number, $N_A \sim 6.022 \cdot 10^{23}$ mol^{-1}, and $F = N_A e$ is the Faraday constant, F ~ 96485 C mol^{-1}). Such equation can be written as:[225,226]

$$m = \frac{QA}{zF} \tag{1.12}$$

where m represents the mass of the deposited metal (in grams), Q symbolizes the net electric charge passed through the circuit (in coulombs), and A corresponds the atomic weight of the metal. Such equation holds significant importance and finds extensive practical application in the determination, for example, of the quantity of metal deposited in the electrodeposition process or the electrodeposition time required to achieve a specific thickness.[225] Furthermore, when applied to coatings, it can be rewritten as:[225,227,228]

$$h = \left(\frac{V_m}{zF}\right)\left(\frac{I}{S}\right)\tau \tag{1.13}$$

where $h = \frac{m}{Sd}$ represents the deposit thickness (S is the cathode surface area, d is the density of the deposited material), $V_m = \frac{A}{d}$ corresponds to the molar volume of the material, I is the applied current, and τ denotes the electroplating duration. From such equation, it is possible to verify that the current density ($J = \frac{I}{S}$) plays an important role in the electrodeposition process, since it regulates its rate.[229] Moreover, this parameter is the most convenient measure of the rate associated with an electrochemical process, as it can be easily calculated from an ammeter reading and by knowing the cathode surface area (S).[225,229]

Furthermore, the electrodeposition of less noble metals, such as Fe-group metals, is accompanied by a significant hydrogen evolution at the cathode surface, since they have reduction potentials that are generally more similar to that of hydrogen ions, leading to a higher competition for the available electrons.[230,231] The hydrogen evolution reaction can be described as:[232]

$$2H^+ + 2e^- \rightarrow H_2 \quad (1.14)$$

However, when in an aqueous solution, the protons form hydronium ions (H_3O^+) with the water molecules, due to the molecular interaction of water dipoles with electrical charges.[233] The formation of this ion occurs according to the following chemical equation:[234]

$$2H^+ + H_2O \rightarrow H_3O^+ \quad (1.15)$$

This leads to a different mechanism of the cathodic evolution of hydrogen, which consists of two steps:[224]

- First step - charge transfer:

$$H_3O^+ + e(M) \rightarrow MH_2 \quad (1.16)$$

- Second step - hydrogen combination:

$$2MH \rightarrow 2M + H_2 \quad (1.17)$$

where M(H) represents the hydrogen adsorbed at the electrode M.

On the other hand, at the anode an oxidation reaction occurs, which can be represented as:[209,235]

$$2H_2O \rightarrow 4H^+ + O_2 + 4e^- \quad (1.18)$$

Regarding electrodeposition into AAO templates, the mass transport within the nanopores is limited by the diffusion of metal ions to the cathode surface and, consequently, the process is diffusion-limited.[236,237] In this context, different methods have been developed for producing uniform arrays of nanostructures inside those membranes (figure 1.30).[88] Consequently, in the following sections, the most relevant ones will be addressed.

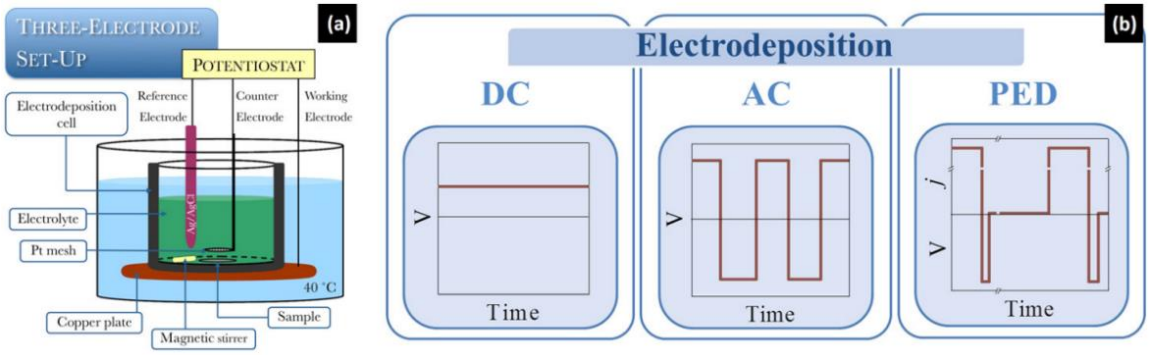

Figure 1.30 - Representation of (a) a three-electrode setup for electrodeposition; and (b) three different voltage-time curves for three distinct electrodeposition strategies (DC: direct current, AC: alternating current, PED: pulsed electrodeposition) that can be used to grow nanostructures inside AAO nanoporous templates. Reprinted from [88], with the permission of AIP Publishing.

1.2.2.1.3.1. Direct Current (DC) Electrodeposition

As previously mentioned, AAO is an electrically insulating material, forming a barrier layer at the bottom of the pores that prevents current flow between two electrodes. Consequently, in order to fabricate nanostructures inside AAO templates by electrodeposition such layer has to be removed or thinned.[196]

In the particular case of direct current (DC) electrodeposition, such barrier layer is removed by a chemical etching process.[238] Therefore, it is necessary to initially create a sufficiently thick AAO template on the Al substrate so that it does not break or dissolve during the template preparation process.[88] Then, this membrane is released from the metal by chemical etching so as to obtain a freestanding membrane and, subsequently, the barrier layer at the bottom of the pores is removed.[239] Subsequently, a thin metallic layer, e.g. Au, is deposited on one of the membrane's surfaces, serving as an electrical contact during the electrodeposition procedure (figure 1.31).[173]

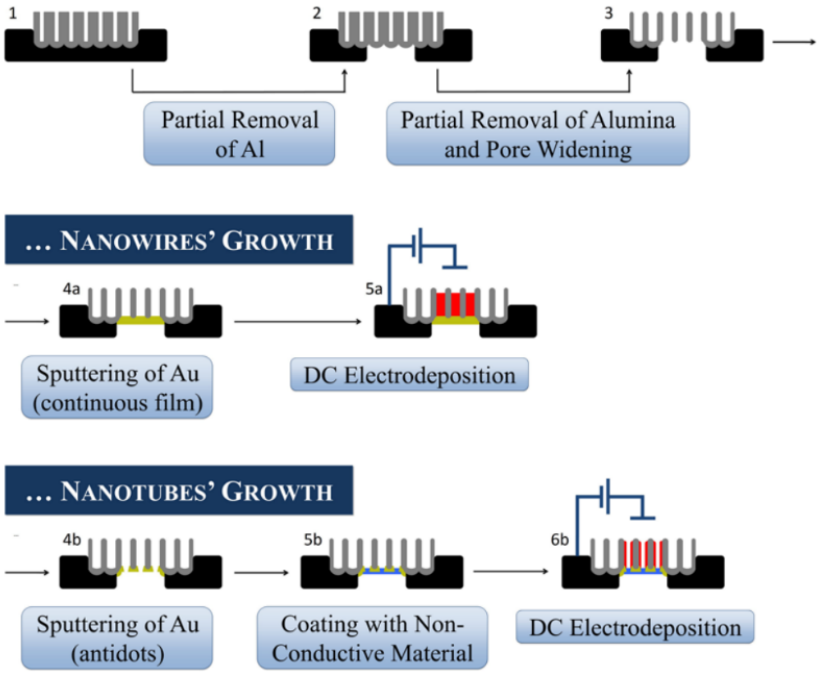

Figure 1.31 - Illustration of the template fabrication process for the synthetization of NWs and NTs through DC electrodeposition. Reprinted from [88], with the permission of AIP Publishing.

After this process, the electrodeposition of nanostructures can be carried out using either a two-electrode system, for galvanostatic methods, or a three-electrode setup, for potentiostatic approaches, in either a static or a pulsed mode.[212,240] The static approach involves maintaining a constant current or potential during the electroplating duration, while in the pulsed strategy a cycle composed of a potentiostatic, or galvanostatic, deposition pulse followed by a rest pulse (0 V/0 mA/cm^2) is repeated during the

electrodeposition process.[241,242] In this last approach, the introduction of a rest pulse permits a renewal of the concentration of metal ions at the deposition interface and limits hydrogen evolution, which allows a more homogeneous growth of the nanoarchitectures.[243] On the other hand, such strategy requires more sophisticated equipment, which translates into higher costs, and it typically involves a more complex optimization process due to the various parameters involved, such as pulse frequency and duty cycle.[242,244,245]

Regardless of the selected approach, the DC electrodeposition process is governed by Faraday's law, i.e. the amount of chemical reaction induced by the electrical current's flow is directly proportional to the quantity of electricity that has passed through the electrolyte, considering the characteristics of the membrane (such as pore size, pore density, porosity, etc.) and the filling efficiency.[88,246] Furthermore, as the nanostructures start growing from the bottom of the template towards its top, it is possible to control their length by simply adjusting the deposition time.[247–249] Additionally, it is also possible to adjust the d of the resulting nanostructures by widening the nanopores through chemical etching.[250]

Moreover, this electrodeposition technique not only allows a considerable control over the composition and crystallinity of the produced nanostructures, but also provides the ability to modulate the composition along the nanoarchitectures' length.[88,251] In addition to these advantages, it is also possible to fabricate tubular nanostructures and tune their wall dimensions through this approach, by adjusting the thickness of the deposited metallic contact.[252,253]

Nevertheless, this electroplating technique has some disadvantages, such as the facts that it is not practical for industry, due to the labour-intensive template preparation process, and its applicability is restricted to thick (> 20 μm) membranes.[198,251]

1.2.2.1.3.2. Alternating Current (AC) Electrodeposition

In contrast to the previous strategy, the AC electrodeposition process does not involve the removal of the AAO layer from the Al substrate after the anodization process (figure 1.32).[254] Instead, the barrier layer at the bottom of the pores is thinned through the reduction of the anodization potential, under either a steady-state or a non-steady-state regime (section 1.2.2.1.1.1.).[255,256] This process allows electrical conductivity to be established as the thickness at the bottom of the membrane is reduced.[257]

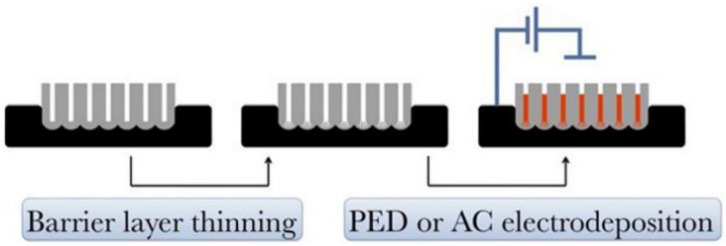

Figure 1.32 - Illustration representing the AC and pulsed electrodeposition (PED) methods. Reprinted from [88], with the permission of AIP Publishing.

Nonetheless, since it is not possible to completely remove the barrier layer, electrical conductivity remains limited, as it acts as the dielectric of a capacitor.[88,258] Therefore, the use of AC deposition with a high voltage and frequency becomes necessary to deposit material inside the nanopores.[259]

Compared to DC electrodeposition, this approach is simpler and can be more easily scaled for industrial applications. Furthermore, it allows to avoid concentration polarization in reverse cycles, leads to lower the Joule heating, and it is possible to control the deposition mechanism by different AC parameters.[260–262] However, it is important to note that the filling percentage of nanopores using AC deposition is typically reduced because of the larger applied voltages in comparison to the DC approach, which results in higher hydrogen evolution that inhibits the deposition process.[263]

1.2.2.1.3.3. Pulsed Electrodeposition (PED)

In order to address the previously mentioned limitations, Nielsch et al.[264] introduced a new electroplating technique known as PED (figure 1.32). This approach involves using the Al substrate as the cathode and applying a modulated signal, composed of three successive potentiostatic and galvanostatic pulses, to plate the desired material from a given electrolyte.[243,265] However, similarly to the previous approach, prior to the deposition process the thickness of the alumina barrier layer present at the bottom of the nanopores has to be reduced. In this case, such process is performed through a non-steady-state anodization, where the anodization potential is exponentially decreased (section 1.2.2.1.1.1.).[236,266–268]

PED has some advantages when compared to other electrodeposition techniques, the main ones being the ability to control the amplitude and duration of the applied pulses, as well as the capacity to implement a rest pulse, like in the pulsed DC approach, while maintaining a relatively simple template synthesis process.[243,264] However, a drawback of this fabrication method is that the resulting nanostructures have a dendritic structure at one end, which modifies their physical properties and is undesirable for biomedical

applications.[266,269] Another disadvantage of this approach is that a constant current density is typically applied to deposit the material, since the resistance of the system varies greatly due to the presence of the oxide barrier layer. This implies that the reaction rate stays constant and the potential (reaction driving force) changes with time, translating into a variation of the NWs composition along their length, when electrodepositing alloys.[270–272] Also, the high potential needed for deposition, due to the presence of a thin oxide layer at the pore's bottom, can lead to a significant hydrogen evolution at the cathode, creating defects along the wire or even inhibiting its growth.[270–272]

1.2.2.2. Interference Lithography Templates

Laser interference lithography is an efficient technique for patterning regular arrays of fine features, whose limits are determined by light diffraction, over a large substrate surface area (cm^2) using relatively short exposure times, without the need for complex optical systems or photomasks.[273–275] This method is based on the interference of two, or more, coherent light beams, which originates a periodic pattern of intensity, i.e. an interference pattern, that is then recorded on a photosensitive material.[276,277] A typical interference lithography setup is represented in figure 1.33.

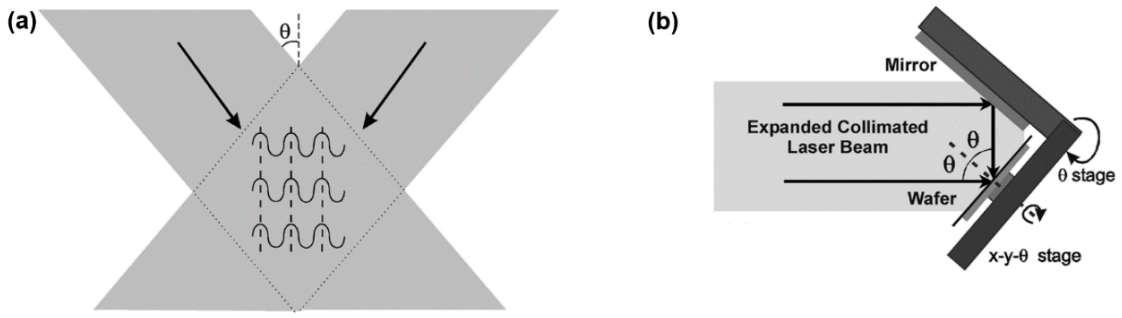

Figure 1.33 - (a) Illustration representing the interference between two coherent beams and (b) scheme depicting a typical interference lithography setup (θ: half angle between the two interfering beams). Adapted from [278]. © 2005 IEEE.

As illustrated the previous figure, the light emitted by a laser illuminates both the mirror and the substrate. As a result, the part of the beam reflected by the mirror interferes with the part that directly illuminates the sample, originating a periodic intensity line pattern that is transferred to a photoresist-coated substrate (figure 1.34) and whose periodicity (p) is given by:[279]

$$\mathrm{p} = \frac{\lambda}{2\sin(\theta)} \tag{1.19}$$

where λ is the wavelength of the light used in the system and θ is the half angle of the two interfering beams. As a result, it is possible to adjust p by changing the angle between the incident beams or, since the mirror and the sample holder are mounted on a rotation stage, by simply rotating that stage. On the other hand, the lateral size of the pattern can be adjusted by controlling the exposure dose.[279,280]

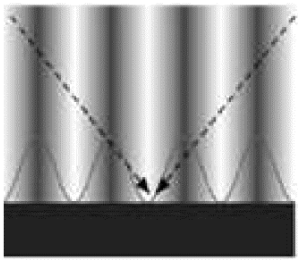

Figure 1.34 - The fringe pattern resulting from the interference between the directly incident beam and the beam reflected by the mirror. Adapted from [279]. Copyright 2018 Authors licensed under a Creative Commons Attribution (CC BY 4.0) license.

Furthermore, it is possible to combine various interference patterns in a single substrate to obtain more complex designs (figure 1.35).

Figure 1.35 - Pattern on a photoresist resulting from the sum of two interference patterns offset by 90º. Adapted from [281]. Copyright 2016 Authors licensed under a Creative Commons Attribution (CC BY 4.0) license.

Following the exposure, the photoresist is developed. This reveals the periodic pattern on top of the substrate, which can be used as a mask for subsequent deposition processes, such as, for example, thermal and electron beam evaporation or ion beam deposition.[279,282,283] As a result, it is possible to obtain an array of nanostructures over a given substrate by combining various interference patterns (e.g. figure 1.35) and, then, depositing the desired materials over the revealed pattern.[279]

1.3. Biomedical Applications of Magnetic Nanomaterials

Nanomedicine is regarded as one of the most significant and emerging areas of modern science, ranging from the application of nanomaterials and biological devices in biomedicine to biosensors.[284,285] Among all the nanomaterials types employed in this field, magnetic nano-objects are among the most promising, since they can exhibit low toxicity, biocompatibility, and inducible magnetic moments, which allow their remote control by the application of an external magnetic field.[286,287] Consequently, there are

various biomedical contexts where these nanomaterials can be employed, such as cellular therapy involving cell labelling and targeting, separation and purification of cell populations, regenerative medicine, targeted drug delivery, contrast agents in magnetic resonance imaging (MRI), magnetic hyperthermia (MHT), or magneto-mechanically induced cell death.[288,289] Furthermore, it is possible to combine diagnostic and treatment capabilities in a single magnetic nano-object, which, as result, can be used as a theragnostic agent.[290] Therefore, in the following sections, the main biomedical applications of magnetic nanomaterials will be addressed.

1.3.1. Magnetic Hyperthermia (MHT)

MHT explores the ability of magnetic nanomaterials to generate heat when subjected to an alternating magnetic field (AMF).[291] When the temperature in the local environment of a tumour is raised to a certain threshold (≥ 42 ºC), the cancer cells suffer irreversible damage, which induces apoptosis and necrosis (figure 1.36).[292,293] Particularly, higher temperatures (> 50 ºC) lead to more necrosis than apoptosis, while the opposite is verified for lower temperatures.[294] Consequently, the principle of MHT is that the heating generated by magnetic nanomaterials under an AMF, in the local environment of a tumour, leads to cancer cell death.[295]

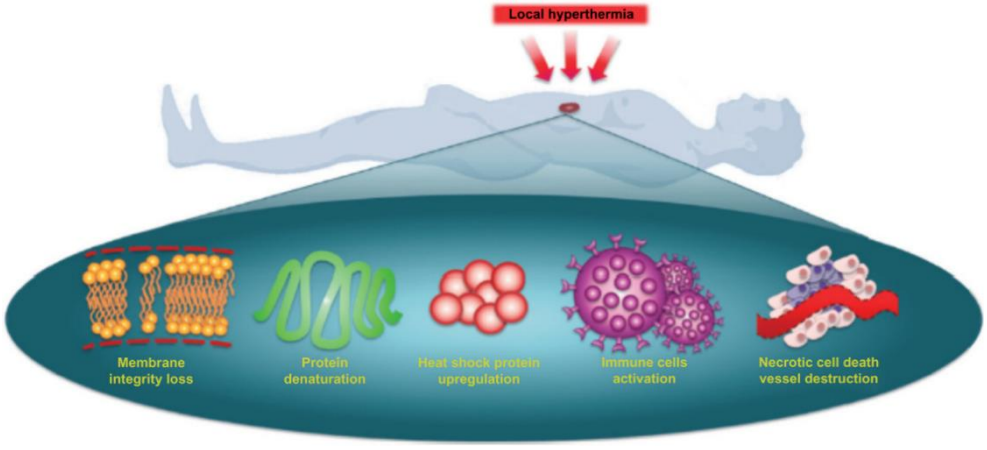

Figure 1.36 - Mechanisms of cancer cell death caused by MHT. From [291]. Used with permission of Elsevier Science & Technology Journals from [291]; permission conveyed through Copyright Clearance Center, Inc.

The capacity to convert magnetic energy into thermal energy has led to the possibility of utilizing magnetic nanomaterials for MHT cancer treatment.[291] Particularly, the heat generated by magnetic materials when subjected to AMF can result from four distinct physical mechanisms, namely hysteresis losses, Néel/Brownian relaxation, eddy currents, and frictional losses in viscous suspensions.[296] In the specific context of MHT, SPIONs stand out as one of the most widely studied and used nanomaterials, principally

due to their simple and low-cost fabrication process, biocompatibility, and zero remanence. The latter is a crucial requirement for the biomedical application of nanomagnets, as it prevents them from agglomerating when dispersed in a solution.[297–300] For this particular type of NPs (typically ferrites), the eddy currents loss is typically negligible due to their reduced conductivity and small dimensions. This last factor leads to a weak induced voltage because of the extremely small size of potential eddy current loops in a NP.[301,302] Moreover, since SPIONs exhibit a superparamagnetic behaviour, their hysteresis losses are negligible or even non-existent. Therefore, the heat produced by this type of NPs is mainly attributed to relaxation losses, which are also related to frictional losses resulting from the viscous resistance encountered by NPs as they rotate within a given medium.[303,304]

The heat dissipation resulting from relaxation losses is a consequence of the energy required to overcome the rotational energy barrier, when SPIONs are exposed to an AMF.[305] In such context, two relaxation processes occur simultaneously, namely Néel relaxation, which is related to internal dynamics of the NP, and Brownian relaxation, which is associated with its external dynamics (figure 1.37).[306] Particularly, the energy loss resulting from Néel relaxation is attributed to the internal friction between the rotating magnetic moments and the crystal lattice, when a particle's magnetic dipole flips between two stable orientations, overcoming an energy barrier. As a result, this relaxation leads to the release of energy in the form of heat, without the physical rotation of the NP [figure 1.37(a)].[307,308] On the other hand, the Brownian relaxation occurs when the NP undergoes a reorientation in response to an external magnetic field, aligning itself with the changes in the direction of its internal magnetic moment. Consequently, when in an AMF, this process leads to the physical rotation of the NP and, as it rotates, energy is dissipated in the form of heat due to friction with its surrounding environment [figure 1.37(b)].[309–311]

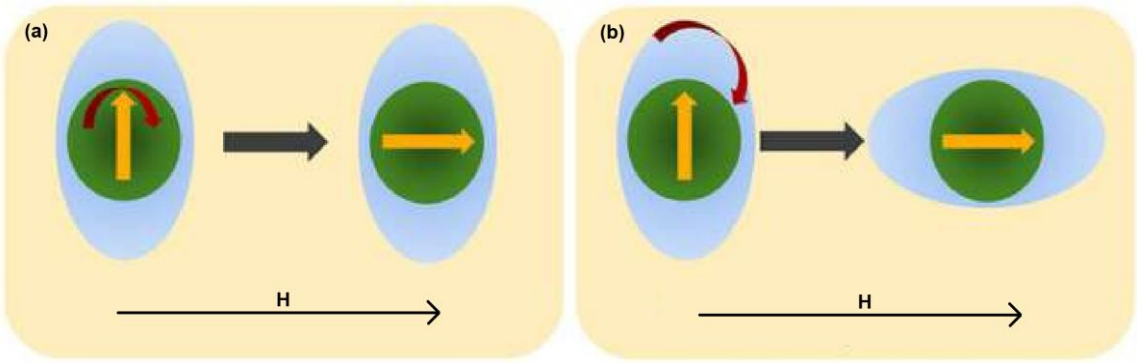

Figure 1.37 - (a) Néel and (b) Brownian relaxation after the application of an external magnetic field, H. Adapted from [312]. Copyright 2022 Authors licensed under a Creative Commons Attribution (CC BY 4.0) license.

These two relaxation processes occur simultaneously; however, one can dominate the heating effects. Nevertheless, it is hard to determine the extent of the contribution associated with each mechanism. Typically, Néel relaxation is dominant in NPs with d's smaller than 20 nm, while in NPs larger than 20 nm the Brownian relaxation, which is also dependent on the viscosity of the surrounding medium, prevails.[304,307,313]

The heating efficiency of magnetic NPs under an AMF is typically evaluated by a parameter known as specific heat absorption rate (SAR), or by equivalent parameters, such as specific loss power (SLP) or intrinsic loss power (ILP).[90] Nevertheless, SAR is the most commonly used figure of merit, being defined as the quantity of heat released by unit mass of the magnetic material, per unit time, during the exposure to an AMF with a defined frequency and field strength.[307,314–316] The SAR is generally expressed in W/g and it is calculated according to the following equation:[317–320]

$$\mathrm{SAR} = \frac{\mathrm{C_{p,s}}}{\mathrm{m_{MNPs}}}\left|\frac{\mathrm{dT}}{\mathrm{dt}}\right|_{\mathrm{t=0}} \tag{1.20}$$

being related to the ILP through the following expression:

$$\mathrm{ILP} = \frac{\mathrm{SAR}}{(\mathrm{f}\cdot\mathrm{H}^2)} \tag{1.21}$$

where $\mathrm{C_{p,s}} = \mathrm{C_{p,d}m_d} + \mathrm{C_{p,MNPs}m_{MNPs}}$ represents the heat capacity of the sample ($\mathrm{C_{p,d}}$: specific heat capacity of the dispersion medium; $\mathrm{m_d}$: mass of the dispersion medium in the analyzed sample; $\mathrm{C_{p,MNPs}}$: specific heat capacity of the magnetic NPs; $\mathrm{m_{MNPs}}$: mass of magnetic NPs present in the considered sample), T stands for the sample's temperature, t is the time, f is the frequency of the magnetic field, and H is its strength.

In order to determine the time derivative of temperature in the previous formula, the dynamic equation that describes the evolution of temperature over time has to be known. This equation can be determined by recording the time evolution of sample temperature. Particularly, considering a completely adiabatic sample holder, the variation of the sample's temperature as a function of time is described by an equation of the form:[320]

$$\mathrm{T(t)} = \mathrm{t}\left|\frac{\mathrm{dT}}{\mathrm{dt}}\right|_{\mathrm{t=0}} + \mathrm{T_0} \tag{1.22}$$

where $\mathrm{T_0}$ is the initial temperature. Nonetheless, in most SAR measurements, non-adiabatic sample holders are typically employed due to the complexities and challenges associated with creating a well-isolated holder.[321] Consequently, in order to minimize the errors that may result from heat losses, SAR is typically determined by the Box-Lucas

method, widely recognized in the literature as one of the primary approaches for determining such parameter.[322–325] This method serves as a figure-of-merit for quantifying and comparing the NPs' heating efficiency, being based on data fitting and analysis and it assumes a non-adiabatic set-up, accounting for convective heat losses.[326] Hence, this is a suitable model for describing the sample's temperature-time relationship that encompasses heat exchanges between the sample and its surrounding environment.[325] The Box-Lucas equation can be formulated as:[325–329]

$$T(t) = A\left(1 - e^{-B\tau}\right) + C \tag{1.23}$$

where A represents the saturation temperature [$A = T(\tau = \infty)$], B is related to the curvature of the heating curve, i.e. the heating rate, and τ corresponds to the AMF exposure time. The product between A and B, at t=0, is known as the initial heat rise rate and it corresponds to the dT/dt ratio used in the SAR formula (equation 1.20), allowing its calculation through the following approach:[326,330]

$$\left|\frac{dT}{dt}\right|_{t=0} = A \cdot B \tag{1.24}$$

$$SAR \approx \frac{m_d}{m_{MNPs}} C_{p,d} \cdot A \cdot B \tag{1.25}$$

The possibility of using SPIONs for MHT cancer treatment was first reported by Gilchrist et al.[331] in 1957. Subsequently, throughout the years several authors have been studying the potential of those and other types of nanomaterials for this therapeutic approach, which has become a new promising alternative for cancer treatment.[291] In this context, some clinical trials have already been performed for glioblastoma, colon cancer, breast cancer, as well as prostate cancer, having been obtained encouraging results.[332-335] Nevertheless, some disadvantages associated with this therapeutic approach, such as limited heat production because of aggregation effects, uneven distribution of magnetic NPs within tumour sites, difficulty in the precise control of heat exposure, as well as safety concerns associated with strong AMF possessing high frequencies, have motivated the development of research with the purpose of improving the traditional MHT approach.[336-339]

A particularly promising strategy involves using the temperature increase as a means to trigger drug release or activate therapeutic molecules at a target site, rather than exclusively focusing on the heating capabilities of magnetic NPs for inducing cell death, when exposed to an AMF.[340] This method involves the use of multifunctional magnetic NPs, which not only can be used for MHT, but can also be loaded with anticancer drugs

and functionalized with specific ligands for targeted drug delivery, among other capabilities (figure 1.38).[341]

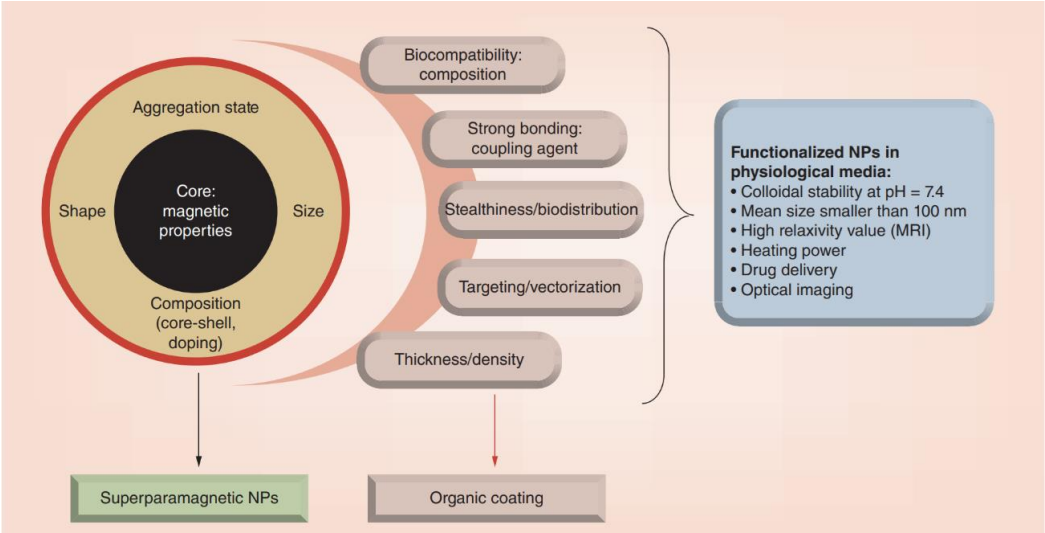

Figure 1.38 - Design of functionalized iron oxide-based NPs suitable for different biomedical applications. Used with permission of Future Medicine Ltd, from [342]; permission conveyed through Copyright Clearance Center, Inc.

In this context, various works have been developed. For example, Gupta et al.[343] reported promising results, in pre-clinical studies, regarding the use of MHT based on anticancer drug-loaded magnetic NPs for the treatment of glioblastoma. The authors indicated that these nanomaterials were able to cross the blood–brain barrier (BBB) when exposed to an AMF, by temporarily reducing the permeability of such barrier. Consequently, they led to an increase in the concentration of anticancer drug at the target tumour site, while, simultaneously, inducing cancer cell death through MHT. Another study, by Jia et al.[344], reported the fabrication of glioma-targeting exosomes with theragnostic capabilities. These extracellular vesicles were produced by first loading SPIONs and curcumin into exosomes, followed by the conjugation of the exosome membrane with neuropilin-1-targeted peptide. As a result, the authors verified that, when administered to glioma cells as well as orthotopic glioma models, these glioma-targeting exosomes were able to not only cross the BBB with ease, but the SPIONs-mediated MHT and Cur-mediated therapy also demonstrated a strong synergistic antitumoral effect, while providing good, targeted imaging. In a different study, Ha et al.[345] fabricated multifunctional SPIONs functionalized with a folate factor for a dual cancer treatment approach, namely MHT in combination with anticancer drug release [doxorubicin (DOX)], at the target site. Here, the authors verified that the heating from the magnetic NPs was sufficient for both effective MHT and triggering drug release. Additionally, *in vivo* studies, considering lung cancer-bearing mice, demonstrated that these NPs had a high efficacy for cancer treatment. More

recently, Beola et al.[346] produced multifunctional lipid-based nanovectors encapsulating SPIONs and anticancer drug, i.e. temozolomide, and tested their suitability for a dual treatment approach of glioblastoma multiforme on an *in vivo* model. As a result, these authors verified that this nanoplatform was able to accumulate at the tumour site, allowing a significant reduction of cancer cell viability when exposed to an AMF, due to the synergy between their MHT and chemotherapeutic capabilities. Furthermore, numerous studies have also suggested that an increase in temperature has additive effect on tumour cell death when certain drugs, such as DOX, cyclophosphamide, ifosfamide, and others, are loaded in multifunctional magnetic NPs.[347]

Besides magnetic NPs, magnetic NWs have also demonstrated potential to act as MHT agents.[348-350] In this context, some theoretical studies have concluded that magnetic nanomaterials possessing larger net magnetic moments, as well as higher magnetic anisotropy, may be more suitable for this biomedical application, since higher SAR values can be achieved at lower sizes, when compared to magnetic NPs.[350] Following on these results, Alonso et al.[350] performed an experimental comparative study on the suitability of FeCo NWs presenting various diameters and lengths for MHT, considering dispersions with a concentration of 0.5 mg-FeCo/ml. From the performed analysis, it was verified that the NWs SAR increases as they get longer (particularly over 10 μm), as represented in figure 1.39, as well as with increasing diameter. Nevertheless, even for the shorter NWs considered in this study, a significant SAR value was observed (up to 350 W/g, at H = 300 Oe and f = 310 kHz vs, for example, 168 W/g, at H = 590 Oe and f = 313 kHz [351]), indicating that these nanostructures are a promising candidate for MHT treatments.

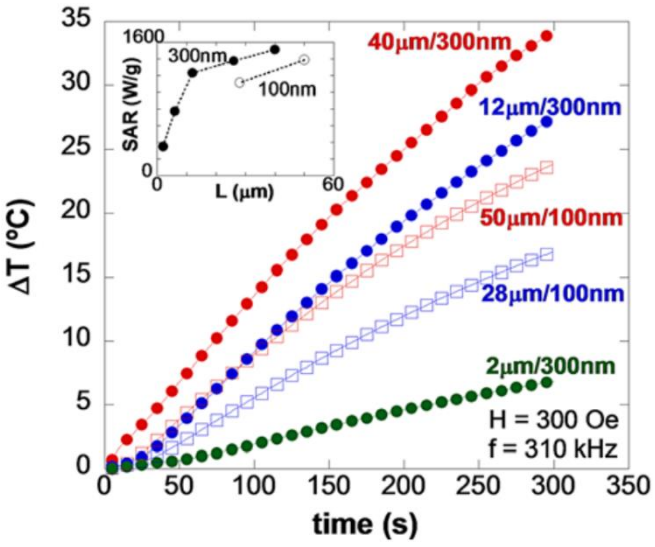

Figure 1.39 - Heating curves for FeCo NWs of varying lengths and diameters, measured through calorimetric methods. Inset: variation of the SAR with the NW's length. Reprinted from [350], with the permission of AIP Publishing.

1.3.2. Cell Manipulation and Separation

Efficient isolation and sorting of particular cells from complex biological mixtures are essential for clinical research, as well as for various cell-based applications in multiple areas, such as cell and molecular biology, biochemistry, and immunology.[352-353] In the clinical practice, the detection and purification of specific cells is fundamental for diagnosing, treating, and preventing diseases, being required, for example, in the acquisition of a particular population for transplantation and gene therapy or to separate stem and progenitor cells for cancer treatment.[353,354]

Over time, multiple cell isolation and manipulation techniques based on physical characteristics, such as density or size, and on electric, magnetic, or adhesive properties of cells, have been developed.[57] The standard processes for separating cellular populations include steps of filtration, density gradient centrifugation, and sedimentation.[57,355] However, when different types of cells have similar sizes or densities, techniques based on those features cannot perform an effective separation.[355] Consequently, other methods, such as fluorescence-activated cell sorting (FACS) and magnetic-activated cell sorting (MACS), where magnetic nanomaterials play a key role, must be used.[57,356]

A common approach involves using core-shell superparamagnetic iron oxide beads, i.e., a nonmagnetic matrix filled with superparamagnetic NPs, coated with antibodies that are specific for the surface antigens of target cells.[355,357,358] In this methodology, the beads attach via antibody-antigen interactions to the cells of interest, located, for example, in a heterogeneous cell population, and, then, these biological entities are separated through the application of an external magnetic field.[362] However, due to the reduced net magnetic moments of the employed NPs, this process frequently requires high external magnetic fields to efficiently isolate the target cells.[57] Therefore, such an approach could be enhanced if the superparamagnetic iron oxide beads were replaced by a nanoarchitecture with a larger net magnetic moment. In this context, ferromagnetic NWs and synthetic antiferromagnetic (SAF) nanostructures have emerged as potential candidates for the improvement of the current magnetic cell separation and manipulation techniques.

Ferromagnetic NWs are promising nanomaterials for this biomedical application, due to their large shape anisotropy (which leads to a single domain structure), tunable remanence, and high saturation magnetization, i.e., the maximum possible magnetic moment per unit volume.[353,359,360] Moreover, various studies on the separation and manipulation of different cell lines, using ferromagnetic Ni NWs functionalized with

antibodies, showed that such nanostructures perform better than the typical superparamagnetic beads of comparable volume, due to their higher saturation magnetization (figure 1.40).[353,361-364]

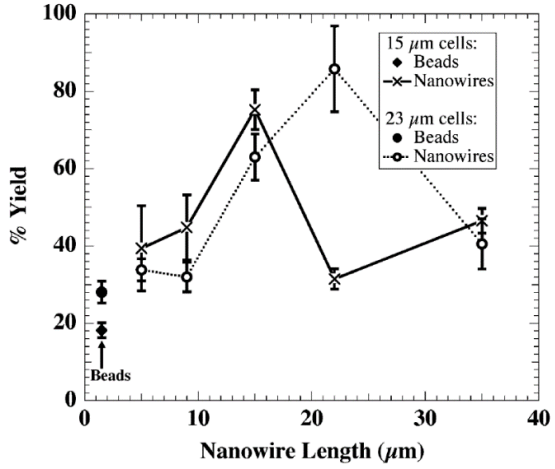

Figure 1.40 - Percentage of the initial number of cells, loaded with magnetic beads or Ni NWs of different lengths, that were captured (% Yield) in the magnetic separation of mouse fibroblast (3T3) populations with average diameters of 15 μm and 23 μm. From [361]. © 2004 IEEE.

Nevertheless, it is crucial to assess the biocompatibility of these nanostructures, due to the potential toxic effects associated with some materials (for example, Ni).[365] In this scope, Byrne et al.[366] studied the cellular response of a human monocytic cell line (THP-1) to Ni NWs, having demonstrated that there were little to no toxic effects on the cells for short incubation periods (10 h) and at low concentrations (< 100 NWs per cell). Felix et al.[367] also addressed this topic, but on human fibroblasts (WI-38). In their work, it was verified that for incubation times shorter than 48 h and at low concentrations of NWs (< 11.88 μg/ml) more than 80% of the cells remained viable; however, for longer periods, a significant decrease in their metabolic activity was observed. Furthermore, considerable toxic effects on the cells occurred mostly after 48 h and at high concentrations of NWs (> 22.5 μg/ml), with cell viability decreasing as incubation time increased.

Consequently, it would be of interest to fabricate and characterize magnetic NWs with similar physical properties but constituted by more biocompatible materials. In this context, Ivanov et al.[359] fabricated and analysed Fe NWs as well as hybrid metallic/nonmetallic NWs, composed of a Fe core and a Fe oxide (magnetite/ Fe_3O_4) shell. Their magnetic characterization showed that both kinds of nanostructures presented a single-domain magnetic state with a longitudinal magnetic anisotropy at remanence. Afterward, a cell viability test (figure 1.41), performed on colon carcinoma epithelial cells (HCT 116), indicated that these nanostructures have a high level of biocompatibility. Moreover, it was also proved that the coercive field, as well as the

saturation and remanent magnetizations, of the core-shell NWs can be tuned by varying the oxidation time, i.e. changing their shell thickness.

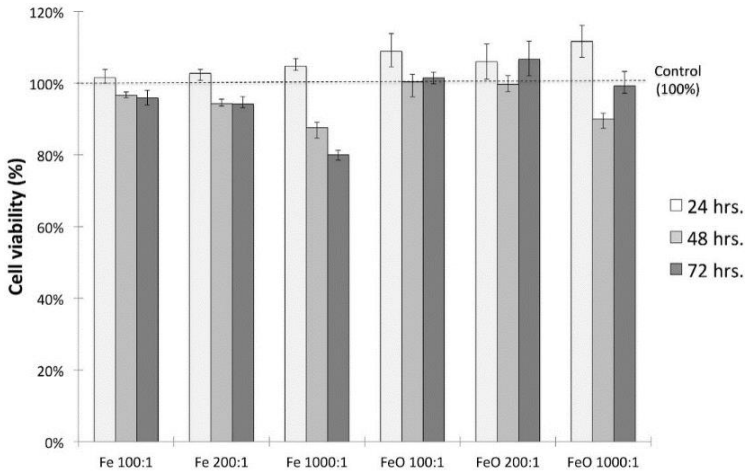

Figure 1.41 - Percentage of viable HCT 116 cells after incubation with different concentrations of Fe and Fe-Fe_3O_4 core-shell NWs for 24, 48, and 72 h. The concentrations on the x-axis indicate the NW-to-cell ratio. From [359]. Copyright 2016 Authors licensed under a Creative Commons Attribution (CC BY 4.0) license.

Additionally, Alsharif[368] and Alsharif et al.[369] studied the toxicity of functionalized Fe NWs, with longitudinal magnetic anisotropy, in leukemic cells (HL60). In these cases, the considered magnetic nanostructures (average diameter of 35 nm and around 3 μm in length) were coated with bovine serum albumen (BSA), Fe-BSA NWs. Then, the BSA-coated NWs were functionalized with a specific antibody (anti-CD44) that targets a surface marker (Cluster of differentiation 44; CD44) overexpressed on leukemic cells, Fe-BSA-CD44 NWs. Subsequently, after the incubation of the one-dimensional nanostructures with the cancer cells, a high level of *in vitro* biocompatibility for both BSA-coated Fe NWs and antibody-coated NWs was observed (figure 1.42).

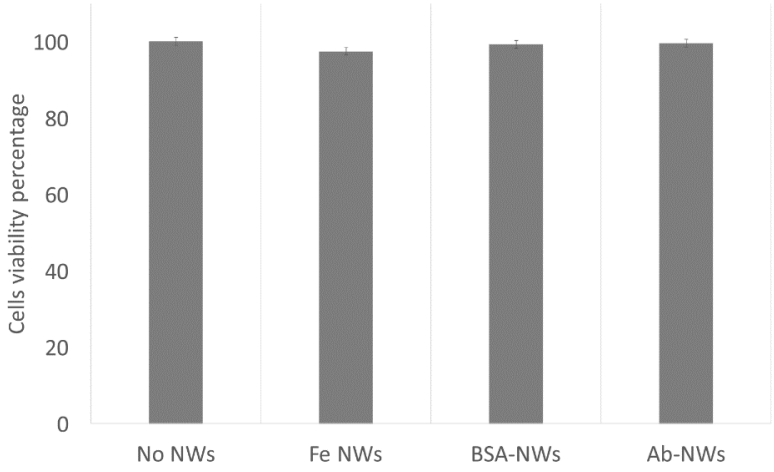

Figure 1.42 - Cell viability after incubating, for 24 h, HL60 cells with Fe NWs, Fe-BSA NWs and Fe-BSA-CD44 NWs (Ab-NWs). The positive control was composed by HL60 cells without NWs (No NWs). From [369]. © 2018 IEEE.

Besides NWs, SAF nanostructures have also been evaluated as possible surrogates to superparamagnetic beads in this biomedical application. For example, by functionalizing the surface of SAF nanoarchitectures, composed by a [Ta/Ru/CoFe/Ru/CoFe/Ru/Ta] layered structure, with a protein (streptavidin), Fu et al.[370] demonstrated that these nanostructures allow a better detection of biomolecules at low analyte concentrations (10 pM), when compared to the typical superparamagnetic materials.

Furthermore, the fluorescent labelling of those nanoarchitectures allowed the authors to see their motion in response to a small external magnetic field gradient (10 $T \cdot m^{-1}$). Additionally, by adjusting the thickness of the SAFs magnetic layers, they also observed a dramatic modification in their movements, which can be very useful for separating and manipulating biological targets or materials linked to SAF surfaces through the application of magnetic fields. Therefore, from this report, it is possible to conclude that SAF nanostructures, due to their high magnetic moment per particle and multifunctional (optical, magnetic, and specific targeting) properties, provide a promising new path for multiple biomedical applications, such as biomolecule detection and magnetic manipulation.

An *in vitro* study on the utilization of SAF nanostructures in this biomedical application was performed by Zhang et al.[371] Here, SAF nanoarchitectures, constituted by the following sequence of layers: [Si 3 nm/ Ti 5 nm/Fe 10 nm/Ti 3 nm/Fe 10 nm/Ti 5 nm/Si 3 nm], were used to separate lung cancer cells (H1650) from blood samples. Therefore, firstly, such nanostructures were coated with a silica shell and then conjugated with streptavidin in order to be capable of linking to the cells of interest, making those biological entities highly magnetically responsive. Then, after incubating the cancer cells with the nanoarchitectures, blood samples were mixed with the stained cells. Afterward, the spiked blood samples were pushed through a magnetic separation device (figure 1.43) and the captured cells were analysed using an optical microscope. As a result, a capture efficiency of 46.8% was achieved, indicating that SAF nanostructures can indeed be used for separating cells from blood samples, being promising nanomaterials for detecting cancer at early stages.

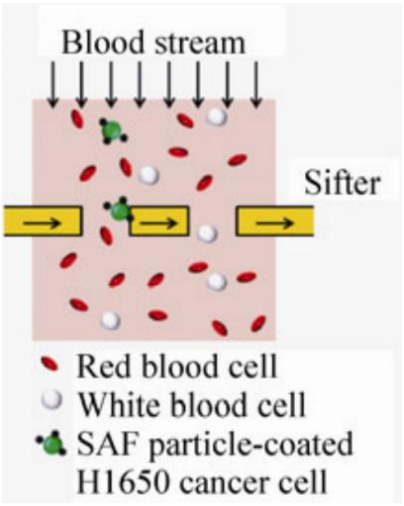

Figure 1.43 - Illustration of a blood sample, spiked with lung cancer cells, passing through the magnetic separation device (sifter); only cells linked to SAF nanostructures are captured by the sifter. Adapted from [371]. Reproduced with permission from Springer Nature.

More recently, the suitability of magnetic NDs with a spin-vortex ground state for this biomedical application has been analysed by various authors. For example, Gregurec et al.[372] addressed the use of these nanostructures for magneto-mechanical neural stimulation. Particularly, such nanomaterials were employed as transducers of torque for remote control of mechanosensory neurons, having demonstrated the ability to exert torques on the membranes of those cells, which allowed a remote triggering of the Ca^{2+} influx, when exposed to weak and slowly varying AMFs. In a similar work, Collier et al.[373] studied the wireless stimulation of primary neuronal circuits via mechanotransduction, using magnetic microdiscs as transducers of AMFs into mechanical forces. As a result, the authors verified an activation of the response associated with specific mechanosensitive ion channels expressed on the cell membranes, which originated from the magneto-mechanical actuation of the microdiscs when exposed to weak AMFs with a low frequency.

1.3.3. Contrast Agents in Magnetic Resonance Imaging (MRI)

MRI is a non-invasive imaging technique, frequently performed all over the world, that makes use of the magnetic properties that certain atomic nuclei possess.[374,375] In this thesis, such diagnostic modality will be addressed using classical mechanics, since it is a more intuitive and simpler approach when compared to the explanation based on quantum mechanics, which, however, is more complete.[376-379]

In this context, when a strong external magnetic field (B_0) is applied to a given sample, the randomly oriented nuclear magnetic moments present in that medium, resulting from

the spin of the hydrogen nuclei[1], will start precessing about B_0 in either the parallel (lower energy state) or antiparallel (higher energy state) orientations relative to the to the applied field.[383-385]

The energy difference between these two alignments is very small, nevertheless the parallel one is slightly favoured because it is a lower energy state. Consequently, more protons will be precessing in that orientation, originating a net magnetization vector (M_0) along B_0 that is constituted by a component parallel to B_0, i.e. the longitudinal magnetization (M_z), which results from the difference between the number of nuclear magnetic moments in the two states, and a component transverse to B_0, i.e. the transverse magnetization (M_{xy}), which is equal to zero due to the dephasing of the nuclear magnetic moments (figure 1.44).[383,384,386-388]

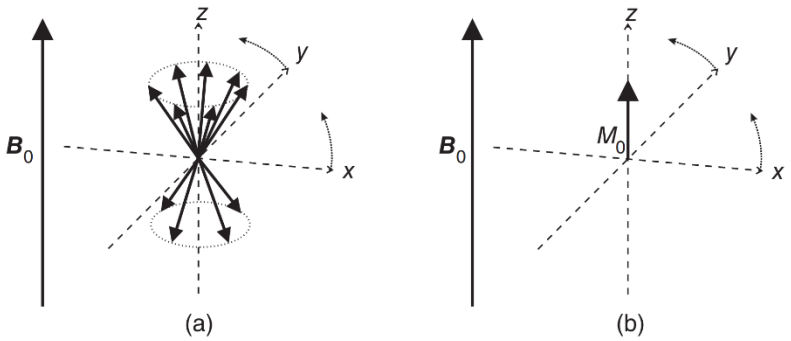

Figure 1.44 - (a) Collection of nuclear magnetic moments (black arrows) in the presence of B_0; (b) M_0 resulting from the difference between the number of nuclear magnetic moments in the two orientations. In this situation M_0 is equal to M_z, while M_{xy} is zero due to the dephasing of the nuclear magnetic moments. Reprinted with permission from [389]. Copyright 2015 WILEY-VCH Verlag GmbH and Co. KGaA, Weinheim.

Since M_z is much smaller than B_0 and parallel to that field, it is virtually impossible to measure any signal in such direction.[386-388] However, by applying a radiofrequency (RF) pulse tuned to the Larmor frequency, i.e. the precession rate (or frequency) of the nuclei around B_0, it is possible to misalign M_0 and, as a result, generate a nonzero M_{xy} that can be measured.[335,390,391] Then, when the RF transmitter is switched off, the two magnetization components will go back, or "relax," to their previous states in the presence of B_0.[389,392] This means that the transverse magnetization will decay towards zero, due to the dephasing of the nuclear magnetic moments, and the longitudinal magnetization will return to its initial maximum value parallel to B_0.[294,380,393] Therefore, the precession of the nuclear magnetic moments, together with the relaxation processes, originate a changing magnetic field in the transverse direction, which, as a consequence of the Faraday's law of induction, generates a small RF electric current in the RF receiver

[1] In MRI the signal from the hydrogen nuclei, which are composed by a single proton, is the most frequently used, because these are the most abundant nuclear species with nonzero spin in the human body.[380-382]

coils [magnetic resonance (MR) signal] that is subsequently processed so as to produce an image.[384,394,395]

The main advantages of MRI over other imaging methods are the use of nonionizing radiation, high spatial resolution, great anatomic detail, and improved soft tissue contrast.[374,396] Such properties make this technique an appealing option to diagnose various physiological diseases and lesions, as well as to assess the effect of therapeutic treatments.[374] However, since this approach has a low sensitivity, contrast agents are often employed to improve the contrast between the different tissues in the resulting pictures and, consequently, increasing the information content of the diagnostic images.[374,396-398] These substances enhance the image quality by lowering the relaxation times of the water protons in their vicinity, modifying, as a result, the signal intensity of the water present in body tissues that contain the contrast agent.[399-404]

All MRI contrast agents affect the rates of the two relaxation processes previously mentioned, with a predominant effect on one of them.[405-407] Therefore, based on such aspect, it is possible to classify these substances as:

- T_1 (or positive) contrast agents - mainly reduce the relaxation time of the longitudinal component of the magnetization;[395,396,408,409]
- T_2 (or negative) contrast agents - mainly lower the relaxation time of the transverse component of the magnetization.[395,396,408,409]

The performance of a contrast agent is assessed by determining its longitudinal and transverse relaxivities (r_1 and r_2, respectively), which are defined as the amount of increase in the longitudinal or transverse relaxation rates of the water protons, correspondingly, produced by a concentration of the contrast agent equal to 1 mmol/L (or mM).[410-416] Then, the relaxivity ratio, i.e. transverse relaxivity (r_2)/longitudinal relaxivity (r_1), is calculated and if the analysed substance has a small r_2/r_1 ratio (≤ 5) it is classified as a T_1 contrast agent, however if it presents a higher r_2/r_1 ratio (> 5) it is considered a T_2 contrast agent. [417-420]

The most widely used contrast agents in clinical practice are Gd^{3+}-complexes; however, these have raised various toxicity concerns.[413,421-424] Consequently, it has arisen an interest for searching and studying new and safer alternatives. In this context, SPIONs have been developed as a viable alternative to the typical Gd^{3+}-complexes. Such particles are suitable as T_2 contrast agents, due to their biocompatibility, ability to be metabolized, high saturation magnetization, and easy surface functionalization.[374,396]

Nevertheless, the dimensions of these NPs are restricted by the superparamagnetic limit, which implies a maximum d of 10–20 nm per particle in order to keep them in the superparamagnetic state so that they have zero remanence and, consequently, do not aggregate in the absence of a magnetic field.[425,426] As a result of this condition, the magnetic moment of each NP is limited and, unfortunately, their ideal size for this specific biomedical application, as determined by simulations, surpasses the superparamagnetic threshold.[427]

To overcome this difficulty, multiple approaches have been considered, such as increasing the magnetization of the NPs within the superparamagnetic limit by using dopants, or designing methods for controlled clustering of NPs.[428,429] However, these approaches are tedious and produce clusters with sizes that are difficult to control.[428] Therefore, a more viable solution for this issue may be using magnetic nanostructures possessing greater magnetic moments, but that exhibit zero remanence as well. In this context, several authors have studied various promising nanomaterials.

For example, Bailey et al.[430] fabricated RE_2O_3-based NDs (d ~ 10–14 nm), where RE = Gd, dysprosium (Dy), or ytterbium (Yb), passivated with a biocompatible polymer (Poly(acrylic acid)), (PAA), grafted with short methoxy-terminated polyethylene oxides), and analysed their suitability as MRI contrast agents. The relaxation times of these nanostructures, measured at 37 ºC (body temperature) in a magnetic field of 1.41 T, were compared against the values reported for their spherical counterparts or small molecule chelates based on the commonly used pentetic acid (DTPA) ligand. The authors also performed MRI scans of a phantom for all the considered contrast agents, using T1- and T2-weighted pulse sequences. As a result, it was observed that the Gd_2O_3 NDs, in particular, presented significant advantages over the commercially available Gd-DTPA contrast agents, one of which being higher longitudinal and transverse relaxivities (r_1 = 12.6-12.7 mM^{-1} s^{-1}; r_2=16.5-17.2 mM^{-1} s^{-1}). This aspect should increase the efficiency of *in vivo* targeted imaging schemes, since it becomes possible to get a high amount of proton relaxation without requiring multiple small molecules in contact with the imaging target. Additionally, their potential as T_1 and T_2 contrast agents, pointed out by the measured r_1 and r_2 values, was confirmed through the MR images of the phantom that were acquired. Moreover, the polymer-coated Gd_2O_3 and Dy_2O_3 nanoarchitectures were incubated with a human cell line derived from cervical cancer cells (HeLa) and, as a result, no significant cytotoxic effects were observed on those biological entities (figure 1.45).

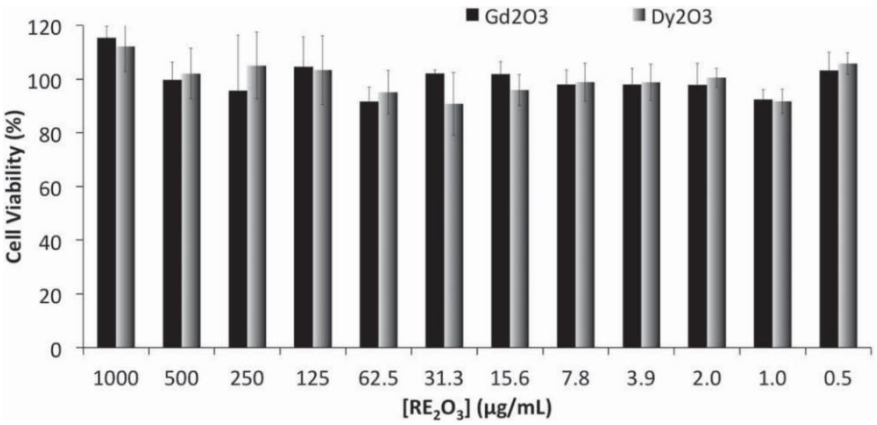

Figure 1.45 - Cell viability after a 48 h incubation with Gd_2O_3 and Dy_2O_3 NDs passivated with a biocompatible polymer. Reprinted with permission from [430]. Copyright 2012 WILEY-VCH Verlag GmbH and Co. KGaA, Weinheim.

On another study, Singh et al.[431] fabricated and analysed the suitability of three polyethylene glycol (PEG)-coated nanostructures, with different dimensions, as MRI contrast agents, namely Gd_2O_3 paramagnetic NDs as well as Gd-doped iron oxide superparamagnetic NPs with a cubic and spherical shape. Here, the relaxivities of the various nanoarchitectures were measured using a 7.0 T MR scanner, having been demonstrated that all the smaller sized nanostructures (< 5 nm) are suitable as T_1 contrast agents (r_2/r_1= 3.70-5.17). However, as their dimensions increased (> 5 nm), they became more appropriate for reducing the T_2 relaxation time (r_2/r_1 = 6.39-74.30). Furthermore, the researchers also verified that no acute *in vitro* toxicity was induced by the fabricated nanoarchitectures on glioblastoma-astrocytoma cells.

Besides NDs, NWs have also been addressed by some reports in the context of this biomedical application. For example, Bañobre-López et al.[374] evaluated the relaxivity properties of PAA-coated Ni NWs, which possessed a longitudinal magnetic anisotropy, in a colloidally stable water dispersion. This dispersion was produced through a process of pulsed electrodeposition of Ni/Au multilayer NWs inside a nanoporous AAO template in a three-electrode cell at room temperature, followed by the liberation of the Ni/Au multilayer NWs from the template and a subsequent two-step acidic etching. The relaxation times of these nanostructures, which presented a monodisperse average d and length of ~ 36 nm and ~ 600 nm, respectively, were measured using a relaxometer operated at 60 MHz and 37 ºC under two magnetic fields, namely, 1.41 and 3.0 T. In both situations, the obtained results indicated that these nanostructures are efficient T_2 contrast agents (r_2 at 1.41 T = 82 mM^{-1} s^{-1}; r_2 at 3.0 T = 28 mM^{-1} s^{-1}). Moreover, the contrast effect of the PAA-coated Ni NWs was confirmed by acquiring MR images of a phantom, which contained various dilutions of Ni NWs and a control sample constituted by water, at a 3.0 T magnetic field (figure 1.46).

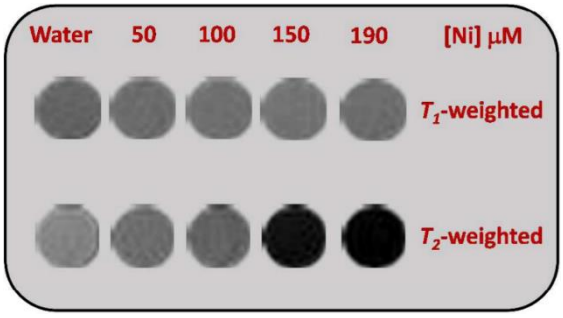

Figure 1.46 - MR image of a phantom obtained at 3.0 T and 37 ºC, using both T_1- as well as T_2-weighted sequences. Used with permission of Royal Society of Chemistry, from [374]; permission conveyed through Copyright Clearance Center, Inc.

Shore et al.[396] also studied NWs in this context, particularly Fe and Fe-Au NWs with various lengths and d's. Here, these nanostructures were coated with compounds, namely, dopamide-PEG (Dop-PEG) and/or thiol-PEG-carboxyl (SH-PEG-COOH), which allow the binding of other biomolecules to target the NWs to specific cell types. The magnetic characterization of both nanostructures indicated that the Fe-Au NWs exhibited a larger saturation magnetization, which was attributed to the fact that their Fe layers are thinner than the d of the nanostructures, allowing them to be more easily magnetized in the direction perpendicular to the long axis of the nanoarchitecture than pure Fe NWs. Furthermore, the relaxivity properties of the analysed NWs were measured at 25 ºC in a 1.5 T magnetic field and compared against those of Fe and Fe-Au NPs. As a result, it was verified that the Fe NWs with a length of 0.7 μm and d = 110 nm, coated with Dop-PEG, were the best suited as T_1 contrast agents (r_1 = 2.0 mM^{-1} s^{-1}). On the other hand, the 1 μm long Fe-Au NWs possessing d = 32.8 nm and coated with both SH-PEG-COOH as well as Dop-PEG were the most appropriate as T_2 contrast agents, having a r_2 (77.1 mM_{-1} s^{-1}) comparable to that of commercial Fe oxide NPs. Moreover, in order to confirm the contrast effect of these nanostructures, the authors acquired T_2-weighted MR images of some samples containing Fe and Fe-Au NWs at various concentrations (figure 1.47).

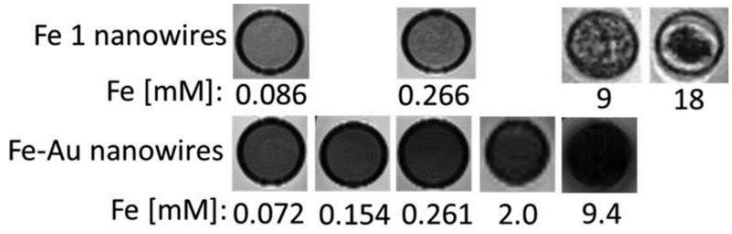

Figure 1.47 - T_2-weighted MR images of samples containing different concentrations of Fe and Fe-Au NWs. Used with permission of Royal Society of Chemistry, from [396]; permission conveyed through Copyright Clearance Center, Inc.

In another work, Martínez-Banderas et al.[432] fabricated distinct one-dimensional nanostructures composed of an iron core together with an iron oxide shell (Fe-Fe_xO_y

core–shell NWs) and assessed their suitability as MRI contrast agents. Here, the r_1, r_2, and r_2/r_1 ratio of these nanostructures were assessed under a 1.5 T magnetic field, having been verified that they possessed great potential as T_2 contrast agents (r_2= 34.4-70.5 mM^{-1} s^{-1}; r_2/r_1 = 32.0-64.8). Furthermore, the effects of various oxidation levels, as well as different surface coatings, on their relaxivity properties were evaluated under a 7.0 T field. As a result, it was shown that their r_2 could be adjusted not only by changing the oxide shell thickness, but also by adding coating agents. Subsequently, the authors inserted into tissue-mimicking phantoms several dilutions of breast cancer cells (MDA-MB-231) labelled with Fe-Fe_xO_y core–shell NWs, which possessed a native oxide layer and two different coatings, namely BSA and (3-aminopropyl) triethoxysilane (APTES). T_2-weighted MR images of those cells under a 7.0 T magnetic field were acquired, so as to assess the efficiency of such nanostructures as T_2 contrast agents. From this analysis, it was observed that the BSA coating improved the dispersion and the cellular internalization when compared to APTES, while providing identical cell identification efficiency through MRI. This permits the use of a lower concentration of nanostructures to efficiently mark the desired cells, thereby lowering the probability of toxic effects. For example, using the BSA coating, the authors were able to detect ~ 25 cells/μL by employing a NW concentration of 0.8 μg/mL of Fe, while for the APTES-coated nanoarchitectures it was required a concentration equal to 2.5 μg/mL of Fe to achieve the same result. Subsequently, MDA-MB-231 cells labelled with BSA-coated nanostructures were implanted inside a mouse's brain and several T_2-weighted MR images of that organ were acquired at various time intervals after implantation, using a static magnetic field of 11.7 T. As a result, about 10 NW-labelled cells could be observed in the brain parenchyma of the mouse and were detectable during at least 40 days after implantation.

A distinct approach to this topic, also based on NWs, was reported by Peci.[433] Here, the author filled the central capillary of carbon NTs with continuous ferromagnetic α-Fe NWs, producing a structure with two different competing anisotropy contributions that result in a small effective anisotropy, and functionalized their surface with paramagnetic Gd^{3+}. Then, these nanostructures were analysed as candidates for a dual approach, namely, MHT cancer therapy and contrast enhancement in MRI. Their suitability for this latter application was assessed by measuring the longitudinal relaxivity of the filled carbon NTs at magnetic fields of 9.4 T and 14.0 T. As a result, it was demonstrated that these nanostructures are viable as high-relaxivity contrast agents for high-field MRI, having the largest r_1 values (r_1 at 9.4 T = 200.5 mM^{-1} s^{-1}; r1 at 14.0 T = 160.5 mM^{-1} s^{-1}) when compared to all the candidate high-field T_1 contrast media considered in this study.

The suitability of a different type of one-dimensional nanomaterial, i.e. Fe_3O_4 nanostructures with rod-like morphologies (NWs with low aspect ratio), for this biomedical application was examined by Mohapatra et al.[434] Such nanoarchitectures exhibited d's of 4–12 nm and lengths ranging from 30 to 70 nm, having been verified that the increase of the NRs length was associated with a linear augment in their r_2 (from 312 until 608 mM^{-1} s^{-1}). Such increasing trend was attributed to the enhancement of both the magnetization value and the outer sphere surface area of the nanostructures. Moreover, *in vitro* assays using HeLa cells demonstrated that those biological entities exhibited normal growth in the presence of Fe_3O_4 NRs and, even after their incubation with 1 mg/mL of NRs, approximately 90% the cells remained alive, suggesting that these nanostructures have an acceptable biocompatibility and possess low cytotoxicity.

In a different study by Leung et al.[435], one-dimensional magnetic Mn-Fe nanostructures, namely, nanoneedles, NRs, and NWs, were fabricated by self-assembly of Mn-doped iron oxide NPs, using cystamine as the linker. Then, the suitability of these nanoarchitectures as MRI contrast agents was evaluated in a clinical 1.5 T whole-body MR system, considering various dilutions of nanostructures in distilled water. The obtained results showed that all the considered nanostructures had notable T_2 relaxivities, especially the nanoneedles ($r_{2\text{-nanoneedles}}$ = 20.81 ± 0.58 mM^{-1} s^{-1}; $r_{2\text{-NRs}}$ = 8.10 ± 0.31 mM^{-1} s^{-1}; $r_{2\text{-NWs}}$ = 6.62 ± 0.42 mM^{-1} s^{-1}). Additionally, a cell viability test was performed on a cell line established from a tumour induced by the Abelson murine leukaemia virus (RAW264.7), having been also obtained a growth curve. Then, the analysis of the acquired data revealed that these nanoarchitectures have acceptable safety profiles.

Leung et al.[436] also investigated the suitability of Mn–Fe oxide NWs, synthesized through the ligand-induced self-organization of Mn–Fe oxide NPs, as MRI contrast agents. Via transmission electron microscopy (TEM), it was observed that these nanostructures possessed a mean d equal to 35 nm and, on average, were 1 μm long. Additionally, the elemental content of the Mn-Fe oxide nanoarchitectures was analysed by inductively coupled plasma-optical emission spectroscopy (ICPOES) as well as through energy-dispersive X-ray (EDS) spectroscopy. These techniques indicated a Fe percentage of ~ 40.65 %. Moreover, the influence of these nanostructures on the T_2 relaxation time was assessed using a 1.5 T MRI system. As a result, it was shown that they considerably increased the MRI signal decay speed at concentrations of 100 μg/mL or 10 μg/mL, which demonstrated their potential as T_2 contrast agents (r_2 not specified by the authors). Moreover, the cell labelling efficiency of these nanoarchitectures was assessed by

incubating them the RAW264.7 cell line, having been achieved an effective incorporation of the Mn–Fe oxide NWs into the considered biological entities (100%).

A more recent work by Gu et al.[437], analysed the suitability of mesoporous silica-coated Fe/Mn multilayered NWs as T_1–T_2 dual-mode contrast agents. Here, a 1.5 T MRI scanner was used to perform such study, having been verified that these nanostructures had a considerable T_1–T_2 imaging effect, which was dependent on their concentration. Particularly, r_1 and r_2 values of 1.25 ± 0.0329 · 10^{-4} mM^{-1} s^{-1} and 5.13 ± 0.123 · 10-4 mM^{-1} s^{-1}, respectively, were observed for these multilayered NWs, which are about twice the r_1 value of Mn NWs (0.654 ± 0.00899 · 10^{-4} mM^{-1} s^{-1}) and the and r_2 value associated with Fe NWs (2.96 ± 0.0415 · 10^{-4} mM^{-1} s^{-1}).

The suitability of magnetic NWs composed of a different metal, i.e. Cu, for this biomedical application was addressed by Thirumurugan et al.[438] Particularly, the authors fabricated copper (II) benzene-1,3,5-tricarboxylate NWs, which were coated with a polydopamine shell to enhance their biocompatibility. This biopolymer can also act as a photothermal therapy agent, improving the near-infrared (NIR) absorption of the nanostructure. As a result, it was verified that these nanoarchitectures possessed an adequate r_1 value (3.01 mg^{-1} s^{-1}) in a 7 T magnetic field, while presenting a good photothermal stability and a photothermal conversion efficiency equal to 13.32 %. *In vitro* studies using HepG-2 cells, revealed that, after incubation with the fabricated NWs, an 808 nm laser irradiation reduced their viability by 58%, indicating that these Cu-based nanostructures have a significant potential as theragnostic agents for cancer therapy.

Also aiming at the development of novel MRI contrast agents, Corr et al.[400] fabricated linear arrays of magnetite NPs, using polyelectrolyte molecules to cross-link neighbouring NPs, and studied their suitability for this specific biomedical application. Here, the authors observed that these nanoarchitectures could be rearranged into parallel arrays by applying an external magnetic field during their drying process. Furthermore, these suspensions were analysed using field-cycling nuclear magnetic resonance (NMR), having been observed, at 37 ºC, a significant reduction in the relaxation times at all considered fields (at 9 MHz: r_1 = 22.5 mM^{-1} of Fe s^{-1}, r_2/r_1 = 5.88; at 59 MHz: r_1 = 7.2 mM^{-1} of Fe s^{-1}, r_2/r_1 = 12.5). The authors also acquired MR images of live rats injected with these nanostructures, in order to assess their effect on the brain. As a result, it was verified that these nanoarchitectures had good biocompatibility and possessed potential as T_2-contrast agents for *in vivo* MRI, since a significant darkening of the rats' brain was observed in the acquired T_2-weighted MR images.

In addition to the previously addressed nanoarchitectures, SAF nanostructures have also been studied as potential contrast agents for MRI. For example, Roosbroeck et al.[428] fabricated phospholipid-coated, disc-shaped SAF nanoarchitectures, composed by a [Au(10 nm)/$Ni_{80}Fe_{20}$(5 nm)/Au(2.5 nm)/$Ni_{80}Fe_{20}$(5 nm)/Au(10 nm)] layered structure, with diameters ranging from 89.8 nm to 523.2 nm, using a colloidal lithography technique. The magnetic characterization of these NDs indicated that they have a very low remanence as well as a high magnetization, being, therefore, adequate nanomaterials for biomedical applications. Then, the performance of these nanostructures as T_2 contrast agents was assessed, having shown improved transverse relaxivities, at 24.85 ºC in a 9.4 T magnetic field, when compared to commercial options, especially the smallest nanoarchitectures (diameter = 90 nm; r_2 = 355 mM^{-1} s^{-1}). Then, these last nanostructures were coated with 1,2-distearoyl-snglycero3-phosphoethanolamine-N-[carboxy(PEG)-2000] (an a amphiphilic phospholipid) and, subsequently, the authors employed them in an *in vitro* MRI study using an ovarian cancer cell line (SKOV3), which confirmed the increased T_2 relaxation rate for cells labelled with such nanostructures (figure 1.48).

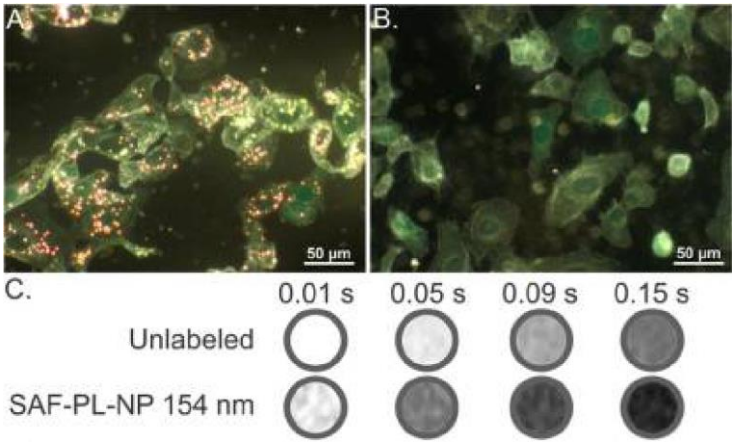

Figure 1.48 - (a) Dark-field image of SKOV3 cells after overnight incubation with 154 nm phospholipid-coated SAF NPs (SAF-PL-NPs); (b) darkfield image of unlabelled SKOV3 cells; (c) MR images of labelled and unlabelled SKOV3 cells at various echo times. Adapted with permission from [428]. Copyright 2014 American Chemical Society.

The use of antiferromagnetic nanomaterials as MRI contrast agents was also investigated by different authors. Namely, Na et al.[439] fabricated antiferromagnetic Mn(II) oxide (MnO) NPs of different sizes, specifically, 7, 15, 20, and 25 nm, coated with a PEG-phospholipid shell, and assessed their suitability as positive contrast agents. By measuring the relaxivities of the MnO NPs (7 nm: r_1 = 0.37 mM^{-1} s^{-1}, r_2 = 1.74 mM^{-1} s^{-1}; 15 nm: r_1 = 0.18 mM^{-1} s^{-1}, r_2 = 0.57 mM^{-1} s^{-1}; 20 nm: r_1 = 0.13 mM^{-1} s^{-1}, r_2 = 0.52 mM^{-1} s^{-1}; 25 nm: r_1 = 0.12 mM^{-1} s^{-1}, r_2 = 0.44 mM^{-1} s^{-1}) and acquiring both T_1- as well as T_2-weighted MR images of a mouse into which the 25 nm nano-objects were injected, the

authors verified that these NPs do, in fact, have potential as T_1 contrast agents. Furthermore, by conjugating the 25 nm nano-objects with a tumour-specific antibody, it was possible to selectively image, through T_1-weighted MRI, breast cancer cells in a metastatic brain tumour present in the mouse. Moreover, their cytotoxicity was assessed in eight human cell lines originating from different tissues, not having been observed a significant toxicity for a MnO concentration below 0.82 mM.

Neves et al.[440] also analysed the use of MnO NPs (average size of ~ 20 nm) as MRI contrast agents; however, in this study, they were coated with carboxymethyl-dextran and the *in vivo* study was not performed. Similarly to the previous work, the authors considered this nanomaterial suitable to be utilized as T_1 MRI contrast agents, having been verified that it possesses a longitudinal relaxivity of 0.44 mM^{-1} s^{-1} as well as a r_2/r_1 ratio equal to 7.84 (in this work, contrast agents were classified as positive if their r_2/r_1 ratio was < 10). Moreover, it was observed that these NPs have a negligible *in vitro* cytotoxicity in healthy cells at concentrations lower than 25 μg/ml, however, for HeLa cells a notable toxicity was observed, even when considering low concentrations of NPs in the cell line (5 μg/ml).

The suitability of spherical nanostructures, exhibiting antiferromagnetic properties, as MRI contrast agents was investigated as well by Liu et al.[441] These nanoarchitectures were glutathione-functionalized iron-oxide NPs, having been produced at room temperature in an aqueous-phase by a facile, extremely efficient, as well as eco-friendly, one-step reduction process, using tetrakis(hydroxymethyl)phosphonium (THCP) chloride as the reducing agent. After the synthesis procedure, the characterization of the nanostructures revealed that they possessed a d = 3.72 ± 0.12 nm, a small r_2 (8.28 mM^{-1} s^{-1}), a low r_2/r_1 ratio (2.28), reduced remanence, plus adequate water dispersion. Additionally, through their incubation with HeLa cells, it was observed that they had a high biocompatibility and, as the concentration of NPs inside the considered biological entities increased, it was verified an improvement in the MR signal intensity in T_1-weighted images. Moreover, these NPs were injected into mice and rat models so as to study not only their circulation and metabolic path *in vivo*, but also the contrast they create in MR images of a living organism. As a result, it was noticed that the nanostructures escaped the hepatic reticuloendothelial system and, subsequently, were expelled from the body via the urinary system, enabling the assessment of the renal function. This factor also leads to a longer circulation period of the NPs in the vasculature in comparison to the traditional Gd-based T_1 contrast agents, which translated into a strong vascular enhancement at the internal carotid artery and superior sagittal sinus in

the T_1-weighted MRI of the *in vivo* mice brain. Additionally, various T_1- and T_2-weighted MR images of a rat's kidney injected with these nanostructures were acquired. As a result, the authors were able to obtain detailed information about the cortical-medullary anatomy and the renal physiological functions.

On a different work, Peng et al.[442] fabricated antiferromagnetic α-iron oxide-hydroxide nanocolloids, with d = 2–3 nm, in the mesopores of worm-like mesoporous silica and studied their suitability for contrast enhancement in MRI. The relaxation times of these NPs were measured at 40 ºC using a 0.47 T Minispec spectrometer, having been verified that they had the lowest r_2/r_1 ratio, i.e. 1.97 (r_1 = 4.03 mM^{-1} s^{-1}), reported, until 2013, for iron-based colloidal T_1 contrast agents and also possessed a significant longitudinal relaxivity. Additionally, by acquiring MR images it was shown that such nanocolloids have great potential as T_1 contrast agents for both *in vitro* (HeLa cells) and *in vivo* (rat and mouse) MRI. Furthermore, these nanocolloids also demonstrated a high level of biocompatibility (in HeLa cells) and biodegradability (in fetal bovine serum).

More recently, Sorouri et al.[443] reported the synthetization of MnO_2 with two distinct shapes, namely flower-like and near-spherical, and assessed their potential as dual-active nanozymes and MRI contrast agents. In this study, it was verified that the paramagnetic characteristics of the produced nanomaterials increased with their surface area. As a result, the flower-like nanomaterials exhibited a more efficient contrast improving effect in comparison to the near-spherical ones, exhibiting a higher longitudinal relaxivity value ($r_{1\text{-flower-like}}$ = 5.73 mM^{-1} s^{-1} vs $r_{1\text{-near-spherical}}$ = 3.17 mM^{-1} s^{-1}), which was confirmed through *in vitro* cellular imaging assays (MCF-7 and MCF-10A cells). Additionally, these flower-like nanostructures not only displayed an adequate biocompatibility, but also presented a more potent pH-sensitive oxidase and peroxidase mimetic activity in comparison to the near-spherical nanoarchitectures. Consequently, the authors concluded that these flower-like nanomaterials are a promising candidate for future theragnostic applications.

1.3.4. Magneto-Mechanical Induction of Cancer Cell Death

Nowadays, the therapeutic modalities most commonly used to treat cancer, i.e. surgery, radiotherapy, and chemotherapy, are considerably stressful for the human body and may have undesirable side effects.[444,445] Therefore, it would be beneficial to the oncologic patient if the shortcomings associated with those therapies could be surpassed.[446] In this context, nanomaterials have emerged as promising candidates for next generation oncologic treatments with reduced side effects.[445] Particularly, there exists an increasing interest for the use of magnetic nanostructures to mechanically stimulate and destroy

specific cells, since magnetic nanomaterials can be remotely controlled by applying external magnetic fields and also due to the fact that cells convert mechanical stimuli into biochemical signals, via a process known as mechanotransduction.[299,446-448]

The capacity to manipulate cellular signals through the use of magnetic nanomaterials and external magnetic fields opens up multiple possibilities for the development of new approaches to cancer treatment.[299] In this framework, most of the experimental studies performed analyse superparamagnetic NPs, however, their reduced saturation magnetization implies that high magnetic fields must be applied to manipulate those nanomaterials.[135] Therefore, concerning cancer therapy, the use of nanostructures with larger magnetic moments presents an interesting alternative to these NPs, having opened doors for an eventual novel treatment modality known as magneto-mechanical induced cell death.[445] This technique consists of exerting forces or torques on cells, using magnetic nanoarchitectures controlled by low-frequency magnetic fields, to induce cell apoptosis, i.e. the programmed cell death.[447,449] Specifically, the basis of the magneto-mechanical actuation in cells is the spatial rotation that the magnetic nanostructures perform, to align themselves with an externally applied magnetic field through the Brown relaxation process. Consequently, it is produced a magnetic torque that depends on the applied magnetic field characteristics, as well as upon the magnetic moment and magnetic susceptibility of the nanoarchitectures.[446,447]

This novel approach is promising for cancer therapy since it has various advantages when compared to other techniques. Namely, the possibility to specifically target cancer cells by functionalizing the surface of the magnetic nanostructures, therefore significantly reducing the toxic side effects of chemotherapy, as well as the considerably lower strength and frequency of the external magnetic field required for manipulating the nanoarchitectures in comparison to MHT, making it easier to implement while eliminating the risk of destroying healthy tissues by undesired local overheating.[447,450]

Driven by the improvement of such technique, various authors have studied the suitability of different magnetic nanoarchitectures for this specific biomedical application. Generally, these nanostructures have a large saturation magnetization and low field magnetic susceptibility, as well as a reduced remanence, therefore requiring lower magnetic fields for manipulation and not agglomerating in the absence of a magnetic field.[71,445,446,451] In this context, micro/nanodiscs with a spin-vortex ground state, i.e. an in-plane flux-closure spin distribution, are a particular interesting nanomaterial, since they possess no remanence and have a large single domain, when compared to the typical superparamagnetic NPs.[452,453]

A search through the literature revealed that the first reported experimental study addressing the use of such disc-shaped nanostructures in this particular biomedical application was carried out by Kim et al.[453] In that work, Py microdiscs with a spin-vortex ground state, with a thickness equal to 60 nm, possessing d ~ 1 μm, and coated on both sides with a 5 nm thick Au layer (for biocompatibility and surface modification), were prepared by magnetron sputtering and optical lithography. Afterward, the surface of these nanoarchitectures was functionalized with an antibody that recognizes a receptor overexpressed on the surface of glioma cells (IL13α2r), in order to specifically target the NDs to human glioblastoma multiforme cells (N10 glioma cancer cells), an aggressive form of brain cancer. Then, these cells were incubated with the functionalized microdiscs and, after that process, it was observed an average of 10 discs per cell. Subsequently, such biological entities were exposed to spatially uniform AC magnetic fields with different intensities and frequencies (figure 1.49). As a result, the authors were able to produce a biologically relevant cell damage (90 % cell death) by applying, for only 10 min, considerably weak magnetic fields (< 10 mT), with frequencies of a few tens of Hz (10–20 Hz). On the other hand, in the typical heating-induced cell toxicity using superparamagnetic particles, considerably stronger AC magnetic fields, with frequencies of hundreds of kHz, are required for achieving significant results, being, therefore, more difficult to implement than the magneto-mechanically induced cell annihilation.[453]

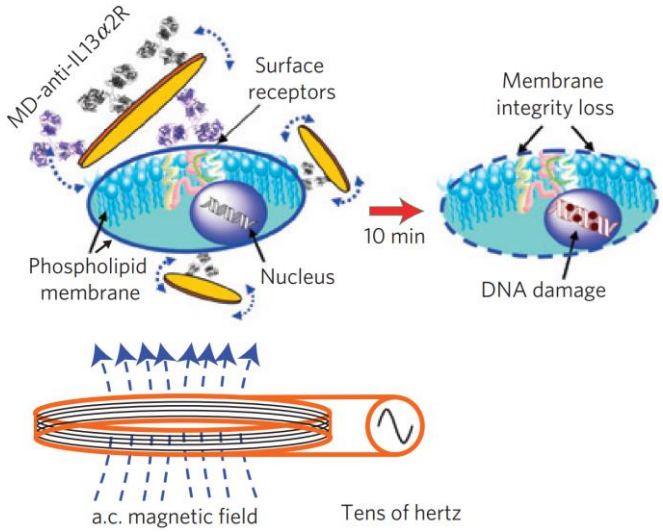

Figure 1.49 - The idea of targeted magneto-mechanical cancer cell annihilation employing disc-shaped magnetic structures with a spin-vortex ground state. From [453], reproduced with permission from SNCSC.

Similar works were performed by Rozhkova et al.[454], Novosad et al.[455], and Vitol et al.[71]; however, in the latter case, a different cell line was considered, specifically A172 glioblastoma cells, which was exposed for 15 min to a 10 mT AC magnetic field, with a

frequency of 10 Hz, and the magneto-mechanically induced controlled drug release was also investigated. Even so, the results acquired in the different works by the various authors were similar to the ones obtained in the study authored by Kim et al.[453]

Also in the context of this biomedical application, Leulmi et al.[447] prepared and characterized three types of disc-shaped anisotropic magnetic nanostructures, namely, SAF nanoarchitectures composed by (NiFe/Ru 0.8 nm/)$_n$/NiFe-based magnetic multilayers, $Ni_{80}Fe_{20}$ microdiscs with a spin-vortex ground state, and polycrystalline magnetite nanostructures with random anisotropy. All these structures had d = 1.3 μm and, similarly to the previous studies, they were coated with Au layers. Afterward, the magnetic properties of the synthesized nanoarchitectures, as well as their deposition process, were compared and the $Ni_{80}Fe_{20}$ microdiscs were considered the best option to start an *in vitro* study on the magneto-mechanically induced death of human renal carcinoma cells, due to their magnetic softness and ease of fabrication.

Consequently, the surface of those microdiscs was functionalized with ligands so that they could target specific renal cancer cells (SKRC-59). Then, after incubating such biological entities with the considered nanostructures, the authors observed an average of 30 nanoarchitectures per cell. Subsequently, an alternating magnetic field (30 mT) with a low frequency (~ 20 Hz) was applied to those cells for 1 h, and afterward the impact of the microsdiscs movement on the considered biological entities was analysed. The statistical results (shown in figure 1.50), obtained by measuring the proportion of the different categories of cells (live vs apoptotic vs necrotic) after the procedure, indicated a significant increase in cancer cell death by apoptosis (~ 70 %), having been demonstrated, therefore, that this strategy is capable of inducing the destruction of target cells *in vitro*. Through the observation of the caspase activation after a 45 min exposure to an identical AC magnetic field, the authors also confirmed that the movement of magnetic particles linked to human renal carcinoma cells induces apoptosis.

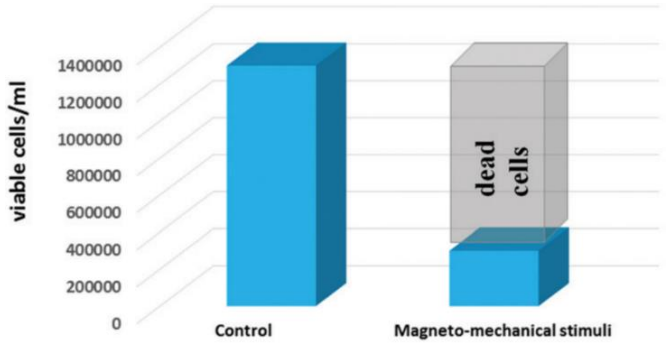

Figure 1.50 - Renal cancer cell viability after incubation with $Ni_{80}Fe_{20}$ microdiscs and subsequent exposure to an AC magnetic field for 45 min. Adapted from [447]. Used with permission of Royal Society of Chemistry, from [447]; permission conveyed through Copyright Clearance Center, Inc.

In another work, Cheng et al.[456] studied the application of Au-coated Py microdiscs, with a spin-vortex ground state, in the magneto-mechanically induced death of human glioblastoma cells (U87), having also demonstrated a distinct method for the *in vivo* destruction of those cells through the movement of the considered nanostructures in a low frequency rotating magnetic field. These magnetic microdiscs, which were fabricated through optical lithography followed by thermal evaporation, had d = 2 μm and a thickness equal to 70 nm. Then, the *in vitro* toxicity of such nanostructures was assessed on U87 glioma cells loaded with magnetic nanoarchitectures (average of 39 microdiscs per cell), by exposing those biological entities to a low frequency (20 Hz) rotating magnetic field of 1 T for 30 min (figure 1.51). After this procedure, it was observed that up to 89 % of the cells were nonviable. Additionally, a trypan blue exclusion test was performed to assess the integrity of the nanomagnet-loaded U87 cells membrane, after a 5-min treatment. Through this assay, it was demonstrated that, by applying a rotating magnetic field, such microdiscs can indeed generate enough mechanical force to affect the structure of the cell's membrane.

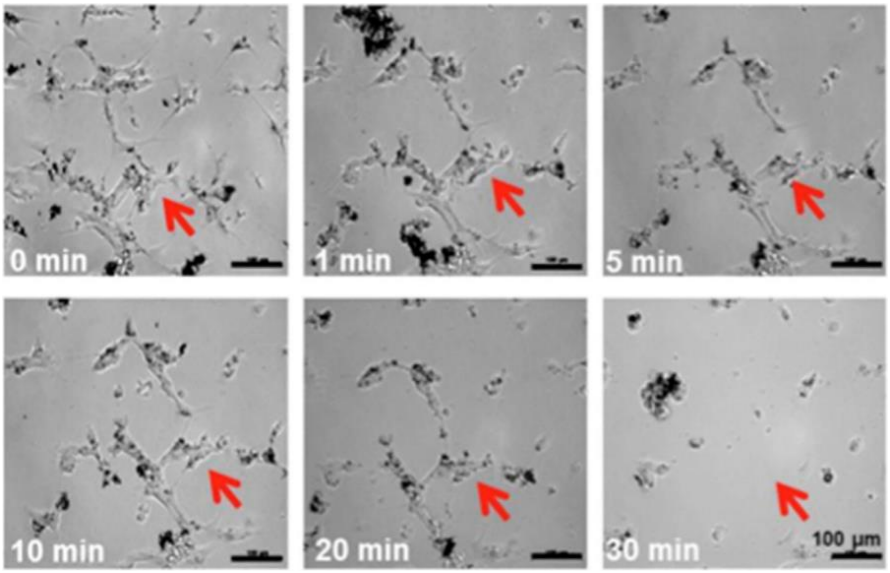

Figure 1.51 - Images of U87 cells, loaded with microdiscs, acquired from 0 min to 30 min after the treatment. The red arrow shows that the same area was tracked. Reprinted from [456], Copyright (2016), with permission from Elsevier.

Additionally, the suitability of these nanoarchitectures for inducing the magneto-mechanical cell destruction *in vivo* was assessed by implanting U87 glioma cells, preincubated for 24 h prior to injection with magnetic microdiscs at a ratio of 50 nanostructures per cell, on mice. Then, a low frequency rotating magnetic field, with identical characteristics, was applied daily for 1 h during 7 days. After such treatment, a reduced tumour size and an improved survival rate for the treated glioma-bearing mice, was verified, indicating that these microdiscs can damage cancer cells *in vivo* when

subject to a rotating magnetic field. In order to get a better understanding of the *in vivo* cell destruction mechanism in a therapeutic model, the microdiscs were injected inside a glioma, which established by intracranially injecting U87 cells on the mice's brain, at a ratio of 50:1 magnetic nanostructures to injected cell, and then a rotating magnetic field (1 T) with a frequency of 20 Hz was applied daily to those animals for 1 h during 7 days. As a result, the brain tissues, acquired after the treatment and examined by histology studies, showed an increase in the intratumoral apoptosis on the treated mice, therefore suggesting that the movement of these magnetic nanostructures in a rotating magnetic field is sufficient to damage the cancer cells *in vivo* and induce their apoptosis.

Searching for new paths, Goiriena-Goikoetxea[457] and Goiriena-Goikoetxea et al.[458] studied the suitability of NDs, i.e. disc-shaped structures with dimensions in the nanoscale, for this biomedical application, having performed a comparison between use of Py microdiscs (R = 1 μm and thickness of 60 nm) and NDs (R = 70 nm and thickness of 50 nm), with a spin-vortex ground state, for the magneto-mechanical induction of human lung cancer cells (A549) death. Consequently, several aspects related to the interaction of those magnetic structures with the considered cells were analysed, namely, their internalization, cytotoxicity, and magnetomechanical actuation effectiveness. To compare the internalization of the different discs by the cancer cells, they were coated with a biocompatible material, namely, Au (NDs) and Au or titanium (microdiscs). Furthermore, to ease their internalization by the lung carcinoma cells, the disc-shaped structures were not functionalized. Then, after incubating these materials with the considered biological entities, it was verified that the number of cells that had internalized NDs (average of 100 per cell) was a slightly larger than the ones loaded with microdiscs (average of 6 per cell). This result was attributed to the better distribution of NDs within the medium.

Subsequently, the cytotoxic effect of the Py discs on the lung carcinoma cells was evaluated. For that purpose, a nominal proportion of 25 microdiscs and 2000 NDs per cell was added and, after incubating them with the magnetic structures, the vital functions of the cells, as well as their proliferation rates, were analysed (see figure 1.52). The obtained results demonstrated that the discs did not affect the viability of the cells; however, they seemed to inhibit their proliferation. Finally, the efficiency of the magneto-mechanically actuated micro- and NDs in the induction of cancer cell death was analysed. This investigation was performed by exposing the cancer cells, previously incubated for 24 h with a nominal proportion of 25 titanium-coated microdiscs or 2000 gold-coated NDs per cell, to a 10 mT AC magnetic field, with a frequency of 10 Hz, for

30 min. 4 h after this procedure, a 15 % viability reduction among the cells that internalized microdiscs was observed. On the other hand, regarding the cells loaded with NDs, it was verified that 30 % died. Consequently, it was proven that Py NDs can also cause irreparable alterations in the integrity of cancer cells, despite the reduced number of experiments performed as well as the lack of a cytometer. The increase in cell death resulting from the use of NDs was not explicitly addressed by the authors, nevertheless, they verified that when a magnetic field was applied, these nanostructures formed chains, and, when the field was turned off, those chains broke quickly and the nanostructures redispersed, as opposed to the microdiscs, which continued to form chains in the absence of a magnetic field. Therefore, the researchers concluded that this chaining and redispersion of the NDs, originated by an AC magnetic field, could possibly disrupt the lysosomal membrane, which is where the nanostructures are accumulated, leading to the release of lysosomal hydrolases into the cytosol and, as a result, triggering apoptosis.

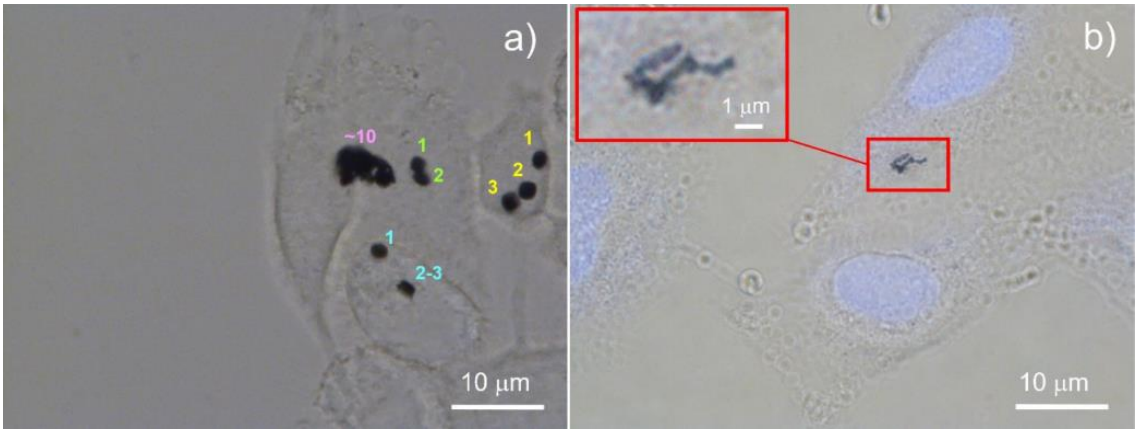

Figure 1.52 - Micrographs of lung carcinoma cells after a 24 h incubation with (a) microdiscs (coated with Au) and (b) NDs (coated with Au). From [457]. Copyright 2017 Authors licensed under a Creative Commons Attribution (CC BY 4.0) license.

The suitability of other types of magnetic nanoarchitectures and magnetic fields for this biomedical application has also been investigated by various authors. An example is the work by Wong et al.[446], where biaxial pulsed magnetic fields (14 ± 1 mT; 1–20 Hz) were applied for 10 min to suspensions of HeLa cells possessing a concentration of magnetic nanostructures equal to 0.1 mg/ml. In this study, the analysed nanoarchitectures, which exhibited a triple vortex state, had three different d's, namely, 150 nm, 250 nm, or 350 nm, and a length of 500 nm. Here, the cell apoptosis caused by applying uniaxial AC and DC pulsed magnetic fields to the cell suspensions with nanostructures exhibiting d = 150 nm, was compared against the cell death resulting from the application of biaxial pulsed fields to identical suspensions [figure 1.53(a)]. As a result, it was verified that a larger

magnetic torque is induced in the nanostructures when applying a biaxial pulsed magnetic field, leading, consequently, to an increased *in vitro* magneto-mechanically induced cell death. The authors also concluded that the nanoarchitecture with the smaller diameter had the greatest low field susceptibility and remanence, therefore allowing the application of larger forces to the cells while not agglomerating in the absence of a magnetic field. This discovery was confirmed in the cell viability test performed, where the particles with d = 150 nm originated more 12% cell death than the remaining nanostructures, which, in turn, led to a cellular mortality of around 20% at best, under identical conditions [figure 1.53(b)].

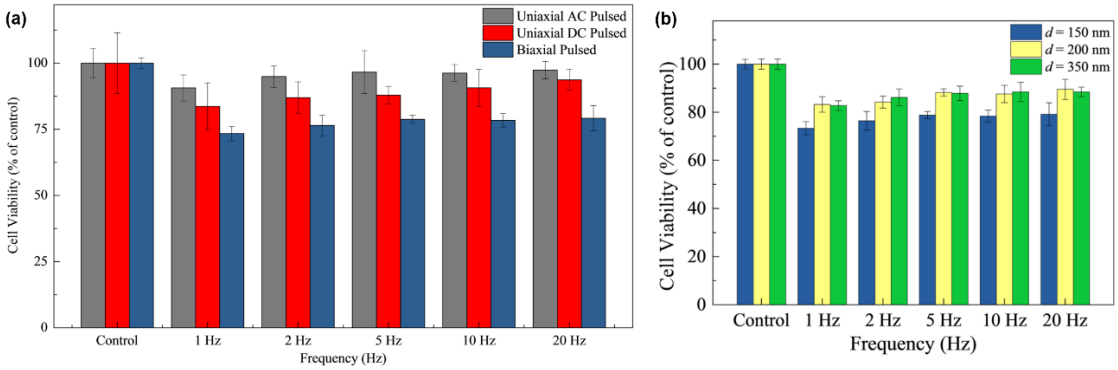

Figure 1.53 - (a) HeLa cells' viability after a treatment by magneto-mechanical actuation of nanostructures with d = 150 nm a length equal to 500 nm, using different magnetic field configurations. (b) Comparison of HeLa cells' viability after a treatment by magneto-mechanical actuation of nanostructures with d = 150–350 nm and length = 500 nm, using a biaxial pulsed magnetic field. Adapted from [446]. Copyright 2017 Authors licensed under a Creative Commons Attribution (CC BY 4.0) license.

Magnetic NWs have also been studied in the context of magneto-mechanically induced cancer cell death by various authors. One of the first reports addressing this one-dimensional nanostructure in such biomedical application is authored by Fung et al.[459] In that work, ferromagnetic Ni NWs, with d's ranging from 198 nm to 280 nm, possessing an average length of 4.4 μm, and presenting longitudinal magnetic anisotropy, were prepared by electrodeposition in nanoporous AAO templates and then incubated with fibroblasts (NIH/3T3) in culture for about 12 h (figure 1.54). Subsequently, it was verified that these nanostructures did not significantly affect the cell viability in the absence of a magnetic field, despite Ni being an agent of hypersensitivity and moderately cytotoxic. Then, the NW-loaded cells were exposed to a weak (240 mT) and low-frequency (1 Hz) rotating magnetic field for 20 min. After this process, it was observed an 89 % reduction in the viability of the cell cultures, indicating that the movement of the one-dimensional magnetic nanostructures induces, in fact, cell death.

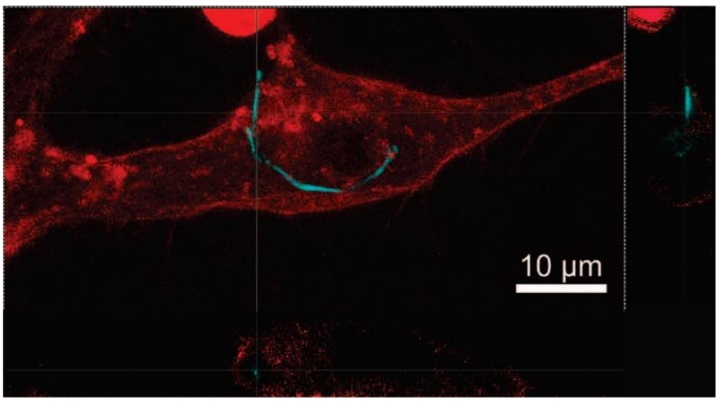

Figure 1.54 - Confocal projection and cross sections of a 3T3 fibroblast (red) possessing various Ni NWs internalized (blue). Reprinted with permission from [459]. Copyright 2008 American Chemical Society.

Complementing the previous study, Choi et al.[460] demonstrated that human embryonic kidney cells (HEK293) died as a result of the rotation of internalized Ni NWs, which had an average nominal d equal to 150 nm and longitudinal magnetic anisotropy. Such rotational motion occurred when an external AC magnetic field was applied to the NW-loaded cells, having been verified that the AC modulation amplitude and rate were fundamental parameters for determining the rotation of the nanostructures located inside the cells, however, the authors did not specify the field intensity and frequency, or the cell death rate achieved through this technique.

Also in this framework, Contreras et al.[461] analysed the magneto-mechanically induced death of human colon cancer cells (HCT116) incubated with two concentrations of Ni NWs (2.4 and 12 µg/ml). These nanostructures had d = 35 nm, were 4 µm long, and exhibited longitudinal magnetic anisotropy. Following the incubation, the viability of the cells was confirmed and, subsequently, they were exposed to an AC magnetic field (0.5 mT; 1 Hz or 1 kHz) for 10 or 30 min. Similarly to the previous reports, [459, 460], after applying the magnetic field, a drop in cell viability was verified, having been observed a maximum decrease of 38 % in cell survival when considering a nanostructures concentration of 12 µg/ml and a 1 kHz magnetic field. Furthermore, it was also demonstrated that there was no significant difference between applying the field for 10 min or 30 min, which indicates that the cell death induction mechanisms affect those biological entities fast.

Considering the same experimental conditions, Contreras[462] investigated the use of Fe and Ni NWs, with longitudinal shape anisotropy, in this specific biological application, having verified that the first nanostructures are better tolerated by the cell lines taken into account (HCT 116 and HeLa). Additionally, the effect of the NWs length on their cytotoxicity was also examined considering 1 µm and 5 µm long nanostructures,

however, it was not observed a significant influence of this parameter on the cell viability for nanostructures composed of the same material. Afterward, Fe and Ni NWs (with d = 35 nm and ~ 4 μm long) were incubated with cells (HCT 116) at two different NW-to-cell concentrations (100:1 and 500:1), and then AC magnetic fields (0.5 mT; 1 Hz or 1 kHz) were applied. Similarly to the previous study, it was verified that the magneto-mechanical actuation led to a reduction in cell viability, having been observed that when using Ni nanostructures at a 500:1 concentration and performing a 1 h exposure the percentage of dead cells was the highest (60%). Additionally, it was apparent that a 1 h incubation time was optimal for the application of this treatment.

In another work, Alsharif et al.[463] studied the feasibility of using functionalized NWs (d = 70 ± 7 nm and length equal to 1.2 ± 0.6 μm) in a combined cancer treatment approach, which consisted of magneto-mechanical (100 mT; 10 Hz) and photothermal (808 nm; 0.7 W/cm^2) therapies. Such nanostructures were composed by an iron core together with an iron oxide shell and, after their fabrication, they were functionalized with anti-CD44 antibodies (CD44-NWs), so as to actively target them to colon cancer cells (HCT116). Subsequently, these nanoarchitectures were incubated with HCT116 colon cancer cells as well as with control cells that did not express the human CD44 antigen (CHO-K1), and their internalization into those biological entities was compared against that of IgG isotype-functionalized NWs. As a result, it was verified that the anti-CD44 functionalization improved both the targeting as well as the internalization of the nanostructures in the HCT116 cells by 49.7 ± 7 %, when compared to the IgG isotype functionalization, while not affecting the antigenicity and magnetic properties of the nanoarchitecture. Furthermore, it was observed that the CD44-NWs internalization into colon cancer cells was 3 times higher than in CHO-K1 cells. Then, the combined treatment was performed for 10 min on HCT116 cells loaded with the two types of nanostructures. After such procedure, it was verified that the isotype-functionalized nanoarchitectures led to a 35 ± 1 % cell death, while the CD44-NWs produced a reduction in cell viability of 71 ± 2 %, having also been shown that the combined therapy originated greater cell mortality than the individual treatments alone. Consequently, through the obtained results, the researchers demonstrated that functionalized core-shell NWs are a very good nanotherapeutics tool for multimodal cancer cell destruction, increasing the cell-killing efficacy and specificity.

Other study regarding the application of magnetic NWs in this particular context was authored by Martínez-Banderas et al.[445] Here, the researchers developed a bimodal strategy for inducing cancer cell death, which consisted in combining the chemotoxic

effect caused by an anticancer drug (DOX) with the mechanical perturbation exerted by Fe NWs (average length of 6.4 ± 1.3 μm and d = 30 - 40 nm), when they were exposed to a low frequency (10 Hz) AC magnetic field (1 mT) for 10 min. The considered nanostructures, shown in figure 1.55, were coated with APTES or with BSA, which allowed their subsequent functionalization with DOX.

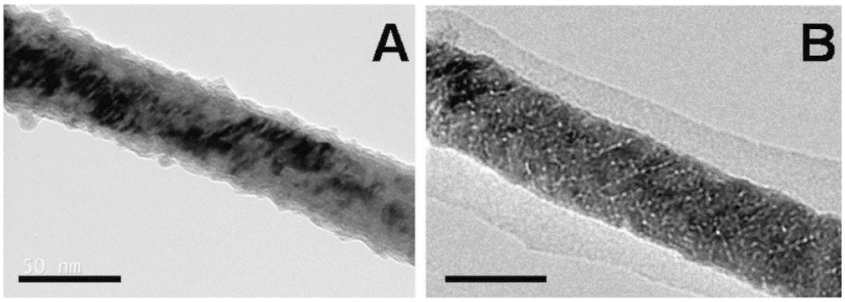

Figure 1.55 - TEM micrographs of (a) APTES-coated NWs, and (b) BSA-coated NWs. The scale bars represent 50 nm. From [445]. Copyright 2016 Authors licensed under a Creative Commons Attribution (CC BY 4.0) license.

In this work, the efficiency of such approach for inducing cell death was determined by assessing the reduction it produced in the viability of breast cancer cells (MDAMB-231). For that purpose, the APTES- and BSA-coated nanostructures were incubated with the cancer cells, at a concentration of 0.05 mg-Fe/mL for 24 h, having been verified that the functionalized NWs possessed good biocompatibility as well as a high degree of internalization in the considered cell line, being therefore efficient carriers for drug delivery. Furthermore, it was observed that the BSA-coated NWs had a higher cellular internalization (26 ± 3 pg of Fe per cell) and a wider distribution within the cells, besides forming smaller and less compact clusters. Consequently, these nanoarchitectures were considered a more efficient option for the induction of cell death. Subsequently, the authors analysed the capacity of the DOX-functionalized NWs to induce cancer cell death, through the combination of the selective drug release with the mechanical disturbance upon the application of the low-frequency AC magnetic field previously described. As a result, it was observed a large cytotoxic effect in the NW-loaded cells after their exposure to the magnetic field, having been obtained a maximum reduction of 69 % and 73 % in cell viability when using APTES- or BSA-coated nanostructures, respectively, functionalized with DOX. Additionally, the authors found that the combination of the chemotoxic and magneto-mechanical treatment modes, using magnetic NWs, had synergistic effects, turning this technique into an attractive approach for novel cancer therapies.

Serrà et al.[464] studied the suitability of a different type of NW for this biomedical application. Such nanostructures, fabricated through a single-bath potentiostatic-pulsed

electrodeposition process, were multisegmented, nontoxic, and biocompatible $(Au/NiNiO)_8$ NWs with longitudinal magnetic anisotropy. These particular nanoarchitectures have a triple functionality, since they can carry two types of functional molecules and induce cell death by magneto-mechanical actuation, having been functionalized, in this specific work, with protoporphyrin IX zinc and with 1,9-nonanedithiol. Then, to assess their suitability for inducing cell death, HeLa cells were incubated with different concentrations of $(Au/NiNiO)_8$ NWs (0-375 μg/ml) and, after their internalization into the cells and subsequent cytotoxicity evaluation, AC magnetic fields, with a frequency of 20 Hz and strengths ranging from 2 to 40 mT, were applied to the NW-loaded cells, which caused the nanostructures to vibrate and move inside those biological entities. After this procedure, it was verified that the motion of the NWs induced the apoptosis in the HeLa cells, not having been noticed any evidence of mechanical destruction. Additionally, it was also shown that cell death increased (up until 24 %) as the applied magnetic field got stronger. Therefore, these multisegmented nanostructures provide a novel platform that induces the death of cancer cells, allowing the combination of a magneto-mechanical actuation with drug release.

Besides NWs and discs with a spin-vortex ground state, some authors have also analysed the suitability of SAF nanostructures for the magneto-mechanical induction of cell death. An example is the report by Mansell et al.[465], where the efficiency of disc-shaped SAFs, possessing d = 2 μm and with perpendicular magnetic anisotropy, for inducing cancer cell destruction through magneto-mechanical actuation was assessed by performing an *in vitro* study using glioma (U87) cells. These nanostructures were fabricated from a repeated motif of ultrathin CoFeB/Pt layers and their efficiency for this biomedical application was compared against that of Py microdiscs with a spin-vortex ground state, which have an easy magnetization plane, under the same conditions (figure 1.56).

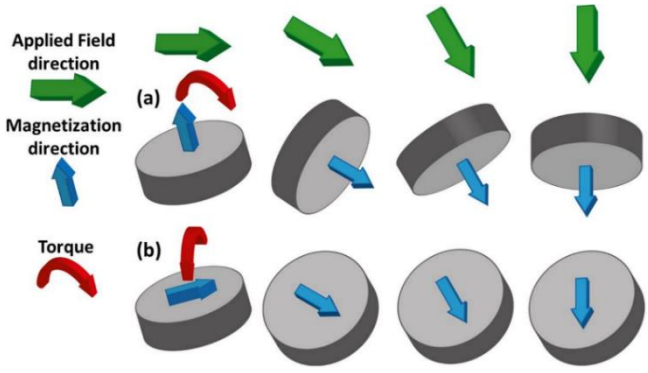

Figure 1.56 - Illustration demonstrating the magnetization direction and torques in (a) a disc-shaped CoFeB/Pt nanostructure and (b) a Py magneticvortex microdisc; in the presence of a rotating magnetic field. From [465]. Copyright 2017 Authors licensed under a Creative Commons Attribution (CC BY 4.0) license.

To achieve such goal, first the two types of nanoarchitectures were incubated with U87 cells at a ratio of 50 particles per cell for 24 h. Then, a rotating (20 Hz) magnetic field (1 T) was applied during 1 min to the magnet-loaded cells, and, subsequently, the cell damage was quantified. As a result, it was verified that the CoFeB/Pt microdiscs were able to induce 62 ± 3 % cell death, however, under the same conditions, the Py microdiscs only originated a cell mortality of 12 ± 2 %. Additionally, the torque applied by the two types of structures was measured, having been obtained maximum values of 20 fNm and 75 fNm for the CoFeB/Pt nanostructures and the Py microdiscs, respectively. Therefore, in this work it was shown that the symmetry of the anisotropy is more relevant than the magnitude of the torque for causing effective cell destruction. Consequently, the ability to explore the anisotropy of nanostructures can also open new paths for this biomedical application.

Kwon[466] also investigated the suitability of disc-shaped SAF nanostructures for the magneto-mechanical induction of cell death. Such nanoarchitectures were composed by a [Ti_{cap}/(Fe_3O_4/Ti)$_{X-1}$/Fe_3O_4/Ti_{cap}] layered structure and had a d ~ 350 nm. Then, after their fabrication, they were internalized into HeLa cells and, subsequently, it was applied an AC magnetic field (200 mT; 1 Hz) to those biological entities, having been assessed the effect of the NDs concentration, as well as the influence of treatment time, in the cell viability after the magneto-mechanical actuation. As a result, it was observed that the cell viability decreased as the concentration of nanostructures increased, having been noticed the existence of a “threshold” concentration, corresponding to ratio of 1 nanostructure:4 cells, at which the cell viability decreased abruptly. Additionally, it was verified that with an exposure of 8 min to the magnetic field (considering a ratio of 1 nanostructure:1 cell), 80 % of the cells were viable; however, when that period was increased to 16 min, less than 8% of the biological entities survived. Therefore, the obtained results showed that these nanoarchitectures, depending on the analysed parameters, induce different levels of cell mortality when exposed to an AC magnetic field.

The use of a different type of magnetic nanoarchitecture with a rectangular-shape (figure 1.57), prepared by wet milling of superferromagnetic Fe-Cr-Nb-B precursor glassy ribbons, in this biomedical application was investigated Chiriac et al.[289] These nanostructures possess an improved torque in a rotating magnetic field, due to the shape anisotropies induced not only by their shape, but also by the superferromagnetism of the glassy alloys. To assess their effectiveness in cell death induction, the authors incubated human osteosarcoma cells (MG-63) with different concentrations of these

nanostructures, namely 0.5, 1, 2, 3, and 5 mg of nanoarchitectures in 1 ml of cell culture, and afterward exposed the nanostructure-loaded cells to a rotating magnetic field (1 mT; 20 Hz) for 10 min. In this work, the effect of the exposure time on cell mortality was also investigated by exposing a nanoarchitectures concentration of 2 mg/ml for 0, 5, 10, 15, and 20 min to the same magnetic field. Then, the cell viability (figure 1.58) was analysed, having been verified that the rotation of these NPs caused relevant damage to the considered cells, leading to greater cell death as the nanoarchitectures concentration and exposure time increased. Therefore, it was demonstrated here that this type of nanostructures is also suitable for the magneto-mechanical induction of cell death.

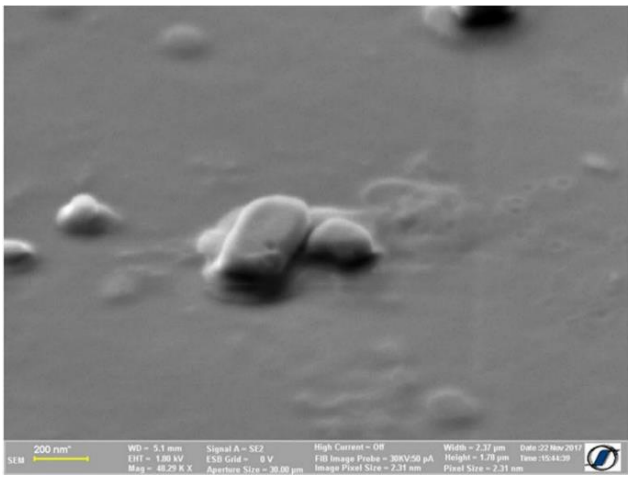

Figure 1.57 - SEM image of the rectangular-shaped magnetic nanoarchitectures. Adapted from [289]. Copyright 2018 Authors licensed under a Creative Commons Attribution (CC BY 4.0) license.

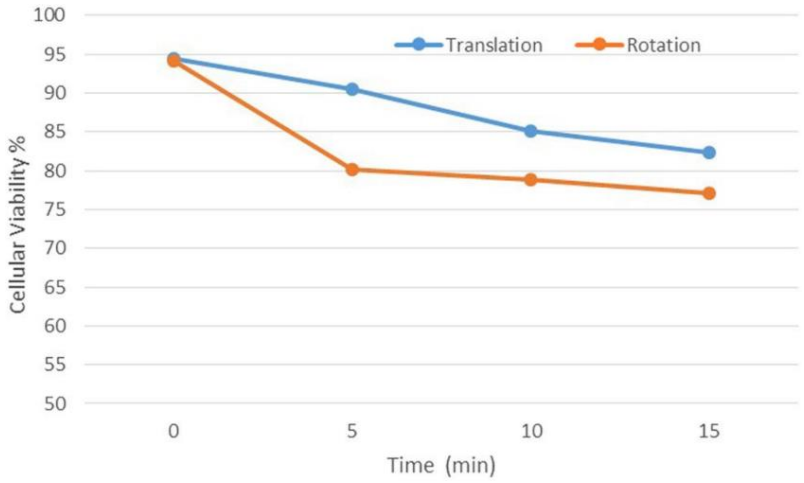

Figure 1.58 - Viability of MG-63 cells loaded with rectangular-shaped magnetic nanostructures, as a function of the exposure time to an AC magnetic field, which can cause the translation or rotation of the nanoarchitectures. From [289]. Copyright 2018 Authors licensed under a Creative Commons Attribution (CC BY 4.0) license.

In a different work, Shen et al.[467] investigated the feasibility of using another type of nanomaterial in this biomedical application. Here, cube-shaped iron oxide NPs doped

with Zn were fabricated and then functionalized with the epidermal growth factor (EGF) peptide, so as to target them to human glioblastoma cells (U87) *in vitro*. Consequently, after incubating the NPs with the cells at a concentration of 100 μg/ml, the nanomagnet-loaded cells were exposed to a low frequency (15 Hz) rotating magnetic field (40 mT) for 30 min per day for 3 days. As a result, it was verified that the application of the magnetic field led to the formation of elongated NP aggregates with longitudinal magnetic anisotropy, which generated forces in the order of hundreds of pN inside the cells. Furthermore, after the 3-day procedure, it was observed that more than 90% of the cells were damaged, indicating, therefore, that such clusters are in fact capable of inducing the death of cancer cells.

More recently, Yao et al.[468] addressed the dependence of the magneto-mechanical therapeutic effect and cell death pathway on the geometry of the magnetic nanomaterials. For such purpose, these authors synthesized two magnetic nanocomposites with the same composition, i.e. $Zn_{0.2}Fe_{2.8}O_4$-Poly(lactic-co-glycolic acid), but possessing different shapes, namely spherical (magnetic nanospheres) and chain (magnetic nanochains) geometries. When exposed to a rotating magnetic field, the magnetic nanospheres presented a corkscrewed circular propulsion mode, while the magnetic nanochains exhibited a steering propulsion mode, indicating that the shape of the magnetic nanomaterials affects their behaviour when exposed to a changing magnetic field. Then, in order to assess the influence of the nanomaterials' geometry on their potential for magneto-mechanical induction of cancer cell death, numerical simulations and *in vitro* assays with both types of nanomagnets, using MCF-7 cells, were performed. As a result, it was verified that the strength of the rotating magnetic field, as well as the rotating speed of the magnetic nanostructures, had a significant impact on the induction of cell death via magneto-mechanical actuation (figure 1.60). Particularly, cell death increased with increasing field strength, however the rotating speed of the magnetic field did not have such a linear relationship with cell death, leading to a performance plateau at 200 rpm and 500 rpm for magnetic nanospheres and magnetic nanochains, respectively. Regarding their therapeutic performance, the *in vitro* studies carried out revealed a that the magnetic nanochains led to better results, than magnetic nanospheres, despite the fact that their internalization was lower. This result was attributed to the fact that magnetic nanochains exert higher forces on cell constituents, due to their greater size. Moreover, the authors verified that the magneto-mechanical effects of magnetic nanospheres have a higher likelihood of triggering cell apoptosis, since their predominant cell death pathway was lysosomal membrane damage. On the

other hand, those of magnetic nanochains tend to promote cell necrosis, as they predominantly caused a cell membrane rupture.

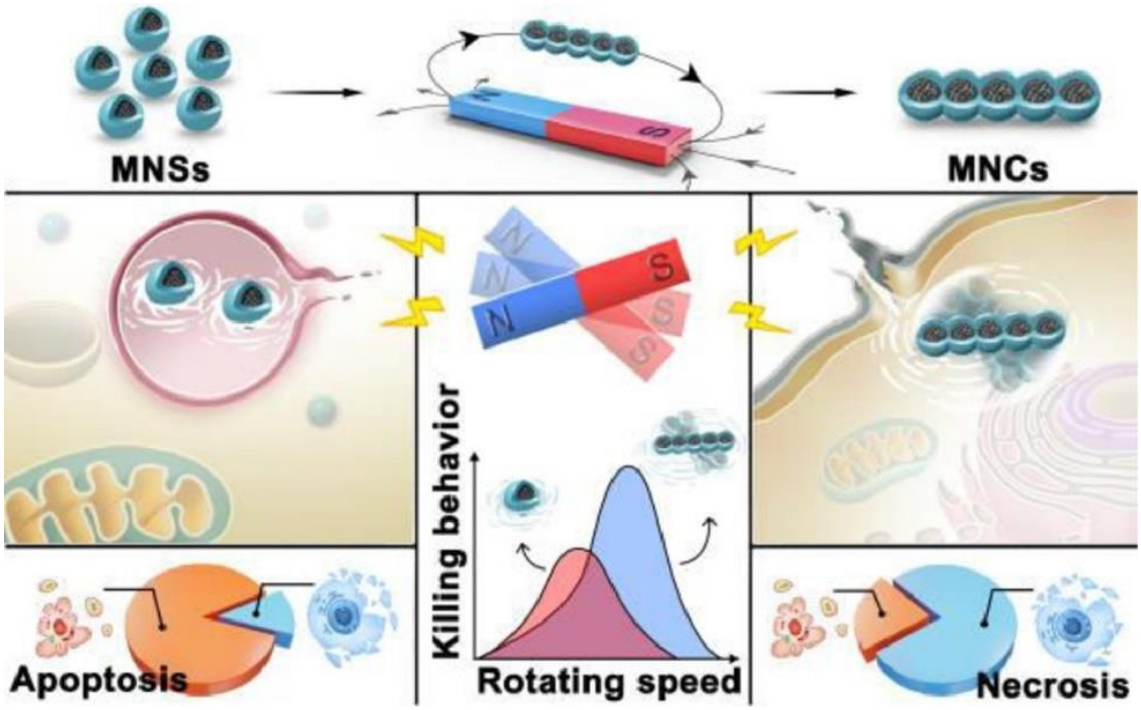

Figure 1.59 - Magneto-mechanical effects of magnetic nanospheres (MNSs) and magnetic nanochains (MNCs) on cancer cells. Reprinted from [468], Copyright (2023), with permission from Elsevier.

1.3.5. Nanostructured Lipid Carriers (NLCs)

As previously mentioned, the introduction of nanomaterials in the biomedical field has led to the development of a new viewpoint regarding drug delivery that holds the potential to minimize adverse effects on healthy tissues, since that type of materials has the capability to traverse the blood vessels and deliver drugs directly to the target site.[469] Furthermore, the use of nanomaterials for this biomedical application offers additional benefits, including the enhancement of the solubility of hydrophobic substances and shielding against unwanted interactions before arriving at the target site. Consequently, this enhances the drug stability, alters its pharmacokinetics, and influences its biodistribution.[470,471]

A search through the literature reveals that various authors have already studied multiple NP-based drug delivery systems (figure 1.60), such liposomes and pegylated liposomes[472], polymeric micelles[473], microemulsions[474], solid lipid NPs (SLNs)[475], nanostructured lipid carriers (NLCs)[476], carbon NTs[477], as well as magnetic NPs.[487]

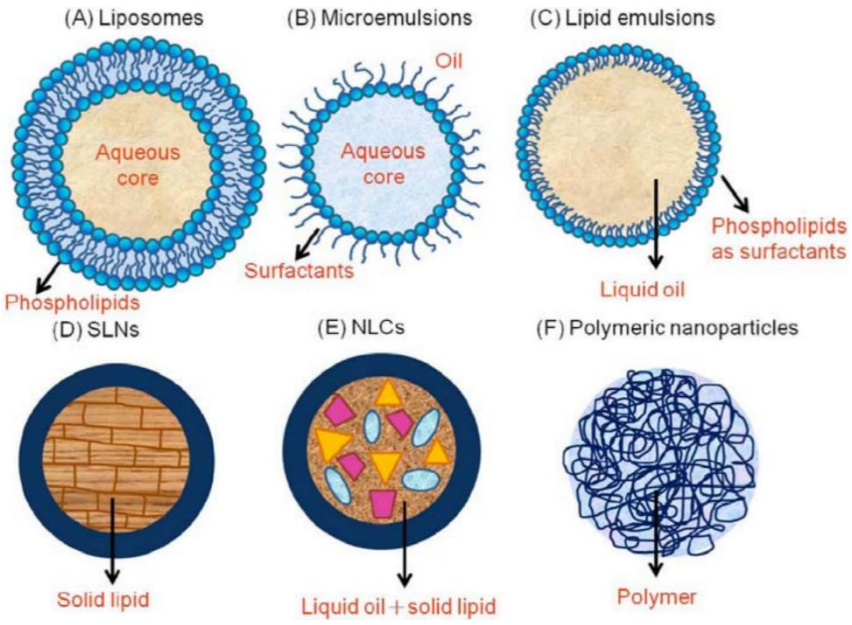

Figure 1.60 - Illustration of various categories of nanostructured particles: (a) liposomes, (b) microemulsions, (c) lipid emulsions, (d) SLNs, (e) NLCs, and (f) polymeric NPs. Used with permission of EUREKA SCIENCE (FZC), from [479]; permission conveyed through Copyright Clearance Center, Inc.

Among all these drug delivery systems, lipid NPs, such as liposomes, SLNs, or NLCs, are particularly promising, since they are biocompatible and biodegradable, have a high capacity to incorporate both hydrophilic and lipophilic drugs, are easily synthesized, and can be administered by various routes.[480,481] In this context, liposomes are the most widely studied drug delivery system, having been approved for use in the clinical practice in 1995.[482] These are self-assembled, spherical lipid vesicles made up of amphiphilic phospholipids, possessing a bilayer membrane structure and a central aqueous compartment, being capable of incorporating both hydrophilic and lipophilic drugs [figure 1.60(a)].[483-486] Currently, there are several liposomal products on the market, including liposomal formulations of DOX (Doxil®), daunorubicin (DaunoXome), cytarabine (DepoCyt), as well as vincristine (Onco-TCS).[487] Nevertheless, a limitation of liposomes is their susceptibility to rapid degradation when exposed to the stomach's acidic pH, or by the action of intestinal enzymes and bile salts, during oral administration, which hinders their physical and chemical stability.[488-490] Moreover, they exhibit a reduced drug encapsulation efficiency (EE) and have high production costs, as well as a complex production method, which makes their large-scale production difficult.[491,492]

To try overcoming the limitations associated with liposomes, SLNs were proposed in the early 90's as a promising marketable alternative.[493] These NPs are composed of a solid lipid core (e.g. triglycerides, fatty acids, waxes) surrounded by a surfactant layer (e.g. poloxamers, polysorbates) in an aqueous medium [figure 1.60(d)].[494-496] The simplicity

and versatility of this type of nanomaterials have made them popular options for drug delivery applications in diverse sectors, including cosmetics, the food industry, and pharmaceutical.[497-500] Furthermore, they can be prepared without the use of toxic organic solvents.[501] Nevertheless, SLNs have some disadvantages, such as limited loading capacity and increased risk of drug expulsion during storage, as a result of polymorphic transitions of the lipid crystals or a decrease in their number of imperfections.[502-504]

Consequently, a second generation of lipid NPs known as NLCs were developed in the late 90s, so as to try overcoming the disadvantages associated with SLNs.[505,506] The difference between this type of nanomaterials and SLNs is that the NLCs' core is composed of a mixture of solid and liquid lipids, as represented in figure 1.60(e).[507] The introduction of the liquid lipid leads to a less crystalline and more imperfect lipid matrix, which increases the drug loading capacity.[508-510] Furthermore, NLCs are recognized for their enhanced physical stability, minimal toxicity, superior drug solubility, and improved bioavailability when compared to other drug delivery systems. Additionally, they hold promise in circumventing the mechanisms associated with multidrug resistance.[511-515] Moreover, they can be fabricated at a large scale with relatively low production costs, not requiring the use of organic solvents.[516,517] Besides these advantages, it is possible to combine various systems in a single NLC, such as magnetic NPs, allowing a wider range of applications in both diagnostic and therapeutic contexts.[518]

1.3.5.1. Targeted Anticancer Drug Delivery

Currently, the use of chemotherapy to treat various types of cancer continues to encounter obstacles, including issues like limited specificity and drug solubility, heightened toxicity towards healthy tissues, and the development of multidrug resistance, leading to low response rates.[519-521] In this context, NLCs have emerged as promising anticancer drug carriers for the targeted delivery of chemotherapeutic agents, due to their large drug loading capacity, high stability, potential for surface functionalization, capacity to protect labile pharmaceuticals from degradation, and straightforward synthetization process.[522,523]

NLCs loaded with anticancer drugs, and with a suitable size, can selectively accumulate in tumour sites due to the enhanced permeability and retention (EPR) effect. This passive targeting strategy allows small particles to escape through the leaky, disorganized, and underdeveloped blood vessels within tumours, which are characterized by large fenestrations (ranging from 60-400 nm), leading to an increase of the anticancer drug concentration at the tumour site.[524-526] Additionally, it is possible to conjugate the drug-loaded NLCs with a targeting molecule for an active targeting of the cancer site.[527] One

example is folic acid that is recognized by folate receptors, which are selectively overexpressed in tumour cells.[528]

Moreover, the drug release from NLCs can be triggered by various factors, including intracellular conditions like pH and temperature, as well as external stimuli such as AMF, ultrasound, and laser, depending on their design. For example, it is possible to leverage the differences in the acidic microenvironment of cancerous cells (pH 4.5 - 6.5) compared to the physiological microenvironment of normal cells (pH 7.5), combining pH as a stimulus with another external trigger offers the potential for more precise control over drug release rates. This approach can enhance the therapeutic efficacy of the treatment while reducing systemic toxicity.[529-532]

A search through the literature reveals that the use of NLCs for targeted delivery of different anticancer drugs generally leads to improved IC_{50} values in *in vitro* assays, as well as increased tumour inhibition rates in *in vivo* experiments, in a wide range of cancer types.[533-538] For example, Li et al.[539] analysed the suitability of NLCs to co-deliver β-lapachone and DOX (LDNLC) for treating multidrug-resistant breast cancer. Using MCF-7 ADR cells, the authors verified that lapachone led to the production of reactive oxygen species and downregulated the P-glycoprotein efflux pump activity, which, in turn, substantially enhanced the intracellular accumulation of the co-administered DOX, thereby allowing to overcome multidrug resistance in cancer cells. Furthermore, *in vitro* assays revealed an increased DOX retention, considered breast cancer cells, when administering LDNLCs in comparison to using NLCs only loaded with DOX. These authors also performed *in vivo* assays using MCF-7 ADR tumour bearing mice, having observed a notably superior efficacy of LDNLC when compared to the single-drug delivery NLCs (DOX-loaded NLCs and lapachone-loaded NLCs). In another work, Fernandes et al.[540] assessed the anticancer activity of NLCs loaded with DOX and of NLCs loaded with DOX and α-tocopherol succinate, in both two breast cancer cell lines (MDAMB-231 and 4T1) and in 4T1 tumour-bearing mice. As a result, the authors verified a synergic effect between α-tocopherol succinate and DOX, which led to an increase of the antitumor efficacy in comparison to free DOX and NLCs loaded with that anticancer drug. Another study, by Ong et al.[541], addressed the suitability of NLCs loaded with another potential chemotherapeutic drug, i.e. thymoquinone, for cancer treatment, using 4T1 tumour-bearing mice. Here, the authors observed that by incorporating thymoquinone into NLC, the therapeutic potential of that drug was increased, leading to a higher mice survival rate when compared to its free form.

Nevertheless, the recognition and clearance of the NPs by macrophages, as well as resident reticuloendothelial cells in the circulatory system, present a challenge for this type of drug delivery systems. To overcome such problem, some approaches have been reported, such as lowering the NPs' dimensions to less than 5.5 nm or maintaining a nearly neutral charge on their surface, which prevents plasma proteins from adhering and, consequently, helps them evade clearance by macrophages.[542-544] An alternative approach involves coating the surface of NPs with hydrophilic polymers, which provide an aqueous shield around them, minimizing the interaction between the NP and proteins in the bloodstream that can mark them as foreign entities for subsequent elimination by immune cells.[545] A typically used polymer for this purpose is PEG, since it possesses an adequate biocompatibility and is classified as Generally Recognized as Safe (GRAS) by the Food and Drug Administration (FDA).[546,547] The coating of NPs with PEG protects their surface from aggregation, opsonization, and phagocytosis, which in turn, extends their circulation time and, ultimately, enhances the delivery of therapeutic cargo. Furthermore, PEG coatings can enhance the ability to overcome various biological barriers, by, for example, minimizing interactions with tissue extracellular matrix, cellular barriers, as well as biological fluids like mucus, and, as a result, improve the delivery of the desired compounds.[548]

Taking this into account, Moraes et al.[549] fabricated PEG-Folic Acid-conjugated NLCs loaded with DOX and assessed their potential for the targeted delivery of that anticancer drug to breast cancer cells (MDA-MB-231). In this work, the authors designed and optimized two different NLC formulations, where only the solid lipid was varied, having been obtained an EE % > 65 %. Additionally, *in vitro* assays demonstrated that all the formulations successfully reached the tumour microenvironment carrying 50 % of the encapsulated DOX.

1.3.5.2. Hybrid Magnetic Lipid-Based Nanoparticles for Cancer Therapy

Besides anticancer drugs, it is possible to load NLCs with other types of therapeutic agents, to enhance their capacity for inducing the death of cancer cells. A particularly promising approach involves loading magnetic NPs into those nanomaterials to obtain hybrid magnetic lipid-based nanoparticles with multifunctional capabilities.[550]

One example is the work by Rodenak-Kladniew et al.[551], where chitosan-coated bioactive NLCs, loaded with 1,8-cineole (a monoterpene with antiproliferative properties) and maghemite NPs were developed. Their characterization revealed a d ~ 250 nm and zeta potential of +10.2 mV, as well as monodispersed particle sizes. Furthermore, it was achieved a high encapsulation efficiency (over 75 %) of 1,8-cineole, which was effectively

released in 24 h. Additionally, the incorporation of 1,8-cineole into the lipid matrix promoted the nanostructuration of the NLCs. Moreover, the incorporation of maghemite NPs into those lipid NPs was successful, having led to the production of NLCs with a superparamagnetic behaviour, which could potentially be used for MHT and/or physical targeting. Particularly, it was observed a greater release of 1,8-cineole as the temperature increased from 37 ºC to 45 ºC (figure 1.61), indicating the potential of these NPs for a dual treatment approach, involving MHT together with local drug delivery promoted by the temperature increase. *In vitro* cell studies, using these NPs, revealed that they were not toxic in healthy human fetal lung fibroblast cells (WI-38), but were capable of reducing the viability of both lung (A549) and liver (HepG2) cancer cells, in the absence of a magnetic field. Moreover, the cytotoxic effect of 1,8-cineole was increased when that compound was incorporated into the NLCs, in comparison to its free form. Additionally, the chitosan-coating of these NPs, improved the selective cellular uptake of these hybrid NPs into the cancer cells.

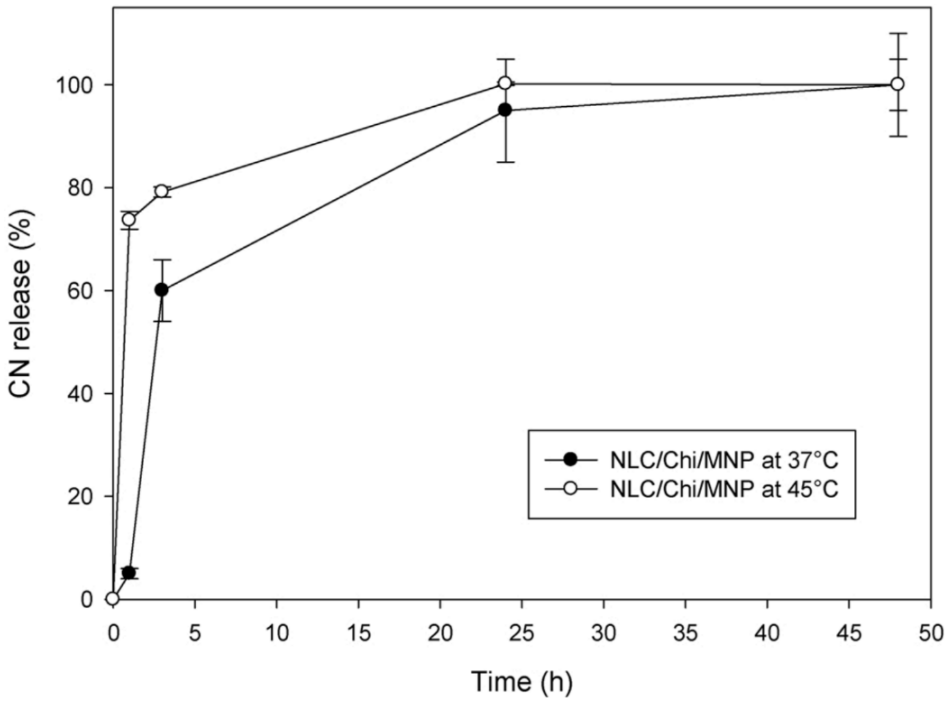

Figure 1.61 - Release profile of 1,8-cineole (CN) from the produced NLCs at 37 ºC and 45 ºC. The values are expressed as the mean ± standard deviation from the mean (n = 3). Reprinted from [551], Copyright 2021, with permission from Elsevier.

Chitosan-coated lipid NPs were also developed by Ahmadifarda et al.[552] In this work, Letrozole, an anticancer drug, was co-loaded together with magnetic NPs into magnetic SLNPs, which were coated with chitosan, and the potential of this system for the delivery of the compound to cancer cells through active and passive targeting was analysed. The characterization of the produced revealed a size of 193.2 nm, a polydispersity index

(PDI) equal to 0.2, and a surface charge of -20.0 mV. Additionally, an EE and drug loading of 90.1% and 26.2 %, were achieved. By analysing the release profile of Letrozole, it was verified that 50% of the drug was exerted by applying a low frequency pulsed magnetic field (8 mT; 50 Hz) for 1 h, while in the absence of a magnetic field it took 12 h to release the same quantity of drug. Moreover, a 2,2-Diphenyl-1-picrylhydrazyl (DDPH) free radical scavenging test was performed to analyse the antioxidant capacity of this novel system, having been observed a considerable concentration-dependent DPPH radical scavenging effect, similar to that of butylated hydroxytoluene. Moreover, *in vitro* cell assays using a normal endothelial cell line (HUVEC), as well as different cancer cell lines, namely breast adenocarcinoma (MCF-7), breast carcinoma (Hs 578Bst), infiltrating ductal cell carcinoma (Hs 319.T), infiltrating lobular carcinoma of breast (UACC-3133), inflammatory carcinoma of the breast (UACC-732), and metastatic carcinoma (MDA-MB-453) cell lines, were performed. As a result, it was verified that by using a low-frequency pulsed magnetic field, it was possible to promote the anticancer drug release from this lipidic system, resulting in an increased cancer cell death.

In another study, On et al.[553] synthesized NLCs co-loaded with methotrexate, an anti-neoplastic agent used for treating breast cancer, and SPIONs, so as try developing a new strategy for treating that type of tumour, based on an improved drug release mediated by MHT. The characterization of the resulting formulations revealed a mean d ~ 200 nm, PDI below 0.1, highly negative zeta potential, high encapsulation efficiency, good biocompatibility and an adequate haemocompatibility. Moreover, they exhibited a high storage stability for 3 months at room temperature, having also maintained their physicochemical properties after being incubated for 24 h in various biological media. *In vitro* cell assays revealed a time-dependent cytotoxic effect towards a breast cancer cell line (MDA-MB-231), having presented IC_{50} values of 137 µg/mL and 12 µg/mL at 48 and 72 h, correspondingly. Regarding their uptake by the same cell line, it was verified that these NPs were internalized through caveolae-mediated endocytosis in a time-dependent way. Moreover, by exposing the produced NLCs to an external alternating magnetic field (20 mT; 869 kHz), a hyperthermia effect was observed, which originated a localized temperature increase at the cellular level that was sufficient to promote the apoptotic cell death, indicating their potential as a multi-modal system for treating breast cancer.

A similar work was carried out by Tan et al.[554], where zerumbone, an anticancer agent also used for breast cancer, was loaded, together with SPIONs, into NLCs, forming a multimodal platform for improving the therapeutic effectiveness of that drug for treating

that type of cancer (figure 1.62). These systems were optimized, having been obtained an average size equal to 140.32 ± 1.14 nm, a polydispersity index of 0.18 ± 0.02, and zeta potential of -13.37 ± 0.61 mV. Additionally, they presented an adequate hemocompatibility with human blood, a high encapsulation efficiency, as well as a good storage stability for 3 months, when stored at 4 ºC. Regarding the drug release, it was verified that it followed zero-order kinetics, being independent of the medium's pH. *In vitro* cell assays using two different breast cancer cell lines, i.e. MCF-7 and MDA-MB-231, revealed that these lipid NPs were internalized through different mechanisms, namely clathrin- and caveolae-mediated endocytosis and energy-dependent active transport, respectively. Moreover, the produced NLCs exhibit a significant cytotoxicity towards both cell lines, having been obtained IC_{50} values equal to 1.81 and 1.85 µg/mL for MDA-MB-231 and MCF-7, respectively, after a 72 h incubation with those NPs. Furthermore, by exposing this multimodal platform to a 0.5 T magnetic field, the authors verified that it was possible to direct the lipid NPs, leading to an increase in their uptake by 40.41 % in MDA-MB-231 cells and 19.35 % in MCF-7 cells, when compared to NLCs not exposed to a magnetic field.

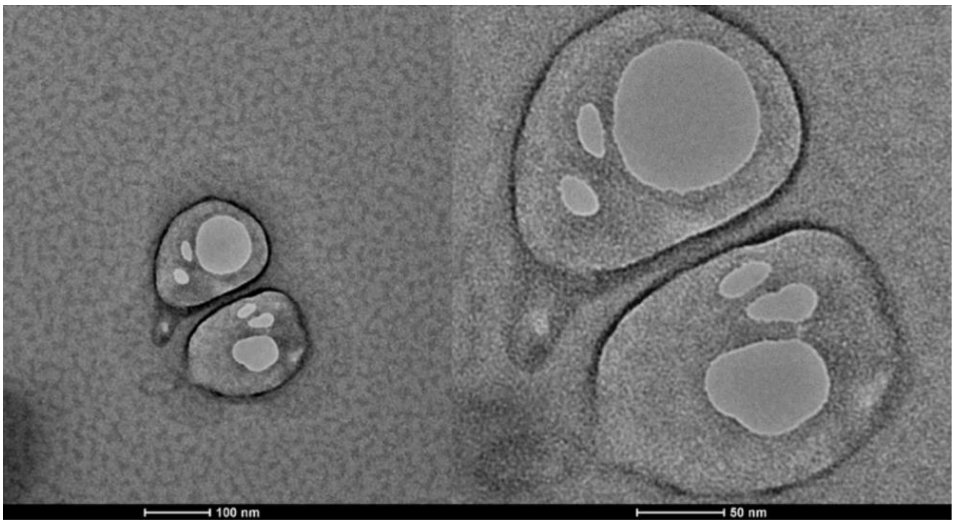

Figure 1.62 - TEM micrographs of the produced NLCs loaded with SPIONs and zerumbone. From [554]. Copyright 2023 Authors licensed under a Creative Commons Attribution (CC BY 4.0) license.

Yoozbashi et al.[555] reported the fabrication of a different type of magnetic NLCs, loaded with curcumin. In this case, magnetite NPs worked as the magnetic core of the targeted carriers and their characterization revealed sizes of 140 ± 3.6 nm, PDI equal to 0.196, a zeta potential of -22.6 mV, as well as promising magnetic properties. Moreover, it was observed a greater release rate of curcumin at 42 ºC, than at 37 ºC. suggesting a temperature-dependent behaviour. Additionally, the effect of these NLCs on different mitochondrial functions were analysed using isolated rat liver mitochondria, having been

verified that they do not present specific mitochondrial toxicity. Karami et al.[556] also reported the production of NLCs co-loaded with SPIONs and curcumin for the targeted delivery of that compound to human breast cancer cells, to address chemotherapy's shortcomings by improving drug accumulation at tumour sites while minimizing adverse effects on healthy cells. The characterization of the fabricated NLCs, revealed adequate properties, including a particle size equal to 166.7 ± 14.20 nm, zeta potential of -27.6 ± 3.8 mv, as well as a PDI of 0.24 ± 0.14. Moreover, an EE % of 99.95 ± 0.015 % and a drug-loading capacity (LC) equal to 3.76 ± 0.005 % were obtained. Then, *in vitro* cell assays, demonstrated an improved cytotoxic activity of these NPs towards breast cancer cells (MCF-7) compared to free curcumin, highlighting its potential for targeted cancer therapy.

Another study, by Abbas et al.[518], addressed the use of NLCs co-loaded with clonazepam, an anti-epileptic, and SPIONs for targeting that compound to the brain via the intranasal olfactory mucosa, through the use of an external magnetic field. These nanolipid carriers were incorporated in a pluronic F127-based thermosensitive mucoadhesive in situ gel composed of 15% pluronic 127 and 0.75% sodium alginate, so as to improve their delivery by prolonging the retention at the application site. Furthermore, the researchers assessed the anticonvulsant characteristics of these NPs in chemically-induced convulsive Swiss Albino mice, observing significantly prolonged onset times for convulsions and a considerable protection of the animals from death. Additionally, it was verified that the NPs more effectively directed towards the olfactory nerve endings through the application of an external magnetic field.

References

[1]R. Amin, S. Hwang, and S. H. Park, Nanobiotechnology: An interface between nanotechnology and biotechnology, *Nano* **6**, 101–111 (2011).

[2]P. Chee, W. Toh, P. Yew, S. Peng, and D. Kai, Introduction of Nanotechnology and Sustainability. In: *Sustainable Nanotechnology*, 1–32 (The Royal Society of Chemistry, 2022).

[3]S. Balasubramanyam, *Nanoengineering of Two-Dimensional WS2 by Atomic Layer Deposition*. PhD Thesis, Technische Universiteit Eindhoven (2020).

[4]S. Gul, S. B. Khan, I. U. Rehman, M. A. Khan, and M. Khan, A Comprehensive Review of Magnetic Nanomaterials Modern Day Theranostics. *Frontiers in Materials* **6**, 179 (2019).

[5]A. K. Hauser, R. J. Wydra, N. A. Stocke, K. W. Anderson, and J. Z. Hilt, Magnetic Nanoparticles and Nanocomposites for Remote Controlled Therapies. *Journal of Controlled Release* **219**, 76–94 (2015).

[6]U. Schubert and N. Hüsing. *Synthesis of Inorganic Materials.* Wiley (2012).

[7]F. Han, *A Modern Course in the Quantum Theory of Solids*. World Scientific (2012).

[8] I. I. Lungu, A. M. Grumezescu, and C. Fleaca, Unexpected Ferromagnetism—A Review. *Applied Sciences* **11**, 6707 (2021).

[9]H. R. Ong, W. M. E. Iskandar, M. Y. Joo, M. M. R. Khan, and M. K. A. Mohamed, Effects of natural-based SiO_2 nanocoolant on car radiator: Thermal profile. *Materials Today: Proceedings* **66**, 2734–2737 (2022).

[10]S. Das, S. Choi, W. Yu, and T. Pradeep, *Nanofluids: Science and Technology*. Wiley (2007).

[11]J. McCrea and G. Palumbo, Nanocoatings for Commercial and Industrial Applications. In: *Nanostructured Metals and Alloys*. Woodhead Publishing, 663–686 (2011).

[12]Mercury Learning and Information, *MLI Physics Collection*. Mercury Learning & Information (2018).

[13]R. Stamps and R. Camley, *Solid State Physics, Volume 66*. Elsevier Science (2015).

[14]J. Dubowik and I. Gościańska, Micromagnetic Approach to Exchange Bias, *Acta Physica Polonica A* **127**, 147–152 (2015).

[15]J. Kimling, Magnetization Reversal in Cylindrical Nanowires and in Nanowires with Perpendicular Magnetic Anisotropy. Cuvillier Verlag (2013).

[16]D. Claudio Gonzalez, *Design, Fabrication, and Characterization of Magnetic Nanostructures*. PhD thesis, University of Southampton (2008).

[17]J. Hang, *Spin Transfer Driven Magnetization Dynamics in Spin Valves and Magnetic Tunnel Junctions*. PhD thesis, New York University (2018).

[18]L. Weissitsch, F. Staab, K. Durst, and A. Bachmaier, Magnetic Materials via High-Pressure Torsion of Powders. *MATERIALS TRANSACTIONS* **64**, 1537–1550 (2023).

[19]K. Buschow, *Handbook of Magnetic Materials*. Elsevier Science (2006).

[20]M. G. Pini and P. Politi, Single-domain versus two-domain configuration in thin ferromagnetic prisms. *Journal of Magnetism and Magnetic Materials* **313**, 273–282 (2007).

[21]H. Gavilán, K. Simeonidis, E. Myrovali, E. Mazarío, O. Chubykalo-Fesenko, R. Chantrell, L. Balcells, M. Angelakeris, M. Morales, and D. Serantes, How size, shape and assembly of magnetic nanoparticles give rise to different hyperthermia scenarios. *Nanoscale* **13**, 15631–15646 (2021).

[22]C. Nayek, K. Manna, A. Imam, A. Alqasrawi, and I. Obaidat, Size-dependent magnetic anisotropy of PEG coated Fe_3O_4 nanoparticles; comparing two magnetization methods. In: *IOP Conference Series: Materials Science and Engineering, Vol. 305*, 012012 (IOP Publishing, 2018).

[23]D. Sarkar, *Nanostructured Ceramics: Characterization and Analysis*. CRC Press, (2018).

[24]S. Sharma, *Exchange Bias: From Thin Film to Nanogranular and Bulk Systems, Monograph Series in Physical Sciences*. CRC Press (2017).

[25]R. Singh, *Solid State Physics*. Dorling Kindersley (2012).

[26]N. Bagdassarov, *Fundamentals of Rock Physics*. Cambridge University Press (2021).

[27]M. H. Salaheldeen, *Fabrication and magnetic characterization of ferromagnetic antidot arrays thin films*. PhD Thesis, University of Oviedo (2019).

[28]E. Vedmedenko, *Competing Interactions and Pattern Formation in Nanoworld*. Wiley (2007).

[29]M. Wuttig and X. Liu, *Ultrathin Metal Films: Magnetic and Structural Properties*. Springer Berlin Heidelberg (2004).

[30]I. Suetake, R. Sharma, and H. Hojo, Analytical Techniques for the Elucidation of Protein Function. Wiley (2023).

[31]M. Morini and V. Slastikov, Reduced Models for Ferromagnetic Thin Films with Periodic Surface Roughness. *Journal of Nonlinear Science* **28**, 513–542 (2018).

[32]G. Dasmohapatra, *Chemistry-I*. Vikas Publishing House (2019)

[33]V. Borisenko and S. Ossicini, *What is What in the Nanoworld: A Handbook on Nanoscience and Nanotechnology*. Wiley (2013).

[34]F. Schwabl, *Statistical Mechanics*. Springer Science & Business Media (2006).

[35]T. Burkert, *Materials for Magnetic Recording Applications*. PhD thesis, Uppsala University (2005).

[36]V. Marghussian, Magnetic Properties of Nano-Glass Ceramics. In: *Nano-Glass Ceramics*, 181–223, William Andrew Publishing (2015).

[37]D. Majumder, D. Majumder, and S. Karan, Magnetic properties of ceramic nanocomposites. In: *Ceramic Nanocomposites*, 51–91, Woodhead Publishing (2013)

[38]A. B. Seabra, M. T. Pelegrino, and P. S. Haddad, Antimicrobial Applications of Superparamagnetic Iron Oxide Nanoparticles: Perspectives and Challenges. In: *Nanostructures for Antimicrobial Therapy*, 531–550, Elsevier (2017).

[39]Wahajuddin and S. Arora, Superparamagnetic iron oxide nanoparticles: magnetic nanoplatforms as drug carriers. *International Journal of Nanomedicine* **7**, 3445–3471 (2012).

[40]Q. A. Pankhurst, J. Connolly, S. K. Jones, and J. Dobson, Applications of magnetic nanoparticles in biomedicine. *Journal of Physics D: Applied physics* **36**, R167 (2003).

[41]I. Robinson, *Synthesis, Characterisation and Functionalisation of Magnetic Nanoparticles for Biomedical Applications*. PhD Thesis, University of Liverpool (2009).

[42]V. V. Mody, A. Singh, and B. Wesley, Basics of magnetic nanoparticles for their application in the field of magnetic fluid hyperthermia. *European Journal of Nanomedicine* **5**, 11–21 (2013).

[43]W. Zheng, *Interplay of Size- and Site-Dependence on the Magnetic Propertices of Diluted Magnetic Semiconductor Quantum Dots*. PhD Thesis, Florida State University (2011).

[44]S. A. Majetich, T. Wen, and O. T. Mefford, Magnetic nanoparticles. *MRS Bulletin* **38**, 899-903 (2013).

[45]G. W. Fernando, Magnetic Anisotropy in Transition Metal Systems. In: *Metallic Multilayers and their Applications, Volume 4*, 89–110, Elsevier (2008).

[46]J. Zhang and K. Hoshino, *Molecular Sensors and Nanodevices: Principles, Designs and Applications in Biomedical Engineering, Micro and Nano Technologies.* Elsevier Science (2018).

[47]K. Krishnan, *Fundamentals and Applications of Magnetic Materials*. OUP Oxford (2016).

[48]J. Sherwood, *Shape Dependent Iron Oxide Nanoparticles for Simultaneous Imaging and Therapy*. PhD Thesis, University of Alabama (2018).

[49]N. Lee and T. Hyeon, Magnetic Nanoparticles for Magnetic Resonance Imaging Contrast Agents. In: *Magnetic Nanoparticles in Biosensing and Medicine*, 228–250, Cambridge University Press (2019).

[50]M. Vázquez, C. Luna, M. Morales, R. Sanz, C. Serna, and C. Mijangos, Magnetic nanoparticles: synthesis, ordering and properties. *Physica B: Condensed Matter* **354**, 71–79 (2004).

[51]A. Lascialfari, M. Filibian, C. Sangregorio, and P. Carretta, In vivo biomedical applications of magnetic resonance and magnetic materials. *La Rivista del Nuovo Cimento* **36**, 211–271 (2013).

[52]P. M. Enriquez-Navas and M. L. Garcia-Martin, Application of Inorganic Nanoparticles for Diagnosis Based on MRI. In: *Nanobiotechnology: Inorganic Nanoparticles vs Organic Nanoparticles*, 233–245, Elsevier (2012)

[53]A. Sezer, *Recent Advances in Novel Drug Carrier Systems*. IntechOpen (2012).

[54]Y. Lin, Advanced Nano Deposition Methods. Wiley (2016).

[55]A. Grumezescu and A. Ficai, *Nanostructures for cancer therapy, Nanostructures in Therapeutic Medicine*. Elsevier Science (2017).

[56]N. Katta, *Essentials of Nanoscience & Nanotechnology*. Prowess Publishing (2021).

[57]B. D. Plouffe, S. K. Murthy, and L. H. Lewis, Fundamentals and application of magnetic particles in cell isolation and enrichment: a review. *Reports on Progress in Physics* **78**, 016601 (2014).

[58]R. M. Fratila, S. Rivera-Fernandez, and J. M. de La Fuente, Shape matters: synthesis and biomedical applications of high aspect ratio magnetic nanomaterials. *Nanoscale* **7**, 8233–8260 (2015).

[59]C. Hussain, *Analytical Applications of Functionalized Magnetic Nanoparticles*. Royal Society of Chemistry (2021).

[60]T. Shinjo, T. Okuno, R. Hassdorf, K. Shigeto, and T. Ono, Magnetic Vortex Core Observation in Circular Dots of Permalloy. *Science* **289**, 930–932 (2000).

[61]E. Kamenetskii, Chirality, *Magnetism and Magnetoelectricity: Separate Phenomena and Joint Effects in Metamaterial Structures*. Springer International Publishing (2021).

[62]L. Peixoto, R. Magalhães, D. Navas, S. Moraes, C. Redondo, R. Morales, J. Araújo, and C. Sousa, Magnetic nanostructures for emerging biomedical applications. *Applied Physics Reviews* **7**, 011310 (2020).

[63]K. Y. Guslienko, V. Novosad, Y. Otani, H. Shima, and K. Fukamichi, Field evolution of magnetic vortex state in ferromagnetic disks. *Applied Physics Letters* **78**, 3848–3850 (2001).

[64]R. P. Cowburn, D. Koltsov, A. Adeyeye, M. Welland, and D. Tricker, Single-Domain Circular Nanomagnets. *Physical Review Letters* **83**, 1042 (1999).

[65]M. Schneider, H. Hoffmann, S. Otto, T. Haug, and J. Zweck, Stability of magnetic vortices in flat submicron permalloy cylinders. *Journal of Applied Physics* **92**, 1466–1472 (2002).

[66]J. García-Martín, A. Thiaville, J. Miltat, T. Okuno, L. Vila, and L. Piraux, Imaging magnetic vortices by magnetic force microscopy: experiments and modelling. *Journal of Physics D: Applied Physics* **37**, 965 (2004).

[67]V. Novosad, K. Y. Guslienko, H. Shima, Y. Otani, S. Kim, K. Fukamichi, N. Kikuchi, O. Kitakami, and Y. Shimada, Effect of interdot magnetostatic interaction on magnetization reversal in circular dot arrays. *Physical Review B* **65**, 060402 (2002).

[68]X. Zhu, V. Metlushko, B. Ilic, and P. Grutter, Direct observation of magnetostatic coupling of chain arrays of magnetic disks. *IEEE Transactions on Magnetics* **39**, 2744–2746 (2003).

[69]M. Schneider, H. Hoffmann, and J. Zweck, Lorentz microscopy of circular ferromagnetic permalloy nanodisks. *Applied Physics Letters* **77**, 2909–2911 (2000).

[70]D. Prior, E. Rutter, and D. Tatham, Deformation mechanisms, rheology and tectonics: microstructures, mechanics and anisotropy. *Geological Society, London, Special Publications* **360**, 1–5 (2011).

[71]E. A. Vitol, V. Novosad, and E. A. Rozhkova, Multifunctional Ferromagnetic Disks for Modulating Cell Function. *IEEE Transactions on Magnetics* **48**, 3269–3274 (2012).

[72]K. L. Metlov and K. Y. Guslienko, Stability of magnetic vortex in soft magnetic nano-sized circular cylinder. *Journal of Magnetism and Magnetic Materials* **242**, 1015–1017 (2002).

[73]M. Goiriena-Goikoetxea, K. Guslienko, M. Rouco, I. Orue, E. Berganza, M. Jaafar, A. Asenjo, M. Fernández-Gubieda, L. F. Barquín, and A. García-Arribas. Magnetization reversal in circular vortex dots of small radius. *Nanoscale* **9**, 11269–11278 (2017).

[74]K. Y. Guslienko and V. Novosad, Vortex state stability in soft magnetic cylindrical nanodots. *Journal of Applied Physics* **96**, 4451–4455 (2004).

[75]K. Y. Guslienko, Magnetic Vortex State Stability, Reversal and Dynamics in Restricted Geometries. *Journal of Nanoscience and Nanotechnology* **8**, 2745–2760 (2008).

[76]A. Fernandez, M. Gibbons, M. Wall, and C. Cerjan, Magnetic domain structure and magnetization reversal in submicron-scale Co dots. *Journal of Magnetism and Magnetic Materials* **190**, 71–80 (1998).

[77]B. Van Waeyenberge, A. Puzic, H. Stoll, K. Chou, T. Tyliszczak, R. Hertel, M. Fähnle, H. Bräckl, K. Rott, G. Reiss, I. Neudecker, D. Weiss, C. H. Back, and G. Schütz, Magnetic vortex core reversal by excitation with short bursts of an alternating field. *Nature* **444**, 461–464 (2006).

[78]X. Cui, *Research on the development of electrical evaluation method for static and dynamic properties of magnetic vortex systems in patterned ferromagnetic dots*. PhD Thesis, Kyushu University (2015).

[79]Y. Gaididei, D. D. Sheka, and F. G. Mertens, Controllable switching of vortex chirality in magnetic nanodisks by a field pulse. *Applied Physics Letters* **92**, 012503 (2008).

[80]V. Uhlíř, M. Urbánek, L. Hladík, J. Spousta, M. Im, P. Fischer, N. Eibagi, J. Kan, E. Fullerton, and T. Šikola, Dynamic switching of the spin circulation in tapered magnetic nanodisks, *Nature Nanotechnology* **8**, 341–346 (2013).

[81]J. Mejía-López, D. Altbir, A. Romero, X. Batlle, I. V. Roshchin, C.-P. Li, and I. K. Schuller, Vortex state and effect of anisotropy in sub-100-nm magnetic nanodots. *Journal of Applied Physics* **100**, 104319 (2006).

[82]K. Y. Guslienko, V. Novosad, Y. Otani, H. Shima, and K. Fukamichi, Magnetization reversal due to vortex nucleation, displacement, and annihilation in submicron ferromagnetic dot arrays. *Physical Review B* **65**, 024414 (2001).

[83]L. Heyderman, H. Solak, C. David, D. Atkinson, R. Cowburn, and F. Nolting, Arrays of nanoscale magnetic dots: Fabrication by x-ray interference lithography and characterization. *Applied Physics Letters* **85**, 4989–4991 (2004).

[84]J. Neal, H. Roberts, M. Connolly, S. Crampin, S. Bending, G. Wastlbauer, and J. Bland, Magnetisation reversal in epitaxial Fe (1 0 0) disks studied by high resolution scanning Hall probe microscopy. *Ultramicroscopy* **106**, 614–619 (2006).

[85]E. C. Stoner and E. Wohlfarth, A mechanism of magnetic hysteresis in heterogeneous alloys. *Philosophical Transactions of the Royal Society of London. Series A, Mathematical and Physical Sciences* **240**, 599–642 (1948).

[86]H. Frei, S. Shtrikman, and D. Treves, Critical Size and Nucleation Field of Ideal Ferromagnetic Particles. *Physical Review* **106**, 446 (1957).

[87]A. Arrott, B. Heinrich, and A. Aharoni, Point singularities and magnetization reversal in ideally soft ferromagnetic cylinders. *IEEE Transactions on Magnetics* **15**, 1228–1235 (1979).

[88]C. Sousa, D. Leitao, M. Proenca, J. Ventura, A. Pereira, and J. Araujo, Nanoporous alumina as templates for multifunctional applications. *Applied Physics Reviews* **1**, 031102 (2014).

[89]S. Ishrat, K. Maaz, K.-J. Lee, M.-H. Jung, and G.-H. Kim, Fabrication and temperature-dependent magnetic properties of one-dimensional multilayer Au–Ni–Au–Ni–Au nanowires. *Journal of Solid State Chemistry* **210**, 116–120 (2014).

[90]L.-F. Liu, W.-Y. Zhou, S.-S. Xie, O. Albrecht, and K. Nielsch, Microstructure and temperature-dependent magnetic properties of Co/Pt multilayered nanowires. *Chemical Physics Letters* **466**, 165–169 (2008).

[91]T. Böhnert, A. C. Niemann, A.-K. Michel, S. Bäßler, J. Gooth, B. G. Tóth, K. Neuróhr, L. Péter, I. Bakonyi, V. Vega, V. M. Prida, and K. Nielsch, Magnetothermopower and

magnetoresistance of single CoNi/Cu multilayered nanowires. *Physical Review B* **90**, 165416 (2014).

[92]M. Susano, M. Proenca, S. Moraes, C. Sousa, and J. Araújo, Tuning the magnetic properties of multisegmented Ni/Cu electrodeposited nanowires with controllable Ni lengths. *Nanotechnology* **27**, 335301 (2016).

[93]S. Moraes, D. Navas, F. Béron, M. P. Proenca, K. R. Pirota, C. T. Sousa, and J. P. Araújo, The Role of Cu Length on the Magnetic Behaviour of Fe/Cu Multi-Segmented Nanowires. *Nanomaterials* **8**, 490 (2018).

[94]S. Caspani, S. Moraes, D. Navas, M. P. Proenca, R. Magalhães, C. Nunes, J. P. Araújo, and C. T. Sousa, The Magnetic Properties of Fe/Cu Multilayered Nanowires: the Role of the Number of Fe Layers and Their Thickness. *Nanomaterials* **11**, 2729 (2021).

[95]W. Wernsdorfer, B. Doudin, D. Mailly, K. Hasselbach, A. Benoit, J. Meier, J.-P. Ansermet, and B. Barbara, Nucleation of Magnetization Reversal in Individual Nanosized Nickel Wires. *Physical Review Letters* **77**, 1873 (1996).

[96]R. Ferré, K. Ounadjela, J. George, L. Piraux, and S. Dubois, Magnetization processes in nickel and cobalt electrodeposited nanowires. *Physical Review B* **56**, 14066 (1997).

[97]M. Proenca, K. Merazzo, L. Vivas, D. Leitao, C. Sousa, J. Ventura, J. Araujo, and M. Vazquez, Co nanostructures in ordered templates: comparative FORC analysis. *Nanotechnology* **24**, 475703 (2013).

[98]R. Hertel, Micromagnetic simulations of magnetostatically coupled Nickel nanowires. *Journal of Applied Physics* **90**, 5752–5758 (2001).

[99]R. Hertel and J. Kirschner, Magnetization reversal dynamics in nickel nanowires. *Physica B: Condensed Matter* **343**, 206–210 (2004).

[100]G. Strijkers, J. Dalderop, M. Broeksteeg, H. Swagten, and W. De Jonge, Structure and magnetization of arrays of electrodeposited Co wires in anodic alumina. *Journal of Applied Physics* **86**, 5141–5145 (1999).

[101]R. M. Metzger, V. V. Konovalov, M. Sun, T. Xu, G. Zangari, B. Xu, M. Benakli, and W. Doyle, Magnetic nanowires in hexagonally ordered pores of alumina. *IEEE Transactions on Magnetics* **36**, 30–35 (2000).

[102]S. Pal, S. Saha, D. Polley, and A. Barman, Magnetization reversal dynamics in Co nanowires with competing magnetic anisotropies. *Solid State Communications* **151**, 1994–1998 (2011).

[103]L.-P. Carignan, C. Lacroix, A. Ouimet, M. Ciureanu, A. Yelon, and D. Ménard, Magnetic anisotropy in arrays of Ni, CoFeB, and Ni/Cu nanowires. *Journal of Applied Physics* **102**, 023905 (2007).

[104]D. Leitao, A. Silva, R. Ferreira, E. Paz, F. Deepack, S. Cardoso, and P. Freitas, Linear nanometric tunnel junction sensors with exchange pinned sensing layer. *Journal of Applied Physics* **115**, 17E526 (2014).

[105]D. Leitao, J. Ventura, C. Sousa, A. Pereira, J. Sousa, M. Vazquez, and J. Araujo, Insights into the role of magnetoelastic anisotropy in the magnetization reorientation of magnetic nanowires. *Physical Review B* **84**, 014410 (2011).

[106]S. Pignard, G. Goglio, A. Radulescu, L. Piraux, S. Dubois, A. Declemy, and J. Duvail, Study of the magnetization reversal in individual nickel nanowires. *Journal of Applied Physics* **87**, 824–829 (2000).

[107]K. Nielsch, R. Wehrspohn, J. Barthel, J. Kirschner, U. Gösele, S. Fischer, and H. Kronmüller, Hexagonally ordered 100 nm period nickel nanowire arrays. *Applied Physics Letters* **79**, 1360–1362 (2001).

[108]H. Xiang, D. Jiang, J. Yao, Y. Zheng, W. Lu, G. Li, H. Saito, S. Ishio, X. Tan, and Y. Lin, Micromagnetic simulations of magnetization reversal of iron nanowire. *Journal of Physics: Conference Series* **266**, 012022 (2011).

[109]X. Qin, C. Deng, Y. Liu, X. Meng, J. Zhang, F. Wang, and X. Xu, Magnetization Reversal of High Aspect Ratio Iron Nanowires Grown by Electrodeposition. *IEEE Transactions on Magnetics* **48**, 3136–3139 (2012).

[110]Y. P. Ivanov, M. Vázquez, and O. Chubykalo-Fesenko, Magnetic reversal modes in cylindrical nanowires. *Journal of Physics D: Applied Physics* **46**, 485001 (2013).

[111]L. Plessis, M. Labuschagne, and M. Westcott, *Human and Social Sciences*. Project literacy (2004).

[112]H. Guo and J. Wu, *Space Science & Technology in China: A Roadmap to 2050*. Springer Berlin Heidelberg (2010).

[113]A. Bhatnagar, *Environmental Cardiology: Pollution and Heart Disease*. Royal Society of Chemistry (2010).

[114]N. Sottos, R. Rowlands, and K. Dannemann, *Experimental and Applied Mechanics, Volume 6: Proceedings of the 2014 Annual Conference on Experimental and Applied Mechanics*. Springer International Publishing (2014).

[115]Z. Wang, J. Ruan, and D. Cui, Advances and Prospect of Nanotechnology in Stem Cells. *Nanoscale Research Letters* **4**, 593 (2009).

[116]P. Dutta and J. Dutta, Multifaceted *Development and Application of Biopolymers for Biology, Biomedicine and Nanotechnology*. Springer Berlin Heidelberg (2013).

[117]F. Matteucci, R. Giannantonio, F. Calabi, A. Agostiano, G. Gigli, and M. Rossi, Deployment and exploitation of nanotechnology nanomaterials and nanomedicine. In: *AIP Conference Proceedings, Volume 1990*, 020001, (AIP Publishing, 2018).

[118]F. Zhang, *Photon Upconversion Nanomaterials*. Springer Berlin Heidelberg (2014).

[119]S. Roy, C. Ghosh, and C. Sarkar, *Nanotechnology: Synthesis to Applications*. CRC Press (2017).

[120]B. Ankamwar, S. Kirtiwar, and A. C. Shukla, Plant-mediated green synthesis of nanoparticles. In: *Advances in Pharmaceutical Biotechnology: Recent Progress and Future Applications*, 221–234 (Springer, 2020).

[121]X. Zhou, F. Boey, F. Huo, L. Huang, and H. Zhang, Chemically functionalized surface patterning. *Small* **7**, 2273–2289 (2011).

[122]N. S. Awwad, H. A. Ibrahium, M. Abd El-Kader, H. E. Ali, A. M. Mostafa, and A. Menazea, Improvement in electrical conductivity characterization of chitosan/Poly (ethylene oxide) incorporated with V_2O_5 NPs via laser ablation. *Journal of Materials Research and Technology* **16**, 1272–1282 (2022).

[123]G. James, *Introduction to nanotechnology*. Gilad James Mystery School (2023).

[124]Y. Lee, *Self-Assembly and Nanotechnology Systems: Design, Characterization, and Applications*. Wiley (2011).

[125]J.-S. Huang, DNA-origami assisted unidirectional single meta-emitters. In: *Fiber Lasers and Glass Photonics: Materials through Applications III*, PC1214203 (SPIE, 2022).

[126]D. Grewal, *Nanoelectronics with a Background in Nanotechnology*. Archers & Elevators Publishing House (2022).

[127]R. Rawat, Dense Plasma Focus - From Alternative Fusion Source to Versatile High Energy Density Plasma Source for Plasma Nanotechnology. *Journal of Physics: Conference Series* **591**, 012021 (2015).

[128]P. G. Jamkhande, N. W. Ghule, A. H. Bamer, and M. G. Kalaskar, Metal nanoparticles synthesis: An overview on methods of preparation, advantages and disadvantages, and applications. *Journal of Drug Delivery Science and Technology* **53**, 101174 (2019).

[129]M. Kaneria and K. Rakholiya, *Nanotechnology and In Silico Tools: Natural Remedies and Drug Discovery*. Elsevier Science (2023).

[130]K. Dhaliwal, *Synthesis and Applications of Semiconductor Nanostructures*. Bentham Science Publishers (2023).

[131]S. Samukawa, Neutral beam technology—Defect-free nanofabrication for novel nano-materials and nano-devices. In: *2015 International Symposium on VLSI Technology, Systems and Applications*, 1-2 (IEEE, 2015).

[132]N. Olteanu, A. Meghea, M. Enachescu, and M. Mihaly, Tunning gold nanoparticles size and surface charge by oil-in-water microemulsion template. *Digest Journal of Nanomaterials and Biostructures* **8**, 1687–1697 (2013).

[133]K. Park and J.-S. Lee, Flexible resistive switching memory with a Ni/CuO_x/Ni structure using an electrochemical deposition process. *Nanotechnology* **27**, 125203 (2016).

[134]A. V. Rane, K. Kanny, V. Abitha, and S. Thomas, Methods for Synthesis of Nanoparticles and Fabrication of Nanocomposites. In: *Synthesis of Inorganic Nanomaterials*, 121–139 (Woodhead Publishing, 2018).

[135]M. Yusefi, K. Shameli, and A. F. Jumaat, Preparation and Properties of Magnetic Iron Oxide Nanoparticles for Biomedical Applications: A Brief Review. *Journal of Advanced Research in Materials Science* **75**, 10–18 (2020).

[136]L. D. Dias, K. H. Gonçalves, J. E. Queiroz, G. M. Vila Verde, and G. L. Aquino, An eco-friendly and alternative method of forced degradation of fluoroquinolone drugs by microwave irradiation: a new application for analytical eco-scale. *Journal of Microwave Power and Electromagnetic Energy* **52**, 162–181 (2018).

[137]J. Lill, Microwave Assisted Proteomics. Royal Society of Chemistry (2009).

[138]M. V. Sullivan, W. J. Stockburn, P. C. Hawes, T. Mercer, and S. M. Reddy, Green synthesis as a simple and rapid route to protein modified magnetic nanoparticles for use in the development of a fluorometric molecularly imprinted polymer-based assay for detection of myoglobin. *Nanotechnology* **32**, 095502 (2020).

[139]F. Scé, I. Cano, C. Martin, G. Beobide, O. Castillo, and I. de Pedro, Comparing conventional and microwave-assisted heating in PET degradation mediated by

imidazolium-based halometallate complexes. *New Journal of Chemistry* **43**, 3476–3485 (2019).

[140]M. Llenas, S. Sandoval, P. M. Costa, J. Oré-Solé, S. Lope-Piedrafita, B. Ballesteros, K. T. AlJamal, and G. Tobias, Microwave-Assisted Synthesis of SPION-Reduced Graphene Oxide Hybrids for Magnetic Resonance Imaging (MRI). *Nanomaterials* **9**, 1364 (2019).

[141]A. Tyagi and R. Ningthoujam, Handbook on Synthesis Strategies for Advanced Materials: Volume-I: Techniques and Fundamentals. Springer Nature Singapore (2021).

[142]W.-s. T. Chow, Solvent-Free Route for Microwave-Assisted Organic Synthesis. MSc Thesis, Hong Kong Polytechnic University (2006).

[143]K. Μυρτώ. Synthesis and characterization of magnetite/β-cyclodextrin (Fe3O4/β-CD) nanoparticles. MSc Thesis, National Technical University of Athens (2020).

[144]A. Gallo-Cordova, M. d. P. Morales, and E. Mazarío, Effect of the Surface Charge on the Adsorption Capacity of Chromium (VI) of Iron Oxide Magnetic Nanoparticles Prepared by Microwave-Assisted Synthesis. Water 11, 2372 (2019).

[145]M. Irshad, F. Ahmad, N. Mohamed, and M. Abdullah, Preparation and Structural Characterization of Template Assisted Electrodeposited Copper Nanowires. International *Journal of Electrochemical Science* **9**, 2548– 2555 (2014).

[146]W. J. Stepniowski and M. Salerno, Fabrication of nanowires and nanotubes by anodic alumina template-assisted electrodeposition. In: *Manufacturing Nanostructures* 321–357 (One Central Press, 2014).

[147]L. A. Meier, A. E. Alvarez, S. Garcia, and M. C. del Barrio, Formation of Cu and Ni nanowires by electrodeposition. *Procedia Materials Science* **8**, 617–622 (2015).

[148]H. Tijjani, A. Olatunde, M. H. Zangoma, C. Egbuna, A. M. Danyaro, H. Abdulkarim, F. A. Mahmoud, and M. Muhammad, Nanoformulation of antioxidant supplements. In: *Applications of Nanotechnology in Drug Discovery and Delivery*, 45–70 (Elsevier, 2022).

[149]A. Ertan, S. N. Tewari, and O. Talu, Electrodeposition of nickel nanowires and nanotubes using various templates. *Journal of Experimental Nanoscience* **3**, 287–295 (2008).

[150]J. Holman and P. Stone, *Chemistry*. Nelson Thornes Limited (2001).

[151]H. Dong, *Surface engineering of light alloys: Aluminium, magnesium and titanium alloys*. Elsevier Science (2010).

[152]W. Lee and S.-J. Park, Porous Anodic Aluminum Oxide: Anodization and Templated Synthesis of Functional Nanostructures. *Chemical reviews* **114**, 7487–7556 (2014).

[153]A. Orsi, *Control of Aluminium Anodization to Regulate the Optical Properties of Porous Aluminium Oxide Membranes*. PhD Thesis, Imperial College London (2013).

[154] D. Vojtěch, J. Fojt, L. Joska, and P. Novák, Surface treatment of NiTi shape memory alloy and its influence on corrosion behavior. *Surface and Coatings Technology* **204**, 3895–3901 (2010).

[155]Z. Zhigang, G.-G. Luis, L. Qiang, F. Andrew, M. William I, and M. Francis, Size-Tunable Porous Anodic Alumina Nano-structure for Biosensing. *Soft Nanoscience Letters* **2011**, 55-60 (2011).

[156]M. Paz Martínez-Viademonte, S. T. Abrahami, T. Hack, M. Burchardt, and H. Terryn, A Review on Anodizing of Aerospace Aluminum Alloys for Corrosion Protection. *Coatings* **10**, 1106 (2020).

[157]G. E. J. Poinern, N. Ali, and D. Fawcett, Progress in Nano-Engineered Anodic Aluminum Oxide Membrane Development. *Materials* **4**, 487–526 (2011).

[158]N. Kumar, J. Jindal, K. Singh, and A. Mittal, Anodic Oxide Nanostructures: Theories of Anodic Nanostructure Self-Organization. In: *Advanced Coating Materials*, 235–254 (Wiley, 2018)

[159]R. Abdel-Karim and S. El-Raghy, Fabrication of Nanoporous Alumina. In: *Nanofabrication using Nanomaterials*, 197–218 (One Central Press, 2014).

[160]S. Upreti, K. Mukherjee, M. Palit, A. Bag, S. Mallik, S. Chattopadhyay, and C. Maiti, Porous Anodic Alumina Template Formation: Deposition Technique Dependence. In: *Physics of Semiconductor Devices*, 725–728 (Springer, 2014).

[161]L. K. Tan, M. A. Chong, and H. Gao, Free-Standing Porous Anodic Alumina Templates for Atomic Layer Deposition of Highly Ordered TiO_2 Nanotube Arrays on Various Substrates. *Journal of Physical Chemistry C* **112**, 69–73 (2008).

[162]M. Aramesh and J. Cervenka, Surface Modification of Porous Anodic Alumina for Medical and Biological Applications. In: *Nanomedicine*, 439-467 (One Central Press, 2014).

[163]L. Zaraska, M. Jasku la, and G. D. Sulka, Porous anodic alumina layers with modulated pore diameters formed by sequential anodizing in different electrolytes. *Materials Letters* **171**, 315– 318 (2016).

[164]T. M. David, P. R. Dev, P. Wilson, P. Sagayaraj, and T. Mathews, A critical review on the variations in anodization parameters toward microstructural formation of TiO_2 nanotubes. *Electrochemical Science Advances* **2**, e202100083 (2022).

[165]T. Stergiopoulos, A. Valota, V. Likodimos, T. Speliotis, D. Niarchos, P. Skeldon, G. Thompson, and P. Falaras, Dye-sensitization of self-assembled titania nanotubes prepared by galvanostatic anodization of Ti sputtered on conductive glass. *Nanotechnology* **20**, 365601 (2009).

[166]D. Losic and D. Losic Jr, Preparation of Porous Anodic Alumina with Periodically Perforated Pores. *Langmuir* **25**, 5426–5431 (2009).

[167]D. Borgohain, R. K. Dash, and G. K. Mamidipudi, Effect of conductive and non-conductive substrates on the formation of anodic aluminum oxide (AAO) template for mask-less nanofabrication. *Microelectronic Engineering* **157**, 1–6 (2016).

[168]L. Zaraska, E. Wierzbicka, E. Kurowska-Tabor, and G. D. Sulka, Synthesis of Nanoporous Anodic Alumina by Anodic Oxidation of Low Purity Aluminum Substrates. In: *Nanoporous Alumina: Fabrication, Structure, Properties and Applications*, 61–106 (Springer, 2015).

[169]M. Pashchanka, Conceptual Progress for Explaining and Predicting Self-Organization on Anodized Aluminum Surfaces. *Nanomaterials* **11**, 2271 (2021).

[170]I. Ryshchenko, I. Lyashok, V. Gomozov, S. Vodolazhchenko, and S. Deribo, “Formation of nanostructures on the basis of porous anodic niobium oxide. *Functional Materials* **26**, 729-733 (2019).

[171]Q. Li, J. Jensen, and N. Bjerrum, Chemistry, electrochemistry, and electrochemical applications: Aluminum. In: Encyclopedia of Electrochemical Power Sources, 695–708 (Elsevier 2009).

[172]L. Zaraska, G. D. Sulka, and M. Jaskuła, Anodic alumina membranes with defined pore diameters and thicknesses obtained by adjusting the anodizing duration and pore opening/widening time. *Journal of Solid State Electrochemistry* **15**, 2427–2436 (2011).

[173]K. S. Choudhari, C.-H. Choi, S. Chidangil, and S. D. George, Recent Progress in the Fabrication and Optical Properties of Nanoporous Anodic Alumina. *Nanomaterials* **12**, 444 (2022).

[174]A. Ruiz-Clavijo, O. Caballero-Calero, and M. Martín-González, Revisiting anodic alumina templates: from fabrication to applications. *Nanoscale* **13**, 2227–2265 (2021).

[175]D. Losic and A. Santos, *Nanoporous Alumina: Fabrication, Structure, Properties and Applications*. Springer International Publishing (2015).

[176]K. Yasuda, J. M. Macak, S. Berger, A. Ghicov, and P. Schmuki, Mechanistic aspects of the self-organization process for oxide nanotube formation on valve metals. *Journal of The Electrochemical Society* **154**, C472 (2007).

Journal of the electrochemical society, 154(9), C472.[177]M. Mir, M. Shah, and P. Ganai, Dielectric study of nanoporous alumina fabricated by two-step anodization technique. *Chemical Papers* **75**, 503–513 (2021).

[178]C. Cheng and A. Ngan, Theoretical Pore Growth Models for Nanoporous Alumina, In: *Nanoporous Alumina: Fabrication, Structure, Properties and Applications*, 31–60 (Springer International Publishing, 2015).

[179]V. Vega, J. García, J. M. Montero-Moreno, B. Hernando, J. Bachmann, V. M. Prida, and K. Nielsch, Unveiling the Hard Anodization Regime of Aluminum: Insight into Nanopores Self-Organization and Growth Mechanism. *ACS Applied Materials & Interfaces* **7**, 28682–28692 (2015).

[180]W. Lee, K. Nielsch, and U. Gösele, Self-ordering behavior of nanoporous anodic aluminum oxide (AAO) in malonic acid anodization. *Nanotechnology* **18**, 475713 (2007).

[181]L. Yi, L. Zhiyuan, H. Xing, L. Yisen, and C. Yi, Investigation of intrinsic mechanisms of aluminium anodization processes by analyzing the current density. *RSC advances* **2**, 5164–5171 (2012).

[182]L. Yi, L. Zhiyuan, H. Xing, L. Yisen, and C. Yi, Formation and microstructures of unique nanoporous AAO films fabricated by high voltage anodization. *Journal of Materials Chemistry* **21**, 9661–9666 (2011).

[183]W. Lee, R. Ji, U. Gösele, and K. Nielsch, Fast fabrication of long-range ordered porous alumina membranes by hard anodization. *Nature materials* **5**, 741–747 (2006).

[184]H. Masuda, K. Yada, and A. Osaka, Self-Ordering of Cell Configuration of Anodic Porous Alumina with Large-Size Pores in Phosphoric Acid Solution. *Japanese Journal of Applied Physics* **37**, L1340 (1998).

[185]K. M. Chahrour, N. M. Ahmed, M. Hashim, N. G. Elfadill, A. M. Al-Diabat, and M. Bououdina, Influence of wet etching time cycles on morphology features of thin porous Anodic Aluminum Oxide (AAO) template for nanostructure's synthesis. *Journal of Physics and Chemistry of Solids* **87**, 1–8 (2015).

[186]D. Leitao, A. Apolinario, C. Sousa, J. Ventura, J. Sousa, M. Vazquez, and J. Araujo, Nanoscale Topography: A Tool to Enhance Pore Order and Pore Size Distribution in Anodic Aluminum Oxide. *Journal of Physical Chemistry C* **115**, 8567–8572 (2011).

[187]K. Hebert, R. Lillard, B. MacDougall, and E. S. C. Division, *Oxide Films: Proceedings of the International Symposium*. Electrochemical Society (2000).

[188]Z. Ling and Y. Li, Mechanisms of Nanoporous Alumina Formation and Self-Organized Growth. *Nanoporous Alumina: Fabrication, Structure, Properties and Applications*, 1–30 (Springer International Publishing, 2015).

[189]Y. Patel, G. Janusas, A. Palevicius, and A. Vilkauskas, Development of Nanoporous AAO Membrane for Nano Filtration Using the Acoustophoresis Method. *Sensors* **20**, 3833 (2020).

[190]N. Panwar, *Magnetism and Magnetic Materials*. IntechOpen (2018).

[191]C. T. de Sousa, A. Apolinário, M. P. Proença, D. C. Leitão, J. Azevedo, J. Ventura, and J. P. Araújo, Dendritic Nanostructures Grown in Hierarchical Branched Pores. In: *Advances in Nanotechnology, Volume 12,* 123–154 (Nova Science Publishers, 2014).

[192]C. Sousa, D. Leitao, M. Proenca, A. Apolinario, J. Correia, J. Ventura, and J. Araujo, Tunning pore filling of anodic alumina templates by accurate control of the bottom barrier layer thickness. *Nanotechnology* **22**, 315602 (2011).

[193]L. Péter, *Electrochemical Methods of Nanostructure Preparation*. Springer International Publishing (2021).

[194]C. Shuoshuo, L. Zhiyuan, H. Xing, Y. Hui, and L. Yi, Competitive growth of branched channels inside AAO membranes. *Journal of Materials Chemistry* **20**, 1794–1798 (2010).

[195]C. Shuoshuo, L. Zhiyuan, H. Xing, and L. Yi, Controlled growth of branched channels by a factor of 1/√n anodizing voltage? *Journal of Materials Chemistry* **19**, 5717–5719 (2009).

[196]W. Cheng, M. Steinhart, U. Gösele, and R. B. Wehrspohn, Tree-like alumina nanopores generated in a non-steady-state anodization. *Journal of Materials Chemistry* **17**, 3493–3495 (2007).

[197]N. Hassanzadeh, H. Omidvar, and S. H. Tabaian, The Effect of Gradual Varying of Anodizing Voltage on the Morphology of Alumina Nanochannels. *Nanoscience and Nanotechnology Letters* **4**, 553–558 (2012).

[198]C. Sousa, A. Apolinario, D. Leitao, A. Pereira, J. Ventura, and J. Araujo, Precise control of the filling stages in branched nanopores. *Journal of Materials Chemistry* **22**, 3110–3116 (2012).

[199]T. Shimizu, *Self-Assembled Nanomaterials II: Nanotubes*. Springer Berlin Heidelberg (2008).

[200]G. Sulka, Nanostructured Anodic Metal Oxides: Synthesis and Applications. Elsevier Science (2020).

[201]O. P. Gujela, V. Gujela, and Gayatri, Anodic Aluminum Axide (AAO) nano membrane fabrication under different conditions. In: *2016 International Conference on Recent Advances and Innovations in Engineering (ICRAIE)*, 1–6 (IEEE, 2016).

[202]A. Apolinário, P. Quitério, C. Sousa, M. Proença, J. Azevedo, M. Susano, S. Moraes, P. Lopes, J. Ventura, and J. Araújo, Bottom-up nanofabrication using self-organized porous templates. *Journal of Physics: Conference Series* **534**, 012001 (2014).

[203]J. M. T. Alvarez, *Hard Anodic Films for Aluminium Alloys*. PhD Thesis, University of Manchester (2018).

[204]A. Khalilian-Gurtani and S. A. Hassanzadeh-Tabrizi, Synthesis and photoluminescence properties of nanoporous anodic aluminum oxide (NAAO): Sm^{3+} nanocomposite layer: effect of anodizing parameters (time and voltage), Sm^{3+} concentrations, and annealing temperatures. *Optical Materials* **102**, 109821 (2020).

[205]M. Noormohammadi, Z. S. Arani, A. Ramazani, M. A. Kashi, and S. Abbasimofrad, Super-fast fabrication of self-ordered nanoporous anodic alumina membranes by ultra-hard anodization. *Electrochimica Acta* **354**, 136766 (2020).

[206]B. Attaf, *Advances in Composite Materials for Medicine and Nanotechnology*. IntechOpen (2011).

[207]K. Wandelt, *Encyclopedia of Interfacial Chemistry: Surface Science and Electrochemistry*. Elsevier Science (2018).

[208]I. Gurrappa and L. Binder, Electrodeposition of nanostructured coatings and their characterization-A review. *Science and Technology of Advanced Materials* **9**, 043001 (2008).

[209]U. S. Nur, K. Ying, and N. Khuan, Electrodeposition: Principles, Applications and Methods. In: *Nuclear Technical Convention 2011, Malaysia* (2011).

[210]P. Wasserscheid and T. Welton, *Ionic Liquids in Synthesis*. Wiley (2006).

[211]M. Schlesinger and M. Paunovic, *Modern Electroplating*. Wiley (2011).

[212]F. Nasirpouri, *Electrodeposition of Nanostructured Materials*. Springer International Publishing (2016).

[213]Y. Champion and H. Fecht, *Nano-Architectured and Nanostructured Materials: Fabrication, Control and Properties*. Wiley (2006).

[214]G. Cao, Q. Liu, Y. Huang, W. Li, and S. Yao, Generation of gold nanostructures at the surface of platinum electrode by electrodeposition for ECL detection for CE. *Electrophoresis* **31**, 1055–1062 (2010).

[215]A. Mukhtar, B. S. Khan, and T. Mehmood, A study of Growth Mechanism of Fe Nanowires and Nanotube via Template-Based Electrodeposition. *International Journal of Electrochemical Science* **12**, 4574–4584 (2017).

[216]K. J. Stine, Biosensor Applications of Electrodeposited Nanostructures. *Applied Sciences* **9**, 797 (2019).

[217]C. T. Sousa, *Development of Nanoporous Alumina Templates for Biotechnological Applications*. PhD Thesis, University of Porto (2011).

[218]V. Kumar, V. Sharma, H. Swart, and S. Das, *Metal Oxides for Next-Generation Optoelectronic, Photonic, and Photovoltaic Applications*. Elsevier Science (2023).

[219]S. Sripad, D. Korff, S. C. DeCaluwe, and V. Viswanathan, Kinetics of lithium electrodeposition and stripping. *Journal of Chemical Physics* **153**, 194701 (2020).

[220]R. Jose and F. Ezema, *Surface Modification and Functionalization of Ceramic Composite*s. Elsevier Science (2023).

[221]U. Erb, G. Palumbo, and J. McCrea, The processing of bulk nanocrystalline metals and alloys by electrodeposition. In: *Nanostructured Metals and Alloys*, 118–151 (Elsevier, 2011).

[222]F. Campbell and J. von Fraunhoffer, Some uses of pyrophosphates in metal finishing part I. Bismuth to copper-tin alloys. *Surface Technology* **4**, 303–330 (1976).

[223]E. Guinea, A. Salicio-Paz, A. Iriarte, H.-J. Grande, E. Medina, and E. García-Lecina, Robust Aluminum Electrodeposition from Ionic Lquid Electrolytes Containing Light Aromatic Naphta as Additive. *ChemistryOpen* **8**, 1094–1099 (2019).

[224]M. Paunovic and M. Schlesinger, *Fundamentals of Electrochemical Deposition*. Wiley (2006).

[225]Y. D. Gamburg and G. Zangari, *Theory and Practice of Metal Electrodeposition*. Springer Science & Business Media (2011).

[226]R. Gaikwad, *Nanochemistry and Characteristics*. Lulu Publication (2022).

[227]A. Mulone, *Characterization of Fe-W Alloys Electrodeposited from Environmentally Friendly Electrolyte*. PhD thesis, Chalmers University of Technology (2020).

[228]S. S. Moraes, *Multimodal Magnetic Lipid Nanocarriers for Cancer Therapies*. PhD thesis, University of Porto (2021).

[229]S. Martinuzzi. *Analysis and study of industrially and technologically interesting surfaces*. PhD Thesis, University of Florence (2023).

[230]M. F. de Carvalho, E. P. Barbano, and I. A. Carlos, Electrodeposition of copper-tin-zinc ternary alloys from disodium ethylenediaminetetraacetate bath. *Surface and Coatings Technology* **262**, 111–122 (2015).

[231]H. Schloerb, V. Haehnel, M. S. Khatri, A. Srivastav, A. Kumar, L. Schultz, and S. Faehler, Magnetic nanowires by electrodeposition within templates. *physica status solidi (b)* **247**, 2364– 2379 (2010).

[232]R. Gautam and M. Chattopadhyaya, Advanced Nanomaterials for Wastewater Remediation. CRC Press (2016).

[233]A. Turan, E. Unveren, and A. Bulutcu, The Prediction of Membrane Transport Numbers in the Salt Splitting of Lithium Sulfate. *Journal of The Electrochemical Society* **163**, F969 (2016).

[234]L. Kaur, *Science for Tenth Class Part 2 Chemistry*. S. Chand Publishing (2016)

[235] Djaenudin, D. R. Wulan, H. R. Hariyadi, Effect of Electrodeposition Reactor Type on Nickel Recovery from Electroplating Wastewater. *Procedia Chemistry* **16**, 155–163 (2015).

[236]J. Azevedo, C. Sousa, J. Ventura, A. Apolinario, A. Mendes, and J. Araujo, Ultra-long Fe nanowires by pulsed electrodeposition with full filling of alumina templates. *Materials Research Express* **1**, 015028 (2014).

[237]Y. Wu and M. Han, Electrodeposited Fe-P nanowire arrays in hard-anodic aluminum oxide templates with controllable magnetic properties by thermal annealing. *Journal of Alloys and Compounds* **688**, 783–789 (2016).

[238]Z. B. Akinci and M. Urgen, A Simple Method for the Production of AAO Templates for DC Electrodeposition of Nanostructures. *ECS Electrochemistry Letters* **3**, D46 (2014).

[239]S. Ramanathan, *Optical and electrical properties of compound and transition metal doped compound semiconductor nanowires*. PhD Thesis, Virginia Commonwealth University (2009).

[240]L. Menon, C. Richter, A. Friedman, Z. Wu, and E. Panaitescu, Synthesis of Nanomaterials Using Self-Assembled Nanotemplates. *Journal of Nanoscience and Nanotechnology* **12**, 7658–7676 (2012).

[241]G. Capuano, D.C. Pulse Plating and Barrel Electrodeposition of Aluminum and Aluminum Alloys from Alkylbenzene Electrolytes. *Canadian Metallurgical Quarterly* **27**, 155–161 (1988).

[242]H. Mori, T. Korenaga, N. Hosomi, T. Terui, and S. Shingubara, Filling of FePt in AAO Nanohole Array by DC Pulsed Electrodeposition. *ECS Transactions* **16**, 65 (2009).

[243]J. Azevedo, C. Sousa, A. Mendes, and J. Araújo, Influence of the Rest Pulse Duration in Pulsed Electrodeposition of Fe Nanowires. *Journal of Nanoscience and Nanotechnology* **12**, 9112–9117 (2012).

[244]D. T. Horvath, Towards Plasmonic Solar to Fuel Conversion. MSc Thesis, University of California (2015).

[245]W. Li, J. Zhang, T. Shen, G. A. Jones, and P. J. Grundy, Magnetic nanowires fabricated by anodic aluminum oxide template—a brief review. *Science China Physics, Mechanics and Astronomy* **54**, 1181–1189 (2011).

[246]A. Alagarasi, Introduction to Nanomaterials. In: *Introduction to Nanomaterials*, 1–24, (Indian Institute of Technology Madras, 2013).

[247]A. Ganapathi, P. Swaminathan, and L. Neelakantan, Anodic Aluminum Oxide Template Assisted Synthesis of Copper Nanowires using a Galvanic Displacement process for Electrochemical Denitrification. *ACS Applied Nano Materials* **2**, 5981–5988 (2019).

[248]D. T. Crouse, A. A. Ikram, A. E. Miller, and M. Crouse, Design and fabrication of novel II-IV semiconductor quantum wire infrared detectors/sensors. In: *Nanofabrication: technologies, devices, and applications, Volume* 5592, 296–305 (SPIE, 2005).

[249]S. Ruiz-Gómez, C. Fernández-González, and L. Perez, Electrodeposition as a Tool for Nanostructuring Magnetic Materials. *Micromachines* **13**, 1223 (2022).

[250]S. Mátéfi-Tempfli and M. Mátéfi-Tempfli, Vertically Aligned Nanowires on Flexible Silicone using a Supported Alumina Template Prepared by Pulsed Anodization. *Advanced Materials* **21**, 4005– 4010 (2009).

[251]A. Ramazani, M. A. Kashi, and G. Seyedi, Crystallinity and magnetic properties of electrodeposited Co nanowires in porous alumina. *Journal of Magnetism and Magnetic Materials* **324**, 1826–1831 (2012).

[252]M. P. Proenca, C. T. Sousa, J. Ventura, M. Vazquez, and J. P. Araujo, Distinguishing nanowire and nanotube formation by the deposition current transients. *Nanoscale Research Letters* **7**, 1–9 (2012).

[253]M. Proenca, C. Sousa, J. Ventura, and J. Araujo, Electrochemical synthesis and magnetism of magnetic nanotubes. In: *Magnetic Nano- and Microwires*, 727–781, (Elsevier, 2015).

[254]J. Puigmartí-Luis, E. Pellicer, B. Jang, G. Chatzipirpiridis, S. Sevim, X.-Z. Chen, B. J. Nelson, and S. Pané, Magnetically and chemically propelled nanowire-based swimmers. In: *Magnetic Nano- and Microwires*, 777–799 (Elsevier, 2020).

[255]C.-W. Hsieh, *A Simplified Approach to Produce Carbon Nanotubes using Alumina Substrate*. MSc Thesis, University of Nevada (2007).

[256]M. Ahmadzadeh, M. Almasi-Kashi, A. Ramazani, and A. Montazer, Electrodeposition efficiency of Ni in the fabrication of highly ordered nanowire arrays: The roles of Cu pre-plating and barrier layer temperature. *Applied Surface Science* **356**, 687–694 (2015).

[257]N. John, K. Divya, and K. Abraham, Electrical properties of Mn_3O_4 nanorods developed through aluminum anodic membranes. In: *AIP Conference Proceedings, Volume 2162*, 020012 (AIP Publishing, 2019).

[258]L. N. Sacco, *Synthesis of carbon nanotubes within porous anodic alumina templates for electronic applications*. PhD Thesis, Ecole Polytechnique (2015).

[259]V. Prida, V. Vega, J. García, L. Iglesias, B. Hernando, and I. Minguez-Bacho, Electrochemical methods for template-assisted synthesis of nanostructured materials. In: *Magnetic Nano- and Microwires*, 3–39 (Elsevier, 2015).

[260]M. Seyedi and M. Saba, Fabrication of highly ordered An nanowires in Anodic Aluminum Oxide templates by using AC electrochemical method. *ChemRxiv* (2018).

[261]I. Tiginyanu, V. Ursaki, and E. Monaico, Template Assisted Formation of Metal Nanotubes. In: *Nanostructures and Thin Films for Multifunctional Applications: Technology, Properties and Devices*, 473–506 (Springer, 2016).

[262]F. Nasirpouri, Template Electrodeposition of Nanowires Arrays. In: *Electrodeposition of Nanostructured Materials*, 187–259 (2017).

[263]X. Peng, *Nanowires: Recent Advances*. IntechOpen (2012).

[264]K. Nielsch, F. Müller, A.-P. Li, and U. Gösele, Uniform Nickel Deposition into Ordered Alumina Pores by Pulsed Electrodeposition. *Advanced Materials* **12**, 582–586 (2000).

[265]L. M. Mota, D. N. N. Nicomedes, A. P. M. Barboza, S. L. L. de Moraes Ramos, R. Vasconcellos, N. V. Medrado, E. C. de Alvarenga, G. Machado, K. R. Juste, C. K. de Vasconcelos, A. Righi, S. M. Manhabosco, R. R. Resende, R. J. C. Batista, J. S. Soares, and T. M. Manhabosco, Soapstone reinforced hydroxyapatite coatings for biomedical applications. *Surface and Coatings Technology* **397**, 126005 (2020).

[266]C. T. Sousa, D. C. Leitao, J. Ventura, P. B. Tavares, and J. P. Araújo, A versatile synthesis method of dendrites-free segmented nanowires with a precise size control. *Nanoscale Research Letters* **7**, 1–7 (2012).

[267]K. Nielsch, J. Choi, K. Schwirn, R. B. Wehrspohn, and U. Gösele, Self-ordering Regimes of Porous Alumina: The 10 Porosity Rule. *Nano Letters* **2**, 677–680 (2002).

[268]A. Yadav, M. Bobji, and S. J. Bull, Controlled Growth of Highly Aligned Cu Nanowires by Pulse Electrodeposition in Nanoporous Alumina. *Journal of Nanoscience and Nanotechnology* **19**, 4254– 4259 (2019).

[269]R. Furneaux, W. Rigby, and A. Davidson, The formation of controlled-porosity membranes from anodically oxidized aluminium. *Nature* **337**, 147–149 (1989).

[270]A. Llavona, L. Pérez, M. C. Sánchez, and V. de Manuel, Enhancement of anomalous codeposition ´ in the synthesis of Fe–Ni alloys in nanopores. *Electrochimica Acta* **106**, 392–397 (2013).

[271]Q. Wang, *Anodic electrochemical synthesis and characterization of nanocrystalline cerium oxide and cerium oxide/montmorillonite nanocomposites*. PhD Thesis, University of North Texas (2003).

[272]O. Yevtushenko, *Electrocrystallization and characterization of nanostructured gold and gold alloys*. PhD Thesis, Saarland University (2007).

[273]W. Mao, I. Wathuthanthri, and C.-H. Choi, Tunable two-mirror interference lithography system for wafer-scale nanopatterning. *Optics Letters* **36**, 3176–3178 (2011).

[274]N. Mojarad, J. Gobrecht, and Y. Ekinci, Interference lithography at EUV and soft X-ray wavelengths: Principles, methods, and applications. *Microelectronic Engineering* **143**, 55–63 (2015).

[275]J.-J. Lin, H.-J. Chang, P.-C. Chang, and Y.-J. Hung, Superior wafer-scale uniformity in a laser interference lithography system equipped with a refractive beam shaper. In: *2017 Conference on Lasers and Electro-Optics Pacific Rim* (CLEO-PR), 1–2 (IEEE, 2017).

[276]J.-H. Seo, J. H. Park, S.-I. Kim, B. J. Park, Z. Ma, J. Choi, and B.-K. Ju, Nanopatterning by Laser Interference Lithography: Applications to Optical Devices. *Journal of Nanoscience and Nanotechnology* **14**, 1521–1532 (2014).

[277]C. Lu and R. Lipson, Interference lithography: a powerful tool for fabricating periodic structures. *Laser & Photonics Reviews* **4**, 568–580 (2010).

[278]S. R. Brueck, Optical and Interferometric Lithography-Nanotechnology Enablers. *Proceedings of the IEEE* **93**, 1704–1721 (2005).

[279]B. M. Cuadrado, *Patterned magnetic nanostructures for biomedical applications*. PhD Thesis, University of the Basque Country (2018).

[280]W. Wang, Y. Song, S. Jiang, M. Pan, and Bayanheshig, Beam drift error and control technology for scanning beam interference lithography. *Applied Optics* **56**, 4138–4145 (2017).

[281]Z. Santybayeva, A. Meghit, R. Desgarceaux, R. Teissier, F. Pichot, C. de Marin, B. Charlot, and F. Pedaci, Fabrication of quartz microcylinders by laser interference lithography for angular optical tweezers. *Journal of Micro/Nanolithography, MEMS, and MOEMS* **15**, 034507–034507 (2016).

[282]F. Smidt, Use of ion beam assisted deposition to modify the microstructure and properties of thin films. *International Materials Reviews* **35**, 61–128 (1990).

[283]L. Peixoto, *Magnetic nanostructures for biotechnological applications*. MSc thesis, University of Porto (2019).

[284]N. H. Abd Ellah, S. F. Gad, K. Muhammad, G. E Batiha, and H. F. Hetta, Nanomedicine as a promising approach for diagnosis, treatment and prophylaxis against COVID-19. *Nanomedicine* **15**, 2085–2102 (2020).

[285]P. Decuzzi, D. Peer, D. Di Mascolo, A. L. Palange, P. N. Manghnani, S. M. Moghimi, Z. S. Farhangrazi, K. A. Howard, D. Rosenblum, T. Liang, Z. Chen, Z. Wang, J.-J. Zhu, Z. Gu, N. Korin, D. Letourneur, C. Chauvierre, R. Meel, F. Kiessling, and T. Lammers, Roadmap on nanomedicine. *Nanotechnology* **32**, 012001 (2020).

[286]Y. Gao, Y. Liu, and C. Xu, Magnetic Nanoparticles for Biomedical Applications: From Diagnosis to Treatment to Regeneration. In: *Engineering in Translational Medicine*, 567–583 (Springer, 2013).

[287]P. E. G. Casillas, I. O. Armendariz, C. C. Gonzalez, K. C. Parga, and C. A. M. Pérez, Magnetic Nanostructures for Biomedical Applications. In: *Microspheres: Technologies, Applications and Role in Drug Delivery Systems*, 137–159 (Nova Science Publishers, 2015).

[288]N. Tran and T. J. Webster, Magnetic nanoparticles: biomedical applications and challenges. *Journal of Materials Chemistry* **20**, 8760–8767 (2010).

[289]H. Chiriac, E. Radu, M. Țibu, G. Stoian, G. Ababei, L. Lăbușcă, D.-D. Herea, and N. Lupu, Fe-Cr-Nb-B ferromagnetic particles with shape anisotropy for cancer cell destruction by magnetomechanical actuation. *Scientific Reports* **8**, 11538 (2018).

[290]C. Hally, B. Rodríguez-Amigo, R. Bresolí-Obach, O. Planas, J. Nos, E. Boix-Garriga, R. Ruiz-González, and S. Nonell, Photodynamic Therapy. In: *Theranostics and Image Guided Drug Delivery*, 86–122 (Royal Society of Chemistry, 2018).

[291]R. Bohara and N. Thorat, *Hybrid Nanostructures for Cancer Theranostics*. (Elsevier Science, 2018).

[292]E. I. Gkanas, *In vitro* magnetic hyperthermia response of iron oxide mnp's incorporated in DA3, MCF-7 and HeLa cancer cell lines. *Central European Journal of Chemistry* **11**, 1042–1054 (2013).

[293]J. Li and N. Wu, Biosensors Based on Nanomaterials and Nanodevices. CRC Press (2017).

[294]Y. Hou and D. Sellmyer, *Magnetic Nanomaterials: Fundamentals, Synthesis and Applications*. Wiley (2017).

[295]D. Lachowicz, A. Kaczyńska, R. Wirecka, A. Kmita, W. Szczerba, A. Bodzoń-Kułakowska, M. Sikora, A. Karewicz, and S. Zapotoczny, A Hybrid System for Magnetic Hyperthermia and Drug Delivery: SPION Functionalized by Curcumin Conjugate. *Materials* **11**, 2388 (2018).

[296]G. Nedelcu, Magnetic nanoparticles impact on tumoral cells in the treatment by magnetic fluid hyperthermia. *Digest Journal of Nanomaterials and Biostructures* **3**, 103–107 (2008).

[297]K. Wu, D. Su, J. Liu, and J.-P. Wang, Estimating saturation magnetization of superparamagnetic nanoparticles in liquid phase. *Journal of Magnetism and Magnetic Materials* **471**, 394–399 (2019).

[298]A. Vashist, A. Kaushik, A. Ghosal, R. Nikkhah-Moshaie, A. Vashist, R. D. Jayant, and M. Nair, Journey of Hydrogels to Nanogels: A Decade After. In: *Nanogels for Biomedical Applications*, 1–8 (Royal Society of Chemistry, 2017).

[299]B. Mora, A. Perez-Valle, C. Redondo, M. D. Boyano, and R. Morales, Cost-Effective Design of High-Magnetic Moment Nanostructures for Biotechnological Applications. *ACS Applied Materials & Interfaces* **10**, 8165–8172 (2018).

[300]B. Pani, P. Kumar, H. Kumar, P. D. S. P. Justa, P. D. S. N. Jaswal, M. S. D. Deepshikha, and M. S. K. Devi, Biomedical Applications of Superparamagnetic Iron Oxide Nanoparticles (SPIONS) as a Theranostic agent. In: *Iron Ores and Iron Oxides*, 1–20 (IntechOpen, 2023).

[301]S. Dutz and R. Hergt, Magnetic particle hyperthermia—a promising tumour therapy? *Nanotechnology* **25**, 452001 (2014).

[302]X. Zuo, H. Ding, J. Zhang, T. Fang, and D. Zhang, Carbothermal treated iron oxide nanoparticles with improving magnetic heating efficiency for hyperthermia. *Results in Physics* **32**, 105095 (2022).

[303]G. Schmid, *Nanoparticles: From Theory to Application*. John Wiley & Sons (2011).

[304]A. G. Kolhatkar, A. C. Jamison, D. Litvinov, R. C. Willson, and T. R. Lee, Tuning the Magnetic Properties of Nanoparticles. *International Journal of Molecular Sciences* **14**, 15977–16009 (2013).

[305]A. Ehrmann, T. Nguyen, M. Ahmadi, A. Farmani, and P. Nguyen-Tri, *Magnetic Nanoparticle-Based Hybrid Materials: Fundamentals and Spplications*. Elsevier Science (2021).

[306]D. Kumar and A. Girija, *Bionanotechnology in Cancer: Diagnosis and Therapy*. Jenny Stanford Publishing (2022).

[307]G. Ortega and E. Reguera, Biomedical applications of magnetite nanoparticles. In: *Materials for Biomedical Engineering*, 397–434 (Elsevier, 2019).

[308]E. Myrovali, K. Papadopoulos, G. Charalampous, P. Kesapidou, G. Vourlias, T. Kehagias, M. Angelakeris, and U. Wiedwald, Toward the Separation of Different Heating Mechanisms in Magnetic Particle Hyperthermia. *ACS Omega* **8**, 12955–12967 (2023).

[309]S. A. Altmeyer, Ferrofluids. *Scholarpedia* **15**, 55163 (2020).

[310]O. Baffa, R. Matsuda, S. Arsalani, A. Prospero, J. Miranda, and R. Wakai, Development of an optical pumped gradiometric system to detect magnetic relaxation of magnetic nanoparticles. *Journal of Magnetism and Magnetic Materials* **475**, 533–538 (2019).

[311]N. J. Wagner and J. Mewis, *Theory and Applications of Colloidal Suspension Rheology*. Cambridge University Press (2021).

[312]G. G. Flores-Rojas, F. López-Saucedo, R. Vera-Graziano, E. Mendizabal, and E. Bucio, Magnetic Nanoparticles for Medical Applications: Updated Review. *Macromol* **2**, 374–390 (2022).

[313]C. Payne, *Minimally invasive therapies for the brain using magnetic particles*. PhD Thesis, University College London (2021).

[314]R. Verma, A. Chauhan, R. Kalia, K. M. Batoo, and R. Kumar, Magnetic nanoferrites as an alternative for magnetic resonance imaging application. In: *Magnetic Nanoferrites and their Composites*, 237–256 (Elsevier, 2023).

[315]B. Aslibeiki, N. Eskandarzadeh, H. Jalili, A. G. Varzaneh, P. Kameli, I. Orue, V. Chernenko, A. Hajalilou, L. Ferreira, and M. Cruz, Magnetic hyperthermia properties of $CoFe_2O_4$ nanoparticles: Effect of polymer coating and interparticle interactions. *Ceramics International* **48**, 27995–28005 (2022).

[316]A. J. Fagan, A. K. Bitz, I. M. Björkman-Burtscher, C. M. Collins, V. Kimbrell, A. J. Raaijmakers, and I. S. Committee, 7T MR Safety. *Journal of Magnetic Resonance Imaging* **53**, 333–346 (2021).

[317]P. Eslami, M. Albino, F. Scavone, F. Chiellini, A. Morelli, G. Baldi, L. Cappiello, S. Doumett, G. Lorenzi, C. Ravagli, A. Caneschi, A. Laurenzana, and C. Sangregorio, Smart Magnetic Nanocarriers for Multi-Stimuli On-Demand Drug Delivery. *Nanomaterials* **12**, 303 (2022).

[318]T. Sojková, G. M. Rizzo, A. Di Girolamo, S. K. Avugadda, N. Soni, N. B. Milbrandt, Y. H. Tsai, I. Kuběna, M. Sojka, N. Silvestri, A. C. Samia, R. Gröger, and T. Pellegrino, From Core–Shell FeO/Fe_3O_4 to Magnetite Nanocubes: Enhancing Magnetic Hyperthermia and Imaging Performance by Thermal Annealing. *Chemistry of Materials* **35**, 6201–6219 (2023).

[319]E. Garaio, J. M. Collantes, J. A. Garcia, F. Plazaola, S. Mornet, F. Couillaud, and O. Sandre, A wide-frequency range AC magnetometer to measure the specific absorption rate in nanoparticles for magnetic hyperthermia. *Journal of Magnetism and Magnetic Materials* **368**, 432–437 (2014).

[320]E. A. Perigo, G. Hemery, O. Sandre, D. Ortega, E. Garaio, F. Plazaola, and F. J. Teran, Fundamentals and advances in magnetic hyperthermia. *Applied Physics Reviews* **2** (2015).

[321]F. J. Teran, C. Casado, N. Mikuszeit, G. Salas, A. Bollero, M. Morales, J. Camarero, and R. Miranda, Accurate determination of the specific absorption rate in superparamagnetic nanoparticles under non-adiabatic conditions. *Applied Physics Letters* **101**, 062413 (2012).

[322]R. Wildeboer, P. Southern, and Q. Pankhurst, On the reliable measurement of specific absorption rates and intrinsic loss parameters in magnetic hyperthermia materials. *Journal of Physics D: Applied Physics* **47**, 495003 (2014).

[323]H. L. Ring, A. Sharma, R. Ivkov, and J. C. Bischof, The impact of data selection and fitting on SAR estimation for magnetic nanoparticle heating. *International Journal of Hyperthermia* **37**, 100–107 (2020).

[324]O. L. Lanier, O. I. Korotych, A. G. Monsalve, D. Wable, S. Savliwala, N. W. Grooms, C. Nacea, O. R. Tuitt, and J. Dobson, Evaluation of magnetic nanoparticles for magnetic fluid hyperthermia. *International Journal of Hyperthermia* **36**, 686–700 (2019).

[325]B. Sanz, M. P. Calatayud, N. Cassinelli, M. R. Ibarra, and G. F. Goya, Long-Term Stability and Reproducibility of Magnetic Colloids Are Key Issues for Steady Values of Specific Power Absorption over Time. *European Journal of Inorganic Chemistry* **2015**, 4524–4531 (2015).

[326]S. C. Freitas, J. H. Belo, A. Granja, M. Canhota, A. S. Silva, S. Reis, H. Crespo, J. P. Araújo, and C. T. Sousa, Key Parameters in Phototherapy with Gold Nanorods Using Continuous Near Infrared Radiation. *Advanced Materials Interfaces* **10**, 2202214 (2023).

[327]A. Shokuhfar and S. S. Seyyed Afghahi, The heating effect of iron-cobalt magnetic nanofluids in an alternating magnetic field: application in magnetic hyperthermia treatment. *Nanoscale Research Letters* **8**, 1–11 (2013).

[328]B. Aslibeiki, M. Ehsani, F. Nasirzadeh, and M. Mohammadi, The effect of interparticle interactions on spin glass and hyperthermia properties of Fe_3O_4 nanoparticles. *Materials Research Express* **4**, 075051 (2017).

[329]A. Chauhan, S. Midha, R. Kumar, R. Meena, P. Singh, S. K. Jha, and B. K. Kuanr, Rapid tumor inhibition *via* magnetic hyperthermia regulated by caspase 3 with time-dependent clearance of iron oxide nanoparticles. *Biomaterials Science* **9**, 2972–2990 (2021).

[330]M. Kallumadil, M. Tada, T. Nakagawa, M. Abe, P. Southern, and Q. A. Pankhurst, Suitability of commercial colloids for magnetic hyperthermia. *Journal of Magnetism and Magnetic Materials* **321**, 1509–1513 (2009).

[331]R. Gilchrist, R. Medal, W. D. Shorey, R. C. Hanselman, J. C. Parrott, and C. B. Taylor, Selective Inductive Heating of Lymph Nodes. *Annals of Surgery* **146**, 596 (1957).

[332]F. K. van Landeghem, K. Maier-Hauff, A. Jordan, K.-T. Hoffmann, U. Gneveckow, R. Scholz, B. Thiesen, W. Brück, and A. von Deimling, Post-mortem studies in glioblastoma patients treated with thermotherapy using magnetic nanoparticles. *Biomaterials* **30**, 52–57 (2009).

[333]S. Mannucci, L. Ghin, G. Conti, S. Tambalo, A. Lascialfari, T. Orlando, D. Benati, P. Bernardi, N. Betterle, R. Bassi, P. Marzola, and A. Sbarbati, Magnetic Nanoparticles from *Magnetospirillum gryphiswaldense* Increase the Efficacy of Thermotherapy in a Model of Colon Carcinoma. *PLOS ONE* **9**, e108959 (2014).

[334]E. Alphandéry, Perspectives of Breast Cancer Thermotherapies. *Journal of Cancer* **5**, 472 (2014).

[335]M. Johannsen, U. Gneveckow, B. Thiesen, K. Taymoorian, C. H. Cho, N. Wald¨ofner, R. Scholz, A. Jordan, S. A. Loening, and P. Wust, Thermotherapy of Prostate Cancer Using Magnetic Nanoparticles: Feasibility, Imaging, and Three-Dimensional Temperature Distribution. *European Urology* **52**, 1653–1662 (2007).

[336]A. Espinosa, J. Kolosnjaj-Tabi, A. Abou-Hassan, A. Plan Sangnier, A. Curcio, A. K. Silva, R. Di Corato, S. Neveu, T. Pellegrino, L. M. Liz-Marzán, and C. Wilhelm, Magnetic (Hyper) Thermia or Photothermia? Progressive Comparison of Iron Oxide and Gold Nanoparticles Heating in Water, in Cells, and In Vivo. *Advanced Functional Materials* **28**, 1803660 (2018).

[337]A. Espinosa, G. R. Castro, J. Reguera, C. Castellano, J. Castillo, J. Camarero, C. Wilhelm, M. A. García, and A. Muñoz-Noval, Photoactivated Nanoscale Temperature Gradient Detection Using X-ray Absorption Spectroscopy as a Direct Nanothermometry Method. *Nano Letters* **21**, 769–777 (2020).

[338]R. Sharma and C. Chen, Newer nanoparticles in hyperthermia treatment and thermometry", *Journal of Nanoparticle Research* **11**, 671–689 (2009).

[339]R. Di Corato, A. Espinosa, L. Lartigue, M. Tharaud, S. Chat, T. Pellegrino, C. Ménager, F. Gazeau, and C. Wilhelm, Magnetic hyperthermia efficiency in the cellular environment for different nanoparticle designs. *Biomaterials* **35**, 6400–6411 (2014).

[340]D. Mertz, O. Sandre, and S. Begin-Colin, Drug releasing nanoplatforms activated by alternating magnetic fields. *Biochimica et Biophysica Acta (BBA)-General Subjects* **1861**, 1617–1641 (2017).

[341]C. Comanescu, Recent Advances in Surface Functionalization of Magnetic Nanoparticles. *Coatings* **13**, 1772 (2023).

[342]C. Blanco-Andujar, A. Walter, G. Cotin, C. Bordeianu, D. Mertz, D. Felder-Flesch, and S. Begin-Colin, Design of iron oxide-based nanoparticles for MRI and magnetic hyperthermia. *Nanomedicine* **11**, 1889–1910 (2016).

[343]R. Gupta and D. Sharma, Evolution of Magnetic Hyperthermia for Glioblastoma Multiforme Therapy. *ACS Chemical Neuroscience* **10**, 1157–1172 (2019).

[344]G. Jia, Y. Han, Y. An, Y. Ding, C. He, X. Wang, and Q. Tang, NRP-1 targeted and cargoloaded exosomes facilitate simultaneous imaging and therapy of glioma *in vitro* and *in vivo*. *Biomaterials* **178**, 302–316 (2018).

[345]P. T. Ha, T. T. H. Le, T. Q. Bui, H. N. Pham, A. S. Ho, and L. T. Nguyen, Doxorubicin release by magnetic inductive heating and *in vivo* hyperthermia-chemotherapy combined cancer treatment of multifunctional magnetic nanoparticles. *New Journal of Chemistry* **43**, 5404–5413 (2019).

[346]L. Beola, N. Iturrioz-Rodríguez, C. Pucci, R. Bertorelli, and G. Ciofani, Drug-Loaded Lipid Magnetic Nanoparticles for Combined Local Hyperthermia and Chemotherapy against Glioblastoma Multiforme. *ACS Nano* **17**, 18441-18455 (2023).

[347]R. Issels, Hyperthermia Combined with Chemotherapy–Biological Rationale, Clinical Application, and Treatment Results. *Oncology Research and Treatment* **22**, 374–381 (1999).

[348]D. Choi, J. Park, S. Kim, D. Gracias, M. Cho, Y. Kim, A. Fung, S. Lee, Y. Chen, S. Khanal, S. Baral, and J.-H. Kim, Hyperthermia with Magnetic Nanowires for Inactivating Living Cells. *Journal of Nanoscience and Nanotechnology* **8**, 2323–2327 (2008).

[349]P. W. Egolf, N. Shamsudhin, S. Pané, D. Vuarnoz, J. Pokki, A.-G. Pawlowski, P. Tsague, B. De Marco, W. Bovy, S. Tucev, M. H. D. Ansari, and B. J. Nelson, Hyperthermia with rotating magnetic nanowires inducing heat into tumor by fluid friction. *Journal of Applied Physics* **120** (2016).

[350]J. Alonso, H. Khurshid, V. Sankar, Z. Nemati, M. Phan, E. Garayo, J. García, and H. Srikanth, FeCo nanowires with enhanced heating powers and controllable dimensions for magnetic hyperthermia. *Journal of Applied Physics* **117** (2015).

[351]Z. Hedayatnasab, A. Dabbagh, F. Abnisa, H. Karimian, N. H. Abu Kasim, and W. M. A. Wan Daud, Synthesis, characterization and in vitro analysis of superparamagnetic iron oxide nanoparticles for targeted hyperthermia therapy. *Chemical Papers* **75**, 669–679 (2021).

[352]E. C. Wang and A. Z. Wang, Nanoparticles and their applications in cell and molecular biology. *Integrative Biology* **6**, 9–26 (2014).

[353]N. Gao, H. Wang, and E.-H. Yang, An experimental study on ferromagnetic nickel nanowires functionalized with antibodies for cell separation. *Nanotechnology* **21**, 105107 (2010).

[354]A. Pors, M. G. Nielsen, and S. I. Bozhevolnyi, Plasmonic Functionalities Based on Detuned Electrical Dipoles. In: *Plasmonics: Theory and Applications*, 401–429 (Springer, 2013).

[355]R. Burger and J. Ducrée, Handling and analysis of cells and bioparticles on centrifugal microfluidic platforms. *Expert Review of Molecular Diagnostics* **12**, 407–421 (2012).

[356]B. Zhu and S. K. Murthy, Stem cell separation technologies. *Current Opinion in Chemical Engineering* **2**, 3–7 (2013).

[357]C. Ruffert, Magnetic Bead—Magic Bullet. *Micromachines* **7**, 21 (2016).

[358]B. J. Kirby, *Micro- and Nanoscale Fluid Mechanics: Transport in Microfluidic Devices*. Cambridge University Press (2010).

[359]Y. P. Ivanov, A. Alfadhel, M. Alnassar, J. E. Perez, M. Vazquez, A. Chuvilin, and J. Kosel, Tunable magnetic nanowires for biomedical and harsh environment applications. *Scientific Reports* **6**, 24189 (2016).

[360]A. Hultgren, M. Tanase, C. Chen, G. Meyer, and D. Reich, Cell manipulation using magnetic nanowires. *Journal of Applied Physics* **93**, 7554–7556 (2003).

[361]A. Hultgren, M. Tanase, C. S. Chen, and D. H. Reich, High-yield cell separations using magnetic nanowires. *IEEE Transactions on Magnetics* **40**, 2988–2990 (2004).

[362]P. C. Pinheiro, C. T. Sousa, J. P. Araújo, A. J. Guiomar, and T. Trindade, Functionalization of nickel nanowires with a fluorophore aiming at new probes for multimodal bioanalysis. *Journal of Colloid and Interface Science* **410**, 21–26 (2013).

[363]D. Reich, M. Tanase, A. Hultgren, L. Bauer, C. Chen, and G. Meyer, Biological applications of multifunctional magnetic nanowires. *Journal of Applied Physics* **93**, 7275–7280 (2003).

[364]A. Hultgren, M. Tanase, E. J. Felton, K. Bhadriraju, A. K. Salem, C. S. Chen, and D. H. Reich, Optimization of Yield in Magnetic Cell Separations Using Nickel Nanowires of Different Lengths. *Biotechnology Progress* **21**, 509–515 (2005).

[365]R. E. McMahon, J. Ma, S. V. Verkhoturov, D. Munoz-Pinto, I. Karaman, F. Rubitschek, H. J. Maier, and M. S. Hahn, A comparative study of the cytotoxicity and corrosion resistance of nickel–titanium and titanium–niobium shape memory alloys. *Acta Biomaterialia* **8**, 2863–2870 (2012).

[366]F. Byrne, A. Prina-Mello, A. Whelan, B. M. Mohamed, A. Davies, Y. K. Gun'ko, J. Coey, and Y. Volkov, High content analysis of the biocompatibility of nickel nanowires. *Journal of Magnetism and Magnetic Materials* **321**, 1341–1345 (2009).

[367]L. P., Felix, J. E. Perez, M. F. Contreras, T. Ravasi, T., and J. Kosel, J., Cytotoxic effects of nickel nanowires in human fibroblasts. *Toxicology reports* **3**, 373-380 (2016).

[368]N. Alsharif, *Towards The Generation of Functionalized Magnetic Nanowires to Target Leukemic Cells*. MSc Thesis, King Abdullah University of Science and Technology (2016).

[369]N. A. Alsharif, A. I. Martiínez-Banderas, J. Merzaban, T. Ravasi, and J. Kosel, Biofunctionalizing Magnetic Nanowires Toward Targeting and Killing Leukemia Cancer Cells. *IEEE Transactions on Magnetics* **55**, 1–5 (2018).

[370]A. Fu, W. Hu, L. Xu, R. J. Wilson, H. Yu, S. J. Osterfeld, S. S. Gambhir, and S. X. Wang, Protein-Functionalized Synthetic Antiferromagnetic Nanoparticles for Biomolecule Detection and Magnetic Manipulation. *Angewandte Chemie International Edition* **48**, 1620–1624 (2009).

[371]M. Zhang, C. M. Earhart, C. Ooi, R. J. Wilson, M. Tang, and S. X. Wang, Functionalization of high-moment magnetic nanodisks for cell manipulation and separation. *Nano Research* **6**, 745– 751 (2013).

[372]D. Gregurec, A. W. Senko, A. Chuvilin, P. D. Reddy, A. Sankararaman, D. Rosenfeld, P.-H. Chiang, F. Garcia, I. Tafel, G. Varnavides, E. Ciocan, and P. Anikeeva, Magnetic Vortex Nanodiscs Enable Remote Magnetomechanical Neural Stimulation. *ACS Nano* **14**, 8036–8045 (2020).

[373]C. Collier, N. Muzzio, R. Thevi Guntnur, A. Gomez, C. Redondo, R. Zurbano, I. K. Schuller, C. Monton, R. Morales, and G. Romero, Wireless Force-Inducing Neuronal Stimulation Mediated by High Magnetic Moment Microdiscs. *Advanced Healthcare Materials* **11**, 2101826 (2022).

[374]M. Bañobre-López, C. Bran, C. Rodriguez-Abreu, J. Gallo, M. Vazquez, and J. Rivas, A colloidally stable water dispersion of Ni nanowires as an efficient T_2-MRI contrast agent. *Journal of Materials Chemistry B* **5**, 3338–3347 (2017).

[375]M. Mohindra and J. K. Jain, *Fundamentals of Orthopedics*. Jaypee Brothers Medical Publishers Ltd (2017).

[376]D. Vanel, M. T. McNamara, O. Arcangioli, L. Arrive, B. Aubert, R. Bénacerraf, J. Bigot, J. Bittoun, S. Blangy, A. Bonnin, A. Bonnin, J. Broussin, D. Buthiau, J.-N. Buy, A.-E. Cabée, J.-M. Caille, S. Chagnon, J.-F. Chateil, A. Chevrot, C. Coffre, D. Couanet, E. Desprès, J. Tœuf, J. Ecoiffier, L. Engelholm, G. Frija, F. Gires, N. Grenier, P. Grenier, C. Guinet, F. Héran, I. Idy-Peretti, J. Jean-Mart, P. Kien, H. Kressel, R. Lavayssière, J. Leclère, A. Leroy-Willig, L. Malbec, M. Marichez, J. Masselot, E. Meary, Y. Menu, G. Pallardy, R.-A. Parienty, J.-D. Piekarski, J.-C. Roucayrol, E. Schouman-Claeys, C. Segebarth, A. Sibert, E. Somveille, A. Taieb, V. Tavière, D. Vadrot, C. Vallée, D. Vanel, M. Zalcman, and M. Wybier, *MRI of the Body*. Springer (1989).

[377]A. Aharoni, *Introduction to the Theory of Ferromagnetism*. Clarendon Press (2000).

[378]J. Armony and P. Vuilleumier, *The Cambridge Handbook of Human Affective Neuroscience*. Cambridge University Press (2013).

[379]M. R. Peres, *The Focal Encyclopedia of Photography*. Taylor & Francis (2013).

[380]T. E. Yankeelov, D. R. Pickens, and R. R. Price, *Quantitative MRI in Cancer*. Taylor & Francis (2011).

[381]M. W. Ross and S. J. Dyson, *Diagnosis and Management of Lameness in the Horse*. Elsevier Health Sciences (2010).

[382]T. W. Shields, *General Thoracic Surgery, Volume 1*. Lippincott Williams & Wilkins (2005).

[383]4G. Placidi, *MRI: Essentials for Innovative Technologies*. CRC Press (2012).

[384]C. Westbrook, *MRI at a Glance*. John Wiley & Sons (2015).

[385]M. Powell, B. Worthington, J. Buckley, and E. Symonds, Magnetic resonance imaging (MRI) in obstetrics. I. Maternal anatomy. *BJOG: An International Journal of Obstetrics & Gynaecology* **95**, 31–37 (1988).

[386]J. J. Dutton, *Radiology of the Orbit and Visual Pathways*. Elsevier Health Sciences (2010).

[387]W. Mai, *Diagnostic MRI in Dogs and Cats*. CRC press (2018).

[388]A. Beqiri, *Parallel Transmission MRI for Optimised Cardiac Imaging and Improved Safety*. PhD Thesis, King's College London (2015).

[389]B. M. Dale, M. A. Brown, and R. C. Semelka, *MRI: Basic Principles and Applications*. John Wiley & Sons (2015).

[390]P. W. Stroman, *Essentials of Functional MRI*. CRC Press (2016).

[391]S. C. White and M. J. Pharoah, *Oral Radiology: Principles and Interpretation*. Elsevier Health Sciences (2014).

[392]S. Aja-Fernandez and G. Vegas-Sanchez-Ferrero, *Statistical Analysis of Noise Estimation in MRI: Modeling, Filtering and Estimation*. Springer International Publishing (2016)

[393]D. W. McRobbie, E. A. Moore, M. J. Graves, and M. R. Prince, *MRI from Picture to Proton*. Cambridge University Press (2017).

[394]G. Karunamuni, *The Cardiac Lymphatic System*. Springer (2013).

[395]R. E. Hendrick, *Breast MRI: Fundamentals and Technical Aspects*. Springer (2008).

[396]D. Shore, S. L. Pailloux, J. Zhang, T. Gage, D. J. Flannigan, M. Garwood, V. C. Pierre, and B. J. Stadler, Electrodeposited Fe and Fe–Au nanowires as MRI contrast agents. *Chemical Communications* **52**, 12634–12637 (2016).

[397]Y.-D. Xiao, R. Paudel, J. Liu, C. Ma, Z.-S. Zhang, and S.-K. Zhou, MRI contrast agents: Classification and application. *International Journal of Molecular Medicine* **38**, 1319–1326 (2016).

[398]M. A. Ibrahim, B. Hazhirkarzar, and A. B. Dublin, Gadolinium Magnetic Resonance Imaging. *StatPearls*, 29494094 (2018).

[399]T. T. T. Yang, *Rare Earth Nanotechnology*. CRC Press (2012).

[400]S. A. Corr, S. J. Byrne, R. Tekoriute, C. J. Meledandri, D. F. Brougham, M. Lynch, C. Kerskens, L. O'Dwyer, and Y. K. Gun'ko, Linear Assemblies of Magnetic Nanoparticles as MRI Contrast Agents. *Journal of the American Chemical Society* **130**, 4214–4215 (2008).

[401]J. W. Bulte and M. De Cuyper, Magnetoliposomes as Contrast Agents. In: *Methods in Enzymology, Volume 373*, 175–198 (Elsevier, 2003).

[402]J. K. Lee, *Computed Body Tomography with MRI Correlation*. Lippincott Williams & Wilkins (2006).

[403]Y. Pathak and D. Thassu, *Drug Delivery Nanoparticles Formulation and Characterization*. CRC Press (2016).

[404]R. Kwong, M. Jerosch-Herold, and B. Heydari, Cardiovascular magnetic resonance imaging, Contemporary Cardiology (Springer New York, 2019).

[405]L. M. De León-Rodríguez, A. F. Martins, M. C. Pinho, N. M. Rofsky, and A. D. Sherry, Basic MR relaxation mechanisms and contrast agent design. *Journal of Magnetic Resonance Imaging* **42**, 545–565 (2015).

[406]M. Carlsson, C. G. Xanthis, S. Smart, S. Bidhult, and A. H. Aletras, Tissue Characterization: T_1, T_2 and T_2^* Techniques. In: *Basic Principles of Cardiovascular MRI: Physics and Imaging Technique*, 167–177 (Springer, 2015).

[407]W. J. Manning and D. J. Pennell, *Cardiovascular Magnetic Resonance*. (Elsevier Health Sciences, 2010).

[408]X. Chen and S. T. Wong, Cancer Theranostics: An Introduction. In: *Cancer Theranostics*, 3–8 (Elsevier, 2014).

[409]J. Bogaert, S. Dymarkowski, A. M. Taylor, and V. Muthurangu, *Clinical Cardiac MRI*. Springer Science & Business Media (2012).

[410]Y. Bao, J. Sherwood, and Z. Sun, Magnetic iron oxide nanoparticles as T_1 contrast agents for magnetic resonance imaging. *Journal of Materials Chemistry C* **6**, 1280–1290 (2018).

[411]N. T. Thanh, *Clinical Applications of Magnetic Nanoparticles: Design to Diagnosis Manufacturing to Medicine*. CRC Press (2018).

[412]J. Stoker, *MRI of the Gastrointestinal Tract*. Springer (2010).

[413]A. S. Merbach, L. Helm, and E. Toth, *The Chemistry of Contrast Agents in Medical Magnetic Resonance Imaging*. John Wiley & Sons (2013).

[414]W. Krause, *Contrast Agents I: Magnetic Resonance Imaging*. Springer Science & Business Media (2002).

[415]T. Trindade and A. L. D. da Silva, *Nanocomposite Particles for Bio-Applications: Materials and Bio-Interfaces*. CRC Press (2011).

[416]E. M. Haacke and J. R. Reichenbach, *Susceptibility Weighted Imaging in MRI: Basic Concepts and Clinical Applications*. John Wiley & Sons (2014).

[417]T. Macher, J. Totenhagen, J. Sherwood, Y. Qin, D. Gurler, M. S. Bolding, and Y. Bao, Ultrathin Iron Oxide Nanowhiskers as Positive Contrast Agents for Magnetic Resonance Imaging. *Advanced Functional Materials* **25**, 490–494 (2015).

[418]M. Vázquez, *Magnetic Nano- and Microwires: Design, Synthesis, Properties and Applications*. Woodhead Publishing (2015).

[419]K. D. Sattler, *Handbook of Nanophysics: Nanomedicine and Nanorobotics*. CRC press (2010).

[420]W. Zhang, L. Liu, H. Chen, K. Hu, I. Delahunty, S. Gao, and J. Xie, Surface impact on nanoparticle-based magnetic resonance imaging contrast agents. *Theranostics* **8**, 2521 (2018).

[421]H.-K. Kim, G. H. Lee, and Y. Chang, Gadolinium as an MRI contrast agent. *Future Medicinal Chemistry* **10**, 639–661 (2018).

[422]M. Rogosnitzky and S. Branch, “Gadolinium-based contrast agent toxicity: a review of known and proposed mechanisms”, Biometals 29, 365–376 (2016).

[423]J. Ramalho, R. Semelka, M. Ramalho, R. Nunes, M. AlObaidy, and M. Castillo, Gadolinium-Based Contrast Agent Accumulation and Toxicity: An Update. *American Journal of Neuroradiology* **37**, 1192–1198 (2016).

[424]Z. Zhou and Z.-R. Lu, Gadolinium-based contrast agents for magnetic resonance cancer imaging. *Wiley Interdisciplinary Reviews: Nanomedicine and Nanobiotechnology* **5**, 1–18 (2013).

[425]A.-H. Lu, E. e. Salabas, and F. Schüth, Magnetic Nanoparticles: Synthesis, Protection, Functionalization, and Application. *Angewandte Chemie International Edition* **46**, 1222–1244 (2007).

[426]D. Andrews, T. Nann, and R. H. Lipson, Comprehensive Nanoscience and Nanotechnology. *Academic press* (2019).

[427]Q. L. Vuong, P. Gillis, and Y. Gossuin, Monte Carlo simulation and theory of proton NMR transverse relaxation induced by aggregation of magnetic particles used as MRI contrast agents. *Journal of Magnetic Resonance* **212**, 139–148 (2011).

[428]R. Van Roosbroeck, W. Van Roy, T. Stakenborg, J. Trekker, A. D’Hollander, T. Dresselaers, U. Himmelreich, J. Lammertyn, and L. Lagae, Synthetic Antiferromagnetic Nanoparticles as Potential Contrast Agents in MRI. *Acs Nano* **8**, 2269–2278 (2014).

[429]L. Li, W. Jiang, K. Luo, H. Song, F. Lan, Y. Wu, and Z. Gu, Superparamagnetic Iron Oxide Nanoparticles as MRI contrast agents for Non-invasive Stem Cell Labeling and Tracking. *Theranostics* **3**, 595 (2013).

[430]M. J. Bailey, R. van der Weegen, P. J. Klemm, S. L. Baker, and B. A. Helms, Stealth Rare Earth Oxide Nanodiscs for Magnetic Resonance Imaging. *Advanced Healthcare Materials* **1**, 437–442 (2012).

[431]G. Singh, B. H. McDonagh, S. Hak, D. Peddis, S. Bandopadhyay, I. Sandvig, A. Sandvig, and W. R. Glomm, Synthesis of gadolinium oxide nanodisks and gadolinium doped iron oxide nanoparticles for MR contrast agents. *Journal of Materials Chemistry B* **5**, 418–422 (2017).

[432]A. I. Martínez-Banderas, A. Aires, S. Plaza-García, L. Colás, J. A. Moreno, T. Ravasi, J. S. Merzaban, P. Ramos-Cabrer, A. L. Cortajarena, and J. Kosel, Magnetic core–shell

nanowires as MRI contrast agents for cell tracking. *Journal of Nanobiotechnology* **18**, 1–12 (2020).

[433]T. Peci, *Carbon nanotubes filled with continuous ferromagnetic α-Fe nanowires and surface-functionalized with paramagnetic Gd(III): A candidate magnetic hyperthermia structure and MRI contrast agent*. PhD Thesis, Queen Mary University of London (2017).

[434]J. Mohapatra, A. Mitra, H. Tyagi, D. Bahadur, and M. Aslam, Iron oxide nanorods as high-performance magnetic resonance imaging contrast agents. *Nanoscale* **7**, 9174–9184 (2015).

[435]K. C.-F. Leung and Y.-X. J. Wang, Mn–Fe Nanowires Towards Cell Labeling and Magnetic Resonance Imaging. In: *Nanowires Science and Technology*, 331–344 (IntechOpen, 2010).

[436]K. C.-F. Leung, Y.-X. Wang, H.-H. Wang, and C.-P. Chak, Novel one-dimensional Mn—Fe oxide nanowires for cell labeling and magnetic resonance imaging. In: 2008 *International Conference on Information Technology and Applications in Biomedicine*, 193–195 (IEEE, 2008).

[437]L. Gu, X. Cao, A. Mukhtar, and K. Wu, Fe/Mn multilayer nanowires as dual mode T_1–T_2 magnetic resonance imaging contrast agents. *Journal of Biomedical Materials Research Part B: Applied Biomaterials* **109**, 477–485 (2021).

[438]S. Thirumurugan, K. Samuvel Muthiah, R. Sakthivel, M.-Y. Liao, H. Kasai, and R.-J. Chung, Polydopamine-Coated Cu-BTC Nanowires for Effective Magnetic Resonance Imaging and Photothermal Therapy. *Pharmaceutics* **15**, 822 (2023).

[439]H. B. Na, J. H. Lee, K. An, Y. I. Park, M. Park, I. S. Lee, D.-H. Nam, S. T. Kim, S.-H. Kim, S.-W. Kim, K.-H. Lim, K.-S. Kim, S.-O. Kim, and T. Hyeon, Development of a T_1 Contrast Agent for Magnetic Resonance Imaging Using MnO Nanoparticles. *Angewandte Chemie* **119**, 5493–5497 (2007).

[440]H. R. Neves, R. A. Bini, J. H. Barbosa, C. E. Salmon, and L. C. Varanda, Dextran-Coated Antiferromagnetic MnO Nanoparticles for a T_1-MRI Contrast Agent with High Colloidal Stability. *Particle & Particle Systems Characterization* **33**, 167–176 (2016).

[441]C.-L. Liu, Y.-K. Peng, S.-W. Chou, W.-H. Tseng, Y.-J. Tseng, H.-C. Chen, J.-K. Hsiao, and P.-T. Chou, One-Step, Room-Temperature Synthesis of Glutathione-Capped Iron-Oxide Nanoparticles and their Application in In Vivo T_1-Weighted Magnetic Resonance Imaging. *Small* **10**, 3962–3969 (2014).

[442]Y.-K. Peng, C.-L. Liu, H.-C. Chen, S.-W. Chou, W.-H. Tseng, Y.-J. Tseng, C.-C. Kang, J.-K. Hsiao, and P.-T. Chou, Antiferromagnetic Iron Nanocolloids: A New Generation in Vivo T_1 MRI Contrast Agent. *Journal of the American Chemical Society* **135**, 18621–18628 (2013).

[443]F. Sorouri, E. Gholibegloo, T. Mortezazadeh, S. Kiani, A. Foroumadi, L. Firoozpour, and M. Khoobi, Tannic acid-mediated synthesis of flower-like mesoporous MnO_2 nanostructures as T_1–T_2 dual-modal MRI contrast agents and dual-enzyme mimetic agents. *Scientific Reports* **13**, 14606 (2023).

[444]S. G. Salvo, *Massage Therapy: Principles and Practice*. Elsevier Health Sciences (2022).

[445]A. I. Martínez-Banderas, A. Aires, F. J. Teran, J. E. Perez, J. F. Cadenas, N. Alsharif, T. Ravasi, A. L. Cortajarena, and J. Kosel, Functionalized magnetic nanowires for chemical and magnetomechanical induction of cancer cell death. *Scientific Reports* **6**, 35786 (2016).

[446]D. W. Wong, W. L. Gan, N. Liu, and W. S. Lew, Magneto-actuated cell apoptosis by biaxial pulsed magnetic field. *Scientific Reports* **7**, 10919 (2017).

[447]S. Leulmi, X. Chauchet, M. Morcrette, G. Ortiz, H. Joisten, P. Sabon, T. Livache, Y. Hou, M. Carrière, S. Lequien, and B. Dieny, Triggering the apoptosis of targeted human renal cancer cells by the vibration of anisotropic magnetic particles attached to the cell membrane. *Nanoscale* **7**, 15904– 15914 (2015).

[448]N. Wang, Review of cellular mechanotransduction. *Journal of physics D: Applied physics* **50**, 233002 (2017).

[449]H. Zabel, *Radiology, Lasers, Nanoparticles and Prosthetics*. Walter de Gruyter GmbH & Co KG (2017).

[450]S. W. Lowe and A. W. Lin, Apoptosis in cancer. *Carcinogenesis* **21**, 485–495 (2000).

[451]D. Shi, *The World Scientific Encyclopedia of Nanomedicine and Bioengineering. II: Bioimplants, Regenerative Medicine, and Nano-Cancer Diagnosis and Phototherapy*. World Scientific (2017).

[452]X.-L. Liu, Y. Yang, J.-P. Wu, Y.-F. Zhang, H.-M. Fan, and J. Ding, Novel magnetic vortex nanorings/nanodiscs: Synthesis and theranostic applications. *Chinese Physics B* **24**, 127505 (2015).

[453]D.-H. Kim, E. A. Rozhkova, I. V. Ulasov, S. D. Bader, T. Rajh, M. S. Lesniak, and V. Novosad, Biofunctionalized magnetic-vortex microdiscs for targeted cancer-cell destruction. *Nature materials* **9**, 165–171 (2010).

[454]E. Rozhkova, I. Ulasov, D.-H. Kim, N. Dimitrijevic, V. Novosad, S. Bader, M. Lesniak, and T. Rajh, Multifunctional nano–bio materials within cellular machinery. *International Journal of Nanoscience* **10**, 899–908 (2011).

[455]V. Novosad and E. A. Rozhkova, Ferromagnets-Based Multifunctional Nanoplatform for Targeted Cancer Therapy. In: *Biomedical Engineering, Trends in Materials Science*, 425–444 (IntechOpen, 2011).

[456]Y. Cheng, M. E. Muroski, D. C. Petit, R. Mansell, T. Vemulkar, R. A. Morshed, Y. Han, I. V. Balyasnikova, C. M. Horbinski, X. Huang, L. Zhang, R. P. Cowburn, and M.j S. Lesniak, Rotating magnetic field induced oscillation of magnetic particles for in vivo mechanical destruction of malignant glioma. *Journal of Controlled Release* **223**, 75–84 (2016).

[457]M. G. Goikoetxea, *Magnetic vortex nanodiscs for cancer cell destruction*. PhD Thesis, University of the Basque Country (2017).

[458]M. Goiriena-Goikoetxea, I. Orue, K. Guslienko, E. Berganza, M. Jaafar, A. Asenjo, D. Munoz, A. Muela, and A. Garcia-Arribas, Properties of Permalloy nanodiscs in magnetic vortex state and magneto-mechanical treatment of cancer cells. In: *2018 IEEE International Magnetics Conference (INTERMAG)*, 1–1 (IEEE, 2018).

[459]A. O. Fung, V. Kapadia, E. Pierstorff, D. Ho, and Y. Chen, Induction of Cell Death by Magnetic Actuation of Nickel Nanowires Internalized by Fibroblasts. *The Journal of Physical Chemistry C* **112**, 15085–15088 (2008).

[460]D. S. Choi, X. Hopkins, R. Kringel, J. Park, I. T. Jeon, and Y. Keun Kim, Magnetically driven spinning nanowires as effective materials for eradicating living cells. *Journal of Applied Physics* **111**, 07B329 (2012).

[461]M. F. Contreras, R. Sougrat, A. Zaher, T. Ravasi, and J. Kosel, Non-chemotoxic induction of cancer cell death using magnetic nanowires. *International journal of nanomedicine* **10**, 2141–2153 (2015).

[462]M. F. Contreras, *Magnetic Nanowires as Materials for Cancer Cell Destruction*. PhD Thesis, King Abdullah University of Science and Technology (2015).

[463]N. A. Alsharif, F. A. Aleisa, G. Liu, B. S. Ooi, N. Patel, T. Ravasi, J. S. Merzaban, and J. Kosel, Functionalization of Magnetic Nanowires for Active Targeting and Enhanced Cell-Killing Efficacy. *ACS Applied Bio Materials* **3**, 4789–4797 (2020).

[464]A. Serrà, G. Vázquez-Mariño, J. García-Torres, M. Bosch, and E. Valles, Magnetic actuation of multifunctional nanorobotic platforms to induce cancer cell death. *Advanced Biosystems* **2**, 1700220 (2018).

[465]R. Mansell, T. Vemulkar, D. C. Petit, Y. Cheng, J. Murphy, M. S. Lesniak, and R. P. Cowburn, Magnetic particles with perpendicular anisotropy for mechanical cancer cell destruction. *Scientific Reports* **7**, 4257 (2017).

[466]B. S. Kwon, *Multilayered magnetic nanoparticles fabricated by nanoimprint lithography for magnetomechanical treatment of cancer*. PhD Thesis, University of Washington (2017).

[467]Y. Shen, C. Wu, T. Q. Uyeda, G. R. Plaza, B. Liu, Y. Han, M. S. Lesniak, and Y. Cheng, Elongated Nanoparticle Aggregates in Cancer Cells for Mechanical Destruction with Low Frequency Rotating Magnetic Field. *Theranostics* **7**, 1735 (2017).

[468]C. Yao, F. Yang, J. Zhang, J. Yao, Y. Cao, H. Peng, S. G. Stanciu, C. A. Charitidis, and A. Wu, Magneto-mechanical therapeutic effects and associated cell death pathways of magnetic nanocomposites with distinct geometries. *Acta Biomaterialia* **161**, 238–249 (2023).

[469]B. Haley and E. Frenkel, Nanoparticles for drug delivery in cancer treatment. In: *Urologic Oncology: Seminars and Original Investigations* **26**, 57–64, (2008).

[470]Y. Li, J. Wang, M. G. Wientjes, and J. L.-S. Au, Delivery of nanomedicines to extracellular and intracellular compartments of a solid tumor. *Advanced Drug Delivery Reviews* **64**, 29–39 (2012).

[471]J. Yang, L. Xiong, M. Li, J. Xiao, X. Geng, B. Wang, and Q. Sun, Preparation and Characterization of Tadpole- and Sphere-Shaped Hemin Nanoparticles for Enhanced Solubility. *Nanoscale Research Letters* **14**, 1–9 (2019).

[472]L.-A. Tai, P.-J. Tsai, Y.-C. Wang, Y.-J. Wang, L.-W. Lo, and C.-S. Yang, Thermosensitive liposomes entrapping iron oxide nanoparticles for controllable drug release. *Nanotechnology* **20**, 135101 (2009).

[473]J. Kreuter, Drug delivery to the central nervous system by polymeric nanoparticles: What do we know? *Advanced Drug Delivery Reviews* **71**, 2–14 (2014).

[474]A. Date, B. Naik, and M. Nagarsenker, Novel Drug Delivery Systems: Potential in Improving Topical Delivery of Antiacne Agents. *Skin Pharmacology and Physiology* **19**, 2–16 (2005).

[475]Y. Luo, Z. Teng, Y. Li, and Q. Wang, Solid lipid nanoparticles for oral drug delivery: Chitosan coating improves stability, controlled delivery, mucoadhesion and cellular uptake. *Carbohydrate Polymers* **122**, 221–229 (2015).

[476]P. Severino, T. Andreani, A. S. Macedo, J. F. Fangueiro, M. H. A. Santana, A. M. Silva, and E. B. Souto, Current State-of-Art and New Trends on Lipid Nanoparticles (SLN and NLC) for Oral Drug Delivery. *Journal of Drug Delivery* **2012**, 750891 (2012).

[477]N. K. Mehra and S. Palakurthi, Interactions between carbon nanotubes and bioactives: a drug delivery perspective. *Drug Discovery Today* **21**, 585–597 (2016).

[478]S. C. Wuang, K. G. Neoh, E.-T. Kang, D. E. Leckband, and D. W. Pack, Acid-sensitive magnetic nanoparticles as potential drug depots. *AIChE Journal* **57**, 1638–1645 (2011).

[479]I. A Aljuffali, C.-H. Huang, and J.-Y. Fang, Nanomedical Strategies for Targeting Skin Microbiomes. *Current Drug Metabolism* **16**, 255–271 (2015).

[480]L. Battaglia and M. Gallarate, Lipid nanoparticles: state of the art, new preparation methods and challenges in drug delivery. *Expert Opinion on Drug Delivery* **9**, 497–508 (2012).

[481]B. Cervantes, L. Arana, S. Murillo-Cuesta, M. Bruno, I. Alkorta, and I. Varela-Nieto, Solid Lipid Nanoparticles Loaded with Glucocorticoids Protect Auditory Cells from Cisplatin-Induced Ototoxicity. *Journal of Clinical Medicine* **8**, 1464 (2019).

[482]C. Zylberberg and S. Matosevic, Pharmaceutical liposomal drug delivery: a review of new delivery systems and a look at the regulatory landscape. *Drug Delivery* **23**, 3319–3329 (2016).

[483]X. Yi, S. Gao, X. Gao, X. Zhang, G. Xia, Z. Liu, H. Shi, and X. Shen, Glycolipids improve the stability of liposomes: The perspective of bilayer membrane structure. *Food Chemistry* **412**, 135517 (2023).

[484]S. Perrett, M. Golding, and W. P. Williams, A Simple Method for the Preparation of Liposomes for Pharmaceutical Applications: Characterization of the Liposomes. *Journal of Pharmacy and Pharmacology* **43**, 154–161 (1991).

[485]A. Barhoum, J. Jeevanandam, and M. Danquah, *Fundamentals of Bionanomaterials*. Elsevier Science (2022).

[486]P. Liu, G. Chen, and J. Zhang, A Review of Liposomes as a Drug Delivery System: Current Status of Approved Products, Regulatory Environments, and Future Perspectives. *Molecules* **27**, 1372 (2022).

[487]P. Parhi, C. Mohanty, and S. K. Sahoo, Nanotechnology-based combinational drug delivery: an emerging approach for cancer therapy. *Drug Discovery Today* **17**, 1044–1052 (2012).

[488]B. C. Keller, Liposomes in nutrition. *Trends in Food Science & Technology* **12**, 25–31 (2001).

[489]A. S. Ulrich, Biophysical Aspects of Using Liposomes as Delivery Vehicles. *Bioscience Reports* **22**, 129–150 (2002).

[490]L. G. Hermida, M. Sabés-Xamaní, and R. Barnadas-Rodríguez, Characteristics and behaviour of liposomes when incubated with natural bile salt extract: implications for their use as oral drug delivery systems. *Soft Matter* **10**, 6677–6685 (2014).

[491]P. Trucillo, R. Campardelli, and E. Reverchon, Liposomes: From Bangham to Supercritical Fluids. *Processes* **8**, 1022 (2020).

[492]Y. Duan, A. Dhar, C. Patel, M. Khimani, S. Neogi, P. Sharma, N. S. Kumar, and R. L. Vekariya, A brief review on solid lipid nanoparticles: part and parcel of contemporary drug delivery systems. *RSC Advances* **10**, 26777–26791 (2020).

[493]R. H. Müller, M. Radtke, and S. A. Wissing, Solid lipid nanoparticles (SLN) and nanostructured lipid carriers (NLC) in cosmetic and dermatological preparations. *Advanced Drug Delivery Reviews* **54**, S131–S155 (2002).

[494]A. Katopodi, K. Safari, A. Kalospyros, K. Politopoulos, E. Alexandratou, and A. Detsi, Preparation and characterization of solid lipid nanoparticles incorporating bioactive coumarin analogues as photosensitizing agents. *Colloids and Surfaces B: Biointerfaces* **229**, 113439 (2023).

[495]T. Wang, N. Wang, Y. Zhang, W. Shen, X. Gao, and T. Li, Solvent injection-lyophilization of tert-butyl alcohol/water cosolvent systems for the preparation of drug-loaded solid lipid nanoparticles. *Colloids and Surfaces B: Biointerfaces* **79**, 254–261 (2010).

[496]K. Mahmoud, S. Swidan, M. El-Nabarawi, and M. Teaima, Lipid based nanoparticles as a novel treatment modality for hepatocellular carcinoma: a comprehensive review on targeting and recent advances. *Journal of Nanobiotechnology* **20**, 109 (2022).

[497]S. A. Wissing and R. H. Müller, Cosmetic applications for solid lipid nanoparticles (SLN). *International Journal of Pharmaceutics* **254**, 65–68 (2003).

[498]J. Weiss, E. A. Decker, D. J. McClements, K. Kristbergsson, T. Helgason, and T. Awad, Solid Lipid Nanoparticles as Delivery Systems for Bioactive Food Components. *Food Biophysics* **3**, 146– 154 (2008).

[499]C. Tapeinos, M. Battaglini, and G. Ciofani, Advances in the design of solid lipid nanoparticles and nanostructured lipid carriers for targeting brain diseases. *Journal of Controlled Release* **264**, 306–332 (2017).

[500]K. Rajpoot, Solid Lipid Nanoparticles: A Promising Nanomaterial in Drug Delivery. *Current Pharmaceutical Design* **25**, 3943–3959 (2019).

[501]V.-A. Duong, T.-T.-L. Nguyen, and H.-J. Maeng, Preparation of Solid Lipid Nanoparticles and Nanostructured Lipid Carriers for Drug Delivery and the Effects of Preparation Parameters of Solvent Injection Method. *Molecules* **25**, 4781 (2020).

[502]T. Dara, A. Vatanara, M. N. Meybodi, M. A. Vakilinezhad, S. S. Malvajerd, F. Vakhshiteh, A. Shamsian, M. Sharifzadeh, H. Kaghazian, and M. H. Mosaddegh, Erythropoietin-loaded solid lipid nanoparticles: Preparation, optimization, and in vivo evaluation. *Colloids and Surfaces B: Biointerfaces* **178**, 307–316 (2019).

[503]A. K. Sailaja, P. Amareshwar, and P. Chakravarty, Formulation of solid lipid nanoparticles and their applications. *Journal of Current Pharma Research* **1**, 197 (2011).

[504]F. Sacchetti, C. Marraccini, D. D'Arca, M. Pelà, D. Pinetti, E. Maretti, M. Hanuskova, V. Iannuccelli, M. P. Costi, and E. Leo, Enhanced anti-hyperproliferative activity of human thymidylate synthase inhibitor peptide by solid lipid nanoparticle delivery. *Colloids and Surfaces B: Biointerfaces* **136**, 346–354 (2015).

[505]N. Dudhipala, K. Y. Janga, and T. Gorre, Comparative study of nisoldipine-loaded nanostructured lipid carriers and solid lipid nanoparticles for oral delivery: preparation, characterization, permeation and pharmacokinetic evaluation. *Artificial Cells, Nanomedicine, and Biotechnology* **46**, 616–625 (2018).

[506]G. Rajalakshmi, C. Dhanapal, and R. Sundhararajan, An Insight to Nanostructured Lipid Carrier System. *Journal of Drug Delivery and Therapeutics* **10**, 173–182 (2020).

[507]K. Wiercigroch, A. Lewi´nska, and K. A. Wilk, Multifunctional di-*N*-oxide surfactants in fabrication of lipid nanoparticles. *Surface Innovations* **2**, 253–264 (2014).

[508]W. Mehnert and K. Mäder, Solid lipid nanoparticles: Production, characterization and applications. *Advanced Drug Delivery Reviews* **64**, 83–101 (2012).

[509]N. Mohamed Noor, *Lipid-based Nanoparticles for Topical Delivery of Hair Growth Therapeutic Molecules*. PhD Thesis, University College London (2017).

[510]A. Granja, A. R. Neves, C. T. Sousa, M. Pinheiro, and S. Reis, EGCG intestinal absorption and oral bioavailability enhancement using folic acid-functionalized nanostructured lipid carriers. *Heliyon* **5**, 1–6 (2019).

[511]S. V. Mussi, R. Sawant, F. Perche, M. C. Oliveira, R. B. Azevedo, L. A. Ferreira, and V. P. Torchilin, Novel Nanostructured Lipid Carrier Co-Loaded with Doxorubicin and Docosahexaenoic Acid Demonstrates Enhanced *in Vitro* Activity and Overcomes Drug Resistance in MCF-7/Adr cells. *Pharmaceutical Research* **31**, 1882–1892 (2014).

[512]K. Bhise, S. K. Kashaw, S. Sau, and A. K. Iyer, Nanostructured lipid carriers employing polyphenols as promising anticancer agents: Quality by design (QbD) approach. *International Journal of Pharmaceutics* **526**, 506–515 (2017).

[513]M. Elmowafy, A. Samy, M. A. Raslan, A. Salama, R. A. Said, A. E. Abdelaziz, W. El-Eraky, S. El Awdan, and T. Viitala, Enhancement of Bioavailability and Pharmacodynamic Effects of Thymoquinone Via Nanostructured Lipid Carrier (NLC) Formulation. *AAPS PharmSciTech* **17**, 663– 672 (2016).

[514]A. B. Kovačević, R. H. Müller, and C. M. Keck, Formulation development of lipid nanoparticles: Improved lipid screening and development of tacrolimus loaded nanostructured lipid carriers (NLC). *International Journal of Pharmaceutics* **576**, 118918 (2020).

[515]V. Andonova and P. Peneva, Characterization Methods for Solid Lipid Nanoparticles (SLN) and Nanostructured Lipid Carriers (NLC). *Current Pharmaceutical Design* **23**, 6630–6642 (2017).

[516]C. Gonçalves, M. J. Ramalho, R. Silva, V. Silva, R. Marques-Oliveira, A. C. Silva, M. C. Pereira, and J. A. Loureiro, Lipid Nanoparticles Containing Mixtures of Antioxidants to Improve Skin Care and Cancer Prevention. *Pharmaceutics* **13**, 2042 (2021).

[517]J. Varshosaz, Lipid-based nanoparticles as promising colloidal drug carriers. *Research in Pharmaceutical Sciences* **7**, 953 (2012).

[518]H. Abbas, H. Refai, and N. El Sayed, Superparamagnetic Iron Oxide–Loaded Lipid Nanocarriers Incorporated in Thermosensitive *In Situ* Gel for Magnetic Brain Targeting of Clonazepam. *Journal of Pharmaceutical Sciences* **107**, 2119–2127 (2018).

[519]M. H. Barcellos-Hoff and N. Cordes, Resistance to radio- and chemotherapy and the tumour microenvironment. *International Journal of Radiation Biology* **85**, 920–922 (2009).

[520]A. Haqyar, H. Raissi, F. Farzad, and H. Hashemzadeh, A strategy toward therapeutic improvement of electric field-sensitive gemcitabine prodrugs in 2D metal–organic frameworks in view of their structure and interactions. *Inorganic Chemistry Communications* **138**, 109281 (2022).

[521]J. J. Lee and S. M. Swain, Development of Novel Chemotherapeutic Agents to Evade the Mechanisms of Multidrug Resistance (MDR). *Seminars in Oncology* **32**, 22– 26 (2005)

[522]S. Nasirizadeh and B. Malaekeh-Nikouei, Solid lipid nanoparticles and nanostructured lipid carriers in oral cancer drug delivery. *Journal of Drug Delivery Science and Technology* **55**, 101458 (2020).

[523]Y. Lu, X. Pan, Q. Nie, Z. Zhou, X. Dai, and O. Liu, Administration methods of lipid-based nanoparticle delivery systems for cancer treatment. *Biomaterials Science* **11**, 3800–3812 (2023).

[524]C. H. Kim, S. G. Lee, M. J. Kang, S. Lee, and Y. W. Choi, Surface modification of lipid-based nanocarriers for cancer cell-specific drug targeting. *Journal of Pharmaceutical Investigation* **47**, 203–227 (2017).

[525]M. Rizwanullah, M. Z. Ahmad, A. Garg, and J. Ahmad, Advancement in design of nanostructured lipid carriers for cancer targeting and theranostic application. *Biochimica et Biophysica Acta (BBA)-General Subjects* **1865**, 129936 (2021).

[526]D. K. Chatterjee, T. Wolfe, J. Lee, A. P. Brown, P. K. Singh, S. R. Bhattarai, P. Diagaradjane, and S. Krishnan, Convergence of nanotechnology with radiation therapy—insights and implications for clinical translation. *Translational Cancer Research* **2**, 256 (2013).

[527]C. Zhao, T. Fan, Y. Yang, M. Wu, L. Li, Z. Zhou, Y. Jian, Q. Zhang, and Y. Huang, Preparation, macrophages targeting delivery and anti-inflammatory study of pentapeptide grafted nanostructured lipid carriers. *International Journal of Pharmaceutics* 450, 11–20 (2013).

[528]M. Kumar, A. Jha, K. Bharti, and B. Mishra, Nanovesicles for hepatic-targeted drug delivery. In: *Applications of Nanovesicular Drug Delivery*, 201–217 (Academic Press, 2022).

[529]S. Zhao, N. Li, V. M. Garamus, U. A. Handge, J. Liu, R. Zhang, R. Willumeit-Römer, and A. Zou, Doxorubicin hydrochloride-oleic acid conjugate loaded nanostructured lipid carriers for tumor specific drug release. *Colloids and Surfaces B: Biointerfaces* **145**, 95–103 (2016).

[530]R. Hamid and I. Manzoor, Nanomedicines: Nano based Drug Delivery Systems Challenges and Opportunities. In: *Alternative Medicine-Update*, 59–78 (IntechOpen, 2020).

[531]H. Li, X. Yang, Z. Zhou, K. Wang, C. Li, H. Qiao, D. Oupicky, and M. Sun, Near-infrared light-triggered drug release from a multiple lipid carrier complex using an all-in-one strategy. *Journal of Controlled Release* **261**, 126–137 (2017).

[532]M. Santos, A. B. C. dos Santos Valle, A. C. M. Gualberto, F. B. Leite, and F. Pittella, Setting Precise Temperature for Triggered Release from Nanostructured Lipid Carriers. *IFAC-PapersOnLine* **51**, 1–6 (2018).

[533]M. Haider, S. M. Abdin, L. Kamal, and G. Orive, Nanostructured Lipid Carriers for Delivery of Chemotherapeutics: A review. *Pharmaceutics* **12**, 288 (2020).

[534]X.-G. Zhang, J. Miao, Y.-Q. Dai, Y.-Z. Du, H. Yuan, and F.-Q. Hu, Reversal activity of nanostructured lipid carriers loading cytotoxic drug in multi-drug resistant cancer cells. *International Journal of Pharmaceutics* **361**, 239–244 (2008).

[535]Y. Wang, H. Zhang, J. Hao, B. Li, M. Li, and W. Xiuwen, Lung cancer combination therapy: co-delivery of paclitaxel and doxorubicin by nanostructured lipid carriers for synergistic effect. *Drug Delivery* **23**, 1398–1403 (2016).

[536]S. Abdolahpour, T. Toliyat, K. Omidfar, H. Modjtahedi, A. J. Wong, M. J. Rasaee, S. Kashanian, and M. Paknejad, Targeted delivery of doxorubicin into tumor cells by nanostructured lipid carriers conjugated to anti-EGFRvIII monoclonal antibody. *Artificial Cells, Nanomedicine, and Biotechnology* **46**, 89–94 (2018).

[537]M. Sun, S. Nie, X. Pan, R. Zhang, Z. Fan, and S. Wang, Quercetin-nanostructured lipid carriers: Characteristics and anti-breast cancer activities in vitro. *Colloids and Surfaces B: Biointerfaces* **113**, 15–24 (2014).

[538]C. W. How, A. Rasedee, S. Manickam, and R. Rosli, Tamoxifen-loaded nanostructured lipid carrier as a drug delivery system: Characterization, stability assessment and cytotoxicity. *Colloids and Surfaces B: Biointerfaces* **112**, 393–399 (2013).

[539]X. Li, X. Jia, and H. Niu, Nanostructured lipid carriers co-delivering lapachone and doxorubicin for overcoming multidrug resistance in breast cancer therapy. *International Journal of Nanomedicine* **13**, 4107–4119 (2018).

[540]R. S. Fernandes, J. O. Silva, H. A. Seabra, M. S. Oliveira, V. M. Carregal, J. M. Vilela, M. S. Andrade, D. M. Townsend, P. M. Colletti, E. A. Leite, V. N. Cardoso, L. A. M. Ferreira, D. Rubello, and A. L. B. Barros, α-Tocopherol succinate loaded nano-structed lipid carriers improves antitumor activity of doxorubicin in breast cancer models in vivo. *Biomedicine & Pharmacotherapy* **103**, 1348–1354 (2018).

[541]Y. S. Ong, L. Saiful Yazan, W. K. Ng, R. Abdullah, N. M. Mustapha, S. Sapuan, J. B. Foo, Y. S. Tor, C. W. How, N. Abd Rahman, and F. H. Z. Ansar, Thymoquinone loaded in nanostructured lipid carrier showed enhanced anticancer activity in 4T1 tumor-bearing mice. *Nanomedicine* **13**, 1567–1582 (2018).

[542]H. Soo Choi, W. Liu, P. Misra, E. Tanaka, J. P. Zimmer, B. Itty Ipe, M. G. Bawendi, and J. V. Frangioni, Renal clearance of quantum dots. *Nature Biotechnology* **25**, 1165–1170 (2007).

[543]M. Elsabahy and K. L. Wooley, Design of polymeric nanoparticles for biomedical delivery applications. *Chemical Society Reviews* **41**, 2545–2561 (2012).

[544]E. Blanco, H. Shen, and M. Ferrari, Principles of nanoparticle design for overcoming biological barriers to drug delivery. *Nature Biotechnology* **33**, 941–951 (2015).

[545]C. L. Bellera, A. V. Enrique, A. Talevi, and L. E. Bruno-Blanch, Advances in Applications of Nanotechnology to Drug Delivery: A Biopharmaceutical Perspective. In: *Nanoscience and Computational Chemistry: Research Progress*, 1–24 (CRC Press, 2013).

[546]S. Petrova, S. Miloshev, R. Mateva, and I. Iliev, Synthesis of amphiphilic PEG-PCL-PEG triblock copolymers. *Journal of the University of Chemical Technology and Metallurgy* **43**, 199–204 (2008).

[547]K. S. Parikh, A. Josyula, T. Inoue, T. Fukunishi, H. Zhang, R. Omiadze, R. Shi, Y. Yazdi, J. Hanes, L. M. Ensign, and N. Hibino, Nanofiber-coated, tacrolimus-eluting sutures inhibit post-operative neointimal hyperplasia in rats. *Journal of Controlled Release* **353**, 96–104 (2023).

[548]J. S. Suk, Q. Xu, N. Kim, J. Hanes, and L. M. Ensign, PEGylation as a strategy for improving nanoparticle-based drug and gene delivery. *Advanced Drug Delivery Reviews* **99**, 28–51 (2016).

[549]S. Moraes, A. Marinho, S. Lima, A. Granja, J. Araújo, S. Reis, C. Sousa, and C. Nunes, Targeted nanostructured lipid carriers for doxorubicin oral delivery. *International Journal of Pharmaceutics* **592**, 120029 (2021).

[550]M. T. Luiz, J. A. P. Dutra, J. S. R. Viegas, J. T. C. de Araújo, A. G. Tavares Junior, and M. Chorilli, Hybrid Magnetic Lipid-Based Nanoparticles for Cancer Therapy. *Pharmaceutics* **15**, 751 (2023).

[551]B. Rodenak-Kladniew, N. Noacco, I. P. de Berti, S. J. Stewart, A. F. Cabrera, V. A. Alvarez, M. G. de Bravo, N. Durán, G. R. Castro, and G. A. Islan, Design of magnetic hybrid nanostructured lipid carriers containing 1, 8-cineole as delivery systems for anticancer drugs: Physicochemical and cytotoxic studies. *Colloids and Surfaces B: Biointerfaces* **202**, 111710 (2021).

[552]Z. Ahmadifard, A. Ahmeda, M. Rasekhian, S. Moradi, and E. Arkan, Chitosan-coated magnetic solid lipid nanoparticles for controlled release of letrozole. *Journal of Drug Delivery Science and Technology* **57**, 101621 (2020).

[553]Y. S. Ong, M. Bañobre-López, S. A. C. Lima, and S. Reis, A multifunctional nanomedicine platform for co-delivery of methotrexate and mild hyperthermia towards breast cancer therapy. *Materials Science and Engineering: C* **116**, 111255 (2020).

[554]L. K. S. Tan, C. W. How, L. E. Low, B. H. Ong, J. S. Loh, S.-Y. Lim, Y. S. Ong, and J. B. Foo, Magnetic-guided targeted delivery of zerumbone/SPION co-loaded in nanostructured lipid carrier into breast cancer cells. *Journal of Drug Delivery Science and Technology* **87**, 104830 (2023).

[555] M. Yoozbashi, H. Rashidzadeh, M. Kermanian, S. Sadighian, M. J., Hosseini, Z. Kaboli, and K. Rostamizadeh, Magnetic nanostructured lipid carrier for dual triggered curcumin delivery: Preparation, characterization and toxicity evaluation on isolated rat liver mitochondria. *Journal of Biomaterials Applications* **36**, 1055-1063 (2022).

[556]S. Karami, K. Rostamizadeh, N. Shademani, and M. Parsa, Synthesis and Investigation of the Curcumin-Loaded Magnetic Lipid Nanoparticles and Their Cytotoxicity Assessment on Human Breast Carcinoma Cell Line. *Jundishapur Journal of Natural Pharmaceutical Products* **15**, e91886 (2020).

2. Goal

The major goal of this thesis was the development of novel strategies for cancer therapy using functionalized magnetic-lipid nanoparticles (NPs) and high aspect-ratio magnetic nanostructures, with unique spin configurations, that can act as multimodal nanocarriers for inducing the cancer cells' death and, at the same time, deliver multiple drug agents at the target site, improving the treatment efficiency.

Building upon the current state of the art, reported in the previous chapter, specific objectives were set so as to reach such innovative goal. These involved the production and characterization of lipid nanoparticles, i.e. nanostructured lipid carriers (NLCs), as well as the development and analysis of biocompatible and multifunctional core-shell magnetic-lipid NPs bi-functionalized with an anticancer drug and folic acid.

Another objective consisted of the fabrication and characterization of high aspect ratio, biocompatible nanostructures, namely FePt nanowires (NWs) and Au/Fe/Au nanodiscs (NDs), by template-assisted methods, particularly electrodeposition into nanoporous anodic aluminium oxide (AAO) templates and thermal evaporation into Si templates, pre-patterned by interference lithography, respectively. Moreover, the development of surface functionalization techniques for this type of nanoarchitectures, so as to increase their biocompatibility and targeting capacity, as well as to prevent their recognition by cells of the mononuclear phagocyte system (MPS), represented another goal of this work.

Then, using the synthesized nanomaterials, the central focus consisted of exploring their boundaries in biomedical applications, with a particular interest in the development of novel strategies for cancer treatment. This involved analysing the suitability of the produced multifunctional core-shell magnetic-lipid NPs for a dual treatment approach, based on magnetic hyperthermia (MHT) together with anticancer drug release, as well as assessing the capacity of the fabricated high aspect ratio magnetic nanostructures for inducing the death of cancer cells, through magneto-mechanical actuation.

3. Experimental Techniques

In this chapter, it is provided a comprehensive overview of the experimental methods employed in this work. Particularly, the nanofabrication techniques used for fabricating the desired nanomaterials are first detailed. Subsequently, a broad description of all the utilized characterization techniques is presented. Finally, the cellular assays involving the use of the produced nanomaterials are described.

3.1. Reagents

For the preparation of superparamagnetic iron oxide nanoparticles (SPIONs), ferric chloride hexahydrate ($FeCl_3 \cdot 6H_2O$; ACS reagent, 97%) and ferrous chloride tetrahydrate ($FeCl_2 \cdot 4H_2O$; puriss. p.a. ≥ 99.0%) were obtained from Sigma-Aldrich® (St Louis, Missouri, USA). Ammonium hydroxide (NH_4OH) was acquired from Fisher Chemical (New Jersey, USA).

Nanostructured Lipid Carriers (NLCs) were prepared using gelucire 43/01 (GEL) and cetyl palmitate (PAL) from Gattefosé SAS (France), hydrochloric acid (HCl), oleic acid (90 %), polysorbate 80 (Tween® 80), folic acid (FA), triethylamine, dimethyl sulfoxide (DMSO) ≥ 99.9, N,N-dicyclohexylcarbodiimide (DCC), as well as Nhydroxysuccinimide (NHS) purchased from Sigma-Adrich® (St Louis, Missouri, USA), doxorubicin (DOX) obtained from LC Laboratories (Canada), and 1,2-distearoyl-sn-glycero-3-phosphoethanolamine-N-[amino(polyethylene glycol)-2000 ($DSPE\text{-}PEG_{2000}\text{-}NH_2$; ammonium salt) acquired from Avanti® Polar Lipids (Merck, Darmstadt, Germany).

The fabrication of FePt nanowires (NWs) was performed using high purity (99.997%) Al foil purchased from Alfa Aesar (Haverhill, Massachusetts, USA), acetone (C_3H_6O; ≥ 99.8%), ethanol (C_2H_5OH; ≥ 99.8%), oxalic acid ($C_2H_2O_4$), and orthophosphoric acid (H_3PO_4; AR grade) acquired from Fisher Chemical (New Jersey, USA), isopropanol (C_3H_8O) obtained from Valente & Ribeiro, Lda (Alcanena, Portugal), perchloric acid ($HClO_4$; 70.0 - 72.0 %), chromium trioxide (CrO_3; ≥ 99.0 %) and boric acid (H_3BO_3; ≥ 99.8 %) purchased from Sigma-Aldrich® (St Louis, Missouri, USA), copper(II) chloride ($CuCl_2$; 99%) and iron (II) sulphate heptahydrate ($FeSO_4 \cdot 7H_2O$; 99.5%) acquired from Acros Organics (New Jersey, USA), hydrochloric acid (HCl; 37%) obtained from Chemlab-Analytical (Zedelgem, Belgium), hexachloroplatinic acid hexahydrate ($H_2PtCl_6 \cdot 6H_2O$; ACS reagent) purchased from PanReac AppliChem (Barcelona, Spain), and Orosene E +4gr/Lt acquired from Italgalvano (Lodi Vecchio, Italy).

On the other hand, Au/Fe/Au nanodiscs (NDs) with a spin-vortex ground state were produced using WIDE8B from Brewer Science Inc. (Rolla, Missouri, USA), TSMR-iN027

purchased from Tokyo Ohka Koygo Co. (Tokyo, Japan), AZ 726 MIF acquired from Clariant AG (Muttenz, Switzerland), 1-methyl-2-pyrrolidonine (NMP) obtained from Sigma-Aldrich® (St Louis, Missouri, USA), and potassium hydroxide (KOH) from PanReac AppliChem (Barcelona, Spain).

The Au/Fe/Au NDs functionalization was performed using amine-polyethylene glycol-thiol [NH_2-PEG-SH; average molecular weight (MW): 2000] purchased from BroadPharm (San Diego, California, USA), and polyethylene glycol methyl ether thiol (PEG-thiol/PEG-SH; average MW: 2000 and 6000), FA, triethylamine, DMSO ≥ 99.9, DCC, as well as NHS obtained from Sigma-Aldrich® (St Louis, Missouri, USA).

Cellular studies were performed using a THP-1 cell line acquired from European Culture Collections (Salisbury, UK) and an MCF-7 cell line obtained from ATCC (Middlesex, UK). Additionally, Roswell Park Memorial Institute (RPMI) 1640 medium, Dulbecco's Modified Eagle's Medium (DMEM), 0.25% Trypsin-Ethylenediaminetetraacetic acid (EDTA) (1X), Penicillin-Streptomycin (PenStrep), and Heat Inactivated Fetal Bovine Serum (FBS) were purchased from Gibco® by Life Technologies (UK).

All experiments were performed with double-deionized water [resistivity (ρ) = 18.2 MΩ·cm] supplied through an ultra-pure water system (Arium Pro, Sartorius AG, Göttingen, Germany or Direct-Pure UP Ultrapure RO Lab Water System, RephiLe Bioscience Ltd, Europe). Additionally, the pH measurements were executed in a Crison pH meter GLP 22, which was equipped with a Crison 52-02 tip (Crison, Barcelona, Spain).

3.2. Nanofabrication

The nanofabrication of the nanomaterials used in this work was performed at the Institute of Physics for Advanced Materials, Nanotechnology and Photonics (IFIMUP) laboratories located at the Faculty of Sciences of the University of Porto (FCUP), at the Associated Laboratory for Green Chemistry (LAQV) of the Network of Chemistry and Technology (REQUIMTE) situated at the Faculty of Pharmacy of the University of Porto (FFUP), and at the laboratories of the Physical Chemistry Department of the University of the Basque Country (UPV). Regarding the nanoporous anodic aluminium oxide (AAO) and interference lithography templates synthetization, as well as the production of the SPIONs and NLCs, the fabrication principles, previously optimized by these research groups and proven suitable for this work, were employed. In this section, the nanofabrication techniques used for producing the desired nanomaterials will be addressed in detail.

3.2.1. Superparamagnetic Iron Oxide Nanoparticles (SPIONs)

The SPIONs used in this work were prepared by a microwave-assisted co-precipitation technique (section 1.2.1.), using a Discover® SP microwave system automated by the Explorer-12 software together with 35 mL glass vessels possessing Teflon caps. These were all purchased from CEM Corporation, North Carolina, USA.

Particularly, the SPIONs were fabricated by first weighting 250 mg of $FeCl_3 \cdot 6H_2O$ and 138 mg of $FeCl_2 \cdot 4H_2O$ into a 35 mL glass vessel with a Teflon cap and a magnetic stir bar. Subsequently, 20 mL of double-deionized water was added under continuous and vigorous magnetic stirring until all the powder was dissolved. Then, in a closed hotte, 3 mL of 25% NH_4OH was added rapidly to the ferrous solution, creating a black solution. Afterwards, the glass vessel was sealed with a Teflon cap, removed from the stirring, and left undisturbed until the precipitate settled down (5-10 min).

Following this process, the sealed glass vessel was placed in the microwave system, under nitrogen pressure, with the following parameters set:

- Temperature: 100°C
- Stirring: maximum
- Time: 10 min
- Maximum wattage: 300 W
- Maximum pressure: 200 psi

When this process ended, the sealed glass vessel was placed in a closed hotte, opened, and the solution was transferred to a 50 mL Falcon® (Falcon, Corning Incorporated, Corning, NY, USA). Then, a strong permanent magnet was placed under the Falcon® and, after most SPIONs aggregated in response to the magnetic field, the clear supernatant was quickly disposed, so as to reduce any potential ammonium volatilization. Subsequently, the resulting ferrofluid was resuspended 25 mL of double-deionized water. This supernatant disposal and resuspension in double-deionized water was performed two more times. Finally, the supernatant was removed, the obtained SPIONs formulation was stored at 4 °C under a N atmosphere and, then, it was lyophilized in a freeze drier (LyoQuest –85 plus v.407, Telstar® Life Science Solutions, Terrassa, Spain) for 24 hours, continuously kept at -80 ºC and 0.40 mbar of pressure, in order to obtain a powder, which is easier to weight..

3.2.2. Nanostructured Lipid Carriers (NLCs)

In this study, different categories of NLCs were fabricated, which are represented in figure 3.1.

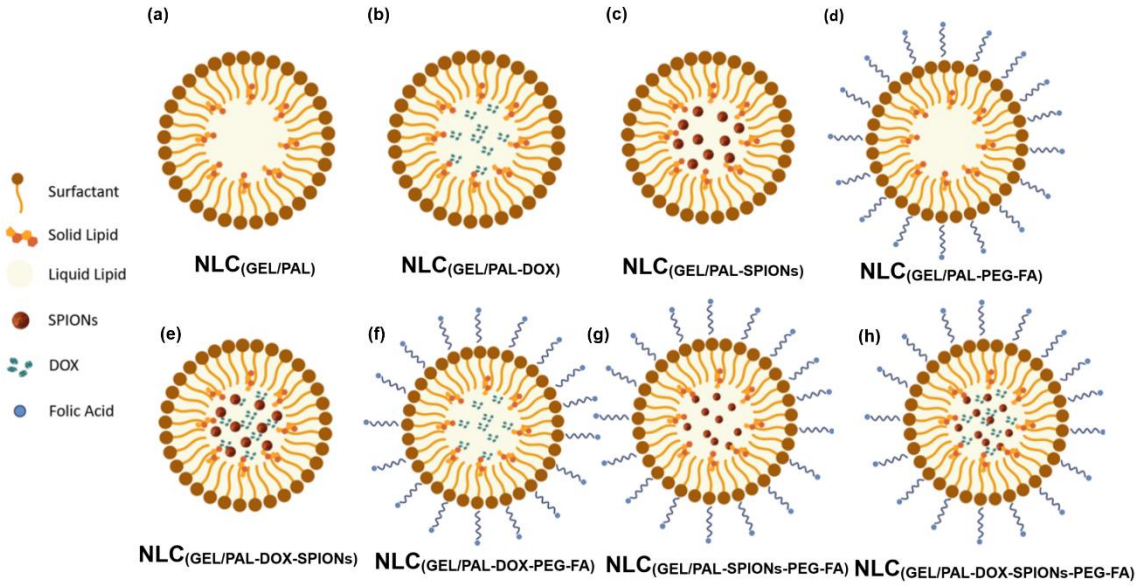

Figure 3.1 - The four different categories of NLCs fabricated in this study: (a) NLC, (b) $NLC_{(DOX)}$, (c) $NLC_{(SPIONs)}$, (d) $NLC_{(PEG-FA)}$ (e) $NLC_{(DOX-SPIONs)}$, (f) $NLC_{(DOX-PEG-FA)}$, (g) $NLC_{(SPIONs-PEG-FA)}$, and (h) $NLC_{(DOX-SPIONs-PEG-FA)}$.

These nanoparticles were fabricated through a hot ultrasonication method, which involves a combination of heat and ultrasonic energy to create a homogeneous and finely dispersed lipid matrix. This process begins by premixing the drugs, or bioactives, with the lipid components and, afterwards, the lipid components are melted, typically by raising the temperature to 5-10 ºC over the temperature of the lipid that has the highest melting point, ensuring a molten state.[1,2] The resulting mixture is then exposed to ultrasonic waves, which generate cavitation bubbles in the liquid.[3] The rapid expansion and collapse of these bubbles create intense local heat and pressure, leading to the formation of microjets and shockwaves.[4,5] These dynamic forces contribute to the breakup of larger lipid droplets into smaller ones, resulting in the formation of nanosized structures.[6] This ultrasonication step not only facilitates the reduction of particle size but also enhances the homogeneity and uniform distribution of the active compound within the lipid matrix.[7]

In this work, the NLCs production started by coating the formulation glass tube with Al foil, to prevent light from affecting DOX, since it is a photosensitive compound. Afterwards, 35 mg of oleic acid (the liquid lipid) and, for the formulations with DOX, a quantity between 1 mg and 10 mg of that compound was weighed into that tube.

Subsequently, the glass recipient placed in an ultrasonic bath (Sonorex Digitec, Bandelin Electronic, Berlin, Germany) for 10 min, to promote their mixing and dispersion. Then, for the formulations with SPIONs, 5 or 60 mg of SPIONs were weighted into the same formulation glass tube, followed by 85 mg of Tween® 80 (the surfactant) and 225 mg of the solid lipid, i.e. GEL or PAL. Subsequently, for the surface functionalized formulations, 5 mg of a PEG-FA conjugate (PEG MW: 2000; see section 3.2.2.1.) was added.

After this process, the formulation glass tube was heated to 55 ºC in a hot water bath, controlled by an immersion thermostat (Variomag Electronicrührer Einhängethermostat MR, H + P Labortechnik GmbH, Oberschleißheim, Germany), for the solid lipid to melt (about 5 min). Then, 5 ml of HCl buffer (pH = 1.0), preheated at the same temperature, was added to that vessel. Subsequently, the resulting mixture was sonicated for 5 min with a sonicator (Vibra-Cell model VCX 130, Sonics and Materials Inc., Newtown, USA) at 80% amplitude (104 W), which possessed a tip diameter of 6 mm. Afterwards, the obtained product was slowly cooled down to room temperature in a water bath, so that the internal oil phase was able to solidify, leading to the formation of NLCs dispersed in the aqueous phase. The resulting formulations were stored at 4 ºC in glass vials, which were protected from light by wrapping them with Al foil.

3.2.2.1. Poly(ethylene glycol)-Folic Acid (PEG-FA) Conjugate

The PEG-FA conjugate was obtained by first dissolving, under anhydrous conditions, 1.0 g of FA in a solution composed of 40 mL of anhydrous DMSO and 0.5 mL of triethylamine, by overnight stirring in the dark at room temperature. Then, 0.5 g of DCC and 0.52 g of NHS were added to the resulting mixture and, subsequently, it was left under overnight stirring at room temperature, under anhydrous conditions and protected from light. Afterwards, the obtained solution was filtered using a 0.45 µm filter and then it was evaporated under vacuum for 3 h, at room temperature and protected from light, using a vacuum pump connected to a desiccator, to remove the precipitated by-product [dicylcohexylurea (DCU)], DMSO, as well as triethylamine.

Subsequently, 50 mg of DSPE-PEG_{2000}-NH_2 dissolved in 1 mL of DMSO was added to 2 mL of the obtained NHS-activated FA solution and left stirring overnight, under anhydrous conditions and protected from light. Afterwards, the resulting mixture was evaporated under vacuum for 3 h, at room temperature and protected from light, using a vacuum pump connected to a desiccator, to remove the DMSO. Then, the DSPE-PEG_{2000}-FA conjugate was dialyzed against 500 mL of ultrapure water, during 48 h, using a T1 dialysis membrane (Cellu.Sep®T1, 3500 Da nominal molecular weight cut off,

Membrane Filtration Products Inc., Seguin, Texas, USA), to remove the non-conjugated FA.

After that process, the obtained solution was lyophilized (LyoQuest –85 plus v.407, Telstar® Life Science Solutions, Terrassa, Spain), resulting in the formation of a yellowish dry orange powder, corresponding to the DSPE-PEG_{2000}-FA conjugate, which was then stored at 4 °C.

3.2.3. FePt Nanowires (NWs)

The FePt NWs used in this thesis were fabricated through two different processes, namely two-step mild anodization of Al substrates, followed by pulsed electrodeposition into the resulting AAO templates, and hard anodization of Al substrates, succeeded by direct current (DC) electrodeposition (either in continuous or pulsed mode) into the obtained nanoporous membranes. In the following sections, these two distinct approaches used for the production of FePt NWs will be addressed in detail.

3.2.3.1. Al Pre-Treatment

The first step for obtaining nanoporous AAO templates is the pre-treatment of the surface of the Al substrates to be anodized, which is fundamental for the formation and organization of the pore structure.[8]

This process consisted of first cutting a high purity (99.997 %) Al foil, with a thickness of 0.25 mm and dimensions of 30 cm X 30 cm, into smaller squares (1.5 cm X 1.5 cm), which were then levelled by applying an appropriate planar pressure with a homemade pressing machine. Afterwards, the resulting Al substrates were subjected to 3 successive ultrasonic baths (Sonorex Super, Bandelin Electronic, Berlin, Germany) of acetone, isopropanol, and 96 % ethanol, each with a duration of 3 min. Acetone works as a degreasing agent, while isopropanol and 96% ethanol were used to eliminate organic contaminations resulting from the industrial rolling process and handling.

After that process, the Al samples were electropolished to improve the AAO surface quality, which translates into better nanopore organization and size uniformity (after the anodization).[9] Electropolishing is a method that involves passing a DC current through an electrolyte to remove material from the surface of an electrically conductive material by anodic dissolution.[10,11] In an electropolishing setup, the material to be electropolished works as the anode and a counter electrode serves as the cathode.[10] These two electrodes are connected to a DC power supply that is switched-off and, subsequently, they are immersed in an electrolytic solution kept at a controlled temperature.[12]

Afterwards, the power supply is turned on, leading to the movement of an electric current from the anode to the cathode. This process leads to the oxidation of the anode's surface, forming an anodic layer that, under adequate conditions, separates from the substrate and, as a result, eliminating surface impurities (figure 3.2), which dissolve in the electrolyte.[13,14] Moreover, the electric field lines tend to concentrate at the edges of points with a higher curvature, such as peaks, being, on the other hand, relatively evenly distributed in the valleys. Consequently, elevated points on the substrate's surface will undergo faster removal compared to those in the valleys, leading to a polished and clean surface with a mirror-like finish.[15–18]

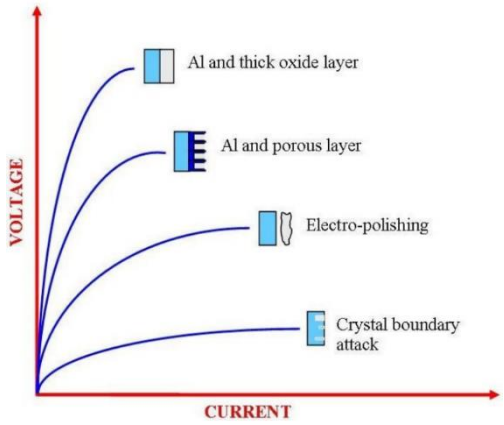

Figure 3.2 - Dependence of the Al anodic layer parameters on the applied voltage/current. From [19]. Copyright 2011 Authors licensed under a Creative Commons Attribution (CC BY-NC-ND 3.0 DEED) license.

Conversely, a reduction reaction typically takes place at the cathode, resulting in the production of hydrogen. In this process, the quantity of material removed depends upon the specific electrolyte solution, temperature, voltage, and the characteristics of the workpiece undergoing electropolishing.[10]

The electropolishing performed in this work was carried out using the previously cleaned Al substrates as the anode and by applying a voltage of 20 V (vs a Pt counter electrode), during 2 min, in a stirred electrolyte maintained at a temperature of around 10 °C, which was composed of $HClO_4$ and C_2H_5OH (volume ratio 1:4). The used setup is represented in figure 3.3.

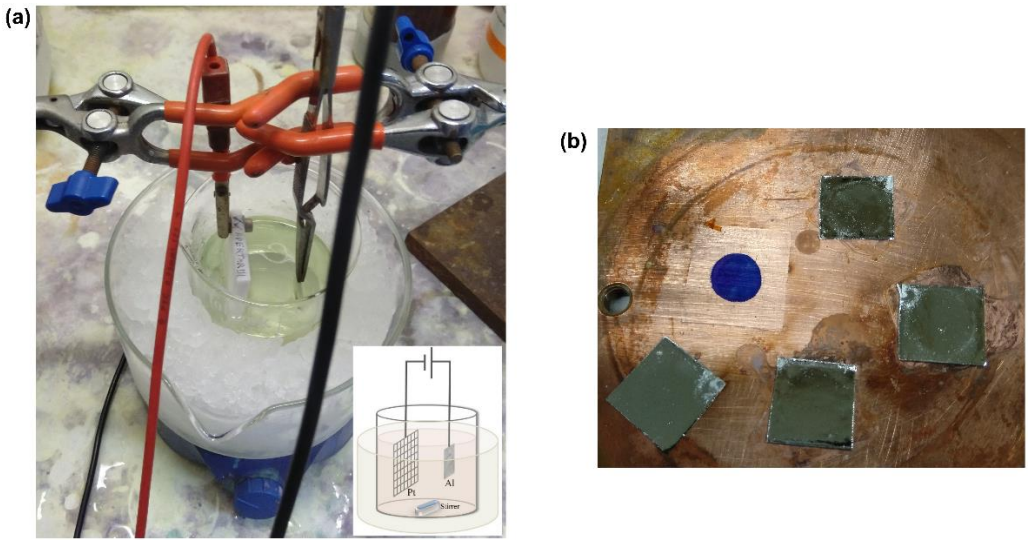

Figure 3.3 - (a) The electropolishing setup used in this work. Inset: schematic diagram of the electropolishing setup representing in the photo. Adapted from [20]. Copyright 2021 Author licensed under a Creative Commons Attribution (CC BY-NC-ND 4.0 DEED) license; (b) Al substrates after the electropolishing step..

Finally, the obtained Al substrates were rinsed in double-deionized water and dried in air.

3.2.3.2. Al Anodization

After the pre-treatment step, the obtained Al substrates were placed in anodization cells for the anodization process. This step was performed using a homemade setup, which was already implemented at IFIMUP. Such system is represented in figure 3.4.

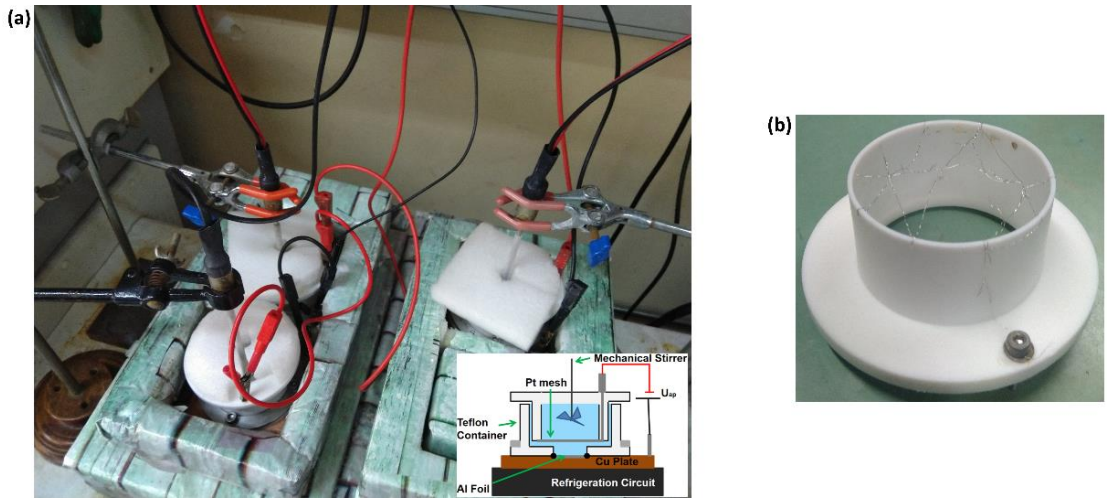

Figure 3.4 - The anodization setup utilized for growing the nanoporous AAO templates used in this work. Inset: schematic diagram anodization setup represented in the photo. From [20]. Copyright 2021 Author licensed under a Creative Commons Attribution (CC BY-NC-ND 4.0 DEED) license; (b) Al substrates after the electropolishing step.

As can be observed, the anodization cell is composed of a Teflon container where the Al substrate (working electrode) is positioned at the bottom, while a Pt mesh is placed at

the top, serving as the counter electrode [figure 3.4(b)]. Teflon was chosen due to its non-reactive nature and suitability for use with acidic solutions, providing, simultaneously, good thermal insulation for the refrigerated electrolyte. Moreover, the bottom of the cell is composed of a Cu plate, which is in direct contact with a refrigeration plate kept at a controlled temperature via a refrigeration circuit composed of a continuous circulating anti-freezing liquid (50% water/50% ethylene glycol, V/V), which is refrigerated and propelled by a Lauda Ecoline E100 immersion circulator (Lauda Brinkmann, LaudaKönigshofen, Germany), allowing the regulation of the Al substrates' temperature. Additionally, the mechanical stirrer allows precise control over the solution stirring (200 - 250 rpm) throughout this process, so as to enhance the uniformity of the electrolyte in terms of temperature, pH, and concentration gradients. Furthermore, the working electrode and the Pt mesh are both connected to a terminal on a Keithley 2400 SourceMeter (Keithley, Cleveland, Ohio USA). A computer, also connected to the SourceMeter, allows the control of the anodization routine and data acquisition throughout the process, through the LabVIEW software (National Instruments, Austin, Texas, USA).

3.2.3.2.1. Two-Step Anodization Process

The nanoporous AAO templates produced, in this work, through the two-step anodization process (see section 1.2.2.1.1.) were fabricated by initially performing a first anodization for 24 h, in 150 mL of a 0.3 M $C_2H_2O_4$ solution kept at 2 °C, under a constant potential of 40 V in DC mode. During this process, the electrolyte was homogeneously stirred with a mechanical stirrer set at a speed of 200 rpm.

Subsequently, the Al samples were placed in a mixture of 0.4 M H_3PO_4 and 0.2 M chromic acid (H_2CrO_4), at room temperature for 24 h, to remove the formed AAO layer. Afterwards, a second anodization of 8 h was performed on those Al substrates, under the same conditions as the ones considered in the first anodization, to obtain a template thick enough to not break in the subsequent steps.

3.2.3.2.1.1. Non-Steady-State Anodization

When the second anodization ended, the applied potential was exponentially decreased (non-steady-state anodization, see section 1.2.2.1.1.1.) from 40 V down to 8 V or 7 V, to reduce the thickness of the alumina barrier layer at the bottom of each nanopore from ~ 52 nm to ~ 10.4 nm or ~ 9.1 nm, according to equation 1.7. This process led to the formation of a tree-like branched structure at the bottom of each nanopore in the AAO template.

3.2.3.2.1.2. Pulsed Electrodeposition

FePt NWs were obtained by pulsed electrodeposition (section 1.2.2.1.3.3.) into the AAO templates (working electrode), produced through a non-steady-state anodization, using an electrolyte composed of 20 g/L $FeSO_4 \cdot 7H_2O$, 1 g/L $H_2PtCl_6 \cdot 6H_2O$, and 30 g/L H_3BO_3. This fabrication process was performed at room temperature, without stirring, using a Keithley 2400 SourceMeter (Keithley, Cleveland, Ohio USA), and it consisted of applying three successive pulses (vs a Pt mesh counter electrode) with different durations:[21–23]

- Deposition pulse (8 ms): this pulse has a negative polarization and a constant current density (6–25 mA/cm^2), being applied to deposit the material inside the nanopores of the template;
- Discharge pulse (2 ms): this pulse has a positive polarization and is applied to discharge the capacitance associated with the alumina barrier layer, as well as to fix eventual fractures that may appear on the template as a result of the first pulse, enhancing its homogeneity. The potential of this pulse corresponds to the final potential applied during the barrier layer thinning process, i.e. 7 V or 8 V;
- Rest pulse (0.7 s): this pulse has 0 mA and 0 V, being applied to introduce a rest time during which the ion concentration at the deposition interface is replenished and, consequently, to assure a homogeneous concentration of ions along each nanopore before the subsequent deposition pulse, thus limiting the hydrogen evolution and enhancing the deposition uniformity.

During the electrodeposition, the deposition voltage and discharge current following each deposition and discharge pulse, respectively, were measured. The deposition times ranged from 5 to 75 min.

3.2.3.2.2. Hard Anodization Process

The hard anodization process was performed using the same electrolyte employed in the fabrication of AAO templates through the two-step anodization approach, i.e. 150 mL of a 0.3 M $C_2H_2O_4$ solution kept at 2 °C, homogeneously stirred at a speed of 150 rpm. As indicated in section 1.2.2.1.2., the first step in this fabrication method was the formation of a thin oxide layer by anodizing the electropolished Al substrate, under mild anodization conditions, i.e. by applying a DC potential of 40 V, during 5 min. Subsequently, the anodization potential was increased to 140 V, at a rate of 0.6 V/s, and maintained at that value for 1 h. Then, the applied potential was switched to 40 V during 1 min, so as to stabilize the barrier layer at the bottom of the nanopores. The resulting

templates were immersed in double-deionized water at room temperature before the subsequent steps.

3.2.3.2.2.1. Al Removal and Nanopore Widening

Following the hard anodization process, the anodized samples were taken out from the double-deionized water and then submerged in 50 mL of an aqueous solution of 0.2 M $CuCl_2$ and 4.1 M HCl, at room temperature, to remove the Al. Subsequently, the resulting AAO membranes were rinsed in double-deionized water and, afterwards, they were floated in a 0.5 M H_3PO_4 aqueous solution kept at ~ 50 ºC, with their bottom side in contact with the etchant, to remove the AAO barrier layer at the bottom of the nanopores. Additionally, the acid solution was placed in a stirred-thermal bath at a stirring speed of 500 rpm, so as to ensure a homogeneous temperature distribution.

The AAO templates remained floating until bubbles were observed on their surface and sunk into the etching solution (~ 30 min), indicating that the nanopores were opened. Afterwards, they were removed from the acid solution, rinsed in double-deionized water, and dried in air.

3.2.3.2.2.2. Deposition of Au Electrical Contacts

To be able to grow nanostructures through electrodeposition into the produced AAO membranes, an electrical contact has to be established between the bottom of the nanopores and the electrodeposition solution. For this purpose, a thin Au layer was sputtered on the backside of those templates, using a DC magnetron sputtering (Scancoat Six, BOC Edwards, UK).

Sputtering is a physical vapor deposition technique, where a solid target material is bombarded by energetic and heavy particles, leading to the ejection of atoms from that target through momentum transfer, which can be deposited on a substrate.[24–26] A sputtering system involves two parallel plates, placed in a vacuum chamber containing an inert gas at low pressure (1-15 mTorr), between which a voltage ranging from a few hundred to a few thousand Vs is applied. These plates correspond to the solid target (the cathode) and the substrate where the material is going to be deposited on (the anode).[27–29] Typically, Ar is chosen for this process, due to its low cost, chemical inertness, and capability to provide a high sputtering yield.[30]

As a result of cosmic radiation, a small quantity of ions and electrons will always exist in the vacuum chamber.[31] Consequently, when an adequate voltage is applied between the two electrodes placed inside the vacuum chamber, free electrons collide with the inert

gas atoms, leading to the formation of gas ions, e.g. (Ar^+), and emission of secondary electrons.[32] The resulting gas ions will be attracted towards the cathode, i.e. the solid target, colliding with its surface, which results in various collisions that, primarily, lead to the removal of neutral atoms from the target by momentum transfer [figure 3.5(a)].[31] Moreover, other particles, e.g. secondary electrons, reflected ions, or photons, can also be scattered from its surface.[33] Nevertheless, the neutral target atoms disperse within the chamber according to a $\cos^n(\theta)$-distribution, indicating that a significant portion of the target atoms will be sputtered in the forward direction. Therefore, placing the substrate holder in this direction ensures that the majority of those atoms will condense on the substrate, forming the thin film.[31,34]

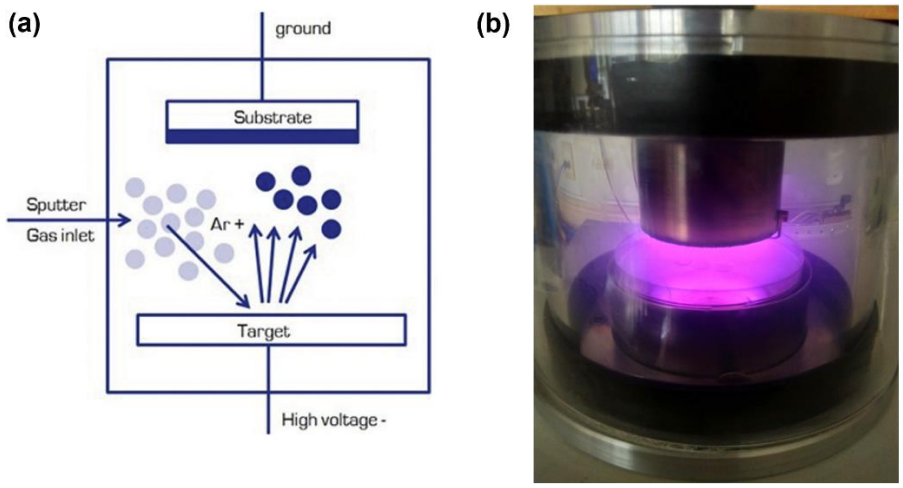

Figure 3.5 - (a) Schematic representation of a sputtering deposition system. Reprinted from [35], Copyright 2021, with permission from Elsevier; (b) the glow observed in the DC magnetron sputtering equipment used for depositing the Au layer on the backside of the AAO templates produced through the hard anodization method.

On the other hand, the free and secondary electrons are accelerated towards the anode, having the potential to collide with other gas atoms, leading to the formation of additional gas ions and secondary electrons. Furthermore, as previously mentioned, the gas ions that hit the cathode originate even more secondary electrons.[32] This results in an avalanche process that leads to a current increase and, as soon as the number of generated electrons is sufficiently high to produce enough gas ions that, in turn, regenerate the same number of electrons that are lost by recombination processes, the discharge is said to be self-sustaining and the gas begins to glow, a phenomenon known as glow discharge [figure 3.5(b)].[32,36,37] The presence of this glow is often an indicator of a stable and sustained plasma state, being primarily attributed to the recombination of free electrons with gas atoms or ions within the plasma, which leads to an energy release in the form of visible light.[38,39]

The previously described sputtering process has been known for various years, having been proven effective for the deposition of various materials. Nevertheless, it presents some limitations due to reduced deposition rates, low ionization efficiencies in the plasma, as well as substrate heating.[40,41] These drawbacks can be overcome by introducing a magnetic field close to the target through the use of a magnetron, which has led to the development of magnetron sputtering.[42] This device is a system of permanent magnets arranged in a specific orientation that is positioned behind the target.[43,44] The presence of a magnetic field constraints the electron motion to the target's vicinity, increasing the probability of electron-ion/atom collisions. Consequently, the ionization efficiency increases, leading to a greater plasma density near the cathode (figure 3.6). This results in higher deposition rates, improving the process efficiency, and, therefore, enhances the quality of the deposited films.[45,46]

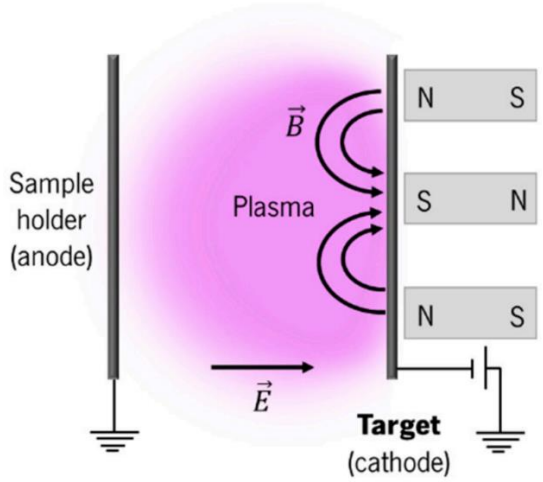

Figure 3.6 - Schematic representation of a magnetron sputtering deposition system. Adapted from [45]. Copyright 2021 Authors licensed under a Creative Commons Attribution (CC BY-NC-ND 4.0 DEED) license; (b) Al substrates after the electropolishing step.

In this work, the sputtering of the Au electrical contacts was performed using a DC magnetron sputtering, meaning that a DC power supply is used to generate a constant electric potential between the cathode and the anode in the magnetron sputtering equipment. The depositions were carried out in an Ar atmosphere (Air Liquide-Alphagaz 1, Paris, France), at a base pressure of $3 \cdot 10^{-2}$ mbar, a working pressure equal to $3 \cdot 10^{-1}$ mbar, a current of 20 mA, and a potential of 0.9 kV. These conditions originated Au thin films with a thickness of ~ 40 - 50 nm, for a deposition time of 5 min.

3.2.3.2.2.3. Direct Current (DC) Electrodeposition

The following step in the fabrication of FePt NWs, using hard anodization AAO templates, was the electrodeposition into those membranes through a DC electrodeposition

method, in both continuous and pulsed modes. This process was performed using an Autolab PGSTAT204 potentiostat/galvanostat (Metrohm AG, Herisau, Switzerland) with a conventional three-electrode system. In this setup, a Pt mesh and an Ag/AgCl electrode were used as counter and reference electrodes, respectively, while the counter electrode was the nanoporous AAO template.

Regarding the continuous DC approach, the considered electrolyte was composed of 20 g/L $FeSO_4 \cdot 7H_2O$, 1 g/L $H_2PtCl_6 \cdot 6H_2O$, plus 30 g/L H_3BO_3 and the applied potential was varied between - 0.8 and - 2.0 V, while the deposition time was kept constant at 15 min. On the other hand, in the pulsed DC approach the influence of multiple parameters on the resulting NWs was assessed by varying one at a time, namely the $FeSO_4 \cdot 7H_2O$ (20 - 120 g/L) and $H_2PtCl_6 \cdot 6H_2O$ (1 - 5 g/L) concentration in the electrolyte, the deposition pulse (t_{on} = 4 - 40 ms), the rest pulse (t_{off} = 4 - 40 ms), the t_{on}/t_{off} ratio (0.1 - 10), as well as the applied potential (- 0.8 — - 10 V). In these experiments, the parameters kept constant were the H_3BO_3 concentration (30 g/L) as well as the electrodeposition duration (15 min). Additionally, it was analysed influence of electrodepositing an Au layer for 5 min, using Orosene 999, before growing the FePt NWs.

3.2.3.2.2.4. Removal of the NWs from the Hard Anodization Anodic Aluminium Template (AAO) Template

After the DC electrodeposition process, the NWs with the desired composition were removed from the AAO templates for the subsequent cellular studies. This process consisted of dissolving the AAO membranes through a chemical etching process. Particularly, the nanoporous membranes containing the NWs were immersed in an aqueous solution composed of 0.4 M H_3PO_4 and 0.2 M H_2CrO_4, which was maintained at 40 ºC. Such etching solution also inhibits the oxidation of metallic NWs.

When the templates were completely dissolved (~ 48 h), the resulting NWs were collected using a magnet and washed three times with double-deionized water. Finally, the obtained nanostructures were suspended in 1 mL of double-deionized water.

3.2.4. Au/Fe/Au Nanodiscs (NDs)

In addition to the previous nanomaterials, Au/Fe/Au NDs with a spin-vortex ground state were fabricated through thermal evaporation into Si templates, pre-patterned by laser interference lithography. Therefore, in the following sections, this synthetization process will be addressed in detail.

3.2.4.1. Interference Lithography Templates

Si(100) wafers with a thickness of 360 μm, covered by an amorphous, 15nm-thick SiO layer were used as the base of the prepared templates. These substrates were first spin-coated with an anti-reflective coating (ARC), WIDE-8B, at 5000 rpm for 60 s, to prevent a second interference pattern on the vertical axis. Afterwards, they were baked on a hotplate in two steps, namely 40 s at 100 ºC and, subsequently, 60 s at 180 ºC. Then, a negative tone photoresist, TSMR-iN027, was spin-coated over the ARC at 4000 rpm during 60 s and, following that process, a baking step at 90 ºC for 90 s was performed, having been obtained a resist stack with a thickness of 280 nm.

Right after, the resist/ARC stack was patterned through laser interference lithography, to reduce the effect of photoresist ageing. The lithographic exposures were performed using a Lloyd's mirror interferometer system where a He-Cd laser (λ = 325 nm) was used as the light source, figure 3.7, which allows the fabrication of ordered patterns in large areas (up to 10x10 cm^2) whose dimensions can be ranged from ≈ 300 nm to a few microns.

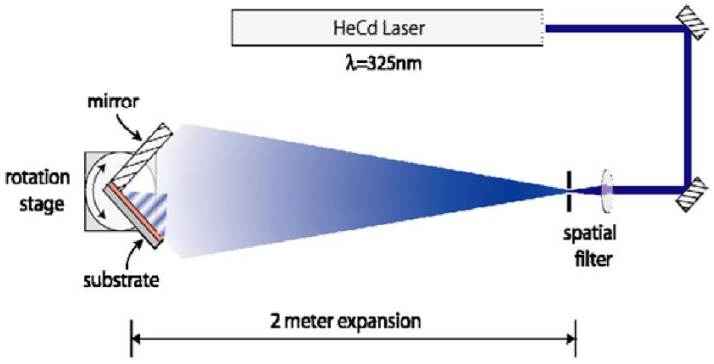

Figure 3.7 - Scheme of the Lloyd's mirror interferometer used to pattern the photoresist-coated Si wafers. From [47].

The working principle of this technique was already addressed in section 1.2.2.2.

In order to obtain a square array of dots on the Si substrates, two 7-min exposures were performed for each sample, considering a 90º rotation of the Si wafer between them. Then, after performing both exposures, the Si wafer was post-baked at 110 ºC during 90 seconds and, subsequently, it was developed in AZ 736 MIF for 1 min. Afterwards, the substrates were cleaned with deionized water and dried using N_2.

3.2.4.2. Thermal Evaporation

Subsequently, Au/Fe/Au NDs, together with an Al sacrificial layer (figure 3.8), were deposited on the pre-patterned Si substrates by thermal evaporation.

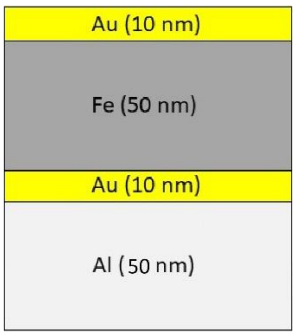

Figure 3.8 - Cross-section schematization of the thermally evaporated multilayered NDs.

Thermal evaporation is a physical vapour deposition technique were the target material, i.e. the evaporant, is heated in a vacuum chamber, by an electric resistance heater, to a temperature that is sufficiently high for its surface atoms to have enough energy to leave the surface.[48–51] Two feedthroughs are utilized to pass a substantial electrical current through the heater, which is made of a refractory material, like W or Mo.[47] In this technique, the most commonly chosen containers are known as ”boats”, being composed of a refractory ribbon featuring a dimple on the upper side, where the target material is positioned, typically in the form of pellets or powders.[47,52–54] Then, the current flow through the boat is gradually increased until the target material begins to evaporate.[55,56] At this stage, increasing the current leads to a faster evaporation rate, and vice versa.[57] The atoms that escape from the target's surface will travel through the vacuum chamber, propelled by thermal energy, and deposit onto a substrate.[58,59] Therefore, the chamber's pressure should be maintained below the threshold where the mean free path of those atoms exceeds the distance between the evaporation source and the substrate.[60] A schematic representation of a typical thermal evaporation setup is illustrated in figure 3.9.

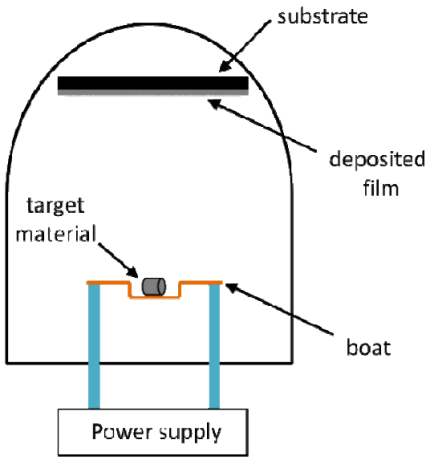

Figure 3.9 - Scheme of a typical thermal evaporation setup. Adapted from [47]. Copyright 2018 Authors licensed under a Creative Commons Attribution (CC BY-NC-ND 4.0 DEED) license.

In this work, the thermal evaporation was performed in a high vacuum chamber equipped with two thermal evaporation sources and a quartz-microbalance to control the deposited film's thickness. Using this equipment, a 50-nm Al layer, which works as the sacrificial layer allowing the removal of the nanostructures from the Si templates, and a 50-nm-thick Fe film sandwiched between two 10-nm-thick Au layers were evaporated sequentially at room temperature with a base pressure in the vacuum chamber of $1 \cdot 10^{-6}$ mbar, and a working pressure of $\sim 6 \cdot 10^{-5}$ mbar.

The deposition rates were 3.5 nm/min for Al, 1 nm/min for Fe, and 2.2 nm/min for Au. In addition to the NDs, a continuous Au/Fe/Au trilayer was also deposited for reference.

Then, the photoresist was removed from the template through a lift-off process involving the use of NMP at 125 ºC, during a few minutes, followed by an ultrasonic bath.

3.2.4.3. Removal of the NDs from the Interference Lithography Template

After depositing the NDs, they were removed from the interference lithography template by etching the Al sacrificial layer located between the nanostructures and the template. This was performed using an aqueous solution of 15 % KOH in an ultrasound bath. The released NDs were then collected using a magnet and placed inside an Eppendorf (Hamburg, Germany) tube. Subsequently, the nanostructures were washed three times with double-deionized water and, finally, suspended in 1 mL of the same type of water.

3.2.4.4. Surface Functionalization

In order to assess the effect of surface functionalization on the suitability of these nanostructures for biomedical applications, two different NDs functionalizations were studied, namely PEG-SH and folic acid-PEG-SH (FA-PEG-SH).

Regarding the first functionalization, two different types of PEG-SH possessing distinct MWs, i.e. 2000 and 6000 g/mol, were used. The functionalization process consisted of the following steps:

- (i) Adding the NDs to a 1 mM PEG-SH solution in pH 7.0 phosphate buffered saline (PBS) solution;
- (ii) Storing the solution with the NDs during 22 hours at room temperature;
- (iii) Aspiration of the PEG-SH solution and rinsing of the NDs with ultrapure double-deionized water;
- (iv) Suspension of the NDs in 1 mL of ultrapure double-deionized water.

The FA-PEG-SH functionalization followed the same steps, but it was preceded by the synthesis of the FA-PEG-SH conjugate. This compound was obtained by first dissolving, under anhydrous conditions, 1.0 g of FA in a solution composed of 40 mL of anhydrous DMSO and 0.5 mL of triethylamine, by overnight stirring in the dark at room temperature. Then, 0.5 g of DCC and 0.52 g of NHS were added to the resulting mixture and, subsequently, it was left under overnight stirring at room temperature, under anhydrous conditions and protected from light. Afterwards, the obtained solution was filtered using a 0.45 µM filter and then it was evaporated under vacuum for 3 h, at room temperature and protected from light, using a vacuum pump connected to a desiccator, so as to remove the precipitated by-product (dicylcohexylurea (DCU)), DMSO, as well as triethylamine. Subsequently, the coupling of the prepared NHS-FA with NH_2-PEG-SH was performed by incubating during 4 h, at room temperature and in the dark, 2 mL of activated FA solution with 13.44 mg of NH_2-PEG-SH dissolved in 1 mL of PBS. After this reaction, the resulting solution was filtered using a 2000 Da filter to remove the excess FA-NHS, EDC, and NHS. Then, the resulting solution was used to functionalize the NDs by immersing the nanostructures in that solution during 22 hours, at room temperature and protected from light. Subsequently, the FA-PEG-SH solution was aspirated and the NDs were rinsed with ultrapure double deionized water. Finally, the nanoarchitectures were suspended in 1 mL of that same type of water.

3.3. Characterization

The fabricated nanomaterials were characterized at IFIMUP, Centro de Microscopia Eletrónica da Universidade do Porto - Portugal (CEMUP), FFUP, Institute for Optoelectronic Systems and Microtechnology - Technical University of Madrid (ISOM-UPM), Autonomous University of Madrid (UAM), and at UPV. In this section, the techniques used for the morphological, structural, compositional, and magnetic characterization of the synthesized nanomaterials are going to be addressed in detail.

3.3.1. Dynamic Light Scattering (DLS)

Dynamic light scattering (DLS) is a non-destructive and simple technique that measures the Brownian motion exhibited by particles within a solution, arising from the continuous impact of solvent molecules that surround them, establishing a relationship between this motion and the particle's size.[61,62] The measurement depends on both the temperature, as well as on the solvent's viscosity.[61] A scheme of a general DLS setup is represented in figure 3.10.

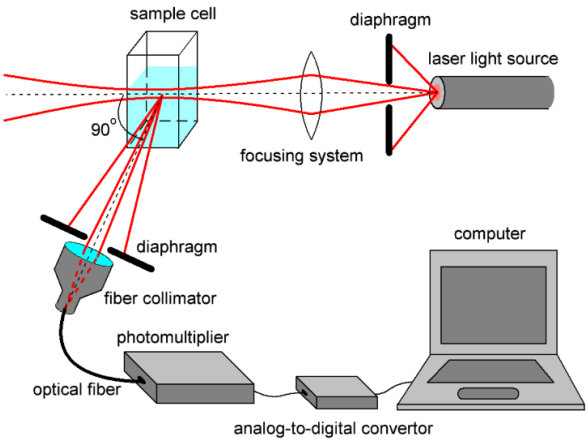

Figure 3.10 - Scheme of a general DLS setup. From [63]. Copyright 2020 Authors licensed under a Creative Commons Attribution (CC BY-NC-ND 4.0 DEED) license.

When particles are irradiated by a laser over a given period, there is a fluctuation in the scattered light intensity, which is determined by the size of the particles. Specifically, smaller particles are projected a greater distance by the solvent molecules and exhibit faster movement, resulting in rapid fluctuations. Conversely, larger particles diffuse more slowly, leading to slower fluctuations.[64]

In a DLS equipment, the intensity of light reaching the detector, at any given moment, depends on the interference pattern created by the light that is scattered by all the particles in the scattering volume. The scattered light can either produce mutually destructive phases that cancel each other out or mutually constructive phases that generate a detectable signal.[64,65] This leads to the generation of a correlogram, where the raw correlation function is represented (3.11).[66]

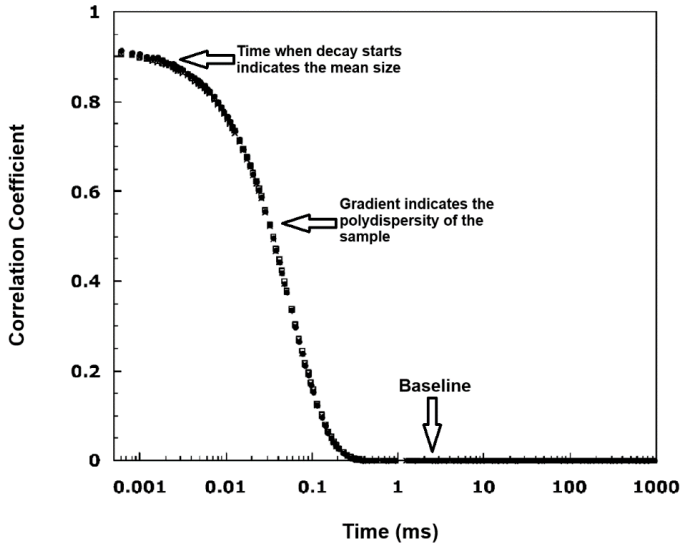

Figure 3.11 - The raw correlation function. Used with permission of Royal Society of Chemistry, from [66]; permission conveyed through Copyright Clearance Center, Inc.

As can be observed, initially, when the particles are not moving significantly, there is a strong correlation between the intensities of the scattered light at different times, resulting in a high correlation coefficient. However, as time passes, the Brownian motion of the particles causes more considerable fluctuations in the scattered light intensity, originating a reduction of the correlation coefficient.[67,68]

Assuming that the particles have a spherical shape and are uniform, the mathematical treatment of the raw correlation function leads to the Stokes-Einstein equation, which allows the determination of their hydrodynamic diameter, d_h:[69,70]

$$d_h = \frac{K_b T}{3\pi\eta D} \quad (3.1)$$

where K_b represents the Boltzmann constant (1.38064852 · 10^{-23} J/K), T is the temperature of the sample, η represents the absolute viscosity of the medium, and D is the diffusion coefficient.

Additionally, DLS also gives information regarding the size distribution of the particles in the form of a polydispersity index (PDI), which is determined by the gradient of the correlation function (figure 3.11). Specifically, steeper lines in the graph signify a more monodispersed system.[71]

In this work, DLS (ZetaPALS, Brookhaven Instruments Corporation, Holtsville, NY, USA) was used to determine the mean NLC size and PDI in the fabricated formulations. For such purpose, 20 µL of each NLC formulation was diluted in 1480 µL of HCl buffer solution (pH = 1). Six runs at room temperature were conducted for each formulation, with each run comprising 10 sub-measurements and lasting 2 min, resulting in a total measurement duration of 12 min. The mean NLC size and PDI were determined by averaging these parameters across all runs. Moreover, three independent batches of each formulation were examined.

Moreover, for assessing thermal stability and pH-sensitivity of the produced formulations, 20 µL of each sample was diluted in 1480 µL of PBS buffer (pH = 5 or 7) and DLS measurements were performed at temperatures ranging from 25 ºC to 70 ºC.

3.3.2. Nanoparticle Tracking Analysis (NTA)

In addition to DLS, nanoparticle tracking analysis (NTA) was also used to assess the mean size of the NLCs, as well as their size distribution. This technique was used because it allows the determination of their concentration in the formulation. On the other

hand, DLS is a faster and simpler technique, capable of analyzing the NP size distribution across a broad range (5 nm to 3 µm).[72–75]

Similarly to DLS, NTA exploits the characteristics of both light scattering and Brownian motion to determine the particle size distribution in a liquid suspension.[76] In this method, a laser beam traverses a prism-edged glass flat located in the sample chamber, below the actual sample [figure 3.12(a)].[77] The angle of incidence, as well as the refractive index associated with the glass flat, are specifically configured to ensure that, when the laser reaches the interface between the glass and the overlying liquid sample layer, it undergoes refraction, leading to a compressed beam with a diminished profile and increased power density.[78,79] Particles in suspension that cross the trajectory of this refracted beam, scatter light in a way that permits their easy visualization using a long working distance, 20X magnification microscope objective, which is fitted to a standard optical microscope that can record a video of those particles.[80] The NTA software monitors the Brownian motion of individual particles at a single-particle level [figure 3.12(b)], determining the single-particle diffusion coefficient, which is derived from the particle's mean displacement between successive frames.[81,82] Then, using the Stokes-Einstein equation, such software computes their sizes and also their total concentration.[73,83]

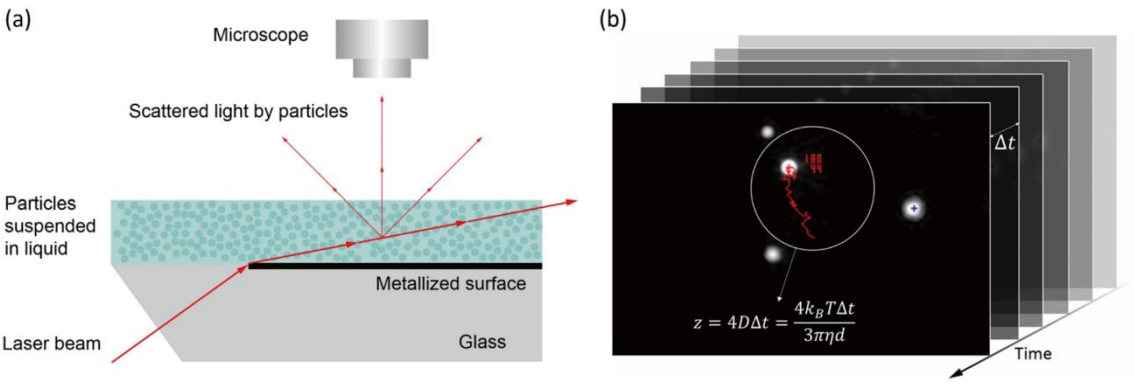

Figure 3.12 - (a) Schematic representation of the NTA detection. Particles suspended in a liquid medium are exposed to a laser beam and the light scattered by these particles is observed through a microscope. The software identifies the positions of the particles based on this scattered light. (b) The software traces the path of the particles and constructs particle tracks. The average squared displacement (z) for each track is subsequently transformed into the corresponding hydrodynamic diameter (d) using the Stokes-Einstein equation. From [84]. Copyright 2019 Authors licensed under a Creative Commons Attribution (CC BY-NC-ND 4.0 DEED) license.

Depending on the particle type, this technique allows the measurement of particle sizes in the range of 10 nm to 1000 nm, at sample concentrations of ~ 10^6 – 10^{12} particles/mL.[85] Particularly, for particles with a high refractive index, such as colloidal Au or Ag particles, NTA allows the determination of sizes as low as 10 nm.[86,87] On the other hand, the upper size limit of this method corresponds to the point where the particles

become so large that their Brownian motion is limited, i.e. they move very slowly, which hinders their accurate tracking, leading to a reduction of this technique's accuracy. Naturally, the viscosity of the solvent also influences this limit, since it affects the particles' movement as well.[88,89]

In this work, NTA was carried out, at FFUP, by performing five runs of measurements for each NLC sample. For such purpose, 20 µL of NLCs formulation were diluted in 1480 µL of HCl buffer solution (pH = 1) and, subsequently, 10 µL of that diluted sample were diluted once more in 1490 µL of the same buffer solution.

3.3.3. Zeta Potential

The zeta potential refers to the potential at the slipping/shear plane of a colloid particle or, in other words, to the potential difference between the dispersion medium and the stationary layer of fluid attached to the dispersed particle (figure 3.13), allowing the assessment of its colloidal stability.[90–93] Particularly, the analysis of the zeta potential can provide a comprehensive understanding of the factors contributing to dispersion, aggregation, or flocculation, which can be used to enhance the colloidal solution conditions.[94,95]

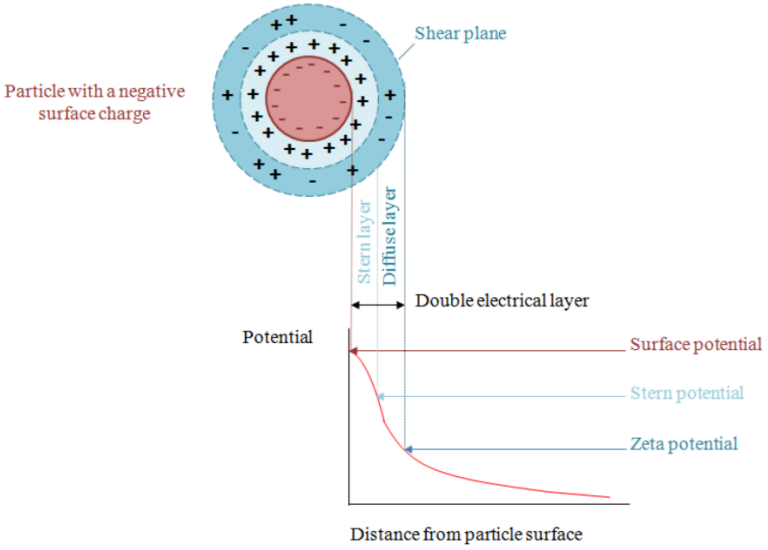

Figure 3.13 - The different charge potentials at a particle's surface. Reprinted from [96], Copyright (2017), with permission from Elsevier.

As depicted in the figure above, there is a strongly attached layer at the particle surface, which is referred to as the Stern layer and it comprises ions with opposite charges. Furthermore, there is an outer layer designated as diffuse layer, consisting of both positive and negative charges that are more loosely associated.[97–99] This double layer structure adsorbed onto the particle surface is known as the electric double layer (EDL),

and its composition is influenced by various factors, including pH, ionic strength, and concentration.[100]

Since the zeta potential cannot be directly measured, various techniques can be used for such purpose.[101,102] In this work, the zeta potential was measured by electrophoretic light scattering (ELS), wherein the mobile NPs in electrophoresis scatter an incident laser (figure 3.14).[103]

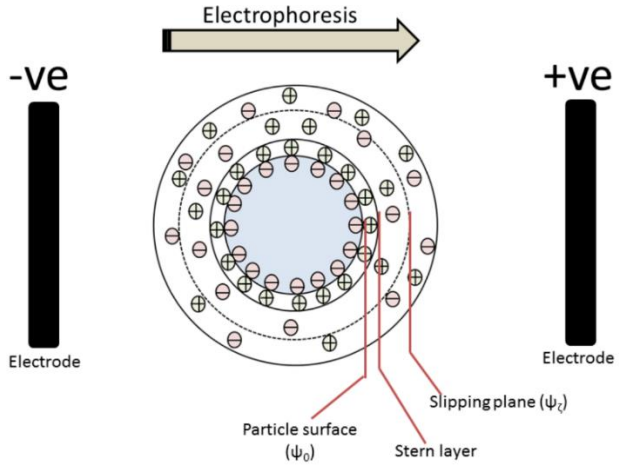

Figure 3.14 - Movement of a particle during electrophoresis. Reprinted from [98], Copyright (2016), with permission from Elsevier.

Particularly, during this process, the particles in a dispersion will migrate toward the electrode that has an opposite charge and a laser light is directed through the dispersion. Therefore, as the particles move the frequency of the light that they scatter is shifted as a result of the Doppler effect. This shift can be analysed to determine the electrophoretic mobility of the particles.[104,105] This electrophoretic mobility (μ_e) is then related to the zeta potential (ζ) through the Henry's equation:[98,106]

$$\mu_e = \frac{2\epsilon_r \epsilon_0 \zeta f(\kappa\alpha)}{3\eta} \quad (3.2)$$

where ϵ_r represents the relative permittivity/dielectric constant of the medium, ϵ_0 is the vacuum permittivity ($\sim 8.85 \cdot 10^{-12}$ F/m), $f(\kappa\alpha)$ is the Henry function, and η represents the viscosity at the experimental temperature.

Typically, NPs exhibiting zeta potential in the ranges of ± 0 - 10 mV, ± 10 - 20 mV, ± 20 -30 mV, and over ± 30 mV are categorized as highly unstable, relatively stable, moderately stable, and highly stable, correspondingly.[107] However, the reality is often more complex as colloid stability is influenced by both Van der Waals attractive forces as well as electrostatic repulsive forces.[108] Consequently, since the zeta potential

provides information solely about the electrostatic repulsive force, it may not fully capture the complexity of colloidal stability. Therefore, colloids with low zeta potential values can also exist.[108,109]

In this work, the NLCs' zeta potential was measured with a ZetaPALS analyser (Brookhaven Instruments Corporation, Holtsville, NY, USA) at 25 ºC, using disposable capillary cells and an electrode working at a scattering angle of 90 º. For every assay, 6 runs, each containing 10 sub-measurements, were performed and the zeta potential was taken as the average value across all runs. Three independent batches of each NLCs formulation were analysed, in terms of zeta potential, and the sample preparation consisted of diluting 2 µL of formulation in 10 mL of Milli-Q® Integral ultrapure water.

3.3.4. Ultraviolet-Visible (UV-Vis) Spectroscopy

Ultraviolet-visible (UV-Vis) spectroscopy was used in this thesis to determine the encapsulation efficiency (EE), as well as the quantity of DOX released from the produced formulations. This technique is frequently employed for quantitatively determining transition metal ions, organic compounds, and biological macromolecules in solutions without causing significant modification or permanent damage to them.[110]

This approach is based on the absorption of electromagnetic radiation by chemical compounds.[111,112] Particularly, in a UV-Vis spectrometer the sample is illuminated by electromagnetic radiation (I_0), with wavelengths ranging from 200 to 800 nm.[113] A part of this radiation is absorbed by the sample, while the other part is transmitted through it (I).[114] The intensity of the transmitted radiation is then is measured as a function of the wavelength, by an appropriate detector.[115] This allows the determination of the transmittance, i.e. $T = \frac{I}{I_0}$, which is used to compute the absorbance of the sample, i.e. $\mathrm{A} = -\log(\mathrm{T})$, for each considered wavelength.[116,117] Considering that the absorbance follows the Beer-Lambert law, its value is directly proportional to the concentration (C) of the absorbing species and to the path length of the absorbing medium (l):[118]

$$\mathrm{A} = \epsilon \mathrm{l} \mathrm{C} = -\log\left(\frac{I}{I_0}\right) \tag{3.3}$$

where ϵ represents the molar absorption or extinction coefficient ($M^{-1} \cdot cm^{-1}$), which is a measure of how strongly a given compound absorbs light with a specific wavelength, under defined temperature and solvent conditions.[119] Consequently, by plotting the absorbance as a function of the wavelength, a UV-Vis spectrum is generated. However, to ensure the applicability of the Beer-Lambert law at each desired wavelength and,

therefore, accurately determine the concentration of the analyte in the sample, a calibration curve should be constructed for every wavelength of interest, under the same conditions used to measure sample (figure 3.15).[120,121] Otherwise, the concentration measurements may be inaccurate, since the absorbance may not be correctly correlated to the analyte concentration.[122]

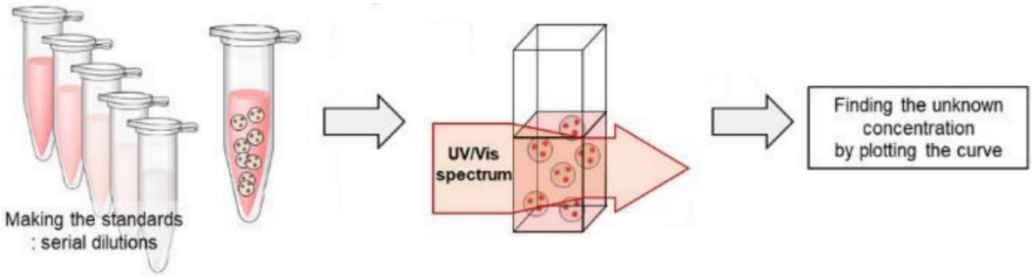

Figure 3.15 - The process of determining the concentration of an analyte in a sample through UV-Vis spectroscopy. Adapted from [123]. Copyright 2019 Authors licensed under a Creative Commons Attribution (CC BY-NC-ND 4.0 DEED) license.

A calibration curve is elaborated by making standard dilutions with known concentrations of the analyte and plotting the absorbance values as a function of the concentration.[124,125] This curve can exhibit both linear and non-linear behaviour, depending on the concentration range of the analyte of interest and the specific characteristics of the chemical system being studied. To obtain accurate and reliable results, it is essential to validate the linearity of the calibration curve within the concentration range of interest. However, if non-linearity is observed, additional calibration methods or techniques may be necessary to correct for these deviations.[126–128]

In this work, a calibration curve of DOX was elaborated from the UV-Vis absorbance at λ_{max} = 253 nm in HCl buffer solution (pH = 1), with concentrations ranging from 0 mg/mL to 0.1 mg/mL.

3.3.4.1. Encapsulation Efficiency (EE) and Loading Capacity (LC)

Using UV-Vis spectroscopy, the EE of DOX in the NLCs was assessed. For this purpose, three independent batches of each formulation were diluted at a ratio of 1:100 in HCl buffer solution (pH = 1) and then transferred to Amicon®Ultra-4 Centrifugal Filter Devices (50 KDa, MERK Milipore, Ltd; Cork, Ireland). Subsequently, they were centrifuged, (HeraeusT M MultifugeT M X1R Centrifuge, USA) at 1006 xg and 20 ºC, for 45 min or until it was observed a total separation between the NLCs retained in the filter unit and the aqueous phase, i.e. the filtrate. Afterwards, the resulting supernatant was collected and used to measure the quantity of DOX that was not incorporated in the NLCs by UV–vis spectrophotometry (Jasco V - 660 Spectrophotometer, USA), at λ_{max} = 253 nm, which

not only corresponds to the wavelength where absorbance is higher for DOX in aqueous solution, but is also a narrow band with high molar absorption coefficients, whose position is independent of the medium pH as opposed to the band located at 480 nm.[129,130] Considering the initial amount of drug added to the NLCs formulation and subtracting from it the free DOX found in the filtrate, it was possible to calculate the drug's incorporation in the NLCs and, consequently, determine the EE through the following equation:

$$\mathrm{EE}\ (\%) = \frac{\text{Amount of DOX Initially Added} - \text{Amount of Free DOX}}{\text{Amount of DOX Initially Added}} \times 100 \qquad (3.4)$$

Using the determined EE the loading capacity (LC) was also determined according to:

$$\mathrm{LC}\ (\%) = \frac{\mathrm{EE} \times \text{Amount of DOX Initially Added}}{\text{Amount of Lipid} + \text{Amount of Surfactant}} \times 100 \qquad (3.5)$$

3.3.4.2. DOX Release Triggered by External Stimuli

The release of the anticancer drug from the produced NLCs, as a result of different external stimuli, i.e. pH, temperature, or alternating magnetic field (AMF), was quantified by first performing a dialysis of the formulation, which was dispersed inside a cellulose dialysis bag (Cellu.Sep®T1, 3500 NMWCO, Membrane Filtration Products, Inc.; Seguin, TX, USA) that, in turn, was placed in a buffer solution, see figure 3.16. Dialysis is a technique based on the diffusion of small solutes, from a solution with a high concentration to one with a lower concentration of that solute, through a semipermeable membrane until the concentrations in both solutions are equal, i.e. equilibrium is reached.[131,132] After this process, the UV-Vis absorbance spectra of the surrounding buffer solution was acquired, allowing the quantification of the amount of drug released from the nanoformulation..

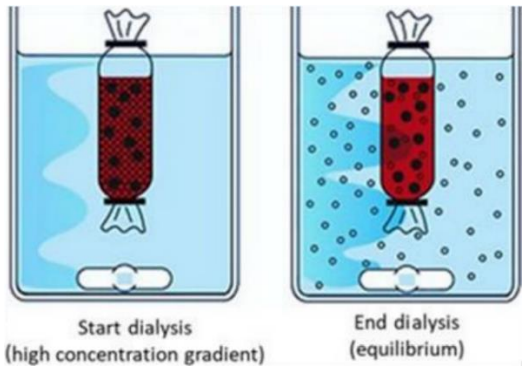

Figure 3.16 - Schematic representation of the dialysis setup used in this work. Adapted from [20]. Copyright 2021 Author licensed under a Creative Commons Attribution (CC BY-NC-ND 4.0 DEED) license.

Before any experiment with the produced formulations, they were filtered by dialysis so as to remove the free DOX. For this purpose, 1 mL of each formulation was placed inside the dialysis bag, which, in turn, was immersed in 80 mL of buffer solution (HCl solution with pH 1.5) for 45 min.

Then, the DOX release from the GEL-based and PAL-based $NLCs_{(DOX\text{-}SPIONs)}$ ([DOX] = 2000 µg/mL; [SPIONs] = 12000 µg/mL) triggered by an AMF was evaluated. For this purpose, the dialysis bag was filled with 150 µL of each formulation and then placed in 1.5 mL of buffer medium (PBS, pH 5 or pH 7), which was located within the magnetic coils of the used MHT system. Subsequently, an AMF was applied for 30 min (556 kHz, 10 mT) and an infrared thermal camera was used to monitor the temperature. A similar protocol was used for assessing the DOX release from the same formulations, but instead of placing the dialysis setup in the magnetic coils, it was placed in water bath at different temperatures (35, 40, 45 and 50 °C).

Moreover, based on the results of the performed studies, the DOX release from GEL-based $NLCs_{(DOX\text{-}SPIONs)}$ ([DOX] = 2000 µg/mL; [SPIONs] = 12000 µg/mL) was analysed in more detail. Particularly, the release profiles of DOX from this formulation at pH 7 and 5, in water bath at different temperatures (35, 40, 45 and 50 ºC) were analysed. For this purpose, 150 µL of sample were diluted in 900 µL of a buffer solution (PBS, pH 5 or pH 7) and, afterwards, the diluted sample was placed inside a dialysis bag, which was immersed in 15 mL of a buffer solution (PBS, pH 5 or pH 7). Then, the quantity of DOX released under each considered condition was measured every 30 min, using UV-Vis spectroscopy every 30 min.

3.3.5. Storage Stability Assessment

The NLCs storage stability was assessed over 61 days. For that purpose, the produced formulations were kept at 4 ºC in glass vials and the mean particle size, zeta potential, PDI, as well as drug content, were measured weekly, through the previously described techniques.

3.3.6. Electron Microscopy

Electron microscopy is based on irradiating a sample with a focused electron beam possessing a controlled kinetic energy, in a high vacuum environment. As these particles interact with the sample, either organic or inorganic, they can provide information about their morphology or composition.[133–135]

Currently, there are various electron microscopy techniques available, such as scanning electron microcopy (SEM), scanning transmission electron microscopy (STEM), transmission electron microscopy (TEM), or energy dispersive X-ray spectroscopy (EDS), which allow the study of different characteristics of the sample. These differ in various aspects, such as the type of detected particles, characteristics of the lighting system (electron beam generation and guidance control), as well as the image construction.[136]

3.3.6.1. Scanning Electron Microscopy (SEM)

SEM consists of the use of a combination of electrostatic and magnetic lenses to manipulate a focused electron beam, with a controlled kinetic energy, to scan the sample. The intensity of emitted particles is then utilized to generate the SEM image by convoluting the spots on the sample that were hit by that beam.[137,138]

Figure 3.17 illustrates the key components of SEM equipment, which include an electron column, condenser lenses, and a detector.

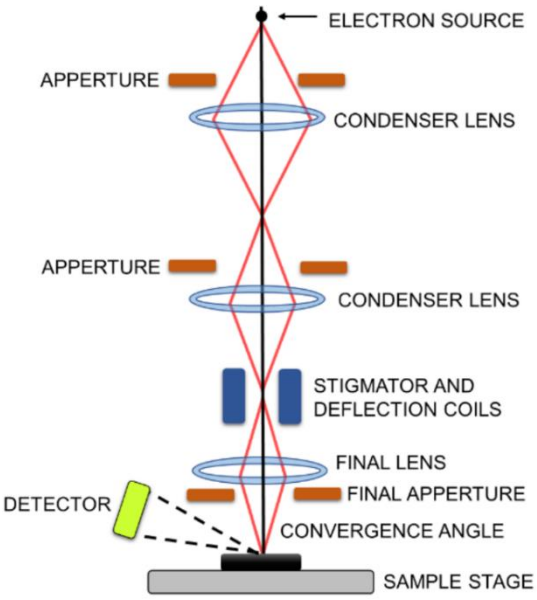

Figure 3.17 - Schematic diagram of the main components of a SEM equipment. Adapted from [139]. Used with permission of Elsevier Science & Technology Journals, from [139]; permission conveyed through Copyright Clearance Center, Inc.

Specifically, the electron column consists of an electron source, such as a W filament cathode, which emits an accelerated electron beam possessing energies ranging from 0.1 to 40 keV, under pressures of about 10^{-4} Pa.[140] The diameter of this electron beam is then decreased, i.e. the beam is focused, by a series of magnetic focusing lenses with defined apertures, to converge the electron beam onto the sample.[141] Inside the sample chamber there are usually two types of detectors, specifically secondary and

backscattered electron detectors.[142] To generate an image, the focused electron beam scans the sample surface in a raster pattern and detectors collect the emitted electrons at each impacted spot. Subsequently, the obtained data is processed and, afterwards, the SEM image is constructed by correlating the intensity of the detected signals to the position of the scanning beam, through point-to-point mapping.[140]

Upon hitting the sample, the focused electron beam interacts with its atoms, leading to the emission of various types of particles at distinct depths within the sample (see Figure 3.18).

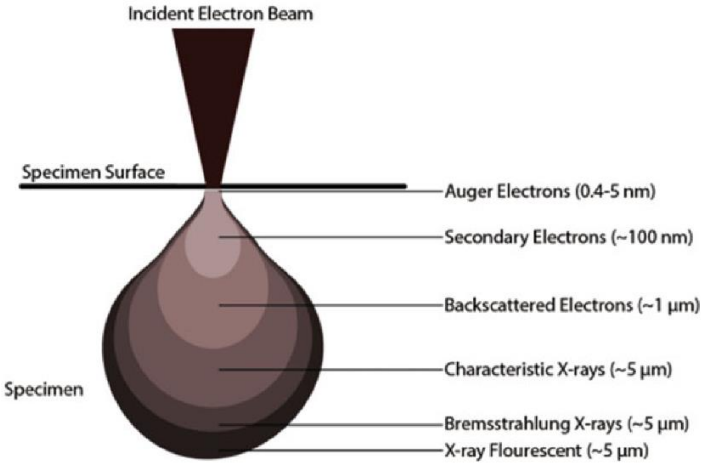

Figure 3.18 - Schematic diagram representing the different particles emitted during electron-sample interaction, at various depths in the sample. Adapted from [143], reproduced with permission from SNCSC.

The most commonly used ones for image formation are secondary and backscattered electrons.[139,140,144,145] Secondary electrons, which have low energy, i.e. < 50 eV, result from inelastic interactions of the primary electron beam with superficial atoms, which are weakly bound and located a few nm from the sample surface. The SEM images generated using these particles provide information about the topography of the sample.[139] On the other hand, backscattered electrons have higher energy, i.e. > 50 eV, and result from elastic interactions between the primary electron beam and atoms located deeper within the sample. These electrons can be used to generate an image with composition contrast, as the intensity of backscattered electron emission is related to the material's atomic number. Specifically, chemical elements with higher atomic numbers emit more backscattered electrons, making them appear brighter in the resulting image.[146,147]

In this work, the morphology of the fabricated NWs and NDs was analysed through SEM using a FEI Quanta 400 FEG ESEM/EDAX Genesis X4M instrument (FEI Company, Oregon, USA). For top-view, the produced samples were fixed on top of a SEM sample

holder using carbon tape. On the other hand, for cross-section view of the produced NW arrays, the templates prepared by mild or hard anodization were bent or broken in the middle, respectively, and then fixed over the edge of a SEM sample holder, also using carbon tape. Then, an image processing software, i.e. ImageJ, was used to analyse the structure of the fabricated arrays, such as diameter and length of the nanopores and NWs.

3.3.6.2. Energy-Dispersive X-Ray Spectroscopy (EDS)

EDS is a technique used to analyse the elemental composition of a sample through the collection and energy dispersion of X-rays, which are emitted when high-energy electrons bombard that sample.[148] Particularly, when an electron experiences an inelastic collision with an orbital electron located in the inner shell of a sample's atom, it can lead to the ejection of that bound electron, if its binding energy is lower than the energy of the incident electron.[149] This creates a vacancy in the atom's electron shell, leading to the ionization of that atom, which is an unstable state.[150] Consequently, an orbital electron present in an outer, higher-energy shell fills that vacancy, leading to the emission of a characteristic X-ray photon, whose energy (typically between 0-20 keV) corresponds precisely to the energy gap between the two energy levels associated with the electron transfer.[151] Therefore, since each element has a unique atomic structure, it is possible to characterize the composition of the sample by analysing the energy of the emitted characteristic X-rays.[152]

In this work, the EDS analysis was employed to assess the composition of the produced NWs and NDs, through the use of an EDS system (EDAX Genesis X4M unit, California, USA) integrated in the previously indicated SEM system.

3.3.6.3. Transmission Electron Microscopy (TEM)

TEM is an imaging technique that also involves the use of a focused electron beam. However, its main difference in comparison to TEM is that the images are generated by detecting the electrons that are transmitted through the sample, not the reflected ones.[153] Consequently, this method provides a detailed information about the interior of the sample, such as crystalline structure, morphology, and stress state.[154]

In this work, TEM (TEM Jeol JEM-1400; JEOL Ltd., Tokyo,Japan) was used to analyse the morphology of unloaded and DOX-loaded NLCs. For this purpose, the produced NLCs suspensions were diluted (1:10) in type 1 Milli-Q® Integral ultrapure water and, subsequently, 10 µL of that dilution was placed over a Cu-mesh grids. After 2 min, the surplus was eliminated and a 0.75% (w/v) uranyl acetate solution (10 µL) was added for

10 seconds to achieve negative staining. Then, the images were obtained using an acceleration voltage equal to 80 kV.

The ImageJ software was used to analyse the geometric characteristics and size distribution of the synthesized SPIONs and NLCs, based on the acquired TEM images.

3.3.7. X-Ray Diffraction (XRD)

X-ray diffraction (XRD) is a characterization method particularly suitable for studying the structural properties of a sample, also allowing the analysis of its composition.[155,156] This technique is based on the diffraction of X-rays on a crystal lattice, according to Bragg's law.[157,158]

Particularly, when X-rays impact matter they interact with the atomic electrons and, as a result, can be scattered.[159] Moreover, the wavelength of that type of electromagnetic radiation is on the order of 0.1 nm (1 Å), therefore it will be diffracted by objects of comparable size, such as atoms or molecules.[160] When the diffracting obstacle is a crystal, its crystal lattice implies that the molecular scattering centres are organized in a well-defined, three-dimensional, ordered array.[161] This means that there is a specific distance between any two molecules, leading to a precisely defined phase relationship between the electromagnetic waves diffracted from any pair of diffraction centers.[162,163] These diffracted waves interact constructively or destructively, providing information about the structure of the sample.[164]

Particularly, the crystal lattice can be divided into repeating units, known as unit cells that, in turn, can be divided into imaginary planes, commonly designated as crystal planes.[165] These planes are described by Miller indices, which are represented by a set of three integers (h k l) that describe a vector perpendicular to that plane, being separated by a fixed distance.[166,167] A schematic representation of X-rays being diffracted from a set of Miller planes with indices (h k) is presented in figure 3.19.

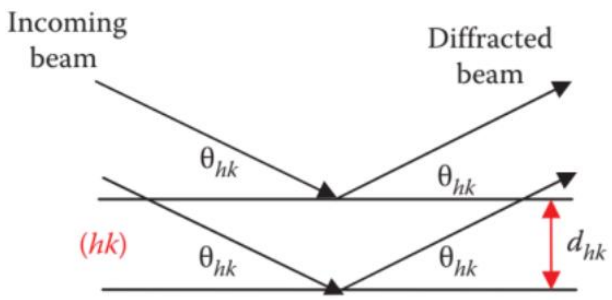

Figure 3.19 - Illustration representing the diffraction of X-rays by a set of crystal planes separated by a distance of d_{hk}. Used with permission of Taylor & Francis Group LLC - Books, from [168]; permission conveyed through Copyright Clearance Center, Inc.

Bragg's law appears in this context, stating that there is a constructive interference between the diffracted X-rays if the path difference between them is equal to an integral multiple (n) of wavelength (λ) associated with the incident X-ray, i.e.:[168,169]

$$n\lambda = 2d_{hk}\sin(\theta_{hk}) \quad (3.6)$$

Consequently, through this law it is possible to calculate the spacing between the crystal planes in a given sample.[170] Furthermore, since the parameters of each crystal plane are specific to each crystal systems, this technique not only allows the determination of those parameters, but also the crystal system of the sample (e.g. cubic, tetragonal, hexagonal, etc).[171]

When considering a complete diffraction spectrum, this law is applied to multiple crystal planes within the crystal lattice.[172] Specifically, each set of crystal planes with specific Miller indices (h k l) contributes to the diffraction pattern at characteristic angles.[173] Therefore, the complete diffraction spectrum is a result of the superposition of all these individual contributions, forming a pattern of constructive and destructive interference.[174]

To obtain such spectrum, the intensity of the diffracted X-rays at distinct angles has to be measured, which can be performed using different measurement geometries.[175] In this work, a Bragg-Brentano θ-2θ geometry was chosen, which consists of maintaining the X-rays' source fixed and rotating the sample by an angle of θ, as well as the detector by 2θ, so as to keep the mirrored geometry (figure 3.20).[176]

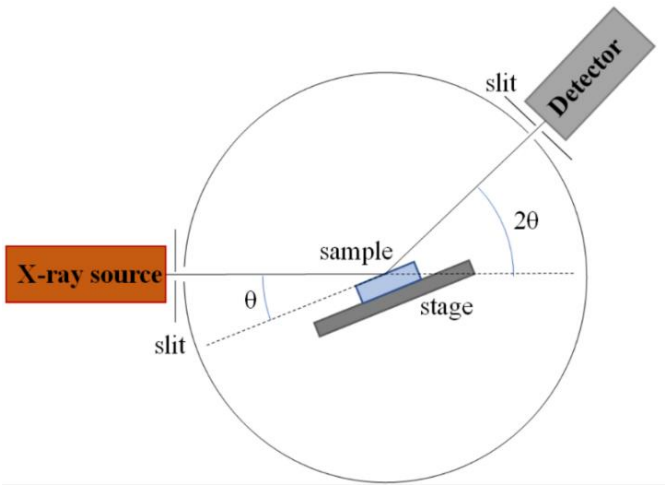

Figure 3.20 - Schematic illustration of an X-ray diffractometer in the Bragg-Brentano θ-2θ geometry. From [177]. https://livrepository.liverpool.ac.uk/3031053/

Such measuring strategy was chosen due to its high angular resolution, short measurement time (typically 10 – 60 min), and ease of sample preparation.[178,179]

In this work, the XRD measurements were performed using a Rigaku® SmartLab diffractometer (Rigaku Co., Tokyo, Japan), with a Cu Kα radiation (λ = 1.540593 Å) and an anode X-ray tube operated at 45 kV and 200 mA.

Moreover, the structural parameters, including crystallite size (D_{hkl}), were determined through peak broadening analysis, employing the Debye-Scherrer equation:[180]

$$D_{hkl} = k\frac{\lambda}{\beta\cos(\theta)} \quad (3.7)$$

where k is a shape factor known as the Scherrer constant (typically $k \sim 0.94$ for spherical grains), λ corresponds to the wavelength of the X-rays, β represents the full width at half maximum associated with diffraction peak, and θ denotes the Bragg diffraction angle.[180,181]

3.3.8. Raman Spectroscopy

Raman spectroscopy is a non-destructive optical technique based on the Raman effect, also known as Raman scattering, allowing the characterization of materials at a molecular level.[182,183] This effect was first described in 1928, by Sir Chandrasekhara Venkata Raman, and it can be defined as the inelastic scattering of photons by molecular bonds.[184-186]

Particularly, when photons strike matter, they can either be transmitted through the material without interacting or they may experience scattering processes where there is or not an energy exchange between the scatterer and the incident photon, corresponding to Raman or Rayleigh scattering, correspondingly.[187–190] Regarding the Raman scattering process, the energy of the scattered photons in comparison to the incident ones can be lower, i.e. there is an energy loss, also known as a red-shift (longer wavelength), or it can be higher, occurring an energy gain, which may also be designated as a blue shift (shorter wavelength), corresponding to a Stokes or anti-Stokes shift, respectively (figure 3.21).[191,192]

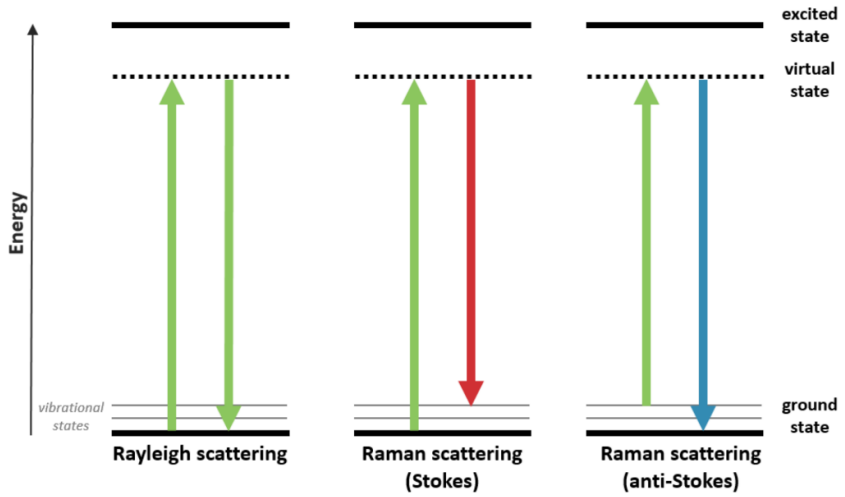

Figure 3.21 - Schematic diagram illustrating the energy transitions that occur in the Rayleigh and Raman scattering processes. Used with permission of The Royal Society (U.K.), from [193]; permission conveyed through Copyright Clearance Center, Inc.

When Raman scattering occurs, the probability of a Stokes shift is higher than that of an anti-Stokes shift, since the majority of the molecules in a sample are at the lower energy (fundamental) level.[194,195] Nevertheless, spontaneous Raman scattering is a very weak effect, being experienced by only 1 in 10^6 -10^{10} of the incident photons, which limits its practical application.[196,197] Consequently, to amplify the Raman signal, coherent Raman scattering techniques, such as coherent anti-Stokes Raman scattering (CARS) and stimulated Raman scattering (SRS), have been developed. These spectroscopic techniques rely on multiphoton scattering processes, utilizing at least two laser beams, i.e. pump beam and Stokes beam, that interact to excite molecular Raman modes.[198,199] Specifically, those two beams irradiate a sample simultaneously and, if the frequency difference between them matches the frequency of a vibrational mode of the molecules, the molecular transition rate to that vibrational state is promoted, as a result of stimulated excitation.[200,201] This effect can lead to a conversion of up to 50% of the incident photons into Raman scattered photons, originating signals that are several orders of magnitude stronger than those of spontaneous Raman scattering.[202,203]

The acquired Raman data is typically expressed in terms of wavenumber (cm^{-1}), which can converted into wavelength, λ, through the following expression:[204]

$$\text{wavenumber}\ (\text{cm}^{-1}) = \frac{10^7}{\lambda(\text{nm})} \tag{3.8}$$

Consequently, it is possible to calculate the Raman shift, $\triangle\omega$, by knowing the wavelengths of the excitation (or pump) laser, λ_1, and of the Raman signal, λ_2, in nm, through the use of the equation below:[205,206]

$$\triangle \omega = \frac{\lambda_1 - \lambda_2}{\lambda_1 \lambda_2} \quad (3.9)$$

In this work, Raman spectroscopy was used to analyse the functionalization of the fabricated Au/Fe/Au NDs. Since the signal of those nanostructures, when dispersed in water, was too low for such study, the NDs were functionalized on top of the Si templates and, subsequently, an InViaTM Qontor® confocal Raman spectrometer (Renishaw, Kingswood, UK) assembled with a Leica DM2700 microscope (Ernst Leitz GmbH, Wetzlar, Germany) and a 50X objective, available at IFIMUP, was used to acquire their Raman spectra. The samples were mounted on an automatized stage with a lateral resolution of 100 nm. For excitation, a He-Ne laser with a wavelength of 633 nm was used at a power of 1.1 mW, considering a spot size between 1 and 2 µm. Additionally, a diffraction grating with a resolution of 1800 lines/mm with high spectral resolution, < 2 cm^{-1}, in all the spectral range was used to collect the data. To improve the signal/noise ratio, the acquisition was performed during 12 h for each sample in the spectral range from 1500 to 3000 cm^{-1}, using the software WiRETM 5.2. (Renishaw Inc., Wotton-under-Edge, UK), since, after searching through the literature, it was concluded that it was the most adequate range for assessing the presence of the PEG molecules on top of the NDs.[207-209]

3.3.9. X-Ray Photoelectron Spectroscopy (XPS)

X-ray photoelectron spectroscopy (XPS) is a technique used for studying a material's surface chemistry, allowing the determination of not only its elemental composition, but also the chemical and electronic state of its atoms, and providing information about the thickness of the overlayer from the top ~ 10 nm of a given sample's surface.[210–212] This characterization method is based on the photoelectric effect, which occurs when a material is irradiated by high-energy photons, typically in the keV range, resulting in the emission of electrons that are known as photoelectrons.[212,213] Furthermore, it is a very surface-sensitive technique, because the photo-emitted electrons can scatter, be absorbed, or interact through other means with the bulk material, consequently, only electrons close to the sample's surface will be capable of escaping without losing energy.[214-216]

In XPS, core electrons are the ones primarily probed (figure 3.22), since their binding energies not only are highly specific to each individual element but can also vary based on the chemical and electronic state of the atoms. Moreover, XPS has a reduced sensitivity at the valence band, due to the reduced photoionization cross-sections at the energies considered for the incident photons, resulting in low peak intensities.

Additionally, valence electrons may be influenced by a broader range of factors, as they are often involved in bonding and may be affected by interactions with neighbouring atoms, possibly leading to peaks in the XPS spectra that are not as sharp and distinctive as those of core electrons, which translates into a lower resolution.[217–220]

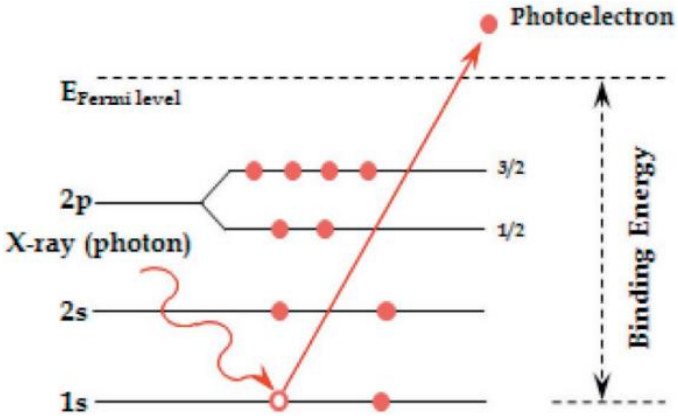

Figure 3.22 - Diagram representing the photoelectric effect. Used with permission of Elsevier Science & Technology Journals, from [212]; permission conveyed through Copyright Clearance Center, Inc.

When an incident photon interacts with a core electron and leads to its emission, the principle of conservation of energy implies that the energy of the incident photon ($h\upsilon$), the initial binding energy of the photoelectron (E_B), and its final kinetic energy (E_K) are related by the following equation:[221,222]

$$E_B = h\upsilon - E_K - \Phi \quad (3.10)$$

where Φ represents the work function of the spectrometer, being a tunable instrumental correction factor that accounts for the few eV (~ 5 eV) of kinetic energy lost by the photoelectron when it is absorbed by the instrument's detector.[223] The XPS spectrum is, therefore, a plot of the number of detected photoelectrons as a function of their binding energy, which is calculated from the measured kinetic energy of ejected photoelectrons.[221,224] Such graph is dominated by a number of sharp emission peaks, each labelled with the core states of the surface atoms from which they originate, allowing, as a result, the identification of specific elemental species in the sample's surface, as each element possesses a distinctive set of binding energies.[225-227] Furthermore, as the quantity of photoelectrons is directly linked to the concentration of the element, once the background resulting from the inelastic scattering of electrons, i.e. the secondary electron background, is eliminated, the areas of the peaks can also be utilized, together with sensitivity factors derived through empirical means, to quantify a particular elemental species in the sample's surface.[212,215,228]

In this work, XPS was used to study the functionalization of surface of the fabricated Au/Fe/Au NDs. This technique was performed at UAM using a SPECS GmbH spectrometer, equipped with a UHV system, possessing a base pressure of 10^{-10} mbar and a hemispherical electron energy analyser (PHOIBOS 150 9 MCD), and using a nonmonochromatic Mg X-ray source at 200 W and 12 kV. The XPS spectra were acquired at normal emission, setting the pass-energy at 50 eV, with an energy step of 1 eV, for the survey scan and using a pass energy of 20 eV, together with an energy step of 0.1 eV, for the narrow scans of Au4f, S2p, C1s, and O1s. This technique was used to study the functionalization of surface of the fabricated Au/Fe/Au NDs.

3.3.10. Magnetometry

The magnetic properties of the fabricated nanomaterials were analysed using different techniques. In this section, those measurement methods will be described in detail.

3.3.10.1. Superconducting Quantum Interference Device (SQUID)

A superconducting quantum interference device (SQUID) is a highly sensitive magnetometer based on superconducting loops, capable of measuring magnetic fields of the order of 10^{-13} Wb/m^2.[229] This device is based on a superconducting loop containing Josephson junctions that is cooled by a cryogenic refrigeration system, so as to maintain superconductivity.[230] Currently, there are two types of SQUID, namely the radiofrequency (RF) SQUID and the DC SQUID, the difference being that the first operates with one Josephson junction, while the latter works with two or more.[231,232] A Josephson junction is made by placing a thin layer of a non-superconducting material between two layers of a superconducting material, allowing the occurrence of the quantum tunnelling effect.[233] These junctions typically exhibit a significantly lower critical current, i.e. the maximum current that can flow before resistance starts to appear, compared to the two superconducting regions that they connect.[234-235]

As the name suggests, in a DC SQUID a bias DC current (typically $\sim$ twice the critical current of a Josephson junction) is applied to the superconducting loop containing the two Josephson junctions and, in the absence of an external magnetic field, that current is equally split between them, converging at the other side of the loop.[235,236] However, when a magnetic flux is applied through the loop and according to the law of Faraday-Lenz, a screening current is induced in it, which generates a magnetic field that opposes the change in the magnetic flux through the loop.[237] As a result, since the bias current flows in a clockwise direction through one junction and in a counterclockwise direction through the other, the currents flowing through each branch become different, as this

screening current is added to the already existing current in one branch and subtracted from the current present in the opposite one.[235,238]

When the Josephson junction is in a superconducting state, it allows the quantum mechanical tunnelling of Cooper pairs of electrons through it without any voltage drop, if the current that flows through the junction is lower than the critical current value.[238] However, when the current passing through the Josephson junction reaches a greater value than that of the critical current, it transitions into a resistive state, resulting in the appearance of voltage across the junction.[238-240]

This is the working principle of the SQUID sensor that, in a SQUID device, is connected to a set of superconducting pickup coils through which the sample is moved (figure 3.23). Such dislocation leads to the appearance of a voltage function with a characteristic shape, presenting an amplitude that is proportional to the magnetic moment of the sample.[241,242] This voltage signal is then transmitted to the SQUID sensor, interrupting that superconducting loop. Subsequently, the superconducting state is re-established by applying an adequate biasing current, allowing the determination of the magnetic moment of the sample.[241,243]

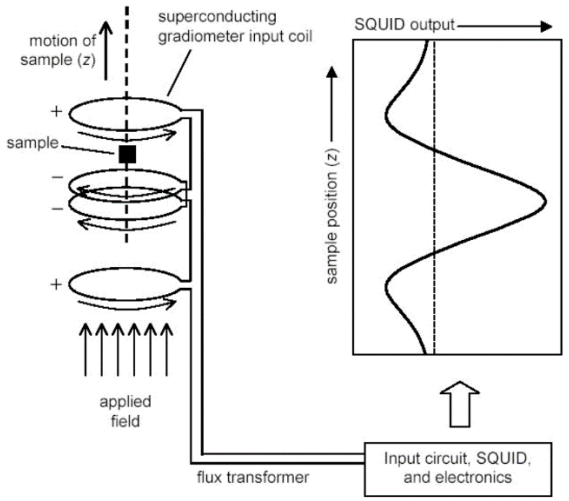

Figure 3.23 - Schematic representation of a SQUID. Used with permission of John Wiley & Sons - Books, from [244]; permission conveyed through Copyright Clearance Center, Inc.

The SQUID measurements performed in this work were carried out using a Quantum Design/EverCool SQUID, MPMS EverCool (Quantum Design Inc., San Diego, CA, USA) magnetometer, available at IFIMUP, using a He bath as the cryogenic refrigeration system. This equipment has a resolution of 10^{-7} emu and is equipped with a 5.5 T superconducting coil, allowing precise magnetization measurements in a temperature range between 5 and 380 k.[245] The magnetic hysteresis loops (M(H)) of the synthesized

samples were obtained at room temperature, considering the external magnetic field (H) applied along the parallel ($H_{\parallel}$) and perpendicular ($H_{\perp}$) directions in relation to the nanostructures' long axis. Additionally, the M(H) curves of SPIONs and NLCs, in powder form, were also acquired through this technique.

Additionally, the M(H) curves of SPIONs and NLCs, in powder form, were also acquired through this technique. Regarding the first, the powder was weighted and then M(H) curves at different temperatures, i.e. 5, 150, and 320 K, were obtained by sweeping the H field between a maximum and a minimum value of ± 50 kOe. Furthermore, in order to further confirm the existence of a superparamagnetic behaviour, the Langevin function was fitted to the hysteresis loop obtained at 320 K.[246] This equation assumes the existence of an ensemble of non-interacting, uniform, magnetic monodomain particles, each possessing the same magnetic moment, μ, being described as:[247–251]

$$\frac{\mathrm{M}}{\mathrm{M_{Sat}}} = \coth\left(\frac{\mu \mathrm{H}}{\mathrm{k_b T}}\right) - \left(\frac{\mathrm{k_b T}}{\mu \mathrm{H}}\right) = \mathrm{L}\left(\frac{\mathrm{k_b T}}{\mu \mathrm{H}}\right) \tag{3.11}$$

where $\mathrm{M_{Sat}}$ represents the saturation magnetization, M is the magnetization of the sample, $\mathrm{k_b}$ corresponds to the Boltzmann constant, T is the measurement temperature, and $\mathrm{L}\left(\frac{\mathrm{k_b T}}{\mu \mathrm{H}}\right)$ represents the Langevin function.

Furthermore, zero-field cooled (ZFC) and field cooled (FC) curves were obtained for these SPIONs, so as to determine their blocking temperature (T_B), i.e. the temperature below which, on the time scale considered for the magnetometry measurements, the net magnetic moments do not fluctuate.[252] In this work, ZFC curves were acquired by first progressively cooling the sample to the desired temperature (5 K) in the absence of an external magnetic field, H. Once the sample reached such temperature and equilibrium was achieved, an H field of 50 Oe was applied. Then, the ZFC curve was obtained by measuring the sample's magnetization while simultaneously increasing the temperature. On the other hand, the FC curves were acquired by performing a similar procedure, but, in this case, the sample was cooled down to 5 K in the presence of an H field of 50 Oe.

Regarding NLCs, a similar measurement procedure was performed, with the exception that the M(H) curves were only measured at 320 K, since, in this work, it is the most relevant temperature for the desired biomedical application of those NPs.

3.3.10.2. Vibrating-Sample Magnetometer (VSM)

A vibrating-sample magnetometer (VSM) is another instrument that allows the measurement of the magnetic properties of materials, with a sensitivity of $\sim 10^{-5}$

emu.[253,254] This device is based on Faraday's law, which states that an electric field appears along a path enclosing a changing magnetic flux.[255] Particularly, in a VSM the sample to measure is first magnetized under an uniform magnetic field and, subsequently, it is sinusoidally vibrated, typically through the utilization of a piezoelectric material, at a known frequency (generally ranging between 50 and 100 Hz) and at a constant amplitude (usually within the range of 1 to 3 mm).[256–259] By placing the vibrating sample between a set of pick-up coils, it is induced an electromotive force in those coils due the changing the magnetic flux, which is proportional to the magnetic moment of the sample.[260,261] A schematic representation of a VSM is presented in figure 3.24.

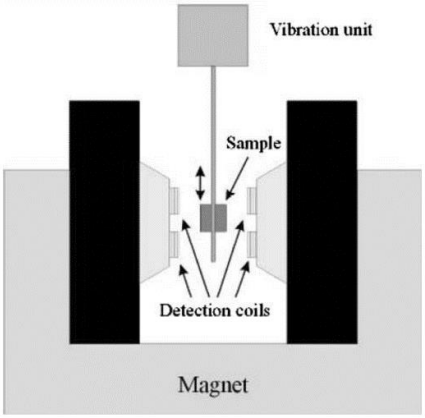

Figure 3.24 - Schematic representation of a VSM. From [262]. Reproduced with permission from Springer Nature.

In this work, the VSM measurements were performed using a LakeShore Controller Model 7304 (Lake Shore Cryotronics Inc., Westerville, OH, USA) located at ISOM-UPM. Similarly to the SQUID measurements, the M(H) curves of the produced samples were acquired at room temperature, considering the H field applied along the parallel ($H_{\parallel}$) and perpendicular ($H_{\perp}$) directions in relation to the nanostructures' long axis.

3.3.10.3. SQUID-VSM

The main disadvantage of SQUID in comparison to VSM is its reduced measurement speed (~ 1 min per point), possessing, however, a higher sensitivity.[263] As a result, in order to try getting the "best of both worlds", the SQUID-VSM was developed, which is an instrument that combines the sensitivity of the SQUID with the data acquisition speed associated with the VSM.[264] Similarly to the SQUID, the detection system in this type of device is based a superconducting loop containing Josephson junctions that is connected to an identical detection coil geometry (figure 3.25).[265]

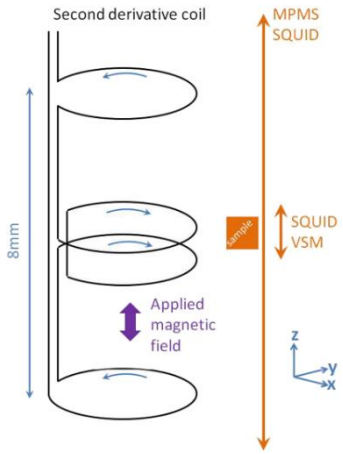

Figure 3.25 - Diagram depicting the pickup coil configuration employed in both the SQUID and SQUID VSM systems, with current direction indicated by the arrows. The vertical (z-axis) centre of the sample is denoted by the orange box. Vertical arrows provide an approximation of the sample's travel length and direction during a measurement. Adapted from [265]. Copyright 2016 Authors licensed under a Creative Commons Attribution (CC BY-NC-ND 4.0 DEED) license..

However, the measurement process in the SQUID-VSM is different from the one used in a SQUID, as in the latter instrument the changing magnetic field is generated by stepping the sample through the detection coils, while in a SQUID-VSM the sample is vibrated at a fixed frequency and the recorded voltage amplitude is averaged over a specified period.[264,266] This leads to much faster acquisition rates, typically ~ 1 s per point, in comparison to the SQUID.[267]

The SQUID-VSM measurements carried out in this work were performed using a Quantum Design MPMS®3 SQUID Magnetometer (Quantum Design Inc., San Diego, CA, USA) available at IFIMUP. This equipment has a sensitivity of ~ 10^{-8} emu, being equipment with a 7 T superconducting magnet and a SQUID detector that are cooled using a cryogenic bath (liquid He). Additionally, measurements can be performed at temperatures ranging from 2K to 380K, by using liquid He to cool the sample chamber. Nevertheless, similarly to the previous magnetometry techniques, the magnetic properties of the fabricated nanomaterials were measured at room temperature, by applying the H field along the parallel ($H_{\parallel}$) and perpendicular ($H_{\perp}$) directions in relation to the nanostructures' long axis.

3.3.10.4. Magneto-Optical Kerr Effect (MOKE)

The magneto-optical Kerr effect (MOKE) is a phenomenon that consists of the rotation of the polarization plane of linearly polarized light, when it is reflected from a magnetic material.[268] The angle of this rotation is designated as Kerr rotation, being proportional to the magnetization of the sample's surface.[269–272]

According to the orientation of the sample's magnetization vector in relation to the reflecting surface and plane of incidence, the MOKE can be categorized into three geometries, which are represented in figure 3.26.[273,274]

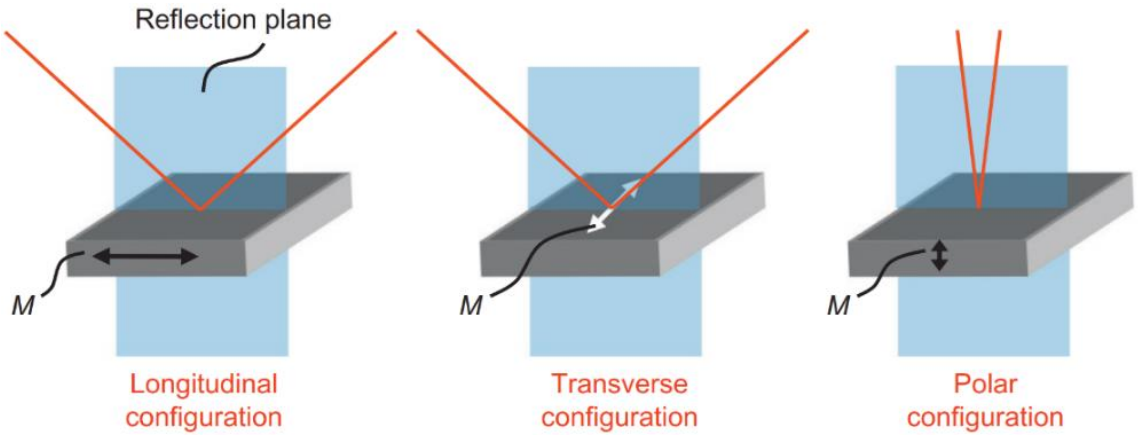

Figure 3.26 - The different MOKE geometries. Reprinted from [273], Copyright (2015), with permission from Elsevier.

As can be observed in the figure above, in the longitudinal configuration the magnetization vector is aligned parallel to the reflection surface and the plane of incidence. On the other hand, in the transverse geometry, the magnetization vector is perpendicular to the plane of incidence and parallel to the reflection surface. Finally, when the magnetization vector is perpendicular to the reflection surface, the configuration is designated as polar.[273,275]

In this work, the MOKE measurements were performed in the longitudinal configuration. This geometry leads to the appearance of an extra polarization component that is perpendicular to the polarization of the incident light, which alters the ellipticity and originates a rotation of the polarization plane. The extent of such rotation is proportional to the sample's magnetization component parallel to the plane of incidence.

In this particular arrangement, an extra polarization component perpendicular to the incoming polarization emerges in the reflected beam. This results in alterations to the ellipticity and a rotation of the polarization plane, with the extent of rotation being directly proportional to the in-plane magnetization component aligned with the plane of incidence.[276,277]

A schematic representation of a MOKE magnetometer in the longitudinal configuration is depicted in figure 3.27.

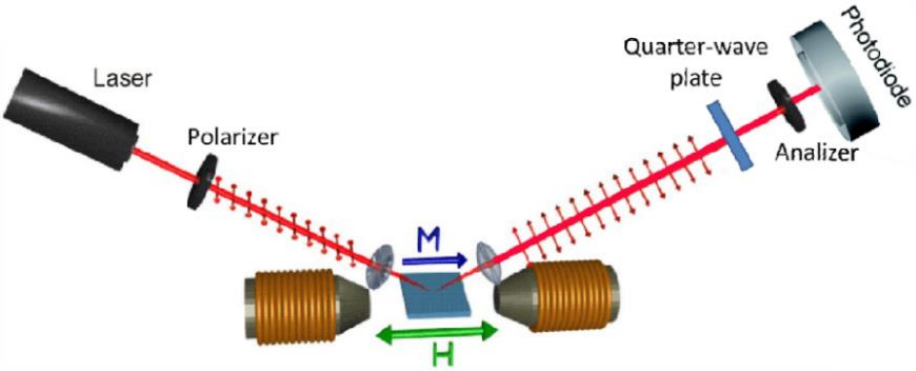

Figure 3.27 - Schematic representation of a MOKE magnetometer with a longitudinal geometry. From [47]. Copyright 2018 Author licensed under a Creative Commons Attribution (CC BY-NC-ND 4.0 DEED) license.

As can be observed in the previous figure, a polarized beam emitted from a laser source is directed and focused onto the surface of a sample, which, in turn, is exposed to an external magnetic field that is aligned parallel to the plane of incidence, being generated by an electromagnet. After hitting the sample's surface, the reflected beam passes through a quarter-wave plate, which eliminates the ellipticity of the signal, but not its rotation. This modified signal is then filtered by an analyser and ultimately captured by a photodiode.[47,278,279]

The MOKE measurements performed in this work were carried out using a NanoMOKE2 (LOTOriel Group Europe, Darmstadt, Germany). This system allows mounting the sample to measure on a movable stage, enabling the laser spot to move over the sample and, therefore, perform a magnetic characterization at the desired location. Additionally, the laser spot possesses a dimension of ~ 3 μm, allowing the acquisition of hysteresis loops from very localized areas of the sample. This technique was used to measure the magnetic hysteresis loops of the fabricated Au/Fe/Au NDs, on top of the interference lithography templates.

3.3.10.5. Magnetic Force Microscopy (MFM)

Magnetic force microscopy (MFM) is a flexible technique used for mapping the stray field, and/or its gradient, originating from a sample's surface, with a high spatial resolution and sensitivity.[280] This method is based on the magnetic interaction between a sample and a nanometric magnetic probe, which is located at the free end of a cantilever probe and raster-scanned in close proximity (~ 30 nm) to its surface.[279,281] Such interaction leads to a deflection of the cantilever that is typically measured by optical means, i.e. using a laser probe (figure 3.28). Generally, the forces measured with this technique are in the order of 30 pN, involving cantilever deflections in the order of nm. This technique typically allows scanning areas between 1 and 200 μm, with imaging times from 5 to 30 min.[282,283]

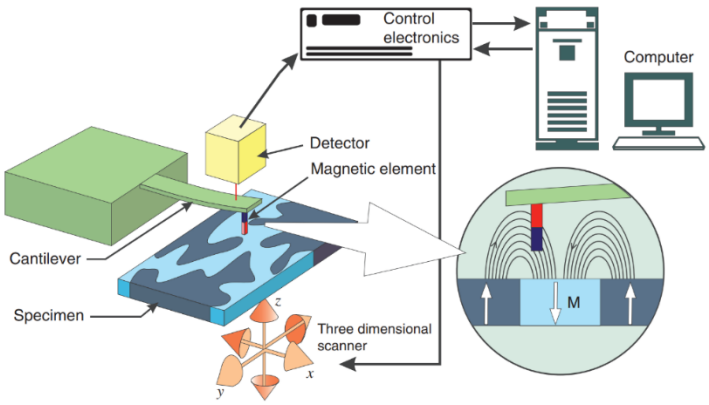

Figure 3.28 - MFM principle. Used with permission of Elsevier Science & Technology Journals, from [282]; permission conveyed through Copyright Clearance Center, Inc.

Generally, a magnetic force microscope has two modes of operation, namely the static (DC) mode, where the stray field from the sample exerts a force on the magnetic tip, leading to the formation of a force image, and the dynamic (alternating current; AC) mode, where the cantilever is set to vibrate close to its resonant frequency and modifications of the phase or frequency of that oscillation, as a result of magnetostatic force gradients, allows the formation of a force gradient image.[279,283,284]

In this work, MFM measurements were carried out on the produced Au/Fe/Au NDs still on top of the interference lithography template, at ambient conditions using a custom modified system from Nanotec Electrónica S.L. (Madrid, Spain).[285] The data analysis was performed with WSxM software (Nanotec, Electronica, S.L., Madrid, Spain).[286]

The standard two-pass Amplitude Modulation (AM) mode of operation has been used to measure magnetic interaction: in the first scan, the topography is mapped whereas in the second pass, the probe lifts a typical distance of 40 nm away from the sample and maps the long-range interactions, via the phase change of the oscillating cantilever. The oscillation amplitude is ~ 20 nm. The positive MFM contrast corresponds to a repulsive interaction, while the negative signal is due to an attractive interaction. Commercial probes from Budget Sensors (Sofia, Bulgaria) MagneticMulti75- G, with CoCr coating were used.

3.3.11. Specific Heat Absorption Rate (SAR) Measurements

In order to assess the heating efficiency of SPIONs and NLCs, they were exposed for 5 min to an AMF, produced by a generator, with a frequency equal to 556 kHz and a peak intensity of 10 mT. These magnetic field values are within the safety limits established by the Hergt and Dutz criterion, i.e. $H \cdot f \leq 5 \cdot 10^9$ A/ms, regarding the clinical application of AMF.[287]

Regarding SPIONs, they were first dispersed in double-deionized water at a concentration of [Fe] = 4 mg/mL. Subsequently, 150 µL of this dispersion was transferred to an Eppendorf (Hamburg, Germany) tube, which was then placed inside the magnetic coils. The temperature in the Eppendorf (Hamburg, Germany) was continuously monitored and record at 1 s intervals, using a thermal infrared camera positioned at the end of the coil cavity (figure 3.29). This methodology was repeated for each considered frequency. Moreover, a similar process was used for the NLCs, with the exception that the formulation was not diluted.

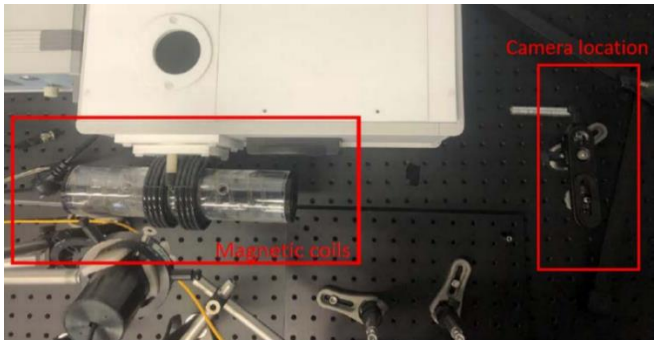

Figure 3.29 - Photograph of the MHT equipment used in this work.

Then, the heating efficiency of these NPs was evaluated through SAR, which was calculated by the Box-Lucas method (section 1.3.1.). Additionally, to ensure a precise in SAR calculation, the initial 5 seconds were excluded from the fitting timeframe, since they correspond to an initial non-linear heating response that leads to a reduction in the exponential factor in the Box-Lucas fitting, possibly leading to inaccurate SAR values.[288–290]

3.4. Micromagnetic Simulations

In order to gain a better understanding of the magnetization behaviour in the fabricated nanostructures, micromagnetic simulations involving the produced nanoarchitectures were carried out and compared with the experimental results.

Particularly, magnetic hysteresis loops of FePt NW arrays were simulated using the object oriented micro-magnetic framework (OOMMF) project.[291] This is a public domain micromagnetic software developed at the National Institute of Standards and Technology (NIST) that operates on the central processing unit (CPU) of the computer.[292,293] OOMMF is designed to possess portability and extensibility, featuring a user-friendly graphical interface. The code is written in both C++ and Tcl/Tk, employing the LLG (Landau-Lifshitz-Gilbert) equation to simulate the magnetization dynamics.[294–296] Additionally, this software uses the finite difference method, which involves discretizing space through a

regular grid comprised of cuboidal cells. Within each of these cells, the magnetization, along with other scalar and vector fields involved in the computation, are assumed to remain constant.[297,298]

In this work, OOMMF was used to study hexagonal arrays of 7 NWs with diameters of 36 nm, centre-to-centre distances of 105 nm, and lengths of 150 nm, using a cubic mesh with a unit cell size of $3 \cdot 3 \cdot 3$ nm^3. The saturation magnetization (M_{Sat}) and stiffness constant (A) values were tuned depending on the Fe atomic percentage (at.%) of the FePt NWs studied. Particularly, for NWs with a Fe at.% of 100 %, $M_{Sat} = 1700 \cdot 10^3$ A/m and $A = 21 \cdot 10^{-12}$ J/m (according to the bulk values provided by OOMMF). On the other hand, for a Fe at.% of x, $M_{Sat} = x \cdot 1700 \cdot 10^3$ A/m and $A = x \cdot 21 \cdot 10^{-12}$ J/m. In all cases, a stopping condition of $\left|\frac{dm}{dt}\right| = 1$ deg/ns and a damping factor of 0.015 were considered.

On the other hand, hysteresis loops of individual and arrays of Au/Fe/Au NDs were simulated using the Mumax^3 software. This is an open source, graphics processing unit (GPU)-accelerated micromagnetic simulation program that can simulate both magnetostatic and dynamic systems in time and space, through the use of a finite-difference discretization.[299,300] The simulations are configured by scripts written on a language based on the Go programming language, instead of a graphical user interface, allowing for more flexibility.[301] Furthermore, it provides a web-based HTML 5 user interface, which enables the inspection and control of the simulations from within a web browser, whether they are being executed locally or remotely.[302]

The simulation process begins by initializing a random magnetic state in the specified geometry and capturing a snapshot of it.[303] Then, the energy is minimized leading to the establishment of the fundamental state, which is also recorded.[304] Following this, the nanostructures are exposed to a magnetic field loop, which induces positive and negative saturation, with the corresponding data being recorded in a table. At each step, a solver based on the Runge-Kutta iterative method is employed to advance the LLG equation.[300,303,305] In this work, the selected algorithm for advancing such equation was the RK45, also known as the Dormand-Prince method, which provides a 5th order convergence as well as a 4th order error estimate, being employed for adaptive time-step control.[300]

The shape and dimensions of the simulated Au/Fe/Au NDs were defined based on an ideal geometry, i.e. perfectly circular, as well as on the acquired SEM images of those nanostructures. In the performed simulations, the material parameters for Fe were chosen in agreement with literature values: $M_{Sat} = 1700 \cdot 10^3$ emu/cm^3, exchange

constant $A = 2.1 \cdot 10^{-11}$ erg/cm and magnetocrystalline anisotropy constant $K_1 = 4.8 \cdot 10^4$ erg/cm^3.[306,307] The XRD analysis of the deposited Fe thin film was used to establish the orientation of the magnetocrystalline axis. Cell size was set to $5 \cdot 5 \cdot 5$ nm^3, which is smaller than Fe exchange length $l_{ex} = \sqrt{\frac{2A}{\mu_0 M_{Sat}^2}} \approx 8.5$ nm and the Gilbert damping parameter, which determines how fast the magnetization relaxes toward the effective magnetic field, was defined as 0.5, so as to guarantee a fast convergence.[308]

Such dimensionless parameter was introduced phenomenologically in the LLG equation and it contains contributions from a variety of processes involved in the dissipation of energy to the non-magnetic degrees of freedom and they are distinguished between intrinsic (usually attributed to the spin-orbit coupling between the spins of electrons and the lattice) and extrinsic contributions (such as the two-magnon scattering and the spin-pumping contributions).[309] This parameter plays a central role in controlling many aspects of the magnetization dynamics, such as the required current for the spin-torque magnetic switching, mobility of magnetic domain walls, or mobility of spin waves.[310-312]

However, the performed micromagnetic simulations of the hysteresis loops are quasi-static simulations. This type of micromagnetic simulations usually use large damping constants, like 0.5 or 1, to ensure that the magnetization reaches a well converged state within a reasonable amount of time and without affecting the final results.[313] Therefore, and although the real magnetic damping constant of Fe should be around 0.01, a larger damping constant, such as 0.5, is a value typically used in this kind of simulations and without affecting the reliability of the final results.

Nevertheless, the real damping parameter is required in case we want to simulate dynamic processes such as studying ferromagnetic resonance, mobility of magnetic domain walls,

3.5. Cellular Studies

The suitability of the fabricated nanomaterials for biomedical applications, in particular for novel cancer therapy strategies, was assessed through *in vitro* studies. These aimed at analysing the nanomaterials' biocompatibility, uptake, as well as their potential for inducing cancer cell death. Therefore, in the following sections the cellular assays carried out in this work will be addressed in detail.

3.5.1 Cell Culture

A human monocytic cell line derived from an acute monocytic leukaemia patient, i.e. THP-1, was cultured in RPMI 1640 medium, supplemented with 10 % FBS (v/v) and 1

% penicillin/streptomycin (v/v), having been maintained at 37 °C in a 5 % CO_2 atmosphere (Unitherm CO_2 Incubator 3503, Uniequip, Planegg, Germany). When the cell culture reached a confluence between 70 % and 80 %, the cells were centrifuged with a Heraeus Multifuge X1R centrifuge (Thermo Fisher Scientific; Waltham, MA, USA) at a speed of 300 x*g* for 5 min and re-suspended in fresh medium.

A human breast cancer cell line derived from a malignant pleural effusion, i.e. MCF-7, was also used in this work, having been cultured in DMEM supplemented with 10 % (v/v) FBS and 1 % (v/v) PenStrep. These cells were also maintained at 37 °C in a 5 % CO_2 atmosphere (Unitherm CO_2 Incubator 3503, Uniequip, Planegg, Germany). When the cell culture reached a confluence between 70 % and 80 %, they were washed with 10 mL of PBS, detached using 3 µL of trypsin-EDTA 0.25% (w/v), and then centrifuged with a Heraeus Multifuge X1R centrifuge (Thermo Fisher Scientific; Waltham, MA, USA) at a speed of 300 xg for 5 min. Subsequently, the cells were re-suspended in fresh medium.

3.5.2. Biocompatibility Assays

The biocompatibility of the produced nanomaterials was evaluated in the two considered cell lines, using the resazurin assay, also known as Alamar Blue® assay. Resazurin is a blue, nonfluorescent dye that, in the presence of metabolically active cells, enters the cytosol and is reduced to a pink and highly fluorescent compound known as resorufin, which is freely released from the cells through a process mediated by intracellular diaphorase enzymes.[314–317] Resorufin can then be detected through fluorescence (excitation λ range = 530-570 nm; emission λ range = 590-620 nm) or absorbance (maximum absorbance λ: 573 nm) measurements (figure 3.30), allowing the estimation of the cells' metabolic activity, which is an indicator of their viability.[318–324]

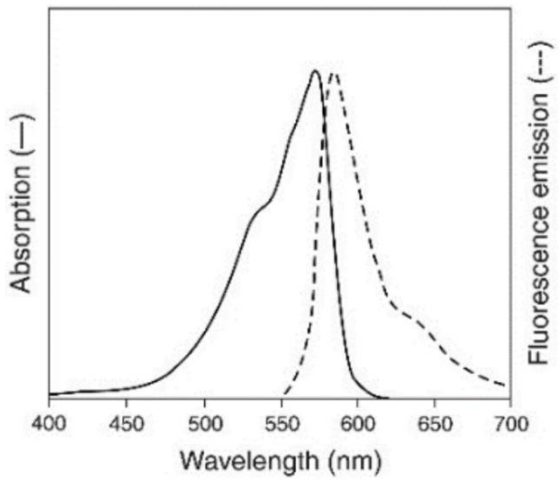

Figure 3.30 - Absorbance and emission spectra of resorufin. From [320]. Copyright 2016 Author licensed under a Creative Commons Attribution (CC BY-NC-ND 4.0 DEED) license.

For each biocompatibility assay performed in this work, either THP-1 or MCF-7 cells were plated in a 96-well microplate (96 wells, surface treated, sterile, VWR Tissue Culture Plate, VWR, Radnor, Pensylvania, USA) at a density of 50.000 cells/well in 50 µL of supplemented RPMI 1640 or DMEM, respectively, and then incubated for 3 h at 37 ºC in a 5% CO_2 atmosphere (Unitherm CO_2 Incubator 3503, Uniequip, Planegg, Germany). The cell counting was performed using a Neubauer chamber (Improved Neubauer Bright-line, Boeco; Hamburg, Germany). Subsequently, different concentrations of nanomaterials, i.e. NLCs, NWs, or NDs, diluted in 50 µL of the same used medium were added to those cells, except to the positive control, which consisted of cells only in supplemented medium (figure 3.31). In every assay, each considered nanomaterials' concentration was repeated 4 times.

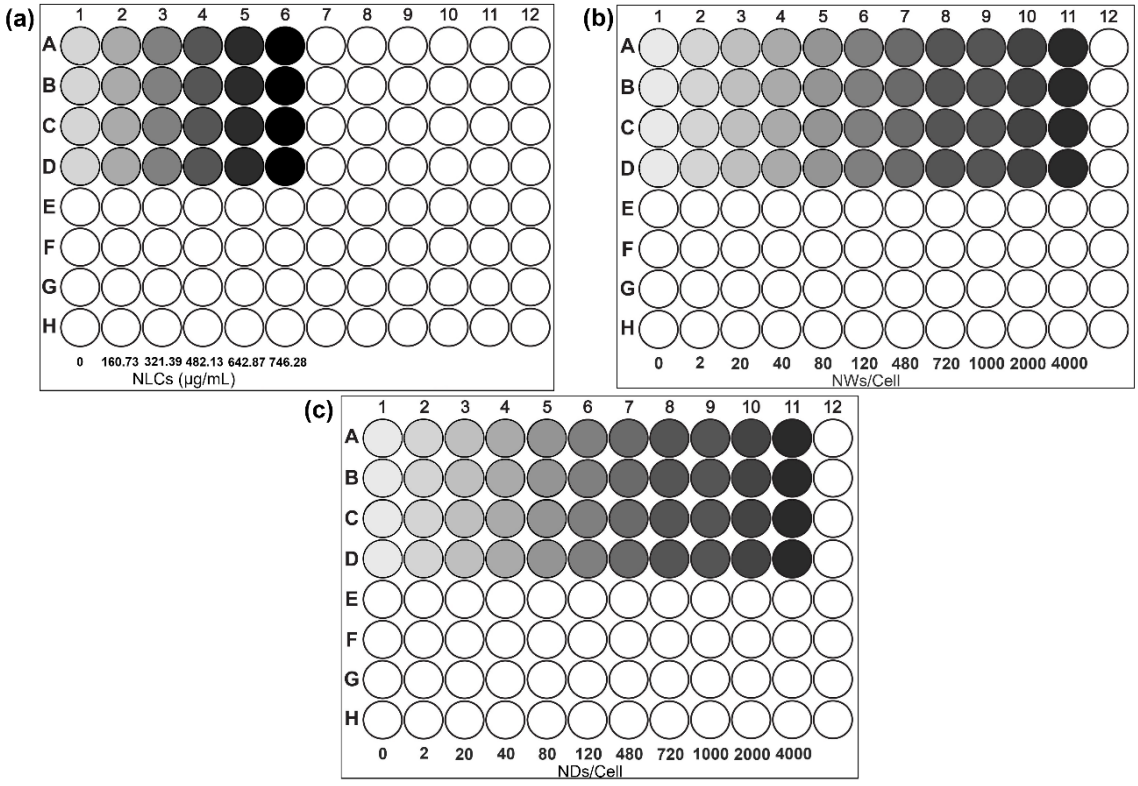

Figure 3.31 - Schemes of the 96-well microplates used in the cell biocompatibility assays considering (a) formulations of NLC, $NLC_{(DOX)}$, $NLC_{(SPIONs)}$, as well as $NLC_{(DOX\text{-}SPIONs)}$ (concentration represents the quantity of solid lipid per µL), (b) FePt NWs, and (c) nonfunctionalized, PEG-thiol (MW = 2000 and 6000) functionalized, and FA-PEG-SH functionalized Au/Fe/Au NDs.

Afterwards, it was performed a 19-h incubation at 37 °C in a 5 % CO_2 atmosphere (Unitherm CO_2 Incubator 3503, Uniequip, Planegg, Germany). Then, the cells were incubated for 3 h with resazurin (0.01 mg/mL per well) (Unitherm CO_2 Incubator 3503, Uniequip, Planegg, Germany). Subsequently, the supernatant was transferred to a 96-well black microplate with a clear bottom (Falcon, Corning Incorporated, Corning, NY,

USA) and the fluorescence intensity in that supernatant was read at a wavelength of 590 nm, after excitation at a wavelength equal to 560 nm, in a microplate reader (BioTek Instruments Inc., Winooski, VT, USA).

This assay was repeated 3 times, under the same conditions, for every type of nanomaterial considered (n = 3). The biocompatibility for each concentration tested was then evaluated by calculating the arithmetic mean of the cell viability from the 3 independent repetitions.

3.5.3. Uptake Assays

The uptake of the synthesized nanomaterials by the two cell lines used in this study was also assessed, since it represents an important aspect for their application in the biomedical context. This factor was evaluated through flow cytometry, which is a technique used to separate, quantify, examine, and categorize cells as they flow in a fluid stream one by one through a sensing point, i.e. beam of light (typically a laser).[326–329] This approach allows the analysis, on a cell-by-cell basis, of different parameters related to various cell characteristics, including relative size (forward scattered light, FSC), relative granularity or internal complexity (side scattered light, SSC), and relative fluorescent intensity (fluorescence).[330–332]

In this work, the uptake of the produced nanomaterials by the two considered cell lines was assessed by measuring the difference in the height of the side scattered light (SSC-H), using a BD AccuriTM C6 (BD Biosciences, Erembodegem, Belgium) flow cytometer. For such purpose, the cells were plated in 24-well microplates (24 wells-F, surface treated, sterile, VWR Tissue Culture Plate, VWR, Radnor, Pensylvania, USA) at a density of 100.000 cells/well in 150 µL of supplemented RPMI 1640 or DMEM, for the THP-1 or MCF-7 cell lines, respectively and, subsequently, they were incubated for 3 h at 37 ºC in a 5 % CO_2 atmosphere (Unitherm CO_2 Incubator 3503, Uniequip, Planegg, Germany). For this purpose, the cell counting was performed using a Neubauer chamber (Improved Neubauer Bright-line, Boeco; Hamburg, Germany). Then, different concentrations of nanomaterials, i.e. NLCs, NWs, or NDs, diluted in 150 µL of the same used medium were added to those cells, except to the positive control, which consisted of cells only in supplemented medium (figure 3.32). In this case, for every assay each considered nanomaterials' concentration was repeated 2 times.

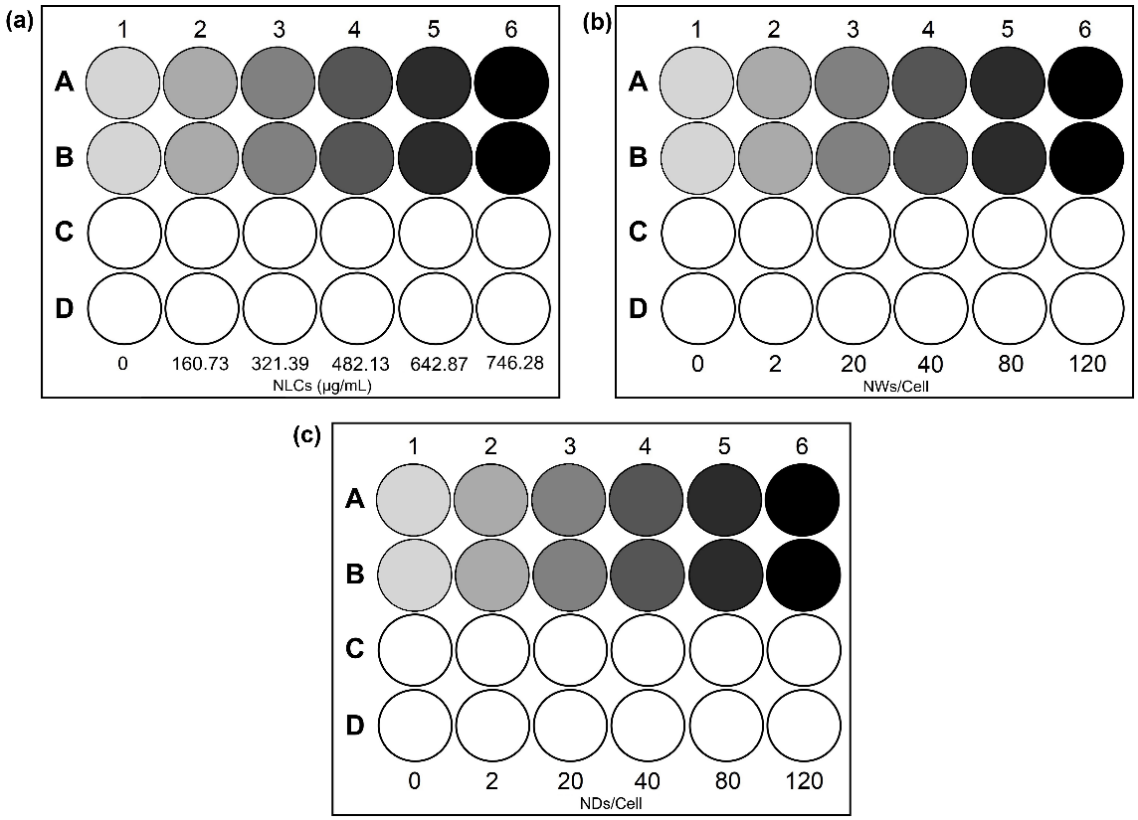

Figure 3.32 - Schemes of the 24-well microplates used in the cell biocompatibility assays considering (a) formulations of NLC, $NLC_{(DOX)}$, $NLC_{(SPIONs)}$, as well as $NLC_{(DOX\text{-}SPIONs)}$ (concentration represents the quantity of solid lipid per µL), (b) FePt NWs, and (c) nonfunctionalized, PEG-thiol (MW = 2000 and 6000) functionalized, and FA-PEG-SH functionalized Au/Fe/Au NDs.

Then, a 19-h incubation was performed at 37 °C in a 5 % CO_2 atmosphere (Unitherm CO_2 Incubator 3503, Uniequip, Planegg, Germany). After this process, the THP-1 cells did not require any treatment before the reading since they grow in suspension. On the other hand, the MCF-7 were washed with 300 µL of PBS, detached using 150 µL of trypsin-EDTA, and then recovered in 300 µL of fresh supplemented DMEM, because they are adherent. Then, the difference in the SSC-H for each considered condition was measured using a BD AccuriTM C6 (BD Biosciences, Erembodegem, Belgium) flow cytometer, since it provides information about the internal complexity or relative granularity of the cells, being a widely used strategy to determine nanomaterials' uptake.

Particularly, when cells pass through the sensing point, the light that is scattered to the side (usually collected at an angle ~ 90 º), as a result of interactions with those cells, is proportional to their internal complexity or granularity (figure 3.33).[333]

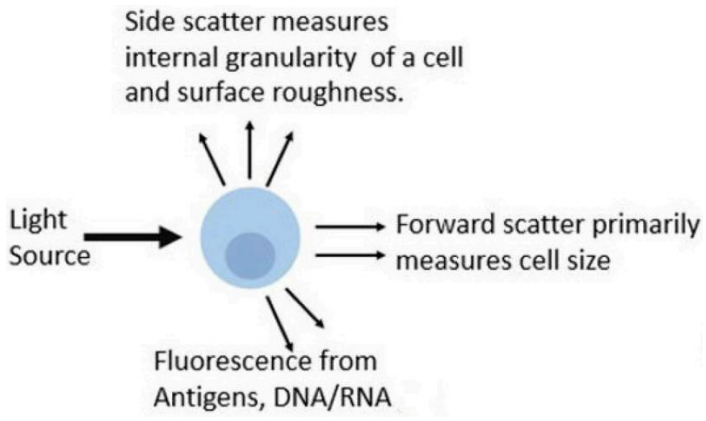

Figure 3.33 - Illustration representing light-scattering by a cell in a flow cytometer. From [328]. Copyright 2019 Author licensed under a Creative Commons Attribution (CC BY-NC-ND 4.0 DEED) license.

The SSC-H represents the peak intensity of the side scatter signal for each individual cell, as it passes through the sensing point. Cells with higher internal complexity or granularity tend to scatter light more intensely to the side, resulting in a greater SSC-H value.[334–336]

3.5.4. Hyperthermia Assays

The hyperthermia assays performed in this study aimed at assessing the effect of the fabricated NLCs on the viability of MCF-7 cells, when exposed to an AMF, having been carried out at IMDEA-Nanoscience, located in the UAM campus. Naturally, only NLCs involving SPIONs, i.e. NLCs, SPIONs, $NLCs_{(DOX\text{-}SPIONs)}$, and $NLC_{(DOX\text{-}SPIONs\text{-}PEG\text{-}FA)}$, were used for this study, since the remaining ones are not able to respond to an AMF.

These experiments were performed by first plating MCF-7 cells in 24-well microplates (24 wells-F, surface treated, sterile, VWR Tissue Culture Plate, VWR, Radnor, Pensylvania, USA) at a density of 100.000 cells/well. Then, after 3 h at 37 °C in a 5 % CO_2 atmosphere, different concentrations of NLCs, ranging between 0 (positive control) and 42.852 µg/mL of SPIONs, were added in duplicate to the wells, followed by an overnight incubation, also at 37 °C in a 5 % CO_2 atmosphere. Subsequently, the cells were detached and collected to Eppendorf (Hamburg, Germany) tubes. Afterwards, for each considered concentration, one of the tubes was placed inside a coil and exposed to an AMF for 30 min, which had a frequency of 556 kHz and a peak intensity of 10 mT. These magnetic field values are within the safety limits established by the Hergt and Dutz criterion, i.e. $H \cdot f \leq 5 \cdot 10^9$ A/ms, for the clinical application of AMF.[329] The cells' temperature was monitored and recorded every 1 s by a thermal infrared camera located at the end of the coil cavity. The second tube, possessing the same amount of cells with internalized NLCs, was placed near the coil under the same room conditions, but it was

not exposed to the magnetic field. Then, the cells were transferred back to the microplate and the viability for each tested concentration was evaluated via the resazurin assay (section 3.5.2.) at two time stamps, namely 24h and 48h after applying the AMF.

3.5.5. Magneto-Mechanical Cell Death Assays

On the other hand, the fabricated FePt NWs, as well as the functionalized and non-functionalized Au/Fe/Au NDs with a spin-vortex ground state, were used to perform magneto-mechanical cell death assays, using the same cell line. For this purpose, these cells were plated in two identical 96-well microplates (96 wells-F, surface treated, sterile, VWR Tissue Culture Plate, VWR, Radnor, Pensylvania, USA) at a density of 50.000 cells/well and, after 3 h at 37 °C in a 5 % CO_2 atmosphere (Unitherm CO_2 Incubator 3503, Uniequip, Planegg, Germany), different concentration of nanostructures, ranging from 0 (positive control) up to 4000 nanostructures/cell, were added in duplicate, followed by an overnight incubation, also at 37 °C in a 5 % CO_2 atmosphere (Unitherm CO_2 Incubator 3503, Uniequip, Planegg, Germany). Then, one of the microplates, containing two wells for each tested concentration, was placed within a homemade magneto-mechanical cell death setup, consisting of two coils facing each other (figure 3.33).

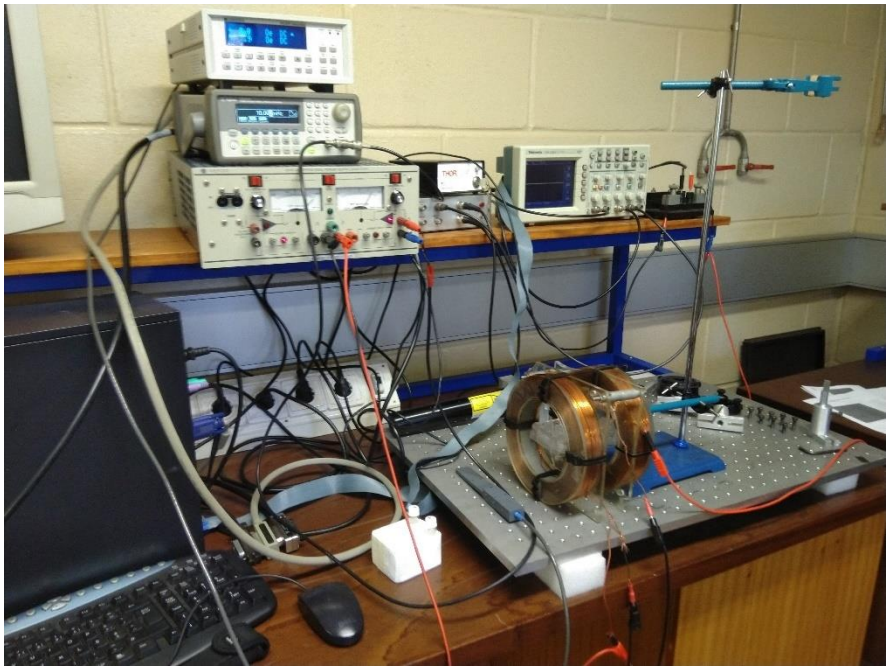

Figure 3.34 - The homemade magneto-mechanical cell death setup..

This setup, available at IFIMUP, consists of two coils facing each other that are connected to a bipolar operational power supply/amplifier (BOP 50-2M, Kepco, Flushing, New York, USA; 0 to ± 50 V, 0 to ± 2 A), which, in turn, is connected to a 20 MHz

function/arbitrary waveform generator (3322OA, Agilent, Santa Clara, California, USA). This generator was used to produce a periodic waveform, i.e. sine, with different frequencies (0.1 Hz to 10 Hz) and peak to peak voltages (5 to 10 V_{pp}), leading to peak magnetic field intensities ranging from 10 to 20 mT. The waveform was monitored using a digital oscilloscope (TDS 2024, Tektronix, Beaverton, Oregon, USA) and the magnetic field strength was measured by placing a magnetic field probe, which was connected to a gaussmeter (Model 425, LakeShore, Carson, California, USA), between the two coils. The duration of the exposure to the magnetic field was established at 60 min.

The second microplate, which was identical to the one positioned between the two coils, was placed near the setup under the same room conditions, but it was not exposed to the magnetic field. Afterwards, both microplates were placed for 24 h in an incubator at 37 °C in a 5 % CO_2 atmosphere (Unitherm CO_2 Incubator 3503, Uniequip, Planegg, Germany). Then, the cell viability was analysed in both plates via the resazurin assay (section 3.5.2.).

3.5.6. Statistical Analysis

The statistical analysis was performed using Python (Python Software Foundation, Wilmington, Delaware, USA). When there were three or more groups to compare, the statistical significance was analysed using a one-way analysis of variance (ANOVA) test. On the other hand, a Mann-Whitney U test was employed to evaluate the statistical significance when only two conditions were considered. The variations were considered statistically significant when * $p < 0.05$, ** $p < 0.01$, *** $p < 0.001$ and **** $p < 0.0001$.

References

[1]S. A. M. Martins, *Drug delivery across blood-brain-barrier by means of intravenous administration of lipid nanoparticles*. PhD Thesis, University of Porto (2012).

[2]N. Nandvikar, R. R. Lala, and A. A. Shinde, Nanostructured Lipid Carrier: The Advanced Lipid Carriers. International Journal of Pharmaceutical Science and Research, 547-561 (2019).

[3]A. Abdullah, M. Malaki, and E. Baghizadeh, On the impact of ultrasonic cavitation bubbles. *Proceedings of the Institution of Mechanical Engineers, Part C: Journal of Mechanical Engineering Science* **226**, 681–694 (2012).

[4]N. Kardava, *Cavitation microjet and shock wave in a signal from impact load measurement*. MSc Thesis, Technical University of Liberec (2020).

[5]T. S. Leong, G. J. Martin, and M. Ashokkumar, Ultrasonic encapsulation – A review. *Ultrasonics Sonochemistry* **35**, 605–614 (2017).

[6]O. K. Ozturk and H. Turasan, Applications of microfluidization in emulsion-based systems, nanoparticle formation, and beverages. *Trends in Food Science & Technology* **116**, 609–625 (2021).

[7]R. Koshani and S. M. Jafari, Ultrasound-assisted preparation of different nanocarriers loaded with food bioactive ingredients. *Advances in Colloid and Interface Science* **270**, 123–146 (2019).

[8]D. Leitao, C. Sousa, J. Ventura, F. Carpinteiro, J. Correia, M. Amado, J. Sousa, and J. Araujo, Influence of surface pre-treatment in the room temperature fabrication of nanoporous alumina. *physica status solidi c* **5**, 3488–3491 (2008).

[9]D. Leitao, A. Apolinario, C. Sousa, J. Ventura, J. Sousa, M. Vazquez, and J. Araujo, Nanoscale Topography: A Tool to Enhance Pore Order and Pore Size Distribution in Anodic Aluminum Oxide. *The Journal of Physical Chemistry C* **115**, 8567–8572 (2011).

[10]G. Yang, B. Wang, K. Tawfiq, H. Wei, S. Zhou, and G. Chen, Electropolishing of surfaces: theory and applications. *Surface Engineering* **33**, 149–166 (2017).

[11]L. Balogh, C. Beaufort, A. Brossard, R. Bunker, J.-F. Caron, M. Chapellier, J.-M. Coquillat, E. Corcoran, S. Crawford, A. D. Fard, Y. Deng, K. Dering, D. Durnford, G. Gerbier, I. Giomataris, G. Giroux, P. Gorel, M. Gros, P. Gros, O. Guillaudin, E. W. Hoppe, I. Katsioulas, F. Kelly, P. Knights, L. Kwon, S. Langrock, P. Lautridou, R. D. Martin, J.-P. Mols, J.-F. Muraz, X.-F. Navick, T. Neep, K. Nikolopoulos, P. O'Brien, R. Owen, M.-C.

Piro, D. Santos, G. Savvidis, I. Savvidis, F. V. S. Fernandez, M. Vidal, R. Ward, M. Zampaolo, NEWS-G Collaboration, S. Alcantar Anguiano, I. J. Arnquist, M.L. di Vacri, K. Harouaka, K. Kobayashi, K.S. Thommasson, Copper electroplating for background suppression in the NEWS-G experiment. *Nuclear Instruments and Methods in Physics Research Section A: Accelerators, Spectrometers, Detectors and Associated Equipment* **988**, 164844 (2021).

[12]B. Sahoo, T. Das, and J. Paul, Anodising and Plasma Electrolytic Oxidation for the Surface Modification of Aluminium Alloys. *Journal of Surface Science and Technology*, **1–14** (2021).

[13]O. Lebedeva, G. Jungurova, D. Kultin, L. Kustov, A. Zakharov, K. Kalmikov, E. Chernikova, and V. Krasovskiy, Ionic liquids based on the imidazolium cation in platinum and titanium electropolishing. *Green chemistry* **13**, 1004–1008 (2011).

[14]C.-H. Chen, C.-Y. Lee, M.-D. Ger, S.-Y. Jian, J.-C. Hung, P.-J. Yang, C.-H. Kao, Y.-C. Ferng, Y.-S. Huang, and K.-K. Jen, The Effect of Oxalic Acid as the Pre-Activator for the Electropolishing of Additive Manufactured Titanium-Based Materials and its Characterization. *Polymers* **14**, 4198 (2022).

[15]V. V. Yuzhakov, H.-C. Chang, and A. E. Miller, Pattern formation during electropolishing. *Physical Review B* **56**, 12608 (1997).

[16]E. Pujiyulianto and S. Suyitno, The Effect of Electropolishing Time Variation at Room Temperature and Low Voltage on the Surface Quality of Cardiovascular Stent. *Advanced Materials Research* **1154**, 91–101 (2019).

[17]K. Alrbaey, D. I. Wimpenny, A. Al-Barzinjy, and A. Moroz, Electropolishing of Re-melted SLM Stainless Steel 316L Parts Using Deep Eutectic Solvents: 3 × 3 Full Factorial Design. *Journal of Materials Engineering and Performance* **25**, 2836–2846 (2016).

[18]L. Cooley, D. Burk, C. Cooper, N. Dhanaraj, M. Foley, D. Ford, K. Gould, D. Hicks, R. Novitski, A. Romanenko, R. Schuessler, C. Thompson, and G. Wu, Impact of Forming, Welding, and Electropolishing on Pitting and the Surface Finish of SRF Cavity Niobium. *IEEE Transactions on Applied Superconductivity* **21**, 2609– 2614 (2010).

[19]G. E. J. Poinern, N. Ali, and D. Fawcett, Progress in Nano-Engineered Anodic Aluminum Oxide Membrane Development. *Materials* **4**, 487–526 (2011).

[20]S. S. Moraes, *Multimodal Magnetic Lipid Nanocarriers for Cancer Therapies*. PhD Thesis, University of Porto, (2021).

[21]J. Azevedo, C. Sousa, A. Mendes, and J. Araújo, Influence of the Rest Pulse Duration in Pulsed Electrodeposition of Fe Nanowires. *Journal of Nanoscience and Nanotechnology* **12**, 9112–9117 (2012).

[22]J. Azevedo, C. Sousa, J. Ventura, A. Apolinario, A. Mendes, and J. Araujo, Ultra-long Fe nanowires by pulsed electrodeposition with full filling of alumina templates. *Materials Research Express* **1**, 015028 (2014).

[23]C. T. Sousa, D. C. Leitao, J. Ventura, P. B. Tavares, and J. P. Araújo, A versatile synthesis method of dendrites-free segmented nanowires with a precise size control. *Nanoscale Research Letters* **7**, 1–7 (2012).

[24]M. Lazzarino, *Cantilever systems for the next generation of biomechanical sensors*. PhD Thesis, University of Groningen (2012).

[25]Z. Guo and L. Tan, Fundamentals and Applications of Nanomaterials. Artech House (2009).

[26]K. Wasa, Sputter deposition technology as a materials engineering. *Bulletin of Materials Science* **16**, 643–663 (1993).

[27]A. Tyagi and R. Ningthoujam, *Handbook on Synthesis Strategies for Advanced Materials: Volume-II: Processing and Functionalization of Materials*. Springer Nature Singapore (2022).

[28]D. Pawar, *Chemical sensors*. CRC Press (2023).

[29]V. Kresin, V. Kresin, S. Ovchinnikov, and S. Wolf, *Superconducting State: Mechanisms and Materials*. Oxford University Press (2021).

[30]H. Ghazal and N. Sohail, Sputtering Deposition. In: *Thin Films*, Chapter 2 (IntechOpen, 2022).

[31]H. Fager, *Growth and Characterization of Amorphous TiAlSiN and HfAlSiN Thin Films*. Licentiate Thesis, University of Linköping (2012).

[32]H. Bartolf, *Fluctuation Mechanisms in Superconductors: Nanowire Single-Photon Counters, Enabled by Effective Top-Down Manufacturing*. Springer Fachmedien Wiesbaden (2015).

[33]A. Daniel, *Electrical studies on cubic boron nitride MIS structures*. PhD Thesis, University of Michigan (2005).

[34]X. Qiu, *High-Temperature Superconductors*. Elsevier Science (2011).

[35]R.M. Pujahari, Solar Cell Technology. In: *Energy Materials Fundamentals to Applications*, 27-60 (Elsevier, 2021).

[36]M. Arce, *Growth of High Permittivity Dielectrics by High Pressure Sputtering from Metallic Targets.* Springer International Publishing (2017).

[37]M. Ohring, *Materials Science of Thin Films: Deposition and Structure*. Elsevier Science (2002).

[38]A. Sarangan, *Nanofabrication: Principles to Laboratory Practice*. CRC Press (2016).

[39]K. S. Kroll. *Development of an H_3^+ Driven Chemical Ionization Source for GC-MS*. PhD Thesis, University of Wuppertal (2021).

[40]A. Lakhtakia and R. Martín-Palma, Engineered Biomimicry. Elsevier Science (2013).

[41]G. Claudio, K. Bass, K. Heasman, A. Cole, S. Roberts, S. Watson, and M. Boreland, Surface passivation by silicon nitride in Laser Grooved Buried Contact (LGBC) silicon solar cells. *Superlattices and Microstructures* **45**, 234–239 (2009).

[42]T. Mieno, *Plasma Science and Technology: Progress in Physical States and Chemical Reactions*. IntechOpen (2016).

[43]S. Zhang, *Hydroxyapatite Coatings for Biomedical Applications*. CRC Press (2013).

[44]A. Piel, *Plasma Physics: An Introduction to Laboratory, Space, and Fusion Plasmas*. Springer International Publishing (2017).

[45]M. S. Rodrigues, J. Borges, C. Lopes, R. M. Pereira, M. I. Vasilevskiy, and F. Vaz, Gas Sensors Based on Localized Surface Plasmon Resonances: Synthesis of Oxide Films with Embedded Metal Nanoparticles, Theory and Simulation, and Sensitivity Enhancement Strategies. *Applied Sciences* **11**, 5388 (2021).

[46]A. Kosari Mehr and A. Kosari Mehr, Magnetron sputtering issues concerning growth of magnetic films: a technical approach to background, solutions, and outlook. *Applied Physics A* **129**, 662 (2023).

[47]B. M. Cuadrado, *Patterned magnetic nanostructures for biomedical applications*. PhD Thesis, University of the Basque Country (2018).

[48]A. Dahiya, S. Chuhadiya, Himanshu, D. Suthar, S. Nehra, and M. Dhaka, Achieving phase stability in ZnSe thin films by thickness and annealing recipes for optical window applications. *Journal of Materials Science: Materials in Electronics* **34**, 410 (2023).

[49]A. K. Kirubaharan, K. G. Saravanan, and V. Vishwakarma, Metallic coatings. In: *Polymetallic Coatings to Control Biofouling in Pipelines: Challenges and Potential*, 97–106 (CRC Press, 2021).

[50]M. Ulmeanu, M. Filipescu, and R. V. Medianu, Fabrication of 2-D nanostructures via metal deposition through a colloidal mask: comparison between thermal evaporation and RF magnetron sputtering. *physica status solidi c* **5**, 3584–3587 (2008).

[51]N. Shah, C. Panchal, V. Kheraj, J. Ray, and M. Desai, Growth, structural and optical properties of copper indium diselenide thin films deposited by thermal evaporation method. *Solar Energy* **83**, 753–760 (2009).

[52]M. Jakešová, *Wireless Bioelectronic Devices Driven by Deep Red Light*. (Linköping University Electronic Press (2021).

[53]H. Gatzen, V. Saile, and J. Leuthold, *Micro and Nano Fabrication: Tools and Processes*. Springer Berlin Heidelberg (2015).

[54]P. U. Londhe, S. Desarada, S. Rane, N. Chaure, and B. Kale, A novel combined thermal evaporation and solvothermal approach to produce highly crystalline and compact CIG $(S_{1-x}Se_x)_2$ thin films. *Applied Materials Today* **35**, 101932 (2023).

[55]K. M. A. Mokhtar, Some Optical Investigations Thin Films of $Ga_{80-x}Se_xTe_{20}$ (where x= 15% and 20%) Chalcogenide glass. *International Journal of Thin Films Science and Technology* **11**, 179–185 (2022).

[56]V. Borra, D. G. Georgiev, and C. R. Grice. Fabrication of optically smooth Sn thin films. *Thin Solid Films* **616**, 311–315 (2016).

[57]E. E. Azrak, *Growth and characterization of in-plane solid-liquid-solid GeSn and SiSn nanowires*. PhD Thesis, University of Rouen Normandy (2018).

[58]K. H. Guenther, B. Loo, D. Burns, J. Edgell, D. Windham, and K.-H. Müller, Microstructure analysis of thin films deposited by reactive evaporation and by reactive ion plating. *Journal of Vacuum Science & Technology A: Vacuum, Surfaces, and Films* **7**, 1436–1445 (1989).

[59]M. Azadi, A. Karrech, M. Elchalakani, and M. Attar, Microfluidic study of sustainable gold leaching using glycine solution. *Hydrometallurgy* **185**, 186–193 (2019).

[60]M. Jakešová, *Wireless Bioelectronic Devices Driven by Deep Red Light*. Linköping University Electronic Press (2021).

[61]J. A. Housmans, G. Wu, J. Schymkowitz, and F. Rousseau, A guide to studying protein aggregation. *The FEBS Journal* **290**, 554–583 (2023).

[62]M. Joshi, A. Bhattacharyya, and S. W. Ali, Characterization techniques for nanotechnology applications in textiles. *Indian Journal of Fibre & Textile Research* **33**, 304-317 (2008).

[63]E. Velichko, S. Makarov, E. Nepomnyashchaya, and G. Dong, Molecular Aggregation in Immune System Activation Studied by Dynamic Light Scattering. *Biology* **9**, 123 (2020).

[64]J. Stetefeld, S. A. McKenna, and T. R. Patel, Dynamic light scattering: a practical guide and applications in biomedical sciences. *Biophysical reviews* **8**, 409–427 (2016).

[65]R. Sandhu, N. Singh, J. Dhankhar, G. Kama, and R. Sharma, Dynamic light scattering (DLS) technique, principle, theoretical considerations and applications. In: *Nanotechnological and Biochemical Techniques for Assessing the Quality and Safety of Milk and Milk Products* 135–137 (ICAR-National Dairy Research Institute, 2018).

[66]J.-L. Putaux, E. Minatti, C. Lefebvre, R. Borsali, M. Schappachera, and A. Deffieuxa, Vesicles made of PS-PI cyclic diblock copolymers: In situ freeze-drying cryo-TEM and dynamic light scattering experiments. *Faraday Discussions* **128**, 163-178 (2005).

[67]Y. Nomura, Evaluation of Mitochondrial DNA Dynamics Using Fluorescence Correlation Analysis. In: *Current Frontiers and Perspectives in Cell Biology*, 525-534 (IntechOpen, 2012).

[68]V. Shukla, K. Niveria, P. Shashidhar, and A. K. Verma, Dynamic light scattering (DLS) particle size analysis for biomedical nanotechnology. In: *Analytical Techniques for Biomedical Nanotechnology*, 16-1-16-25 (IOP Publishing Bristol, 2023).

[69]T. Misono, Dynamic Light Scattering (DLS). In: *Measurement Techniques and Practices of Colloid and Interface Phenomena*, 65–69 (Springer, 2019).

[70]M. Vamvakaki, D. Palioura, A. Spyros, S. Armes, and S. Anastasiadis, Dynamic Light Scattering vs ^{1}H NMR Investigation of pH-Responsive Diblock Copolymers in Water. *Macromolecules* **39**, 5106– 5112 (2006).

[71]F. Varenne, J. Botton, C. Merlet, H. Hillaireau, F.-X. Legrand, G. Barratt, and C. Vauthier, Size of monodispersed nanomaterials evaluated by dynamic light scattering: protocol validated for measurements of 60 and 203 nm diameter nanomaterials is now

extended to 100 and 400 nm. *International Journal of Pharmaceutics* **515**, 245–253 (2016).

[72]T. Bourguignon, A. A. Torrano, L. Houel-Renault, A. Machelart, P. Brodin, and R. Gref, An original methodology to study polymeric nanoparticle-macrophage interactions: nanoparticle tracking analysis in cell culture media and quantification of the internalized objects. *International Journal of Pharmaceutics* **610**, 121202 (2021).

[73]V. Filipe, A. Hawe, and W. Jiskoot, Critical Evaluation of Nanoparticle Tracking Analysis (NTA) by Nanosight for the Measurement of Nanoparticles and Protein Aggregates. *Pharmaceutical Research* **27**, 796–810 (2010).

[74]M. Y. Chan, Q. M. Dowling, S. J. Sivananthan, and R. M. Kramer, Particle Sizing of Nanoparticle Adjuvant Formulations by Dynamic Light Scattering (DLS) and Nanoparticle Tracking Analysis (NTA). In: *Vaccine Adjuvants: Methods and Protocols*, 239–252 (Springer, 2017).

[75]H. Kato, A. Nakamura, N. Ouchi, and S. Kinugasa, Determination of bimodal size distribution using dynamic light scattering methods in the submicrometer size range. *Materials Express* **6**, 175–182 (2016).

[76]H. Masri and J. K. Raynes, Nanoparticle Tracking Analysis of β-Casein Nanocarriers. In: *Protein Nanotechnology: Protocols, Instrumentation, and Applications* 301–309 (Springer, 2020).

[77]F. Varenne, A. Makky, M. Gaucher-Delmas, F. Violleau, and C. Vauthier, Multimodal Dispersion of Nanoparticles: A Comprehensive Evaluation of Size Distribution with 9 Size Measurement Methods. *Pharmaceutical Research* **33**, 1220–1234 (2016).

[78]J. Sanchís, C. Bosch-Orea, M. Farré, and D. Barceló, Nanoparticle tracking analysis characterisation and parts-per-quadrillion determination of fullerenes in river samples from Barcelona catchment area. *Analytical and Bioanalytical Chemistry* **407**, 4261–4275 (2015).

[79]S. Miyamoto, T. Hirakawa, Y. Noguchi, D. Urushiyama, K. Miyata, T. Baba, F. Yotsumoto, S. Yasunaga, K. Nakabayashi, K. Hata, W. Nakagawa, T. Otsuka, Y. Nozawa, I. Furuhata, and J. Mikasa, Physical Properties of Ultrafine Bubbles Generated Using a Generator System. *in vivo* **37**, 2555–2563 (2023).

[80]P. Hole, K. Sillence, C. Hannell, C. M. Maguire, M. Roesslein, G. Suarez, S. Capracotta, Z. Magdolenova, L. Horev-Azaria, A. Dybowska, L. Cooke, A. Haase, S. Contal, S. Manø, A. Vennemann, J.-J. Sauvain, K. C. Staunton, S. Anguissola, A. L., M.

Dusinska, R. Korenstein, A. C. Gutleb, M. Wiemann, A. Prina-Mello, M. Riediker, and P. Wick, Interlaboratory comparison of size measurements on nanoparticles using nanoparticle tracking analysis (NTA). *Journal of Nanoparticle Research* **15**, 1–12 (2013).

[81]M. Lungu, A. Neculae, M. Bunoiu, and C. Biris, *Nanoparticles' Promises and Risks: Characterization, Manipulation, and Potential Hazards to Humanity and the Environment.* Springer International Publishing (2014).

[82]P. Kesharwani and K. Singh, *Nanoparticle Therapeutics: Production Technologies, Types of Nanoparticles, and Regulatory Aspects*. Elsevier Science (2021).

[83]A. Kamanzi, Y. Gu, R. Tahvildari, Z. Friedenberger, X. Zhu, R. Berti, M. Kurylowicz, D. Witzigmann, J. A. Kulkarni, J. Leung, J. Andersson, A. Dahlin, F. Höök, M. Sutton, P. R. Cullis, and S. Leslie, Simultaneous, Single-Particle Measurements of Size and Loading Give Insights into the Structure of Drug-Delivery Nanoparticles. *ACS Nano* **15**, 19244–19255 (2021).

[84]A. Kim, W. B. Ng, W. Bernt, and N.-J. Cho, Validation of Size Estimation of Nanoparticle Tracking Analysis on Polydisperse Macromolecule Assembly. *Scientific Reports* **9**, 2639 (2019).

[85]K. Sałaga-Zaleska, A. Kuchta, B. Bzoma, G. Chyła-Danił, A. Safianowska, A. Płoska, L. Kalinowski, A. Dębska-Ślizień, and M. Jankowski, Nanoparticle Tracking Analysis of Urinary Extracellular Vesicle Proteins as a New Challenge in Laboratory Medicine. *International Journal of Molecular Sciences* **24**, 12228 (2023).

[86]J. Gross, S. Sayle, A. R. Karow, U. Bakowsky, and P. Garidel, Nanoparticle tracking analysis of particle size and concentration detection in suspensions of polymer and protein samples: influence of experimental and data evaluation parameters. *European Journal of Pharmaceutics and Biopharmaceutics* **104**, 30–41 (2016).

[87]A. Malloy and B. Carr, NanoParticle Tracking Analysis – The Halo^{TM} System. *Particle & Particle Systems Characterization* **23**, 197–204 (2006).

[88]D. Griffiths, P. Hole, J. Smith, A. Malloy, and B. Carr, Counting and Sizing of Virus and Protein Aggregates by Nanoparticle Tracking Analysis (NTA). *Nanotechnology* **3**, 176–179 (2010).

[89]B. Carr and A. Malloy, Nanoparticle Measurement Through Visualisation. *Microscopy Today* **16**, 22–25 (2008).

[90]M. Kaszuba, J. Corbett, F. M. Watson, and A. Jones, High-concentration zeta potential measurements using light-scattering techniques. *Philosophical Transactions of the Royal Society A: Mathematical, Physical and Engineering Sciences* **368**, 4439–4451 (2010).

[91]H. Newton, *Handbook of Brain Tumor Chemotherapy, Molecular Therapeutics, and Immunotherapy*. Elsevier Science (2018).

[92]Z. Liu, R. Fu, and Y. Yuying, Preparation and evaluation of stable nanofluids for heat transfer application. In: *Advances in Nanofluid Heat Transfer*, 25–57 (Elsevier, 2022).

[93]A. Doostmohammadi, A. Monshi, R. Salehi, M. H. Fathi, Z. Golniya, and A. U. Daniels, Bioactive glass nanoparticles with negative zeta potential. *Ceramics International* **37**, 2311–2316 (2011).

[94]R. Kohli and K. Mittal, *Developments in Surface Contamination and Cleaning, Volume 8: Cleaning Techniques.* Elsevier Science (2014).

[95]P. Rauta, Y. Mohanta, and D. Nayak, *Nanotechnology in Biology and Medicine: Research Advancements & Future Perspective*s. CRC Press (2019).

[96]V. Forest and J. Pourchez, Preferential binding of positive nanoparticles on cell membranes is due to electrostatic interactions: A too simplistic explanation that does not take into account the nanoparticle protein corona. *Materials Science and Engineering: C* **70**, 889–896 (2017).

[97]A. Langford, M. Bruchsaler, and M. Gupta, Suspension properties and characterization of aluminum-adjuvanted vaccines. In: *Practical Aspects of Vaccine Development*, 225–266 (Academic Press, 2022).

[98]S. Bhattacharjee, DLS and zeta potential – What they are and what they are not? *Journal of Controlled Release* **235**, 337–351 (2016).

[99]T. A. T. Mohd, M. Z. Jaafar, A. A. A. Rasol, and M. F. Hamid, Measurement of Streaming Potential in Downhole Application: An Insight for Enhanced Oil Recovery Monitoring. In: *Matec Web of Conferences, Volume 87*, 03002 (EDP Sciences, 2017).

[100]S. Sharma, P. Shukla, A. Misra, and P. R. Mishra, Interfacial and colloidal properties of emulsified systems: Pharmaceutical and biological perspective. In: *Colloid and Interface Science in Pharmaceutical Research and Development*, 149–172 (Elsevier, 2014).

[101]C. Skyttner, *Peptide-Liposome Model Systems for Triggered Release*. Linkoping University (2018).

[102]T. Tadros, *Dispersion of Powders in Liquids and Stabilization of Suspensions*. Wiley (2012).

[103]A. Rahdar, N. Amini, F. Askari, and M. A. B. H. Susan, Dynamic light scattering: A useful technique to characterize nanoparticles. *Journal of Nanoanalysis* **6**, 80–89 (2019).

[104]J. Han, *Innovations in Food Packaging*. Elsevier Science (2013).

[105]L. Nollet, Handbook of Food Analysis: Methods and Instruments in Applied Food Analysis. Marcel Dekker (2004).

[106]G. V. Lowry, R. J. Hill, S. Harper, A. F. Rawle, C. O. Hendren, F. Klaessig, U. Nobbmann, P. Sayre, and J. Rumble, Guidance to improve the scientific value of zeta-potential measurements in nanoEHS. *Environmental Science: Nano* **3**, 953–965 (2016).

[107]V. R. Patel and Y. Agrawal, Nanosuspension: An approach to enhance solubility of drugs. *Journal of Advanced Pharmaceutical Technology & Research* **2**, 81 (2011).

[108]T. Missana and A. Adell, On the Applicability of DLVO Theory to the Prediction of Clay Colloids Stability. *Journal of Colloid and Interface Science* **230**, 150–156 (2000).

[109]I. T. Radwan, R. I. Eltaly, M. M. Baz, M. Yousif, A. Selim, H. A. Taie, E. A. Manaa, and H. F. Khater, Novel acaricidal and growth-regulating activity of *Aloe vera* and *Rheum rhabarbarum* extracts and their oil/water nanoemulsions against the camel tick, *Hyalomma dromedarii*. *Scientific Reports* **13**, 16802 (2023).

[110]V. Fotopoulos and G. Gohari, *Engineered Nanoparticles in Agriculture: From Laboratory to Field.* De Gruyter (2023).

[111]G. Mul, F. Groot, B. Mojet-Mol, and M. Tromp, Characterization of Catalysts. In: *Catalysis: An Integrated Textbook for Students*, 271-313 (Wiley, 2018).

[112]A. Moazeni, *Investigation of Halogen Bond Interactions of Chiral Molecules Using Infrared, Vibrational Circular Dichroism, NMR, UV-vis Spectroscopy and Density Functional Theory Calculations*. PhD Thesis, University of Alberta (2023).

[113]T. Fahmy, A. Sarhan, I. Elsayed, and M. Ahmed, Effect of UV Irradiation on the Structure and Optical Properties of PVA/$Cucl_2$. *Journal of Advances in Physics* **14**, 5378-5387 (2018).

[114]Y. Doumbia, A. Bouich, D. Soro, and M. S. Bernabé, Improving Stability and Performance of Cesium Mixed Lead Halides for Photovoltaic Applications. *JOM* **75**, 693–700 (2023).

[115]G. Shinde, R. Godage, R. Jadhav, B. Manoj, and B. Aniket, A Review on Advances in UV Spectroscopy. *Research Journal of Science and Technology* **12**, 47–51 (2020).

[116]T. Okazaki, K. Imai, S. Y. Tan, Y. T. Yong, F. A. Rahman, N. Hata, S. Taguchi, A. Ueda, and H. Kuramitz, Fundamental Study on the Development of Fiber Optic Sensor for Real-Time Sensing of $CaCO_3$ Scale Formation in Geothermal Water. *Analytical Sciences* **31**, 177–183 (2015).

[117]J.-J. Poh, W.-L. Wu, N. W.-J. Goh, S. M.-X. Tan, and S. K.-E. Gan, Spectrophotometer onthe-go: The development of a 2-in-1 UV–Vis portable Arduino-based spectrophotometer. *Sensors and Actuators A: Physical* **325**, 112698 (2021).

[118]S. Nimesh, N. Gupta, and R. Chandra, *Nanomaterials: Evolution and Advancement Towards Therapeutic Drug Delivery (Part I)*. Bentham Science Publishers (2021).

[119]R. Narain, *Polymer Science and Nanotechnology: Fundamentals and Applications*. Elsevier Science (2020).

[120]M. H. Penner, Ultraviolet, Visible, and Fluorescence Spectroscopy. In: *Food Analysis*, 89–106 (Springer, 2017).

[121]B. Al-Sabbagh and N. N. Abdulrazzaq, Measuring Dyes Concentration Using a Low-Cost Visible-Light Spectrophotometer. *Iraqi Journal of Chemical and Petroleum Engineering* **23**, 27–33 (2022).

[122]C. Knowles and A. Knowles, *Practical Absorption Spectrometry: UV Spectrometry Group.* Springer Netherlands (2013).

[123]K. Lee, Y. Choi, K. Kim, H.-J. Koo, and J. Choi, Quantification of Unknown Nanoscale Biomolecules Using the Average-Weight-Difference Method. *Applied Sciences* **9**, 130 (2019).

[124]J. Robinson and E. Frame, *Undergraduate Instrumental Analysis*. CRC Press (2004).

[125]B. Cahyono, E. F. Hasanah, M. Suzery, and Widayat, Analysis of piperine content in cabe jawa extracts (*piper retrofractum Vahl*) using UV spectrophotometry and HPLC. In: IOP *Conference Series: Materials Science and Engineering, Volume 509*, 012025 (IOP Publishing, 2019).

[126]K.-H. Hsu and C. Chen, The effect of calibration equations on the uncertainty of UV–Vis spectrophotometric measurements. *Measurement* **43**, 1525–1531 (2010).

[127]A. R. Carvalho, L. C. G. Bazana, M. F. Ferrão, and A. M. Fuentefria, Curve fitting and linearization of UV–Vis spectrophotometric measurements to estimate yeast in inoculum preparation. *Analytical Biochemistry* **625**, 114216 (2021).

[128]M. S. B. Omar and M. Sofi, Uv-Vis Spectrum Analysis of Heavy Metal Detection. *UTP Electronic and Digital Intellectual Asset* (2011).

[129]S. Moraes, A. Marinho, S. Lima, A. Granja, J. Araújo, S. Reis, C. Sousa, and C. Nunes, Targeted nanostructured lipid carriers for doxorubicin oral delivery. *International Journal of Pharmaceutics* **592**, 120029 (2021).

[130]T. A. Ranathunge, D. Karunaratne, R. Rajapakse, and D. L. Watkins, Doxorubicin Loaded Magnesium Oxide Nanoflakes as pH Dependent Carriers for Simultaneous Treatment of Cancer and Hypomagnesemia. *Nanomaterials* **9**, 208 (2019).

[131] R. Onnainty and G. Granero, Chitosan-based nanocomposites: Promising materials for drug delivery applications. In: *Biomedical Applications of Nanoparticles*, 375–407 (Elsevier, 2019).

[132]K. W. Khalid and S. N. Abd Alhammid, Preparation and in-vivo Evaluation of Ticagrelor Oral Liquid Self nano-emulsion. *Journal of Pharmaceutical Negative Results* **13**, 274 (2022).

[133]H. He, M. Booth, C. He, and S. Zhang, Advances in nano-scale systems with optics (nanochemical, nanomaterial, and nano-biomedicine). *Frontiers Research Topics* **10**, 989153 (2022).

[134]M. Janecek and R. Kral, *Modern Electron Microscopy in Physical and Life Sciences*. IntechOpen (2016).

[135]S. Telikepalli, H. E. Shinogle, P. S. Thapa, J. H. Kim, M. Deshpande, V. Jawa, C. R. Middaugh, L. O. Narhi, M. K. Joubert, and D. B. Volkin, Physical Characterization and *In Vitro* Biological Impact of Highly Aggregated Antibodies Separated into Size-Enriched Populations by Fluorescence-Activated Cell Sorting. *Journal of Pharmaceutical Sciences* **104**, 1575–1591 (2015).

[136]L. G. Vivas, *On the magnetic and structural properties of Co and Co-based nanowire arrays*. PhD Thesis, Autonomous University of Madrid (2012).

[137]Y. Zhu and H. Dürr, The future of electron microscopy. *Physics Today* **68**, 32–38 (2015).

[138]L. D. Mafu, T. A. Msagati, and B. B. Mamba, Ion-imprinted polymers for environmental monitoring of inorganic pollutants: synthesis, characterization, and applications. *Environmental Science and Pollution Research* **20**, 790–802 (2013).

[139]C. A. Evans, *Encyclopedia of Materials Characterization: Surfaces, Interfaces, Thin Films.* Gulf Professional Publishing (1992).

[140]P. Echlin, C. Fiori, J. Goldstein, D. C. Joy, and D. E. Newbury, Advanced Scanning Electron Microscopy and X-Ray Microanalysis. *Springer Science & Business Media* (2013).

[141]P. Pant, A. Jaipuria, and C. Gupta, Spectroscopic and Microscopic Techniques: Tools for Characterizing Nanoscale Metal–Organic Frameworks (NMOFs). In: Metal-Organic Frameworks (MOFs) as Catalysts, 127–164 (Springer, 2022).

[142]T. Otsuka, M. Nakamura, K.-i. Yamashita, K. Honda, S.-i. Kitamura, F. Timischl, and M. Kudo, SEM Images Obtained with an Energy and Takeoff Angle Selective Detector. *e-Journal of Surface Science and Nanotechnology* **12**, 279–282 (2014).

[143]A. Ul-Hamid and A. Ul-Hamid, Contrast Formation in the SEM. In: *A Beginners' Guide to Scanning Electron Microscopy*, 77–128 (Springer, 2018).

[144]L. Li, *Versatile Applications of Nanostructured Metal Oxides*. PhD Thesis, University of Cambridge (2014).

[145]W. Zhou, R. Apkarian, Z. L. Wang, and D. Joy, Fundamentals of Scanning Electron Microscopy (SEM). In: *Scanning Microscopy for Nanotechnology: Techniques and Applications*, 1–40 (Springer, 2007).

[146]J. I. Goldstein, D. E. Newbury, J. R. Michael, N. W. Ritchie, J. H. J. Scott, and D. C. Joy, *Scanning Electron Microscopy and X-Ray Microanalysis*. Springer (2017).

[147]K.-H. Grote and H. Hefazi, *Springer Handbook of Mechanical Engineering*. Springer Nature (2021).

[148]S. Mark, *Bioinspired Nanoarchitecture: Nanofabrication of 2-D Metallic and Semiconductor Arrays Using Microbial Surface Layer (S-Layer) Protein Biotemplates*. Cornell University (2006).

[149]Y. Bar-Cohen, Low Temperature Materials and Mechanisms. CRC Press (2016).

[150]M. Lund, *Effect of interfacial disorder on exchange anisotropy in nickel manganese/nickel epitaxial bilayers*. PhD Thesis, University of Minnesota (2006).

[151]D. Zhao, Y. Wan, and W. Zhou, *Ordered Mesoporous Materials*. Wiley (2012).

[152]M. Nasrollahzadeh, *Biopolymer-Based Metal Nanoparticle Chemistry for Sustainable Applications: Volume 1: Classification, Properties and Synthesis*. Elsevier Science (2021).

[153]B. J. Inkson, Scanning electron microscopy (SEM) and transmission electron microscopy (TEM) for materials characterization. In *Materials Characterization Using Nondestructive Evaluation (NDE) Methods*, 17–43 (Elsevier, 2016).

[154]M. Malatesta, Transmission Electron Microscopy as a Powerful Tool to Investigate the Interaction of Nanoparticles with Subcellular Structures. *International Journal of Molecular Sciences* **22**, 12789 (2021).

[155]U. Pohl, *Epitaxy of Semiconductors: Physics and Fabrication of Heterostructures*. Springer International Publishing (2020).

[156]R. Errington, *Advanced Practical Inorganic and Metalorganic Chemistry*. Taylor & Francis (1997).

[157]N. Rao, G. Preminger, and J. Kavanagh, *Urinary Tract Stone Disease*. Springer London (2011).

[158]S. D. Terhune, *An Electron Backscatter Diffraction Analysis of the Microstructure of Pure Aluminum Processed by Equal-Channel Angular Pressing*. MSc Thesis, Naval Postgraduate School (1998).

[159]G. Henderson, D. Neuville, and R. Downs, *Spectroscopic Methods in Mineralogy and Material Sciences*. De Gruyter (2014).

[160]J. Allday, S. Adams, *Advanced Physics*. OUP Oxford (2020).

[161]D. Sherwood and J. Cooper, *Crystals, X-rays and Proteins: Comprehensive Protein Crystallography*. OUP Oxford (2011).

[162]H. Brittain, *Profiles of Drug Substances, Excipients and Related Methodology*. Elsevier Science (2003).

[163]J. Greenberg, *X-ray Diffraction Imaging: Technology and Applications*. CRC Press (2018).

[164]T. Ramabhadran, *Pharmaceutical Design and Development: A Molecular Biology Approach*. CRC Press (1994).

[165]R. Asthana, A. Kumar, and N. Dahotre, *Materials Processing and Manufacturing Science*. Elsevier Science (2006).

[166]M. L, *Chemistry for Degree Students B.Sc. First Year (LPSPE)*. S. Chand & Company Limited (2022).

[167]J. Hasbun and T. Datta, *Introductory Solid State Physics with MATLAB Applications*. CRC Press (2019).

[168]M. Julian, *Foundations of Crystallography with Computer Applications*. CRC Press (2014).

[169]U. Hanefeld and L. Lefferts, *Catalysis: An Integrated Textbook for Students*. Wiley (2018).

[170]A. Fischer-Cripps, *The Materials Physics Companion*. CRC Press (2007).

[171]R. Prasad, *Physics and Technology for Engineers: Understanding Materials and Sustainability*. Springer Nature Switzerland (2023).

[172]M. Mansfield and C. O'Sullivan, *Understanding Physics*. Wiley (2011).

[173]J. E. Parks and R. DeSerio, X-ray Diffraction and Absorption. *Rough Draft 04/15/2015*, University of Tennessee (2015).

[174]R. Brill and R. Mason, *Advances in Structure Research by Diffraction Methods*. Elsevier Science (2013).

[175]D. Dr Geeta Nair, *Material Characterization Techniques for Beginners*. BFC Publications (2023).

[176]J. Owen, *Growth, Etching, and Stability of Sputtered ZnO: Al for Thin-film Silicon Solar Cells*. Forschungszentrum Jülich (2011).

[177]S. Mariotti, *Hybrid and inorganic plumbo-halide perovskites for solar cells*. PhD Thesis, University of Liverpool (2019).

[178]A. Jesche, M. Fix, A. Kreyssig, W. R. Meier, and P. C. Canfield, X-Ray diffraction on large single crystals using a powder diffractometer. *Philosophical Magazine* **96**, 2115–2124 (2016).

[179]J. Bolze, V. Kogan, D. Beckers, and M. Fransen, High-performance small-and wide-angle X-ray scattering (SAXS/WAXS) experiments on a multi-functional laboratory goniometer platform with easily exchangeable X-ray modules. *Review of Scientific Instruments* **89**, 085115 (2018).

[180]M. Sivagami and I. Asharani, Phyto-mediated Ni/NiO NPs and their catalytic applications-a short review. *Inorganic Chemistry Communications* **145**, 110054 (2022).

[181]C. Dawedeit, *Functional foam coatings inside tubing and custom developed diamond ignition targets*. PhD Thesis, Technical University of Munich (2014).

[182]G. James, *Introduction to Nanotechnology*. Gilad James Mystery School (2023)

[183]G. Zhang, L. Ernst, and O. de Saint Leger, *Benefiting from Thermal and Mechanical Simulation in Micro-Electronics*. Springer US (2013).

[184]J. Buffle and H. van Leeuwen, *Environmental Particles: Volume 1*. CRC Press (2019).

[185]G. Jaiswal, *Transition metal-based nonocatalysts for (de)-hydrogenation reactions*. PhD Thesis, Academy of Scientific and Innovative Research (2018).

[186]S. Cohen, *Biophotonics in Pathology: Pathology at the Crossroads*. IOS Press (2013).

[187]R. do Nascimento, O. Ferreira, A. De Paula, and V. de Oliveira Sousa Neto, *Nanomaterials Applications for Environmental Matrices: Water, Soil and Air*. Elsevier Science (2019).

[188]P. Coble, *Aquatic Organic Matter Fluorescence*. Cambridge University Press (2014).

[189]D. Svergun, M. Koch, P. Timmins, and R. May, Small Angle X-Ray and Neutron Scattering from Solutions of Biological Macromolecules. OUP Oxford (2013).

[190]G. Bracco and B. Holst, *Surface Science Techniques*. Springer Berlin Heidelberg (2013).

[191]D. Watson, *Pharmaceutical Analysis: A Textbook for Pharmacy Students and Pharmaceutical Chemists*. Churchill Livingstone Elsevier (2012).

[192]M. Sun and X. Mu, *Computational Simulation in Nanophotonics and Spectroscopy*. Springer Nature Singapore (2023).

[193]C. C. Moura, R. S. Tare, R. O. Oreffo, and S. Mahajan, Raman spectroscopy and coherent anti-Stokes Raman scattering imaging: prospective tools for monitoring skeletal

cells and skeletal regeneration. *Journal of The Royal Society Interface* **13**, 20160182 (2016).

[194]E. S. Allakhverdiev, V. V. Khabatova, B. D. Kossalbayev, E. V. Zadneprovskaya, O. V. Rodnenkov, T. V. Martynyuk, G. V. Maksimov, S. Alwasel, T. Tomo, and S. I. Allakhverdiev, Raman Spectroscopy and its Modifications Applied to Biological and Medical Research. *Cells* **11**, 386 (2022).

[195]E. C. Wellner, *Development of surface-enhanced Raman based sensors*. MSc Thesis, Western Washington University (2013).

[196]A. Schmidt-Ott, *Spark Ablation: Building Blocks for Nanotechnology*. Jenny Stanford Publishing (2019).

[197]R. R. Jones, D. C. Hooper, L. Zhang, D. Wolverson, and V. K. Valev, Raman Techniques: Fundamentals and Frontiers. *Nanoscale Research Letters* **14**, 1–34 (2019).

[198]B. Schrader, *Infrared and Raman Spectroscopy: Methods and Applications*. Wiley (2008).

[199]B. Ross and S. Gambhir, *Molecular Imaging: Principles and Practice*. Elsevier Science (2021).

[200]E. Grassi, S. P. Laptenok, L. Genchi, A. Serdaroglu, and C. Liberale, Frequency-modulation stimulated Raman scattering microscopy with an acousto-optic tunable filter. *Optics Express* **31**, 18290–18299 (2023).

[201]C. Kumar, *Nanotechnology Characterization Tools for Biosensing and Medical Diagnosis*. Springer Berlin Heidelberg (2018).

[202]K. Pang, S. Dong, Y. Zhu, X. Zhu, Q. Zhou, B. Gu, W. Jin, R. Zhang, Y. Fu, B. Yu, D. Sun, Z. Duanmu, and X. Wei, Advanced flow cytometry for biomedical applications. *Journal of Biophotonics* **16**, e202300135 (2023).

[203]M. Diem, *Quantum Mechanical Foundations of Molecular Spectroscopy*. Wiley (2021).

[204]S. Wartewig, *IR and Raman Spectroscopy: Fundamental Processing*. Wiley (2006).

[205]R. Lamb, *Monitoring and Identifying the Rhodamine 6G-Hydroxide Ion Reaction Using In-Situ, Surface-Enhanced Raman Spectroscopy*. MSc Thesis, Western Kentucky University (2020).

[206]I. T. Lucas, D. Bazin, and M. Daudon, Raman opportunities in the field of pathological calcifications. *Comptes Rendus. Chimie* **25**, 83–103 (2022).

[207]V. Kuzmin, V. Novikov, L. Y. Ustynyuk, K. Prokhorov, E. Sagitova, and G. Y. Nikolaeva, Raman spectra of polyethylene glycols: Comparative experimental and DFT study. *Journal of Molecular Structure* **1217**, 128331 (2020).

[208]A. Z. Samuel and S. Umapathy, Energy funneling and macromolecular conformational dynamics: a 2D Raman correlation study of PEG melting. *Polymer Journal* **46**, 330–336 (2014).

[209]J. M. R. Jordão, *Raman Spectroscopy in tumoral tissues*. MSc Thesis, University of Porto (2020).

[210]T. Bond, J. Morton, Z. Al-Rekabi, D. Cant, S. Davidson, and Y. Pei, Surface properties and rising velocities of pristine and weathered plastic pellets. *Environmental Science: Processes & Impacts* **24**, 794–804 (2022).

[211]V. Gurunanthanan, H. Perera, B. Dassanayake, and S. Gunathilake, Development of Fe@ MgO nanoparticles for enhancing the adsorption of methylene blue dye. In: *11th Annual Science Research Sessions 2022 (ASRS-2022) Proceedings on ""Scientific Engagement for Sustainable Futuristic Innovations". 15th November 2022. Faculty of Applied Sciences, South Eastern University of Sri Lanka, Sammanthurai, Sri Lanka*, 32 (2022).

[212]M. H. Engelhard, T. C. Droubay, and Y. Du, X-ray Photoelectron Spectroscopy Applications. In: *Encyclopedia of Spectroscopy and Spectrometry*, 716-724 (2017).

[213]A. M. Venezia, X-ray photoelectron spectroscopy (XPS) for catalysts characterization. *Catalysis Today* **77**, 359–370 (2003).

[214]D. Murzin, *Engineering Catalysis*. De Gruyter (2020).

[215]Z. Amjad and K. Demadis, *Water-Formed Deposits: Fundamentals and Mitigation Strategies*. Elsevier Science (2022).

[216]A. Lanje, S. Sharma, and R. Pode, *Functional Nanomaterial Synthesis and Charaterization Electrical, Magnetic and Optical*. Lambert Academic Publishing (2014).

[217]R. Fehrmann, A. Riisager, and M. Haumann, *Supported Ionic Liquids: Fundamentals and Applications*. Wiley (2014).

[218]The Minerals, Metals & Materials Society, *TMS 2014 143rd Annual Meeting & Exhibition, Annual Meeting Supplemental Proceedings*. Springer International Publishing (2016).

[219]A. Legras, R. Truss, C. Chaleat, and M. T. Heitzmann, A practical toolbox to overcome the multiple challenges of biocomposites extrusion. In: *Composites Australia and CRC ACS 2015 Composites Conference* (2015).

[220]T. Christensen, *Understanding Surface and Thin Film Science*. CRC Press (2022).

[221]D. Briggs, *Surface Analysis of Polymers by XPS and Static SIMS*. Cambridge University Press (1998).

[222]H. Herper, B. Brena, C. Puglia, S. Bhandary, H. Wende, O. Eriksson, and B. Sanyal, *Molecular Nanomagnets: Fundamental Understanding*. Springer Nature Singapore (2020).

[223]R. Valeev, A. Vakhrushev, A. Fedotov, and D. Petukhov, *Nanostructured Semiconductors in Porous Alumina Matrices: Modeling, Synthesis, and Properties*. Apple Academic Press (2019).

[224]G. Greczynski and L. Hultman, X-ray photoelectron spectroscopy: Towards reliable binding energy referencing. *Progress in Materials Science* **107**, 100591 (2020).

[225]D. Woodruff, *Modern Techniques of Surface Science*. Cambridge University Press (2016).

[226]N. Susha, K. Nandakumar, and S. S. Nair, Enhanced photoconductivity in CdS/betanin composite nanostructures. *RSC Advances* **8**, 11330–11337 (2018).

[227]R. Nayak, B. Ray, D. Rout, and K. Mahato, *Hydrothermal Behavior of Fiber- and Nanomaterial-Reinforced Polymer Composites*. CRC Press (2020).

[228]R. Adams, J. Comyn, and W. Wake, *Structural Adhesive Joints in Engineering*. Springer Netherlands (1997).

[229]D. Mulajkar, *S. Chand's Engineering Physics Vol-I*. S. Chand & Company Limited (2010).

[230]H. Kado, H. Ogata, Y. Haruta, M. Higuchi, M. Shimogawara, J. Kawai, Y. Adachi, C. Bertrand, and G. Uehara, The Imaging of a Magnetic Source. In: *Biological Imaging and Sensing*, 117–204 (Springer, 2004).

[231]S. M. Frolov, *Current-phase relations of Josephson junctions with ferromagnetic barriers*. PhD Thesis, University of Illinois at Urbana-Champaign (2005).

[232]G. Bartington, Sensors for low level low frequency magnetic fields. In: *IEE Colloquium on Low Level Low Frequency Magnetic Fields*, 2/1-2/9 (IET, 1994).

[233]M. Anand, *Electronic Instruments and Instrumentation Technology*. PHI Learning (2004).

[234]A. Schneider, *Quantum Sensing Experiments with Superconducting Qubits*. KIT Scientific Publishing (2021).

[235]S. Speller, *A Materials Science Guide to Superconductors: And How to Make Them Super*. OUP Oxford (2022).

[236]R. Fagaly, Superconducting quantum interference device instruments and applications. *Review of scientific instruments* **77**, 101101 (2006).

[237]R. Chaudhury, *Gateway to Condensed Matter Physics and Molecular Biophysics: Concepts and Theoretical Perspectives*. Apple Academic Press (2021).

[238]G. Papaefthymiou, *Nanomagnetism: An Interdisciplinary Approach*. CRC Press (2022).

[239]T. Gandhi, *Microelectronics Fialure Analysis Desk Reference*. ASM International (2019).

[240]G. Krylov and E. Friedman, *Single Flux Quantum Integrated Circuit Design*. Springer International Publishing (2021).

[241]A. Hajalilou, M. Tavakoli, and E. Parvini, *Magnetic Nanoparticles: Synthesis, Characterization, and Applications*. Wiley (2022).

[242]K. Richardson, *The Manufacture of High Temperature Superconducting Tapes and Films*. Universal Publishers (1999).

[243]M. Omar, *Nondestructive Testing Methods and New Applications*. IntechOpen (2012).

[244]R. C. Black and F. C. Wellstood, Measurements of Magnetism and Magnetic Properties of Matter. In: *The SQUID Handbook: Applications of SQUIDs and SQUID Systems, Volume II*, 391-440 (Wiley, 2006).

[245]G. Oliveira, Synthesis, *Macroscopic and Local Probe Characterization of $AgCrO_2$ and $CdCr_2S_4$*. PhD Thesis, University of Porto (2009).

[246]J. Schlief, Temperature optimization of the SuperParamagnetic Quantifier for comparison with standard methods. BSc Thesis, University of Twente (2017).

[247]B. Sutens, T. Swusten, K. Zhong, J. K. Jochum, M. J. Van Bael, E. V. Van der Eycken, W. Brullot, M. Bloemen, and T. Verbiest, Tunability of Size and Magnetic Moment of Iron Oxide Nanoparticles Synthesized by Forced Hydrolysis. *Materials* **9**, 554 (2016).

[248]B. Thakur, S. S. Reddy, U. Deshpande, G. Amarendra, and S. Chakravarty, Evidence of magnetism in rf magnetron sputtered deposited carbon films and investigation of its origin. *Carbon* **154**, 485–496 (2019).

[249]N. Kaur and S. Tiwari, Superparamagnetic behavior of non-interacting antiferromagnetic ferritin nanoparticles. *Journal of Physics and Chemistry of Solids* **185**, 111746 (2024).

[250]E. C. Devi and S. D. Singh, Manifestation of Magnetic Characteristics of Zinc Ferrite Nanoparticles Using the Langevin Function. *Journal of Superconductivity and Novel Magnetism* **34**, 617–622 (2021).

[251]B. Pujada, E. Sinnecker, A. Rossi, and A. Guimarães, Ferromagnetic resonance studies of cobalt-copper alloys. *Physical Review B* **64**, 184419 (2001).

[252]M. L. Schneider, C. A. Donnelly, S. E. Russek, B. Baek, M. R. Pufall, P. F. Hopkins, P. D. Dresselhaus, S. P. Benz, and W. H. Rippard, Ultralow power artificial synapses using nanotextured magnetic Josephson junctions. *Science Advances* **4**, e1701329 (2018).

[253]J. Chauhan, *Nanomaterial Volume 4*. Educreation Publishing (2019)

[254]J. Arnaudas, A. Del Moral, and C. De la Fuente, Mesoscopic Quantum Tunneling in Amorphous Magnets with Strong Random-Axis Anisotropy. In: *Nanomagnetism*, 167–178 (Springer, 1993).

[255]E. Wolf, *Nanophysics and Nanotechnology: An Introduction to Modern Concepts in Nanoscience*. Wiley (2015).

[256]R. Nazir, *Nanotechnology Applications in Environmental Engineering*. IGI Global (2018).

[257]S. C. Acharya, *Dual Beam Detection Technique to Study Magneto-Optical Kerr Effect*. MSc Thesis, Texas State University (2019).

[258]R. Vijapure, *Magnetic Ordering and Hyperfine Interactions in Magnetic Semiconducting Nanoparticles*. Ashok Yakkaldevi (2022).

[259]K. Barmak and K. Coffey, *Metallic Films for Electronic, Optical and Magnetic Applications: Structure, Processing and Properties*. Elsevier Science (2014).

[260]D. Shi, *High-Temperature Superconducting Materials Science and Engineering: New Concepts and Technology*. Elsevier Science (1995).

[261]M. Chang, Y.-J. Chang, P. Y. Chao, and Q. Yu, Exosome purification based on PEG-coated Fe_3O_4 nanoparticles. *PloS one* **13**, e0199438 (2018).

[262]J. Toniolo, A. S. Takimi, M. J. Andrade, R. Bonadiman, and C. P. Bergman, Synthesis by the solution combustion process and magnetic properties of iron oxide (Fe_3O_4 and α -Fe_2O_3) particles. *Journal of Materials Science* **42**, 4785-4791 (2007).

[263]Y. Wang, *Fundamental Elements of Applied Superconductivity in Electrical Engineering*. Wiley (2013).

[264]S. Roy, *Experimental Techniques in Magnetism and Magnetic Materials*. Cambridge University Press (2023).

[265]Z. Boekelheide and C. Dennis, Artifacts in magnetic measurements of fluid samples. *AIP Advances* **6**, 085201 (2016).

[266]J. Anker and O. Mefford, *Biomedical Applications of Magnetic Particles*. CRC Press (2020).

[267]V. Franco and B. Dodrill, *Magnetic Measurement Techniques for Materials Characterization*. Springer International Publishing (2021).

[268]S. Jaiswal, Investigation of the Dzyaloshinskii-Moriya interaction and perpendicular magnetic anisotropy in magnetic thin films and nanowires. PhD Thesis, Johannes Gutenberg University Mainz(2018).

[269]J. Suits and K. Lee, Giant Magneto-Optical Kerr Effect in EuO. *Journal of Applied Physics* **42**, 3258–3260 (1971).

[270]G. Catarina, N. M. Peres, and J. Fernández-Rossier, Magneto-optical Kerr effect in spin split two-dimensional massive Dirac materials. *2D Materials* **7**, 025011 (2020).

[271]C. Mudivarthi, *Magnetic and Structural Characterization of Fe-Ga Using Kerr Microscopy and Neutron Scattering*. PhD Thesis, University of Maryland (2010).

[272]G. Phelps, *Magneto-Optical Effects and Precision Measurement Physics: Accessing the Magnetic Faraday Effect of Polarized ^{3}He with a Triple Modulation Technique*. PhD Thesis, University of Kentucky (2014).

[273]A. Adeyeye and G. Shimon, Growth and Characterization of Magnetic Thin Film and Nanostructures. In: *Handbook of Surface Science, Volume 5*, 1–41 (Elsevier, 2015).

[274]M. Albrecht, *Magneto-optical Kerr Effect Spectroscopy Study of Ferromagnetic Metal/Organic Heterostructures*. PhD Thesis, Chemnitz University of Technology (2010).

[275]X. Wang, *High-Performance Magnetic Materials for RF/Microwave Devices and Memory Applications*. PhD Thesis, Northeastern University (2018).

[276]A. Barman and J. Sinha, *Spin Dynamics and Damping in Ferromagnetic Thin Films and Nanostructures*. Springer International Publishing (2017).

[277]M. Vázquez, *Magnetic Nano- and Microwires: Design, Synthesis, Properties and Applications*. Elsevier Science (2020).

[278]M. Buchmeier, R. Schreiber, D. Bürgler, and C. Schneider, Thickness dependence of linear and quadratic magneto-optical Kerr effects in ultrathin Fe(001) films. *Physical Review B* **79**, 064402 (2009).

[279]C. Kumar, *Surface Science Tools for Nanomaterials Characterization*. Springer Berlin Heidelberg (2015).

[280]E. Meyer, R. Bennewitz, and H. Hug, *Scanning Probe Microscopy: The Lab on a Tip*. Springer International Publishing (2021).

[281]P. Ares, M. Jaafar, A. Gil, J. Gómez-Herrero, and A. Asenjo, Magnetic Force Microscopy in Liquids. *Small* **11**, 4731–4736 (2015).

[282]L. Abelmann, Magnetic Force Microscopy. In: *Encyclopedia of Spectroscopy and Spectrometry*, 675–684 (Academic Press, Oxford, 2017).

[283]Y. Dahman, *Nanotechnology and Functional Materials for Engineers*. Elsevier Science (2017).

[284]H. Nalwa, *Handbook of Thin Films*. Elsevier Science (2001).

[285]O. Kazakova, R. Puttock, C. Barton, H. Corte-León, M. Jaafar, V. Neu, and A. Asenjo, Frontiers of magnetic force microscopy. *Journal of applied Physics* **125**, 060901 (2019).

[286]I. Horcas, R. Fernández, J. Gomez-Rodriguez, J. Colchero, J. Gómez-Herrero, and A. Baro, WSXM: A software for scanning probe microscopy and a tool for nanotechnology. *Review of Scientific Instruments* **78**, 013705 (2007).

[287]D. Kouzoudis, G. Samourgkanidis, A. Kolokithas-Ntoukas, G. Zoppellaro, and K. Spiliotopoulos, Magnetic Hyperthermia in the 400–1,100 kHz Frequency Range Using MIONs of Condensed Colloidal Nanocrystal Clusters. *Frontiers in Materials* **8**, 638019 (2021).

[288]S. C. Freitas, J. H. Belo, A. Granja, M. Canhota, A. S. Silva, S. Reis, H. Crespo, J. P. Araújo, and C. T. Sousa, Key Parameters in Phototherapy with Gold Nanorods Using Continuous Near Infrared Radiation. *Advanced Materials Interfaces* **10**, 2202214 (2023).

[289]R. Wildeboer, P. Southern, and Q. Pankhurst, On the reliable measurement of specific absorption rates and intrinsic loss parameters in magnetic hyperthermia materials. *Journal of Physics D: Applied Physics* **47**, 495003 (2014).

[290]H. L. Ring, A. Sharma, R. Ivkov, and J. C. Bischof, The impact of data selection and fitting on SAR estimation for magnetic nanoparticle heating. *International Journal of Hyperthermia* **37**, 100–107 (2020).

[291]M. J. Donahue and D. G. Porter, *OOMMF User's Guide, version 1.0*. National Institute of Standards (1999).

[292]T. Shinjo, *Nanomagnetism and Spintronics*. Elsevier Science (2013).

[293]M. Lonsky, M. Lang, S. Holt, S. A. Pathak, R. Klause, T.-H. Lo, M. Beg, A. Hoffmann, and H. Fangohr, Developing computational skills through simulation based problem-solving in science. *arXiv* **2303**, 01784 (2023).

[294]Y. Zhou, *Spin-dependent Electron Transport in Nanomagnetic Thin Film Devices*. PhD thesis, University of Plymouth (2011).

[295]F. Ahmadi, M. J. Donahue, Y. Sozer, and I. Tsukerman, Micromagnetic study of soft magnetic nanowires. *AIP Advances* **9**, 125047 (2019).

[296]J. Leliaert and J. Mulkers, Tomorrow's micromagnetic simulations. *Journal of Applied Physics* **125**, 180901 (2019).

[297]D. Chernyshenko and H. Fangohr, Computing the demagnetizing tensor for finite difference micromagnetic simulations via numerical integration. *Journal of Magnetism and Magnetic Materials* **381**, 440–445 (2015).

[298]J. W. K los, D. Kumar, J. Romero-Vivas, H. Fangohr, M. Franchin, M. Krawczyk, and A. Barman, Effect of magnetization pinning on the spectrum of spin waves in magnonic antidot waveguides. *Physical Review B* **86**, 184433 (2012).

[299]N. Bäckström, J. Löfgren, and V. Rydén, *Study of Magnetic Nanostructures using Micromagnetic Simulations and Monte Carlo Methods*. BSc Thesis, Uppsala University (2014).

[300]M. A. Frantiu, *Micromagnetic Simulations of Magnetic Thin Films using MuMax^3*. BSc Thesis, University of Groningen (2019).

[301]Y. Liu, *Spin Waves in Magnetic Insulators: Electrical Control of Damping and Low Dissipative Transmission*. PhD Thesis, University of California, Los Angeles (2021).

[302]A. Vansteenkiste, J. Leliaert, M. Dvornik, M. Helsen, F. Garcia-Sanchez, and B. Van Waeyenberge, The design and verification of MuMax^3. *AIP Advances* **4**, 107133 (2014).

[303]L. Peixoto, C. Sousa, D. Navas, and J. Araújo, Micromagnetic study of the vortex state in sub-micron iron discs. In: *EPJ Web of Conferences, Volume 233*, 05002 (EDP Sciences, 2020).

[304]S. Li, J. Xia, L. Shen, X. Zhang, M. Ezawa, and Y. Zhou, Mutual conversion between a magnetic Néel hopfion and a Néel toron*. Physical Review B* **105**, 174407 (2022).

[305]H. Belrhazi and M. E. Hafidi, An alternative numerical method to study spin transfer-induced magnetic reversals in nanopillar devices with non-zero damping. *Physica B: Condensed Matter* **648**, 414441 (2023).

[306]N. Dao, S. Homer, and S. L. Whittenburg, Micromagnetics simulation of nanoshaped iron elements: Comparison with experiment. *Journal of Applied Physics* **86**, 3262–3264 (1999).

[307]Y. P. Ivanov, M. Vázquez, and O. Chubykalo-Fesenko, Magnetic reversal modes in cylindrical nanowires. *Journal of Physics D: Applied Physics* **46**, 485001 (2013).

[308]T. Gilbert, A phenomenological theory of damping in ferromagnetic materials. *IEEE Transactions on Magnetics* **40**, 3443 (2004).

[309]M. Farle, Ferromagnetic resonance of ultrathin metallic layers. *Reports on Progress in Physics* **61**, 755–826 (1998).

[310]A. Brataas, A. D. Kent, and H. Ohno, Current-induced torques in magnetic materials. *Nature Materials* **11**, 372 (2012).

[311]T. Weindler, H. G. Bauer, R. Islinger, B. Boehm, J.-Y. Chauleau, and C. H. Back, Magnetic Damping: Domain Wall Dynamics versus Local Ferromagnetic Resonance. *Physical Review Letters* **113**, 237204 (2014).

[312]A. V. Chumak, V. I. Vasyuchka, A. A. Serga, and B. Hillebrands, Magnon spintronics. *Nature Physics* **11**, 453 (2015).

[313]A. Baker, M. Beg, G. Ashton, M. Albert, D. Chernyshenko, W. Wang, S. Zhang, M.-A. Bisotti, M. Franchin, C. L. Hu, R. Stamps, T. Hesjedal, and H. Fangohr, Proposal of a micromagnetic standard problem for ferromagnetic resonance simulations. *Journal of Magnetism and Magnetic Materials* **421**, 428–439 (2017).

[314]S. Foerster, V. Desilvestro, L. J. Hathaway, C. L. Althaus, and M. Unemo, A new rapid resazurin-based microdilution assay for antimicrobial susceptibility testing of *Neisseria gonorrhoeae*. *Journal of Antimicrobial Chemotherapy* **72**, 1961–1968 (2017).

[315]J. S. Uzarski, M. D. DiVito, J. A. Wertheim, and W. M. Miller, Essential design considerations for the resazurin reduction assay to noninvasively quantify cell expansion within perfused extracellular matrix scaffolds. *Biomaterials* **129**, 163–175 (2017).

[316]C. Almeida, B. Bottazzi, K. Lawlor, and D. De Nardo, *Immunomodulation of Innate Immune Cells*. Frontiers Media SA (2020).

[317]I. Osaka and P. S. Hefty, Simple Resazurin-Based Microplate Assay for Measuring Chlamydia Infections. *Antimicrobial Agents and Chemotherapy* **57**, 2838–2840 (2013).

[318]B. Vieira-da-Silva and M. A. Castanho, Resazurin Reduction-Based Assays Revisited: Guidelines for Accurate Reporting of Relative Differences on Metabolic Status. *Molecules* **28**, 2283 (2023).

[319]C. Mancusi, *Identification of novel therapeutic approaches for the treatment of tumours characterised by mutations in the Retinoblastoma tumour suppressor gene (RB1)*. PhD Thesis, University College London (2021).

[320]D. H. M. Dam, *Aptamer-loaded Gold Nanoconstructs for Targeted Cancer Therapy*. PhD Thesis, Northwestern University (2014).

[321]A. Sharipova, R. E. Unger, A. Sosnik, and E. Gutmanas, Dense drug-eluting biodegradable Fe-Ag nanocomposites. *Materials & Design* **204**, 109660 (2021).

[322]A. Panchal, L. T. Swientoniewski, M. Omarova, T. Yu, D. Zhang, D. A. Blake, V. John, and Y. M. Lvov, Bacterial proliferation on clay nanotube pickering emulsions for oil spill bioremediation. *Colloids and Surfaces B: Biointerfaces* **164**, 27–33 (2018).

[323]J. K. Magtaan, B. Fitzpatrick, and R. Murphy, Elucidating the Biological Activity of Fish-Derived Collagen and Gelatine Hydrolysates using Animal Cell Culture - A Review. *Current Pharmaceutical Design* **27**, 1365–1381 (2021).

[324]S. Sharma and Y. Javed, *Magnetic Nanoheterostructures: Diagnostic, Imaging and Treatment*. Springer International Publishing (2020).

[325]E. Stanzani, *Molecular mechanisms underlying radioresistance of glioblastoma initiating cells*. PhD Thesis, University of Barcelona (2016).

[326]M. Ormerod, Flow Cytometry: A Practical Approach. OUP Oxford (2000).

[327]P. Quirke, Introduction to Flow Cytometry. *Journal of Clinical Pathology* **45**, 275 (1992).

[328]L. G. Nguyen, *Cytotoxicity of eluates from denture base materials*. MSc thesis, University of Bergen (2015).

[329]M. Leach, M. Drummond, and A. Doig, *Practical Flow Cytometry in Haematology Diagnosis*. Wiley (2013).

[330]E. Combrier, P. Métézeau, X. Ronot, H. Gachelin, and M. Adolphe, Flow cytometric assessment of cell viability: a multifaceted analysis. *Cytotechnology* **2**, 27–37 (1989).

[331]A. Macheta, K. Radko, S. Szymczyk, and M. Podhorecka, The technique of flow cytometry in diagnostic research. *Advances in Science and Technology. Research Journal* **7,** 55--59 (2013).

[332]G. Ozbay and M. Jackson, Flow cytometry application in marine phytoplankton study: a case study investigating effects of formalin preservation on phytoplankton count and cell integrity. *Journal of Biotech Research* **2**, 79 (2010).

[333]A. Vembadi, A. Menachery, and M. A. Qasaimeh, Cell Cytometry: Review and Perspective on Biotechnological Advances. *Frontiers in Bioengineering and Biotechnology* **7**, 147 (2019).

[334]M. Kamioka, Y. Goto, K. Nakamura, Y. Yokoi, R. Sugimoto, S. Ohira, Y. Kurashima, S. Umemoto, S. Sato, J. Kunisawa, Y. Takahashi, S. E. Domino, J.-C. Renauld, S. Nakae, Y. Iwakura, P. B. Ernst, T. Ayabe, and H. Kiyono, Intestinal commensal microbiota and cytokines regulate Fut2^{+} Paneth cells for gut defense. *Proceedings of the National Academy of Sciences* **119**, e2115230119 (2022).

[335]A. Andrievski and R. C. Wilkins, The response of gamma-H2AX in human lymphocytes and lymphocytes subsets measured in whole blood cultures*. International Journal of Radiation Biology* **85**, 369–376 (2009).

[336]B. Biosciences, *FACSymphony™ A1 Flow Cytometer User's Guide*. BD Biosciences (2021).

4. Superparamagnetic Iron Oxide Nanoparticles and Nanostructured Lipid Carriers

4.1. Introduction

In this chapter, the characterization of the produced nanostructured lipid carriers (NLCs) formulations and superparamagnetic iron oxide nanoparticles (SPIONs) is addressed in detail, focusing on critical aspects such as size, stability, storage stability, and biocompatibility. Moreover, the morphological and structural characterization of such nanomaterials is presented. Additionally, the thermal stability and pH-sensitivity of the formulations, as well as their doxorubicin (DOX) release as a result of external stimuli, i.e. pH, temperature, and alternating magnetic field (AMF), are also assessed. Furthermore, the magnetic properties and specific heat absorption rate (SAR) of both SPIONs and NLCs are analysed.

The SPIONs used in this work were fabricated using a microwave-assisted co-precipitation technique, already optimized by the LAQV-REQUIMTE group. On the other hand, the NLCs were produced through a hot ultrasonication method optimized by [1]. That author performed an experimental optimization of the NLCs' manufacturing parameters through a univariate methodology, by varying the solid lipid, pH, and surfactant quantity. Based on the obtained results, it was implemented a response surface methodology (RSM), using a central composite design, to evaluate if the experimental set followed a multivariate mathematical model, to optimize the fabrication parameters. In this analysis, the size and encapsulation efficiency (EE) were the considered dependent variables, while the most important independent variables (as assessed by the preliminary assays) were the pH and surfactant amount. This optimization process led to the development of two NLCs formulations, which differed concerning the solid lipid [gelucire 43/01 (GEL) or cetyl palmitate (PAL)], presenting adequate parameters, i.e. stability for at least 30 days, a DOX encapsulation rate over 65%, a loading capacity (LC) > 2 %, a diameter of ~ 300 nm, and a polydispersity index (PDI) < 0.2, for the pretended biomedical application. As a result, these two formulations were the ones produced (section 3.2.2.) and studied in this work.

4.2. Size and Size Distribution

Using dynamic light scattering (DLS) the mean hydrodynamic diameter of the produced NLCs was analysed and the obtained results are presented in figure 4.1.

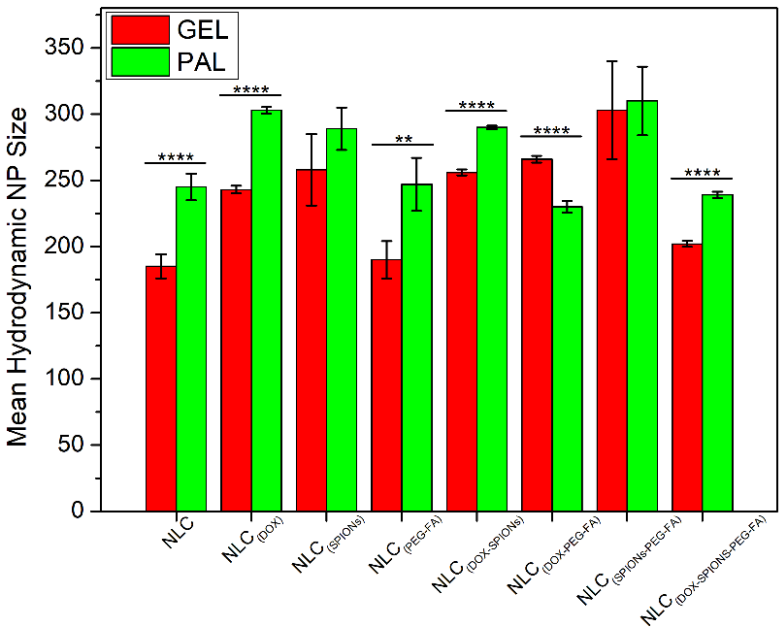

Figure 4.1 - The mean hydrodynamic nanoparticle (NP) size in the different produced formulations measured using DLS. [DOX] = 2000 µg/mL; [SPIONs] = 12000 µg/mL. Asterisks in bars indicate the statistical significance between the tested conditions (*P ≤ 0.05; **P ≤ 0.01; ***P ≤ 0.001; ****P ≤ 0.0001).

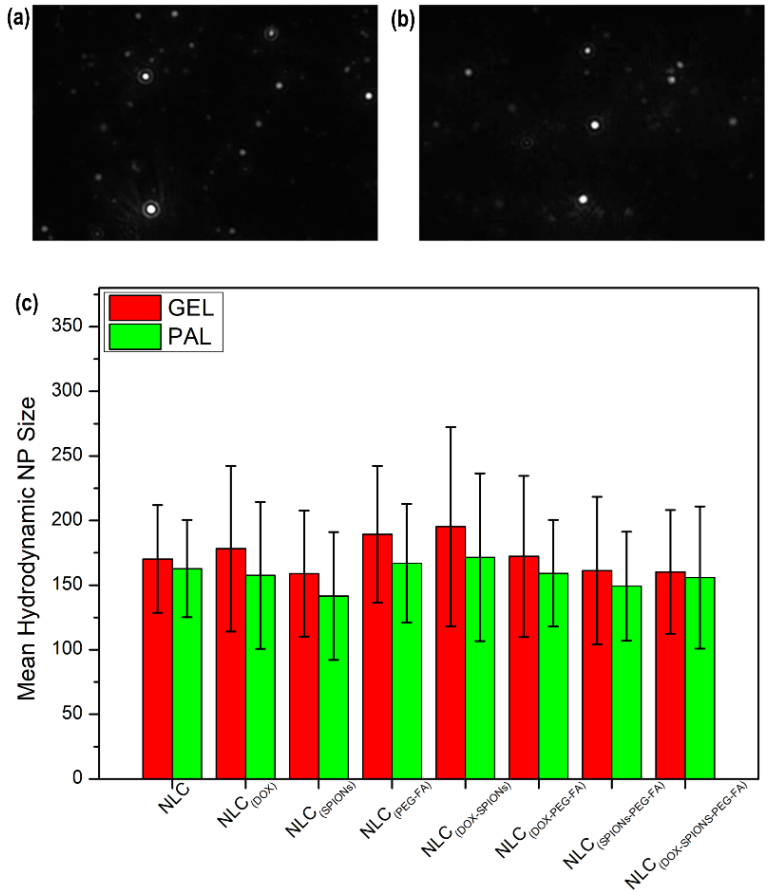

Figure 4.2 - (a, b) NTA video frame of an $NLC_{(DOX\text{-}SPIONs)}$ formulation with (a) GEL and (b) PAL. [DOX] = 2000 µg/mL, [SPIONs] = 12000 µg/mL; (c) The mean hydrodynamic NP size in the different produced formulations measured using NTA. [DOX] = 2000 µg/mL; [SPIONs] = 2000 µg/mL. Asterisks in bars indicate the statistical significance between the tested conditions (*P ≤ 0.05; **P ≤ 0.01; ***P ≤ 0.001; ****P ≤ 0.0001).

As can be observed, when considering DLS, the hydrodynamic diameter of the produced NLCs was in the range of 185 nm to 310 nm, depending on the formulation. This makes them suitable as carriers for chemotherapeutic agents, since it has been reported that, for an increased uptake by the cancer cells, the NLCs' diameter should range between 50 and 300 nm.[2] On the other hand, when using nanoparticle tracking analysis (NTA), similar NP sizes were observed for both GEL and PAL-based NLCs formulations (figure 4.2). Additionally, no large particle aggregations were detected in the videos, suggesting that the nanoparticles (NPs) possess high stability.

Comparing the two techniques, it is possible to verify that lower mean hydrodynamic sizes were measured through NTA than by DLS. On the other hand, a significantly higher standard deviation was obtained when using NTA to measure the mean hydrodynamic size of the NLCs. This result can be attributed to the fact that the intensity of scattered light in DLS is directly proportional to the sixth power of the particle diameter. Such aspect makes that technique particularly sensitive to the existence of large particles in the sample, which represents a significant limitation for precise size determination.[3] In contrast, NTA relies on tracking individual particles and it is expected to be more accurate and reliable, since it has a lower sensitivity to the presence of a small number of large NPs.[3,4] Regarding standard deviation, DLS provides an ensemble average over a larger number of particles (2 - 4 orders of magnitude more particles), contributing to a more stable and reliable statistical representation, leading to a lower standard deviation.[5,6]

The NLCs' size as a function of the DOX and SPIONs concentration was also analysed for the $NLC_{(DOX\text{-}SPIONs)}$ formulations (figure 4.3), to examine if there was a synergistic effect between them that would affect the NP size.

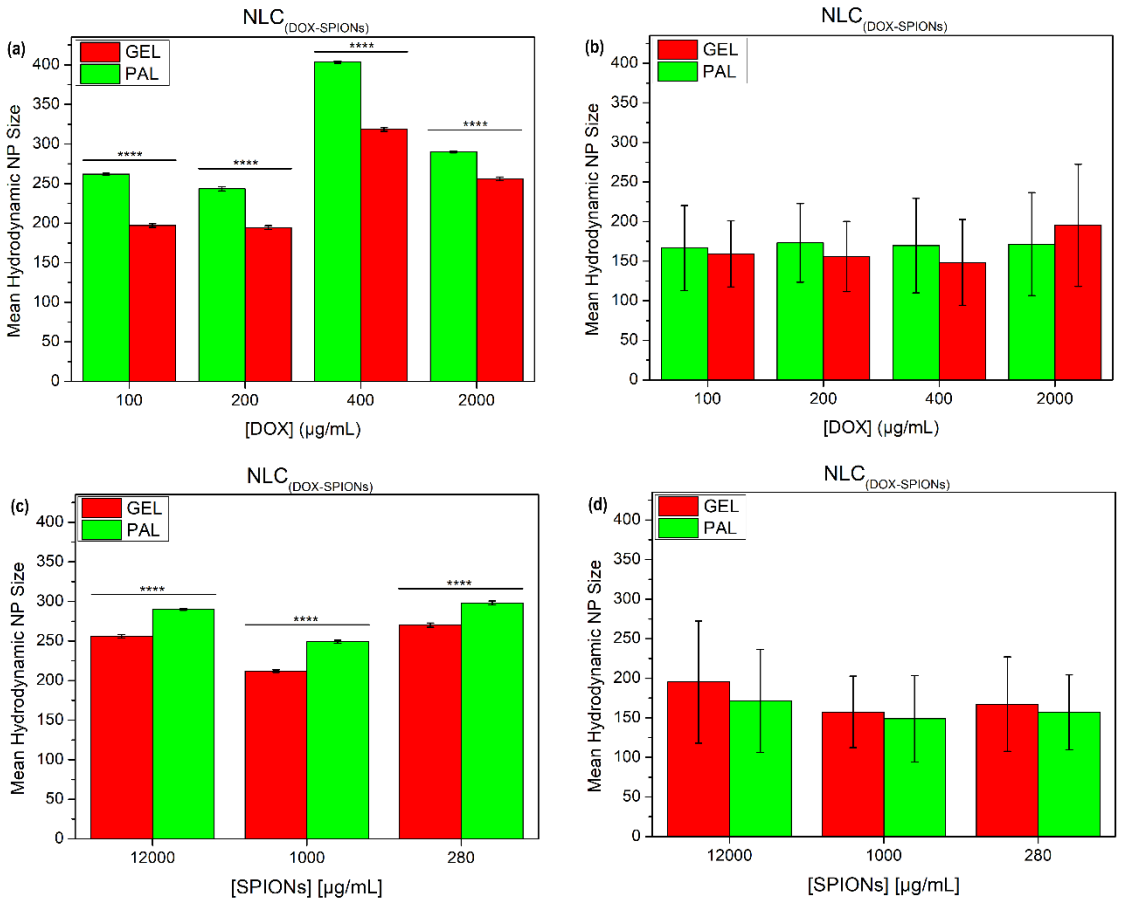

Figure 4.3 - The mean hydrodynamic NP size in the fabricated $NLC_{(DOX\text{-}SPIONs)}$ formulations measured through (a, c) DLS and (b, d) NTA, as a function of the (a, b) DOX and (c, d) SPIONs concentration. Asterisks in bars indicate the statistical significance between the tested conditions (*P ≤ 0.05; **P ≤ 0.01; ***P ≤ 0.001; ****P ≤ 0.0001).

From the analysis of figure 4.3, it is possible to conclude that there is no significant relationship between the concentration of DOX or SPIONs and the mean hydrodynamic NP size, since the concentration of those two constituents is relatively low.

Additionally, to gain a better understanding of the particles' size distribution and the respective contributions of each population to the overall concentration, three parameters were derived from the NTA data, namely the mode, representing the most frequent particle size; D50, which is the size below which 50% of the particles are contained; and D90, denoting the size below which 90% of the particles are included (figure 4.4).

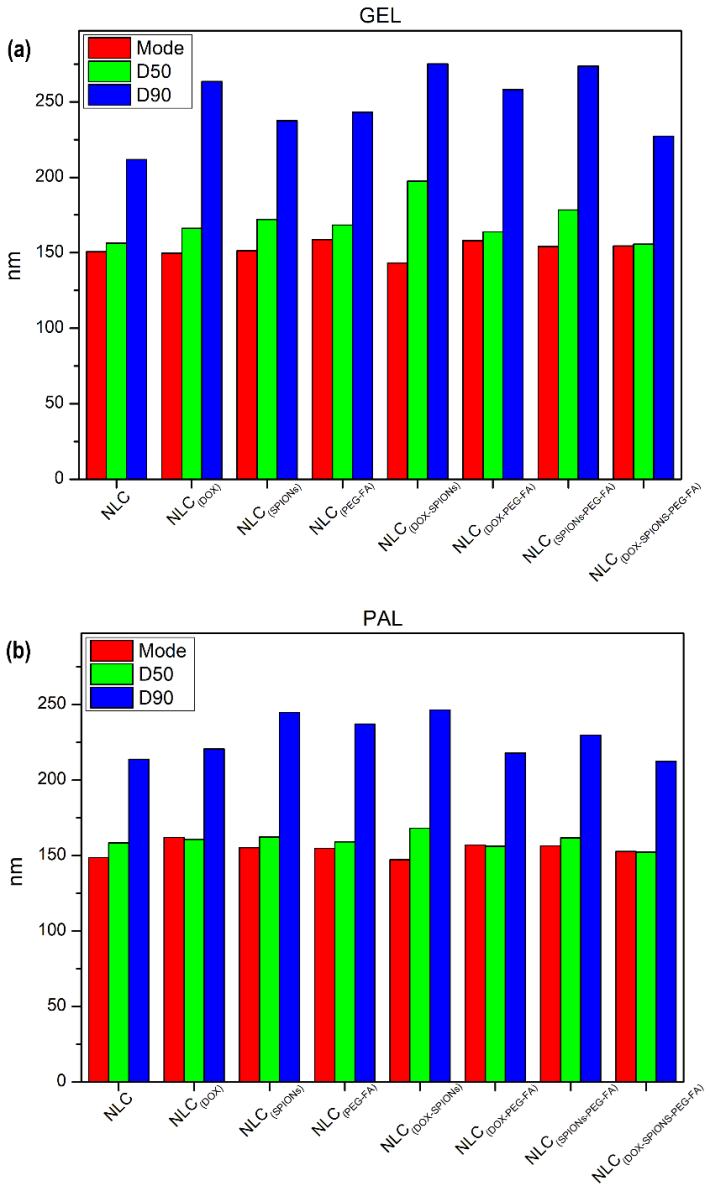

Figure 4.4 - The mode, D50, and D90 of the produced NLCs formulations considering (a) GEL and (b) PAL as the solid lipid.

Across all samples, it is evident that the majority of NPs possess sizes below 200 nm in all formulations. Additionally, every D90 value was consistently below 300 nm, falling within the optimal diameter range for uptake by cancer cells.[2]

Furthermore, using DLS, the PDI of the synthesized formulations was studied as well and the obtained results are presented in figure 4.5.

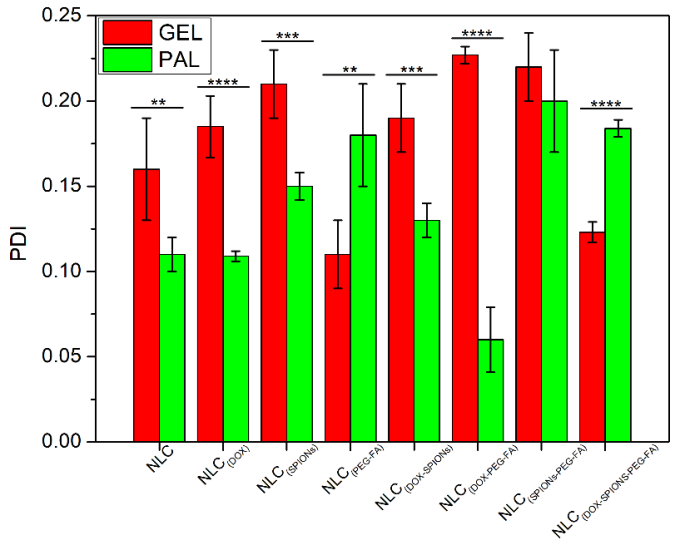

Figure 4.5 - The PDI on the fabricated NLC formulations. [DOX] = 2000 µg/mL; [SPIONs] = 12000 µg/mL. Asterisks in bars indicate the statistical significance between the tested conditions (*P ≤ 0.05; **P ≤ 0.01; ***P ≤ 0.001; ****P ≤ 0.0001).

As can be noted, for all the formulations a PDI lower than 0.25 was obtained, which, according to the literature, indicates that the NPs are relatively homogeneous with a narrow size distribution.[7,8] Additionally, these values point to a uniform functionalization process. Moreover, the GEL-based NLCs formulations typically exhibit a slightly larger PDI than those based on PAL.

4.3. Stability

The stability of the fabricated NLCs formulations was assessed through their zeta potential (figures 4.6 and 4.7).

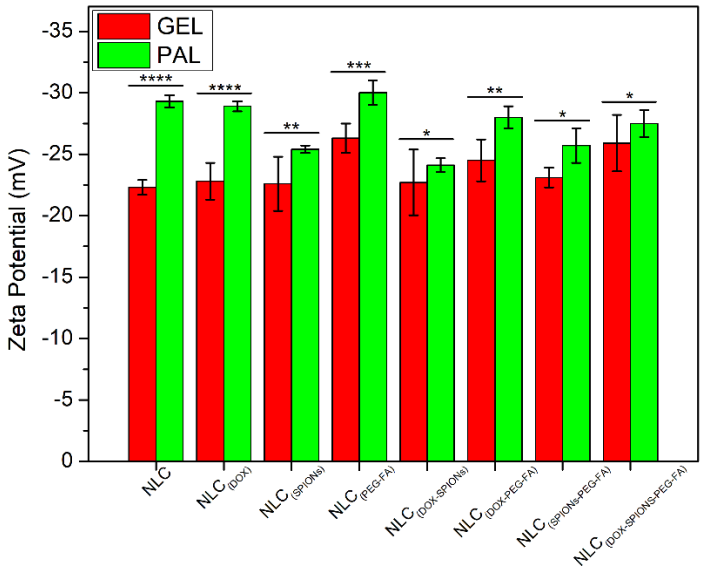

Figure 4.6 - The zeta potential of the fabricated NLC formulations. [DOX] = 2000 µg/mL; [SPIONs] = 12000 µg/mL. Asterisks in bars indicate the statistical significance between the tested conditions (*P ≤ 0.05; **P ≤ 0.01; ***P ≤ 0.001; ****P ≤ 0.0001).

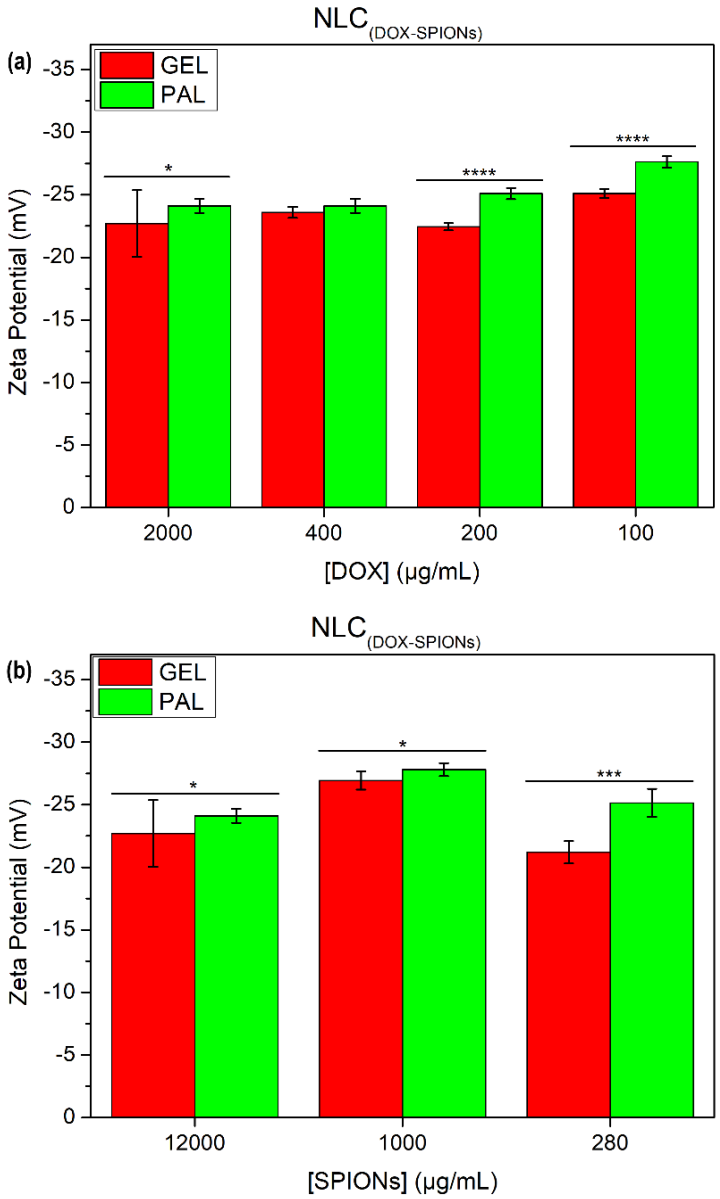

Figure 4.7 - The zeta potential of the fabricated $NLC_{(DOX\text{-}SPIONs)}$ formulations as a function of the (a) DOX and (b) SPIONs concentration. Asterisks in bars indicate the statistical significance between the tested conditions (*P ≤ 0.05; **P ≤ 0.01; ***P ≤ 0.001; ****P ≤ 0.0001).

From the presented results, it is possible to verify that the zeta potential of all the analysed NLCs was not only lower than -20 mV, but also independent of the DOX or SPIONs concentration, indicating that they are relatively stable.[9] Additionally, the PAL-based NLCs presented a slightly higher zeta potential in comparison to the GEL-based ones. Nevertheless, it is accepted that particle aggregation or flocculation is prevented when the zeta potential is < |20| mV, especially for NPs modified with a steric stabilization agent, such as polyethylene glycol (PEG), polysorbate 80 (Tween® 80), or oleic acid.[9–13]

Moreover, a negative zeta potential indicates that the analysed NPs have a negative charge, which may be attributed to the presence of ionized oleic acid in the formulation

composition.[14] This aspect suggests that the synthesized NLCs are suitable for biomedical applications since it has been reported that negatively charged particles exhibit a lower cytotoxicity compared to cationic particles, which are associated to increased cell membrane disruption, causing, consequently, greater cell death.[15] Furthermore, NPs with a negative charge have a higher tendency to accumulate more efficiently in tumour tissues, as they are associated with a longer blood circulation time compared to positively charged ones of a similar size.[16]

4.4. Encapsulation Efficiency (EE) and Loading Capacity (LC)

The EE and LC of the produced drug-loaded NLCs are presented in figure 4.8.

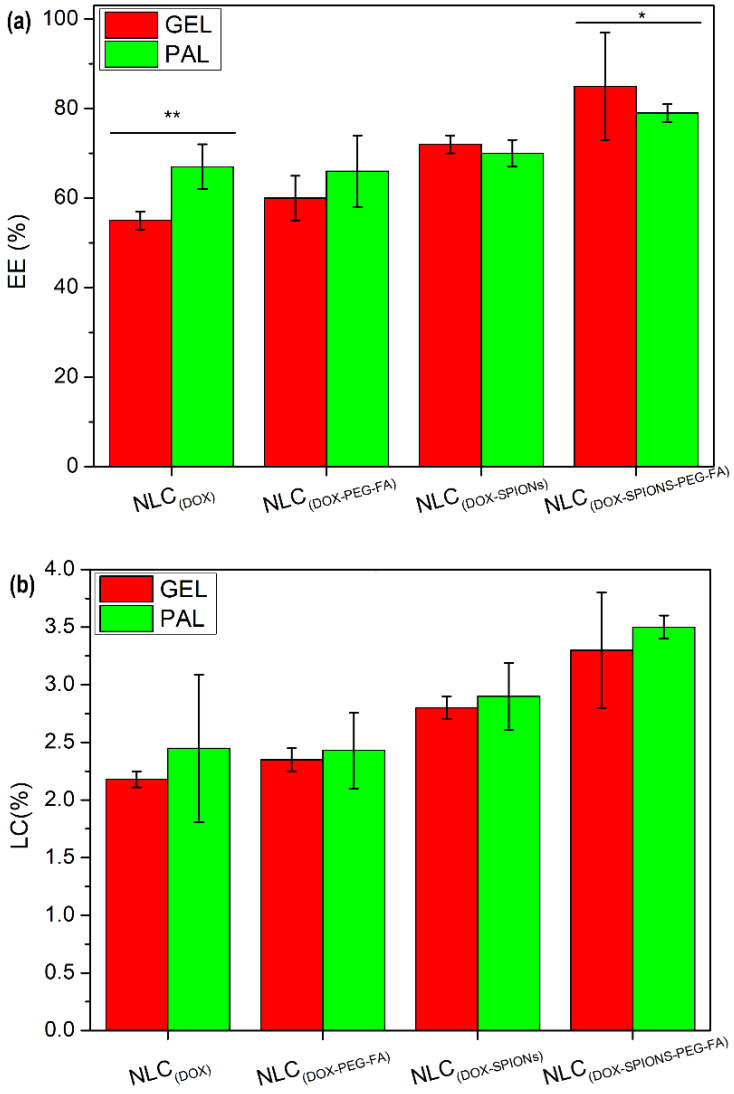

Figure 4.8 - (a) EE (%) and (b) LC (%) of the fabricated drug-loaded NLCs. Asterisks in bars indicate the statistical significance between the tested conditions (*P ≤ 0.05; **P ≤ 0.01; ***P ≤ 0.001; ****P ≤ 0.0001).

As can be observed, the used preparation methodology allows for achieving an EE of ~ 85 % and a LC of ~ 3.5 % for DOX. Moreover, minimal differences were noted in both

EE and LC values when comparing NLCs without SPIONs. On the other hand, it is possible to verify that the co-encapsulation of DOX and SPIONs promoted the DOX encapsulation, leading to higher EE (%) and LC (%). This may occur due to multiple reasons namely, SPIONs could interact synergistically with DOX or the lipid matrix of the NLCs, possibly through mechanisms like electrostatic attraction or hydrophobic interactions, which might lead to a stronger association between DOX and the NPs, resulting in higher EE and LC.[17–19] Additionally, SPIONs could contribute to the overall stability of the lipid matrix, potentially preventing premature drug release and supporting an increased encapsulation efficiency.[20] The specific mechanisms may include improved drug-lipid interactions, enhanced lipid bilayer integrity, and modifications to the particle characteristics influenced by the presence of SPIONs.[20,21]

4.5. Morphological Characterization

To analyse the morphology of the produced NLCs formulations, they were observed in suspension using transmission electron microscopy (TEM; figures 4.9 and 4.10).

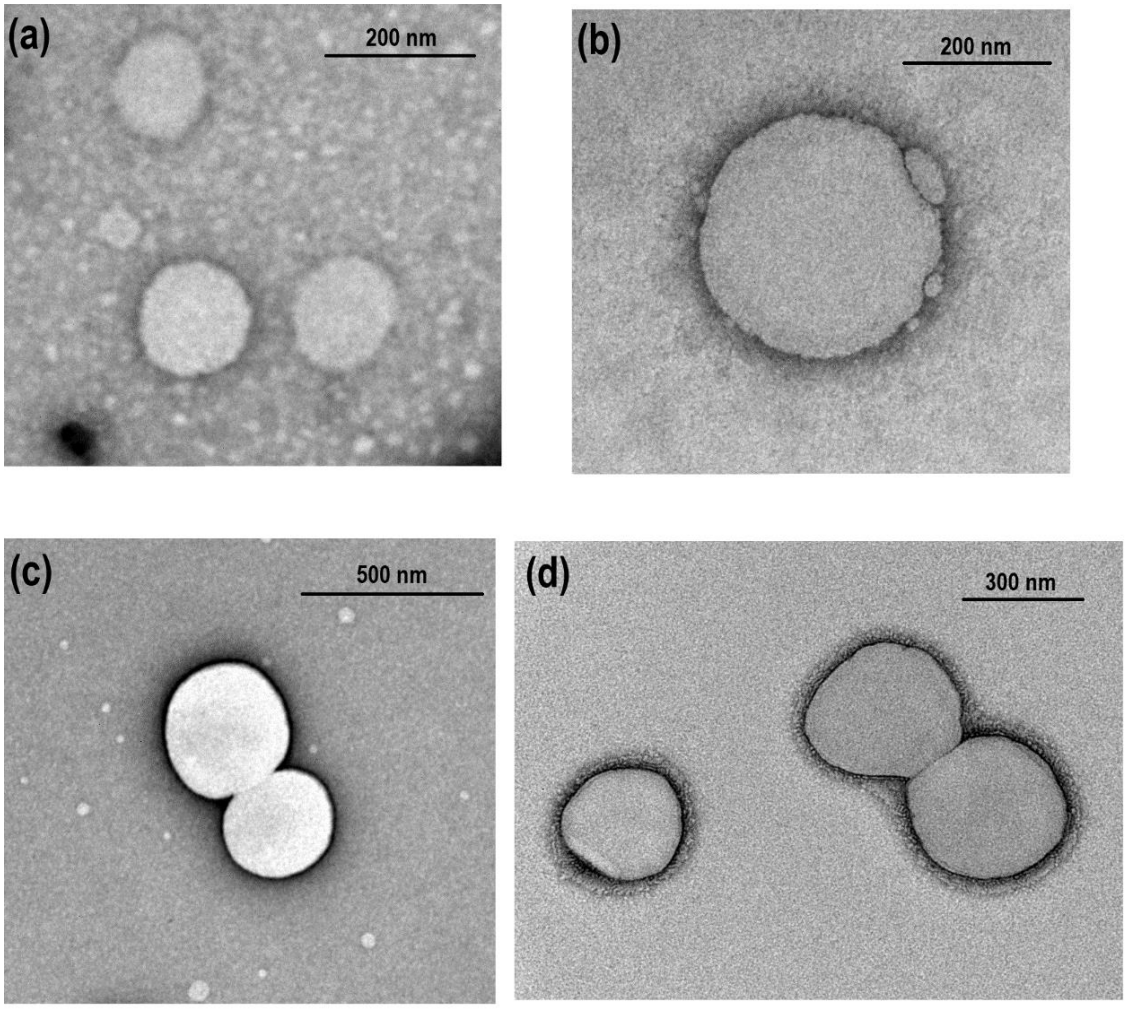

Figure 4.9 - TEM images of the (a, b) GEL-based and (c, d) PAL-based (a, c) NLC and (b, d) $NLC_{(DOX\text{-}PEG\text{-}FA)}$.

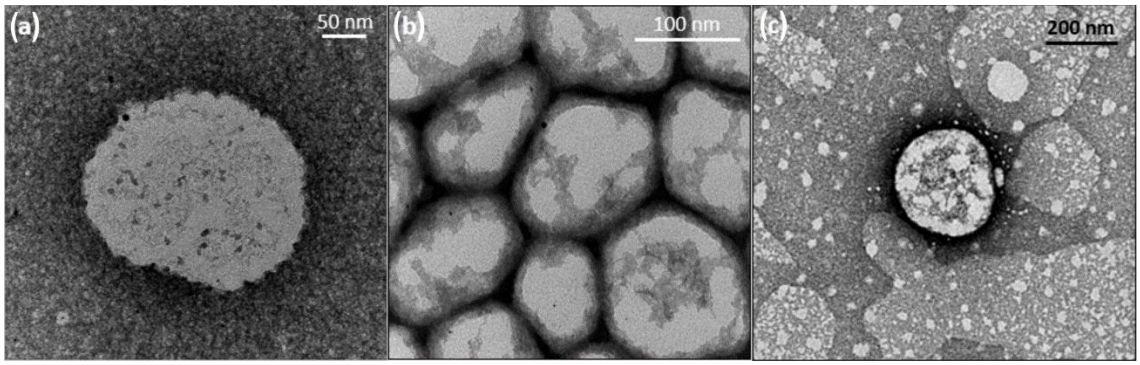

Figure 4.10 - TEM images of GEL-based (a) $NLC_{(SPIONs)}$; (b) $NLC_{(DOX\text{-}SPIONs)}$; and (c) $NLC_{(DOX\text{-}SPIONs\text{-}PEG\text{-}FA)}$.

For all the formulations, the TEM images revealed that the NLCs' had a spherical shape, which was not significantly affected by the functionalization process. Furthermore, it was verified that such NPs presented some aggregation, which could be attributed to the drying required for their analysis through this technique, modifying their behaviour. Additionally, using ImageJ, the diameters of the NLCs were analysed, having been obtained sizes slightly different to those measured through DLS or NTA. Particularly, for GEL-based NLC and $NLC_{(DOX\text{-}PEG\text{-}FA)}$ average dimensions of 146 ± 70 nm and 213 ± 81 nm (n = 6), respectively, were acquired, while mean sizes equal to 137 ± 25 nm and 151 ± 64 nm (n = 6) were obtained for PAL-based NLC and $NLC_{(DOX\text{-}PEG\text{-}FA)}$, correspondingly. On the other hand, for GEL-based formulations involving SPIONs, namely $NLC_{(SPIONs)}$, $NLC_{(DOX\text{-}SPIONs)}$, and $NLC_{(DOX\text{-}SPIONs\text{-}PEG\text{-}FA)}$, average diameters of 143 ± 79 nm, 129 ± 54 nm, and 201 ± 67 nm (n = 6), respectively, were determined through this method.

These differences can be attributed to the fact that DLS and NTA provide the mean hydrodynamic diameter of the NPs over an ensemble, while this approach allows the measurement of their average core diameter (figure 4.11), but over a much smaller sample size (~ 1-10 NPs). As a result, the reduced number of acquired images and low count of NLCs per image did not allow the execution of a statistical analysis.

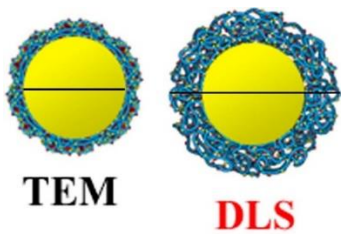

Figure 4.11 - The different diameters measured through TEM and DLS. Reprinted from [22], with permission from Elsevier.

The presence of the PEG-folic acid (FA) conjugate [figure 4.9(b, d) and figure 4.10(c)] could be detected by the existence of a distinct outline, or halo, around the NP, which is

commonly observed in pegylated functionalized surfaces.[23] On the other hand, SPIONs could not be clearly identified inside the NLCs based on the acquired images, which can be attributed to the thickness of their lipid membrane as well as to the presence of uranyl contrast agent.[24]

4.5.1. Superparamagnetic Iron Oxide Nanoparticles' (SPIONs) Size Distribution

The dimensions of the synthesized SPIONs fell below the detection limit of NTA for this type of NPs, i.e. ~ 30 nm.[25] Given this limitation and considering the DLS's high sensitivity to the existence of agglomerates, which can result from attractive van der Waals forces as well as hydrophobic and magnetic interactions between SPIONs when in suspension, the assessment of the size and size distribution of these NPs was conducted using TEM, which is known for its high resolution (~ 0.2 nm).[26,27] Subsequently, ImageJ was employed to analyse a TEM micrograph, enabling a precise measurement of the SPIONs' dimensions. This approach was selected to overcome the limitations of NTA and DLS, ensuring an accurate characterization of the produced SPIONs. The selected TEM image and respective size distribution histogram are presented in figure 4.12.

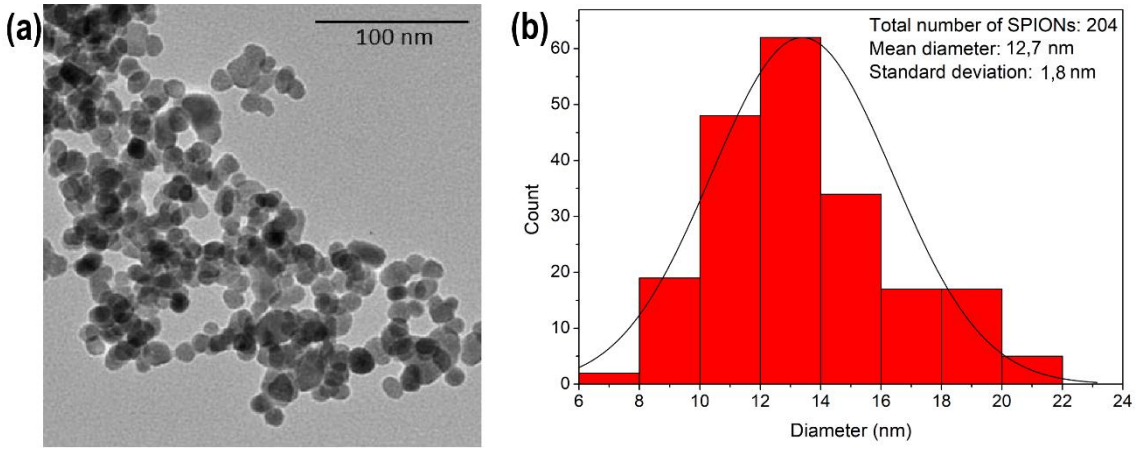

Figure 4.12 - (a) the TEM image selected for analysing the size of the SPIONs fabricated in this work and (b) the obtained size distribution histogram with a normal distribution fit.

As can be observed, the mean diameter of the produced SPIONs was 12.7 ± 1.8 nm, falling within the estimated particle size required to achieve superparamagnetism in magnetite/maghemite NPs, i.e. 20 nm.[28,29]

From the presented histogram, it is possible to verify that the synthesized SPIONs possess a moderately broad size distribution. This fact represents one of the main limitations associated with the co-precipitation synthesis method, which is its tendency to yield SPIONs with a larger standard deviation in mean size compared to alternative

methods. The motives for such poor mono-dispersity in co-precipitated SPIONs are thought to be the extremely large reactivity of Fe ions under high pH conditions, as well as the low controllability of supersaturation in a dynamic reaction environment.[30]

4.6. Structural Characterization

The structural characterization of the fabricated SPIONs and NLCs was performed using X-ray diffraction (XRD). In this context, the structure of the SPIONs was first analysed (figure 4.13).

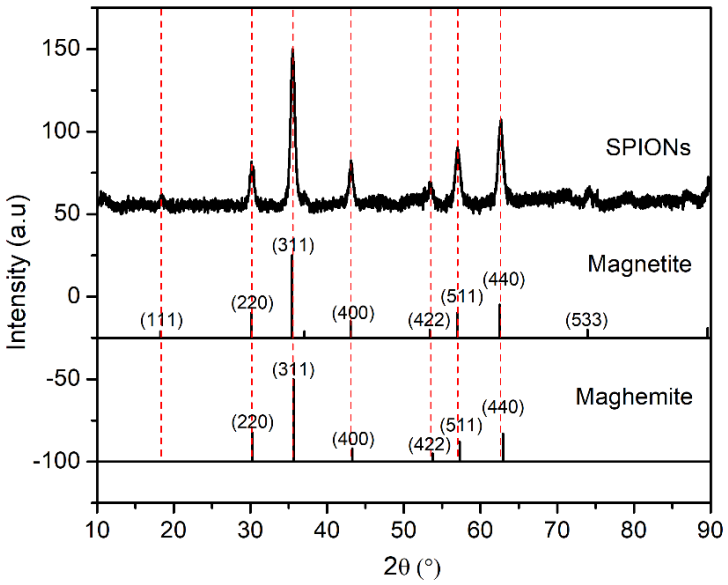

Figure 4.13 - XRD pattern of the SPIONs produced in this work.

From the obtained results, it was concluded that the resulting XRD pattern of the SPIONs corresponded to a spinel structure characteristic of magnetic Fe oxides, i.e. maghemite (γ-Fe_2O_3) and magnetite (Fe_3O_4). Particularly, the peaks located at 2θ ~ 30.1º, 35.4º, 43.1º, 53.4º, 57.1º, and 62.6º can be indexed to the (220), (311), (400), (422), (511) and (440) lattice planes of the cubic magnetite phase, correspondingly.[31] In this context, due to the similarities between the inverse spinel structure and comparable patterns at the nm scale observed in γ-Fe_2O_3 and Fe_3O_4, as illustrated in figure 4.13, the lattice parameter can be used to differentiate them. Nevertheless, alternative techniques, like extended X-ray absorption fine structure (EXAFS), Mössbauer spectroscopy, X-ray photoelectron spectroscopy (XPS), or magnetic measurements would be required to distinguish between those two Fe oxides.[32,33]

Regardless of that aspect, the mean X-ray crystallite diameter of SPIONs was determined using Scherrer's equation (Eq. 3.7), considering the peak values of the (311), (511), (440), and (220) crystallographic planes. As a result, it was obtained an average

diameter of 12.5 ± 1 nm, aligning well with the NP size derived from the TEM images of SPIONs, i.e. 13 ± 3 nm, and the dimensions of SPIONs fabricated through alternative techniques.[34]

In addition to SPIONs, NLCs were also structurally characterized through XRD (figure 4.14).

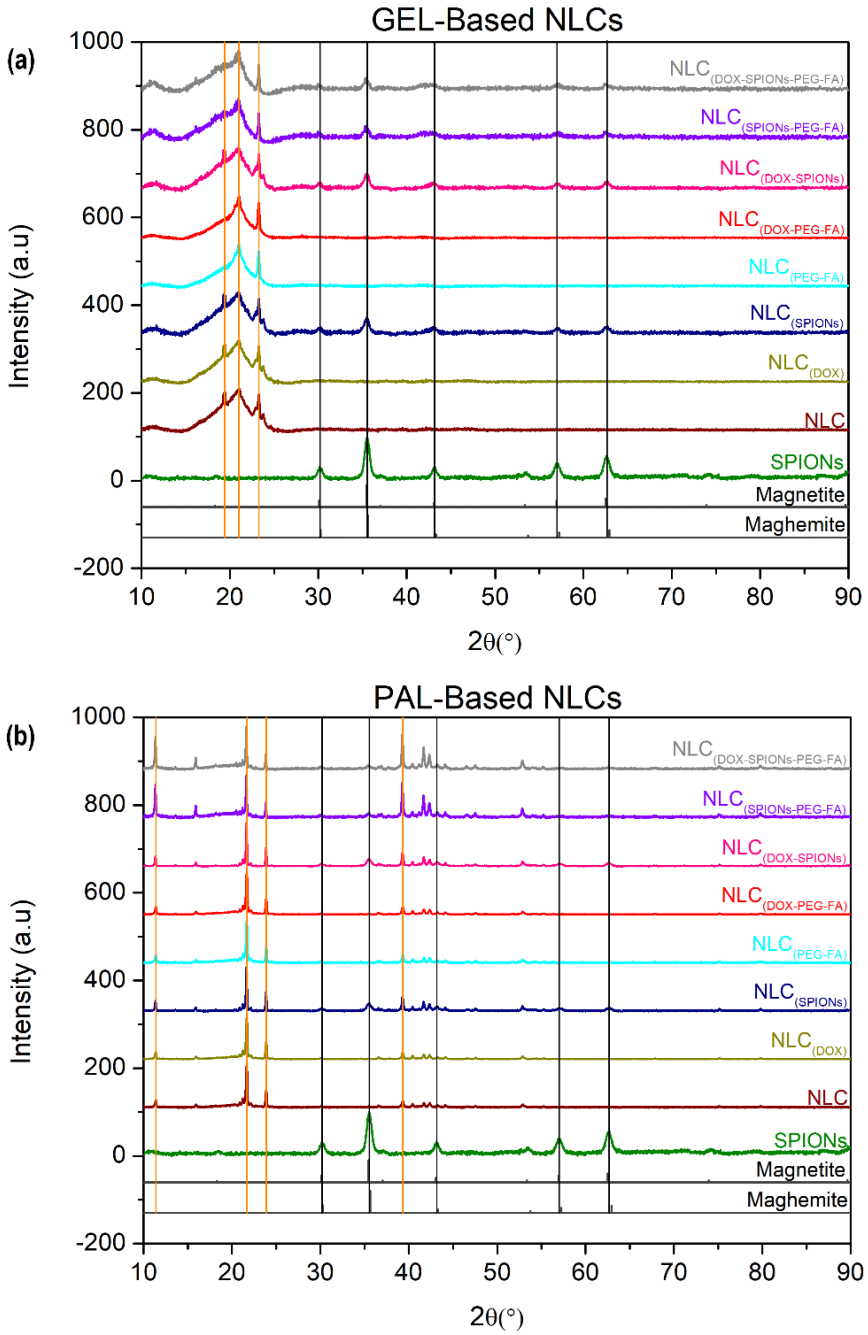

Figure 4.14 - XRD pattern of the (a) GEL-based and (b) Pal-based NLC formulations produced in this work ([DOX] = 2000 μg/mL; [SPIONs] = 12000 μg/mL). The characteristic peaks of the solid lipid and magnetite/maghemite are indicated by the orange and black lines, respectively.

As can be observed in the figure above, all the NLC formulations presented a crystalline structure. Particularly, regarding the GEL-based NLCs [figure 4.14(a)], it was possible to identify two characteristic peaks of GEL located at 2θ = 21.04º and 23.28º, which were already reported in other studies.[35–38] Additionally, when PEG-FA was present, the peak at 2θ = 19.39º, which had a low intensity in the other formulations, disappeared, suggesting that the crystalline structure of these lipid carriers was altered by this surface conjugate. Moreover, the characteristic crystalline peaks of DOX were not detected in all the analysed formulations, indicating the successful encapsulation of DOX in the NLCs, which remained in its molecular form within the lipid matrix.[39] On the other hand, it was possible to distinguish five peaks characteristic of SPIONs, for the formulations involving those nanomaterials.

Regarding PAL-based NLCs [figure 4.14(b)], it was observed a better-defined crystalline structure in comparison to the GEL-based ones. Additionally, in all the analysed formulations, characteristic peaks of PAL located at 2θ = 11.38º, 21.68º, 23.87º, and 39.31º were detected, suggesting that neither DOX nor PEG-FA modified the crystalline structure of these lipid carriers.[37,40–42] However, by comparing those peaks with crystal data of PAL, no correlation with its monoclinic structure was found, suggesting that this type of NLCs are composed of crystallites of a different modification of PAL.[43,44] Regardless of that fact, for the formulations with SPIONs, it was possible to distinguish five peaks that are characteristic of those NPs.

As a result, the XRD analysis of the produced NLCs confirmed the presence of SPIONs in all the predicted formulations. Furthermore, the characteristic peaks of the solid lipid were not altered by the presence of SPIONs and/or DOX, indicating that those two constituents do not affect the crystalline structure of the NLC shell and, consequently, do not compromise its stability. Moreover, the diffraction peaks associated with DOX were not identified in any formulation. This confirms that the drug is either dispersed in a molecular form within the lipid matrix or exists in an amorphous state, which is highly desirable for enhancing solubility and bioavailability in drug delivery systems.[45]

4.7. GEL-based vs PAL-based NLCs

To determine the most suitable type of NLCs (GEL-based or PAL-based) for the desired biomedical application, i.e. the combination of magnetic hyperthermia (MHT) with targeted anticancer drug delivery for inducing the death of cancer cells at a target site, further studies were performed. These experiments aimed at assessing the NLCs' thermal stability and pH-sensitivity, the DOX release triggered by an AMF, under conditions that mimic those found in a physiological environment, as well as their

biocompatibility in the absence of any stimulus. For such purpose, GEL-based and PAL-based NLCs loaded with DOX ([DOX] = 2000 µg/mL) and SPIONs ([SPIONs] = 12000 µg/mL) were the selected ones, since they are the most relevant for the goal of this study.

4.7.1. Thermal Stability and pH-Sensitivity

The influence of temperature (25 - 70 ºC) and pH (5 – 7.4) on the stability of the considered NLCs was evaluated by analysing the particle size through DLS (figure 4.15).

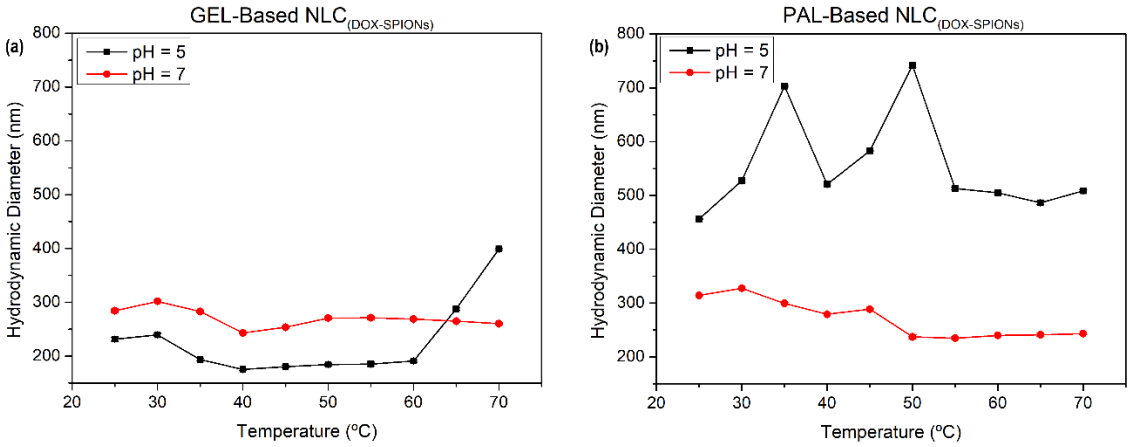

Figure 4.15 - Variation of the NLCs' hydrodynamic diameter with temperature for (a) GEL-based $NLC_{(DOX\text{-}SPIONs)}$ at pH 5 and at pH 7.4 and (b) PAL-based $_{NLC(DOX\text{-}SPIONs)}$ at pH 5 and at pH 7.4.

From the presented results, it is possible to conclude that the GEL-based NLCs and PAL-based NLCs are sensitive to the temperature, as well as to the pH of the environment. Particularly, in the pH 7.4 buffer solution [figure 4.15(a)], both types of NLCs demonstrated a good stability across the tested temperature range, despite experiencing some fluctuations in the hydrodynamic diameter, with a tendency for decreasing size with increasing temperature. On the other hand, when the NLCs were dispersed in the buffer solution with a pH of 5 [figure 4.15(b)], they exhibited an unstable behaviour, having been observed more significant differences in their hydrodynamic size as the temperature increased.

Overall, the NLCs based on PAL presented a greater hydrodynamic diameter than those based on GEL, which indicates the potential existence of particle aggregations. In contrast, NLCs based on GEL maintained a nearly constant diameter at lower temperatures but experienced a sudden increase in size at 60ºC, likely due to the thermally-induced breakdown of the lipid membrane. As a result, it was concluded that the GEL-based NLCs have a higher temperature sensitivity, which can be associated with the fusion point of the solid lipid as GEL possesses a lower fusion temperature (43 ºC) than PAL (~ 53 ºC).[46,47] This greater sensitivity to temperature is highly advantageous

for drug release systems, as it enables a control over the release of the loaded therapeutic agents, allowing a targeted and efficient delivery under specific physiological conditions.

4.7.2. pH-Triggered DOX Release

Another critical aspect, regarding the use of drug-loaded NLCs for the previously mentioned biomedical application, is the ability to not only prevent the drug release in healthy tissues, but also control its delivery to the target site, through the application of an AMF. Consequently, drug release tests from the aforementioned NLC formulations, using an AMF stimulus (556 kHz, 10 mT) for 30 min, were performed under different pH conditions, so as to simulate distinct physiological environments. The obtained results are presented in figure 4.16.

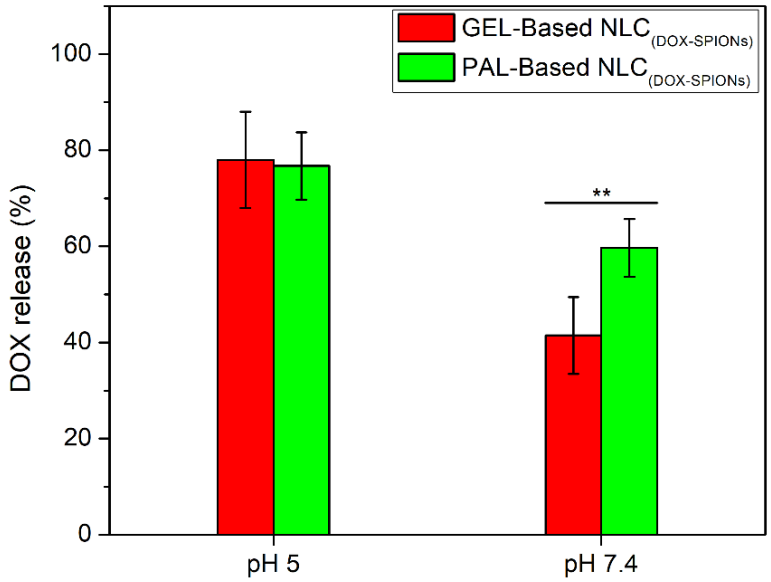

Figure 4.16 - Drug release % of GEL-based and PAL-based $NLC_{(DOX\text{-}SPIONs)}$ at pH 5 and at pH 7, when exposed to an AMF (556 kHz, 10 mT) for 30 min. Asterisks in bars indicate the statistical significance between the tested conditions (*P ≤ 0.05; **P ≤ 0.01; ***P ≤ 0.001; ****P ≤ 0.0001).

As can be observed in the figure 4.16, it was verified that, under the same conditions, the release of DOX from the two types of considered formulations increased at lower pH, which is characteristic of a tumour environment.[48]

These results suggested that the used NLCs possess an effective pH-responsive behaviour. Consequently, both formulations could be employed for AMF-triggered DOX release, as the localized heating produced by SPIONs was sufficient for facilitating the drug release process. Nevertheless, no macroscopic heating was observed through the thermal infrared camera. This indicates the existence of a ”hot spot” effect, where the nanoscopic temperature increase within the lipid carriers, caused by the localized

heating of SPIONs, that can be sufficient to promote the DOX release, as a result of their thermal sensitivity.[49,50] Furthermore, the GEL-based NLCs exhibited a lower DOX release when in an environment simulating normal physiological conditions (pH = 7.4).[51] Therefore, these NPs may be less harmful for the healthy tissues, when administered *in vivo*.

4.7.3. Temperature-Triggered DOX Release

Moreover, to estimate the local temperature within the NLCs, further drug release experiments were conducted in a water bath, utilizing identical samples, sample volumes, and dialysis procedures (figure 4.17).

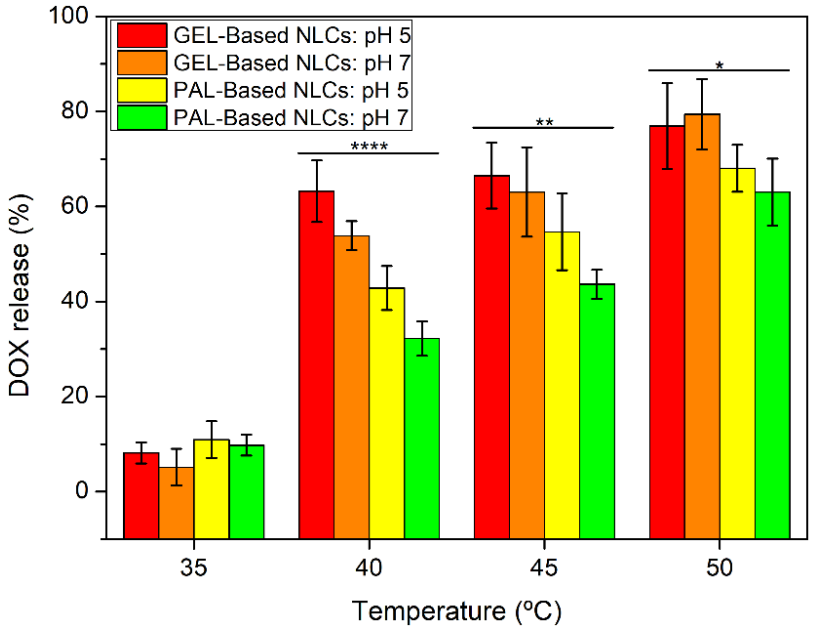

Figure 4.17 - Drug release % of GEL-based and PAL-based $NLC_{(DOX\text{-}SPIONs)}$ at pH 5 and at pH 7.4, triggered by water bath at 35, 40, 45, and 50 ºC. Asterisks in bars indicate the statistical significance between the tested conditions (*P ≤ 0.05; **P ≤ 0.01; ***P ≤ 0.001; ****P ≤ 0.0001).

By comparing the results of both assays, it is possible to conclude that, during the AMF-triggered DOX release experiments, a local temperature of up to 50 ºC, at pH 5, may have been attained inside the NLCs. On the other hand, at a pH of 7, a lower temperature was reached, indicating that the heating capacity of SPIONs was suppressed. This suggests that the pH of the external medium can affect the surface properties of the NLCs, which, in turn, may influence their interactions with SPIONs, altering the distribution and mobility of those magnetic NPs within the lipid matrix and, as a result, impacting their efficiency for generating heat when exposed to an AMF.[52-55]

Nevertheless, by comparing the results obtained for the GEL-based and PAL-based NLCs, it was possible to conclude that the first ones exhibited a greater sensitivity to the

temperature increase. This translates into a smaller DOX release at lower temperatures and a higher DOX release when the temperature in the NLC increases, allowing a more precise control over the anticancer drug release.

4.7.4. Biocompatibility

The biocompatibility of the aforementioned formulations and free DOX, in the absence of external stimuli, was evaluated on MCF-7 cells, so as to analyse the suitability of each type of NLC, for the desired biomedical application. The obtained results are presented in figure 4.18.

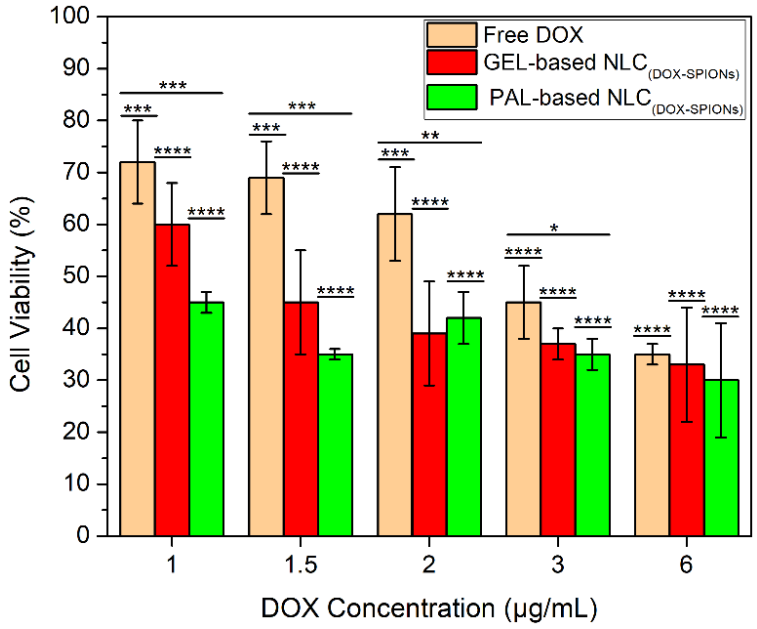

Figure 4.18 - Viability of MCF-7 cells after a 19-h incubation with free DOX, as well as with GEL-based and PAL-based $NLC_{(DOX\text{-}SPIONs)}$. Asterisks in short bars indicate statistical significance in relation to control and asterisks in long bars indicate statistical between the tested conditions (*P ≤ 0.05; **P ≤ 0.01; ***P ≤ 0.001; ****P ≤ 0.0001).

As a result, it was verified a concentration-dependent reduction in the viability of the MCF-7 cells for all the considered conditions. Particularly, as the concentration of DOX increased, the number of viable cells decreased. By comparing the various evaluated scenarios, it is possible to conclude that free DOX had the lowest cytotoxicity. On the other hand, the lipid carriers presented the highest cytotoxicity, suggesting that the DOX loaded in the NLCs together with the SPIONs, which may interfere with the drug release process, are the main reasons for the observed cell death, as NLCs are generally regarded as biocompatible.[56]

Nevertheless, the presented results indicate that the DOX uptake by the cancer cells is higher when such compound is loaded into NLCs, revealing its promising potential for targeted anticancer drug delivery. Furthermore, by comparing the results obtained for

the two types of NLCs considered, it is possible to conclude that the GEL-based ones have a slightly lower cytotoxicity, although the difference is typically within the standard deviation value.

4.7.5. Conclusion

From the results presented in the previous sections, it was concluded that the GEL-based NLCs were more suitable for the desired biomedical application, i.e. the combination of MHT with targeted anticancer drug delivery for inducing the death of cancer cells at a target site. Therefore, these were the selected NPs for the subsequent studies.

4.8. Magnetic Characterization

A fundamental aspect for using nanomaterials towards this type of biomedical application is their magnetic properties. Therefore, in this section we will address the magnetic characterization of not only the NLCs, but also the SPIONs, that was performed in this work.

4.8.1. Superparamagnetic Iron Oxide Nanoparticles

The fabricated SPIONs exhibited a magnetic behaviour in suspension that could be observed by the naked eye (figure 4.19). Particularly, before the exposure to the magnetic field, the suspension was well-dispersed, presenting a homogeneous black colour. However, after approaching a magnet to that suspension, it was possible to observe that the majority of SPIONs concentrated close to the magnet, originating a black precipitate with a nearly transparent supernatant.

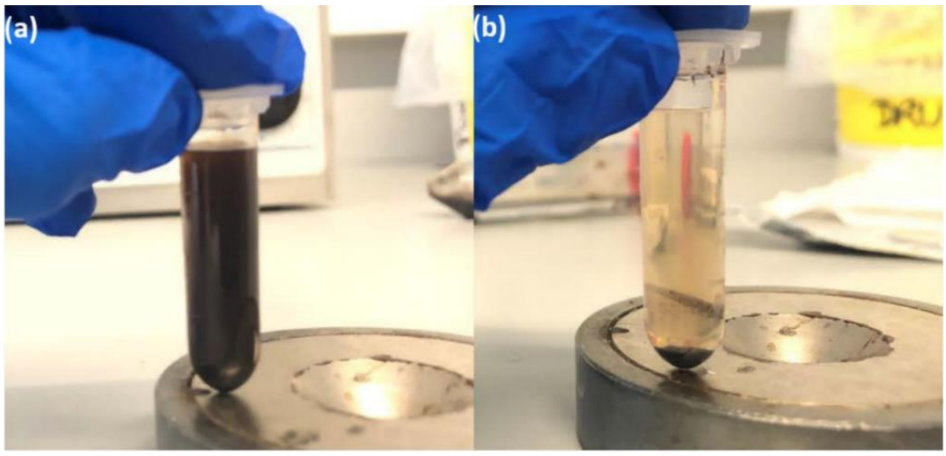

Figure 4.19 - Magnetic response of SPIONs in suspension to a magnet. (a) The SPIONs suspension prior to the magnetic field exposure; (b) the same suspension 10 s after exposure to the magnetic field.

Nevertheless, this test does not constitute a rigorous analysis of the magnetic properties of these NPs. For that purpose, the magnetic characterization of these SPIONs, in powder form, was performed by measuring their magnetic hysteresis loops at various temperatures, i.e. 5, 150, and 320 k, using a superconducting quantum interference device (SQUID). The obtained results are represented in figure 4.20.

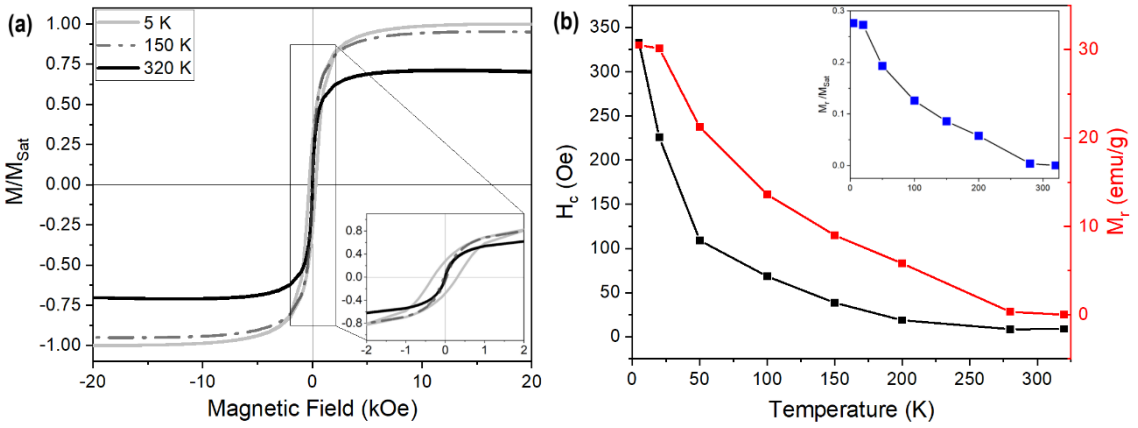

Figure 4.20 - (a) Hysteresis loops of SPIONs measured at 5, 150 and 320 K, using a SQUID. Inset: magnified view of the magnetization behaviour at lower magnetic fields. (b) Coercive field (H_c) and remanent magnetization (M_r) of SPIONs as a function of temperature. Inset: variation of the SPIONs squareness (M_r/M_{Sat}) with the temperature.

From figure 4.20(a), it is possible to verify that the SPIONs have a significantly larger coercivity (H_c) and remanent magnetization (M_r) at a temperature of 5 K, which was anticipated because, at that temperature, they are in a magnetically blocked state.[57] Nevertheless, as represented in figure 4.20(b), the values of those two parameters decreased fast with increasing temperature, having been observed negligible H_c and M_r beyond 280 K, indicating that the SPIONs are in a superparamagnetic state. Additionally, it was noticed that M_{Sat} was reached at a relatively low external magnetic field, indicating a high magnetic susceptibility.

The specific M_{Sat} obtained for these SPIONs, at 320 K, was 70 emu/g, a value that is quite reasonable when compared to the saturation magnetization (M_{Sat}) of bulk magnetite, which is ~ 85–100 emu/g, or that of maghemite, i.e. ~ 76 emu/g.[58,59] Nevertheless, this slight decrease can be attributed to the nature of monodispersed and ultrafine particles, surface disorder, and cation distribution.[58] Furthermore, it is reported that magnetite undergoes spontaneous oxidation when in contact with air, forming maghemite, which has a M_{Sat} of ~ 80 % of that observed in magnetite, leading to the existence of a mixture between magnetite and maghemite NPs.[60] Therefore, the analysed sample may also contain that compound, leading to a further reduction of its M_{Sat}.

Additionally, it was concluded that M_{Sat} decreased as the temperature got higher. This behaviour can be attributed to the increasing thermal energy, which tends to disrupt the alignment of the magnetic dipoles along the applied magnetic field, consequently reducing the magnetization of the sample.[61]

Regarding the squareness [figure 4.20(b)], a value below 0.5 was obtained for all the considered temperatures, suggesting that these were indeed single-domain NPs possessing a randomly oriented easy axis of magnetization and a uniaxial anisotropy.

To further validate the existence of a superparamagnetic behaviour in the synthesized SPIONs, as well as their diameter, the Langevin function was fitted to the M(H) curves measured at 320 K [figure 4.21(a)].

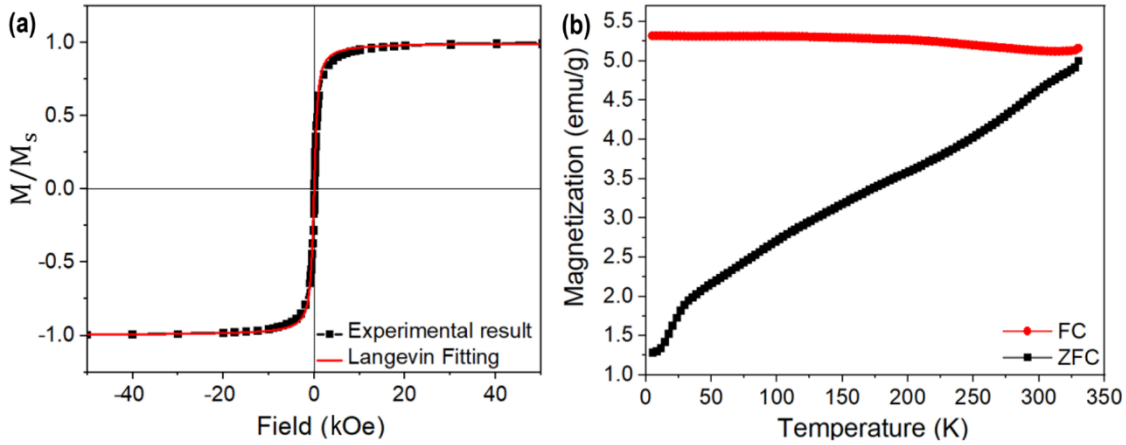

Figure 4.21 - (a) Fitting of the Langevin function to the SPIONs' hysteresis loop measured at 320 K, using a SQUID. (b) ZFC and FC curves of the produced SPIONs measured under an H field equal to 50 Oe.

The fitting of the Langevin function to the M(H) curve of the fabricated SPIONs, measured at 320 K, originated a coefficient of determination (R^2) of 0.998, indicating that such function fitted well to the experimental data. However, it is important to mention that this function does not take into account the size distribution of the NPs, as it assumes that they possess homogeneous dimensions. Nevertheless, this result indicated that these NPs possess a superparamagnetic behaviour, at the considered temperature. Moreover, taking into account that the magnetic moment per NP, i.e. μ, is defined as $\mu = M_{Sat} \cdot V$, where M_{Sat} is the saturation magnetization of the bulk material and V represents the NP's volume (for a spherical NP: $V = \frac{\pi D^3}{6}$, where D is the NP diameter) it was possible to estimate the mean diameter of these SPIONs, having been obtained a value of 7.14 ± 3 nm, which is lower than that determined through TEM.[65–68] Such difference can be associated with the potential presence of a nonmagnetic (or "magnetically dead") layer on the magnetic NPs' surface, resulting from the employed

fabrication process.[69] This issue might be reduced through surface modification, to an extent that depends on the specific interactions or bonding between the surface capping agent and the NP surface.[69,70]

Additionally, the zero-field cooled (ZFC) and field cooled (FC) curves obtained for these SPIONs are represented in figure 4.21(b). Regarding the latter, it is possible to observe a well-defined plateau of the magnetization with varying temperature, revealing the existence of strong dipolar interactions between the NPs.[71] These interactions can also explain the resulting ZFC curve, which presents a quasi-linear behaviour without pronounced inflections. Particularly, at low temperatures, the overall magnetization presents its lowest values, suggesting that the magnetic moments of the SPIONs are blocked along a random direction, since the thermal energy is lower than the magnetic anisotropy energy.[72,73] Then, as the temperature increases, the thermal energy get higher and, consequently, more magnetic moments are able to align along the external magnetic field, leading to an increasing magnetization.[74] The magnetization reaches its maximum value when the thermal energy surpasses the magnetic anisotropy energy and, therefore, all the magnetic moments are able to align with the external magnetic field, corresponding to the blocking temperature (T_B). A further increase of the temperature results in a reduction of the magnetization, as the thermal energy tends to disrupt the alignment of the magnetic dipoles along the external magnetic field.[75,76]

Consequently, in the ZFC curve, the T_B corresponds to its maximum, or inflection point.[75] From the presented results, it is possible to verify that such curve did not present a maximum, indicating the existence of a T_B over 330 K. This may be attributed to the strong dipolar interactions among the NPs, causing a shift of T_B to a higher value.[77] Another indication of those interactions is the divergence between the ZFC and the FC curves across the entire temperature range.[78] As a result, this analysis does not allow to conclusively determine whether the analysed NPs are, indeed, superparamagnetic, despite the evidence obtained by their hysteresis loop and the fitting of the Langevin function.

Nevertheless, it is possible to notice a subtle change in the ZFC curve's slope at $\sim$ 25 and $\sim$ 150 K, which may represent the "unblocking" of smaller NPs within the sample, as it was previously concluded that these SPIONs had a moderately broad size distribution.[79]

4.8.2. Nanostructured Lipid Carriers

The magnetic behaviour of the produced $NLC_{(DOX\text{-}SPIONs)}$ is presented in figure 4.22.

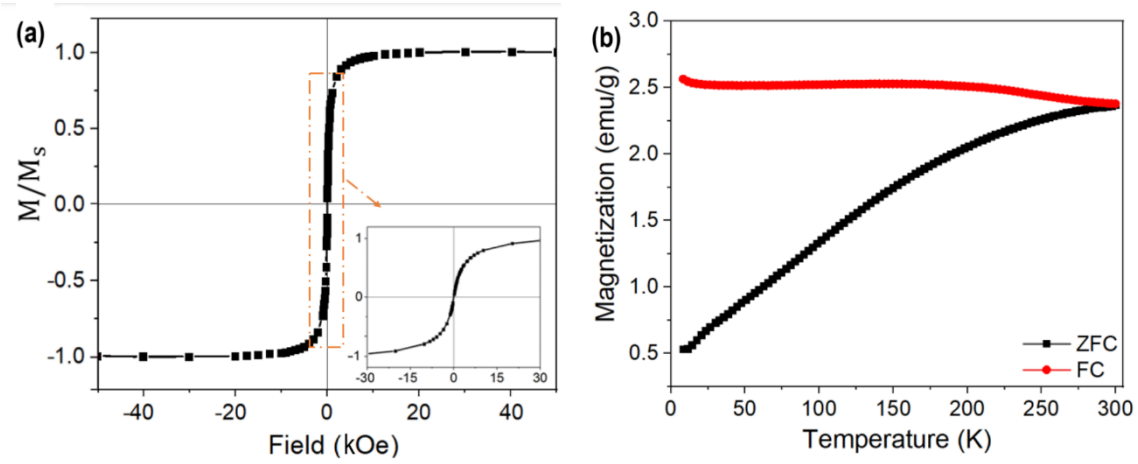

Figure 4.22 - (a) Hysteresis loop of $NLC_{(DOX\text{-}SPIONs)}$ ([DOX] = 2000 µg/mL; [SPIONs] = 12000 µg/mL) measured at 320 K, using a SQUID. Inset: magnified view of the magnetization behaviour at lower magnetic fields. (b) ZFC and FC curves of the $NLC_{(DOX\text{-}SPIONs)}$ ([DOX] = 2000 µg/mL; [SPIONs] = 12000 µg/mL) measured under an H field equal to 50 Oe.

From the measured hysteresis loop, a H_c and M_r of ~ 3.33 Oe and ~ 0.69 emu/g, respectively, were determined. These relatively low values, i.e. H_c < 10 Oe and M_r < 1 emu/g, indicate the existence of a superparamagnetic state, suggesting that the presence of NLCs and DOX did not impact the intrinsic superparamagnetic properties of the SPIONs.[80–82] On the other hand, regarding M_{Sat} it was obtained a value similar to that observed in the SPIONs, i.e. 70.2 emu/g. Therefore, it was concluded that the encapsulation of SPIONs within NLCs did not affect their magnetic behaviour, revealing the potential of this system as a combined drug delivery and MHT platform.

The obtained ZFC and FC curves [figure 4.21(b)] further suggested the existence of a superparamagnetic behaviour in the SPIONs-loaded NLCs, as the FC curve exhibits a continuous decrease as the temperature increases, while the ZFC curve increases up until reaching an inflection point, corresponding to T_B, after which it starts to decrease. At higher temperatures, both curves converge, exhibiting identical temperature dependence as temperature increases.[83] In this case, the T_B was ~ 300 K, being lower than that observed for the free SPIONs, i.e. > 330 K. This suggests a decrease in the magnetic dipolar interactions between the SPIONs when encapsulated within lipid carriers.

4.9. Specific Heat Absorption Rate (SAR)

Subsequently, the heating capacity of the produced SPIONs and NLCs was assessed by determining their SAR. Regarding the first, the temperature increase during their exposure to the AMF with a frequency of 556 kHz is depicted in figure 4.23.

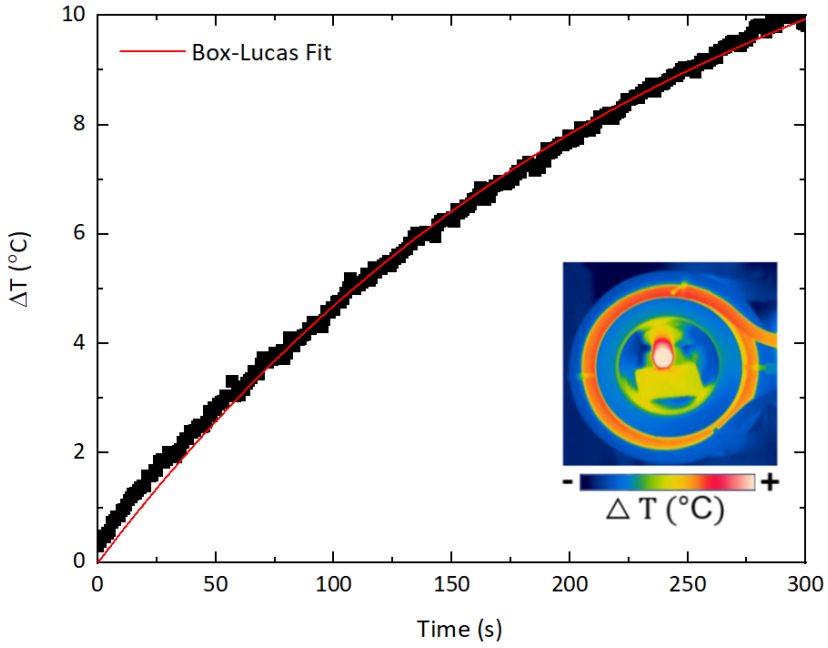

Figure 4.23 - Variation of temperature (ΔT) as a function of time for a SPIONs' sample, with a volume of 150 µL ([Fe] = 4 mg/mL), exposed to a 10 mT AMF with a frequency of 556 kHz. Inset: thermal image, captured by a thermal camera, of a SPIONs' sample inside the magnetic coils, after a 5 min of exposure to the AMF.

The Box-Lucas fit to the experimental data led to an $R^2 \sim 0.996$, indicating a good level of correlation between the model and the observed data. Then, based on equation 1.25 and the A and B values acquired from the performed fit, i.e. 14.18289 ± 0.14416 and $0.00402 \pm 6.3318 \cdot 10^{-5}$ respectively, the SAR of these SPIONs was calculated, having been obtained a value of ~ 59.89 W/g, which is within the range reported for most commercially available SPION dispersions (4 - 100 W/g).[84]

Regarding NLCs and similarly to the results presented in section 4.7.2., no macroscopic temperature increase was detected, indicating a low heat generation from the SPIONs within the lipid NPs. As indicated in section 1.2.1., the heat resulting from this type of NPs, when exposed to an AMF, and, therefore, their SAR, is mainly attributed to relaxation losses, particularly Néel and Brownian relaxation processes. However, the Brownian relaxation of the SPIONs may be affected when they are enclosed within the NLCs. This can be attributed to a greater movement restriction when the NPs are inside the lipid carriers, due to the viscosity of the lipid matrix, and, simultaneously, to the increased dipolar interactions between SPIONs, as they are in closer proximity in the lipid matrix.[85]

Nevertheless, in addition to the sample volume, SAR is also influenced by the AMF parameters, i.e. strength and frequency, as well as the geometry (size and shape), crystal structure, and magnetic properties (magnetic anisotropy and temperature

dependence of the magnetization) of the NPs.[86] Therefore, a meaningful comparison can only be made when considering samples of identical volume and concentration, which are composed of nanomaterials with the same size, shape, and composition that are placed in a sample vessel of the same size, shape, and material.[87]

4.10. pH- and Temperature-Triggered DOX Release

In addition to the AMF-triggered drug release (section 4.7.2.), the drug release from the GEL-based $NLC_{(DOX\text{-}SPIONs)}$ formulation, with [DOX] = 2000 µg/mL and [SPIONs] = 12000 µg/mL), under different pH (5 and 7.4) and temperature (35, 40, 45 and 50 ºC) conditions as a function of time was also analysed, to get a more comprehensive understanding of the release profiles of those nanomaterials. The obtained results are presented in figure 4.24.

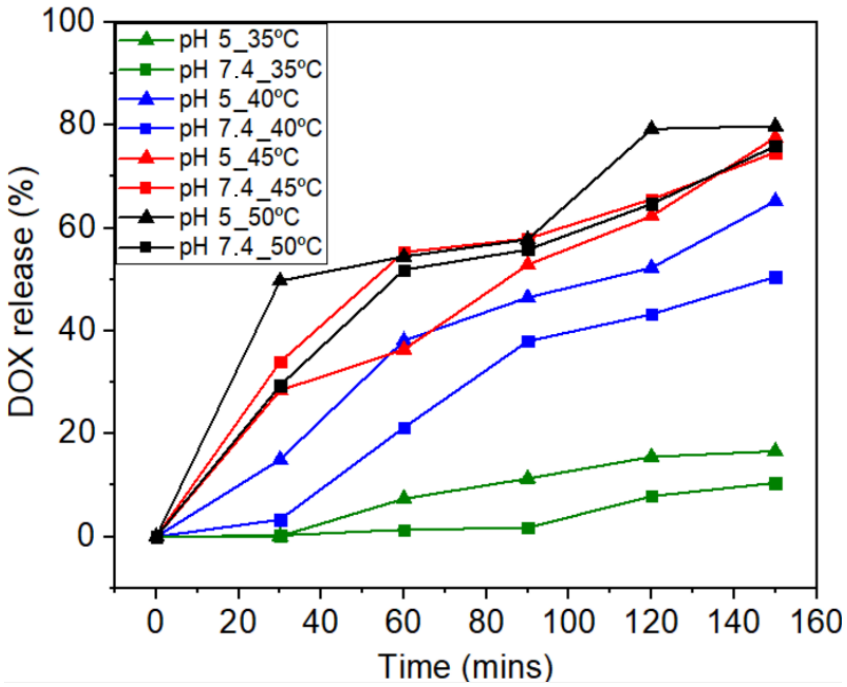

Figure 4.24 - Cumulative DOX release profiles (%) as a function of time for the GEL-based $NLC_{(DOX\text{-}SPIONs)}$ ([DOX] = 2000 µg/mL; [SPIONs] = 12000 µg/mL) in a PBS buffer solution (pH 5 or 7) at different temperatures (35, 40, 45, and 50ºC).

As can be observed in the figure above, the release of DOX from $NLC_{(DOX\text{-}SPIONs)}$ at 35 ºC was considerably lower compared to higher temperatures, suggesting that they are stable below the body temperature. On the other hand, it was verified a significant increase of the DOX release % at temperatures over 40 ºC. Furthermore, for the same temperature, an increased DOX release consistently occurred under lower pH conditions (pH 5), which represents an advantage for cancer therapy as such pH value is similar to that found in the acidic microenvironment for cancer cells (pH 4.5 - 6.5).[49] Particularly, the maximum DOX release, i.e. 79.8%, was attained at 50ºC under a pH of 5.0.

4.11. Storage Stability

The physical stability of the produced GEL-based NLC formulations, with [DOX] = 2000 µg/mL and/or [SPIONs] = 12000 µg/mL, which are the most relevant for the desired biomedical application, was analysed for 10 weeks, so as to assess their long-term structural integrity over a long storage period. This examination was performed by measuring weekly the hydrodynamic diameter, PDI, zeta potential, EE, and LC of each considered formulation, stored at 4 ºC. The acquired results are depicted in figure 4.25.

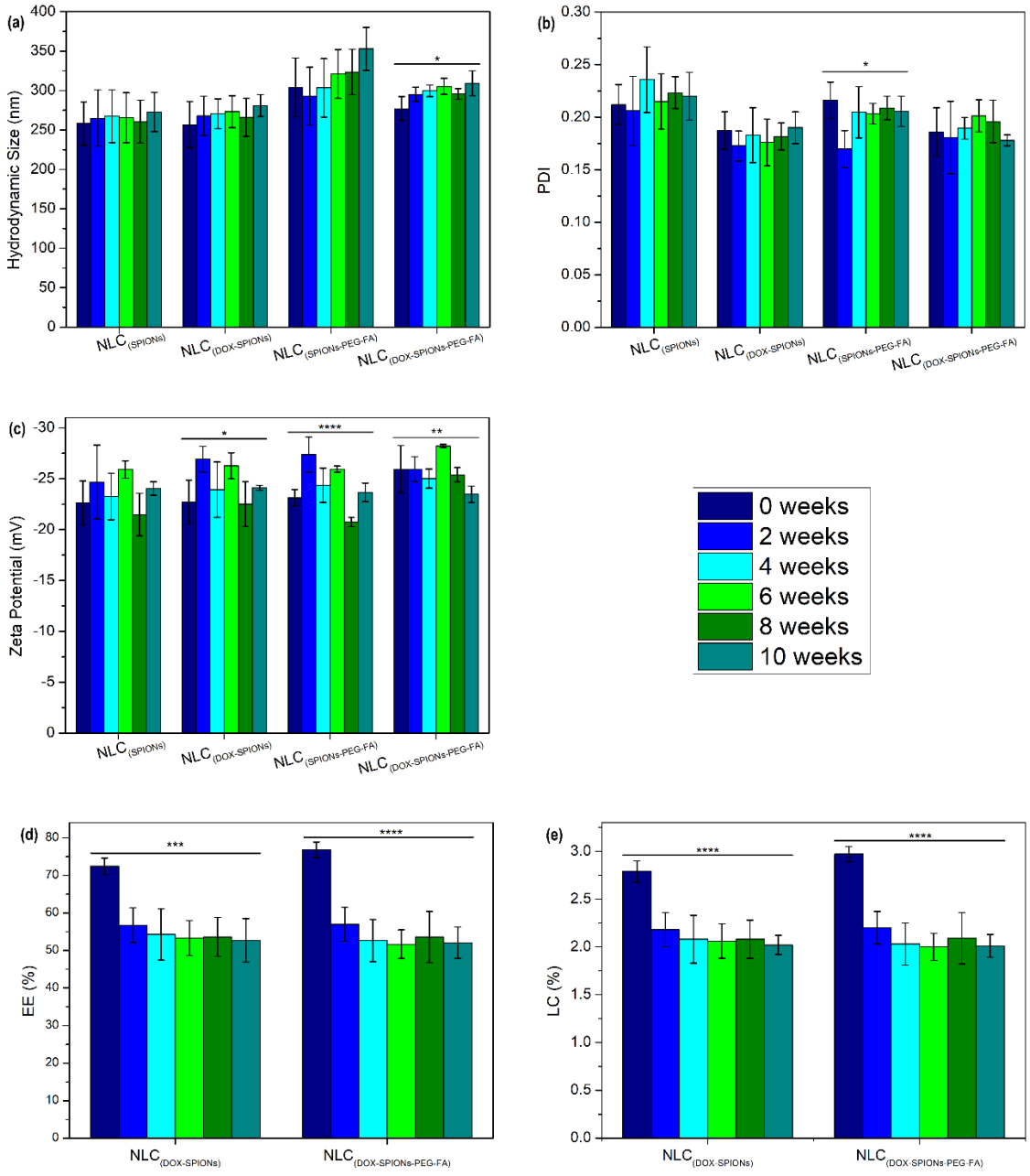

Figure 4.25 - Physical stability of the GEL-based formulations during 10 weeks: (a) hydrodynamic diameter, (b) PDI, (c) zeta potential, (d) EE, and (e) LC. The values represent the mean of three readings (n = 3) ± standard deviation. Asterisks in bars indicate the statistical significance between the considered time points (*P ≤ 0.05; **P ≤ 0.01; ***P ≤ 0.001; ****P ≤ 0.0001).

The statistical analyses detected some statistically significant differences in the studied parameters, for each considered formulation. Furthermore, regarding EE and LC, it was verified that the DOX release was higher during the initial two weeks, but, after 8 weeks, the values of those two parameters appear to have stabilized.

Consequently, from the presented results, it is possible to conclude that the produced DOX- an/or SPIONs-loaded NLCs based on GEL are relatively stable over time, being suitable for therapeutic administration during, at least, 10 weeks after synthetization, when stored under the tested conditions.

4.12. Conclusions

In this chapter, it was presented the characterization of a novel biocompatible and multi-responsive drug delivery system composed of NLCs co-loaded with DOX and SPIONs. This platform was produced with the aim of developing a dual cancer treatment strategy, involving the delivery and targeting of cancer cells, through lipid carriers and surface modifications, in combination with MHT. In this context, it was verified that it was possible to control the anticancer drug release by an external AMF stimulus, as a result of the heat-generating properties of SPIONs.

Particularly, the NLCs characterization carried out revealed physicochemical properties that make them suitable for the desired biomedical application, as they presented an adequate hydrodynamic diameter, a PDI suggesting homogeneous NPs with a narrow size distribution, and a zeta potential indicating that they are relatively stable. Additionally, through XRD, it was possible to identify characteristic peaks of maghemite/magnetite in both SPIONs and SPIONs-loaded NLCs. Regarding the latter, the presence of DOX and PEG-FA conjugate was also detected by this technique.

Moreover, by comparing the thermal stability, AMF-triggered DOX release, and biocompatibility of GEL-based and PAL-based NLCs, it was concluded that the GEL-based NPs were more suitable for the pretended application, consequently these were the ones selected for the subsequent studies. These involved a magnetic characterization that revealed the existence of a superparamagnetic behaviour, at room temperature, for both SPIONs and GEL-based NLCs. Furthermore, it was measured a SAR value of 62.41 W/g for the NLCs co-loaded with DOX and SPIONs, under a 10 mT AMF with a frequency of 556 kHz, which makes them potential candidates for MHT. These NLCs also demonstrated pH and thermal sensitivity, leading to an increased release of DOX under greater temperatures and lower pH conditions. Additionally, the

synthesized GEL-based NLCs presented good stability for a period of, at least, 10 weeks, when stored at 4 ºC.

References

[1]S. S. Moraes, *Multimodal Magnetic Lipid Nanocarriers for Cancer Therapie*s. PhD Thesis, University of Porto (2021).

[2]M. Haider, S. M. Abdin, L. Kamal, and G. Orive, Nanostructured Lipid Carriers for Delivery of Chemotherapeutics: A Review. *Pharmaceutics* **12**, 288 (2020).

[3]V. Filipe, A. Hawe, and W. Jiskoot, Critical Evaluation of Nanoparticle Tracking Analysis (NTA) by Nanosight for the Measurement of Nanoparticles and Protein Aggregates. *Pharmaceutical Research* **27**, 796–810 (2010).

[4]B. Q. Chaudhry, *Nanoparticle Systems for Raman Micro-spectroscopy: Synthesis and Characterisation*. PhD Thesis, King's College London (2021).

[5]M. Zhang, J. Yang, L. Tang, X. Pan, and D. Zhang, What occurs in colloidal gas aphron-induced separation of titanium dioxide nanoparticles? Particle fate analysis by tracking technologies. *Science of The Total Environment* **716**, 137104 (2020).

[6]A. Dikpati, *Size exclusion of radioactive polymers to study the biodegradation and stability of polymeric nanoparticles*. PhD Thesis, Laval University (2023).

[7]T. Boztepe, S. Scioli-Montoto, M. E. Ruiz, V. A. Alvarez, G. R. Castro, and I. E. Leon, 8-Hydroxyquinoline platinum (II) loaded nanostructured lipid carriers: synthesis, physicochemical characterization and evaluation of antitumor activity. *New Journal of Chemistry* **45**, 821–830 (2021).

[8]M. Pradhan, D. Singh, and M. R. Singh, Influence of selected variables on fabrication of tri- amcinolone acetonide loaded solid lipid nanoparticles for topical treatment of dermal disorders. *Artificial Cells, Nanomedicine, and Biotechnology* **44**, 392–400 (2016).

[9]V. R. Patel and Y. Agrawal, Nanosuspension: An approach to enhance solubility of drugs. *Journal of Advanced Pharmaceutical Technology & Research* **2**, 81 (2011).

[10]S. Nimesh, R. Chandra, and N. Gupta, *Advances in Nanomedicine for the Delivery of Therapeutic Nucleic Acids*. Woodhead Publishing (2017).

[11]A. Kumar and C. K. Dixit, Methods for characterization of nanoparticles. In: *Advances in Nanomedicine for the Delivery of Therapeutic Nucleic Acids*, 43–58, Elsevier (2017), pp. 43–58.

[12]L. Portilla, *Functionalization of Metal Oxide Nanostructures via Self-Assembly. Implications and Applications*. PhD Thesis, University of Erlangen–Nuremberg (2017).

[13]S. Honary and F. Zahir, Effect of Zeta Potential on the Properties of Nano-Drug Delivery Systems - A Review (part 2). *Tropical Journal of Pharmaceutical Research* **12**, 265–273 (2013).

[14]R. S. Fernandes, J. O. Silva, S. V. Mussi, S. C. Lopes, E. A. Leite, G. D. Cassali, V. N. Cardoso, D. M. Townsend, P. M. Colletti, L. A. Ferreira, D. Rubello, and A. L. B. de Barros, Nanostructured Lipid Carrier Co-loaded with Doxorubicin and Docosahexaenoic Acid as a Theranostic Agent: Evaluation of Biodistribution and Antitumor Activity in Experimental Model. *Molecular Imaging and Biology* **20**, 437–447 (2018).

[15]A. M. Farnoud and S. Nazemidashtarjandi, Emerging investigator series: interactions of engineered nanomaterials with the cell plasma membrane; what have we learned from membrane models?. *Environmental Science: Nano* **6**, 13–40 (2019).

[16]A. C. Ortiz, O. Yañez, E. Salas-Huenuleo, and J. O. Morales, Development of a Nanostructured Lipid Carrier (NLC) by a Low-Energy Method, Comparison of Release Kinetics and Molecular Dynamics Simulation. *Pharmaceutics* **13**, 531 (2021).

[17]J. Gautier, E. Munnier, L. Douziech-Eyrolles, A. Paillard, P. Dubois, and I. Chourpa, SERS spectroscopic approach to study doxorubicin complexes with Fe^{2+} ions and drug release from SPION-based nanocarriers. *Analyst* **138**, 7354–7361 (2013).

[18]J. Gautier, E. Allard-Vannier, E. Munnier, M. Soucé, and I. Chourpa, Recent advances in theranostic nanocarriers of doxorubicin based on iron oxide and gold nanoparticles. Journal of Controlled Release 169, 48–61 (2013).

[19]W.-H. Chiang, W.-C. Huang, C.-W. Chang, M.-Y. Shen, Z.-F. Shih, Y.-F. Huang, S.-C. Lin, and H.-C. Chiu, Functionalized polymersomes with outlayered polyelectrolyte gels for potential tumor-targeted delivery of multimodal therapies and MR imaging. *Journal of Controlled Release* **168**, 280–288 (2013).

[20]J. Qu, Z. Tian, Q. Wang, S. Peng, J.-b. Luo, Q.-h. Zhou, and J. Lin, Surface design and preparation of multi-functional magnetic nanoparticles for cancer cell targeting, therapy, and imaging. *RSC Advances* **8**, 35437–35447 (2018).

[21]A. Szuplewska, A. Rękorajska, E. Pocztańska, P. Krysiński, A. Dybko, and M. Chudy, Magnetic field-assisted selective delivery of doxorubicin to cancer cells using magnetoliposomes as drug nanocarriers. *Nanotechnology* **30**, 315101 (2019).

[22]B. K. Wilson, R. K. Prud'homme, Nanoparticle size distribution quantification from transmission electron microscopy (TEM) of ruthenium tetroxide stained polymeric nanoparticles. *Journal of Colloid and Interface Science* **604**, 208-220 (2021).

[23]J. Lopes-de-Araújo, A. R. Neves, V. M. Gouveia, C. C. Moura, C. Nunes, and S. Reis, Oxaprozin-Loaded Lipid Nanoparticles towards Overcoming NSAIDs Side-Effects. *Pharmaceutical Research* **33**, 301–314 (2016).

[24]J. Poletaeva, I. Dovydenko, A. Epanchintseva, K. Korchagina, D. Pyshnyi, E. Apartsin, E. Ryabchikova, and I. Pyshnaya, Non-Covalent Associates of siRNAs and AuNPs Enveloped with Lipid Layer and Doped with Amphiphilic Peptide for Efficient siRNA Delivery. *International Journal of Molecular Sciences* **19**, 2096 (2018).

[25]T. Fülöp, R. Nemes, T. Mészáros, R. Urbanics, R. J. Kok, J. A. Jackman, N.-J. Cho, G. Storm, and J. Szebeni, Complement activation in vitro and reactogenicity of low-molecular weight dextran-coated SPIONs in the pig CARPA model: Correlation with physicochemical features and clinical information. *Journal of Controlled Release* **270**, 268–274 (2018).

[26]M. Mahmoudi, S. Sant, B. Wang, S. Laurent, and T. Sen, Superparamagnetic iron oxide nanoparticles (SPIONs): Development, surface modification and applications in chemotherapy. *Advanced Drug Delivery Reviews* **63**, 24–46 (2011).

[27]N. Tanaka, Present status and future prospects of spherical aberration corrected TEM/STEM for study of nanomaterials. *Science and Technology of Advanced Materials* **9**, 014111 (2008).

[28]Q. Li, C. W. Kartikowati, S. Horie, T. Ogi, T. Iwaki, and K. Okuyama, Correlation between particle size/domain structure and magnetic properties of highly crystalline Fe_3O_4 nanoparticles. *Scientific Reports* **7**, 9894 (2017).

[29]M. Desimone and R. Jotania, *Magnetic Nanoparticles for Biomedical Applications*. Materials Research Forum LLC (2023).

[30]S. Yoffe, T. Leshuk, P. Everett, and F. Gu, Superparamagnetic Iron Oxide Nanoparticles (SPIONs): Synthesis and Surface Modification Techniques for use with MRI and Other Biomedical Applications. *Current Pharmaceutical Design* **19**, 493–509 (2013).

[31]Á. de Jesús Ruíz-Baltazar, S. Y. Reyes-López, and R. Pérez, Magnetic structures synthesized by controlled oxidative etching: structural characterization and magnetic behavior. *Results in Physics* **7**, 1828–1832 (2017).

[32]K. Shibano, S. Kubuki, K. Akiyama, Z. Homonnay, E. Kuzmann, S. Krehula, M. Ristić, and T. Nishida, Local structure and water cleaning ability of iron oxide nanoparticles prepared by hydro-thermal reaction. *Hyperfine Interactions* **226**, 489–497 (2014).

[33]C. Piquer, M. Laguna-Marco, A. G. Roca, R. Boada, C. Guglieri, and J. Chaboy, Fe K-Edge X-Ray Absorption Spectroscopy Study of Nanosized Nominal Magnetite. *The Journal of Physical Chemistry C* **118**, 1332–1346 (2014).

[34]Z. Hedayatnasab, A. Dabbagh, F. Abnisa, H. Karimian, N. H. Abu Kasim, and W. M. A. Wan Daud, Synthesis, characterization and in vitro analysis of superparamagnetic iron oxide nanoparticles for targeted hyperthermia therapy. *Chemical Papers* **75**, 669–679 (2021).

[35]F. Notario-Pérez, R. Cazorla-Luna, A. Martín-Illana, R. Ruiz-Caro, J. Peña, and M.-D. Veiga, Tenofovir Hot-Melt Granulation using Gelucire® to Develop Sustained-Release Vaginal Systems for Weekly Protection against Sexual Transmission of HIV. *Pharmaceutics* **11**, 137 (2019).

[36]S. H. Peczek, A. P. S. Tartari, I. C. Zittlau, C. Diedrich, C. S. Machado, and R. M. Mainardes, Enhancing Oral Bioavailability and Brain Biodistribution of Perillyl Alcohol Using Nanostructured Lipid Carriers. *Pharmaceuticals* **16**, 1055 (2023).

[37]E. T. Maggio, Polysorbates, peroxides, protein aggregation, and immunogenicity–a growing concern. *Journal of Excipients and Food Chemicals* **3**, 45-53 (2016).

[38]A. E.-H. I. El Assasy, N. F. Younes, and A. I. Makhlouf, Enhanced Oral Absorption of Amisulpride *Via* a Nanostructured Lipid Carrier-Based Capsules: Development, Optimization Applying the Desirability Function Approach and *In Vivo* Pharmacokinetic Study. *AAPS PharmSciTech* **20**, 1–14 (2019).

[39]F. Chai, L. Sun, X. He, J. Li, Y. Liu, F. Xiong, L. Ge, T. J. Webster, and C. Zheng, Doxorubicin-loaded poly (lactic-co-glycolic acid) nanoparticles coated with chitosan/alginate by layer by layer technology for antitumor applications. *International Journal of Nanomedicine* **12**, 1791–1802 (2017).

[40]W. Soeratri, R. Hidayah, and N. Rosita, Effect of Combination Soy Bean Oil and Oleic Acid to Characteristic, Penetration, Physical Stability of Nanostructure Lipid Carrier Resveratrol. *Folia Medica Indonesiana* **55**, 213–222 (2019).

[41]M.-H. Kim, K.-T. Kim, S.-Y. Sohn, J.-Y. Lee, C. H. Lee, H. Yang, B. K. Lee, K. W. Lee, and D.-D. Kim, Formulation And Evaluation Of Nanostructured Lipid Carriers (NLCs) Of 20 (S)-Protopanaxadiol (PPD) by Box-Behnken Design. *International Journal of Nanomedicine*, 8509–8520 (2019).

[42]V. Teeranachaideekul, E. B. Souto, V. B. Junyaprasert, and R. H. Müller, Cetyl palmitate-based NLC for topical delivery of Coenzyme Q_{10} – development,

physicochemical characterization and *in vitro* release studies. *European Journal of Pharmaceutics and Biopharmaceutics* **67**, 141–148 (2007).

[43]U. Ruktanonchai, S. Limpakdee, S. Meejoo, U. Sakulkhu, N. Bunyapraphatsara, V. Junyaprasert, and S. Puttipipatkhachorn, The effect of cetyl palmitate crystallinity on physical properties of gamma-oryzanol encapsulated in solid lipid nanoparticles. *Nanotechnology* **19**, 095701 (2008).

[44]G. Lukowski, J. Kasbohm, P. Pflegel, A. Illing, and H. Wulff, Crystallographic investigation of cetylpalmitate solid lipid nanoparticles. *International Journal of Pharmaceutics* **196**, 201–205 (2000).

[45]S. Kumar and J. K. Randhawa, Paliperidone-loaded spherical solid lipid nanoparticles. *RSC Advances* **4**, 30186–30192 (2014).

[46]S. H. Sofi and P. Sonia, Gelucire: A Versatile Formulation Excipient. *International Journal of Pharmacy and Pharmaceutical Research* **10**, 55–73 (2017).

[47]F. Shoviantari, T. Erawati, and W. Soeratri, Skin Penetration of Coenzyme Q10 in Nanostructure Lipid Carriers Using Olive Oil and Cetyl Palmitate. *International Journal of Pharmaceutical and Clinical Research* **9**, 142–5 (2017).

[48]Y. Zhu, M. Wu, X. Miao, B. Wang, J. He, and X. Qiu, Delivery of paclitaxel by carboxymethyl chitosan-functionalized dendritic fibrous nano-silica: fabrication, characterization, controlled release performance and pharmacokinetics. *International Journal of Biological Macromolecules* **256**,128431 (2023).

[49]E. Cazares-Cortes, A. Espinosa, J.-M. Guigner, A. Michel, N. Griffete, C. Wilhelm, and C. Ménager, Doxorubicin Intracellular Remote Release from Biocompatible Oligo(ethylene glycol) Methyl Ether Methacrylate-Based Magnetic Nanogels Triggered by Magnetic Hyperthermia. *ACS Applied Materials & Interfaces* **9**, 25775-25788 (2017)

[50]N. Griffete, J. Fresnais, A. Espinosa, D. Taverna, C. Wilhelm, and C. Ménager, Thermal Polymerization on the Surface of Iron Oxide Nanoparticles Mediated by Magnetic Hyperthermia: Implications for Multishell Grafting and Environmental Applications. *ACS Applied Nano Materials* **1**, 547–555 (2018).

[51]D. Lee and P. N. Kumta, Chemical synthesis and stabilization of magnesium substituted brushite. *Materials Science and Engineering: C* **30**, 934–943 (2010).

[52]N. Osman, C. A. Omolo, R. Gannimani, A. Y. Waddad, S. Rambharose, C. Mocktar, S. Singh, R. Parboosing, and T. Govender, Novel fatty acid-based pH-responsive

nanostructured lipid carriers for enhancing antibacterial delivery. *Journal of Drug Delivery Science and Technology* **53**, 101125 (2019).

[53]S. Scialla, N. Genicio, B. Brito, M. Florek-Wojciechowska, G. J. Stasiuk, D. Kruk, M. Bañobre-López, and J. Gallo, Insights into the Effect of Magnetic Confinement on the Performance of Magnetic Nanocomposites in Magnetic Hyperthermia and Magnetic Resonance Imaging. *ACS Applied Nano Materials* **5**, 16462–16474 (2022).

[54]H. A. Gad, R. S. Elezaby, M. Mansour, and R. M. Hathout, Novel Approaches of Solid Lipid Nanoparticles as Drug Carrier. In: *Nanoengineering of Biomaterials* 107–143, Wiley (2022).

[55]A. Grillone, E. R. Riva, A. Mondini, C. Forte, L. Calucci, C. Innocenti, C. de Julian Fernandez, V. Cappello, M. Gemmi, S. Moscato, F. Ronca, R. Sacco , V. Mattoli, and G. Ciofani, Active Targeting of Sorafenib: Preparation, Characterization, and In Vitro Testing of Drug-Loaded Magnetic Solid Lipid Nanoparticles. *Advanced Healthcare Materials* **4**, 1681–1690 (2015).

[56]S. Moraes, A. Marinho, S. Lima, A. Granja, J. Araújo, S. Reis, C. Sousa, and C. Nunes, Targeted nanostructured lipid carriers for doxorubicin oral delivery. *International Journal of Pharmaceutics* **592**, 120029 (2021).

[57]M. Tadić, V. Kusigerski, D. Marković, M. Panjan, I. Milošević, and V. Spasojević, Highly crystalline superparamagnetic iron oxide nanoparticles (SPION) in a silica matrix. *Journal of Alloys and Compounds* **525**, 28–33 (2012).

[58]M. Darroudi, M. Hakimi, E. Goodarzi, and R. K. Oskuee, Superparamagnetic iron oxide nanoparticles (SPIONs): Green preparation, characterization and their cytotoxicity effects. *Ceramics International* **40**, 14641–14645 (2014).

[59]J. Queiros Campos, M. Boulares, M. Raboisson-Michel, G. Verger-Dubois, J. García Fernández, G. Godeau, and P. Kuzhir, Improved Magneto-Microfluidic Separation of Nanoparticles through Formation of the β-Cyclodextrin–Curcumin Inclusion Complex. *Langmuir* **37**, 14345–14359 (2021).

[60]P. Kucheryavy, J. He, V. T. John, P. Maharjan, L. Spinu, G. Z. Goloverda, and V. L. Kolesnichenko, Superparamagnetic Iron Oxide Nanoparticles with Variable Size and an Iron Oxidation State as Prospective Imaging Agents. *Langmuir* **29**, 710–716 (2013).

[61]L. Maldonado-Camargo, M. Unni, and C. Rinaldi, Magnetic Characterization of Iron Oxide Nanoparticles for Biomedical Applications. In: *Biomedical Nanotechnology: Methods and Protocols* 47–71, Springer (2017).

[62]S. Ammar, A. Helfen, N. Jouini, F. Fievet, I. Rosenman, F. Villain, P. Molinie, and M. Danot, Magnetic properties of ultrafine cobalt ferrite particles synthesized by hydrolysis in a polyol medium. *Journal of Materials Chemistry* **11**, 186–192 (2001).

[63]B. D. Cardoso, A. R. O. Rodrigues, M. Bañobre-López, B. G. Almeida, C. O. Amorim, V. S. Amaral, P. J. Coutinho, and E. M. Castanheira, Magnetoliposomes Based on Shape Anisotropic Calcium/Magnesium Ferrite Nanoparticles as Nanocarriers for Doxorubicin. *Pharmaceutics* **13**, 1248 (2021).

[64]D. Caruntu, G. Caruntu, and C. J. O'Connor, Magnetic properties of variable-sized Fe_3O_4 nanoparticles synthesized from non-aqueous homogeneous solutions of polyols. *Journal of Physics D: Applied Physics* **40**, 5801 (2007).

[65]M. Feygenson, *Magnetic and structural properties of thin films and nanoparticles studied by scattering methods*. Forschungszentrum Julich (2007).

[66]M. Chapline, C. Papusoi, A. Ajan, P. Dorsey, M. Desai, and R. Acharya, Characterization of the Magnetic Properties of HAMR Media Using the Temperature Dependence of the AC Susceptibility. *IEEE Transactions on Magnetics* **52**, 1–4 (2015).

[67]M.-J. Kim, Y.-H. Choa, D. H. Kim, and K. H. Kim, Magnetic Behaviors of Surface Modified Superparamagnetic Magnetite Nanoparticles. *IEEE Transactions on Magnetics* **45**, 2446–2449 (2009).

[68]A. U. Lorente, *Open problems in the magnetic behavior of iron-oxide nanoparticles*. Prensas Universitarias de Zaragoza (2011).

[69]M. Unni, A. M. Uhl, S. Savliwala, B. H. Savitzky, R. Dhavalikar, N. Garraud, D. P. Arnold, L. F. Kourkoutis, J. S. Andrew, and C. Rinaldi, Thermal Decomposition Synthesis of Iron Oxide Nanoparticles with Diminished Magnetic Dead Layer by Controlled Addition of Oxygen. *ACS Nano* **11**, 2284–2303 (2017).

[70]G. Kandasamy and D. Maity, Recent advances in superparamagnetic iron oxide nanoparticles (SPIONs) for *in vitro* and *in vivo* cancer nanotheranostics. *International Journal of Pharmaceutics* **496**, 191–218 (2015).

[71]C. Pereira, A. M. Pereira, C. Fernandes, M. Rocha, R. Mendes, M. P. Fernández-García, A. Guedes, P. B. Tavares, J.-M. Grenèche, J. P. Araújo, and C. Freire, Superparamagnetic MFe_2O_4 (M = Fe, Co, Mn) Nanoparticles: Tuning the Particle Size and Magnetic Properties through a Novel One-Step Coprecipitation Route. *Chemistry of Materials* **24**, 1496–1504 (2012).

[72]L. Cabana, M. Bourgognon, J. T.-W. Wang, A. Protti, R. Klippstein, R. T. De Rosales, A. M. Shah, J. Fontcuberta, E. Tobías-Rossell, J. K. Sosabowski, K. T. Al-Jamal, and G. Tobias, The Shortening of MWNT-SPION Hybrids by Steam Treatment Improves Their Magnetic Resonance Imaging Properties In Vitro and In Vivo. *Small* **12**, 2893–2905 (2016).

[73]C. Altavilla, E. Ciliberto, D. Gatteschi, and C. Sangregorio, A New Route to Fabricate Monolayers of Magnetite Nanoparticles on Silicon. *Advanced Materials* **17**, 1084–1087 (2005).

[74]S. Guo, W. Liu, X. Liu, W. Gong, J. Feng, and Z. Zhang, Influence of ferromagnetic layer on the exchange coupling of antiferromagnetic NiO-based films. *Journal of Magnetism and Magnetic Materials* **324**, 3933–3936 (2012).

[75]H. K. Kim, L. T. Schelhas, S. Keller, J. L. Hockel, S. H. Tolbert, and G. P. Carman, Magnetoelectric Control of Superparamagnetism. *Nano Letters* **13**, 884–888 (2013).

76D. Psimadas, G. Baldi, C. Ravagli, M. C. Franchini, E. Locatelli, C. Innocenti, C. Sangregorio, and G. Loudos, Comparison of the magnetic, radiolabeling, hyperthermic and biodistribution properties of hybrid nanoparticles bearing $CoFe_2O_4$ and Fe_3O_4 metal cores. *Nanotechnology* **25**, 025101 (2013).

[77]A. M. Pereira, C. Pereira, A. S. Silva, D. S. Schmool, C. Freire, J.-M. Grenèche, and J. P. Araújo, Unravelling the effect of interparticle interactions and surface spin canting in γ-Fe_2O_3@SiO_2 superparamagnetic nanoparticles. *Journal of Applied Physics* **109** (2011).

[78]A. Carvalho, J. Gallo, D. M. Pereira, P. Valentão, P. B. Andrade, L. Hilliou, P. M. Ferreira, M. Bañobre-López, and J. A. Martins, Magnetic Dehydrodipeptide-Based Self-Assembled Hydrogels for Theragnostic Applications. *Nanomaterials* **9**, 541 (2019).

[79]D. Serantes, D. Baldomir, M. Pereiro, C. Hoppe, F. Rivadulla, and J. Rivas, Nonmonotonic evolution of the blocking temperature in dispersions of superparamagnetic nanoparticles. *Physical Review B* **82**, 134433 (2010).

[80]P. M. de Faria Mendes, *Desenvolvimento de magnetolipossomas baseados em magnetite para aplicações na entrega de fármacos antitumorais*. MsC Thesis, University of Minho (2013).

[81]T. Okada, S. Ozono, M. Okamoto, Y. Takeda, H. M. Minamisawa, T. Haeiwa, T. Sakai, and S. Mishima, Magnetic Rattle-Type Core–Shell Particles Containing Iron Compounds

with Acid Tolerance by Dense Silica. *Industrial & Engineering Chemistry Research* **53**, 8759–8765 (2014).

[82]R. Hachani, *Development of novel magnetic nanoparticles to track stem cells in tissue-engineered organs*. PhD Thesis, University College London (2018).

[83]P. De la Presa, T. Rueda, A. Hernando, J. Ramallo-Lopez, L. Giovanetti, and F. Requejo, Spontaneous oxidation of disordered fcc FePt nanoparticles. *Journal of Applied Physics* **103**, 103909 (2008).

[84]S. M. Dadfar, D. Camozzi, M. Darguzyte, K. Roemhild, P. Varvarà, J. Metselaar, S. Banala, M. Straub, N. Güvener, U. Engelmann, U. Engelmann, I. Slabu, M. Buhl, J. van Leusen, P. Kögerler, B. Hermanns-Sachweh, V. Schulz, F. Kiessling, and T. Lammers, Size-isolation of superparamagnetic iron oxide nanoparticles improves MRI, MPI and hyperthermia performance. *Journal of Nanobiotechnology* **18**, 1–13 (2020).

[85]A. Espinosa, J. Kolosnjaj-Tabi, A. Abou-Hassan, A. Plan Sangnier, A. Curcio, A. K. Silva, R. Di Corato, S. Neveu, T. Pellegrino, L. M. Liz-Marzán, and C. Wilhelm, Magnetic (Hyper)Thermia or Photothermia? Progressive Comparison of Iron Oxide and Gold Nanoparticles Heating in Water, in Cells, and In Vivo. *Advanced Functional Materials* **28**, 1803660 (2018).

[86]C. S. Kumar and F. Mohammad, Magnetic nanomaterials for hyperthermia-based therapy and controlled drug delivery. *Advanced Drug Delivery Reviews* **63**, 789–808 (2011).

[87]Y. Patil-Sen, E. Torino, F. De Sarno, A. M. Ponsiglione, V. Chhabria, W. Ahmed, and T. Mercer, Biocompatible superparamagnetic core-shell nanoparticles for potential use in hyperthermia-enabled drug release and as an enhanced contrast agent. *Nanotechnology* **31**, 375102 (2020).

5. FePt Nanowires

5.1. Introduction

In this chapter, it is introduced a detailed characterization of the obtained FePt nanowires (NWs) that were produced through different electrodeposition techniques into nanoporous anodic aluminium oxide (AAO) templates. The used electrolyte was composed of Fe and Pt precursors, $FeSO_4 \cdot 7H_2O$ and $H_2PtCl_6 \cdot 6H_2O$, as well as H_3BO_3, which works as a buffer to constrain the pH change resulting from the reduction of the H^+ ions at the working electrode, consequently limiting the formation of metal hydroxides and hydrogen evolution.[1-3]

Particularly, the effect of different fabrication parameters on the composition of the resulting nanoarchitectures is analysed. These include the AAO barrier layer thickness and the electrodeposition current density for the NWs with a tree-like branched structure and, for the nanostructures without those formations, the electrodeposition approach, voltage (-0.8 – -2.0 V), Pt (1 – 5 g/L) and Fe (20 – 120 g/L) precursors concentration, duration of the deposition pulse (t_{on}; 4 – 40 ms) and rest pulse (t_{off}; 4 – 40 ms), as well as the t_{on}/t_{off} ratio (0.1 – 10). Moreover, a magnetic characterization at room temperature of the synthetized nanoarchitectures is presented, to analyse the impact of the NWs composition on their hysteresis loop. Moreover, micro-magnetic simulations of FePt NW arrays are compared with the experimental results, in order to gain a better understanding of the magnetization behaviour in these nanostructures.

5.2. FePt Nanowires (NWs) with a Tree-Like Branched Structure

FePt NWs with a tree-like branched structure were fabricated through pulsed electrodeposition into AAO templates. In the following sections, a detailed analysis of this type of nanostructures, ranging from their synthesis to a thorough analysis of their magnetic properties, is presented.

5.2.1. Porous Anodic Alumina Template with a Tree-Like Branched Structure

First, AAO templates with a thickness of 20 μm, an interpore distance equal to 105 nm, and nanopores with 35 nm in diameter were produced and then, used to vertically grow FePt NWs through PED. The porosity of this type of membranes, which determines the effective electrodeposition area, was studied by [4], who found that the self-ordering in AAO produced through electrochemical anodization requires a porosity of 10 % regardless of the considered anodization conditions, which is known as the 10 % porosity rule. This porosity value is associated with a volume expansion of Al to Al oxide equal to

~ 1.2. However, before the electrodeposition, the thick insulating Al oxide layer existing between each nanopore and the Al substrate, which is formed after the second anodization (figure 5.1), has to be thinned, so that electrons can tunnel through it. The thickness of such layer determines the electron flux that occurs during the pulsed electrodeposition (PED) process, which allows the metal ions reduction.[5] Therefore, it is possible to control the deposition by adjusting such parameter.

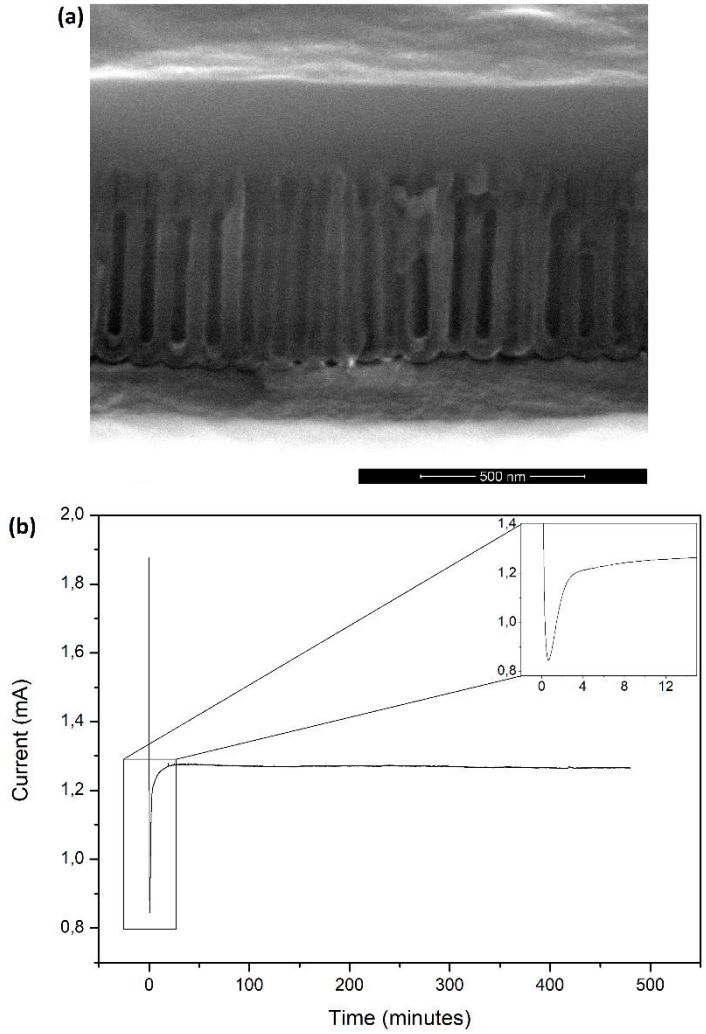

Figure 5.1 - (a) Scanning electron microscopy (SEM) cross-sectional image of a AAO membrane after the second anodization and (b) corresponding variation of the current with time during its formation. Inset: magnified view of the initial behaviour of the curve.

In this work, the Al oxide barrier layer was thinned by exponentially decreasing the anodization potential from 40 V down to 8 V or 7 V, to reduce its thickness from ~ 52 nm to ~ 10.4 nm or ~ 9.1 nm (figure 5.2), respectively, and, consequently, analyse the influence of such parameter on the resulting nanostructures. Moreover, this process originated a reproducible tree-like branched structure (also known as dendritic structure)

at the bottom of each nanopore. The porosity, P, of the resulting template can be calculated through the following equation:[6]

$$P = \frac{2\pi}{\sqrt{3}}\left[\frac{\frac{D_p}{2}}{D_{int}}\right] \quad (5.1)$$

where D_p is the pore diameter and D_{int} is the interpore distance.

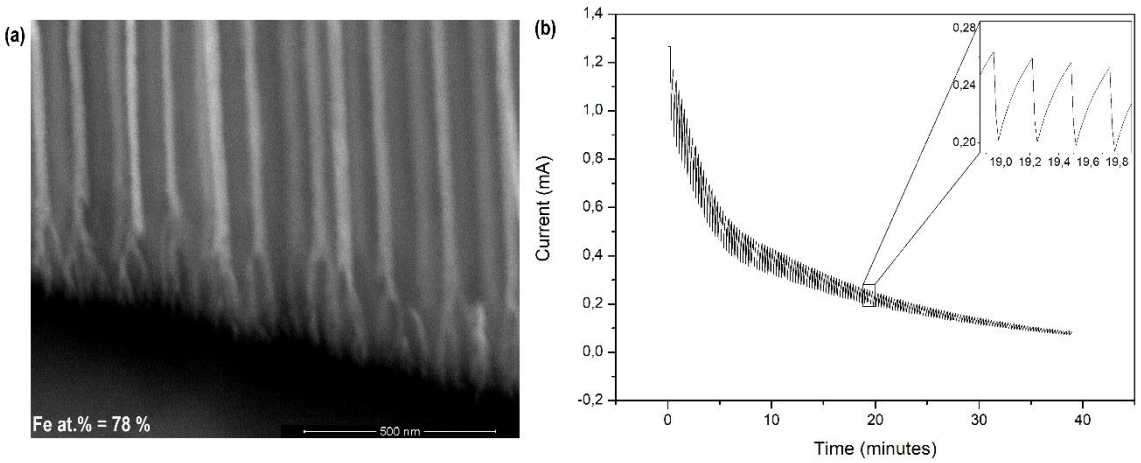

Figure 5.2 - (a) SEM cross-sectional image of a AAO template filled with electrodeposited FePt NWs evidencing the dendritic structures at the bottom of the nanopores, which resulted from the barrier layer thinning process, and (b) variation of the current with time during the exponential decrease of the anodization potential (from 40 V down to 7 V). Inset: magnified view of the curve behaviour.

In the particular case of AAO templates anodized in oxalic acid under 40 V, followed by an anodization potential reduction down to 7 V, their porosity varies from 8 to 10% in the pore region up to 32% in the last generation of dendrites.[6]

5.2.2. Electrodeposition Behaviour

Such modification in the porosity along the various generations of dendrites directly influences the effective electrodeposition area during the NWs growth. Particularly, as observed in figure 5.3, during the filling of the template section with a constant porosity, which corresponds to stage II, the electrodeposition potential (V_{dep}) hardly changes, being rather independent of the deposited nanostructures' length, since the electroplating area remains constant.

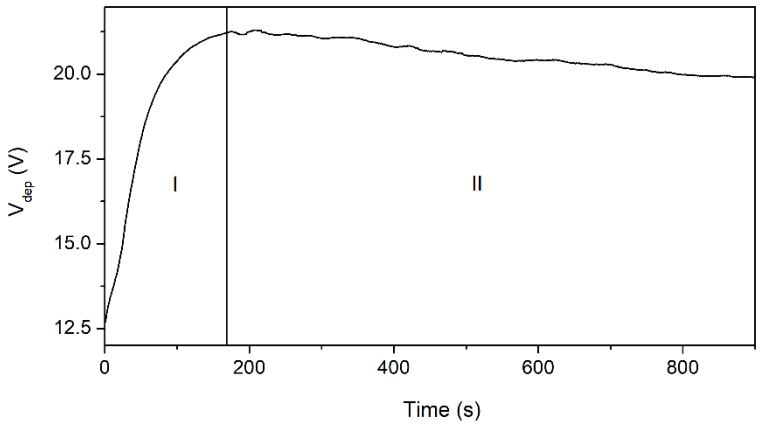

Figure 5.3 - Behaviour of the V_{dep} during PED into AAO templates, which possess dendritic structures at the bottom of the nanopores that were generated in a non-steady-state anodization process.

However, during the filling of the dendritic structures at the bottom of the nanopores (figure 5.3; stage I), it is possible to verify that there is an increase of V_{dep}. This occurs due to the change of the effective electrodeposition area associated with the decrease of the local porosity from 32 % to 10 %. Moreover, if the deposited nanoarchitectures reach the surface of the template, the deposition area increases rapidly, which translates into a sudden reduction of V_{dep}.[6] Furthermore, if deposition continues, hemispherical caps on top of each NW start to develop, which will ultimately merge, originating a thin film at the surface of the template.

Taking this into account and after fabricating the AAO templates, FePt nanostructures were synthesized through PED, at a constant current density, into the nanopores of those membranes. In this process, the formation of the desired nanoarchitectures can be divided into four steps:[7,8]

1. Transfer of the metal ions from the bulk electrolyte to the electrode interface;
2. Adsorption of the metal ions on the electrode surface;
3. Charge transfer, originating metal atoms;
4. Nucleation and growth of the nanostructures.

The nanoporous structure of the template does not influence the last three steps; however, the first one is a mass transport process and, consequently, it is affected by the diameter and length of the nanopores.[7,9] As a result, the electrodeposition into nanoporous structures is diffusion-limited, since the mass transport within the nanopores is limited by the diffusion of metal ions to the electrode surface.[9–11] Furthermore, as previously mentioned (section 1.2.2.1.3.), the electrodeposition of less noble metals, such as Fe, is typically accompanied by hydrogen evolution at the cathode surface, leading to the formation of gaseous H_2 bubbles.[12,13] In the case of nanoporous templates,

this reaction can inhibit the NW growth, since a bubble can completely fill the pore and, as a result, prevent more metal ions from reaching the electrode surface.[7]

Taking into account these effects, different current densities, AAO barrier thicknesses, and electrodeposition time pulses were considered in order to analyse the impact of such parameter on the resulting nanoarchitectures.

5.2.3. Morphological Characterization

The obtained samples were analysed through SEM to evaluate the NWs length and homogeneity. As observed in figure 5.2(a), despite the dendrites at the template's bottom being homogeneously filled, the electrodeposited nanostructures presented varying lengths. This result was more evident for the cases where current densities lower than 40 mA/cm^2 were considered [figure 5.4(a)], where non-continuous nanostructures were obtained. On the other hand, for higher current densities, the template filling was considerably more homogeneous [figure 5.4(b)].

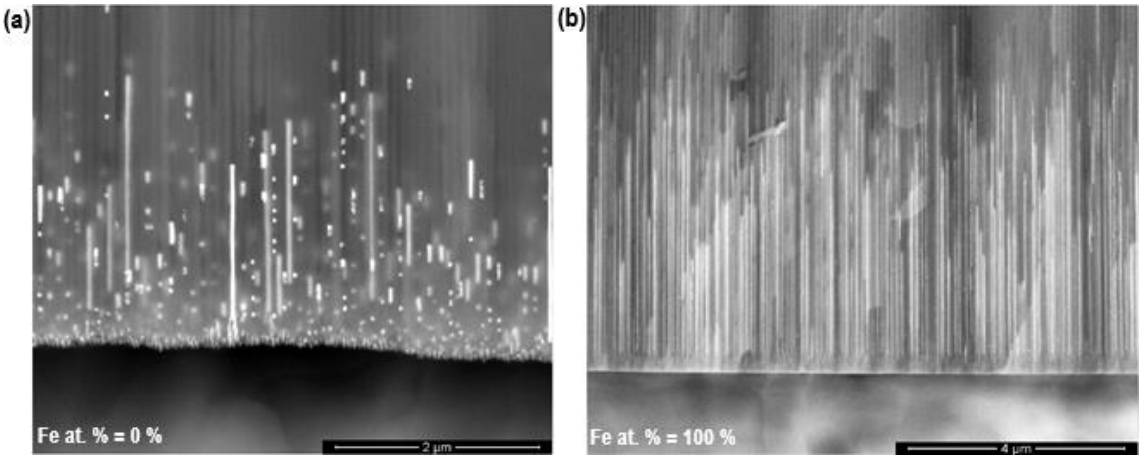

Figure 5.4 - SEM images of the samples electrodeposited at (a) 6 mA/cm^2 and (b) 40 mA/cm^2, considering a barrier layer thickness of ~ 9.1 nm.

Additionally, from the acquired SEM images, average sizes of 106.4 ± 404 nm and 4456.0 ± 1055.3 nm for the NWs fabricated using a current density of 6 mA/cm^2 or 40 mA/cm^2, respectively, were determined. Moreover, considering that a deposition time of 15 min was used for fabricating these samples, it was possible to calculate the deposition rate of the produced NWs, having been obtained values equal to ~ 7.09 nm/min and ~ 296.07 nm/min for the nanostructures synthesized under a current density of 6 mA/cm^2 or 40 mA/cm^2, correspondingly.

5.2.4. Composition Analysis

Then, the fabricated samples were analysed by energy-dispersive X-ray spectroscopy (EDS), to determine the composition of the electrodeposited nanoarchitectures. For the same electrolyte composition, when using a barrier layer thickness of ~ 10.4 nm, it was verified that only Pt was present in the resulting nanoarchitectures, regardless of the applied current density (12 – 70 mA/cm^2). On the other hand, when thinning the barrier layer down to ~ 9.1 nm, the EDS analysis (figure 5.5) revealed that at lower current densities only Pt was electrodeposited, but as the current density increased, the percentage of that element in the fabricated samples decreased and the Fe percentage increased until only Fe was electrodeposited at the higher current densities.

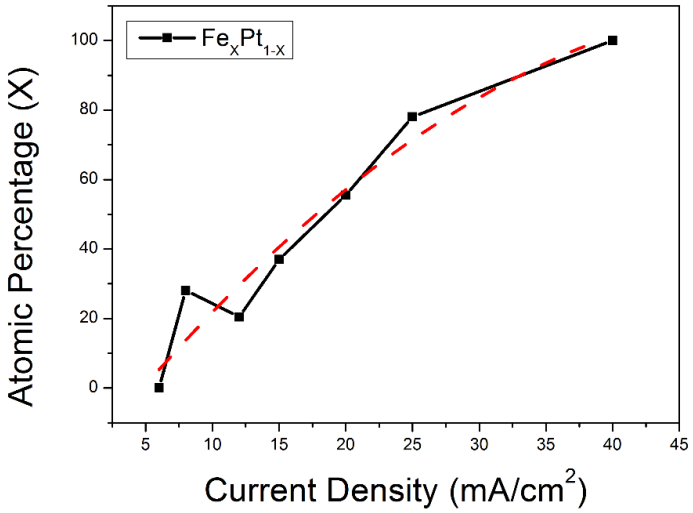

Figure 5.5 - Atomic percentage of Fe and Pt as a function of the electrodeposition current density, with a barrier layer thickness of ~ 9.1 nm. The dashed red line is a polynomial trend line fitted to the acquired data and a guide to the eye.

From figure 5.5, we can verify that for current densities lower than 7 mA/cm^2 only Pt is deposited, at very low deposition rates (15 min to grow 227 nm). Moreover, the percentage of Fe in the NWs increases quasi linearly with this parameter up to $Fe_{80}Pt_{20}$; however, for current densities higher than 40 mA/cm^2 only Fe is deposited. This is an expected result, as lower voltages typically favour the reduction of the more noble metal, i.e. Pt, since it has a higher reduction potential, meaning that it requires a weaker electric field to undergo reduction compared to less noble metal.[14]

Therefore, it is possible to conclude that both the barrier layer thickness and the current density applied during the electrodeposition process influence the composition of the resulting FePt nanostructures, allowing a control over the atomic percentage of the two elements involved.

5.2.5. Magnetic Characterization

Afterwards, the parallel and perpendicular hysteresis loops of the synthesized NW arrays, with a Fe at.% of 28.07, 20.47, 37, 55.46, 78, and 100, were measured at room temperature using a vibrating-sample magnetometer (VSM), as well as a superconducting quantum interference device (SQUID) (figure 5.6). In that figure, the anisotropy field distribution (AFD) curves are also represented. These were determined, for each sample, by performing a cubic b-spline interpolation of the descendant branch of the hard axis hysteresis loop (perpendicular orientation) from the positive saturation down to the remanence value, then calculating the second derivative of the resulting data, and finally performing the following operation for each point (H_A):[15,16]

$$\sigma(H_A) = -H\frac{d^2}{dH^2} < M(H) > \Big|_{H=H_A} \quad (5.2)$$

where $\sigma(H_A)$ is the AFD value at the point H_A, H is the external magnetic field, and $M(H)$ is the magnetization of the sample under an applied magnetic field of H.

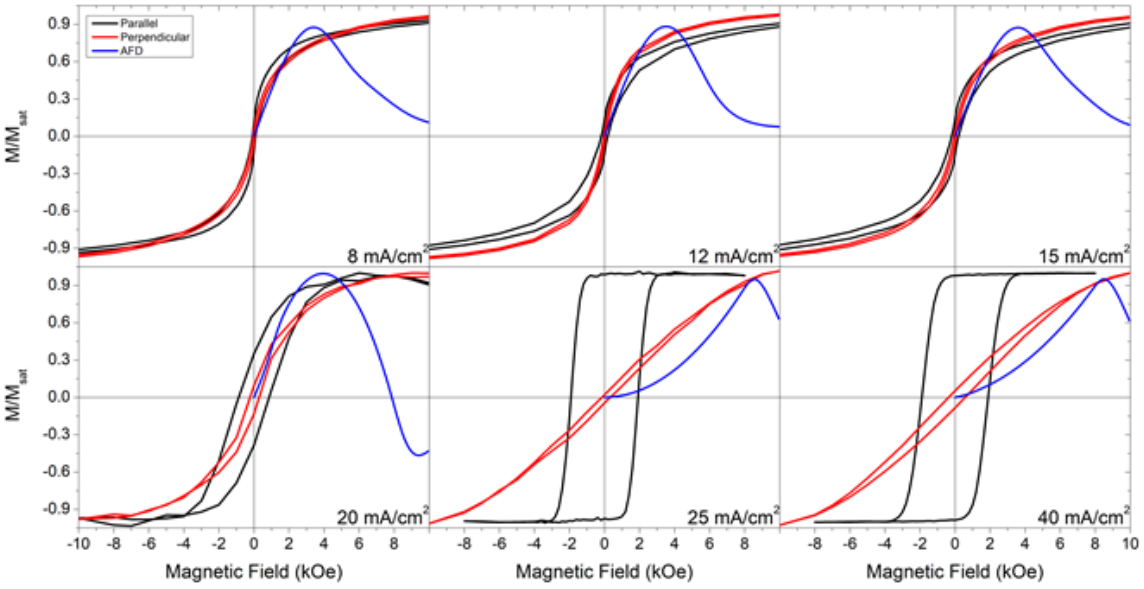

Figure 5.6 - Parallel and perpendicular hysteresis loops and AFD curves of the NWs electrodeposited at 8, 12, 15, 20, 25, and 40 mA/cm^2, which possessed an Fe at.% of 28.07, 20.47, 37, 55.46, 78, and 100, respectively.

Based on the acquired data, it is possible to conclude that the nanostructures' easy magnetization axis is parallel to their longitudinal axis. Additionally, it is observed a significant increase of the magnetic hysteresis as the current density applied during the fabrication process gets higher. Furthermore, we can also verify that the increase of such electrodeposition parameter originates samples with a larger remanent magnetization (M_r) in both orientations, being, such dependence, more significant in the parallel

orientation. Another relevant property of these materials is their coercivity (H_c). From figure 5.6, it is noticeable that the H_c of the samples synthesized under higher current densities is larger in the two considered orientations, when compared to those produced by applying a lower current density. Additionally, and in similar fashion to the remanent magnetization, the variation of the coercivity is more pronounced for the parallel orientation.

These results, regarding the magnetic hysteresis, M_r, and H_c of the fabricated nanoarchitectures, can be attributed to the fact that the Fe at.% in the nanostructures is larger when higher current densities are applied, as observed in the EDS analysis (figure 5.5).

Another important parameter of the fabricated samples is the mean anisotropy field ($< H_A >$), or perpendicular saturation field ($H_{Sat}^{\perp}$), which is the minimum magnetic field required to saturate the magnetization of a material along its hard axis direction.[17–20] Such field can be determined from the calculated AFD curves, since it corresponds to the magnetic field at which that curve reaches its maximum.[16,21] The $H_{Sat}^{\perp}$ values obtained through this method are illustrated in figure 5.8(a), where it is possible to verify that such field increases as the Fe at.% in the fabricated nanostructures gets higher.

5.2.6. Micromagnetic Simulations

Additionally, the magnetic hysteresis loops of an array of 7 NWs with different Fe_xPt_{1-x} stoichiometries were also simulated by applying the magnetic field parallel and perpendicular to the NWs' long axis. The Fe at.% values simulated were 30 %, 55 %, and 100 %, always considering a uniform distribution of Fe along the NWs' length.

As a result, it was verified that the hysteresis loops simulated for the 100 % Fe NWs arrays illustrated a similar behaviour when compared to the ones experimentally measured [figure 5.7(a)]. Furthermore, as the Fe at.% got lower, it was observed a reduction of the perpendicular saturation field values in both the simulated and experimentally measured hysteresis loops [figure 5.8(a)]. However, when analysing the simulated parallel hysteresis loops for Fe at.% of 55 % and 30 % and comparing them to the experimental ones, the differences were noticeable. Specifically, much higher coercivity values were obtained in the calculated loops [figure 5.8(b)]. This might be ascribed to the inhomogeneous length distribution of the NWs array deposited at smaller current densities, as observed in the SEM images (figure 5.4). In addition, slight differences in the FePt stoichiometry along the NWs' length were also found by EDS, as usually occurs when using PED techniques inside long and narrow nanoporous

templates. In particular, the dendrites present at the bottom of the wires appeared to have less Fe at.% than the rest of the nanostructure.

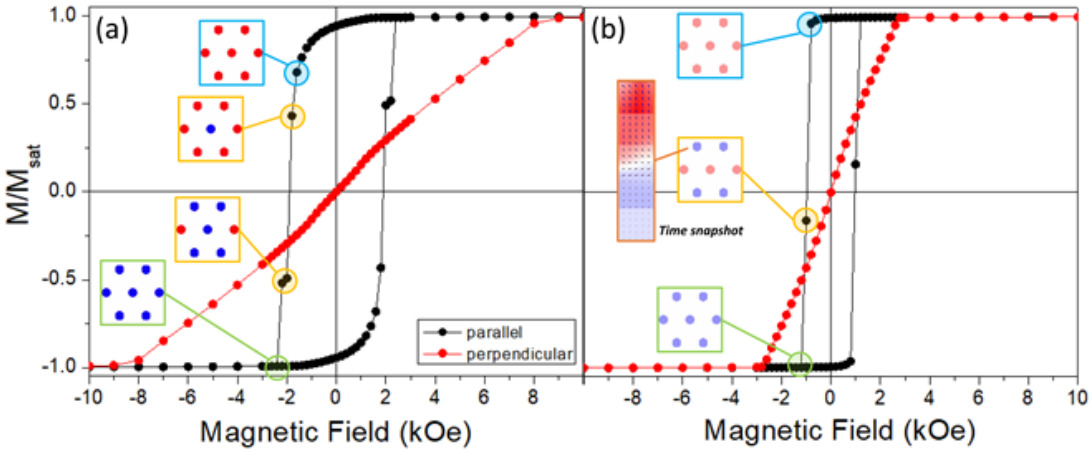

Figure 5.7 - Simulated magnetic hysteresis loops of an array of 7 FePt NWs with an Fe at.% of (a) 100% and (b) 10–20–30–40–50% (gradient), obtained by applying the magnetic field parallel and perpendicular to the NWs' long axis. Insets show cross-sectional views of the magnetic configurations at specific applied fields, with a colour scale of red ($M^{//}/M_{Sat}$ = 1), white ($M^{//}/M_{Sat}$ = 0), and blue ($M^{//}/M_{Sat}$ = -1), where $M^{//}$ is the magnetization along the NWs' long axis..

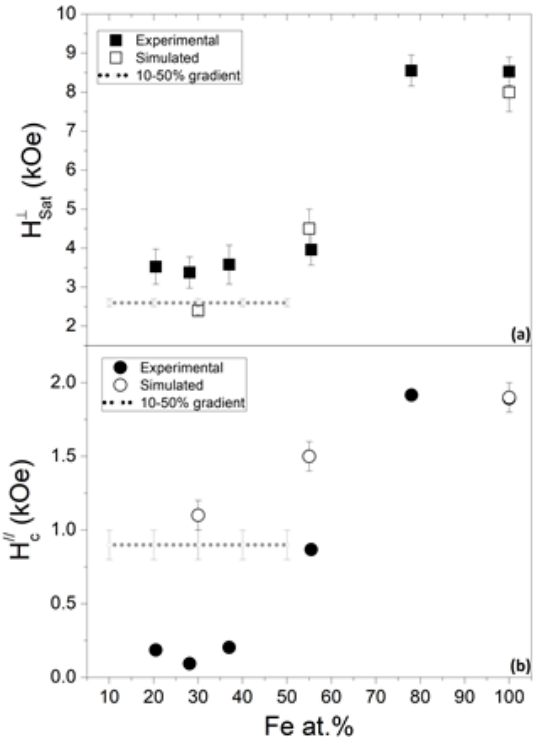

Figure 5.8 - Experimental and simulated (a) $H_{Sat}^{\perp}$, and (b) parallel coercive feld, $H_C^{//}$.

To better understand the effect of a possible change in stoichiometry along the nanostructures, a NW array with a change in stoichiometry along the wires' length was also simulated. In this case, the NWs length was divided into 5 equal parts (each with 30 nm in thickness) and the Fe at.% was set to 10 %, 20 %, 30 %, 40 %, and 50 % at each

consecutive segment. As a result, the simulated parallel hysteresis loop evidenced a decrease in coercivity when compared to the ones simulated for Fe at.% of 30 % and 55 % [figure 5.8(b)]. This result confirms the important effect that stoichiometry has in the magnetization reversal process of FePt NWs. Further analysis of their magnetic configuration using the object oriented micro-magnetic framework (OOMMF) revealed that the reversal of the magnetization in FePt NW arrays with a gradient stoichiometry occurred by the nucleation of a transverse domain wall at the segment with the lowest Fe at.%, which then propagated along the neighbouring segments [figure 5.7(b)]. This led to a reduction of the parallel coercivity, as observed in the simulated parallel hysteresis loops [figure 5.7(b)].

In summary, the micromagnetic simulation results suggest that FePt NWs deposited at lower current densities might have regions with lower Fe at.%, which induce the reversal of the NWs magnetization at smaller magnetic field values. Therefore, the much lower parallel coercivities experimentally measured might be ascribed to existence of nucleation sites along the NWs' length with a lower Fe at.%.

By comparing these results with those from a study where micromagnetic simulations of NWs composed of two different Fe alloys were performed, it is possible to verify the existence of some similarities. Particularly, [22] verified that the magnetic moment and coercive field of $Fe_{(1-x)}M_x$ (M=Co/Ni) NWs monotonically decreased with the content of Co or Ni. A similar effect was observed in our work, where the lowering of the Fe at.% in the FePt nanostructures reduced those two properties of the NWs. The authors of such paper also verified that the Co, or Ni, content influenced the orientation of the easy axis of magnetization of the analysed nanoarchitectures, however, in this work, Pt did not seem have such effect.

5.3. FePt NWs without a Tree-Like Branched Structure

The FePt NWs produced through PED into AAO templates presented in the previous sections are potential candidates for biomedical applications. However, aspects like non-uniform length, heterogeneous composition along their length, and presence of dendritic structures at one end, which modify their properties and are undesirable in biomedicine, make them not suitable for cancer therapy strategies.[23,24] As a result, it emerged an interest for overcoming those limitations by synthesizing FePt NWs through a different strategy. This fabrication approach involved combining hard anodization templates with direct current (DC) electrodeposition, in either the continuous or pulsed mode. Consequently, in the following section, it is presented a detailed characterization of the nanostructures obtained through this process.

5.3.1. Hard Anodization Template

The fabrication of FePt NWs without dendritic structures started with the production of hard anodization templates, using the process described in sections 3.2.3.2.2.1. and 3.2.3.2.2.2. As a result, nanoporous templates with a thickness of ~ 50 µm, an interpore distance equal to 300 nm, and nanopores with ~ 130 nm in diameter, possessing a conducting Au layer in place of the insulating Al oxide layer at the bottom, were obtained (figure 5.9).

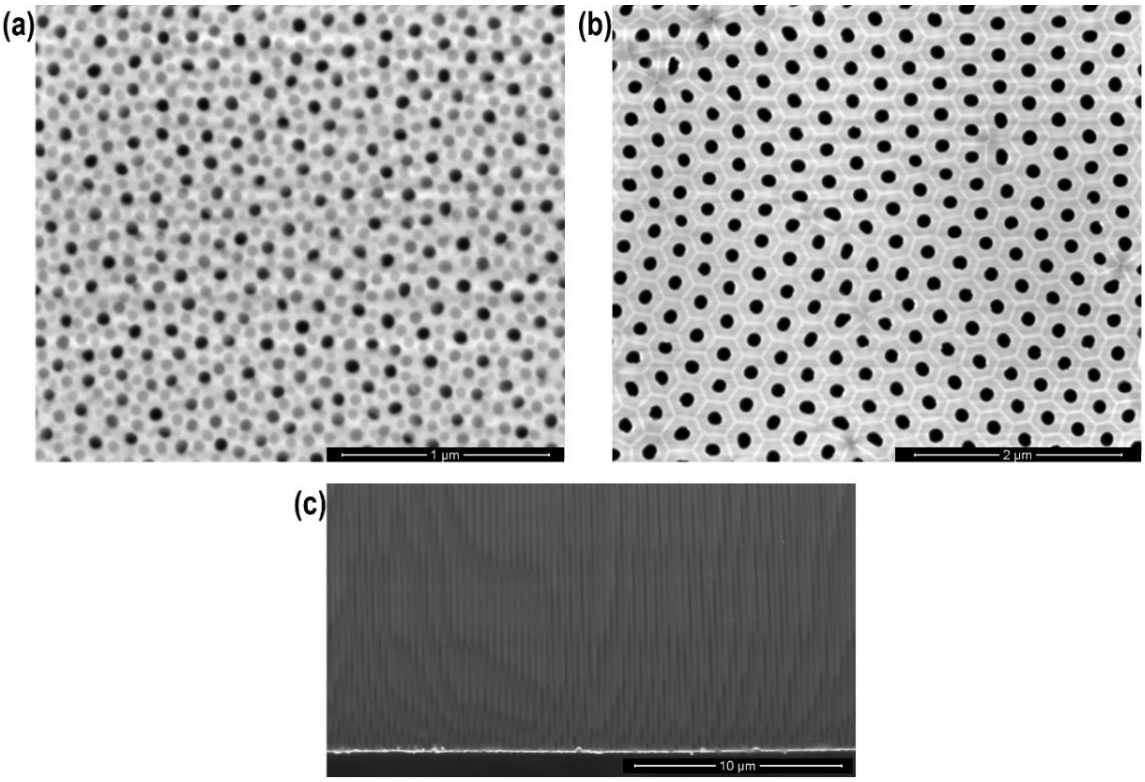

Figure 5.9 - SEM micrographs showing the (a) top, (b) bottom, and (c) cross-section of a hard anodization template, with an Au layer sputtered at the bottom.

The variation of the current density (J) as a function of time (t) during a hard anodization process is represented in figure 5.10.

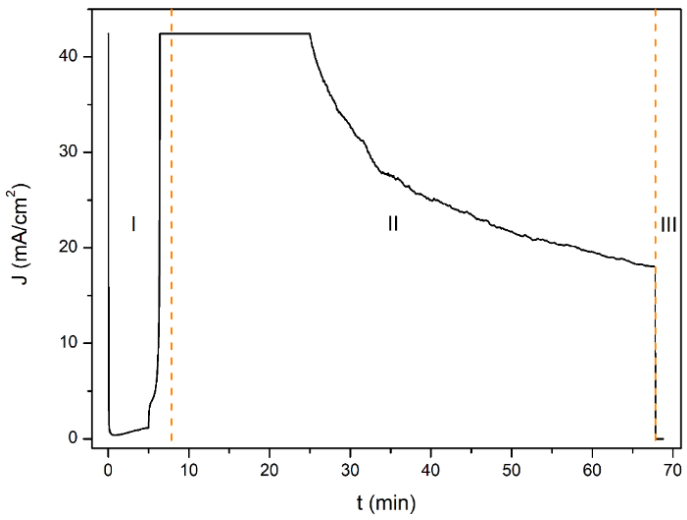

Figure 5.10 - Variation of the current density (J) during a hard anodization process. I: pre-anodization; II: anodization; III: after-anodization.

As can be observed in the figure above, a hard anodization curve can be divided in three phases. The first section corresponds to the pre-anodization, where it is possible to notice, in the first 5 min, a behaviour similar what is verified in a mild anodization curve [figure 5.1(b)], involving a steep decrease of the current density followed by its gradual increase. However, after that period, the current density increases at a significantly faster rate, as a result of the potential increase from 40 V to 140 V, in a stepwise manner. After reaching 140 V, it follows the second step, where such voltage is maintained for 60 min. As can be observed, there is a current density plateau, but, after about 17 min, it starts to decrease in an approximately exponential fashion. This can be attributed to the diffusion-limited electrochemical oxidation of Al at the bottom of the nanopores, due to the extremely fast and uniform growth of the oxide film (50 - 70 µm/h) across the entire sample area. Particularly, it is considered that the anodization current is primarily associated with the movement of ionic species (O^{2-}, OH^{-}, Al^{3+}) through the oxide layer at the nanopores' bottom. Consequently, the current density throughout the anodization is governed by the mass transport of oxygen-containing anions from the bulk reservoir, i.e. the electrolyte, to the oxide/metal interface. Therefore, as the diffusion path gets longer, due to the growing nanopores, the ionic current gradually decreases over time.[25,26] Finally, the third phase corresponds to the after-anodization, where the anodization potential is abruptly reduced to 40 V and a drop in the current density is naturally observed.

In contrast to the AAO templates produced through mild anodization, hard anodization membranes possess a significantly lower porosity, ranging between 3.4 and 3.5 %, deviating from the 10 % porosity rule.[26] Moreover, as a result of the higher anodization

potential, the volume expansion from Al to Al oxide increases from ~ 1.2 at 40 V up to ~ 1.7 at 140 V.[27]

5.2.3. Electrodeposition Behaviour

FePt NWs were grown inside the produced AAO templates through DC electrodeposition, in either continuous or pulsed mode, under potentiostatic conditions, so as to obtain a uniform composition along their length. Similarly, to the previous electroplating approach, these fabrication techniques are diffusion-limited, as a result of the nanopores' shape.[28,29]

In the following sections, such synthetization strategies will be addressed in detail.

5.2.3.1. Continuous Direct Current (DC) Electrodeposition

A typical continuous DC electrodeposition curve, obtained under potentiostatic conditions, is presented in figure 5.11(a).

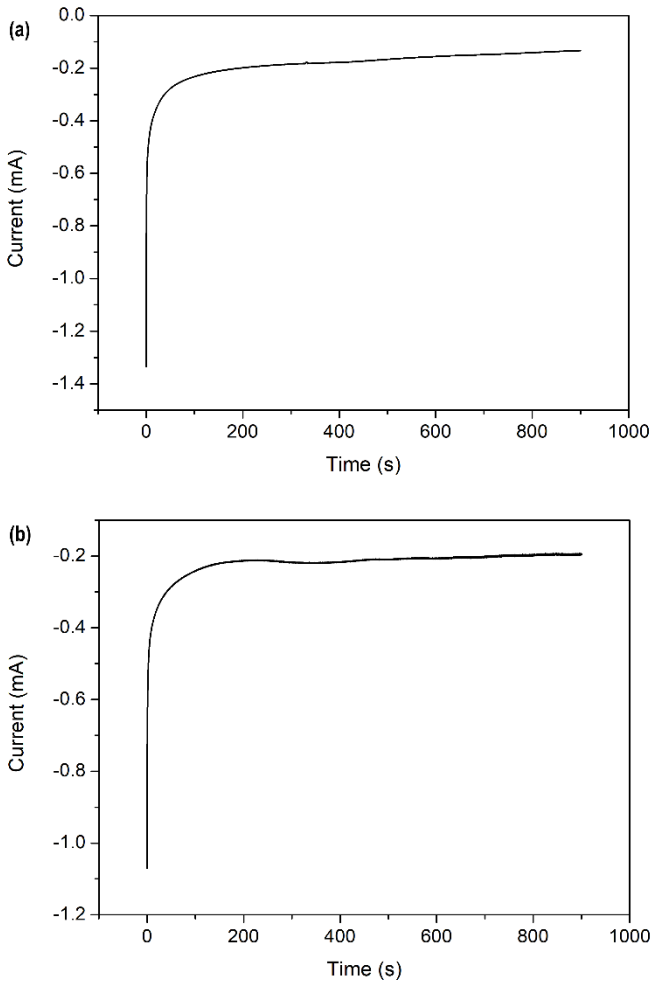

Figure 5.11 - Variation of the current with time, during the electrodeposition of FePt NWs into hard anodization AAO templates through a (a) continuous or (b) pulsed DC approach, considering the application of a deposition potential of 1 V ([$H_2PtCl_6 \cdot 6H_2O$] = 1 g/L; [$FeSO_4 \cdot 7H_2O$] = 20 g/L).

As can be observed, in the initial moments of electrodeposition, there is a steep decrease, in modulus, of the current density. This behaviour is commonly associated with a diffusion-limited growth, where the reduction in that parameter is indicative of a limited availability of ions or reactants at the electrode surface.[30,31] Therefore, the rate of mass transport from the bulk electrolyte to the electrolyte/electrode interface becomes a limiting factor, influencing the electrodeposition process.[32]

Moreover, it is not observed an initial increase of the current density modulus, which was anticipated as it corresponds to the nucleation process where there is a 3D expansion and/or the formation of additional nuclei in the initial stages of electrodeposition, resulting in an increase of the electroplating surface area.[32,33] In this case, the absence of such behaviour can be attributed to the FePt high deposition rate, as a result of the large V_{dep} applied, leading to an instantaneous nucleation, wherein the nucleation sites become saturated after a very brief period.[31,34–36]

In this work, the effect of different V_{dep} and concentrations of precursors in the electrolyte on the composition of the resulting NWs, when considering continuous DC electrodeposition, was assessed.

5.3.2.2. Pulsed DC Electrodeposition

In addition to the DC electrodeposition in the continuous mode, FePt NWs were also produced through a pulsed DC electroplating technique into the same type of templates. An electrodeposition curve, obtained using this fabrication strategy, is presented in figure 5.11(b).

By comparing this curve with the one presented in the one of continuous DC approach, it is possible to verify that, in both cases, the current decreases steeply with time, in the initial moments of electrodeposition. However, as the process progresses, that parameter presents a slower reduction in the pulsed strategy, which can be attributed to fact that the introduction of a rest pulse allows the renewal of the concentration of metal ions at the deposition interface and limits hydrogen evolution, as opposed to the continuous DC electroplating technique.[37,38]

Regarding this fabrication strategy, besides the influence of different V_{dep} and concentrations of precursors in the electrolyte on the composition of the produced nanostructures, it was also analysed the role played by the t_{on}, t_{off}, t_{on}/ t_{off} ratio, and prior Au electrodeposition, on that same physical property.

5.3.3. Morphological Characterization and Composition Analysis

After fabricating the FePt through DC electrodeposition, their morphology and composition was evaluated using SEM and EDS, respectively, in order to analyse the effect of each varied parameter on those two physical properties. In the following sections, the influence of each fabrication parameter will be addressed in detail.

5.3.3.1. Electrodeposition Potential

For the two DC approaches considered, it was evaluated the effect of V_{dep} on the composition and quality of the resulting NWs (figure 5.12).

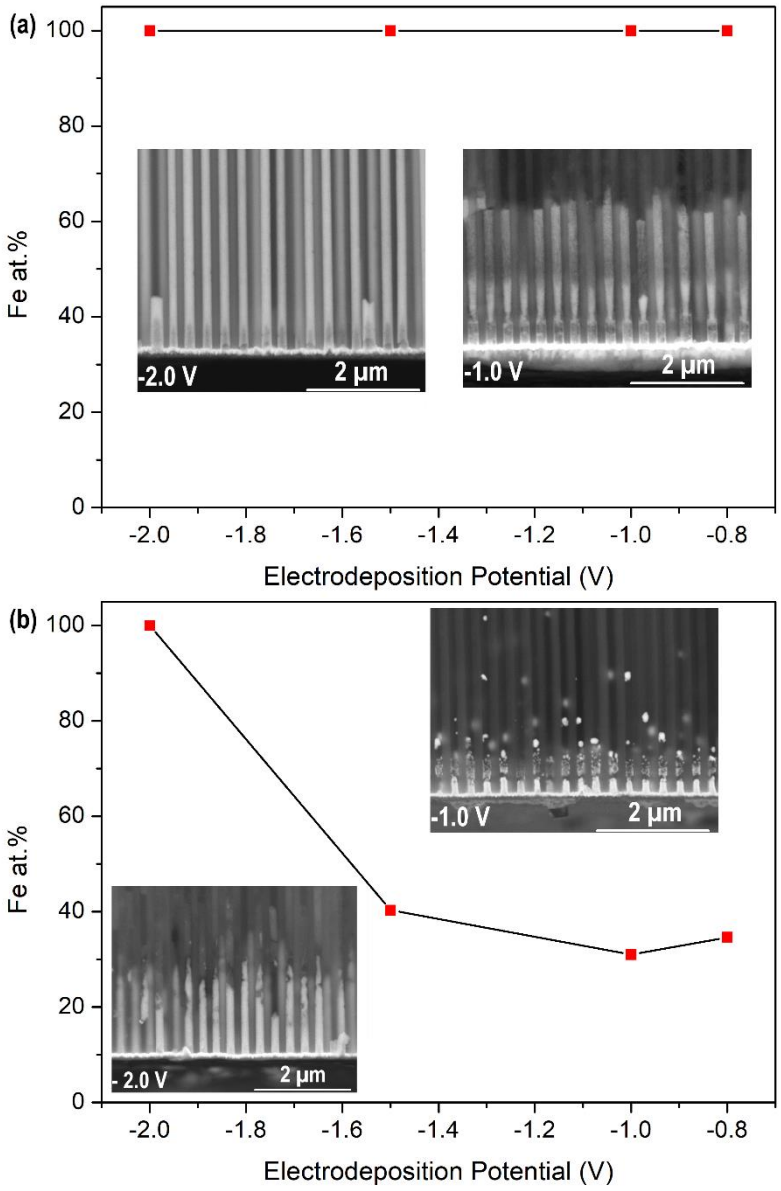

Figure 5.12 - Composition of the NWs fabricated through (a) continuous and (b) pulsed DC electrodeposition as a function on the applied V_{dep} ($[H_2PtCl_6 \cdot 6H_2O]$ = 1 g/L; $[FeSO_4 \cdot 7H_2O]$ = 20 g/L; t_{on} = 4 ms; t_{off} = 40 ms).

Regarding the DC electrodeposition in the continuous mode [figure 5.12(a)], it is possible to conclude that varying V_{dep} does not change the composition of the resulting NWs, which are composed of only Fe. Moreover, reducing, in modulus, V_{dep} appears to produce lower-quality NWs, leading to the formation of a tubular structure at the bottom of the nanopore that grows into a NW with a tapered end. This can be attributed to the intricate interplay between several factors involved in the NWs' development, such as the nanopore geometry, ion diffusion and transport dynamics, as well as the kinetics governing their growth.[39–42]

On the other hand, from results obtained with pulsed DC electrodeposition [figure 5.12(b)], it is verified that, despite the existence of a composition variation with V_{dep}, the electroplating quality is low, particularly when considering lower potentials, in modulus. Naturally, due to the fact that in some samples only a residual amount of material is deposited, the EDS measurements are not precise. Therefore, the presented Fe at.% values may not correspond to the values in those sample with a lower deposition quality.

5.3.3.2. Concentration of Pt and Fe Precursors in the Electrolyte

In addition to V_{dep}, the influence of the concentration of $FeSO_4 \cdot 7H_2O$ and $H_2PtCl_6 \cdot 6H_2O$ in the electrolyte on the morphology and composition of the resulting FePt NWs was also analysed. Regarding continuous DC electrodeposition, the obtained results are presented below (figure 5.13).

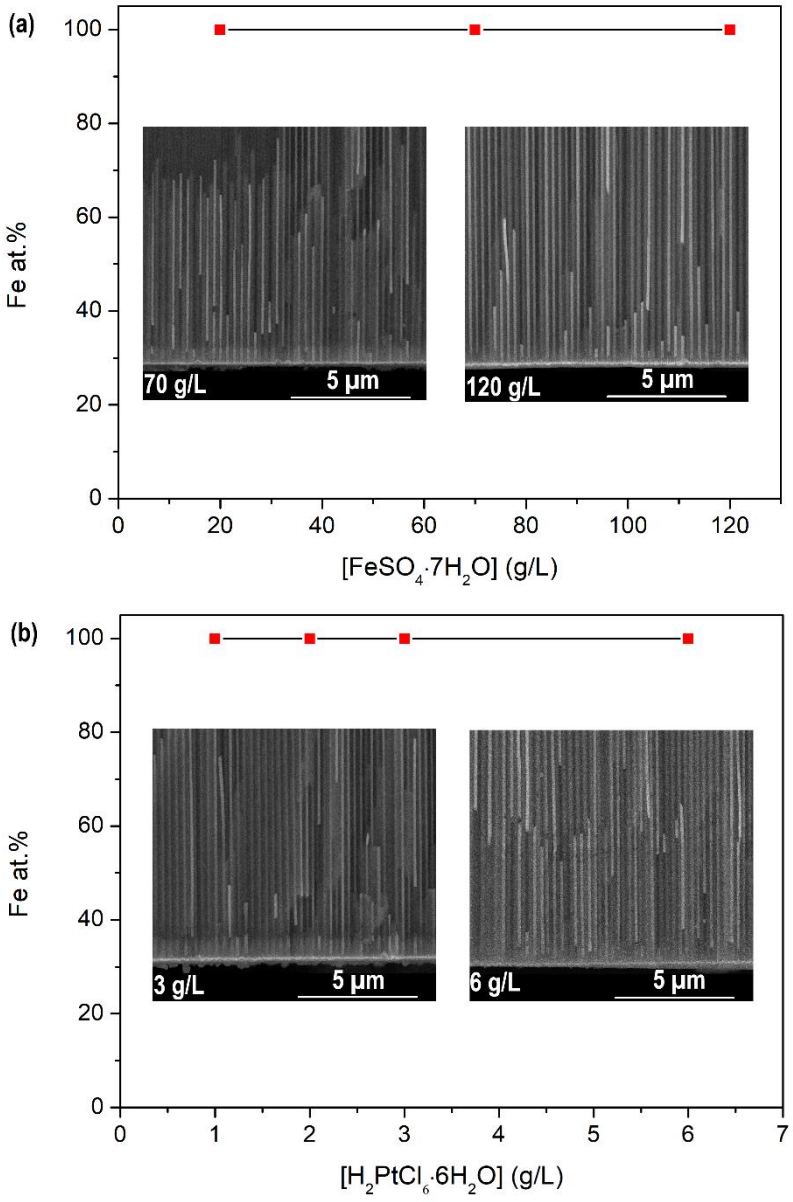

Figure 5.13 - Composition of the NWs fabricated through continuous DC electrodeposition as a function of the concentration of (a) [$FeSO_4 \cdot 7H_2O$] ($H_2PtCl_6 \cdot 6H_2O$] = 1 g/L and (b) $H_2PtCl_6 \cdot 6H_2O$] ([$FeSO_4 \cdot 7H_2O$] = 20 g/L) in the electrolyte, (V_{dep} = -2.0 V).

As can be observed, the concentration of the two metal precursors in the electrolyte does not affect the composition or the morphology of the resulting NWs, which are composed of only Fe.

This study was also performed for pulsed DC electrodeposition and the acquired results are represented in figure 5.14.

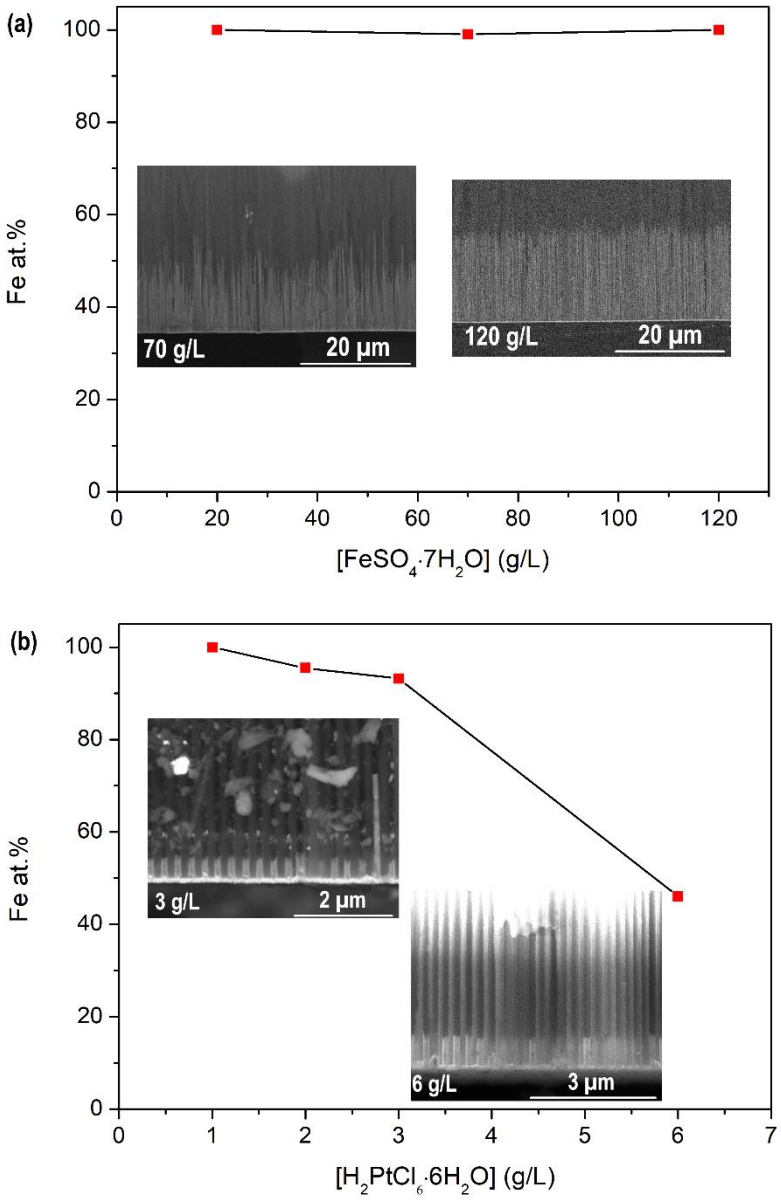

Figure 5.14 - Composition of the NWs fabricated through pulsed DC electrodeposition as a function of the concentration of (a) [$FeSO_4 \cdot 7H_2O$] ([$H_2PtCl_6 \cdot 6H_2O$] = 1 g/L and (b) $H_2PtCl_6 \cdot 6H_2O$] ([$FeSO_4 \cdot 7H_2O$] = 20 g/L) in the electrolyte, (V_{dep} = -2.0 V; t_{on} = 20 ms; t_{off} = 20 ms).

From the presented results, it is possible to verify that the concentration of $FeSO_4 \cdot 7H_2O$ does not influence the composition of the resulting NWs, which are only composed of Fe. Nevertheless, regarding their morphology, higher [$FeSO_4 \cdot 7H_2O$] leads to an improved deposition quality, resulting in longer NWs presenting more homogeneous lengths. Conversely, increasing the concentration of $H_2PtCl_6 \cdot 6H_2O$ appears to have a similar effect, i.e. the electrodeposition quality improves, but the quantity of material deposited is reduced. This may occur as a result of the increase of H^+ ions in the electrolyte, due to the higher quantity of Pt precursor, leading to a modification in the chemical environment of the Pt ions during the deposition process, which may inhibit the

nanostructures' growth.[43] Nevertheless, similarly to the previous section, in this case the EDS results should not be considered completely precise, due to the low amount of material grown inside the nanopores.

5.3.3.3 Duration of the Deposition Pulse (t_{on})

Based on the results acquired in the two previous studies, it was decided that the use of pulsed DC electrodeposition for the fabrication of FePt NWs was the most promising approach, as it appeared to allow a higher control of the composition of the resulting nanostructures, despite leading to a worse deposition quality. Therefore, to try improving those two aspects, the influence of other electrodeposition parameters, namely t_{on} and t_{off} was analysed. Regarding the first, the obtained results are presented below (figure 5.15).

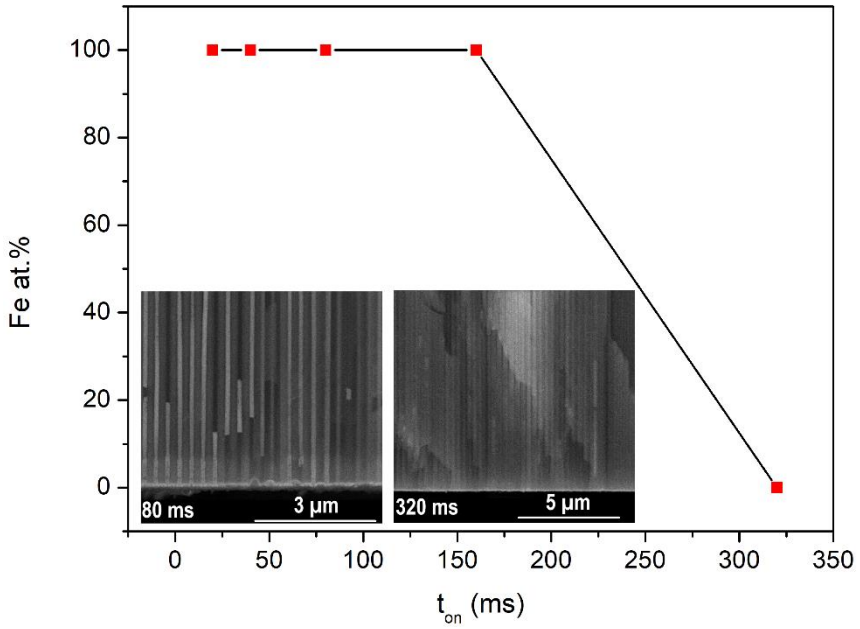

Figure 5.15 - Composition of the NWs fabricated through pulsed DC electrodeposition as a function of t_{on} ([$FeSO_4 \cdot 7H_2O$] = 20 g/L; [$H_2PtCl_6 \cdot 6H_2O$] = 1 g/L; V_{dep} = -2.0 V; t_{off} = 20 ms).

As can be observed, changing t_{on} up until 160 ms does not appear to have a significant impact on the composition of the NWs, leading, nevertheless, to an improved morphology. However, it was verified that, when using a t_{on} of 320 ms, no material was deposited, suggesting that this parameter has an impact on the successful deposition of the FePt NWs. This suggests a complex interplay of factors, where the pulse duration in pulsed DC electrodeposition acts as a critical parameter influencing the nucleation, growth, and precursor reactivity, ultimately leading to a lack of FePt deposition with longer pulses.[44] Particularly, a longer ton in combination with a relatively short toff may promote unfavourable reactions, such as excessive precursor decomposition or

competing reactions, that disrupt the conditions required for the formation of the FePt NWs.[44-46]

5.3.3.4. Duration of the Rest Pulse (t_{off})

In addition to t_{on}, the influence of t_{off} on the FePt NWs produced through pulsed DC electrodeposition was assessed as well (figure 5.16).

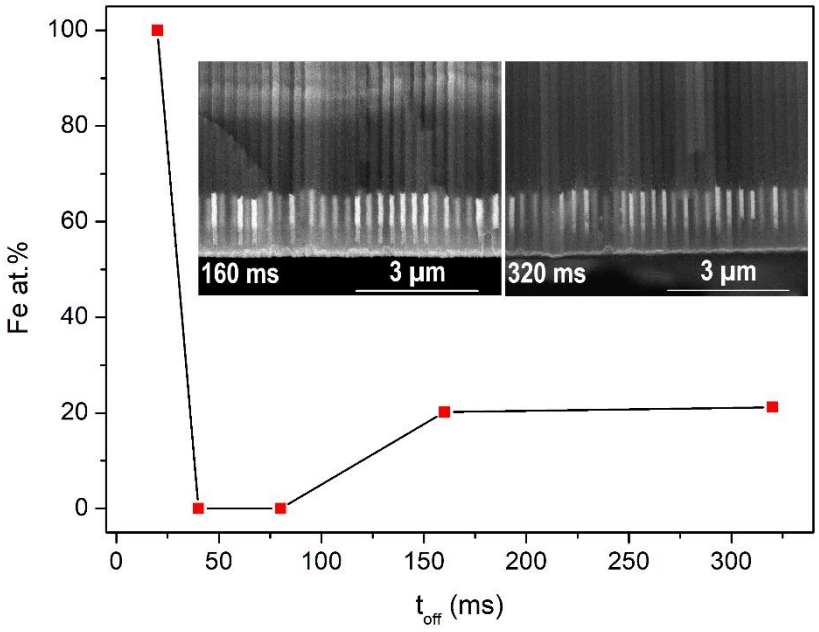

Figure 5.16 - Composition of the NWs fabricated through pulsed DC electrodeposition as a function of t_{off} ([$FeSO_4 \cdot 7H_2O$] = 20 g/L; [$H_2PtCl_6 \cdot 6H_2O$] = 1 g/L; V_{dep} = -2.0 V; t_{on} = 20 ms).

From the presented results, it is possible to verify that, for a sufficiently long t_{off} (160 ms, in this case), the resulting FePt NWs present a relatively homogeneous length. Additionally, a further increase of t_{off} does not appear to have a significant impact on the morphology or composition of the deposited nanostructures. This result may be attributed to the fact that longer t_{off} values allow the concentration of metal ions at the deposition interface to be properly renewed before the following deposition pulse.[32,37]

5.3.3.5. Prior Au Electrodeposition

In order to try improving the quality of the fabricated NWs, it was analysed the effect of electrodepositing ~ 250 nm of Au before growing the FePt NWs, as it was hypothesized that it could enhance the nucleation and growth processes of the FePt NWs, ultimately leading to improved structural integrity, crystallinity, and magnetic properties (figure 17).[47,48]

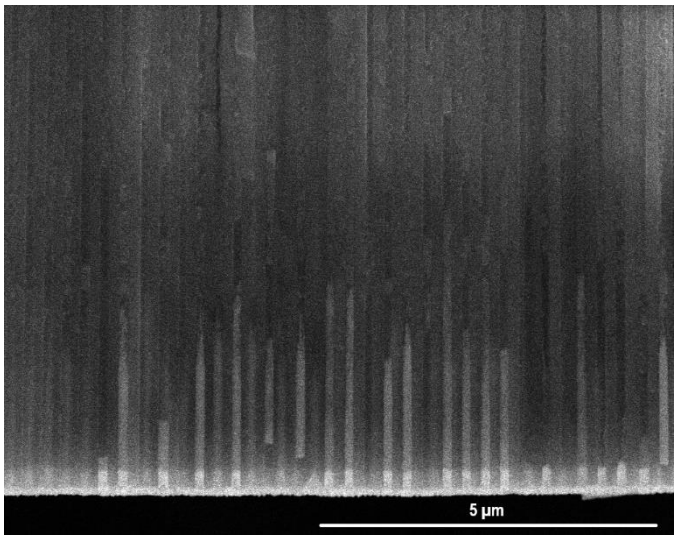

Figure 5.17 - NWs fabricated through pulsed DC electrodeposition after depositing a ~ 250 nm-thick Au layer at the bottom of the nanopores ([$FeSO_4 \cdot 7H_2O$] = 20 g/L; [$H_2PtCl_6 \cdot 6H_2O$] = 1 g/L; V_{dep} = -2.0 V; t_{on} = 20 ms; t_{off} = 20 ms).

By comparing this sample with the one previous obtained under the same conditions, but without depositing the Au layer inside the nanopores (e.g. figure 5.14), it is possible to verify that the Au layer appears to originate nanostructures with slightly less defects. Furthermore, in terms of composition, it was observed a slight reduction of the Fe at.% in this sample (90.98 %).

Consequently, for the subsequent experiments, it was decided to deposit a ~ 250 nm-thick Au layer at the bottom of the nanopores before the deposition of FePt.

5.3.3.6. t_{on}/t_{off} Ratio

Based on the results acquired up until this point, it is verified that both t_{on} and t_{off} play a role on the ability to produce FePt NWs through this approach. Consequently, in order to better comprehend such relation and, therefore, improve the electrodeposition quality as well as the control over the nanotructures' composition, it was decided to analyse the impact of the t_{on}/t_{off} ratio on those two aspects (figure 5.18).

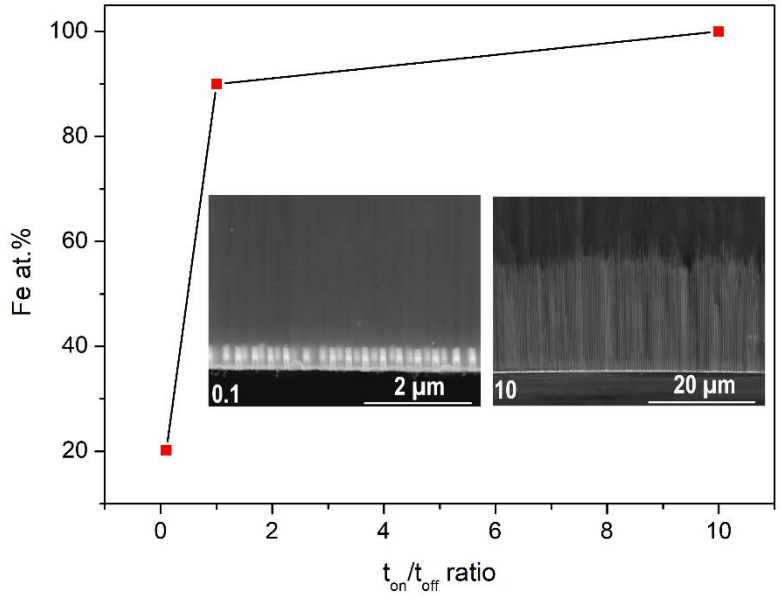

Figure 5.18 - Composition of the NWs fabricated through pulsed DC electrodeposition as a function of the t_{on}/t_{off} ratio ($[FeSO_4 \cdot 7H_2O]$ = 20 g/L; $[H_2PtCl_6 \cdot 6H_2O]$ = 1 g/L; V_{dep} = -2.0 V).

From the presented results, it is possible to conclude that the Fe at.% increases with increasing t_{on}/t_{off} ratio. Therefore, this appears to be a parameter that controls the composition of the FePt NWs. However, as the Fe at.% in the nanostructures decreases, the electrodeposition quality significantly degrades.

To try overcoming this limitation, a similar experiment was performed under the same conditions, but considering a higher concentration (3 g/L) of $H_2PtCl_6 \cdot 6H_2O$ in the electrolyte (figure 5.19).

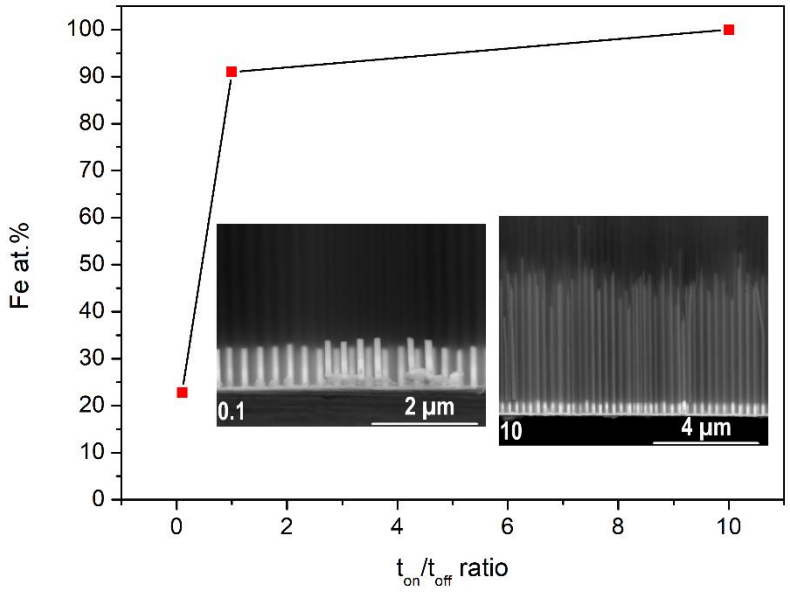

Figure 5.19 - Composition of the NWs fabricated through pulsed DC electrodeposition as a function of the t_{on}/t_{off} ratio ($[FeSO_4 \cdot 7H_2O]$ = 20 g/L; $[H_2PtCl_6 \cdot 6H2O]$ = 3 g/L; V_{dep} = -2.0 V).

As can be observed, increasing the concentration of Pt in the electrolyte significantly improved the quality of the electrodeposited NWs with lower Fe at.%, which were obtained for t_{off} times longer than t_{on} times. This may occur for various reasons, such as, for example, reduction of the likelihood of impurities or competing ions being incorporated into the nanostructures, thus minimizing structural irregularities.[49-53] Furthermore, a higher concentration of Pt in the electrolyte means that there are more Pt ions available for nucleation, allowing more uniform nucleation and growth processes.[7,9]

Additionally, the Fe at.% appears to follow a trend similar to that presented in figure 5.19, where that parameter increases with increasing t_{on}/t_{off}. Consequently, this ratio appears to be the main factor for controlling the FePt NWs composition.

To further validate this fact, it was analysed the influence of the V_{dep} on the composition and morphology of FePt NWs, obtained under the same conditions used for fabricating the NWs presented in figure 5.19 with a t_{on}/t_{off} ratio equal to 0.1 (figure 5.20).

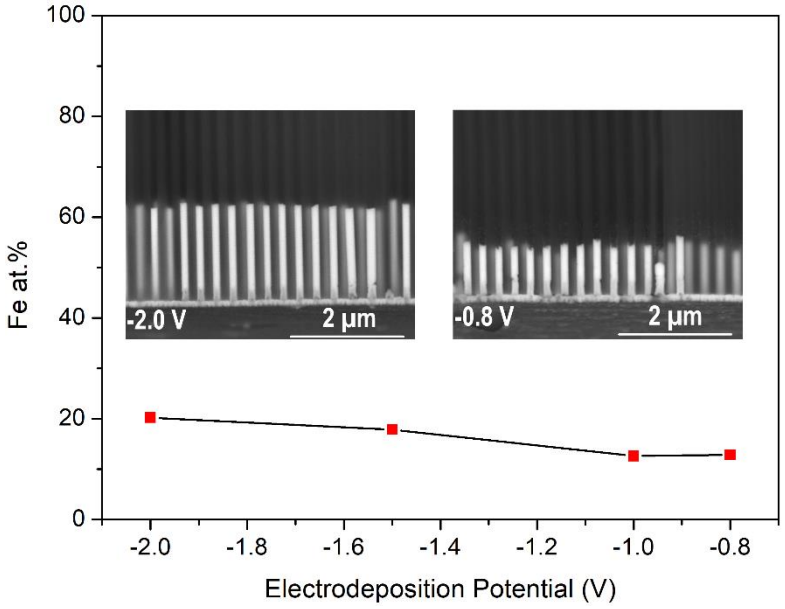

Figure 5.20 - Composition of the NWs fabricated through pulsed DC electrodeposition as a function of the applied V_{dep} ($[H_2PtCl_6 \cdot 6H_2O]$ = 3 g/L; $[FeSO_4 \cdot 7H_2O]$ = 20 g/L; t_{on}/t_{off} = 0.1).

The obtained results seem to indicate that V_{dep} is not, in fact, the main parameter for controlling the composition of the electrodeposited FePt NWs, as the variation of their Fe at.% over the considered potential range is low. Nevertheless, the Fe content in the produced nanostructures appears to slightly increase with increasing V_{dep}, in modulus. This is an expected result, as the Pt concentration is considerably lower than the Fe concentration in the electrolyte. As a result, since Pt has a greater reduction potential,

larger voltages lead to a faster depletion of the Pt ions allowing, therefore, a higher deposition of Fe.[54-56]

Since it was demonstrated that higher concentration of $H_2PtCl_6 \cdot 6H_2O$ in the electrolyte improved the homogeneity of the resulting nanostructures, it was decided to analyse the impact of the t_{on}/t_{off} ratio on a new batch of samples, where a concentration of $H_2PtCl_6 \cdot 6H_2O$ equal to 6 g/L was considered in the fabrication process (figure 5.21).

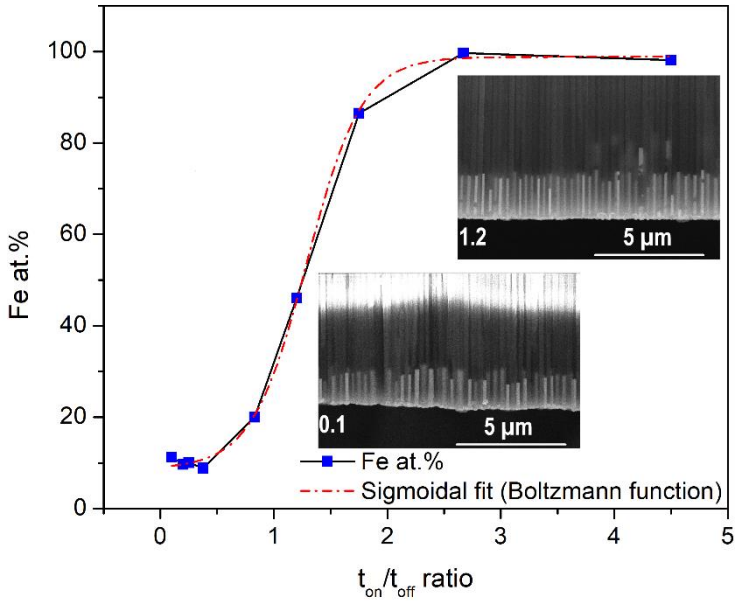

Figure 5.21 - Composition of the NWs fabricated through pulsed DC electrodeposition as a function of the t_{on}/t_{off} ratio ($[FeSO_4 \cdot 7H_2O]$ = 20 g/L; $[H_2PtCl_6 \cdot 6H_2O]$ = 6 g/L; V_{dep} = -2.0 V).

From the presented results, it is possible to conclude that the Fe at.% increases with increasing t_{on}/t_{off} ratio, ranging between ~ 0.1 Fe at.% at t_{on}/t_{off} = 0.1 to ~ 100 Fe at.% at $t_{on}/t_{off} \geq 2.67$. Moreover, it was performed a sigmoidal fit, using the Boltzmann function, to the acquired data, having been obtained a R^2 of 0.99925, indicating a good fit to the experimental data. This suggests the existence of a threshold (possibly related to the t_{on}/t_{off} ratio) at which the Fe at.% starts to significantly increase. Such behaviour may indicate a modification in the underlying mechanisms governing the growth of the FePt NWs.[57-59]

Additionally, the morphology of the produced NWs is significantly improved in comparison to the ones previously synthesized, which can be attributed to the increase of the concentration of $H_2PtCl_6 \cdot 6H_2O$ in the used electrolyte.

5.3.4. Magnetic Characterization

After optimizing the fabrication process of FePt NWs, the parallel and perpendicular hysteresis loops of FePt NW arrays possessing different Fe at.% were acquired at room temperature, using a SQUID-VSM (figures 5.22 and 5.23).

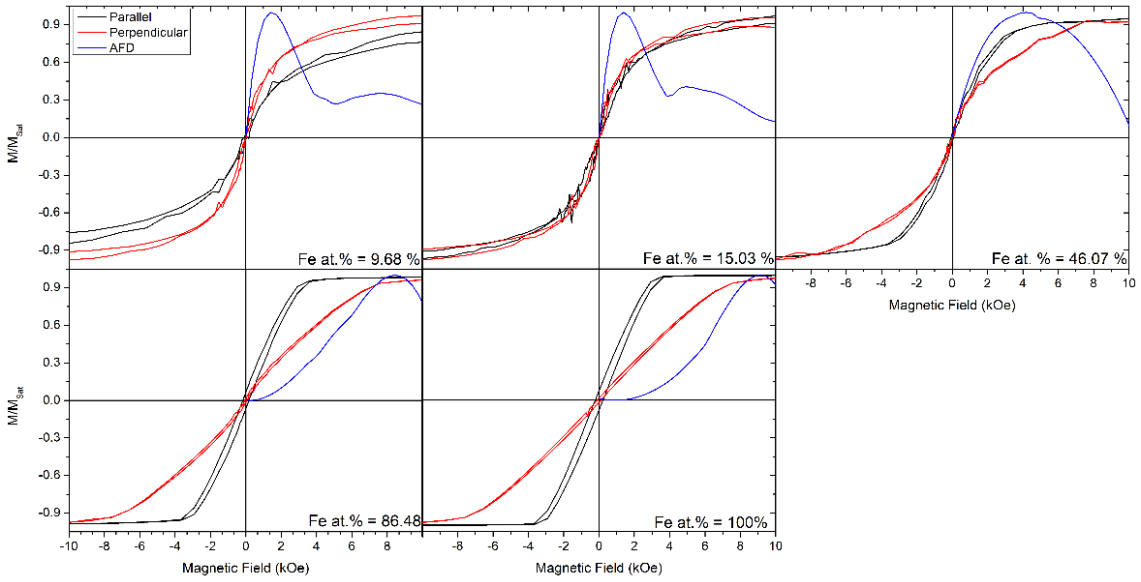

Figure 5.22 - Parallel and perpendicular hysteresis loops and AFD curves of the produced FePt NWs with different Fe at.% (100, 86.48, 46.07, 15.03, and 9.68 %).

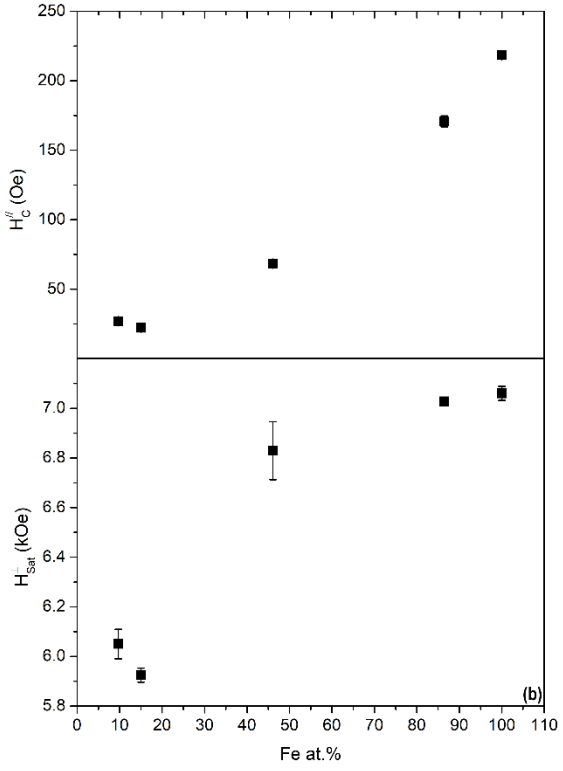

Figure 5.23 - Experimental (a) $H_C^{//}$ and (b) $H_{Sat}^{\perp}$.

Similarly to the results obtained for the NWs fabricated through PED, it is possible to verify that the easy magnetization axis of these nanostructures is parallel to their longitudinal axis. Furthermore, it is observed a decrease of the magnetic hysteresis, as well as of the M_r in both orientations, as the Fe at.% gets lower. Additionally, regarding their $H_C^{//}$ [figure 5.23(a)] it is noticeable that such parameter also has a smaller value for lower Fe at.%. This variation of M_r and H_c appears to be more evident for the parallel orientation.

As in the case of FePt NWs with dendritic structures, this variation of the magnetic hysteresis, M_r, and H_c can be ascribed to the different Fe at.% in the nanostructures, which was previously determined through EDS. Moreover, the $H_{Sat}^{\perp}$ values [figure 5.23(b)], obtained from the calculated AFD curves, present a similar behaviour, where lower Fe at.% lead to a smaller $H_{Sat}^{\perp}$.

In order to verify if there was a stoichiometry change along the length of these nanostructures that could affect their magnetic properties, it was decided to remove from the AAO template and disperse FePt NWs with a Fe at.% of $\sim$ 80 %, previously determined through EDS, and then perform a morphological and compositional characterization of individual nanoarchitectures, using SEM and EDS (figure 5.23). These were the selected nanomaterials because their biocompatibility, together with magnetic properties and oxidation resistance, makes them the most promising candidates for the desired biomedical application.[60-62] Moreover, this analysis was not carried out for the FePt nanostructures produced through PED, as it is not possible to remove them from the template without breaking the dendritic structures.

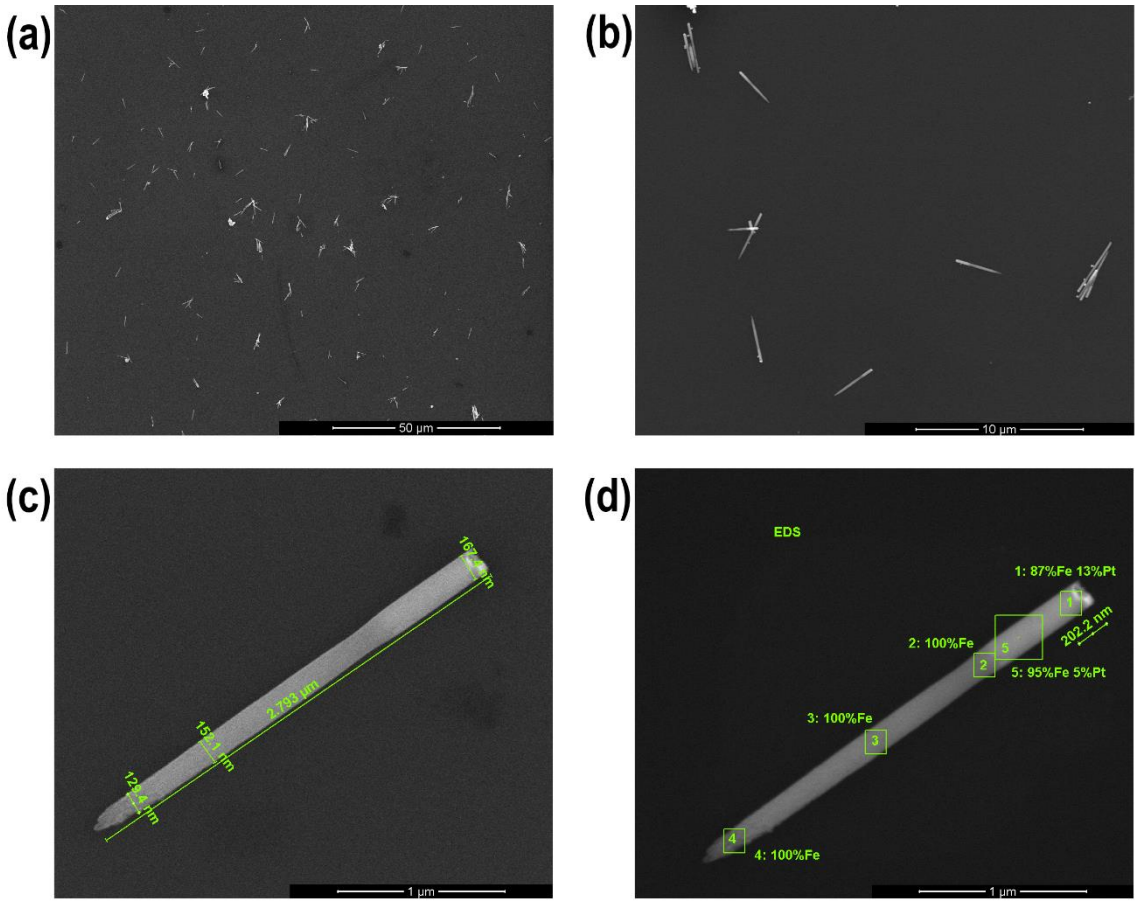

Figure 5.24 - (a, b) SEM images of dispersed FePt NWs; (c) morphological and (d) compositional analysis of a single FePt NW.

From the presented results, it is possible to verify that both the diameter and composition of the FePt NWs vary along their longitudinal axis. Particularly, the nanostructures become narrower and the Fe at.% increases as they get longer. Regarding their composition, the obtained results indicate that during the initial stages of electrodeposition, the more noble metal, i.e. Pt, is preferentially deposited, as it possesses a higher reduction potential. However, since the concentration of Pt ions in the electrolyte is considerably lower than that of Fe ions, the preferential deposition of Pt diminishes over time as Fe ions become even more predominant in that solution. Consequently, as the electrodeposition process progresses, there is a shift towards a higher Fe at.% in the FePt NWs. This problem should be addressed in the future, through the design of an electrolyte where the reduction potentials of Fe and Pt are brought closer together using a selective complexing agent, i.e. one that only forms complexes with Pt ions but not Fe ions, narrowing the gap between the reduction potentials of those two cations. [63,64] Examples of those compounds include 5,5-dimethylhydantoin (DMH) or ethylenediamine.[65,66]

Nevertheless, for biomedical applications the dimensions of these nanoarchitectures should not exceed 1 μm, so as to prevent a partial or even total occlusion of the capillaries.[67,68] In this context, as presented in figure 5.24(c, d), it is possible to obtain FePt NWs with a homogeneous morphology and possessing the desired composition for lengths up until ~ 200 nm. Consequently, by calculating the electrodeposition rate, i.e. ~ 3.103 nm/min, it is possible to produce FePt nanostructures with an adequate length for pretended biomedical application.

5.4. Conclusion

In this chapter, two methods for fabricating FePt NWs, based on pulsed or DC electrodeposition into AAO templates, were demonstrated. Regarding the first approach, it was concluded that the composition of the resulting nanostructures could be controlled by adjusting the thickness of the barrier layer at the bottom of the template, as well as the current density applied during the electroplating process. However, the length of the resulting nanoarchitectures grown at lower current densities was not homogeneous. Furthermore, the magnetic characterization of the obtained samples revealed that there is an increase of the magnetic hysteresis, remanent magnetization, coercivity, and $H_{Sat}^{\perp}$ with the increase of the Fe at.%. Additionally, micromagnetic simulations of FePt NW arrays with various stoichiometries indicated that the nanostructures produced at lower current densities may possess a varying stoichiometry along their length.

On the other hand, when using continuous and pulsed DC electrodeposition, it was demonstrated that the composition of the synthesized NWs was controlled by the t_{on}/t_{off} ratio considered in the pulsed mode, while the continuous approach did not lead to any significant modification of their composition. In comparison to the pulsed strategy, it was possible to obtain NWs with a more uniform length when Pt was deposited. Regarding their magnetic properties, as similar result was obtained, where the magnetic hysteresis, remanent magnetization, coercivity, and $H_{Sat}^{\perp}$ values increased with increasing Fe at.% in the nanostructures. However, the analysis of the morphology and composition of individual FePt NWs obtained through this approach revealed that both their diameter and composition vary along their longitudinal axis, becoming narrower and possessing a higher Fe content as they got longer. This fact should be addressed in the future by further improving the electrodeposition conditions. Nevertheless, for the desired biomedical application, such fact does not play a significant role, as it is possible to obtain nanostructures with suitable dimensions that present a relatively homogeneous length, diameter, and composition.

References

[1]J.-W. Kang, K. Kuroda, and M. Okido, Effect of Heat Treatment of Al Substrate on GaN Film Electrodeposited in Aqueous Solution. *Journal of Surface Engineered Materials and Advanced Technology* **10**, 1 (2020).

[2]J. Um, *Template-Assisted Electrodeposited Nanowires and Their Applications*. PhD Thesis, University of Minnesota (2021).

[3]R. R. D. Djouani and X. Qian, Mechanism of electrodeposition of nickel. *International Journal of Current Research* **10**, 64228-64239 (2018).

[4]K. Nielsch, J. Choi, K. Schwirn, R. B. Wehrspohn, and U. Gösele, Self-ordering Regimes of Porous Alumina: The 10 Porosity Rule. *Nano Letters* **2**, 677–680 (2002).

[5]C. Sousa, D. Leitão, M. Proença, A. Apolinário, J. Correia, J. Ventura, and J. Araújo, Tunning pore filling of anodic alumina templates by accurate control of the bottom barrier layer thickness. *Nanotechnology* **22**, 315602 (2011).

[6]C. Sousa, A. Apolinario, D. Leitao, A. Pereira, J. Ventura, and J. Araujo, Precise control of the filling stages in branched nanopores. *Journal of Materials Chemistry* **22**, 3110–3116 (2012).

[7]H. Schloerb, V. Haehnel, M. S. Khatri, A. Srivastav, A. Kumar, L. Schultz, and S. Faehler, Magnetic nanowires by electrodeposition within templates. *physica status solidi (b)* **247**, 2364–2379 (2010).

[8]M. Paunovic and M. Schlesinger, *Fundamentals of Electrochemical Deposition*. John Wiley & Sons (2006).

[9]T. Mehmood, A. Mukhtar, B. S. Khan, A. Saeed, W. Ahmad, and W. kaiming, Electrochemical Process and Phase Formation of Fe-Based Alloy Nanowires into Anodic Alumina Oxide. *International Journal of Electrochemical Science* **12**, 1203–1215 (2017).

[10]J. Azevedo, C. Sousa, J. Ventura, A. Apolinario, A. Mendes, and J. Araujo, Ultra-long Fe nanowires by pulsed electrodeposition with full filling of alumina templates. *Materials Research Express* **1**, 015028 (2014).

[11]C.-C. Wang, *Verification of Electrodeposition Patterns Caused by Interfacial Instability*. PhD Thesis, University of Florida (2016).

[12]A. Kavner, S. John, S. Sass, and E. Boyle, Redox-driven stable isotope fractionation in transition metals: Application to Zn electroplating. *Geochimica et Cosmochimica Acta* **72**, 1731–1741 (2008).

[13]Z. Zhang, A. Kitada, K. Fukami, Z. Yao, and K. Murase, Electrodeposition of an iron thin film with compact and smooth morphology using an ethereal electrolyte. *Electrochimica Acta* **348**, 136289 (2020).

[14]A. Fardi-Ilkhchy, F. Nasirpouri, C. Bran, and M. Vázquez, Compositionally graded $Fe_{(1-x)}$-$Pt_{(x)}$ nanowires produced by alternating current electrodeposition into alumina templates. *Journal of Solid State Chemistry* **244**, 35–44 (2016).

[15]V. Vega, T. Böhnert, S. Martens, M. Waleczek, J. M. Montero-Moreno, D. Görlitz, V. Prida, and K. Nielsch, Tuning the magnetic anisotropy of Co–Ni nanowires: comparison between single nanowires and nanowire arrays in hard-anodic aluminum oxide membranes. *Nanotechnology* **23**, 465709 (2012).

[16]J. G. Fernández, *Magnetization processes in transition metal based nanowire arrays*. PhD Thesis, University of Oviedo (2014).

[17]F. Mukhtar, S. Riaz, A. Awan, F. Rubab, Z. N. Kayani, and S. Naseem, Structural and magnetization crossover in electrodeposited $FeAl_2o_4$ – effect of *in situ* oxidation. *RSC Advances* **9**, 38183–38194 (2019).

[18]P. Tameerug, *Enhanced AMR in thin $Ni_{80}Fe_{20}$ film using $(Ni_{80}Fe_{20})_{56}Cr_{44}$ or $Ni_{58}Fe_{42}$ underlayer*. MSc Thesis, San Jose State University (2000).

[19]P. M. Shepley, *Effect of piezoelectric strain on the magnetic properties of Pt/Co thin films*. PhD Thesis, University of Leeds (2015).

[20]A. Nowick, Rare Earth Permanent Magnets. Elsevier (2012).

[21]M. Méndez, S. González, V. Vega, J. M. Teixeira, B. Hernando, C. Luna, and V. M. Prida, Ni-Co Alloy and Multisegmented Ni/Co Nanowire Arrays Modulated in Composition: Structural Characterization and Magnetic Properties. *Crystals* **7**, 66 (2017).

[22]S. Assa Aravindh, S. Mathi Jaya, M. Valsakumar, and C. Sundar, Compositional variation of magnetic moment, magnetic anisotropy energy and coercivity in $Fe_{(1-x)}M_x$ (M = Co/Ni) nanowires: an ab initio study. *Applied Nanoscience* **2**, 409–415 (2012).

[23]C. T. Sousa, D. C. Leitao, J. Ventura, P. B. Tavares, and J. P. Araújo, A versatile synthesis method of dendrites-free segmented nanowires with a precise size control. *Nanoscale Research Letters* **7**, 1–7 (2012).

[24]R. Furneaux, W. Rigby, and A. Davidson, The formation of controlled-porosity membranes from anodically oxidized aluminium. *Nature* **337**, 147–149 (1989).

[25]M. Norek, W. J. Stepniowski, and D. Siemiaszko, Effect of ethylene glycol on morphology of anodic alumina prepared in hard anodization. *Journal of Electroanalytical Chemistry* **762**, 20–28 (2016).

[26]W. Lee, R. Ji, U. G¨osele, and K. Nielsch, Fast fabrication of long-range ordered porous alumina membranes by hard anodization. *Nature Materials* **5**, 741–747 (2006).

[27]E. Gordeeva, I. Roslyakov, A. Sadykov, T. Suchkova, D. Petukhov, T. Shatalova, and K. Napolskii, Formation Efficiency of Porous Oxide Films in Aluminum Anodizing. *Russian Journal of Electrochemistry* **54**, 990–998 (2018).

[28]F. Nasirpouri, Template electrodeposition of nanowires arrays. In: *Electrodeposition of Nanostructured Materials*, 187–259 (Springer, 2017).

[29]A. Apolinário, P. Quitério, C. Sousa, M. Proença, J. Azevedo, M. Susano, S. Moraes, P. Lopes, J. Ventura, and J. Araújo, Bottom-up nanofabrication using self-organized porous templates. *Journal of Physics: Conference Series* **534**, 012001 (2014).

[30]A. Radisic, F. Ross, and P. Searson, In Situ Study of the Growth Kinetics of Individual Island Electrodeposition of Copper. *The Journal of Physical Chemistry B* **110**, 7862–7868 (2006).

[31]L. Guo, G. Oskam, A. Radisic, P. M. Hoffmann, and P. C. Searson, Island growth in electrodeposition. *Journal of Physics D: Applied Physics* **44**, 443001 (2011).

[32]S. Gonçalves, V. Andrade, C. T. Sousa, J. P. Araújo, J. H. Belo, and A. Apolinário, Tunable Iron–Cobalt Thin Films Grown by Electrodeposition. *Magnetochemistry* **9**, 161 (2023).

[33]M. F. Dupont and S. W. Donne, Nucleation and Growth of Electrodeposited Manganese Dioxide for Electrochemical Capacitors. *Electrochimica Acta* **120**, 219–225 (2014).

[34]A. Gupta and C. Srivastava, Nucleation and growth mechanism of tin electrodeposition on graphene oxide: A kinetic, thermodynamic and microscopic study. *Journal of Electroanalytical Chemistry* **861**, 113964 (2020).

[35]M. R. Khelladi, L. Mentar, A. Azizi, F. Kadirgan, G. Schmerber, and A. Dinia, Nucleation, growth and properties of Co nanostructures electrodeposited on n-Si(1 1 1). *Applied Surface Science* **258**, 3907–3912 (2012).

[36]S. S. Moraes, *Multimodal Magnetic Lipid Nanocarriers for Cancer Therapies*. PhD Thesis, University of Porto (2021).

[37]J. Azevedo, C. Sousa, A. Mendes, and J. Araújo, Influence of the Rest Pulse Duration in Pulsed Electrodeposition of Fe Nanowires. *Journal of Nanoscience and Nanotechnology* **12**, 9112–9117 (2012).

[38]R. Ji, C. Cao, Z. Chen, and R. Yao, Synthesis of crystalline $CoFe_x$ nanowire arrays through high voltage pulsed electrochemical deposition. *Journal of Magnetism and Magnetic Materials* **363**, 95–102 (2014).

[39]K. Fu, S.-R. Kwon, D. Han, and P. W. Bohn, Single Entity Electrochemistry in Nanopore Electrode Arrays: Ion Transport Meets Electron Transfer in Confined Geometries. *Accounts of Chemical Research* **53**, 719–728 (2020).

[40]Z. Ma, B. Jiang, Y. Dong, J. Qiang, D. Drummer, and L. Zhang, Electrodeposition model with dynamic ion diffusion coefficients for predicting void defects in electroformed microcolumn arrays. *Physical Chemistry Chemical Physics* **25**, 7407–7416 (2023).

[41]W. Si, Z. Zhu, G. Wu, Y. Zhang, Y. Chen, and J. Sha, Encoding Manipulation of DNA-Nanoparticle Assembled Nanorobot Using Independently Charged Array Nanopores. *Small Methods* **6**, 2200318 (2022).

[42]G. M. Crouch, Nanoholes and Nanowires: Electrochemistry in Optically-active Nanostructures. PhD Thesis, University of Notre Dame (2019).

[43]W. Spieker, J. Liu, J. Miller, A. Kropf, and J. Regalbuto, An EXAFS study of the co-ordination chemistry of hydrogen hexachloroplatinate(IV): 1. Speciation in aqueous solution. *Applied Catalysis A: General* **232**, 219–235 (2002).

[44]Y. Zhang, N. S. Mbugua, H. Jin, and L. Chen, Preparation and Investigation of Ni–Co–P Alloy Coatings Using Jet Electrodeposition with Varying Pulse Parameters. *Crystals* **13**, 303 (2023).

[45]A. W. Black, W. Zhang, Y. J. Noori, G. Reid, and P. N. Bartlett, Temperature effects on the electrodeposition of semiconductors from a weakly coordinating solvent. *Journal of Electroanalytical Chemistry* **944**, 117638 (2023).

[46]J. Orozco-Messana and R. Camaratta, ZnO Electrodeposition Model for Morphology Control. *Nanomaterials* **12**, 720 (2022).

[47]L. Soleimany, A. Dolati, and M. Ghorbani, A study on the kinetics of gold nanowire electrodeposition in polycarbonate templates. *Journal of Electroanalytical Chemistry* **645**, 28–34 (2010).

[48]S. Caspani, *Magnetic nanoparticles as potential contrast agents in Magnetic Resonance Imaging*. MSc Thesis, University of Porto (2019).

[49]X. Zhang, K. Zuo, X. Zhang, C. Zhang, and P. Liang, Selective ion separation by capacitive deionization (CDI) based technologies: a state-of-the-art review. *Environmental Science: Water Research & Technology* **6**, 243–257 (2020).

[50]U.-S. Mohanty, B. Tripathy, P. Singh, S. Das, and V. Misra, Electrodeposition of nickel in the presence of Al^{3+} from sulfate baths. *Journal of Applied Electrochemistry* **35**, 545–549 (2005).

[51]M. Mikolasek, P. Ondrejka, F. Chymo, P. Novak, M. Pavuk, I. Novotny, V. Rehacek, J. Breza, A. Vincze, and I. Hotovy, Potentiostatic electrodeposition under light irradiation for preparation of highly photoactive Cu_2O for water splitting applications. *Applied Surface Science* **461**, 196–201 (2018).

[52]K.-L. Tsai, C.-M. Chen, and C.-E. Ho, Synergistic effects of additives on impurity residues in high-speed copper electrodeposition and voiding propensity in solder joints. *Journal of the Taiwan Institute of Chemical Engineers* **156**, 105391 (2024).

[53]Z. L. Bao, S. Majumder, A. A. Talin, A. S. Arrott, and K. L. Kavanagh, Epitaxial $Fe_x Ni_{1-x}$ Thin Film Contacts to GaAs via Electrochemistry. *Journal of The Electrochemical Society* **155**, H841 (2008).

[54]M. Sundaram, A. B. Kamaraj, and G. Lillie, Experimental study of localized electrochemical deposition of Ni-Cu alloy using a moving anode. *Procedia CIRP* **68**, 227-231 (2018).

[55]G. L. Schnable, Electrodeposition of Molten Metals and Alloys from Glycerine Solutions. *Journal of the Electrochemical Society* **108**, 964 (1961).

[56]A. Laghrissi and M. Es-Souni, Porous PtPd alloy nanotubes: towards high performance electrocatalysts with low Pt-loading. *Catalysis Science & Technology* **9**, 4355–4364 (2019).

[57]M. Rahaman, A. Aldalbahi, P. Govindasami, N. P. Khanam, S. Bhandari, P. Feng, and T. Altalhi, A New Insight in Determining the Percolation Threshold of Electrical

Conductivity for Extrinsically Conducting Polymer Composites through Different Sigmoidal Models. *Polymers* **9**, 527 (2017).

[58]R. Samba, T. Herrmann, and G. Zeck, PEDOT–CNT coated electrodes stimulate retinal neurons at low voltage amplitudes and low charge densities. *Journal of Neural Engineering* **12**, 016014 (2015).

[59]H. Boudouh, S. Guessasma, R. Essehli, and A. Aissat, Monte Carlo Simulation of Ion-Exchange Response of Copper Sulfide Ion Selective Electrode for Metal Pollutant Detection. *Journal of The Electrochemical Society* **159**, D148 (2011).

[60]P. Tartaj, M. P. Morales, S. Veintemillas-Verdaguer, T. Gonzalez-Carreño, and C. J. Serna, Synthesis, Properties and Biomedical Applications of Magnetic Nanoparticles. In: *Handbook of Magnetic Materials*, 403–482 (2006).

[61]J. Lyubina, O. Gutfleisch, K.-H. Müller, and L. Schultz, Structure and hysteresis properties of nanocrystalline FePt powders. *Journal of Magnetism and Magnetic Materials* **290**, 547–550 (2005).

[62]H. Cha, Y. Kim, C. Kim, and Y. Kang, Study of the Magnetic Phase of Fe-Pt Alloy Nanoparticles. *Journal of Nanoscience and Nanotechnology* **8**, 4666–4669 (2008).

[63]C. Rodríguez, P. Tobosque, M. Maril, C. Camurri, L. Basáez, M.-P. Delplancke, and C. Carrasco, Effect of different complexing agents on Pb–Co thin-film electrodeposition. *Journal of Materials Science* **52**, 3388–3401 (2017).

[64]O. El Khouja, A. C. Galca, K. Nouneh, M. Y. Zaki, M. E. Touhami, M. Taibi, E. Matei, C. C. Negrila, M. Enculescu, and L. Pintilie, Structural, morphological and optical properties of Cu–Fe–Sn–S thin films prepared by electrodeposition at fixed applied potential. *Thin Solid Films* **721**, 138547 (2021).

[65]D. Wang, G. Hu, P. Yang, X. Pan, H. Xu, L. Liu, J. Zhang, and M. An, Using DMH as a complexing agent for pulse electrodeposition of platinum nanoparticles towards oxygen reduction reaction. *Ionics* **26**, 3473–3482 (2020).

[66]T. Nakamoto, Y. Terui, S. Tsuchida, R. Seki, Y. Ueyama, S. Yokoyama, H. Takahashi, and K. Tohji, Oxidation-Reduction Potential Control for One Step Synthesis of Cu-Pt Core-Shell Nanoparticles. *ECS Transactions* **85**, 1517 (2018).

[67]M. Elsabahy and K. L. Wooley, Design of polymeric nanoparticles for biomedical delivery applications. *Chemical Society Reviews* **41**, 2545–2561 (2012).

[68]P. Decuzzi, B. Godin, T. Tanaka, S.-Y. Lee, C. Chiappini, X. Liu, and M. Ferrari, Size and shape effects in the biodistribution of intravascularly injected particles. *Journal of Controlled Release* **141**, 320–327 (2010).

6. Au/Fe/Au Nanodiscs

6.1. Introduction

In this chapter, it is presented a detailed characterization of the Au/Fe/Au nanodiscs (NDs) fabrication by thermal evaporation into Si templates, which were pre-patterned by laser interference lithography. Particularly, these nanoarchitectures were analysed through scanning electron microcopy (SEM), energy-dispersive X-ray spectroscopy (EDS), X-ray diffraction (XRD), superconducting quantum interference device (SQUID), magneto-optical Kerr effect (MOKE), and magnetic force microscopy (MFM). Additionally, micromagnetic simulations were performed to get a better comprehension and support the experimental results.

6.2. Interference Lithography Template

As it was previously described, the Au/Fe/Au NDs were fabricated through thermal evaporation on the interference lithography templates. An example template is represented in figure 6.1.

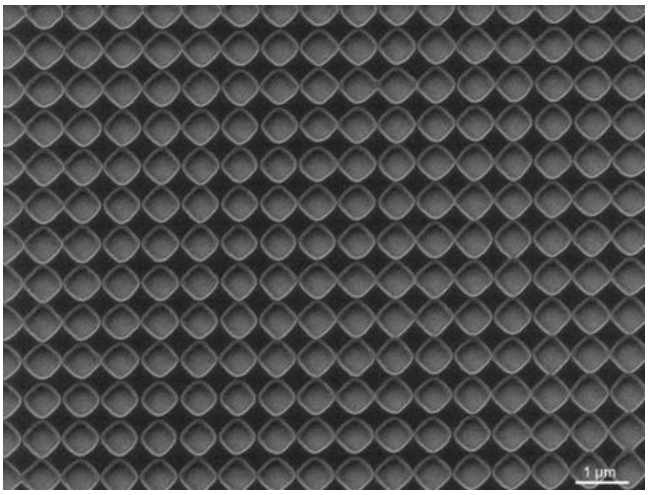

Figure 6.1 - SEM image of an interference lithography template after the developing process.

As can be observed, the dots' shape is not a perfect circle, being more like a lozenge with two axes of slightly different dimensions (figure 6.2).

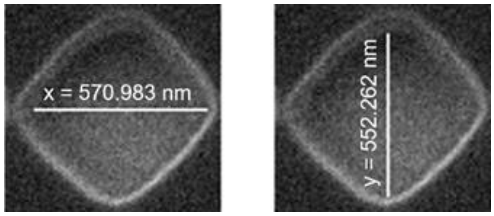

Figure 6.2 - Dimensions of a single dot along the considered x- and y-axis.

This is an expected result due to the nature of the interference lithography process, namely the superposition of the two diffraction patterns offset by 90º [figure 6.3(a)].

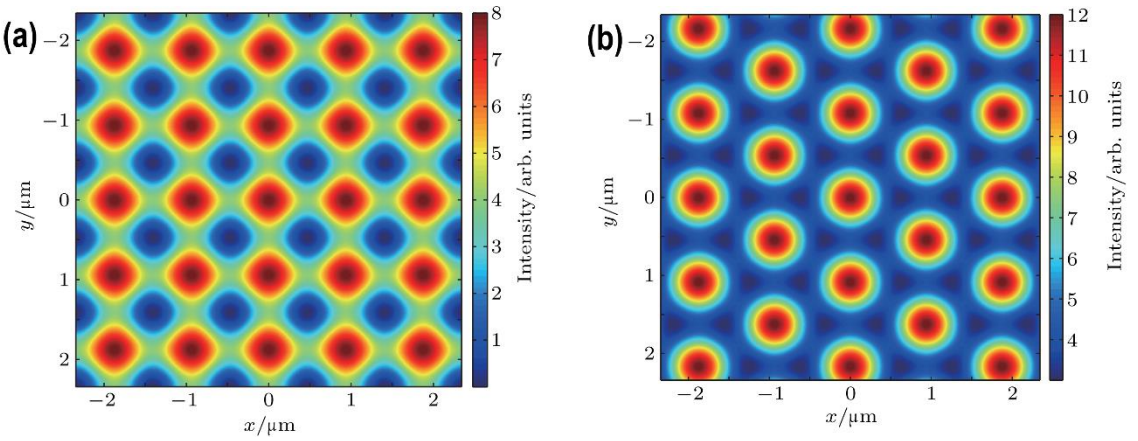

Figure 6.3 - Numerically simulated 2D optical field distribution for different exposures in an interference lithography system: (a) two exposures considering a 90º rotation of the sample between them; or (b) three exposures considering a 60º rotation of the sample between them. Adapted from [1].

Such effect could be reduced by performing 3 exposures, offset by 60º [figure 6.3(b)], instead the two considered in these templates. Nevertheless, taking this into account, histograms representing the size distribution along each axis of the dots were elaborated (figure 6.4).

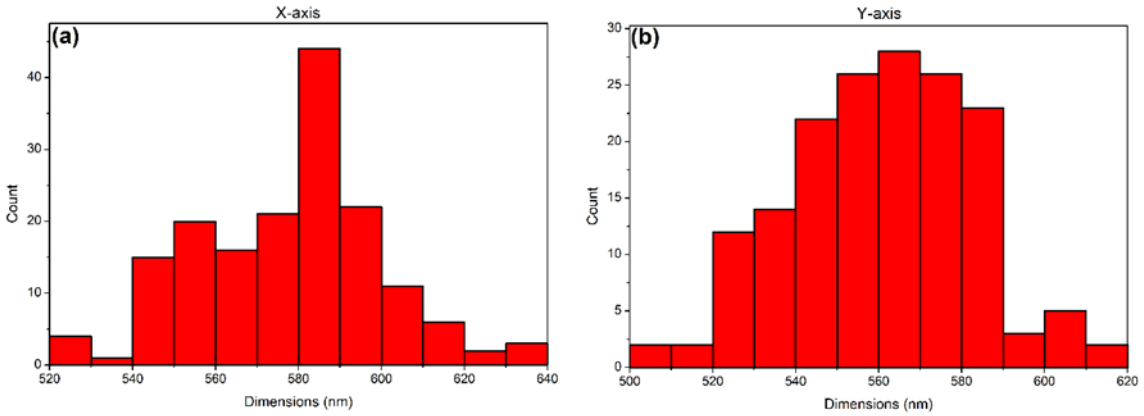

Figure 6.4 - Histograms representing the dimensions of the dots along the (a) x- and (b) y-axis.

Based on this analysis, it was possible to conclude that the mean dot size along the x-axis was equal to 576.980 nm, with a standard deviation of 24.360 nm, whilst along the y-axis the analysed dots presented a mean size of 559.577 nm, with a standard deviation of 22.969 nm.

6.3. Morphological Characterization

Afterwards, the NDs were thermally evaporated [figure 6.5(a)] and the photoresist was removed through a lift-off process, leading to the nanostructures presented in figure 6.5(b).

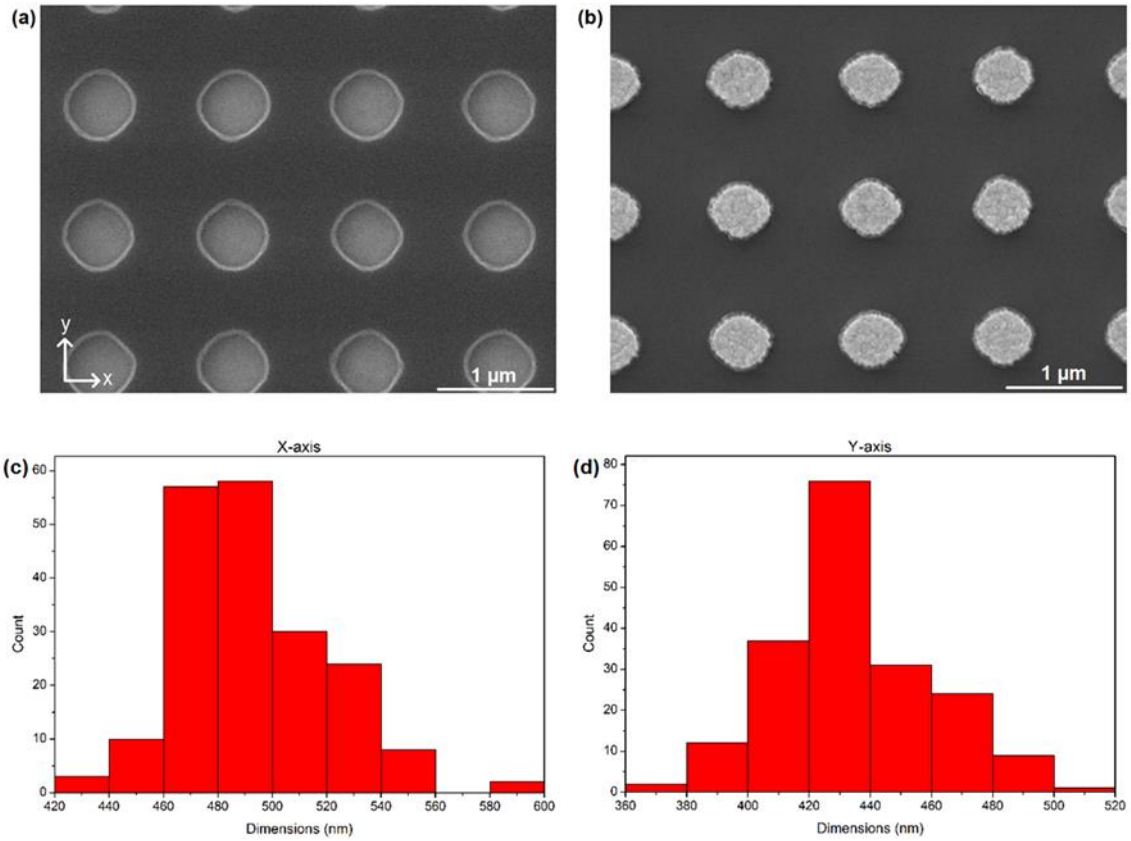

Figure 6.5 - (a, b) SEM images of NDs thermally evaporated on the pre-patterned Si wafer (a) before and (b) after the lift-off process; (c, d) histograms representing the dimensions of the fabricated NDs along the (c) x- and (d) y-axis.

Subsequently, histograms depicting the size of the obtained NDs along their two main axes were created [figure 6.5(c, d)]. As a result, it was estimated that the average dimensions of the fabricated NDs were (490 ± 30) nm and (430 ± 30) nm along the x- and y-axis, respectively.

Additionally, an EDS analysis was performed, which allowed to confirm the presence of the deposited metals (figure 6.6).

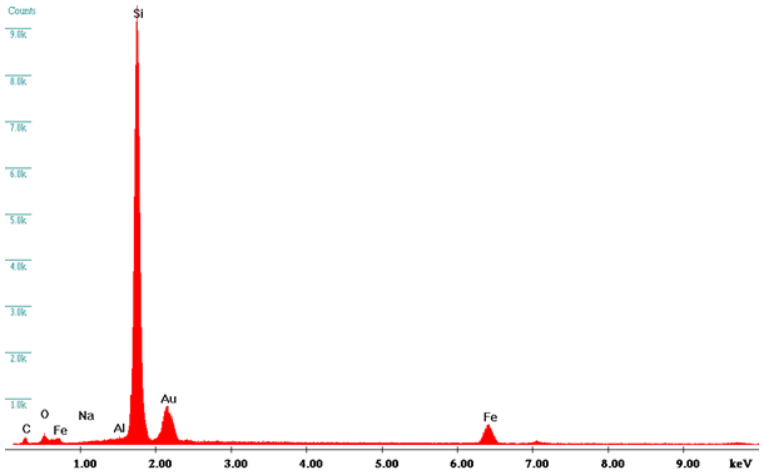

Figure 6.6 - EDS analysis of the NDs over the Si template.

6.4. Structural Characterization

Then, the fabricated nanostructures, as well as the continuous thin film, or reference sample, were structurally characterized through XRD in the θ - 2θ mode. The obtained scans and respective analysis are presented in figure 6.7.

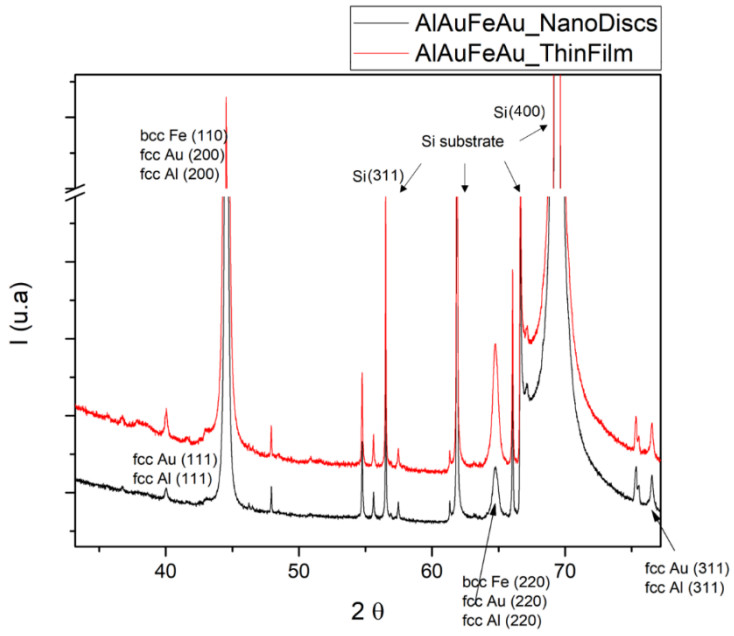

Figure 6.7 - XRD patterns obtained for the NDs and thin film samples, together with the respective analysis.

Through this technique, it was possible to confirm the presence of Al, Au, and Fe in the synthesized samples, and it was confirmed that Fe shows a body-centred cubic (bcc) structure with a preferred growth along the (110) direction. Additionally, it was verified that the peaks of both the thin film and the NDs were identical. However, there was an overlapping of the Fe peaks with those of Au and Al, which not only impeded a

quantitative analysis, but also impossibilities the determination of the grain size. Hence, alternative techniques, like extended X-ray absorption fine structure (EXAFS) or Mössbauer spectroscopy, should be employed to confirm the Fe's texture. However, it was still possible to gather some information about that aspect through careful analysis of the presented spectrum. For instance, by examining the peaks' relative intensity and shape, clues about the crystalline structure and preferred orientation of Fe were obtained. Additionally, by comparing the observed XRD pattern with reference patterns for known Fe textures qualitative insights were also acquired. Nevertheless, due to the overlapping peaks, these results required a cautious interpretation. Moreover, some peaks were not identified, which could indicate the presence of Fe oxides or other contaminants resulting from the thermal evaporation process.

6.5. Magnetic Characterization

Afterwards, the magnetic characterization of these nanoarchitectures was performed, having been used various techniques, namely SQUID, MOKE, and MFM. In the following sections, the results obtained with each one of those methods will be addressed.

6.5.1. SQUID

The SQUID measurements were carried out by applying the external magnetic field in the parallel and perpendicular direction in relation to the sample plane. An obtained hysteresis loop is represented in figure 6.8, where it is possible to observe the existence of a diamagnetic behaviour, which results from the large contribution of the Si substrate, whose thickness is multiple times that of the active sample.

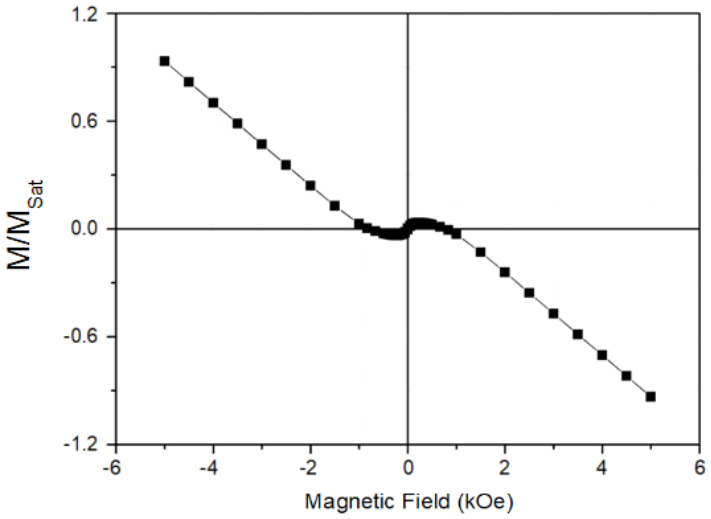

Figure 6.8 - Hysteresis loop of a NDs sample, measured with a SQUID magnetometer where the external magnetic field was applied along the sample plane.

To account for this effect, the linear parts of the obtained hysteresis loops were fitted and, subsequently, this diamagnetic contribution was subtracted from the real behaviour of the active sample in all the measured curves. Examples of hysteresis loops obtained after this process are represented in figure 6.9.

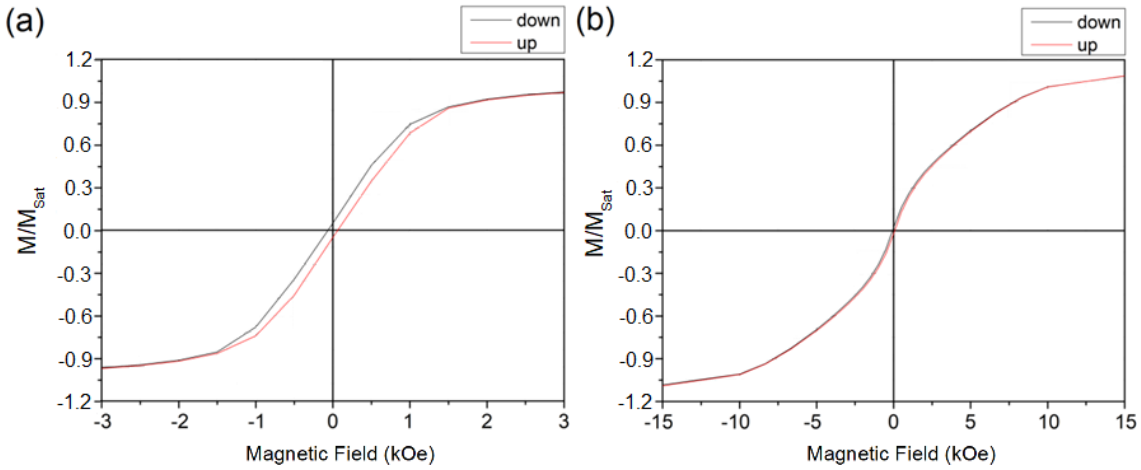

Figure 6.9 - SQUID measurements of a NDs sample, after removing the Si diamagnetic contribution, considering the external magnetic field applied along the (a) parallel and (b) perpendicular directions in relation to the sample's plane.

As a result, it was verified that the obtained hysteresis loops did not demonstrate the expected behaviour, when applying the external magnetic field parallel to the sample plane (figure 1.6). This could be attributed to the fact that the Si substrate, which had a thickness that was many times larger than that of the NDs, was hindering, or masking, the measurements of the NDs' hysteresis loops.

6.5.2. MOKE

In order to overcome such problem, MOKE measurements of the Fe NDs array and the Fe thin film were performed and the obtained hysteresis loops are presented in figure 6.10.

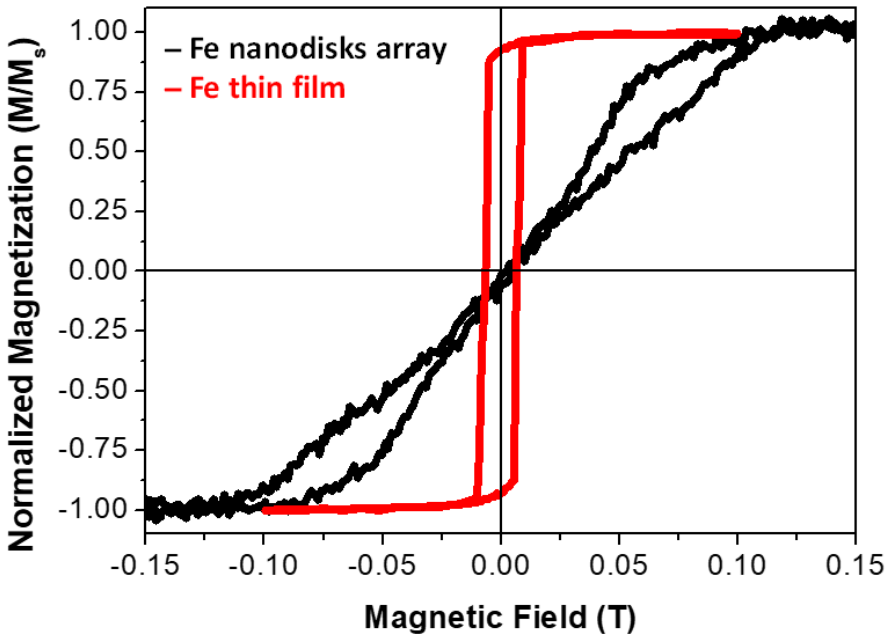

Figure 6.10 - MOKE hysteresis loops of the Fe thin film (red line) and the Fe NDs array (black line).

As can be observed, the hysteresis loop of the reference sample shows the typical shape of a soft magnetic material with small coercive field ($H_c \approx 73$ Oe) and large reduced remanence value ($M_r/M_{Sat} \approx 0.13$). Meanwhile, the hysteresis loop of the Fe ND array clearly indicates the presence of a spin-vortex ground state with a vortex annihilation field ($H_a \approx 1200$ Oe), i.e. the magnetic field at which the ND transitions to a single-domain state, the vortex nucleation field ($H_n \approx 650$ Oe), i.e. the magnetic field at which the nanostructure transitions back to a spin-vortex state, and the remanence value as low as 2.5% of the saturation magnetization.[2] This confirms that such spin arrangement is adequate for biomedical applications, as it provides us with nanostructures with a reduced total magnetic moment in remanence, which prevents the magnetic aggregation of the NDs in the absence of magnetic fields.

Nevertheless, it is important to consider that any potential in-plane texture variations in the Fe can also influence these results, as they affect how the nanostructures respond to magnetic fields and light, which are fundamental to this type of measurements. This fact should be more evident in epitaxial thin films, such as those prepared by molecular beam epitaxy (MBE), where the bcc crystal structure of Fe is well-defined and the magnetocrystalline anisotropy should be an important term. However, our Au/Fe/Au NDs were prepared by thermal evaporation, which results in the growth of polycrystalline thin films. In this case, the contribution of magnetocrystalline anisotropy can be neglected and the magnetic behaviour is basically controlled by the shape anisotropy.

Additionally, the direction of the applied external magnetic field should influence the results of the MOKE hysteresis loops. However, these differences must be small discrepancies in both the nucleation and annihilation fields of the vortex state. For the purpose of this work, which was to obtain nanostructures with magnetic configuration in vortex state under the application of a zero external magnetic field, these differences were neglected.

Furthermore, it is possible to verify that there is a similarity between the MOKE loops of the blanket Fe film and the NDs array, despite the absence of a vortex in the first. This suggests a deviation of the magnetic behaviour of the nanostructures, from the expected magnetic state, and/or that the MOKE sensitivity is not sufficient for obtaining an accurate hysteresis loop of the produced nanostructures.

6.5.3. MFM

To further confirm the presence of a spin-vortex ground state in the synthesized NDs, MFM measurements were performed (figure 6.11).

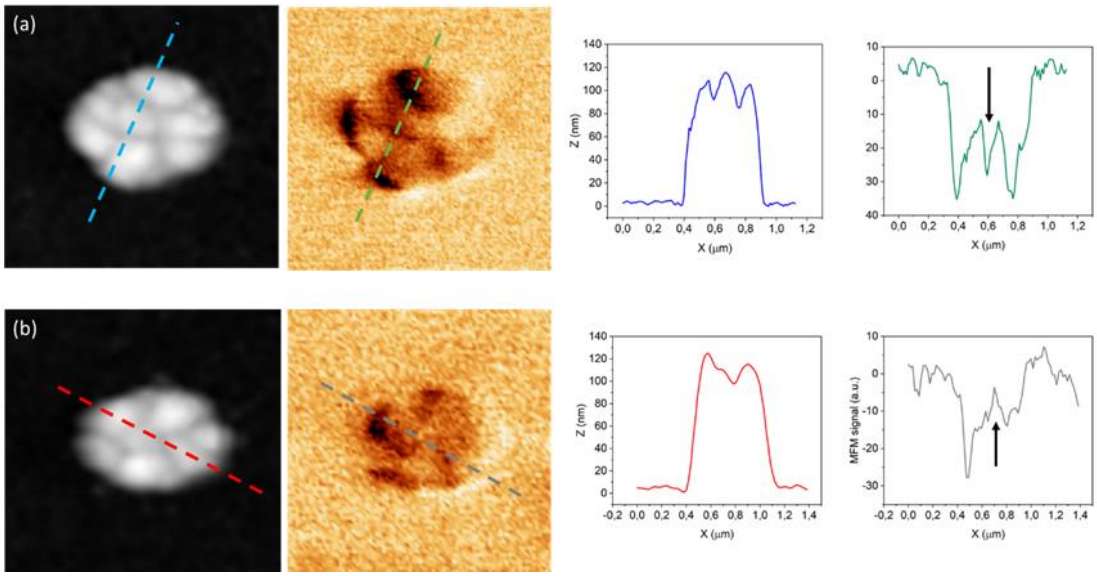

Figure 6.11 - Topography and MFM micrographs of a ND possessing a vortex core pointing (a) down or (b) up, in relation to the ND's plane. The black arrow indicates the location of the spin-vortex core.

In the acquired images, it is possible to distinguish the MFM contrast corresponding to four in-plane domains with clockwise or counterclockwise rotation, i.e. in-plane flux-closure magnetic state, encircling a point near the disc centre where magnetization points in the up or down direction (black or white contrast, respectively at remnant state), which is known as the vortex core.[3] The orientation of the core magnetization appears to oscillate arbitrarily between up and down for different discs in the array. This behaviour

is consistent with the idea that both states are energetically equivalent in the absence of an external magnetic field, explaining why they can arbitrarily appear in our samples. It is also relevant to notice that the MFM technique is mainly sensitive to the magnetic pole density that concentrates around the domain walls and the vortex core.

Furthermore, it is possible to calculate a numerical estimate of the minimum vortex core radius, r_c, through the following expression:[4]

$$r_c = \sqrt[3]{\frac{l_{ex}^2 R}{12\kappa\beta}} \tag{6.1}$$

where l_{ex}^2 is the exchange length of Fe, i.e. 2.4 nm, R is the nanodisc radius (~ 250 nm), κ is a numerical constant equal to 4.12 x 10^2, and β is the aspect ratio, i.e. radius/length, of the nanostructure (~ 5).[5] Using this formula, it was obtained a minimum vortex core radius of ~ 8.35 nm.

Nevertheless, through MFM, it was also verified that not only the vortex core was not located exactly at the centre of the nanostructure, but there were also some defects in those nanoarchitectures, such as different grain sizes, which may result from the thermal evaporation process. These aspects may influence overall magnetic behaviour of the produced NDs, leading to the similarities with the blanket Fe film observed in the MOKE measurement (figure 6.10).

6.6. Micromagnetic Simulations

The study of the magnetic properties of these nanostructures was completed by performing micromagnetic simulations using the mumax^3 software.[6] The geometries of the nanostructures considered in these simulations were defined based on the acquired SEM images of the NDs [figure 6.12(a)]. Additionally, periodic boundary conditions were established, as in the real sample.

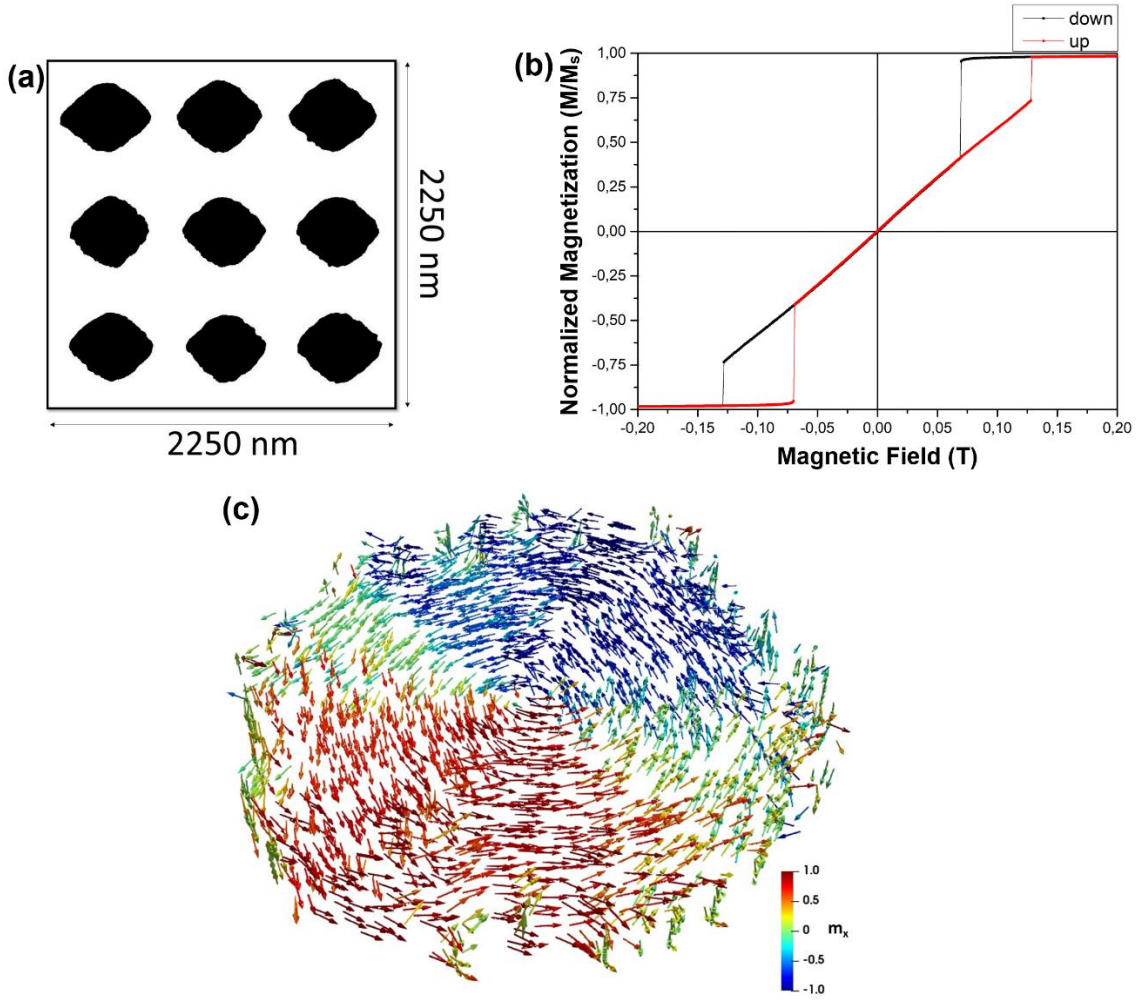

Figure 6.12 - Geometry of (a) a single disc and (b) an array of NDs, defined using the obtained SEM images, which was used in the micromagnetic simulations carried out (black - magnetic region; white - non-magnetic region). (c) 3D scheme of a spin-vortex ground state.

As it was experimentally observed, when the external magnetic field was parallel to the ND's plane, two clear and abrupt transitions exist, corresponding to H_n and H_a. Additionally, there is a linear section that represents the movement of the vortex core. Particularly, when the magnetic field is decreased from the saturation, a magnetic vortex nucleates (H_n), which is accompanied by an abrupt decrease in magnetization. Then, as the applied magnetic field is further reduced, the magnetization accompanies that variation until another abrupt transition is observed, corresponding to the point where the spin-vortex is annihilated (H_a) or ejected from disc. In good agreement with the experimental data, the simulated vortex characteristic fields along the x-axis were H_n = 698 Oe and H_a = 1290 Oe and, along the y-axis were H_n = 1129 Oe, H_a = 1718 Oe.

Additionally, it is possible to observe differences between the experimental and simulated hysteresis loop, which can not only be attributed to defects in the fabricated

nanostructures, but also to the sensitivity and resolution of the MOKE technique used to measure the loops. Particularly, differences in sensitivity or resolution between the experimental setup and the simulation method could lead to discrepancies in the observed features.

Subsequently, micromagnetic simulations of a NDs array with periodic boundary conditions were performed and compared against those carried out for an individual ND. From this comparison, it was observed that the differences between the two cases were negligible, supporting the assumption that the inter-dot distances observed in the fabricated samples, i.e. ~250 nm, did not play a significant role. On the other hand, in figure 6.13, there are represented snapshots of an array of nine NDs at six different magnetic fields, not considering periodic boundary conditions, so as to demonstrate the spin-vortex nucleation process.

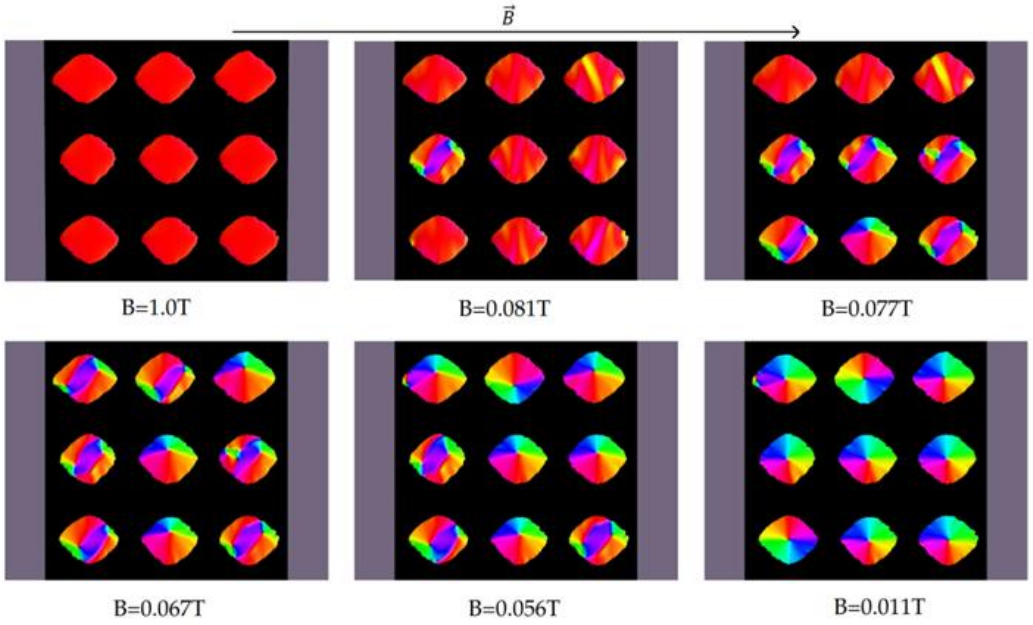

Figure 6.13 - Simulated field evolution of an array of 9 Fe NDs, each with 50 nm in thickness, without periodic boundary conditions.

6.7. Conclusions

In this chapter, it was demonstrated a method for synthesizing Au/Fe/Au NDs with a spin-vortex ground state. Moreover, their morphological and structural characterization was presented and, to confirm the presence of that magnetic state in those nanostructures, their magnetic characterization was detailed. Additionally, micromagnetic simulations were performed to better understand and support the experimental results confirming the formation of a spin-vortex state.

References

[1]Y. Chen, X. Wang, R. Wang, H. Yang, and Y. Qi, Theoretical study of micro-optical structure fabrication based on sample rotation and two-laser-beam interference. *Chinese Physics B* **26**, 054203 (2017).

[2]R. P. Cowburn, D. Koltsov, A. Adeyeye, M. Welland, and D. Tricker, Single-Domain Circular Nanomagnets. *Physical Review Letters* **83**, 1042 (1999).

[3]T. Shinjo, T. Okuno, R. Hassdorf, K. Shigeto, and T. Ono, Magnetic Vortex Core Observation in Circular Dots of Permalloy. *Science* **289**, 930–932 (2000).

[4]S. S. P. K. Arekapudi, B. B¨ohm, L. Ramasubramanian, F. Ganss, P. Heinig, S. Stienen, C. Fowley, K. Lenz, A. M. Deac, M. Albrecht, and O. Hellwig, Direct imaging of distorted vortex structures and magnetic vortex annihilation processes in ferromagnetic/antiferromagnetic disk structures. *Physical Review B* **103**, 014405 (2021).

[5]C. Gatel, F. J. Bonilla, A. Meffre, E. Snoeck, B. Warot-Fonrose, B. Chaudret, L.-M. Lacroix, and T. Blon, Size-Specific Spin Configurations in Single Iron Nanomagnet: From Flower to Exotic Vortices. *Nano Letters* **15**, 6952–6957 (2015).

[6]A. Vansteenkiste, J. Leliaert, M. Dvornik, M. Helsen, F. Garcia-Sanchez, and B. Van Waeyenberge, The design and verification of MuMax3. *AIP Advances* **4**, 107133 (2014).

7. Biomedical Applications

7.1. Introduction

In this chapter, it is analysed the suitability of the previously characterized nanomaterials for different biomedical applications. Particularly, regarding nanostructured lipid carriers (NLCs), it is evaluated their potential for a dual cancer treatment approach, involving the delivery of anticancer drugs in combination with magnetic hyperthermia (MHT). On the other hand, the applicability of nanowires (NWs) and nanodiscs (NDs) in a different oncological therapeutic strategy, i.e. magneto-mechanical induction of cancer cell death, considering both functionalized and non-functionalized nanostructures is also assessed.

Nevertheless, before such studies, a critical preliminary examination is performed, which involves conducting cytotoxicity studies and uptake assays on the nanomaterial-incubated cells. This investigation aimed at assessing not only the safety of those nanomaterials but also their behaviour in the absence of an external magnetic field.

7.2. Nanostructured Lipid Carriers (NLCs)

The suitability of the fabricated NLCs, previously described in chapter 4, for a biomedical application that can be designated as dual chemo-MHT therapy was evaluated. This treatment approach is based on a combined action at the target site, involving MHT together with anticancer drug release promoted by the temperature increase. The produced NLCs, loaded with superparamagnetic iron oxide nanoparticles (SPIONs) and anticancer compounds, are particularly promising for this type of application, since they can selectively accumulate in tumour sites due to the enhanced permeability and retention (EPR) effect. Moreover, as previously demonstrated, when they are exposed to an alternating magnetic field (AMF), the localized heating caused by the SPIONs facilitates the anticancer drug release, possibly further increasing the cancer cells' death.[1–3] Additionally, it is possible to functionalize their surface with compounds that enhance their ability to overcome various biological barriers and accumulate at the target site.[4]

To confirm such proof of concept, various *in vitro* cell assays were performed, which will be addressed in the subsequent sections.

7.2.1. *In Vitro* Cytotoxicity Studies

First, the biocompatibility of different types of gelucire 43/01 (GEL)-based NLCs, i.e. NLC, $NLC_{(DOX)}$, $NLC_{(SPIONs)}$, and $NLC_{(DOX\text{-}SPIONs)}$, was analysed, to evaluate their safety and potential impact on cellular systems, in the absence of an external magnetic field.

For such purpose, the MCF-7 cell line was considered and it was decided to initially evaluate the cell viability as a function of the doxorubicin (DOX) concentration, for the GEL-based $NLC_{(DOX\text{-}SPIONs)}$, as it is the most relevant formulation for this specific application. The obtained results are presented in figure 7.1.

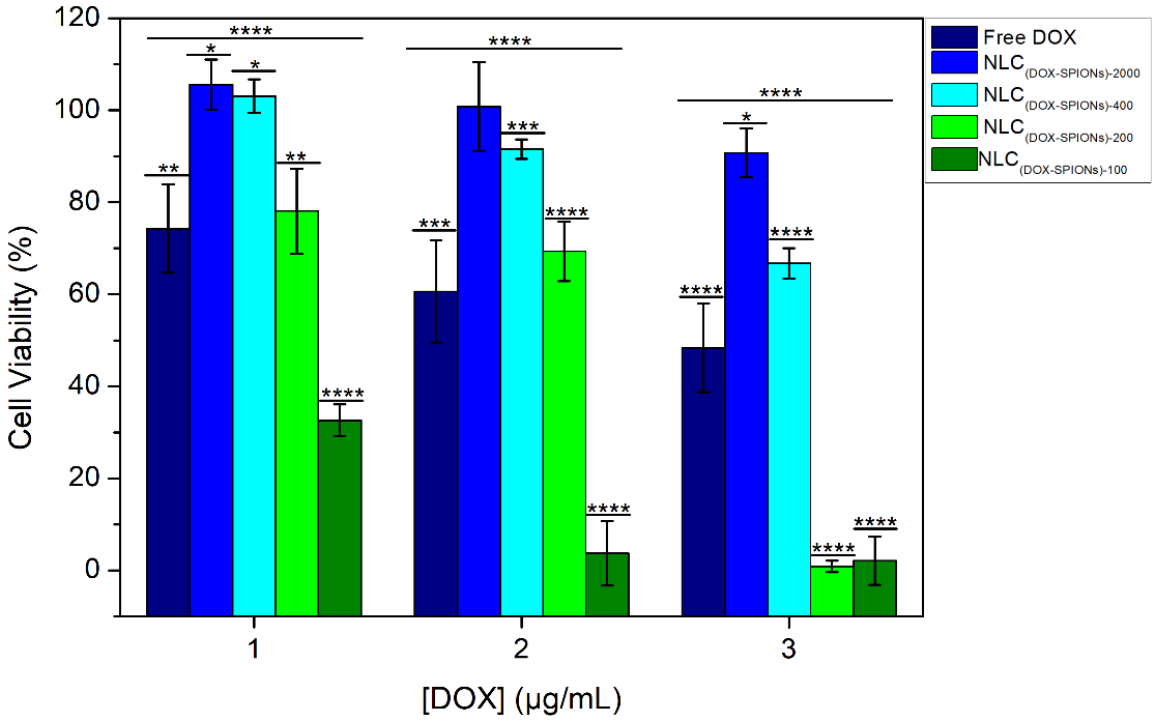

Figure 7.1 - Viability of MCF-7 cells, in relation to control, after a 19-h incubation with various concentrations of distinct $NLC_{(DOX\text{-}SPIONs)}$ formulations that possess different DOX concentrations ([NLCs] = 45 mg/mL, [DOX] = 100 - 2000 µg/mL, [SPIONs] = 12000 µg/mL). Asterisks in short bars indicate statistical significance in relation to control and asterisks in long bars indicate statistical between the tested conditions (*P ≤ 0.05; **P ≤ 0.01; ***P ≤ 0.001; ****P ≤ 0.0001).

As can be observed, there is a concentration-dependent reduction of the cell viability for all the considered scenarios. Additionally, formulations with a higher DOX concentration exhibited a lower toxicity. This result suggests that formulations with lower DOX concentrations may exhibit an improved stability, leading to a higher cellular uptake and cytotoxicity compared to less stable formulations possessing a greater drug concentration. The effect of polyethylene glycol (PEG) functionalization of the NLCs on cell viability was also assessed (figure 7.2), considering the formulation with a DOX concentration of 400 µg/mL. This was the selected concentration because, based on the previous, it is the one that allows the highest concentration of NLCs, while still presenting a relatively high biocompatibility for the tested conditions, representing the best balance between those two aspects. As a result, it was verified an small increased biocompatibility for the functionalized NPs, although without statistical significance (figure 7.2).

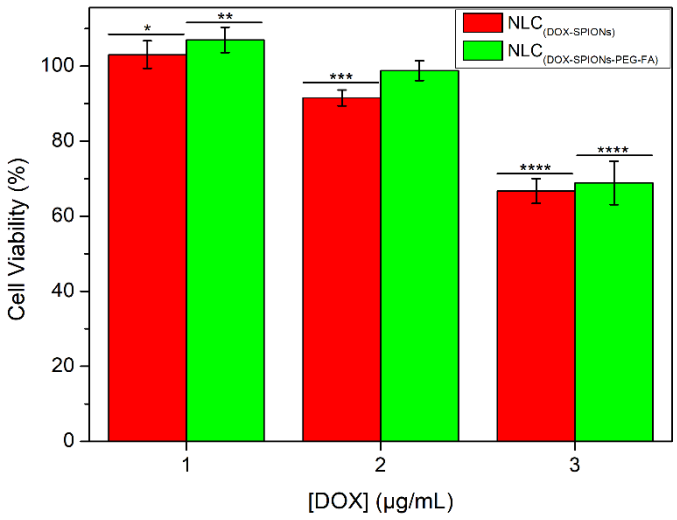

Figure 7.2 - Viability of MCF-7 cells, in relation to control, after a 19-h incubation with various concentrations of an $NLC_{(DOX\text{-}SPIONs)}$ or $NLC_{(DOX\text{-}SPIONs\text{-}PEG)}$ formulation ([NLCs] = 45 mg/mL, [DOX] = 400 μg/mL; [SPIONs] = 12000 μg/mL). Asterisks in short bars indicate statistical significance in relation to control and asterisks in long bars indicate statistical between the tested conditions (*P ≤ 0.05; **P ≤ 0.01; ***P ≤ 0.001; ****P ≤ 0.0001).

Based on the acquired results, it was decided to assess the biocompatibility of a new set of formulations, possessing [DOX] = 280 μg/mL and [SPIONs] = 1000 μg/mL (figure 7.3), to try increasing the number of NLCs per cell without causing significant death and to better understand the toxicity of that type of nanoparticles (NPs).

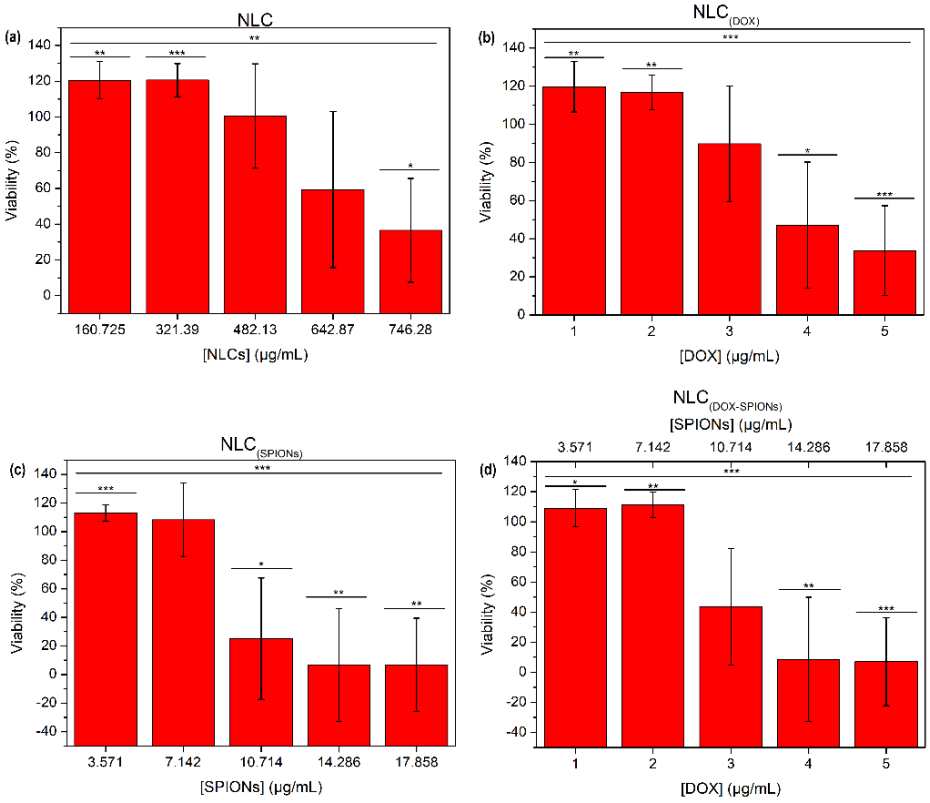

Figure 7.3 - Viability of MCF-7 cells, in relation to control, after a 19-h incubation with various concentrations of (a) NLC; (b) $NLC_{(DOX)}$; (c) $NLC_{(SPIONs)}$; (d) $NLC_{(DOX\text{-}SPIONs)}$ ([DOX] = 280 μg/mL; [SPIONs] = 1000 μg/mL). Asterisks in short bars

indicate statistical significance in relation to control and asterisks in long bars indicate statistical between the tested conditions (*P ≤ 0.05; **P ≤ 0.01; ***P ≤ 0.001; ****P ≤ 0.0001).

As can be observed, the cytotoxic effect of different concentrations of NLCs (160.725 – 746.28 µg/mL), DOX (1 – 5 µg/mL), and SPIONs (3.571 – 17.858 µg/mL) was analysed. Similarly to the previous case, there is a concentration-dependent reduction of the cell viability for every analysed situation. Particularly, it is possible to observe, for sufficiently high concentrations of NLCs, i.e. over 321.39 µg/mL, a significant reduction in cell viability. This suggests the existence of a threshold concentration for that type of NPs, above which a considerable reduction in cell viability is observed. Nevertheless, that behaviour is more pronounced for NPs loaded with DOX and/or SPIONs, particularly for concentrations greater than 2 µg/mL or 7.142 µg/mL, respectively. This indicates that the presence of either or both these agents within the NLCs, leads to the existence of additional effects on the cells, that promotes their death. Nevertheless, it is possible to verify an adequate biocompatibility for the two lowest concentrations of NLCs, i.e. 160.725 µg/mL and 321.39 µg/mL, which are associated with DOX concentrations of 1 and 2 µg/mL, respectively, and SPIONs concentrations equal to 3.571 and 7.142 µg/mL, correspondingly.

Considering these results, it was decided to perform the subsequent studies considering the GEL-based formulations with [DOX] = 280 µg/mL and [SPIONs] = 1000 µg/mL.

7.2.2. Morphological Characterization after Incubation

Using an optical microscope, the morphological modifications on MCF-7 cells resulting from their 19-h incubation with the GEL-based NLCs were analysed (figure 7.4).

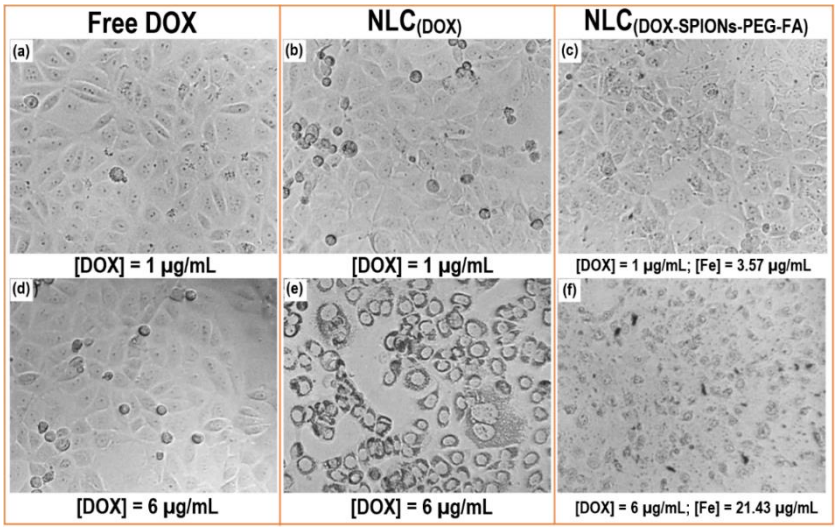

Figure 7.4 - Images of optical microscopy of MCF-7 cells after a 19-h incubation with different concentrations of (a, d) Free DOX; (b, e) $NLC_{(DOX)}$; and (c, f) $NLC_{(DOX\text{-}SPIONs\text{-}PEG\text{-}FA)}$.

From the images above, it is possible to observe that, for a DOX concentration of 1 μg/mL, the MCF-7 cells displayed a similar morphology when incubated with free DOX or $NLC_{(DOX\text{-}SPIONs\text{-}PEG\text{-}FA)}$, presenting a healthy structure. On the other hand, the cells incubated with $NLC_{(DOX)}$, considering the same DOX concentration, exhibited specific apoptotic characteristics, including cell rounding and shrinkage, suggesting that this formulation had an increased cytotoxicity [figure 7.4(b)].[5,6]

When increasing the DOX concentration to 6 μg/mL, a greater toxicity was verified, leading to distinct apoptotic characteristics, as depicted in figures 7.4(e, f). Additionally, the black spots are observed in figure 7.4(e), which correspond to SPIONs located around and inside the MCF-7 cells.

7.2.3. *In Vitro* Magnetic Hyperthermia Assays

MHT assays were performed considering the GEL-based NLC formulations involving only SPIONs and SPIONs together with DOX ([NLCs] = 45 mg/mL; [DOX] = 280 μg/mL; [SPIONs] = 1000 μg/mL), to evaluate if there was a synergistic effect between MHT and drug-release on cell viability. These conditions correspond to the two lowest concentrations of NPs determined as safe in the biocompatibility assays (figure 7.3) were the ones selected, as any eventual viability reduction would probably result from the assisted drug delivery due to the MHT. The results of those assays are presented in figure 7.5.

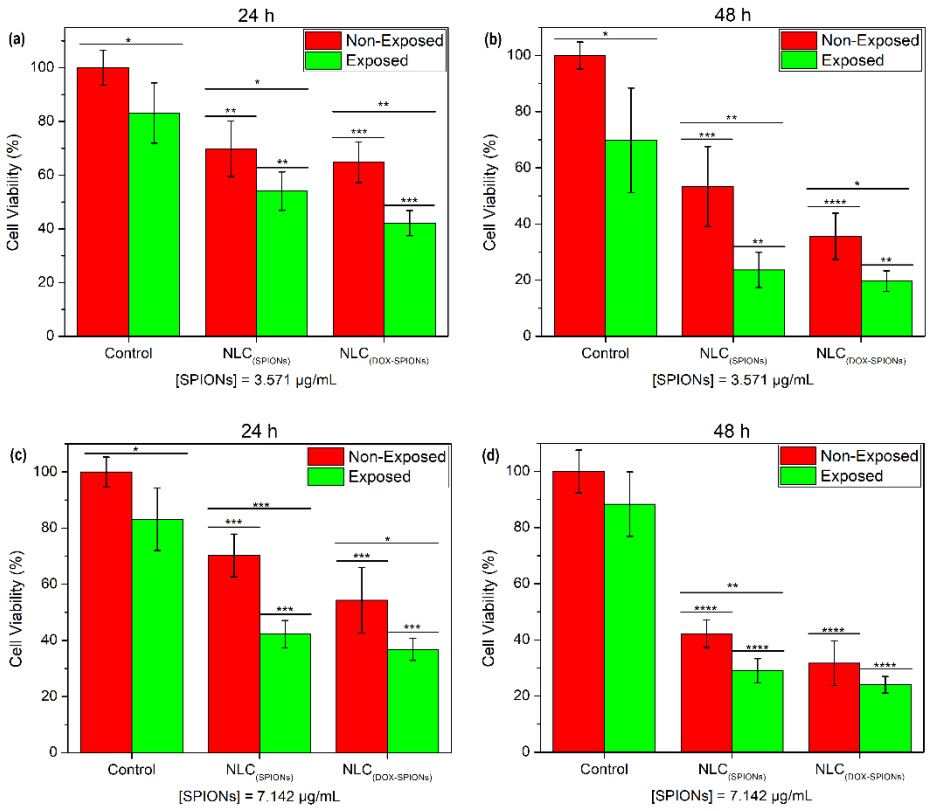

Figure 7.5 - Viability of MCF-7 cells incubated with various types of SPIONs-loaded NLCs at a concentration of (a, b) 3.571 µg/mL or (c, d) 7.142 µg/mL, (a, c) 24 h or (b, d) 48 h after being placed, for 30 min, under similar conditions that differed in regard to the absence (non-exposed) or presence (exposed) of an AMF with a frequency of 556 kHz and a peak intensity equal to 10 mT. Asterisks in short bars indicate statistical significance in relation to the respective control, i.e. exposed or non-exposed, and asterisks in long bars indicate the statistical significance between the tested conditions for each formulation (*P ≤ 0.05; **P ≤ 0.01; ***P ≤ 0.001; ****P ≤ 0.0001).

As can be observed, for all the tested conditions there appears to be a cell viability reduction when the MCF-7 cells are exposed to the AMF, even for those not incubated with NPs. This fact suggests that the AMF is capable of directly affecting the MCF-7 cells' viability through other mechanisms not considered in this work, possibly by interfering with essential biological pathways.[7-9]

On the other hand, when considering the NLCs-incubated cells, it was verified a significant viability reduction for either the non-exposed or exposed cases. Such result possibly suggests that the heating of the coils during operation, which was also mimicked for the not exposed sample, originates a temperature increase in the sample that may be sufficient to promote some DOX-release from the NLCs. In fact, as concluded in section 4.7.3., a temperature as low as 35 ºC can promote DOX release from the considered lipid NPs, which may lead to an increased cell death. This can be a result of using a non-adiabatic sample holder in the performed MHT assays, since good isolated holders are difficult and complex to implement, consequently making environmental interferences hard to avoid.[10,11]

Nevertheless, by comparing the viability reduction for both the non-exposed and exposed NLCs-incubated cells, it was possible to observe a slightly higher cell death in the second case. Particularly, a lower number of viable cells was observed when they were incubated with NLCs loaded with SPIONs and DOX, rather than only SPIONs, indicating the existence of a combined action involving MHT together with DOX release promoted by the hyperthermia temperature increase.

Additionally, a greater cell death was verified 48 h after the assays, suggesting that the cellular response to the combined action of MHT and drug release evolves over time, as a result of the activation of cellular stress response pathways.[12,14]

7.3. FePt Nanowires

After fully characterizing the produced FePt NWs without dendritic structures, obtained through DC electrodeposition, it was decided to analyse their suitability for a biomedical application known as magneto-mechanical induction of cancer cell death (section 1.3.4). For such purpose, and based on the obtained results, it was concluded that nanostructures with a Fe at.% of ~ 80 % would be the most adequate, due to their promising magnetic properties combined with an oxidation resistance capacity (section 5.3.4.).[15,16]

Consequently, multiple anodic aluminum oxide (AAO) templates with electrodeposited $Fe_{80}Pt_{20}$ NWs were produced, based on the previously optimized fabrication process (section 5.3.3.), and then the resulting nanostructures, presenting a diameter of 165.2 ± 6 nm and a length equal to 199.3 ± 31 nm, were removed from the templates (section 3.2.3.2.2.4.) and suspended in double-deionized water. Subsequently, and before the magneto-mechanical cell death assays, the cytotoxicity and uptake of these nanoarchitectures was analysed, in the absence of a magnetic field. All these cell experiments performed using the MCF-7 cell line.

7.3.1. *In Vitro* Cytotoxicity Studies

According to the literature, for the induction of the death of cancer cells through magneto-mechanical action, significantly lower concentrations of nanostructures per cell are required in comparison to MHT, allowing, therefore, a reduction of any potential side effects. Particularly, experiments with concentrations ranging from 10 up to 2000 nanoarchitectures per cell, depending on the type of nanomaterial, have been reported.[17,18] Considering this range, it was determined that, for the magneto-mechanical cell death assays conducted in this study, concentrations of nanomaterials ranging from 80 to 4000 nanostructures per cell would be investigated.

In this context, first it was analysed the biocompatibility of FePt NWs in that concentration range, so as to assess their suitability for biomedical applications (figure 7.6).

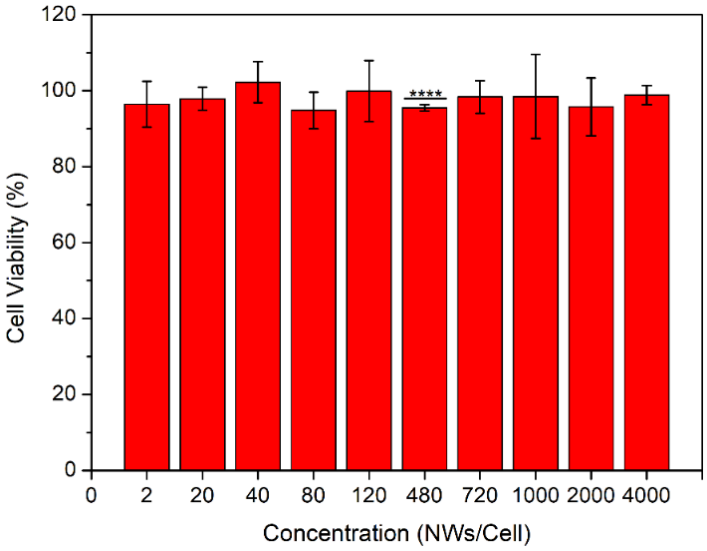

Figure 7.6 - Viability of MCF-7 cells, in relation to control, after a 19-h incubation with various concentrations of $Fe_{80}Pt_{20}$ NWs. Asterisks in short bars indicate statistical significance in relation to control and asterisks in long bars indicate statistical the tested conditions (*P ≤ 0.05; **P ≤ 0.01; ***P ≤ 0.001; ****P ≤ 0.0001).

As represented, for all the FePt NWs' concentrations tested it was observed a cell viability of over 90 %, indicating that these nanostructures have a biocompatibility that makes them promising candidates for not only magneto-mechanical induction of cancer cell death, but also other biomedical applications, e.g. imaging contrast agents or cell manipulation and separation.

7.3.2. *In Vitro* Uptake Assays

In addition to their biocompatibility, the internalization of these nanoarchitectures by the MCF-7 cells was also analysed (figure 7.7).

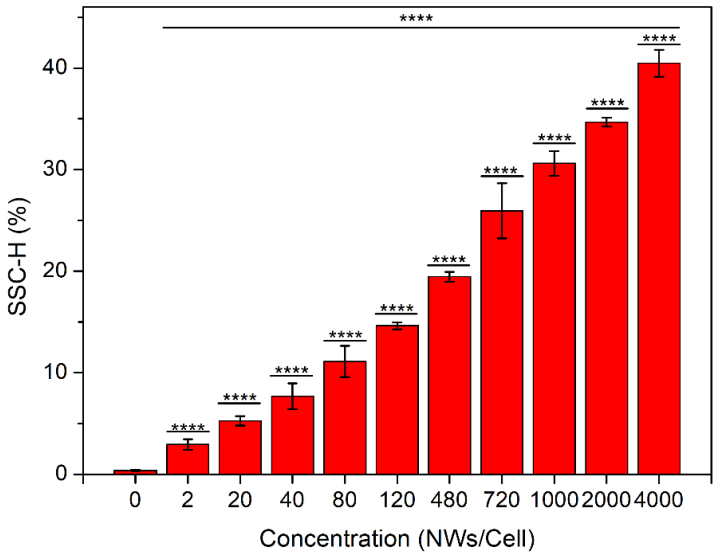

Figure 7.7 - Height of the side scattered light (SSC-H; %) of MCF-7 cells after a 19-h incubation with various concentrations of Fe80Pt20 NWs. Asterisks in short bars indicate statistical significance in relation to control and asterisks in long bars indicate statistical the tested conditions (*P ≤ 0.05; **P ≤ 0.01; ***P ≤ 0.001; ****P ≤ 0.0001).

From the presented results, it is possible to verify that the $Fe_{80}Pt_{20}$ NWs were internalized by the MCF-7 cells. Particularly, there was an increasing SSC-H as higher concentrations of nanostructures were employed, suggesting that the cells possessed greater relative granularity or internal complexity when more NWs were present in the medium. This result can be attributed to the uptake of a larger number of nanoarchitectures per cell, as higher quantities of nanostructures are considered.

7.3.3. *In Vitro* Magneto-Mechanical Cell Death Assays

After analyzing the biocompatibility and uptake of the fabricated $Fe_{80}Pt_{20}$ NWs in MCF-7 cells, magneto-mechanical cell death assays were conducted. These assays were performed on the same cell line to evaluate the suitability of these magnetic nanostructures for the specific biomedical application. According to the magnetic field values reported in the literature for this type of application, it was decided to first perform a 1 h exposure of the NWs-incubated cells to a 10 mT AMF with a frequency of 1 Hz (figure 7.8).[17]

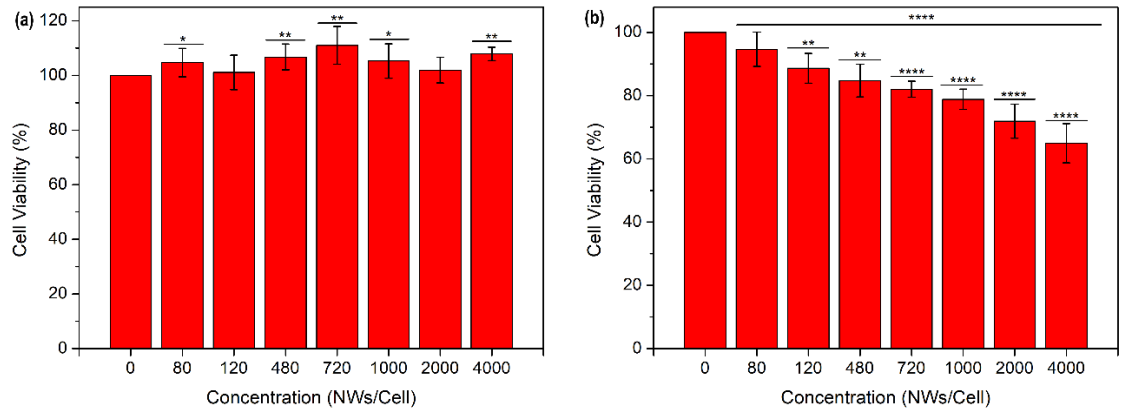

Figure 7.8 - Viability of MCF-7 cells after being placed, for 1 h, under similar conditions, which differ in regard to the (a) absence or (b) presence of a 10 mT magnetic with a frequency of 1 Hz. Asterisks in short bars indicate statistical significance in relation to control and asterisks in long bars indicate statistical the tested conditions (*P ≤ 0.05; **P ≤ 0.01; ***P ≤ 0.001; ****P ≤ 0.0001).

The demonstrated results clearly suggest the induction of cell death in the cells exposed to the magnetic field, which increased with increasing NWs' concentration. This indicates that the produced nanostructures were indeed capable of inducing cancer cell death through magneto-mechanical actuation, when exposed to a relatively weak and low-frequency magnetic field in comparison to the magnetic fields required for MHT, which represents an advantage of this treatment approach.

Since the maximum magnetic field strength in the homemade setup was 10 mT, for the coil separation required to fit the 96 well-microplate, it was analysed the effect of reducing the frequency of that field to 0.1 Hz on the cell viability (figure 7.9).

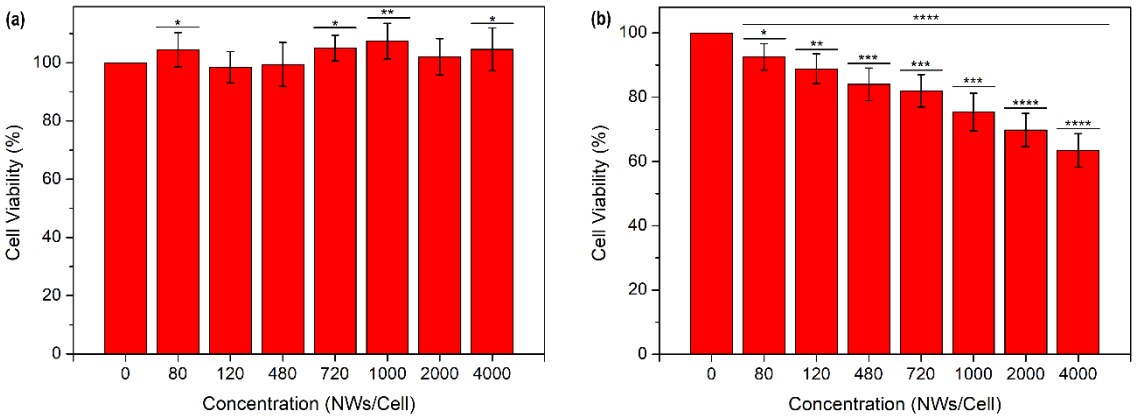

Figure 7.9 - Viability of MCF-7 cells, previously incubated with FePt NWs, after being placed, for 1 h, under similar conditions that differed in regard to the (a) absence or (b) presence of a 10 mT magnetic field with a frequency of 0.1 Hz. Asterisks in short bars indicate statistical significance in relation to control and asterisks in long bars indicate statistical the tested conditions (*P ≤ 0.05; **P ≤ 0.01; ***P ≤ 0.001; ****P ≤ 0.0001).

The results obtained by reducing the magnetic field frequency from 1 Hz to 0.1 Hz are quite similar, although small differences were observed that, however, are within the

standard deviation range. Therefore, it is possible to conclude that the magnetic field frequency does not have a significant effect on the magneto-mechanical induction of cancer cell death. Nevertheless, lower magnetic field frequencies may be more adequate for applications in the clinical practice, as the equipment requirements are less demanding and those magnetic fields are associated with a lower $H \cdot f$, which is important for complying with the limit established by the Hergt and Dutz criterion.[19,20] Additionally, based on the hysteresis loops of these nanostructures, which are presented in figure 5.22, it was determined that, at 10 mT, the magnetization in the NWs, along their easy and hard magnetization axes, was 5.34 ± 3.85 % or 1.99 ± 1.61 % that of their saturation magnetization, respectively. This indicates that the application of stronger magnetic fields would be a promising way to increase cell death, as it would allow to further exploit the magnetic properties of those nanoarchitectures, which presented a saturation magnetization of 702.74 ± 4.69 mT (figure 5.23), enhancing their effectiveness in this biomedical application. However, since it was not possible to increase the applied magnetic field due to the setup limitations, another approach would involve improving the magnetic properties of the NWs so that it would be required a weaker magnetic field to reach their saturation magnetization.

7.4. Au/Fe/Au Nanodiscs

After characterizing the produced Au/Fe/Au NDs, they were removed from the Si template and suspended in double-deionized water for the subsequent cell assays. In this case, and in contrast to the previous study involving FePt NWs, it was first assessed their cytotoxicity and cellular uptake in the absence of a magnetic field by a macrophage cell-line, i.e. THP-1. For such purpose, both non-functionalized and PEG methyl ether thiol (PEG-SH)-functionalized NDs were considered, so as to evaluate the effect of the surface functionalization on those two aspects.

Then, similarly to the FePt NWs, it was assessed their suitability for the induction of the death of cancer cells through magneto-mechanical action. However, in this case such analysis was performed for both non-functionalized and folic acid (FA)-PEG-SH-functionalized NDs, to evaluate the influence of a cancer-targeting agent on the potential of those nanostructures for this specific biomedical application. As in the previous study, before those assays, the cytotoxicity and uptake of these nanoarchitectures was analysed, in the absence of a magnetic field. These cell experiments were performed using the MCF-7 cell line.

7.4.1. Macrophage Assays

When nanomaterials are introduced into a biological system they face a complex series of biological barriers that considerably hinder the site-specific bioavailability, preventing adequate diagnostic and/or therapeutic results.[21,22] In this context, one of the main obstacles is related to their opsonization and successive sequestration by the mononuclear phagocyte system (MPS).[23,24] Several strategies are been explored to avoid this limitation, such as the functionalization of the nanostructures by using PEG.[25] This approach has been carried out with great success for small NPs with sizes lower than 50 nm.[21] However, the functionalization of larger nanostructures, such as the Au/Fe/Au NDs produced in this work (with sizes greater than 200 nm), is still a challenge.

Therefore, to assess the cytotoxicity and cellular uptake of these nanostructures in the absence of a magnetic field by cells of the MPS, cell assays using the THP-1 cell line were conducted. These experiments involved employing different concentrations of NDs with no functionalization, as well as with two distinct PEG-SH functionalizations, which differed in regard to their average molecular weight (MW), i.e. 2000 (PEG_{2000}) or 6000 (PEG_{6000}) g/mol.

7.4.1.1. Functionalization Analysis

Before carrying out the cytotoxicity and cellular uptake assays with the THP-1 cell line, it was necessary to analyse and confirm the presence of the functionalization on the surface of the nanostructures. This analysis was performed through through two distinct methods, namely Raman spectroscopy and X-ray photoelectron spectroscopy (XPS).

7.4.1.1.1. Raman Spectroscopy

Regarding Raman Spectroscopy, the spectra obtained for the two types of PEG-SH used (in powder), the functionalized magnetic nanostructures (still attached to the Si substrate) with the two different functionalizations, and the Si template without NDs are represented in figure 7.10.

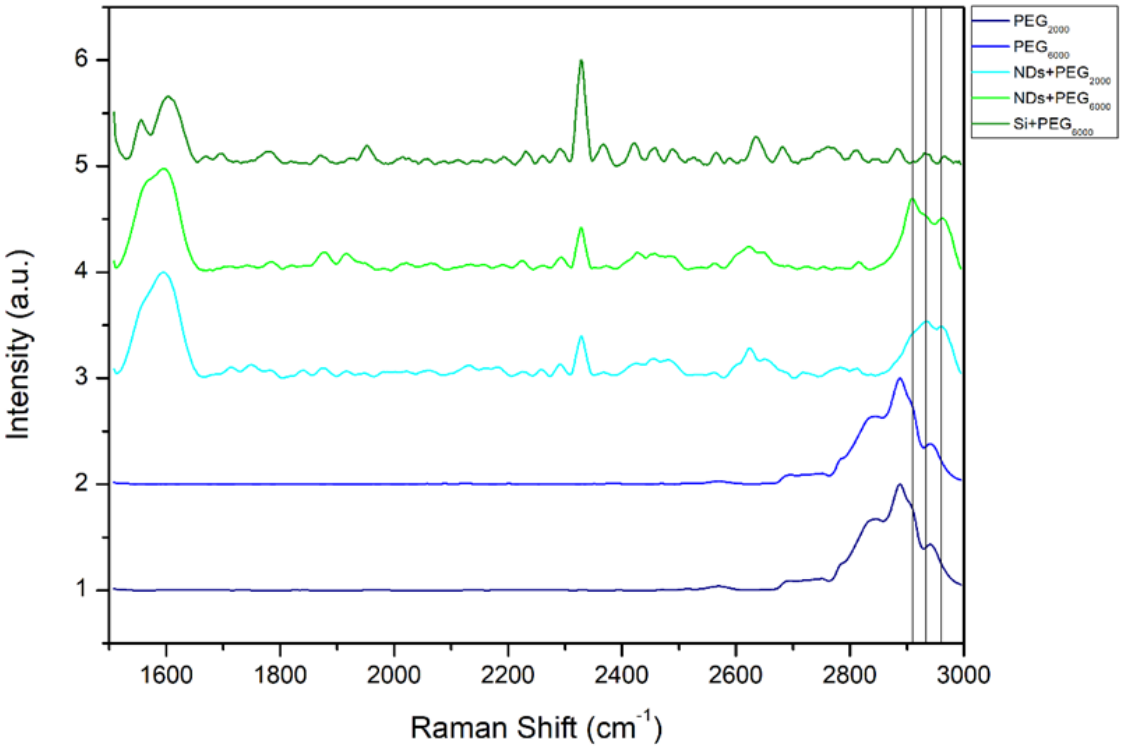

Figure 7.10 - Raman spectra of the two types of PEG-SH considered (PEG_{2000} and PEG_{6000} powder), the functionalized Si template without NDs (Si + PEG_{6000}), and the nanostructures with the two different functionalizations (NDs + PEG_{2000} and NDs + PEG_{6000}).

As can be observed, the PEG-SH powder, for both molecular weights, presents four peaks in the 2800 to 3000 cm^{-1} range, which are related to symmetric (u_s) and anti-symmetric (u_a) stretches of CH_2. Particularly, these Raman spectra present peaks at 2841 cm^{-1}, 2888 cm^{-1}, 2908 cm^{-1}, and 2941 cm^{-1}, corresponding to combination modes from the bending region, $u_s(CH_2)$, CH_2 stretch mode, and $u_a(CH_2)$, respectively.[26-28]

From the comparison of the NDs + PEG spectrum with the spectra of PEG_{2000} and PEG_{6000} represented in figure 7.10, it is possible to verify that 3 peaks appear in the nanostructures (represented by the vertical lines), from which the two with the lowest frequency are also present in the compound of interest, indicating that the NDs were indeed functionalized. Those two peaks are located at Raman shifts of about 2908 and 2937 cm^{-1}, being related with a CH_2 stretch mode influenced by solvent interactions and $u_a(CH_2)$, correspondingly. The remaining peak can be attributed to the Raman signal of the nanostructures, suggesting a successful selective functionalization.

By further analysing the spectra of the NDs + PEG_{2000} and NDs + PEG_{6000}, it is possible to verify that the shift of the peaks in the C-H stretching region can be a result of intensity shifts towards higher wavenumbers, particularly an increase of the intensity of the peak located at 2941 cm^{-1} and a reduction of the intensity of the peak at 2888 cm^{-1}.[26] This

results from a change of the analysed PEG environment.[26] Furthermore, similar spectra were reported by Arib et al.[29] for COOH-terminated PEG-coated Au NPs in the 2800 cm^{-1} to 3000 cm^{-1} region. Consequently, from the Raman analysis, we can claim that there is strong evidence that our nanostructures are functionalized.

7.4.1.1.2. X-Ray Photoelectron Spectroscopy (XPS)

To increase our confidence in such result, an XPS analysis of the NDs over the Si template was also performed considering three conditions, namely NDs without functionalization, functionalized with PEG_{2000}, and functionalized with PEG_{6000}. The detailed spectra for the expected elements, corrected for adventitious C at 284.8 eV in binding energy, are represented in figure 7.11.

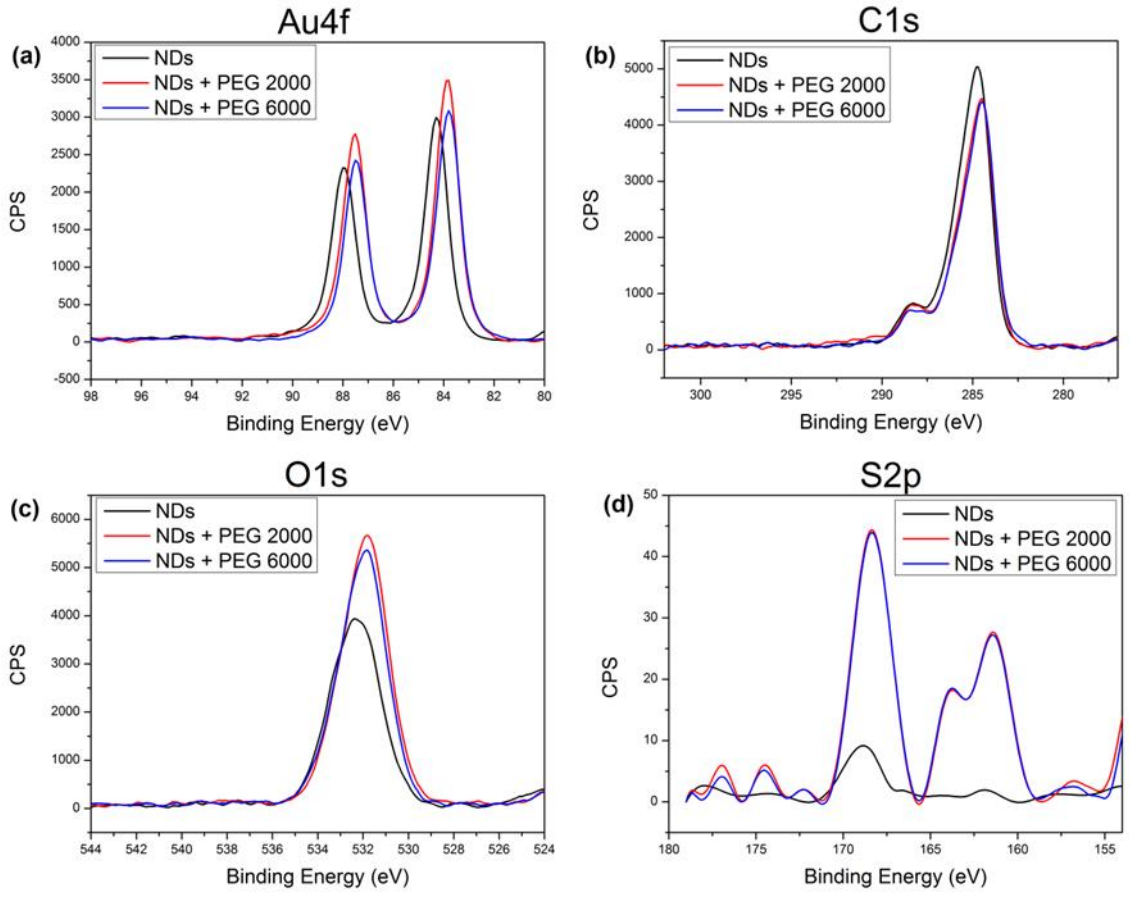

Figure 7.11 - XPS spectra (counts per second, cps vs. binding energy) of (a) Au4f, (b) C1s, (c) O1s, and (d) S2p regions for the NDs without functionalization (NDs), functionalized with PEG_{2000} (NDs + PEG 2000), and functionalized with PEG_{6000} (NDs + PEG 6000).

Regarding figure 7.11(a), it is possible to observe two peaks for the non-functionalized NDs, namely at 84.3 eV and 88.0 eV, corresponding to $4f_{7/2}$ and $4f_{5/2}$ spin orbitals. Furthermore, these two peaks are relatively narrow, indicating that Au is present in the Au^0 metallic form and, consequently, is highly stable.[30,31] On the other hand, after the

functionalization process, these two peaks are shifted towards lower binding energies, i.e. 83.8 eV and 87.5 eV. Such negative shift can be explained by the interaction between PEG-SH and Au, namely, according to the hard-soft acid-base (HSAB) principle, S is a soft base with a high affinity for Au, since it is a soft acid, forming a strong interaction. Consequently, S atoms share their electrons with the Au atoms, which increases the electron density and, therefore, originates a negative shift in the binding energy.[32]

In the C1s spectra [figure 7.11(b)], it is possible to observe that the non-functionalized nanoarchitectures exhibit a spectrum characteristic of adventitious C, which is expected and unavoidable due to the exposure of the sample to air before its transfer to the XPS instrument.[33] In turn, the functionalized NDs present C1s spectra that can be deconvoluted in three peaks: 284.6 eV, which could represent the mean value of the binding energies associated with the different C atom types on the functionalized surface, including C atoms of aliphatic groups (C–C/C–H at 284.6 eV) from PEG-SH; 286.5 eV, indicating the presence of the ether-carbon bonds from the PEG backbone; and 288.4, which is associated with carbon–oxygen bonds.[34-37]

The O1s spectra was also analysed for all the considered nanostructures [figure 7.11(c)], having been observed, for the non-functionalized NDs, a single peak at around 532.3 eV, which, according to the literature, corresponds to adsorbed oxygen species, such as H2O and CO2.[38,39] On the other hand, the O1s spectra of the functionalized nanostructures appears to be shifted towards lower binding energies, presenting a peak at ~ 531.8 eV. This result is consistent with the removal of hydroxyl groups resulting from the functionalization with PEG-SH.[40,41]

From these three XPS spectra, it is possible to conclude that the shifting of the peaks only occurs when functionalization is performed, indicating that the local chemical environment of the surface is indeed altered during that procedure.[42,43] However, in order to confirm the presence of the PEG-SH molecules on the surface of the NDs, it is necessary to assess the presence of S, which was not observed in the survey spectra due to its inherently low concentration in the PEG-SH molecules. Therefore, the high resolution S2p spectra of these nanostructures were also acquired [figure 7.11(d)].

Regarding the functionalized NDs, their S2p spectra can be deconvoluted into three peaks, i.e. 161.5 eV, which, according to the literature, corresponds to thiols covalently bonded to Au atoms at the ND surface; 163.8 eV, representing physisorbed RS-H thiol groups; and 168.4 eV that indicates the presence of high oxidation state S species, such as sulfonate groups.[44-47]

In summary, the acquired XPS data also indicated that the NDs were successfully functionalized with PEG-SH.

7.4.1.2. *In Vitro* Cytotoxicity Studies

Following these results, we were interested in assessing the interaction of these nanostructures by some cells of the MPS. In this context, it was first assessed the cytotoxicity of both functionalized and non-functionalized nanostructures in the THP-1 cell line (figure 7.12).

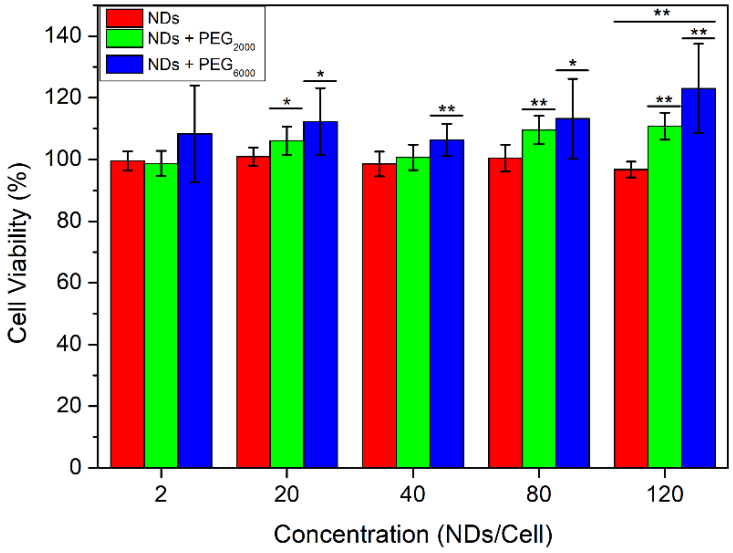

Figure 7.12 - Cell viability as a function of the number of non-functionalized (NDs) and functionalized NDs (NDs + PEG_{2000}; NDs + PEG_{6000}) per cell (n=3). Asterisks in short bars indicate statistical significance in relation to control and asterisks in long bars indicate statistical the tested conditions (*P ≤ 0.05; **P ≤ 0.01; ***P ≤ 0.001; ****P ≤ 0.0001).

As can be observed, for all the concentrations of non-functionalized NDs tested, less than 5% of the cells were dead. Consequently, it was concluded that these nanostructures, without the functionalization, are innocuous to THP-1 cells in the absence of an external magnetic field. Regarding the functionalized nanostructures, they also present high biocompatibility, with the lowest cell viability achieved being 98%. Furthermore, the NDs functionalized with PEG-SH possessing an average molecular weight of 2000 (p-value = 0.02) appear to have a slightly lower level of cytotoxicity.

7.4.1.3. *In Vitro* Uptake Assays

Subsequently, the uptake of both functionalized and non-functionalized NDs was assessed, using the same cell line (figure 7.13).

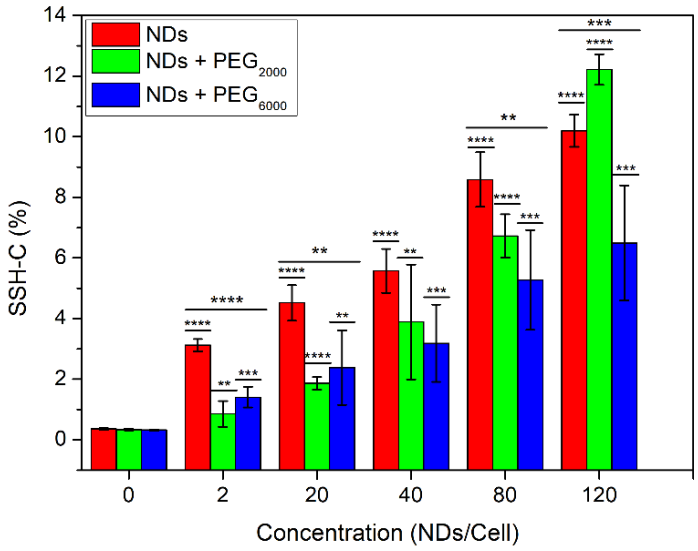

Figure 7.13 - SSC-H as a function of the number of non-functionalized (NDs) and functionalized NDs (NDs + PEG_{2000}; NDs + PEG_{6000}) per cell (n=3). Asterisks in short bars indicate statistical significance in relation to control and asterisks in long bars indicate statistical the tested conditions (*P ≤ 0.05; **P ≤ 0.01; ***P ≤ 0.001; ****P ≤ 0.0001).

Regarding the cellular uptake of the non-functionalized NDs, it was verified that they were internalized by the considered cells, having been observed an increase of the SSC-H with the concentration of nanostructures. On the other hand, regarding the functionalized nanoarchitectures, it is possible to observe that the internalization by the THP-1 cells is, generally, lower when compared to the non-functionalized ones. Such result is particularly pronounced for the NDs functionalized with the PEG-SH possessing a higher average molecular weight. The reason for this observation can be attributed to the fact that such functionalization introduces modifications in the surface properties of the NDs, such as charge and hydrophilicity. These modifications may affect the interaction between the functionalized nanoarchitectures and the THP-1 cell membrane, making them less favourable for internalization.[48]

Consequently, it is possible to conclude that this functionalization has the potential to reduce the opsonisation of these nanostructures by the cells of the MPS, while maintaining their biocompatibility.

7.4.2. Magneto-Mechanical Cell Death Assays

After studying the cytotoxicity and uptake of the produced Au/Fe/Au NDs by the THP-1 cell line, and confirming that the PEG-SH functionalization led to a reduction of their opsonization, it was analysed the potential of those magnetic nanostructures for inducing the death of cancer cells through magneto-mechanical actuation. For such purpose, both non-functionalized and PEG-SH-functionalized NDs were considered. Moreover, another functionalization of those nanostructures with FA-PEG-SH (section 3.2.2.1.) was

also tested, since the folate receptor is overexpressed on numerous tumours, serving as a biomarker for cancer cells.[49]

Nevertheless, similarly to the previously performed experiments with FePt NWs, before the magneto-mechanical cell death assays, the cytotoxicity and uptake of these nanoarchitectures was analysed, in the absence of a magnetic field. These experiments were performed considering the MCF-7 cell line, as well.

7.4.2.1. *In Vitro* Biocompatibility Assays

First, in order to assess the biocompatibility of both non-functionalized and functionalized Au/Fe/Au NDs on the selected cell line, in the absence of an external magnetic field, their cytotoxicity was assessed. As in the previous involving FePt NWs, concentrations ranging between 80 and 4000 nanostructures per cell were tested (figure 7.14).

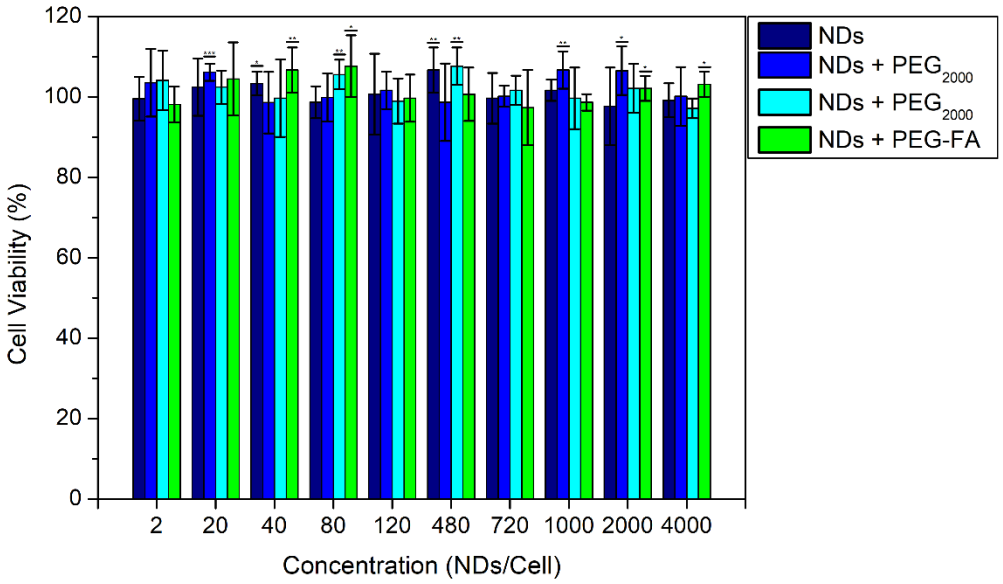

Figure 7.14 - Viability of MCF-7 cells, in relation to control, after a 19-h incubation with various concentrations of (NDs) and functionalized NDs (NDs + PEG_{2000}; NDs + PEG_{6000}; NDs + PEG-FA) per cell (n=3). Asterisks in short bars indicate statistical significance in relation to control and asterisks in long bars indicate statistical the tested conditions (*P ≤ 0.05; **P ≤ 0.01; ***P ≤ 0.001; ****P ≤ 0.0001).

From the presented results, it is possible to verify that for all the concentrations of both non-functionalized and functionalized NDs, less than 4% of the cells were dead. Consequently, it was concluded that these nanostructures, in the absence of an external magnetic field, do not have a significant cytotoxic effect on the MCF-7 cells.

7.4.2.2. *In Vitro* Uptake Assays

The uptake of these nanostructures by the MCF-7, without an applied magnetic field (figure 7.15), was also assessed before the magneto-mechanical cell death assays, to better understand the interactions between the NDs and those cancer cells.

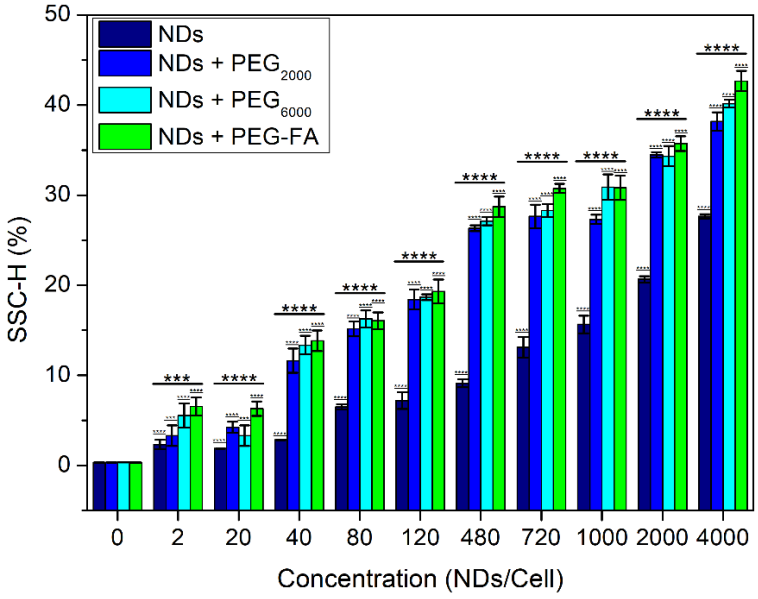

Figure 7.15 - SSC-H as a function of the number of non-functionalized (NDs) and functionalized NDs (NDs + PEG_{2000}; NDs + PEG_{6000}; NDs + PEG-FA) per cell (n=3). Asterisks in short bars indicate statistical significance in relation to control and asterisks in long bars indicate statistical the tested conditions (*P ≤ 0.05; **P ≤ 0.01; ***P ≤ 0.001; ****P ≤ 0.0001).

As can be observed, both functionalized and non-functionalized NDs were internalized by the MCF-7, having been verified a concentration-dependent increase of the SSC-H with increasing concentration of nanostructures. Nevertheless, the functionalized nanoarchitectures were significantly more internalized than the non-functionalized ones, particularly those with FA-PEG-SH at the surface. This result may be attributed to the enhanced stability and reduced aggregation of the PEG-SH-functionalized nanostructures, which can make them more suitable for interaction with the cancer cells' membranes.[50-52] On the other hand, the increased uptake of the FA-PEG-SH-functionalized NDs may result from the overexpression of folate receptors on the surface of the MCF-7 cells.[53,54] Nevertheless, it is possible to observe that the difference between the presence or absence of FA on the surface of the NDs is small, which can be attributed to the fact that most PEG-functionalized nanostructures are internalized, leading to a reduced number of NDs outside the cells. This originates a reduced increase in the internalization of the FA-PEG-SH-functionalized nanostructures by the cancer cells, as most nanoarchitectures were already internalized when functionalized with PEG-SH.

7.4.2.3. *In Vitro* Magneto-Mechanical Cell Death Assays

After analysing the biocompatibility and internalization of both functionalized and non-functionalized Au/Fe/Au NDs, the induction of the death of MCF-7 cells through magneto-mechanical actuation using those nanostructures. In this context, it was assessed the influence of several parameters, namely the magnetic field strength and frequency, as well as the concentration of NDs and their functionalization, on the resulting cell death.

As a result, NDs without any functionalization were selected for the initial assays. Additionally, based on the magnetic field strength and frequency reported in the literature for this type of biomedical application and nanomaterials, it was used a magnetic field with a strength of 10 mT and a frequency of 1 Hz for these first assays.[17] The obtained results are presented in figure 7.16.

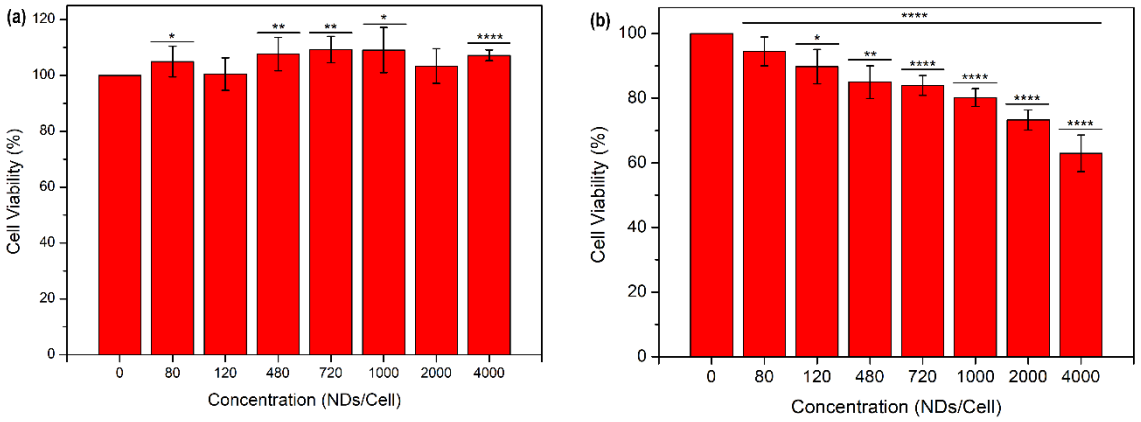

Figure 7.16 - Viability of MCF-7 cells incubated with different concentrations of non-functionalized Au/Fe/Au NDs, after being placed, for 1 h, under similar conditions that differed in regard to the (a) absence or (b) presence of a 10 mT magnetic field with a frequency of 1 Hz. Asterisks in short bars indicate statistical significance in relation to control and asterisks in long bars indicate statistical the tested conditions (*P ≤ 0.05; **P ≤ 0.01; ***P ≤ 0.001; ****P ≤ 0.0001).

From the presented results, it is possible to verify that, for the non-exposed cells, no significant cytotoxicity was observed. On the other hand, regarding the cells exposed to the external AMF, a concentration-dependent decrease of cell viability was noticed, where higher concentrations of nanostructures led to a greater cell death.

Subsequently, it was analysed the impact of reducing the frequency of the external magnetic field from 1 Hz to 0.1 Hz on the cell viability (figure 7.17).

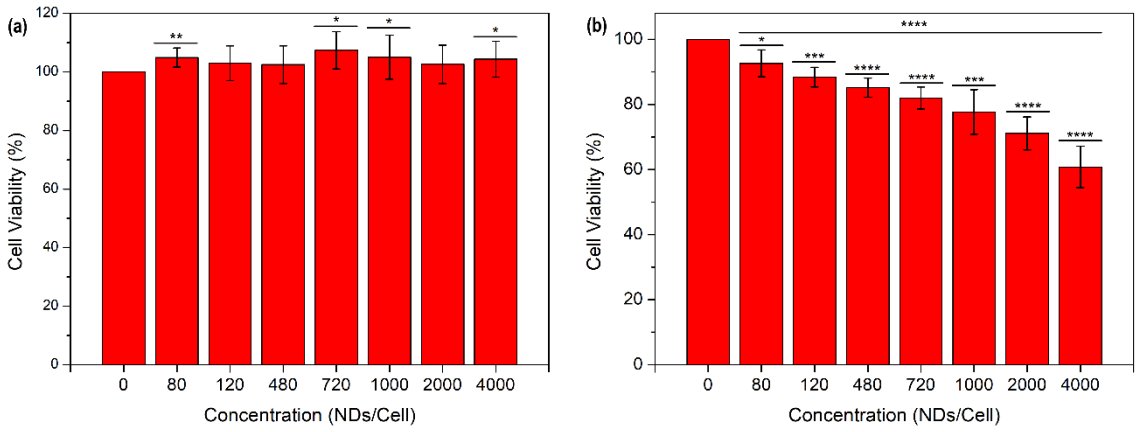

Figure 7.17 - Viability of MCF-7 cells incubated with different concentrations of non-functionalized Au/Fe/Au NDs, after being placed, for 1 h, under similar conditions that differed in regard to the (a) absence or (b) presence of a 10 mT magnetic field with a frequency of 0.1 Hz. Asterisks in short bars indicate statistical significance in relation to control and asterisks in long bars indicate statistical the tested conditions (*P ≤ 0.05; **P ≤ 0.01; ***P ≤ 0.001; ****P ≤ 0.0001).

Similarly to the previous experiment, it was observed that, for the cells exposed to the AMF, higher concentrations of NDs led to a greater cell death, while, for the non-exposed cells, no considerable reduction in cell viability was verified. Additionally, by comparing the two assays, no significant differences in cell death were observed when employing a 10 mT magnetic field with a frequency of 1 or 0.1 Hz, suggesting that, by reducing this parameter, the cytotoxic effect of the NDs exposed to an AMF is not considerably influenced. Moreover, the effect of increasing the frequency of the magnetic field was not tested as it was not possible to achieve higher frequencies with the same field strength in the homemade setup, due to the response time of the system.

In addition to the frequency, the influence of the magnetic field strength on the induction of cell death through this approach was also analysed. However, since the maximum attainable magnetic field in the homemade setup, for a frequency of 1 Hz, was 10 mT, it was decided to use a frequency of 0.1 Hz to perform this study, as it allowed to achieve a maximum magnetic field strength of 20 mT and, as previously concluded, decreasing the frequency of the field did not significantly affect the resulting cell death. The acquired results are represented in figure 7.18.

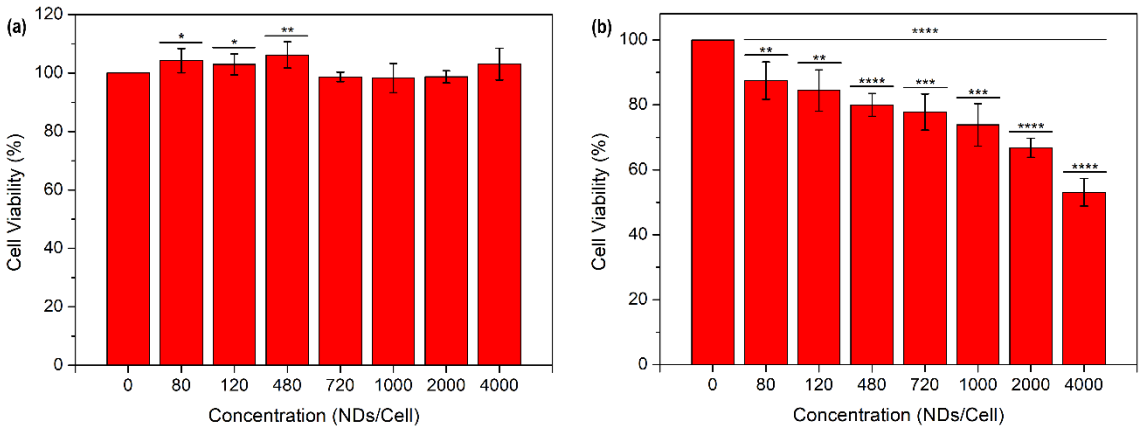

Figure 7.18 - Viability of MCF-7 cells incubated with different concentrations of non-functionalized Au/Fe/Au NDs, after being placed, for 1 h, under similar conditions that differed in regard to the (a) absence or (b) presence of a 20 mT magnetic field with a frequency of 0.1 Hz. Asterisks in short bars indicate statistical significance in relation to control and asterisks in long bars indicate statistical the tested conditions (*P ≤ 0.05; **P ≤ 0.01; ***P ≤ 0.001; ****P ≤ 0.0001).

As can be observed, no noticeable cell death was verified for the non-exposed cells, while those exposed to the AMF presented a viability reduction that depended on the concentration of nanostructrures considered. By comparing these results with those obtained in the previous experiment, a similar concentration-dependent behaviour of the viability of the AMF-exposed MCF-7 cells was observed. Nevertheless, such reduction was slightly more significant when considering a 20 mT AMF (~ 4 %), suggesting that higher magnetic fields promote the cytotoxic effect of these NDs. By analysing the hysteresis loop of this type of nanostructures, presented in figure 6.10, it was possible to verify that, under a magnetic field of 10 mT, their magnetization corresponds to 9.86 ± 3.8 % of their saturation magnetization, while under a magnetic field equal to 20 mT, that value increases to 23.10 ± 3.92 %. In this context, stronger magnetic fields should be applied to further exploit the magnetic properties of these nanostructures to increase the resulting cell death, with their saturation magnetization being reached at 103.67 ± 13.67 mT.

Based on the obtained results, it was concluded that the optimal magnetic field parameters for inducing cell death through magneto-mechanical actuation in this homemade setup, using Au/Fe/Au NDs, were a strength of 20 mT and a frequency equal to 0.1 Hz. Subsequently, considering an AMF with those characteristics, it was assessed the effect of the NDs functionalization with two types of PEG-SH, i.e. PEG_{2000} and PEG_{6000}, on their ability to induce the death of MCF-7 cells through magneto-mechanical actuation (figure 7.19).

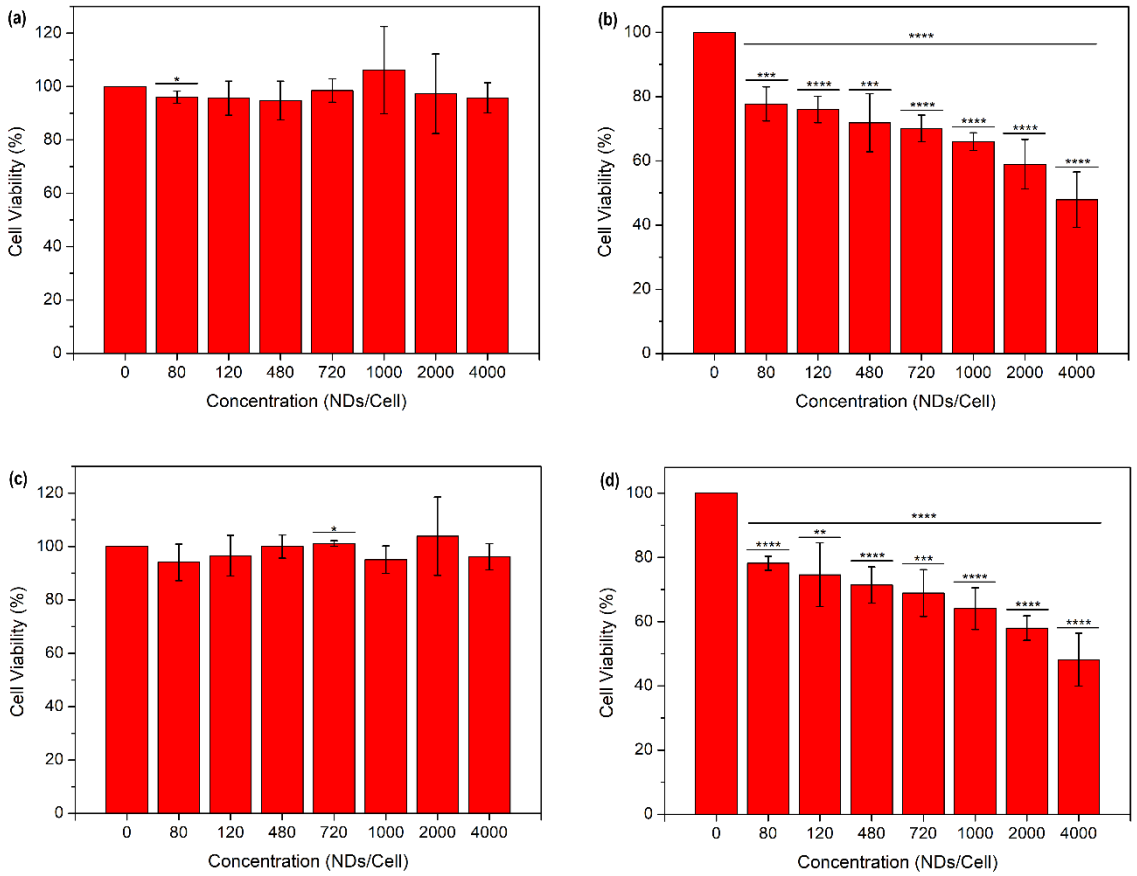

Figure 7.19 - Viability of MCF-7 cells incubated with different concentrations of (a, b) PEG_{2000} or (c, d) PEG_{6000} functionalized Au/Fe/Au NDs, after being placed, for 1 h, under similar conditions that differed in regard to the (a, c) absence or (b, d) presence of a 20 mT magnetic field with a frequency of 0.1 Hz. Asterisks in short bars indicate statistical significance in relation to control and asterisks in long bars indicate statistical the tested conditions (*P ≤ 0.05; **P ≤ 0.01; ***P ≤ 0.001; ****P ≤ 0.0001).

As previously concluded in the biocompatibility assays, no significant cytotoxicity was observed in the cells not exposed to the AMF. Conversely, for those exposed to the AMF, a considerable increase in cell death, which depended on the concentration of the functionalized NDs, was verified. Comparing the two PEG-SH functionalizations, negligible differences were observed between them, indicating that the type of PEG-SH molecule does not significantly affect the cytotoxic effect of these nanostructures. However, a cell death increase of 7.75 ± 1.26 % or 8.41 ± 1.56 % was attained when using the PEG_{2000}- or PEG_{6000}-functionalized NDs, in comparison to the non-functionalized ones, suggesting that such functionalization contributes to an enhanced cytotoxicity of those nanoarchitectures, when under an AMF. This result may be attributed to the increased internalization of PEG-functionalized NDs observed in the uptake assays (figure 7.15), which leads to a higher concentration of these nanostructures within the cells and, consequently, causes a greater magneto-mechanically-induced damage in those biological entities.

Afterwards, similar assays were performed using FA-PEG-SH-functionalized NDs, so as to evaluate the effect of that functionalization on the nanostructures' capacity to promote cell death through magneto-mechanical action (figure 7.20).

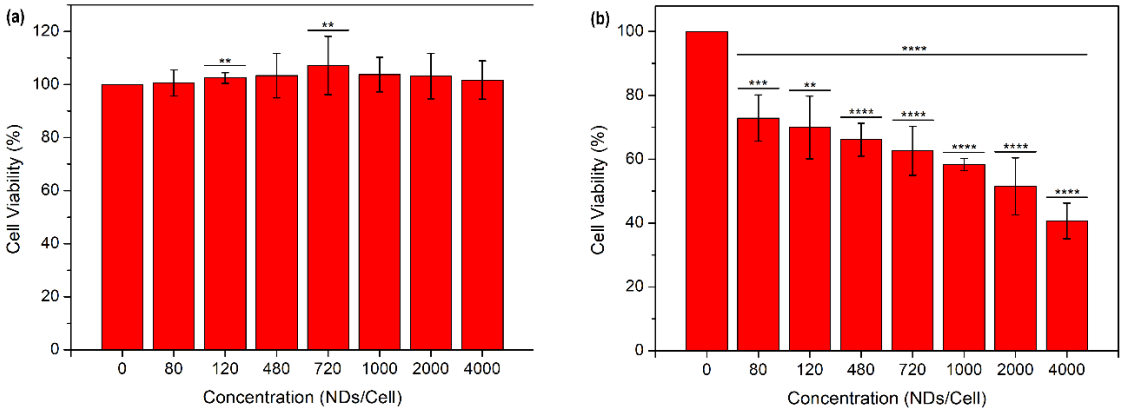

Figure 7.20 - Viability of MCF-7 cells incubated with different concentrations of FA-PEG-SH functionalized Au/Fe/Au NDs, after being placed, for 1 h, under similar conditions that differed in regard to the (a) absence or (b) presence of a 20 mT magnetic field with a frequency of 0.1 Hz. Asterisks in short bars indicate statistical significance in relation to control and asterisks in long bars indicate statistical the tested conditions (*P ≤ 0.05; **P ≤ 0.01; ***P ≤ 0.001; ****P ≤ 0.0001).

As can be observed, the non-exposed cells did not exhibit any significant viability reduction, while those exposed to the AMF presented a death percentage that depended on the concentration of NDs considered in the assay. In comparison to the PEG-SH-functionalized nanostructures, the FA-PEG-SH functionalization led to higher cell death for the same concentration of nanoarchitectures, specifically 6.38 ± 0.33 % larger. This can be attributed to their greater internalization by the cancer cells, as concluded in the uptake assays (figure 7.15). This increased internalization of the FA-PEG-SH NDs can be a result of the overexpression of folate receptors on the surface of the MCF-7 cells.[55]

7.5. Conclusions

In this chapter, the suitability of the produced nanomaterials for different biomedical applications was analysed. Particularly, it was assessed the potential of the produced NLCs for a dual cancer treatment approach involving MHT together with a targeted anticancer drug release. For such purpose, the nano-formulations composition and concentration for this application was first optimized, based on biocompatibility studies and morphology evaluation after incubating cancer cells with those nanomaterials. Then, MHT assays with those NPs were performed, having been obtained evidence of a successful dual action on cancer cells involving MHT together with DOX release promoted by the temperature increase.

The potential of FePt NWs and Au/Fe/Au NDs for a different biomedical application known as magneto-mechanical induction of cell death was also studied. Regarding the first, biocompatibility studies revealed that they were innocuous to cancer cells in the absence of an external AMF, while uptake assays suggested that those biological entities were capable of internalizing the FePt NWs. Then, magneto-mechanical cell death assays indicated a concentration-dependent decrease of the cell viability, where cell death increased with increasing concentration of nanostructures. Furthermore, it was concluded that reducing the frequency of the applied AMF led to a negligible effect on the number of viable cells, after exposure to the AMF.

Subsequently, the potential of the synthesized Au/Fe/Au NDs for this same application was evaluated. However, in this case, it was first assessed their recognition by cells of the MPS. For such purpose, the nanostructures were functionalized with two types of PEG-SH possessing distinct MWs. Raman spectroscopy and XPS allowed to confirm the presence of those compounds in the NDs. Afterwards, cell assays with the non-functionalized and functionalized NDs led to the conclusion that both types of nanostructures are biocompatible and, through PEG-SH functionalization, it is possible to reduce their uptake by the cells of the MPS. Then, it was assessed the suitability of these nanostructures for the previously mentioned biomedical application, using non-functionalized, PEG-SH functionalized, as well as FA-PEG-SH-functionalized NDs. In this context, biocompatibility assays in the absence of an external AMF, revealed that all these nanoarchitectures possessed an adequate biocompatibility. On the other hand, by performing uptake assays, also without an external AMF, it was verified that the functionalized NDs were internalized at a higher degree by the cancer cells than the non-functionalized ones. Subsequently, cells incubated with different concentrations of nanoarchitectures were exposed to AMFs with various parameters, having been concluded that reducing the magnetic field frequency did not significantly impact the cytotoxic ability of these NDs, while increasing the strength of that field led to increased cell death. Additionally, it was verified that functionalized nanostructures were capable of inducing greater cell death, specially those involving FA-PEG-SH.

References

[1]Y. Lu, X. Pan, Q. Nie, Z. Zhou, X. Dai, and O. Liu, Administration methods of lipid-based nanoparticle delivery systems for cancer treatment. *Biomaterials Science* **11**, 3800–3812 (2023).

[2]C. H. Kim, S. G. Lee, M. J. Kang, S. Lee, and Y. W. Choi, Surface modification of lipid-based nanocarriers for cancer cell-specific drug targeting. *Journal of Pharmaceutical Investigation* **47**, 203–227 (2017).

[3]M. Rizwanullah, M. Z. Ahmad, A. Garg, and J. Ahmad, Advancement in design of nanostructured lipid carriers for cancer targeting and theranostic application. *Biochimica et Biophysica Acta (BBA)-General Subjects* **1865**, 129936 (2021).

[4]K. S. Parikh, A. Josyula, T. Inoue, T. Fukunishi, H. Zhang, R. Omiadze, R. Shi, Y. Yazdi, J. Hanes, L. M. Ensign, and N. Hibino, Nanofiber-coated, tacrolimus-eluting sutures inhibit post-operative neointimal hyperplasia in rats. *Journal of Controlled Release* **353**, 96–104 (2023).

[5]S. Rello, J. Stockert, V. Moreno, A. Gamez, M. Pacheco, A. Juarranz, M. Canete, and A. Villanueva, Morphological criteria to distinguish cell death induced by apoptotic and necrotic treatments. *Apoptosis* **10**, 201–208 (2005).

[6]N. Amini-Sarteshnizi, S. Zahri, H. Jafari-Ghahfarokhi, F. K. Hafshejani, and H. Teimori, Morphological changes of apoptosis and cytotoxic effects induced by Caffeic acid phenethyl ester in AGS human gastric cancer cell line. *Journal of HerbMed Pharmacology* **3**, 77–82 (2014).

[7]H. Zadeh-Haghighi and C. Simon, Magnetic field effects in biology from the perspective of the radical pair mechanism. *Journal of the Royal Society Interface* **19**, 20220325 (2022).

[8]D. A. Hart, The Influence of Magnetic Fields, Including the Planetary Magnetic Field, on Complex Life Forms: How Do Biological Systems Function in This Field and in Electromagnetic Fields?. *Biophysica* **4**, 1–21 (2024).

[9]A. Buchachenko and D. Kuznetsov, Genes and Cancer under Magnetic Control. *Russian Journal of Physical Chemistry B* **15**, 1–11 (2021).

[10]E. Natividad, M. Castro, and A. Mediano, Adiabatic vs. non-adiabatic determination of specific absorption rate of ferrofluids. *Journal of Magnetism and Magnetic Materials* **321**, 1497–1500 (2009).

[11]A. Makridis, Magnetic nanostructures and nanomagnetism for modern biomedical applications. PhD Thesis, Aristotle University of Thessaloniki (2019).

[12]K. Ahmed, S. F. Zaidi, R. Rehman, T. Kondo, et al., “Hyperthermia and protein homeostasis: cytoprotection and cell death”, Journal of thermal biology 91, 102615 (2020).

[13]S. Fulda, A. M. Gorman, O. Hori, and A. Samali, Cellular Stress Responses: Cell Survival and Cell Death. *International Journal of Cell Biology* **2010**, 214074 (2010).

[14]X. Liu, Y. Zhang, Y. Wang, W. Zhu, G. Li, X. Ma, Y. Zhang, S. Chen, S. Tiwari, K. Shi, S. Zhang, H. M. Fan, Y. X. Zhao, and X.-J. Liang, Comprehensive understanding of magnetic hyperthermia for improving antitumor therapeutic efficacy. *Theranostics* **10**, 3793 (2020).

[15]J. Lyubina, O. Gutfleisch, K.-H. Müller, and L. Schultz, Structure and hysteresis properties of nanocrystalline FePt powders. *Journal of Magnetism and Magnetic Materials* **290**, 547–550 (2005).

[16]H. Cha, Y. Kim, C. Kim, and Y. Kang, Study of the Magnetic Phase of Fe-Pt Alloy Nanoparticles. *Journal of Nanoscience and Nanotechnology* **8**, 4666–4669 (2008).

[17]L. Peixoto, R. Magalhães, D. Navas, S. Moraes, C. Redondo, R. Morales, J. Araújo, and C. Sousa, Magnetic nanostructures for emerging biomedical applications. *Applied Physics Reviews* **7**, 011310 (2020).

[18]A. A. Nikitin, A. V. Ivanova, A. S. Semkina, P. A. Lazareva, and M. A. Abakumov, Magneto-Mechanical Approach in Biomedicine: Benefits, Challenges, and Future Perspectives. *International Journal of Molecular Sciences* **23**, 11134 (2022).

[19]D. P. Valdés, E. Lima, R. D. Zysler, G. F. Goya, and E. De Biasi, Role of Anisotropy, Frequency, and Interactions in Magnetic Hyperthermia Applications: Noninteracting Nanoparticles and Linear Chain Arrangements. *Physical Review Applied* **15**, 044005 (2021).

[20]D. Kouzoudis, G. Samourgkanidis, A. Kolokithas-Ntoukas, G. Zoppellaro, and K. Spiliotopoulos, Magnetic Hyperthermia in the 400–1,100 kHz Frequency Range Using MIONs of Condensed Colloidal Nanocrystal Clusters. *Frontiers in Materials* **8**, 638019 (2021).

[21]E. Blanco, H. Shen, and M. Ferrari, Principles of nanoparticle design for overcoming biological barriers to drug delivery. *Nature Biotechnology* **33**, 941–951 (2015).

[22]W. Bao, F. Tian, C. Lyu, B. Liu, B. Li, L. Zhang, X. Liu, F. Li, D. Li, X. Gao, S. Wang, W. Wei, X. Shi, and Y. Li, Experimental and theoretical explorations of nanocarriers' multistep delivery performance for rational design and anticancer prediction. *Science Advances* **7**, eaba2458 (2021).

[23]Y.-F. Wang, L. Liu, X. Xue, and X.-J. Liang, Nanoparticle-based drug delivery systems: What can they really do *in vivo*?. *F1000Research* **6**, 681 (2017).

[24]C. Lin, H. Gao, and L. Ouyang, Advance cardiac nanomedicine by targeting the pathophysiological characteristics of heart failure. *Journal of Controlled Release* **337**, 494–504 (2021).

[25]J. Conniot, J. M. Silva, J. G. Fernandes, L. C. Silva, R. Gaspar, S. Brocchini, H. F. Florindo, and T. S. Barata, Cancer immunotherapy: nanodelivery approaches for immune cell targeting and tracking. *Frontiers in Chemistry* **2**, 105 (2014).

[26]R. T. Rooney, K. G. Schmitt, H. F. von Horsten, R. Schmidt, and A. A. Gewirth, Raman and QCM Studies of PPG and PEG Adsorption on Cu Electrode Surfaces. *Journal of The Electrochemical Society* **165**, D687 (2018).

[27]A. Z. Samuel and S. Umapathy, Energy funneling and macromolecular conformational dynamics: a 2D Raman correlation study of PEG melting. *Polymer Journal* **46**, 330–336 (2014).

[28]T. Yoshihara, H. Tadokoro, and S. Murahashi, Normal Vibrations of the Polymer Molecules of Helical Conformation. IV. Polyethylene Oxide and Polyethylene-d_4 Oxide. *The Journal of Chemical Physics* **41**, 2902–2911 (1964).

[29]C. Arib, S. Milano, A. Gerbino, and J. Spadavecchia, Aptamer Grafting onto (on) and into (in) Pegylated Gold Nanoparticles: Physicochemical Characterization and In vitro Cytotoxicity Investigation in Renal Cells. *Journal of Nanomedicine & Nanotechnology* **9**, 2157–7439 (2018).

[30]S. Thambiraj, S. Hema, and D. R. Shankaran, Functionalized gold nanoparticles for drug delivery applications. *Materials Today: Proceedings* **5**, 16763–16773 (2018).

[31]S. Almheiri, A. A. Ahmad, B. Le Droumaguet, R. Pires, A. A. Mohamed, and M. M. Chehimi, Development of Latent Fingerprints via Aryldiazonium Tetrachloroaurate Salts on Copper Surfaces: An XPS Study. *Langmuir* **36**, 74–83 (2019).

[32]S. Kumar, E. Subramani, A. Esokkiya, S. Sudalaimani, Y. Sulaiman, M. M. Khan, C. Jeyabharathi, and K. Giribabu, Self-Assisted Sensing of Spermine by Controlled Dissolution of Polysulfide Modified Gold Electrode. *SSRN* **4058091** (2022).

[33]G. Greczynski and L. Hultman, Impact of sample storage type on adventitious carbon and native oxide growth: X-ray photoelectron spectroscopy study. *Vacuum* **205**, 111463 (2022).

[34]X. Wei, Z. Wang, Z. Zhang, J. Wang, and S. Wang, Surface modification of commercial aromatic polyamide reverse osmosis membranes by graft polymerization of 3-allyl-5, 5-dimethylhydantoin. *Journal of Membrane Science* **351**, 222–233 (2010).

[35]J. R. Hull, G. S. Tamura, and D. G. Castner, Structure and Reactivity of Adsorbed Fibronectin Films on Mica. *Biophysical Journal* **93**, 2852–2860 (2007).

[36]C. Daniel, K. E. Sohn, T. E. Mates, E. J. Kramer, J. O. Rädler, E. Sackmann, B. Nickel, and L. Andruzzi, Structural characterization of an elevated lipid bilayer obtained by stepwise functionalization of a self-assembled alkenyl silane film. *Biointerphases* **2**, 109–118 (2007).

[37]D.G. Xiong, Z. Zhang, X. Y. Huang, Y. Huang, J. Yu, J. X. Cai, and Z. Y. Yang, Boosting the polysulfide confinement in B/N–codoped hierarchically porous carbon nanosheets via Lewis acid–base interaction for stable Li–S batteries. *Journal of Energy Chemistry* **51**, 90–100 (2020).

[38]I. N. Reddy, C. V. Reddy, M. Cho, J. Shim, and D. Kim, Structural, optical and XPS study of thermal evaporated In_2O_3 thin films. *Materials Research Express* **4**, 086406 (2017).

[39]B. Eren and A. R. Head, Carbon Monoxide Adsorption on Manganese Oxide/Cobalt: an Ambient Pressure X-ray Photoelectron Spectroscopy Study. *The Journal of Physical Chemistry C* **124**, 3557–3563 (2020).

[40]R. K. Schulze, M. A. Hill, R. D. Field, P. A. Papin, R. J. Hanrahan, and D. D. Byler, Characterization of carbonated serpentine using XPS and TEM. *Energy Conversion and Management* **45**, 3169–3179 (2004).

[41]I. Shackery, U. Patil, A. Pezeshki, N. M. Shinde, S. Im, and S. C. Jun, Enhanced Non-enzymatic amperometric sensing of glucose using $Co(OH)_2$ nanorods deposited on a three dimensional graphene network as an electrode material. *Microchimica Acta* **183**, 2473–2479 (2016).

[42]C. Ehlert, D. Kroener, and P. Saalfrank, A combined quantum chemical/molecular dynamics study of X-ray photoelectron spectra of polyvinyl alcohol using oligomer models. *Journal of Electron Spectroscopy and Related Phenomena* **199**, 38–45 (2015).

[43]C. Moffitt, Fundamental Aspects of XPS and the Development of XPS Imaging. *Microscopy Today* **19**, 16–21 (2011).

[44]S. Cerra, T. A. Salamone, F. Sciubba, M. Marsotto, C. Battocchio, S. Nappini, F. A. Scaramuzzo, R. L. Voti, C. Sibilia, R. Matassa, A. M. Betlrán, G. Familiari, and I. Fratoddi, Study of the interaction mechanism between hydrophilic thiol capped gold nanoparticles and melamine in aqueous medium. *Colloids and Surfaces B: Biointerfaces* **203**, 111727 (2021).

[45]J. Agúndez, C. Ares, C. Márquez-Álvarez, and J. Pérez-Pariente, Catalytic oxidation of cyclohexene by supported gold nanoclusters synthesized in a two-liquid phases system containing eucalyptus essential oil. *Molecular Catalysis* **488**, 110922 (2020).

[46]N. Wang, Y. Wang, Z. Bai, Z. Fang, X. Zhang, Z. Xu, Y. Ding, X. Xu, Y. Du, S. Dou, and G. Yu, High-performance room-temperature sodium–sulfur battery enabled by electrocatalytic sodium polysulfides full conversion. *Energy & Environmental Science* **13**, 562–570 (2020).

[47]S. Gao, N. Koshizaki, E. Koyama, H. Tokuhisa, T. Sasaki, J.-K. Kim, Y. Cho, D.-S. Kim, and Y. Shimizu, Innovative Platform for Transmission Localized Surface Plasmon Transducers and Its Application in Detecting Heavy Metal Pd(II). *Analytical Chemistry* **81**, 7703–7712 (2009).

[48]J. S. Suk, Q. Xu, N. Kim, J. Hanes, and L. M. Ensign, PEGylation as a strategy for improving nanoparticle-based drug and gene delivery. *Advanced Drug Delivery Reviews* **99**, 28–51 (2016).

[49]M. Fernández, F. Javaid, and V. Chudasama, Advances in targeting the folate receptor in the treatment/imaging of cancers. *Chemical Science* **9**, 790–810 (2018).

[50]S. Yang, Z. Wang, Y. Ping, Y. Miao, Y. Xiao, L. Qu, L. Zhang, Y. Hu, and J. Wang, PEG/PEI-functionalized single-walled carbon nanotubes as delivery carriers for doxorubicin: synthesis, characterization, and in vitro evaluation. *Beilstein Journal of Nanotechnology* **11**, 1728–1741 (2020).

[51]C. Cazan, M. Cosnita, and A. Duta, Effect of PET functionalization in composites of rubber–PET–HDPE type. *Arabian Journal of Chemistry* **10**, 300–312 (2017).

[52]G. Sanità, B. Carrese, and A. Lamberti, Nanoparticle Surface Functionalization: How to Improve Biocompatibility and Cellular Internalization. *Frontiers in Molecular Biosciences* **7**, 587012 (2020).

[53]A. Angelopoulou, A. Kolokithas-Ntoukas, C. Fytas, and K. Avgoustakis, Folic Acid-Functionalized, Condensed Magnetic Nanoparticles for Targeted Delivery of Doxorubicin to Tumor Cancer Cells Overexpressing the Folate Receptor. *ACS Omega* **4**, 22214–22227 (2019).

[54]J. P. Marshalek, P. S. Sheeran, P. Ingram, P. A. Dayton, R. S. Witte, and T. O. Matsunaga, Intracellular delivery and ultrasonic activation of folate receptor-targeted phase-change contrast agents in breast cancer cells *in vitro*. *Journal of Controlled Release* **243**, 69–77 (2016).

[55]E. Faghfuri, M. Sagha, and A. H. Faghfouri, The Cytotoxicity Effect of Curcumin Loaded Folic Acid Conjugated-Nanoparticles on Breast Cancer Cells and Its Association with Inhibition of STAT3 Phosphorylation. *Journal of Cluster Science* **33**, 1–8 (2022).

8. Final Remarks and Future Work

The work developed in this thesis falls within three main research lines: (i) development of core-shell magnetic-lipid nanoparticles (NPs) bi-functionalized with an anticancer drug and folic acid (FA); (ii) synthesis and characterization of biocompatible high-aspect-ratio magnetic nanostructures by template-assisted methods; and (iii) assessment of the suitability of those nanomaterials for magneto-stimulated chemotherapy and magneto-mechanical induction of cancer cells death, respectively.

Regarding the first topic, a biocompatible and multi-responsive drug delivery system involving core-shell magnetic-lipid NPs, with different solid lipids (gelucire 43/01: GEL or cetyl palmitate: PAL), bi-functionalized with an anticancer drug, doxorubicin (DOX) and FA was successfully developed. The characterization of those nanomaterials indicated that they possess adequate physicochemical properties for biomedical applications, presenting a suitable hydrodynamic diameter, a narrow size distribution, and a relatively high stability. Moreover, no significant change in those properties was observed after incorporation of superparamagnetic iron oxide nanoparticles (SPIONs) and/or the functionalization process. Nevertheless, it was verified that the co-encapsulation of DOX and SPIONs increased the DOX encapsulation in the NPs. A morphological analysis of the core-shell magnetic-lipid NPs allowed to confirm the presence of the polyethylene glycol-FA (PEG-FA) functionalization on their surface. The morphology of the produced SPIONs was also studied, having been concluded that their size fell within the estimated particle size required to achieve superparamagnetism in magnetite/maghemite NPs. Furthermore, a structural characterization allowed the identification of characteristic peaks of maghemite/magnetite in both SPIONs and magnetic-lipid NPs. Regarding the latter, such analysis also allowed the detection of DOX and PEG-FA conjugate.

Through comparison of the thermal stability, AMF-triggered DOX release, and biocompatibility between GEL-based and PAL-based magnetic-lipid NPs, it was determined that the former were more appropriate for the intended biomedical application. This application involves a dual cancer treatment strategy, wherein anticancer drugs are targetedly delivered to cancer cells in conjunction with magnetic hyperthermia (MHT). Nevertheless, independently of the considered solid lipid, it was confirmed the possibility to control the DOX release by an external AMF stimulus, as a result of the heat-generating properties of SPIONs. Subsequently, the magnetic characterization of the GEL-based NPs and SPIONs confirmed the existence of a superparamagnetic behaviour, at room temperature, for both. Additionally, the SAR of those magnetic-lipid NPs loaded with SPIONs was measured, having been obtained a

value that makes them potential candidates for MHT. The GEL-based NPs also demonstrated pH and thermal sensitivity, leading to an increased release of DOX under greater temperatures and at lower pH conditions. Moreover, they presented a good stability for a period of, at least, 10 weeks, when stored at 4 ºC.

In addition to those NPs, biocompatible high aspect ratio magnetic nanostructures were also synthesized and characterized. Particularly, FePt nanowires (NWs) were produced through two different approaches involving either pulsed or DC electrodeposition into anodic aluminium oxide (AAO) templates. The first strategy allowed the control of the resulting nanoarchitectures composition by adjusting two parameters, namely the thickness of the barrier layer at the bottom of the template and the current density applied during the electroplating process. Nevertheless, it was verified that the length of the NWs possessing Pt in their composition was not homogeneous. The magnetic characterization of the obtained nanostructures indicated an increase of the magnetic hysteresis, remanent magnetization, coercivity, and perpendicular saturation field ($H_{Sat}^{\perp}$) as the Fe at.% got higher. Furthermore, micromagnetic simulations of FePt NW arrays with various stoichiometries suggested that the nanostructures produced at lower current densities may possess a varying stoichiometry along their length.

Besides the non-uniform length and stoichiometry of these nanoarchitectures, they also present dendritic structures at one end, which alter their properties and are undesirable in biomedicine. Consequently, another synthesis approach for FePt NWs was developed, involving direct current (DC) electrodeposition, in either static or pulsed mode, into AAO templates obtained through hard anodization. In this context, it was analysed the effect of different parameters on the composition of the resulting nanostructures, such as electrodeposition potential (V_{dep}), concentrations of precursors in the electrolyte, deposition pulse (t_{on}), rest pulse (t_{off}), t_{on}/t_{off} ratio, and prior Au electrodeposition. As a result, it was verified that the composition of the produced FePt NWs was controlled by the t_{on}/t_{off} ratio considered in the pulsed mode, while the static approach did not lead to any significant modification of their stoichiometry. In comparison to the pulsed strategy, it was possible to obtain NWs with a more uniform length when Pt was deposited through the DC approach. Moreover, regarding their magnetic characterization, a similar result was obtained, where it was observed higher magnetic hysteresis, remanent magnetization, coercivity, and $H_{Sat}^{\perp}$ values as the Fe at.% in the nanostructures increased. Moreover, the morphology and composition of individual FePt NWs, obtained by dissolving the hard anodization AAO template after the pulsed DC electrodeposition process, revealed that both their diameter and composition vary along

their longitudinal axis. Particularly, it was noticed that those nanostructures become narrower and their Fe content increases as they get longer. Nevertheless, it is possible to obtain nanostructures with suitable dimensions for biomedical applications that present a relatively homogeneous length, diameter, and composition.

Apart from the FePt NWs, Au/Fe/Au nanodiscs (NDs) with a spin-vortex ground state were also produced through a different approach, based on thermal evaporation into templates pre-patterned by laser interference lithography. Then, it was performed a morphological and structural characterization of these nanostructures and, to confirm the presence of the spin-vortex ground state, a detailed magnetic characterization involving various techniques was detailed. Moreover, micromagnetic simulations were performed to better understand and support the obtained experimental results, also validating the formation of a spin-vortex state in the synthesized NDs.

Then, the potential of the produced core-shell magnetic-lipid NPs and high aspect ratio nanostructures for chemo-MHT and magneto-mechanical induction of cancer cell death, respectively, was evaluated. Regarding the first biomedical application, the composition and concentration of the nano-formulations composed of magnetic-lipid NPs were first optimized for this specific use-case. This was performed by carrying out biocompatibility and morphological studies using the MCF-7 breast cancer cell line. Subsequently, MHT assays were conducted using these nanoparticles, having been verified an increase of the cell death due to the synergistic effect between the DOX chemotherapeutic effect and the heating promoted by the external magnetic field.

The suitability of the produced high aspect ratio magnetic nanoarchitectures for a different biomedical application, i.e. magneto-mechanical induction of cancer cell death, was also assessed. When considering FePt NWs, biocompatibility studies indicated that these nanomaterials were harmless to cancer cells when not exposed to an external AMF. Additionally, uptake assays indicated that these biological entities were able to internalize the FePt NWs. Subsequent magneto-mechanical cell death assays demonstrated a concentration-dependent reduction in cell viability, with increasing cell death observed as the concentration of nanostructures increased. Additionally, it was observed that reducing the frequency of the applied AMF had a negligible impact on the number of viable cells following an exposure to the AMF.

The potential of the produced Au/Fe/Au NDs for this same biomedical application was analysed as well. Nevertheless, in contrast to the previous case, their recognition by cells of the mononuclear phagocyte system (MPS) either with no functionalization or functionalized with PEG-SH was first evaluated. The confirmation of the presence of the

PEG-SH on the surface of the nanoarchitectures was obtained through Raman spectroscopy and X-ray photoelectron spectroscopy (XPS) analyses. Then, cell assays with non-functionalized and functionalized NDs indicated that both types of nanostructures are biocompatible. Furthermore, it was observed that the PEG-SH functionalization led to a reduction of the NDs uptake of the NDs by the MPS' cells. After this study, the potential of these nanoarchitectures for the magneto-mechanical induction of cancer cell death was assessed, using non-functionalized, PEG-SH functionalized, as well as FA-PEG-SH-functionalized NDs. The biocompatibility assays, conducted absence of an external AMF, revealed an adequate biocompatibility for all the considered nanostructures. Uptake assays were also performed under the same conditions, having been concluded that the functionalized NDs were internalized to a greater extent by cancer cells compared to the non-functionalized ones. Afterwards, cells incubated with different concentrations of non-functionalized and functionalized were exposed to AMFs with distinct parameters. As a result, it was concluded that reducing the magnetic field frequency did not significantly affect the cytotoxic ability of these NDs, whereas increasing the strength of the field led to higher cell death. Additionally, it was observed that functionalized nanostructures, particularly those involving FA-PEG-SH, could induce greater cell death.

In this thesis, various multifunctional nanoplatforms for the development of novel cancer therapy strategies were successfully produced and characterized in detail. These can constitute the basis for new research in various topics, such as:

- Optimization of new formulations of NLCs with different anticancer drugs or a combination of drugs;
- Optimization of the NLCs so as to prevent anticancer drug release at lower temperatures (< 40 ºC);
- Optimization of the AMF parameters for inducing the cancer cell death using the formulations studied in this work;
- Improvement of the MHT setup for better analysing the *in vitro* induction of cell death using the produced NLC formulations;
- *In vivo* chemo-MHT assays using the studied NLC formulations;
- Development of new NLC formulations, involving the fabricated high aspect ratio magnetic nanostructures together with anticancer drugs and functionalized with targeting agents, for a treatment approach involving magneto-mechanical actuation combined with anticancer drug release at the target site;

- *In vivo* magneto-mechanical assays for the induction of cancer cell death using the produced high aspect ratio nanostructures;
- Development of a more versatile setup for in vitro magneto-mechanical cell death assays;
- Synthesis and characterization of magnetic nanostructures with other shape and/or composition for inducing the cell death through magneto-mechanical actuation;
- Further optimization of the FePt NWs electrodeposition conditions;
- Study of the properties of Au/Fe/Au NDs as a function of their dimensions.